frontiers | Research Topics

Nonlinear analysis and machine learning in cardiology

Edited by
Elena Tolkacheva, Xiaopeng Zhao and Hans Dierckx

Published in
Frontiers in Physiology

ISSN 1664-8714
ISBN 978-2-8325-2293-6
DOI 10.3389/978-2-8325-2293-6

About Frontiers

Frontiers is more than just an open access publisher of scholarly articles: it is a pioneering approach to the world of academia, radically improving the way scholarly research is managed. The grand vision of Frontiers is a world where all people have an equal opportunity to seek, share and generate knowledge. Frontiers provides immediate and permanent online open access to all its publications, but this alone is not enough to realize our grand goals.

Frontiers journal series

The Frontiers journal series is a multi-tier and interdisciplinary set of open-access, online journals, promising a paradigm shift from the current review, selection and dissemination processes in academic publishing. All Frontiers journals are driven by researchers for researchers; therefore, they constitute a service to the scholarly community. At the same time, the *Frontiers journal series* operates on a revolutionary invention, the tiered publishing system, initially addressing specific communities of scholars, and gradually climbing up to broader public understanding, thus serving the interests of the lay society, too.

Dedication to quality

Each Frontiers article is a landmark of the highest quality, thanks to genuinely collaborative interactions between authors and review editors, who include some of the world's best academicians. Research must be certified by peers before entering a stream of knowledge that may eventually reach the public - and shape society; therefore, Frontiers only applies the most rigorous and unbiased reviews. Frontiers revolutionizes research publishing by freely delivering the most outstanding research, evaluated with no bias from both the academic and social point of view. By applying the most advanced information technologies, Frontiers is catapulting scholarly publishing into a new generation.

What are Frontiers Research Topics?

Frontiers Research Topics are very popular trademarks of the *Frontiers journals series*: they are collections of at least ten articles, all centered on a particular subject. With their unique mix of varied contributions from Original Research to Review Articles, Frontiers Research Topics unify the most influential researchers, the latest key findings and historical advances in a hot research area.

Find out more on how to host your own Frontiers Research Topic or contribute to one as an author by contacting the Frontiers editorial office: frontiersin.org/about/contact

Nonlinear analysis and machine learning in cardiology

Topic editors

Elena Tolkacheva — University of Minnesota Twin Cities, United States
Xiaopeng Zhao — The University of Tennessee, Knoxville, United States
Hans Dierckx — KU Leuven Kulak, Belgium

Citation

Tolkacheva, E., Zhao, X., Dierckx, H., eds. (2023). *Nonlinear analysis and machine learning in cardiology*. Lausanne: Frontiers Media SA.
doi: 10.3389/978-2-8325-2293-6

Table of contents

frontiers | Frontiers in Physiology

TYPE Editorial
PUBLISHED 14 April 2023
DOI 10.3389/fphys.2023.1183149

OPEN ACCESS

EDITED AND REVIEWED BY:
Ruben Coronel,
University of Amsterdam, Netherlands

*CORRESPONDENCE
Hans Dierckx,
h.dierckx@kuleuven.be

SPECIALTY SECTION
This article was submitted to Cardiac Electrophysiology, a section of the journal Frontiers in Physiology

RECEIVED 09 March 2023
ACCEPTED 16 March 2023
PUBLISHED 14 April 2023

CITATION
Dierckx H, Zhao X and Tolkacheva EG (2023), Editorial: Non-linear analysis and machine learning in cardiology. *Front. Physiol.* 14:1183149. doi: 10.3389/fphys.2023.1183149

Editorial: Non-linear analysis and machine learning in cardiology

Hans Dierckx[1,2]*, Xiaopeng Zhao[3] and Elena G. Tolkacheva[4,5,6]

[1]Department of Mathematics, KU Leuven Campus Kortrijk (KULAK), Kortrijk, Belgium, [2]iSi Health - KU Leuven Institute of Physics-based Modeling for in silico Health, Leuven, Belgium, [3]Department of Mechanical, Aerospace and Biomedical Engineering, University of Tennessee, Knoxville, TN, United States, [4]Biomedical Engineering Department, University of Minnesota, Minneapolis, MN, United States, [5]Institute for Engineering in Medicine, University of Minnesota, Minneapolis, MN, United States, [6]Lillehei Heart Institute, University of Minnesota, Minneapolis, MN, United States

KEYWORDS

cardiology (basic/technical), machine learning, ML, data analysis, non-linear analysis methodologies, multiscale modeling and analysis

Editorial on the Research Topic
Non-linear analysis and machine learning in cardiology

Cardiovascular diseases remain a major cause of death accounting for about 30% of death worldwide according to the World Health Organization. Over the past decades, various interdisciplinary approaches have been developed *via* close collaboration between clinicians, engineers and basic scientists to reveal fundamental mechanisms and develop approaches to perform analysis of cardiac abnormalities. The analysis can be performed on different available measurements in patients, which can be electrical (*via* electrode recordings), mechanical (*via* imaging), hemodynamic, or even entail overall patient data. As the heart is a complex dynamical system, the simple linear approaches are not always successful, and advances in non-linear signal processing and machine learning (ML) guided analysis techniques could lead to a better understanding, diagnosis and treatment of cardiac diseases.

In addition to traditional methods of ECG analysis based on filtering, spectral analysis and statistical approaches, various non-linear dynamic modeling and ML approaches have been recently developed to perform quantitative analysis of electrical signals from the heart. The contributions to this Research Topic are covering recent advances and novel research trends in such approaches, aiming to discriminate between normal and abnormal cardiac rhythms, to offer insights into fundamental processes, or even predict the future evolution of a cardiac cell from time series.

The fundamental biophysical level is key to understand the collective behaviour of myocytes during arrhythmias. (Béland et al.) improved the analysis of videomicroscopy of cultured myocytes, by assessing not only the rate of activity but also the contractile properties of the beating cells. Such approach is motivated by the use of cell cultures to high-throughput screening of cardiotoxicity in drug development. (Nowak et al.) performed numerical simulations to investigate the effect of ephaptic coupling on conduction velocity in the tissue, and reported a non-linear, biphasic dependency on cell size. They concluded that developmental changes predict changes in cardiac conduction. Interesting results of multiscale modeling were presented by (Shahi et al.), who demonstrated that ML offers a way to construct predictive models for local electrical activity, when cardiac action potentials are predicted either using recurrent neural networks or reservoir computing.

At the tissue level, an important characteristic in cardiac excitation patterns is the activation time. (Ramlugun et al.) presented a comprehensive framework to extract the activation time from optical mapping signals, accounting for the repetitive activation during complex arrhythmia. An alternative representation of activation times is phase mapping, which is a well-established technique to determine the location of phase singularities during recordings of chaotic regimes such as ventricular fibrillation. However, in a clinical context, the phase maps are often noisy or sparse. To enable phase singularity identification in these cases, (Lebert et al.) proposed a self-supervised deep-learning approach that immediately recovers the phase maps from short spatio-temporal sequences of electrical data. Meanwhile, (Arno et al.) assessed shortcomings of traditional phase analysis, integrated the concepts of linear rotor cores and conduction block lines into a structure called "phase defect lines", and showed their presence in optical mapping recordings.

Moving one step further towards clinical applications, two contributions focused on image analysis. (Wu et al.) adopted a deep neural network approach to find objects of interest in medical images without the need for predefined thresholds, and applied it to cardiac images in movie data. (Yang et al.) described a novel way to extract the characteristics of vortex flows in the right atrium, from phase-contrast MRI images.

Non-linear analysis can also be used to support or guide specific therapy. For instance, (Ravikumar et al.) developed a similarity score from analysis of clinical intracardiac electrograms to identify active sites of atrial arrhythmias for potential guiding for ablation therapy. (Khamzin et al.) presented a predictive model for the outcome of cardiac resynchronization therapy. They found that including computational modeling results increased the quality of predictions compared to a pure ML approach from clinical data only.

Finally, two papers in this Research Topic described advances in improving the analysis of ECG signals. (Zheng et al.) developed a ML approach to recover the location of arrhythmia triggers based on the 12-lead ECG. Their method can help to plan ablation procedures for triggers near the right or left-ventricular outflow tracts. (Shinoda et al.) utilized Poincaré mapping and recurrence quantification analysis to characterize stochasticity vs. chaotic dynamics in the heart, to distinguish between naturally varying ECG characteristics and a pathological condition. Their method is then applied to a Parkinson's disease animal model.

Non-linear signal processing and ML guided analysis techniques have played a key role in better understanding, diagnosing, and treating cardiovascular diseases. The contributions to this Research Topic cover recent advances and novel research trends in such approaches, with a focus on discriminating between normal and abnormal cardiac rhythms, offering insights into fundamental processes, or even predicting the future evolution of a cardiac cell from time series. These advances span from analyzing individual myocytes to improving the analysis of ECG signals, to extracting the characteristics of vortex flows in the right atrium from phase-contrast MRI images.

The studies presented in this Research Topic demonstrate the utility of ML approaches in clinical applications for decision support and improving patient outcomes. In the future, the proposed frameworks need to be adjusted to address various disease monitoring and subsequent disease prediction. Further development of various signal processing and data analysis techniques based on different non-linear and ML approaches are also warranted for multiple wearable sensors.

Author contributions

All authors listed have made a substantial, direct, and intellectual contribution to the work and approved it for publication.

Conflict of interest

The authors declare that the research was conducted in the absence of any commercial or financial relationships that could be construed as a potential conflict of interest.

Publisher's note

frontiers in Physiology

ORIGINAL RESEARCH
published: 25 February 2021
doi: 10.3389/fphys.2021.641066

A High-Precision Machine Learning Algorithm to Classify Left and Right Outflow Tract Ventricular Tachycardia

Jianwei Zheng[1†], Guohua Fu[2†], Islam Abudayyeh[3], Magdi Yacoub[4], Anthony Chang[5], William W. Feaster[5], Louis Ehwerhemuepha[5], Hesham El-Askary[1,6], Xianfeng Du[2], Bin He[2], Mingjun Feng[2], Yibo Yu[2], Binhao Wang[2], Jing Liu[2], Hai Yao[7], Huimin Chu[2] and Cyril Rakovski[1]*

[1] Computational and Data Science, Chapman University, Orange, CA, United States, [2] Department of Cardiology, Ningbo First Hospital of Zhejiang University, Hangzhou, China, [3] Department of Cardiology, Loma Linda University, Loma Linda, CA, United States, [4] Harefield Heart Science Center, Imperial College London, London, United Kingdom, [5] CHOC Children's Hospital, Orange, CA, United States, [6] Department of Environmental Sciences, Faculty of Science, Alexandria University, Alexandria, Egypt, [7] Zhejiang Cachet Jetboom Medical Devices Co., Ltd., Hangzhou, China

OPEN ACCESS

Edited by:
Xiaopeng Zhao,
The University of Tennessee, Knoxville, United States

Reviewed by:
Peter Van Dam,
Radboud University Nijmegen, Netherlands
Marianna Meo,
Institut de Rythmologie et Modélisation Cardiaque (IHU-Liryc), France

***Correspondence:**
Huimin Chu
mark.chuhuimin@gmail.com

[†] These authors have contributed equally to this work

Specialty section:
This article was submitted to Cardiac Electrophysiology, a section of the journal Frontiers in Physiology

Received: 13 December 2020
Accepted: 18 January 2021
Published: 25 February 2021

Citation:
Zheng J, Fu G, Abudayyeh I, Yacoub M, Chang A, Feaster WW, Ehwerhemuepha L, El-Askary H, Du X, He B, Feng M, Yu Y, Wang B, Liu J, Yao H, Chu H and Rakovski C (2021) A High-Precision Machine Learning Algorithm to Classify Left and Right Outflow Tract Ventricular Tachycardia. Front. Physiol. 12:641066. doi: 10.3389/fphys.2021.641066

Introduction: Multiple algorithms based on 12-lead ECG measurements have been proposed to identify the right ventricular outflow tract (RVOT) and left ventricular outflow tract (LVOT) locations from which ventricular tachycardia (VT) and frequent premature ventricular complex (PVC) originate. However, a clinical-grade machine learning algorithm that automatically analyzes characteristics of 12-lead ECGs and predicts RVOT or LVOT origins of VT and PVC is not currently available. The effective ablation sites of RVOT and LVOT, confirmed by a successful ablation procedure, provide evidence to create RVOT and LVOT labels for the machine learning model.

Methods: We randomly sampled training, validation, and testing data sets from 420 patients who underwent successful catheter ablation (CA) to treat VT or PVC, containing 340 (81%), 38 (9%), and 42 (10%) patients, respectively. We iteratively trained a machine learning algorithm supplied with 1,600,800 features extracted *via* our proprietary algorithm from 12-lead ECGs of the patients in the training cohort. The area under the curve (AUC) of the receiver operating characteristic curve was calculated from the internal validation data set to choose an optimal discretization cutoff threshold.

Results: The proposed approach attained the following performance: accuracy (ACC) of 97.62 (87.44–99.99), weighted F1-score of 98.46 (90–100), AUC of 98.99 (96.89–100), sensitivity (SE) of 96.97 (82.54–99.89), and specificity (SP) of 100 (62.97–100).

Conclusions: The proposed multistage diagnostic scheme attained clinical-grade precision of prediction for LVOT and RVOT locations of VT origin with fewer applicability restrictions than prior studies.

Keywords: outflow tract ventricular tachycardia, catheter ablation, electrocardiography, classification, artificial intelligence algorithm

INTRODUCTION

One population-based study (Dukes et al., 2015) of 1,139 older adults without any heart-failure signs or systolic dysfunction shows that premature ventricular complexes (PVC) and ventricular tachycardia (VT) burden are significantly associated with an increased risk of adjusted decreased left ventricular ejection fraction (odds ratio, 1.13) and increased adjusted risk of incident heart failure (hazard ratio, 1.06) and death (hazard ratio, 1.04). Catheter ablation (CA) is a commonly considered treatment of VT patients with and without structural heart disease when drugs are ineffective or have unacceptable side effects (Cronin et al., 2019). It has a class I indication for treatment of idiopathic outflow tract ventricular tachycardia (OTVT) (Joshi and Wilber, 2005; Latchamsetty et al., 2015). The OTVT stems from the right ventricular outflow tract (RVOT) in 60–80% of the cases and from the left ventricular outflow tract (LVOT) (Bunch and Day, 2006) in the rest of the cases. An accurate prediction of RVOT and LVOT origins of OTVT can optimize the CA strategy, reduce ablation duration, and avoid operative complications. Previous studies (Kamakura et al., 1998; Hachiya et al., 2000; Ito et al., 2003; Joshi and Wilber, 2005; Tanner et al., 2005; Haqqani et al., 2009; Zhang et al., 2009; Betensky et al., 2011; Yoshida et al., 2011, 2014; Cheng et al., 2013, 2018; Nakano et al., 2014; Efimova et al., 2015; He et al., 2018; Xie et al., 2018; Di et al., 2019; Enriquez et al., 2019; Yamada, 2019) propose several criteria or models to estimate RVOT and LVOT origins. However, these results have been limited by sample size, scope of studies, ECG measurement efficiency, and generalizability of the models. In contrast, we develop an optimal multistage scheme that automatically extracts features from standard 12-lead ECGs and incorporates these features into a machine learning model to predict RVOT and LVOT origins of VT or PVC with clinical-grade precision and provides multiprospective analysis for the most important ECG features.

MATERIALS AND METHODS

Study Design

The institutional review board of Ningbo First Hospital of Zhejiang University has approved this retrospective study and granted a waiver of the requirement to obtain informed consent. The study was conducted in accordance with the Declaration of Helsinki.

From each patient's entire ECG recorder, three cardiac electrophysiologists (EPs) unanimously selected one QRS complex during the sinus rhythm (SR) and one QRS complex during the PVC or VT as the initial input. The features extracted from the two QRS complexes are supplied to an optimal machine learning classification model that provides two possible prediction outputs: RVOT or LVOT. For the purposes of the classification scheme, RVOT is considered a positive outcome and LVOT a negative one. This study employed a training–validation–testing design to correctly assess the performance of the algorithm. This study consists of four phases (shown in **Figure 1**): (Dukes et al., 2015) a feature extraction phase in which two feature extraction methods are studied and compared—our proprietary automated ECG feature extraction method and a method based on conventional QRS morphological ECG measurements (Cronin et al., 2019) a training phase in which the extreme gradient boosting tree classification model is supplied by the features generated in the feature extraction phase (Joshi and Wilber, 2005) a validation phase aimed at finding important features as optimal model input and deciding the optimal discretization cutoff threshold that was applied in the testing phase; and (Latchamsetty et al., 2015) a testing phase aimed at evaluating, interpreting, and reporting the model performance.

Patient Selection

We reviewed patients who underwent mapping and ablation for frequent PVC or VT that originated from either LVOT or RVOT at the Ningbo First Hospital of Zhejiang University from March 2007 to September 2019. A PVC or VT burden above 10% of total test duration was required for a study entry. A total of 420 patients with OTVT were included in this study. Origin sites of OTVT were confirmed by a successful CA, which means the frequent PVC and VT did not occur above 5% of the total test duration in the first 6-month follow-up after CA.

Classification of Anatomic Sites

The anatomical structure of RVOT and LVOT is depicted in **Figure 2**, and the demographic data of the anatomic sites are shown in **Supplementary Section A** and **Table 1**. This study only focuses on the prediction of RVOT and LVOT rather than the subsites (shown in **Figure 2**) under RVOT and LVOT. The effective ablation sites of RVOT and LVOT confirmed by ablation provide evidence to create RVOT and LVOT labels for the subsequent machine learning model development.

Mapping and Ablation Procedure

Anti-arrhythmic drugs were stopped for at least five half-lives before the inception of the ablation procedure. A 4.0-mm 7F irrigated ablation catheter (Navistar; Biosense Webster, Diamond Bar, CA, United States) was initially placed in the RVOT for mapping. Both fluoroscopy and electroanatomic mapping systems (CARTO, Biosense Webster, Diamond Bar, CA, United States or NavX Velocity, St. Jude Medical, St. Paul, MN, United States) were used to localize the anatomic position of the ablation catheter within the outflow tract. The intracardiac echo was used to identify specific anatomical structures, such as cusps and papillary muscles. For example, **Figure 3** presents the fluoroscopy, 3-D mapping, intracardiac echocardiography, and activation mapping for a case with the origin site in commissure of aortic sinus of valsalva LVOT. Using point-by-point mapping, anatomic aggregated maps were created. Activation mapping was performed in all patients during VT and PVC. Pace mapping was also performed with the lowest pacing output (2–20 mA) and pulse width (0.5–10 ms) to capture the ventricular myocardium at the site of the earliest activation. If suitable ablation sites for the RVOT were not located or ablation failed to abolish the arrhythmia, extended mapping to the LVOT site was deployed *via* a retrograde aortic approach. After target sites were located, radiofrequency energy was delivered up to a maximum power

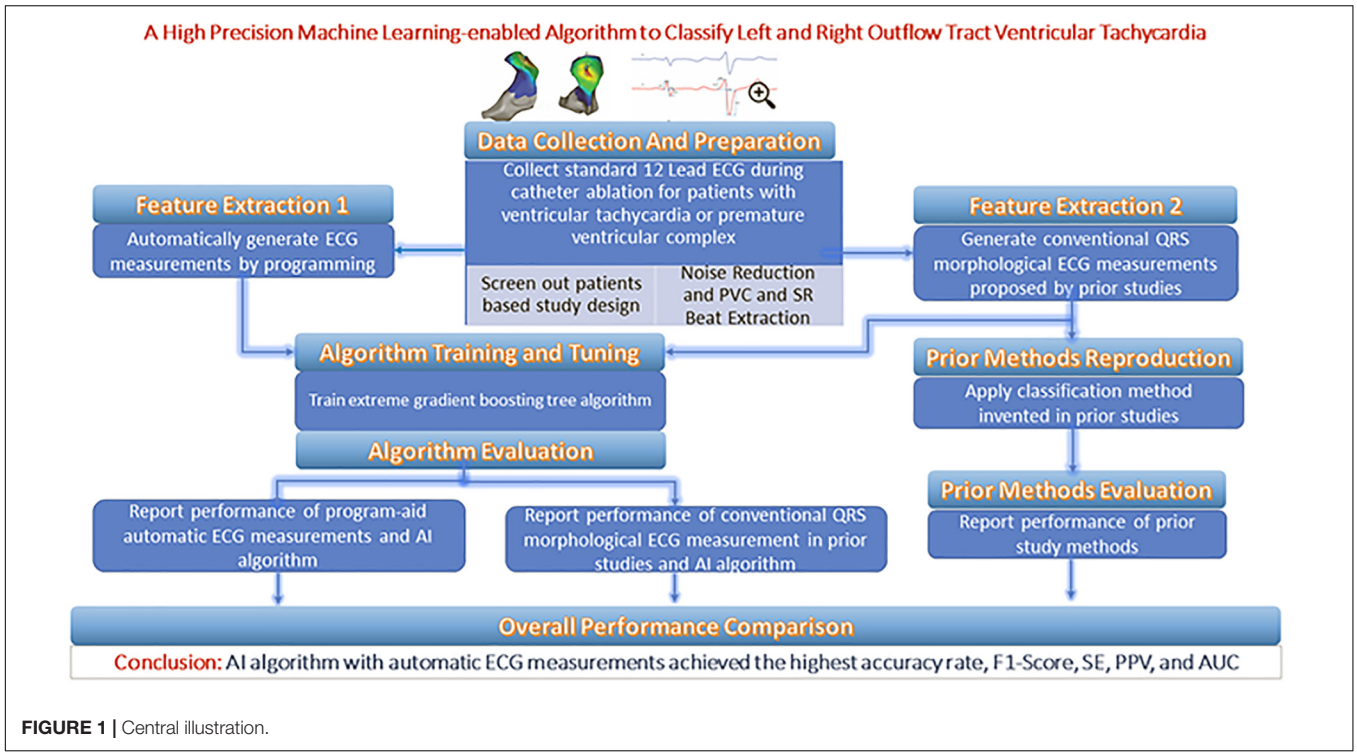

FIGURE 1 | Central illustration.

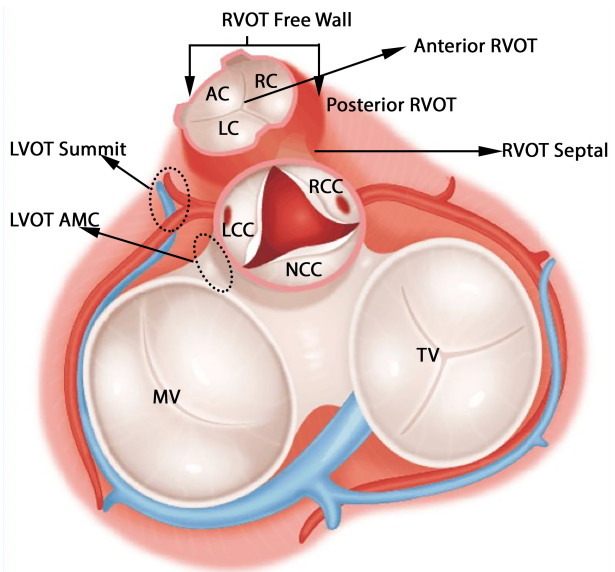

FIGURE 2 | Anatomic structure of LVOT and RVOT. LVOT includes left coronary cusp (LCC), right coronary cusp (RCC), non-coronary cusp (NCC), aortomitral continuity (AMC), and LVOT summit. RVOT includes anterior cusp (AC), left cusp (LC), right cusp (RC), RVOT freewall, and RVOT septal.

of 35 W and a maximum electrode-tissue interface temperature of 43°C. If the VT or PVC disappeared or the frequency of arrhythmias diminished after the first 30 s of ablation, the energy was delivered continuously from 60 to 180 s. Ablation success was defined as the absence of spontaneous or induced VT or PVC at 30 min after the last energy delivery and confirmed by continuous cardiac telemetry in the subsequent 24 h of inpatient care.

The Procedure to Assess the Catheter Ablation Outcomes

In the subsequent 24 h of inpatient care after the ablation procedure, every patient received continuous ECG monitoring. After discharge, the patients underwent a follow-up 2 weeks after the ablation and then every month at the cardiology clinic. A 12-lead surface ECG test was obtained on each clinic visit, and 24-h Holter monitoring was also prescribed at 3 and 6 months after the ablation.

ECG Measurement Protocol

Noise Reduction and QRS Sample Selection

With chest and limb leads placed carefully in a standard position, the 12-lead surface ECGs were collected by the EP workmate system (EP-WorkMate^{TM} System, Abbott, Saint Paul, MI, United States) at a sampling rate of 2,000 Hz before the ablation procedure. The noise sources impacting the ECG database were power line interference, baseline wandering, and random noise. Wavelet transform yields better time–frequency localization results than windowed Fourier transform and naturally has an advantage in noise reduction applications (Abi-Abdallah et al., 2006). Thus, the wavelets technique was used to remove the noise components mentioned above. The coif5 Wavelets (Lahmiri, 2014) and Stein's Unbiased Risk Estimator (SURE)-based (Stein, 1981; David and Johnstone, 1995) threshold were implemented by MATLAB to carry out

TABLE 1 | Summary statistics of demographic data and clinical characteristics of all patients.

	Training cohort			Validation cohort			Testing cohort		
	RVOT	**LVOT**	***P*-value**	**RVOT**	**LVOT**	***P*-Value**	**RVOT**	**LVOT**	***P*-Value**
Patients, *n* (%)	263 (77)	77 (23)	0.921	30 (79)	8 (21)	0.991	33 (79)	9 (21)	<0.01
Age, year, mean ± sd	46.5 ± 10.6	47.5 ± 11.3	0.731	45.1 ± 13.8	46.9 ± 9.2	0.74	43.8 ± 15.0	45.3 ± 17.1	0.652
Male, *n* (%)	80 (66)	41 (34)	<0.01	6 (46)	7 (54)	<0.01	7 (58)	5 (42)	<0.01
BMI (kg/m^2), mean ± sd	28.33 ± 3.24	29.28 ± 2.19	<0.01	30.11 ± 3.17	28.37 ± 4.53	<0.01	27.62 ± 4.15	28.37 ± 4.72	<0.01
PVC, n/24 h mean ± sd	, 28,455.5 ± 9,635.8	29,358.5 ± 12,117.4	0.651	30,356.5 ± 18,587.8	276,565 ± 10,997.8	0.531	23,218.5 ± 11,755.6	33,035.6 ± 18,256.3	0.0273
Frequent PVC, *n* (%)	249 (78)	70 (22)	0.683	22 (76)	7 (24)	0.818	28 (85)	4 (44.5)	0.046
Paroxysm VT, *n* (%)	14 (78)	4 (22)	1	1	0	1	2 (6)	4 (44.5)	0.023
Sustained VT, *n* (%)	6 (67)	3 (34)	0.425	1	1	0.398	3 (9)	1 (11)	1
VT cycle length (ms), mean ± sd	410 ± 57	424 ± 102	0.431	426 ± 74	430 ± 88	0.621	438 ± 93	402 ± 147	0.886
Pre-QRS activation time (ms), mean ± sd	29.38 ± 10.26	31.27 ± 8.25	0.334	33.40 ± 5.51	31.65 ± 8.76	0.63	28.64 ± 9.69	33.48 ± 8.46	0.5
Prior CA, n	2	1	0.533	0	0	1	2	0	1
Myocardiopathy,*n*	1	2	0.127	1	0	1	1	1	0.398
Alcoholic cardiomyopathy, *n*	1	0	1	0	0	1	0	0	1
ICD (VT), *n*	1	0	1	0	0	1	1	0	1
Coronary heart disease, *n*	3	1	1	1	0	1	1	1	0.398

P-values present the probabilities of equal means or proportions of each tested variable. LVOT, left ventricular outflow tract; RVOT, right ventricular outflow tract; BMI, body mass index; LVEF, left ventricular ejection fraction; PVC, premature ventricular complex; VT, ventricular tachycardia; CA, catheter ablation.

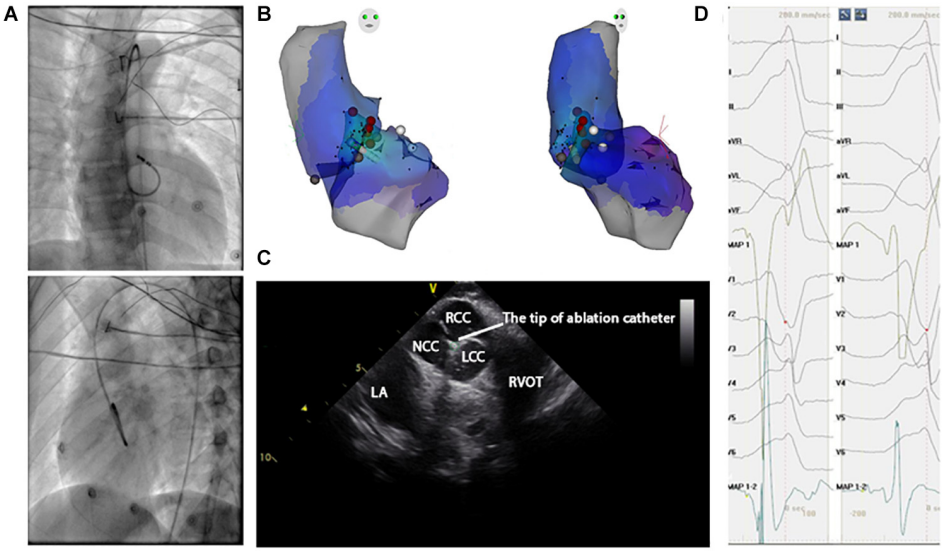

FIGURE 3 | Activation map and fluoroscopic map for VA originating from commissure of aortic sinus of valsalva in LVOT. **(A)** Right and left anterior oblique fluoroscopic views show an ablation catheter in the LVOT. Ablation in the LVOT (LCC–RCC commissure) eliminated the PVC within 3 s. **(B)** The 3-D anatomic representation of the RV endocardium, LV endocardium, and venous system with the ablation catheter positioned at the anterior interventricular vein. **(C)** The green circle indicates the tip of the ablation catheter in LCC–RCC commisure. **(D)** The earliest bipolar and unipolar activation time (–30 ms) are shown.

the noise reduction steps. To get a full understanding of the techniques and schemes that were adopted in this work, please refer to the code availability section. After noise components were removed, three cardiac EPs unanimously selected one QRS complex during the SR and one QRS complex during the PVC or VT to classify RVOT and LVOT.

Automated ECG Feature Extraction Method

We applied the following measurements and transformation protocol to automatically extract ECG morphological features and supply them to the machine learning model. We used the R-wave peak points of PVC and SR heartbeat in lead V_6 as reference lines because they are easy to identify in most conditions. At the first step, for one SR heartbeat, 215 data points (0.11 s) before and after the reference line were truncated, and 335 data points (0.17 s) before and after the reference line were cut for one PVC. The above lengths of 430 and 670 were the means of QRS complex duration plus four times the standard deviation of that for SR beat and PVC. They should cover 99.99% of the QRS complexes in any data due to the normality of the QRS duration distribution and the empirical rule. The mean and standard deviation of QRS duration were computed from the samples in this study; the maximum length of QRS complex for SR beat is 405 data points, and the maximum for PVC is 607 data points. Second, for every lead, we selected the first peak/valley (local maximum or minimum) closest to the reference line (shown in **Figure 4A**) defined in the first step. Third, the three peaks or valleys before the first peak/valley identified in the second step and the four peaks or valleys after the first peak/valley were selected from all peaks and valleys of SR heartbeat and PVC separately. Thus, in every lead, eight peaks and valleys were extracted to represent the SR heartbeat and PVC basic features. The zero-padding method was applied for the cases that did not have eight peaks and valleys around the reference line. The total number of peaks and valleys, eight, is equal to the means of the number of peaks and valleys in all leads plus four times the standard deviation of that for SR beat and PVC, respectively. This automated feature extraction method was verified manually to make sure it captured essential QRS morphological characteristics.

The numerical measurements (shown in **Figure 4B**) of each peak and valley include location, prominence, the distance from peak or valley location to left prominence boundary, the distance from peak or valley location to right prominence boundary, width at half of the prominence, the distance from left prominence boundary to right prominence boundary, amplitude, contour height, and a logic variable to present peak or trough. The prominence of a peak or a valley measures how much the peak or valley stood out due to its intrinsic height and location relative to neighbor peaks or valleys. Thus, the prominence of a peak was defined as the vertical distance between the peak point and its lowest contour line. The measurement of valleys adopted the same method with peaks.

After the above eight numerical measurements of eight peaks or valleys for both SR beat and PVC at every lead were collected, we generated a feature matrix with the size of 192 (2 beats $\times$ 12 leads $\times$ 8 peaks or valleys) by 8 (the number of numerical measurements). We transformed the feature matrix using ratios of features in the rows and columns of the matrix to create a new level of features that can reveal vital details of the ECG morphology. Finally, 1,600,800 features were automatically obtained, and their definitions can be found in **Supplementary Section B.2**. The estimated 95% CI of each

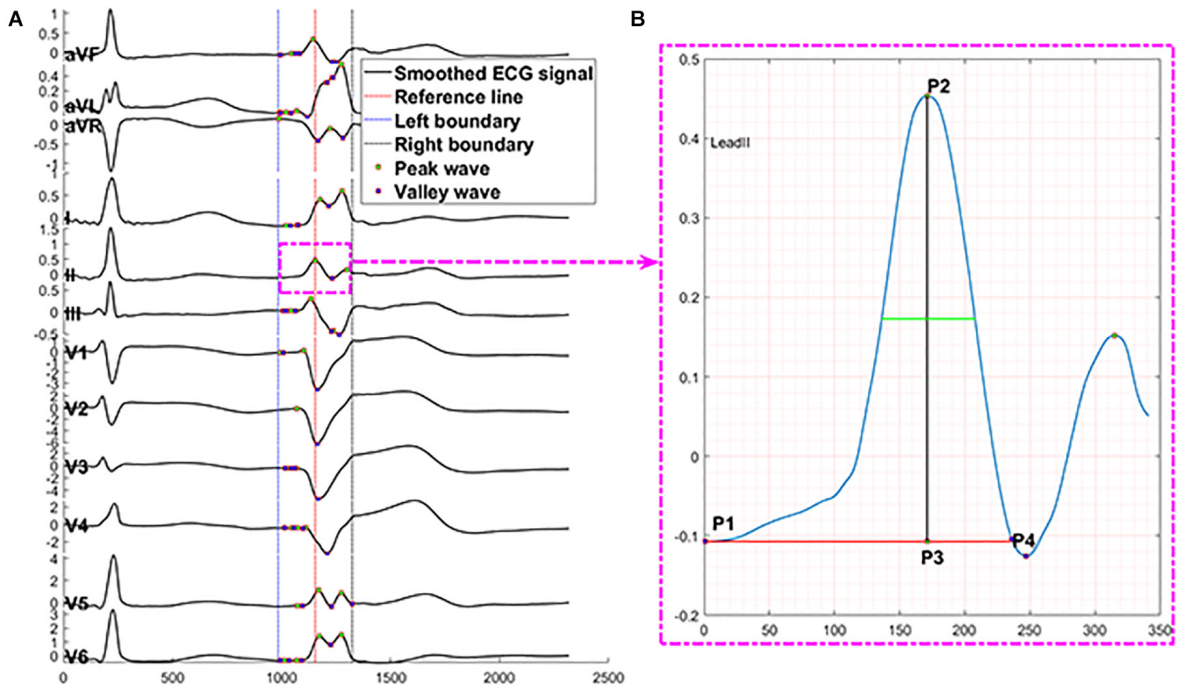

FIGURE 4 | Description of automated ECG feature extraction method. The proposed feature extraction method automatically finds peaks presented by P# and valleys presented by V# in panel **(A)** through 430 data points of one SR beat in 12 leads. Panel **(B)** presents the numerical measurements that capture essential information of a peak, including location = sample points at P3, prominence = distance from P2 to P3, distance from peak or valley location to left prominence boundary = distance from P1 to P3, distance from peak or valley location to right prominence boundary = distance from P3 to P4, width at half of the prominence = the length of green line, distance from left prominence boundary to right prominence boundary = distance from P1 to P4, amplitude = distance from P2 to zero baseline, contour height = prominence – amplitude. *X*-axis presents sampling data points, and *Y*-axis presents voltage.

numerical measurement in the feature matrix is documented in **Supplementary Section B.2** and **Supplementary Table 5**.

Conventional QRS Morphological Feature Extraction

Even though we intended to develop an automated ECG measurement system that is favored by the machine learning algorithm, the conventional QRS morphological ECG measurement method, such as metrics of Q-, R-, and S-waves; segments among them; and the ratios among segments, is studied and compared in this work. The conventional QRS morphological ECG measurement protocol is defined below. SR and VT ECG morphology were measured on the same 12-lead ECG by a customized MATLAB program. During the clinical arrhythmia, the following measurements (presented in **Supplementary Section B.3** and **Figure 1**) were obtained from both one SR beat and one PVC: (Dukes et al., 2015) amplitude of Q-, R-, and S-waves (Cronin et al., 2019) duration of Q-, R-, and S-waves as well as QRS complex; and (Joshi and Wilber, 2005) R/S amplitude ratio (Kamakura et al., 1998; Ito et al., 2003), transitional zone (Hachiya et al., 2000; Tanner et al., 2005), V_2 transition ratio (Betensky et al., 2011), transitional zone index (Yoshida et al., 2011; Di et al., 2019), R-wave deflection interval (Cheng et al., 2013), V_2S/V_3R index (Yoshida et al., 2014), R-wave duration index (Ouyang et al., 2002), and R/S amplitude index (Ouyang et al., 2002). The T-P segment was considered one of the isoelectric baselines to measure R- and S-wave amplitudes. The QRS duration was measured from the site of the earliest initial deflection from the isoelectric line to the time of the latest activation. The R-wave length was calculated from the site of the earliest initial deflection from the isoelectric line to the time at which the R-wave intersected the isoelectric line. For all cases, QRS measurements were performed on an isolated PVC representative of the clinical VT before the induction of sustained VT and compared with the SR QRS complex. All measurements above were used to compare our approach against methods from 12 prior studies (Kamakura et al., 1998; Zhang et al., 2009; Betensky et al., 2011; Yoshida et al., 2011, 2014; Cheng et al., 2013, 2018; Nakano et al., 2014; Efimova et al., 2015; He et al., 2018; Xie et al., 2018; Di et al., 2019).

In addition to the above conventional ECG measurements, we developed the following protocol to generate features to supply to the machine learning model. Amplitudes of Q-, R-, and S-waves based on the voltage at the onset of Q-wave, the offset of S-wave, the Q-wave, and the S-wave were also input variables in the machine learning model. To give the same length input to the machine learning model, we set the measures of Q-, R-, and S-waves for these waves' missing cases to zeros, such as QS morphology in the V_1 lead and RS morphology in the V_5 or V_6 lead. As we implemented the automated feature extraction method, we also transformed the measurements mentioned above into new variables and put them into the machine learning model. The total number of features generated by this method

is 155,784, and the entire definition of features can be found in **Supplementary Section B.3**. The 95% CI of each numerical measurement are listed in **Supplementary Section B.3** and **Supplementary Table 7**.

Statistical Analysis

For the continuous variables of age and ECG measurements, we calculated the mean and standard deviation. For all count variables, total sample size, number of males, number of subjects with frequent PVC, sustained VT, and sublocations under RVOT or LVOT, we calculated frequency counts and percentages. One-sample test for proportions, two-sample *t* test, two-sample test for proportions, and Fisher's exact test were adopted to test the difference of the sample numbers, average ages, genders, and the number of frequent PVC or sustained VT between RVOT and LVOT groups. The Cramer Von Mises, Anderson–Darling, and Shapiro–Wilks tests did not reject the data normality hypothesis, and a two-sample *t* test was used to test for equal means of continuous variables between RVOT and LVOT. Statistical optimization of the gradient boosting tree model was done through iterative training using the extreme gradient booster (XGBoost) package. The following performance measures were formally analyzed, including the area under the curve (AUC) of the receiver operating characteristic (ROC) curve, accuracy (ACC), sensitivity (SE), specificity (SP), and F1-score. A two-sided 95% CI summarizes the sample variability in the estimates. The CI for the AUC was estimated using the Sun and Su optimization of the Delong method implemented in the pROC package. In contrast, CIs for F_1-score, SE, and SP were obtained by the bootstrap method with 20,000 replications. All analyses were done by R version 3.5.3.

RESULTS

We analyzed data from 420 patients who underwent CA of OTVT at the Ningbo First Hospital of Zhejiang University from March 2007 to September 2019. After the CA procedure, two (0.5%) patients developed slight ecchymosis. A total of five (1.2%) patients were excluded from this study because of frequent PVC or VT recurrence in the first 6-month follow-up.

Patient demographic and clinical characteristics data for the RVOT and LVOT groups are shown in **Table 1**. We compare the distributions of these background characteristics in the RVOT and LVOT groups and list the associated *p*-values in the table. The RVOT cohort consists of 20.95% left cusp, 17.62% posterior septal, 14.29% anterior septal, 10% anterior cusp, 7.86% free wall, and 7.14% right cusp. The LVOT cohort consists of 10.71% left coronary cusp, 5.71% aortomitral continuity, 2.62% left coronary cusp and right coronary cusp ommisure, 1.67% right coronary cusp, and 1.43% summit (shown in **Supplementary Section A** and **Table 1**).

The patients were assigned to training, validation, and testing cohorts, consisting of 340 (81%), 38 (9%), and 42 (10%) patients, respectively, using random proportional allocation (demographic summary shown in **Table 1**). For a fair comparison, the machine learning model was supplied with different features from two feature extraction methods. The performance was assessed using the same training, validation, and testing cohorts.

We used 1,600,800 automatically generated ECG features as machine learning model input. The proposed approach achieved an ACC of 97.62 (87.44–99.99); F_1-score of 98.46 (90–100); prediction of RVOT origins with SE of 96.97 (82.54–99.89); and SP of 100 (62.97–100) (shown in **Table 2**), respectively; and AUC of 98.99 (96.89–100) (presented in **Figure 5**). Among the 1,600,800 initial automatically generated ECG features, we found a total of 1,352 critically important features with non-zero Shapley additive explanations (SHAP) values (Lundberg and Lee, 2017), showing the importance of their contributions to RVOT and LVOT prediction. The detailed interpretation of SHAP value is introduced in **Supplementary Section C.1**. We chose and analyzed the top three important features (shown in **Figure 6**) that have significant classification capability: (Dukes et al., 2015) the ratio between the location of the 5th peak or valley at the SR beat V_1 lead and the right boundary of the 5th peak or valley at the V_1 lead of PVC, Cronin et al. (2019) the ratio between the prominence of the 5th peak or valley at the V1 lead of PVC and the prominence of the 5th peak or valley at the V3 lead of PVC, and (Joshi and Wilber, 2005) the difference between the distance of the 5th peak or valley to the left boundary at the V1 lead of PVC and the distance of the 5th peak or valley to the left boundary at the V_1 lead of the SR beat.

Training the machine learning model using 155,784 features extracted from conventional QRS morphological ECG measurements, the proposed method attained an ACC of 92.86 (80.35–98.85), F_1-score of 95.38 (86.62–98.86), prediction of RVOT origins with SE of 93.94 (78.64–98.99) and SP of 88.89 (50.86–99.45) (shown in **Table 2**), and AUC of 95.62 (89.78–100) (presented in **Figure 5**). Among the initial 155,784 features, we found a total of 1,003 critically important features with non-zero SHAP values (Lundberg and Lee, 2017), showing the importance of their contributions to RVOT and LVOT prediction. The top three important features (shown in **Supplementary Section C.1** and **Figure 2**) that show significant classification capability are

TABLE 2 | Classification performance comparison with 95% CI.

	AUC	SE	SP	F_1-Score	ACC
Automated ECG feature extraction	98.99% (96.89–100)	96.97% (82.54–99.89)	100% (62.97–100)	98.46% (90–100)	97.62% (87.44–99.99)
Conventional QRS morphological feature extraction	95.62% (89.78–100)	93.94% (78.64–98.99)	88.89% (50.86–99.45)	95.38% (86.62–98.86)	92.86% (80.35–98.85)
Cardiologists	NA	97.86%	81.72%	96.39%	94.29%

F_1-score = 2 × Precision × recall / (precision + recall); SE, sensitivity; SP, specificity; ACC, accuracy; CI, confidence interval.

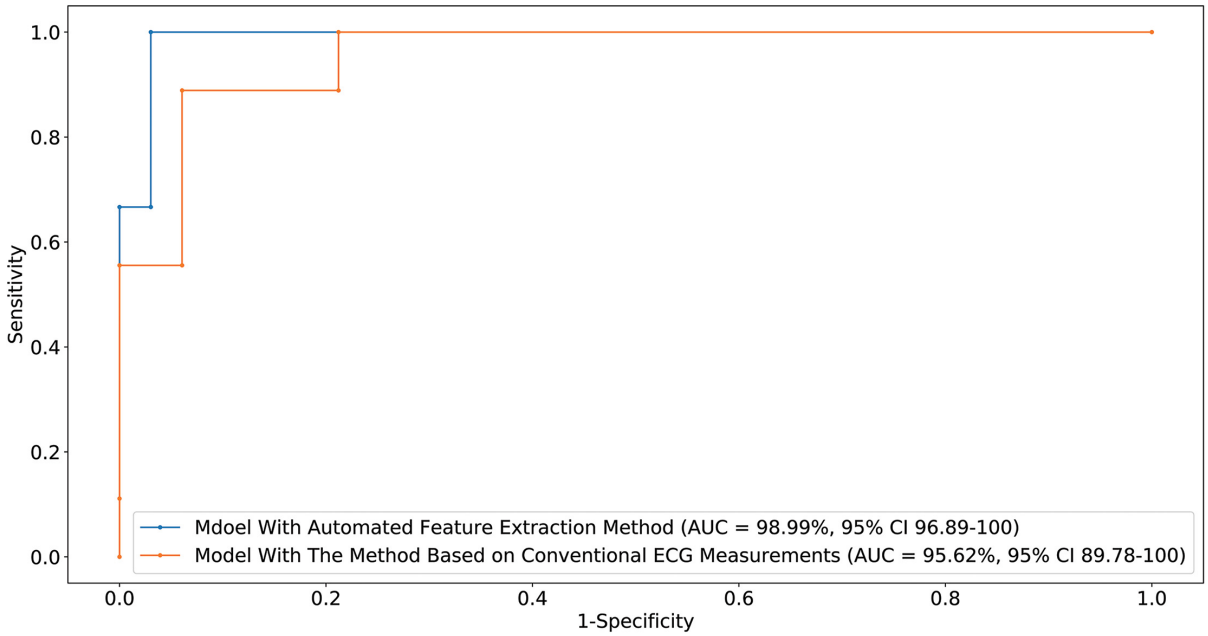

FIGURE 5 | Receiver-operating characteristic curve generated by the optimal machine learning model supplied with two feature extraction methods. The CI for the AUC was estimated using the Sun and Su optimization of the Delong method. Sensitivity and specificity of RVOT prediction are indicated for different thresholds.

(Dukes et al., 2015) the ratio between R-wave amplitude based on the zero isoelectric baselines at lead III PVC and the R-wave amplitude based on the offset of S-wave at V_1 lead PVC, Cronin et al. (2019) the ratio between the R-wave amplitude based on R-wave onset at V_2 lead SR beat and the *R*-wave amplitude based on zero isoelectric baseline at V_3 lead PVC, and (Joshi and Wilber, 2005) the ratio between the R-wave amplitude based on the zero isoelectric baseline at aVL lead SR beat and the R-wave amplitude based on S-wave offset at V_1 lead PVC. The statistical summary of conventional QRS morphological measurements for leads V_1 to V_6 is listed in **Supplementary Section A** and **Table 2**.

Finally, the average performance of eight cardiologists who determined RVOT and LVOT using the same ECG samples in this study is presented in **Table 2**. The classification confusion matrix for these three methods shows correct and incorrect frequency counts in **Supplementary Section A** and **Table 3**. Furthermore, we compared our approach against related methods from 12 prior studies (Kamakura et al., 1998; Zhang et al., 2009; Betensky et al., 2011; Yoshida et al., 2011, 2014; Cheng et al., 2013, 2018; Nakano et al., 2014; Efimova et al., 2015; He et al., 2018; Xie et al., 2018; Di et al., 2019). ACC, F_1-score, SE, SP, positive predictive value, negative predictive value, and AUC were used to compare performances and are shown in **Table 3**.

DISCUSSION

We designed and implemented a high-accuracy algorithm for LVOT and RVOT origins of OTVT classification, using 1,600,800 ECG measurements automatically extracted from 12-lead ECGs using our proprietary method. The prediction accuracy comparison among our method combined with the XGBoost classifier, a conventional QRS feature extraction method combined with XGBoost, and the performance of human experts (shown in **Table 2**) shows that the machine learning model with the automated ECG feature extraction method was uniformly superior. We used DeLong's test (DeLong et al., 1988) to demonstrate that the automated ECG feature extraction method had a significantly higher AUC compared with that attained by the conventional QRS morphological feature extraction approach with a *P*-value = 0.035. The comparison of our approach against methods from 12 prior studies (Kamakura et al., 1998; Zhang et al., 2009; Betensky et al., 2011; Yoshida et al., 2011, 2014; Cheng et al., 2013, 2018; Nakano et al., 2014; Efimova et al., 2015; He et al., 2018; Xie et al., 2018; Di et al., 2019) shows that our algorithm achieved the highest performance scores (shown in **Table 3**). Additionally, we evaluated the general classification capability of each criterion proposed by previous studies using the database in this study. Not surprisingly, we observed significant differences between previously reported performances and the reproduced results of these methods because most of the prior studies used the univariate analysis to make predictions (shown in **Table 3**).

The excellent performance of our machine learning algorithm demands an enormous volume of data and features. It is an extremely time- and cost-consuming task to generate such amount of features by the conventional ECG QRS morphological measurements introduced in prior studies because these measurements are manually obtained. Thus, we did not make any assumptions about ECG criteria before training the machine learning algorithm and intended to exhaust all possible

TABLE 3 | Comparison with prior studies to localize the origins of outflow tract arrhythmia.

Author	Patients	ECG criteria/algorithm	Reported performance in the article	Performance using the database in this study
ThisStudy	420	1,600,800 ECG criteria and extreme gradient boosting tree model	SE 96.97% SP 100% PPV 100% NPV 90% AUC 98.99% ACC 97.62% F_1-Score 98.46%	
Kamakura et al. (1998)	40	The R/S transition (first precordial lead with R/S ration >1) in Lead V_3 to predict LVOT	SE 80% PPV 40% SP 82.86% NPV 96.67%	SE 30.1% PPV 18.92% SP 63.3% NPV 73.4%
Zhang et al. (2009)	65	(a) Transitional zone ≥ V_4 predicts RVOT origin	SE 94.87% PPV 100%	SE 60.86% PPV 72.47%
		(b) R-wave duration index≤0.5 and R/S wave amplitude index≤0.3 in V1/V2 predicts RVOT origin	SE 94.87% PPV 100%	SE 80.24% PPV 73.52%
Betensky et al. (2011)	61	(a) V_2 transition ratio (defined as percentage R wave during VT divided by percentage R wave in SR) ≥ 0.6 predicts LVOT origin	SE 95% SP 100% PPV 100% NPV 95% ACC 91%	SE 78.49% SP 89.6% PPV 68.22% NPV 93.61% ACC 87.14%
		(b) PVC precordial transition later than SR transition predicts RVOT origin	SE 19% SP 100%	SE 23% SP81%
Yoshida et al. (2011)	207	V_2S/V_3R index ≤ 1.5 predicts LVOT origin	SE 89% SP 94% PPV 84% NPV 96%	SE 69.89% SP 85.63% PPV 58.04% NPV 90.9%
Cheng et al. (2013)	94	(a) R/S transition at lead V_1/V_2 predicts LVOT origin	SE 52.4% SP 92.1% PPV 72.6% NPV 85.3% ACC 84.2%	SE 76.34% SP 91.43% PPV 71.72% NPV 93.15% ACC 88.09%
		(b) R/S transition at lead V_3 predicts RVOT origin	SE 39% SP 35.2% PPV 74.2% NPV 29.4% ACC 46.3%	SE 33.33% SP 48.93% PPV 15.66% NPV 72.07% ACC 45.48%
		(c) R/S transition at lead V_4 or later predicts RVOT origin	SE 59.3% SP 93.1% PPV 94.6% NPV 46.7% ACC 68.3%	SE 43.01% SP 52.6% PPV 20.51% NPV 76.44% ACC 50.47%
Yoshida et al. (2014)	112	TZ index = TZ score of OTVT minus TZ score of a sinus beat	To aortic sinus cusp SE 88% SP 82% AUC 0.9	SE 76.05% SP 52.59%
Nakano et al. (2014)	63	(a) R > S concordance in synthesized right-sided chest leads (Syn-V_3R, Syn-V_4R, Syn-V_5R) predicts an LVOT origin	SE 100% SP 100%	Could not be reproduced by standard 12-lead ECG
		(b) R/S index (>0.3): A ratio of R-wave amplitude to S-wave amplitude in leads V_1 or V_2 predicts an LVOT origin	SE 90% SP 98%	SE 53.12% SP 46.05%
Efimova et al. (2015)	105	A QRS-RVA (right ventricular apex) interval ≥ 0.49 ms predicts an LVOT origin. The QRS-RVA interval was measured from the onset of the QRS complex to the distal RVA signal.	SE 98%, SP 94.6%, PPR 94.1%, NPR 98.1%, ACC 96.1%	Could not be reproduced by standard 12-lead ECG
Cheng et al. (2018)	94	R-wave deflection interval in lead V_3 > 80 ms and R-wave amplitude index in lead V_1	SE 100% SP 83% PPV 85.7% NPV 100% ACC 91.7%	SE 59.14% SP 58.1% PPV 28.64% NPV 83.33% ACC 58.33%
He et al. (2018)	488	$Y = -1.15*(TZ) - 0.494*(V_2S/V_3R)$	SE 90% SP 87% AUC 0.88%	SE 78.39% SP 67.23% AUC 0.79%
Xie et al. (2018)	75	R-wave amplitude ≥ 0.1 mV to predict LVOT	SE 75% SP 98% PPV 92.3% NPV 93% AUC 0.85%	SE 67.74% SP 58.1% PPV 31.5% NPV 86.36%
Di et al. (2019)	184	V_1-V_3 transition index to predict RVOT	SE 93% SP 86% AUC 0.931 ACC 95%	SE 70.33% SP 67.74% ACC 69.76%

The first column presents the first author name and the reference number in the main text; TZ, transition zone; SE, sensitivity; SP, specificity; PPV, positive predictive value; NPV, native predictive value; ACC, accuracy; AUC, area under curve.

relationships among morphological measures of Q-, R-, and S-waves as well as the entire QRS complex. We designed and implemented an automated ECG feature extraction method that can generate 1,600,800 ECG signal characteristics. Not only did these features contain a considerable amount of the classical statistics from 12 prior studies (Kamakura et al., 1998; Zhang et al., 2009; Betensky et al., 2011; Yoshida et al., 2011, 2014; Cheng et al., 2013, 2018; Nakano et al., 2014; Efimova et al., 2015; He et al., 2018; Xie et al., 2018; Di et al., 2019), but they also captured morphological measures not considered by previous studies, such

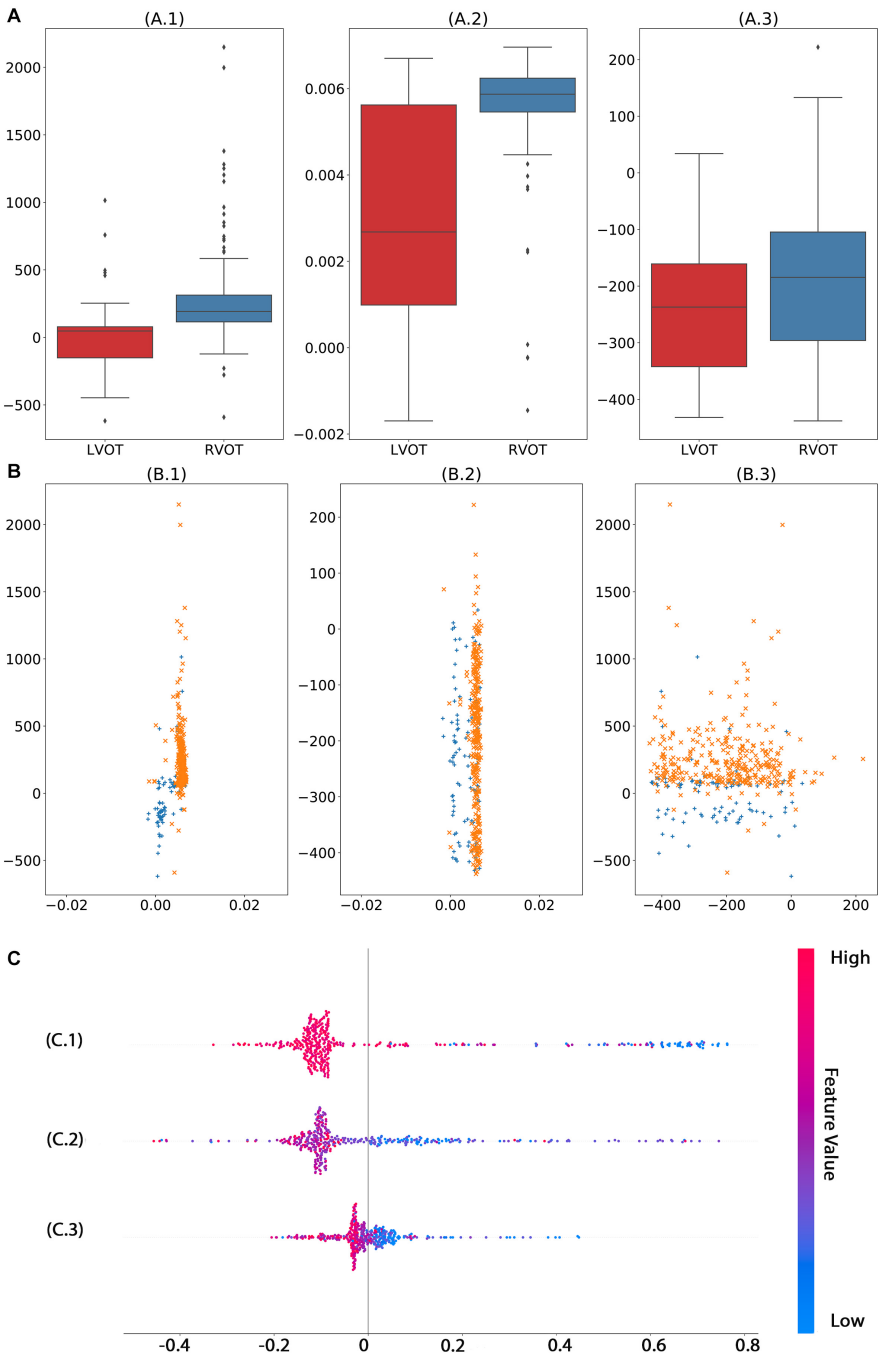

FIGURE 6 | Analysis of top three significant ECG measurements found by machine learning model with automated feature extraction method. The univariate analysis **(A)** shows that features 1 **(A.1)** and 2 **(A.2)** have significant capability to separate RVOT and LVOT. The bivariate analysis **(B)** indicates the classification ability of one–one interaction of the top 3 significant features. In the multivariate analysis **(C)**, the smaller feature 1 **(C.1)**, feature 1 **(C.2)**, and feature 3 **(C.3)** generate a higher probability of LVOT, but the magnitude of influence varies across features. The color in **panel (C)** represents the feature value (red high, blue low).

as rsR' waves and rsr's' waves. However, one may be concerned that such a feature extraction method will include the P- and T-wave within SR beats and retrograde P-waves within PVC. The machine learning model captures and analyzes a large amount of information from every beat but filters out all unimportant features based on their classification accuracy contribution. As we can see from the top three important features (shown in **Figure 6**) selected by the machine learning model, none of the features that presented waves mentioned above played a role in the prediction. The important morphological features of the Rsr' and rsr's waves

may be caused by noise and lead placement of the 12-lead ECG electrodes because the 12-lead ECG electrodes are frequently misplaced due to the mapping patches used during the ablation procedure. In this study, we avoid such a problem because chest and limb leads were placed carefully in a standard position when the 12-lead surface ECGs were collected before the procedure.

Moreover, before the machine learning model is safely applied in practice, an unambiguous interoperation is necessary for cardiologists to gear this advanced tool, such as explaining what crucial criteria are and why they play vital roles. For instance, the machine learning model shows that the smaller the magnitude of the first important feature (shown in **Figure 6C.1**), the higher the possibility of LVOT origin of OTVT. The first important feature is the ratio of the location of the 5th peak or valley at the V1 lead SR beat and the right boundary of the 5th peak or valley at the V_1 lead of PVC. In our feature extraction system, the 5th peak or valley at the V_1 lead of PVC is an S-wave in most cases. The key ECG lead in the initial site prediction of VT origin is the V_1 lead because it is located nearly orthogonal to the septal plane and, thus, is the best lead to resolve initial right- vs. left-sided activation. When the V_1 lead has a positive QRS (R > s), the VT is considered to have the right bundle branch block (RBBB) configuration. Conversely, net negative QRS (r < S) defines a left bundle branch block (LBBB) configuration (Haqqani and Marchlinski, 2019). The top three important features (shown in **Figure 6**) were exactly measured activation time, RBBB, and LBBB configuration. Therefore, such interpretation makes the machine learning decision process not a black box anymore.

Last but not least, the machine learning model proposed in this study can be immediately and effortlessly deployed to EP labs. The pretrained model, source code, and data are available online and found in the "Data Availability Statement" section. The model inputs are only two QRS complexes, one for PVC and one for SR beat, and they can be easily acquired from 12-lead standard ECG. The analysis of one patient's data takes less than a second provided every step of measurement and computation is automatically done by the model and the preprocessing approach. The precise prediction of origins can significantly reduce CA duration and reduce the risk of complications.

Study Limitations

Because the data set did not produce enough well-labeled data to feed a machine learning model, the algorithm currently only predicts LVOT and RVOT rather than subsites of them. For instance, the origin of PVC is sometimes in the middle of septal RVOT/LVOT. The presence of expertly labeled data for three categories, RVOT, LVOT, and septal, will allow the machine learning model to predict the origins with higher accuracy. Although this study includes patients with comprehensive anatomy sites under RVOT and LVOT, the performance of the method could improve in the presence of more cases of RCC and summit under LVOT. Moreover, some conditions, such as cardiomyopathies, reentrant VT coronary heart disease, and prior structural and congenital abnormalities, are underrepresented or absent from the study. Thus, the algorithm potentially has a limitation if applied in such scenarios.

CONCLUSION

Considering the performance of prediction, the capacity of extracting vital information from 12-lead ECG and the robustness of application, our results provide the promising and reliable decision support to guide a successful CA treatment of ventricular arrhythmia by machine learning technology.

DATA AVAILABILITY STATEMENT

The datasets presented in this study can be found in online repositories. The names of the repository/repositories and accession number(s) can be found below: https://doi.org/10.6084/m9.figshare.c.4668086.v2.

AUTHOR CONTRIBUTIONS

JZ, GF, XD, BH, HC, and CR processed the data for analysis. JZ, HC, GF, XD, IA, and CR performed the statistical analysis. All authors contributed to the study design, data interpretation, and writing of the report.

FUNDING

This work was supported by the 2020 Natural Science Foundation of Zhengjiang Province (ID H0205-3202410).

ACKNOWLEDGMENTS

We are grateful for the support from the arrhythmia center of Ningbo First Hospital of Zhejiang University.

SUPPLEMENTARY MATERIAL

The Supplementary Material for this article can be found online at: https://www.frontiersin.org/articles/10.3389/fphys.2021.641066/full#supplementary-material

REFERENCES

Abi-Abdallah, D., Chauvet, E., Bouchet-Fakri, L., Bataillard, A., Briguet, A., and Fokapu, O. (2006). Reference signal extraction from corrupted ECG using wavelet decomposition for MRI sequence triggering: application to small animals. *Biomed. Eng. Online* 5:11.

Betensky, B. P., Park, R. E., Marchlinski, F. E., Hutchinson, M. D., Garcia, F. C., Dixit, S., et al. (2011). The V(2) transition ratio: a new electrocardiographic

criterion for distinguishing left from right ventricular outflow tract tachycardia origin. *J. Am. Coll. Cardiol.* 57, 2255–2262.

Bunch, T. J., and Day, J. D. (2006). Right meets left: a common mechanism underlying right and left ventricular outflow tract tachycardias. *J. Cardiovasc. Electrophysiol.* 17, 1059–1061. doi: 10.1111/j.1540-8167.2006.00577.x

Cheng, D., Ju, W., Zhu, L., Chen, K., Zhang, F., Chen, H., et al. (2018). V3R/V7 index: a novel electrocardiographic criterion for differentiating left from right ventricular outflow tract arrhythmias origins. *Circ. Arrhythm. Electrophysiol.* 11:e006243.

Cheng, Z., Cheng, K., Deng, H., Chen, T., Gao, P., Zhu, K., et al. (2013). The R-wave deflection interval in lead V3 combining with R-wave amplitude index in lead V1: a new surface ECG algorithm for distinguishing left from right ventricular outflow tract tachycardia origin in patients with transitional lead at V3. *Int. J. Cardiol.* 168, 1342–1348. doi: 10.1016/j.ijcard.2012.12.013

Cronin, E. M., Bogun, F. M., Maury, P., Peichl, P., Chen, M., Namboodiri, N., et al. (2019). HRS/EHRA/APHRS/LAHRS expert consensus statement on catheter ablation of ventricular arrhythmias. *Europace* 21, 1143–1144.

David, L. D., and Johnstone, I. M. (1995). Adapting to unknown smoothness via wavelet shrinkage. *J. Am. Stat. Assoc.* 90, 1200–1224. doi: 10.1080/01621459.1995.10476626

DeLong, E. R., DeLong, D. M., and Clarke-Pearson, D. L. (1988). Comparing the areas under two or more correlated receiver operating characteristic curves: a nonparametric approach. *Biometrics* 44, 837–845. doi: 10.2307/2531595

Di, C., Wan, Z., Tse, G., Letsas, K. P., Liu, T., Efremidis, M., et al. (2019). The V1-V3 transition index as a novel electrocardiographic criterion for differentiating left from right ventricular outflow tract ventricular arrhythmias. *J. Interv. Card. Electrophysiol.* 56, 37–43. doi: 10.1007/s10840-019-00612-0

Dukes, J. W., Dewland, T. A., Vittinghoff, E., Mandyam, M. C., Heckbert, S. R., Siscovick, D. S., et al. (2015). Ventricular ectopy as a predictor of heart failure and death. *J. Am. Coll. Cardiol.* 66, 101–109. doi: 10.1016/j.jacc.2015.04.062

Efimova, E., Dinov, B., Acou, W. J., Schirripa, V., Kornej, J., Kosiuk, J., et al. (2015). Differentiating the origin of outflow tract ventricular arrhythmia using a simple, novel approach. *Heart Rhythm* 12, 1534–1540. doi: 10.1016/j.hrthm.2015.04.004

Enriquez, A., Baranchuk, A., Briceno, D., Saenz, L., and Garcia, F. (2019). How to use the 12-lead ECG to predict the site of origin of idiopathic ventricular arrhythmias. *Heart Rhythm* 16, 1538–1544. doi: 10.1016/j.hrthm.2019.04.002

Hachiya, H., Aonuma, K., Yamauchi, Y., Harada, T., Igawa, M., Nogami, A., et al. (2000). Electrocardiographic characteristics of left ventricular outflow tract tachycardia. *Pacing Clin. Electrophysiol.* 23(11 Pt 2), 1930–1934. doi: 10.1111/j.1540-8159.2000.tb07055.x

Haqqani, H. M., and Marchlinski, F. E. (2019). The surface electrocardiograph in ventricular arrhythmias: lessons in localisation. *Heart Lung Circ.* 28, 39–48. doi: 10.1016/j.hlc.2018.08.025

Haqqani, H. M., Morton, J. B., and Kalman, J. M. (2009). Using the 12-lead ECG to localize the origin of atrial and ventricular tachycardias: part 2–ventricular tachycardia. *J. Cardiovasc. Electrophysiol.* 20, 825–832. doi: 10.1111/j.1540-8167.2009.01462.x

He, Z., Liu, M., Yu, M., Lu, N., Li, J., Xu, T., et al. (2018). An electrocardiographic diagnostic model for differentiating left from right ventricular outflow tract tachycardia origin. *J. Cardiovasc. Electrophysiol.* 29, 908–915. doi: 10.1111/jce.13493

Ito, S., Tada, H., Naito, S., Kurosaki, K., Ueda, M., Hoshizaki, H., et al. (2003). Development and validation of an ECG algorithm for identifying the optimal ablation site for idiopathic ventricular outflow tract tachycardia. *J. Cardiovasc. Electrophysiol.* 14, 1280–1286. doi: 10.1046/j.1540-8167.2003.03211.x

Joshi, S., and Wilber, D. J. (2005). Ablation of idiopathic right ventricular outflow tract tachycardia: current perspectives. *J. Cardiovasc. Electrophysiol.* 16(Suppl. 1), S52–S58.

Kamakura, S., Shimizu, W., Matsuo, K., Taguchi, A., Suyama, K., Kurita, T., et al. (1998). Localization of optimal ablation site of idiopathic ventricular tachycardia from right and left ventricular outflow tract by body surface ECG. *Circulation* 98, 1525–1533. doi: 10.1161/01.cir.98.15.1525

Lahmiri, S. (2014). Comparative study of ECG signal denoising by wavelet thresholding in empirical and variational mode decomposition domains. *Healthc Technol. Lett.* 1, 104–109. doi: 10.1049/htl.2014.0073

Latchamsetty, R., Yokokawa, M., Morady, F., Kim, H. M., Mathew, S., Tilz, R., et al. (2015). Multicenter outcomes for catheter ablation of idiopathic premature ventricular complexes. *JACC Clin. Electrophysiol.* 1, 116–123.

Lundberg, S., and Lee, S.-I. (2017). A unified approach to interpreting model predictions. in *Proceedings of the 31st International Conference on Neural Information Processing Systems*. New York, NY: ACM

Nakano, M., Ueda, M., Ishimura, M., Kajiyama, T., Hashiguchi, N., Kanaeda, T., et al. (2014). Estimation of the origin of ventricular outflow tract arrhythmia using synthesized right-sided chest leads. *Europace* 16, 1373–1378. doi: 10.1093/europace/eut355

Ouyang, F., Fotuhi, P., Ho, S. Y., Hebe, J., Volkmer, M., Goya, M., et al. (2002). Repetitive monomorphic ventricular tachycardia originating from the aortic sinus cusp: electrocardiographic characterization for guiding catheter ablation. *J. Am. Coll. Cardiol.* 39, 500–508.

Stein, C. M. (1981). Estimation of the mean of a multivariate normal distribution. *Ann. Stat.* 9, 1135–1151. doi: 10.1214/aos/1176345632

Tanner, H., Hindricks, G., Schirdewahn, P., Kobza, R., Dorszewski, A., Piorkowski, C., et al. (2005). Outflow tract tachycardia with R/S transition in lead V3: six different anatomic approaches for successful ablation. *J. Am. Coll. Cardiol.* 45, 418–423. doi: 10.1016/j.jacc.2004.10.037

Xie, S., Kubala, M., Liang, J. J., Hayashi, T., Park, J., Padros, I. L., et al. (2018). Lead I R-wave amplitude to differentiate idiopathic ventricular arrhythmias with left bundle branch block right inferior axis originating from the left versus right ventricular outflow tract. *J. Cardiovasc. Electrophysiol.* 29, 1515–1522. doi: 10.1111/jce.13747

Yamada, T. (2019). Twelve-lead electrocardiographic localization of idiopathic premature ventricular contraction origins. *J. Cardiovasc. Electrophysiol.* 30, 2603–2617. doi: 10.1111/jce.14152

Yoshida, N., Inden, Y., Uchikawa, T., Kamiya, H., Kitamura, K., Shimano, M., et al. (2011). Novel transitional zone index allows more accurate differentiation between idiopathic right ventricular outflow tract and aortic sinus cusp ventricular arrhythmias. *Heart Rhythm* 8, 349–356. doi: 10.1016/j.hrthm.2010.11.023

Yoshida, N., Yamada, T., McElderry, H. T., Inden, Y., Shimano, M., Murohara, T., et al. (2014). A novel electrocardiographic criterion for differentiating a left from right ventricular outflow tract tachycardia origin: the V2S/V3R index. *J. Cardiovasc. Electrophysiol.* 25, 747–753. doi: 10.1111/jce.12392

Zhang, F., Chen, M., Yang, B., Ju, W., Chen, H., Yu, J., et al. (2009). Electrocardiographic algorithm to identify the optimal target ablation site for idiopathic right ventricular outflow tract ventricular premature contraction. *Europace* 11, 1214–1220. doi: 10.1093/europace/eup231

Zheng, J., Fu, G., Anderson, K., Chu, H., and Rakovski, C. (2020). A 12-Lead ECG database to identify origins of idiopathic ventricular arrhythmia containing 334 patients. *Sci. Data* 7:98.

Conflict of Interest: From the Department of Cardiology, Ningbo First Hospital of Zhejiang University. HC has served as a consultant for Biosense Webster, Boston Scientific, and Abbott. HY was employed by the company Zhejiang Cachet Jetboom Medical Devices Co., Ltd.

The remaining authors declare that the research was conducted in the absence of any commercial or financial relationships that could be construed as a potential conflict of interest.

frontiers in Physiology

ORIGINAL RESEARCH
published: 01 September 2021
doi: 10.3389/fphys.2021.698405

A Hybrid Approach for Cardiac Blood Flow Vortex Ring Identification Based on Optical Flow and Lagrangian Averaged Vorticity Deviation

*Ke Yang[1,2], Shiqian Wu[3], Oluwarotimi W. Samuel[4], Hui Zhang[5], Dhanjoo N. Ghista[6], Di Yang[1,2] and Kelvin K. L. Wong[4]**

[1] Key Laboratory of Metallurgical Equipment and Control Technology, Ministry of Education, Wuhan University of Science and Technology, Wuhan, China, [2] Hubei Key Laboratory of Mechanical Transmission and Manufacturing Engineering, Wuhan University of Science and Technology, Wuhan, China, [3] School of Information Science and Engineering, Wuhan University of Science and Technology, Wuhan, China, [4] Shenzhen Institutes of Advanced Technology, Chinese Academy of Sciences, Shenzhen, China, [5] Ultrasound Department, The Third Affiliated Hospital of Sun Yat-sen University, Guangzhou, China, [6] University 2020 Foundation, Inc., California City, CA, United States

OPEN ACCESS

Edited by:
Xiaopeng Zhao, The University of Tennessee, Knoxville, United States

Reviewed by:
George Haller, ETH Zürich, Switzerland
Alessio Gizzi, Campus Bio-Medico University, Italy

***Correspondence:**
Kelvin K. L. Wong
kelvin.wong@siat.ac.cn

Specialty section:
This article was submitted to Computational Physiology and Medicine, a section of the journal Frontiers in Physiology

Received: *21 April 2021*
Accepted: *05 August 2021*
Published: *01 September 2021*

Citation:
Yang K, Wu S, Samuel OW, Zhang H, Ghista DN, Yang D and Wong KKL (2021) A Hybrid Approach for Cardiac Blood Flow Vortex Ring Identification Based on Optical Flow and Lagrangian Averaged Vorticity Deviation. Front. Physiol. 12:698405. doi: 10.3389/fphys.2021.698405

Objective: The measurement of cardiac blood flow vortex characteristics can help to facilitate the analysis of blood flow dynamics that regulates heart function. However, the complexity of cardiac flow along with other physical limitations makes it difficult to adequately identify the dominant vortices in a heart chamber, which play a significant role in regulating the heart function. Although the existing vortex quantification methods can achieve this goal, there are still some shortcomings: such as low precision, and ignoring the center of the vortex without the description of vortex deformation processes. To address these problems, an optical flow Lagrangian averaged vorticity deviation (Optical flow-LAVD) method is proposed.

Methodology: We examined the flow within the right atrium (RA) of the participants' hearts, by using a single set of scans pertaining to a slice at two-chamber short-axis orientation. Toward adequate extraction of the vortex ring characteristics, a novel approach driven by the Lagrangian averaged vorticity deviation (LAVD) was implemented and applied to characterize the trajectory integral associated with vorticity deviation and the spatial mean of rings, by using phase-contrast magnetic resonance imaging (PC-MRI) datasets as a case study. To interpolate the time frames between every larger discrete frame and minimize the error caused by constructing a continuous velocity field for the integral process of LAVD, we implemented the optical flow as an interpolator and introduced the backward warping as an intermediate frame synthesis basis, which is then used to generate higher quality continuous velocity fields.

Results: Our analytical study results showed that the proposed Optical flow-LAVD method can accurately identify vortex ring and continuous velocity fields, based on optical flow information, for yielding high reconstruction outcomes. Compared with

the linear interpolation and phased-based frame interpolation methods, our proposed algorithm can generate more accurate synthesized PC-MRI.

Conclusion: This study has developed a novel Optical flow-LAVD model to accurately identify cardiac vortex rings, and minimize the associated errors caused by the construction of a continuous velocity field. Our paper presents a superior vortex characteristics detection method that may potentially aid the understanding of medical experts on the dynamics of blood flow within the heart.

Keywords: vortex identification, Lagrangian averaged vorticity deviation, optical flow, cardiac flow analysis, vortex rings, vortex volume

INTRODUCTION

The vortex formation in blood flow within the heart plays an important role in characterizing the function of the blood flow mechanism and energy transfer to the heart chamber, which are important indicators that can be used to quantify the overall heart function. The fluid flow transported by the vortex ring formation is observed to be more efficient than that transported by a steady, straight jet flow of fluid, in terms of aiding the circulation of blood to the various regions of the heart chamber (Dabiri and Gharib, 2005; Kheradvar and Gharib, 2007, 2009; Kheradvar et al., 2007; Wong et al., 2009a). As we know, the cardiac myocardium has inter-twined helical fibers. So when they contract, the heart chamber twists, and this is how blood is efficiently ejected out of the chamber. Now this heart chamber twisting causes the formation of vortex rings of high vorticity in blood flow in the chamber. In contrast, cardiomyopathic hearts have impaired contractility, and hence less twisting; hence, they have smaller vortex rings with lower vorticity (Sengupta et al., 2006). So, the formation of vortex rings is closely associated with cardiac function, and the health status of an individual. This is why, in conjunction with the structural parameters of the heart, the vortex flow analysis provides an insight into its functional analysis, and helps distinguish normal subjects from patients with heart disease (Kheradvar et al., 2019). Therefore, developing a method that can enable quantification of the vortex ring characteristics and its dynamic changes during the cardiac cycle can enable understanding of the vortex ring's physiological functions and facilitate exploration of heart diagnostics and its pathological changes (Kräuter et al., 2020).

Interestingly, phase-contrast magnetic resonance imaging (PC-MRI) allows three-dimensional MR velocity mapping based on the intrinsic sensitivity of MRI to flow, and provides a unique tool for measuring complex blood flow patterns *in vivo* (Markl et al., 2007; Dyverfeldt et al., 2015). Earlier Wong et al. (2009a) conducted a study in which the vorticity of vortex flow was measured by using the flow field obtained from scanned PC-MRI, to characterize the location and strengths of vortices within a cardiac chamber. A major limitation of this study is that it is based on global estimation, and does not include extraction of localized information from the vortex region to elucidate the function of dominant vortexes. The identification of the dominant vortex ring is the key for the comprehensive description of the resulting swirling blood flow within a heart chamber (such as the left ventricle) resulting in blood outflow.

Since there is no uniform definition of vortex (Epps, 2017; Günther and Theisel, 2018), different vortex criteria have been used to extract vortex flow information within the heart chamber (Wong et al., 2010; Töger et al., 2012; Elbaz et al., 2014; Kräuter et al., 2020). Elbaz et al. (2014) adopted the criterion λ_2 for left ventricular (LV) vortex detection in early and late diastolic inflow. Kräuter et al. (2020) computed the divergence-free part of the velocity vector for Q criterion-based identification vortex throughout the cardiac cycle. The above-mentioned methods are region-based and used to extract instantaneous vortex rings in a single frame, which hinders proper exploration of vortex formation processes. Töger et al. (2012) considered Lyapunov exponent values higher than 50% as the Lagrangian vortex ring to identify vortex boundaries. The Lagrangian vortex ring can more accurately describe the developmental process, but the method is conservative and does not include the vortex core (Kräuter et al., 2020). In Yang et al. (2021), we have employed Lagrangian averaged vorticity deviation (LAVD) to identify the cores and regions of the Lagrangian vortices and Eulerian vortices, for measuring the vortex volume and vorticity in the LV blood flow for more accurate quantification of the vortex formation. Wong et al. (2010) identified two dominant vortices of opposite rotation in the right atrium (RA), but they applied an unsupervised data clustering algorithm without considering the characteristics of blood flow. This is what has led to our preparing this paper, to improve the description of the vortex characterization in the RA by employing LAVD for more accurate identification and quantification of blood flow vortex rings.

Therefore, for accurate identification and tracking of the cardiac vortex ring characterization, this study presents a novel method (**Optical flow-LAVD**), which is precise in the extraction of Lagrangian vortex core and associated regions within the heart, based on the PC-MRI data. The proposed algorithm implements the trajectory integral of the normed deviation of vorticity from its spatial mean, for LAVD-based identification and tracking of the cardiac Lagrangian vortex rings (Haller et al., 2015). At the same time, we adopt the Horn-Schunck (Horn and Schunck, 1981) brightness constraint to synthesize the intermediate PC-MRI data for yielding high quality continuous velocity fields to reduce the error caused by the integral process of LAVD. Additionally, we have extensively validated the accuracy of the

proposed Optical flow-LAVD based vortex identification method concerning synthesized PC-MRI data sequences, and we were able to characterize the region of the dominant Lagrangian vortex ring within a cardiac chamber.

MATERIALS AND METHODS

Study Population and PC-MRI Protocol

In order to validate the performance of our proposed method of vortex ring identification and features, normal and healthy male subjects with ages around 22 years were recruited for the PC-MRI dataset collection required for the Optical flow-LAVD model's testing. The volunteers had normal blood pressure, and no history of cardiovascular disease was observed after preliminary examination. Subsequently, we examined the flow within the RA of the participants' hearts, by using a single set of scans pertaining to a slice at a two-chamber short-axis orientation. In this study, the RA is considered, because we can verify more accurately the effectiveness of our novel method, by referring to our previous research work on cardiac flow analysis within the atrium (Wong et al., 2009a, 2010). At the same time, our objective is to analyze the Optical flow-LAVD, and understand the developmental process of the cardiac Lagrangian vortex ring. The study was approved by the local ethical review board, and written informed consent was obtained from the subjects.

The velocity-encoded magnetic resonance imaging was performed by using a Siemens Avanto, 1.5 Tesla, model-syngo MRB15 scanner with Numaris-4, Series No: 26406 software. More precisely, the encoding was set to 100 cm/s in all directions, and this configuration was applied in the case of aliasing. In addition, other parameters such as the echo time (TR) 47.1ms, repetition time (TE) $= 1.6$ ms, field of view (FOV) $(298 = 340)$ mm^2 at a $(134 = 256)$ pixel matrix were configured. Further, we have employed an in-plane resolution of 1.54 $mm/pixel$ determined by the pixel spacing, and the through-plane resolution of 6 mm based on the slice interval. All images were acquired with retrospective gating and 25 phases or time frames (for time frame indices from $Nt = 1$ to 25) for each slice, as shown in **Figure 1**.

Computation of Lagrangian Average Vorticity Deviation

To identify the Lagrangian vortex ring within the right atrium (RA), the Lagrangian average vorticity deviation (LAVD) was computed in each image's plane and consecutive time phase. Haller et al. (2015) derived the LAVD from a dynamic polar decomposition of the deformation gradient (Haller, 2016) to define vortices. The time-dependent motion trajectories of fluid particles generated by $v(x, t)$ within the heart are governed by the following differential equation

$$\dot{x}(t) = v(x, t), \tag{1}$$

defining the cardiac flow map

$$\Delta\mathcal{F}_{t_0}^{t} : x_0 \to x(x_0; t) \;\; t \in [t_o, t_1]. \tag{2}$$

The displacement gradient of $\mathcal{F}_{t_0}^{t}$ can describe the distance of two particles from time t_0 to t_1, one at x_0 and the other is adjacent to it at $x_0 + \delta x(t_0)$. Using mathematical representation, we have the following function

$$\Delta\mathcal{F}_{t_0}^{t}(x_0) = \frac{dx(x_0, t_0, t)}{dx_0} \; t \in [t_0, t_1]. \tag{3}$$

It is to be noted that the $\Delta\mathcal{F}_{t_0}^{t}$ tensor does not provide an objective indication of the rotational component of the deformation, because the polar rotation angle extracting from this mapping depends on the observer (Haller, 2016). To address this issue, Haller et al. (2015) used a technique based on the Dynamic polar Decomposition (DPD) to decompose $\mathcal{F}_{t_0}^{t}$ into the dynamic rotation tensor $O_{t_0}^{t}$ and the right dynamic stretch tensor $M_{t_0}^{t}$, and this is denoted as follows

$$\Delta\mathcal{F}_{t_0}^{t} = O_{t_0}^{t} M_{t_0}^{t} \; t \in [t_0, t_1]. \tag{4}$$

Then, $O_{t_0}^{t}$ can be further factorized into two tensors. Specifically, we have

$$\Delta\mathcal{F}_{t_0}^{t} = \Phi_{t_0}^{t} \Theta_{t_0}^{t} M_{t_0}^{t} \; t \in [t_0, t_1], \tag{5}$$

wherein, $\Phi_{t_0}^{t}$ is relative rotation and $\Theta_{t_0}^{t}$ describes the mean rotation (Haller et al., 2015). The $\Phi_{t_0}^{t}$ has a dynamic consistency, which implies that the total angle swept by this tensor around its axis of rotation is dynamically consistent. Because of the feature of any physical rigid body motion, this angle will satisfy the relationship

$$\psi_{t_0}^{t}(x_0) = \psi_{s}^{t}(x_0) + \psi_{t_0}^{s}(x_0) \;\; s, t \in [t_0, t_1], \tag{6}$$

wherein $\psi_{t_0}^{t}$ is the intrinsic rotation angle. Using the result obtained in Haller (2016), it can be computed as

$$\psi_{t_0}^{t}(x_0) = \frac{1}{2}\int_{t_0}^{t} |\omega(x(x_0, s), s) - \varpi(s)| \, ds, \tag{7}$$

where $\omega(x(x_0, s), s)$ is the vorticity along a material trajectory, and ϖ describes the spatial mean of vorticity. The LAVD is defined by an integral component of the above Eq. (7), as follows

$$LAVD_{t_0}^{t}(x_0) = \int_{t_0}^{t} |\omega(x(x_0, s), s) - \varpi(s)| \, ds. \tag{8}$$

Based on this Eq. (8), a rotationally coherent Lagrangian vortex is defined as a nested set of outward decreasing tubular level sets of LAVD. The LAVD is objective, and we note that this measure is relative to its neighborhood, and its value-range depends on the flow domain. In this study, the region relative to the vortex is large, and of the size of RA, based on manual segmentation. The boundary of the Lagrangian vortex is the outermost closed convex level surface of LAVD, satisfying convexity deficiency, while the vortex core is the local maxima of LAVD enclosed by the boundary (Haller et al., 2015; Yang and Melissa, 2015). Hence, we define the boundaries of Lagrangian vortex within the heart as the outermost members of closed families of LAVD level curves falling below a convexity deficiency threshold.

The LAVD also leads to a difficulty: The Lagrangian vortex is intrinsically tied to a specific finite time interval over which

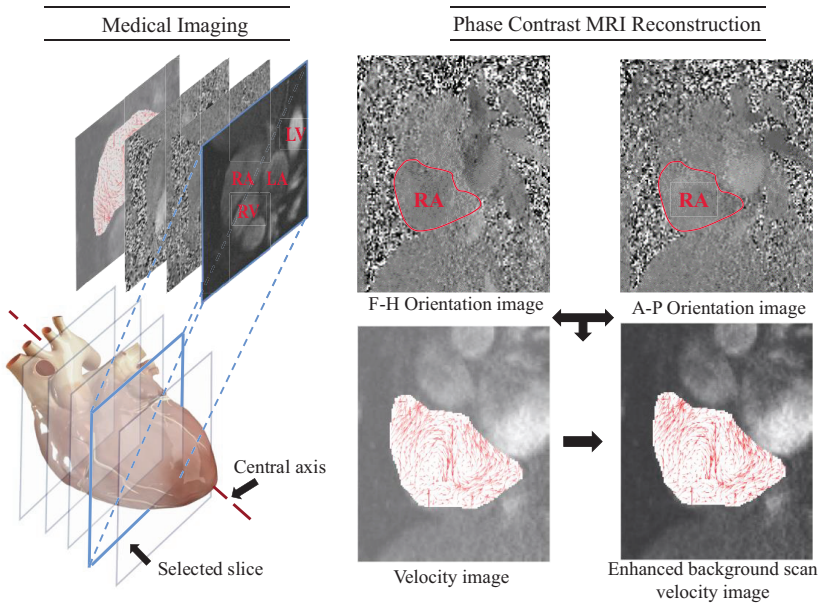

FIGURE 1 | A representation of the MRI scan images through the heart, and PC-MRI based velocity images in a cardiac chamber. The PC-MRI pertains to the Foot-Head (F-H) and the Anterior-Posterior (A-P) orientations, respectively, the intensity of the whose pixels indicates the magnitude of the velocity component in the specified orientation. Combining two orthogonal velocity-encoded images can yield a velocity flow field.

they exert their influence on nearby trajectories (Epps, 2017; Katsanoulis et al., 2017). Short-time variability of flow within a cardiac chamber is often seen as significant in computing the LAVD values. Therefore, we adopt the Horn-Schunck (Horn and Schunck, 1981) optical flow to synthesize the intermediate PC-MR velocity data in time and space, for producing a more accurate continuous velocity field $v(x, t)$.

Intermediate PC-MR Velocity Data Synthesis

As expressed in Eq. (8), the computation of LAVD represents an integral process, but the PC-MR velocity data are obtained within the large discrete frames and have a limited temporal resolution. So in this study, we innovatively introduce the optical flow-based intermediate PC-MR velocity data synthesis to compute LAVD.

Horn-Schunck Optical Flow

Recent optical flow assessment methods (Wulff et al., 2017; Xu et al., 2017) take on the variational approach introduced by Horn and Schunck (HS) (Horn and Schunck, 1981). The HS optical flow can perform on consecutive frames and predict the motion of pixels from one frame to the other, by iteratively settling an optimization issue formulated from two constraints (Afrashteh et al., 2017). The first constraint is "brightness constancy," and it assumes that a pixel has the same brightness level in two frames after movement,

$$I\left(x+u,\ y+v,\ t+dt\right)=I\left(x,\ y,\ t\right), \tag{9}$$

where (i) $I(x,\ y,\ t)$ is the pixel brightness in the first frame at spatial location (x, y) and time t, and (ii) $I(x+u,\ y+v,$ t+dt) is the pixel brightness in the next frame at tdt after (u, v) displacements from (x, y) in x and y directions, respectively. The second constraint is "spatial smoothness," which prevents discontinuities in the flow field, as follows

$$|\nabla u|^2=\left(\frac{\partial u}{\partial x}\right)^2+\left(\frac{\partial u}{\partial y}\right)^2 and,\ |\nabla v|^2=\left(\frac{\partial v}{\partial x}\right)^2+\left(\frac{\partial v}{\partial y}\right)^2. \tag{10}$$

These two constraints are combined to use the first-order form of Tikhonov's formulation for solving the minimization problem (Horn and Schunck, 1981; Liu and Shen, 2008). Mathematically,

$$\min_{u,\ v}\left\{\int\left(I_t+I_x u+I_y v\right)^2 dxdy+\alpha\int\left(|\nabla u|^2+|\nabla v|^2\right)dxdy\right\}, \tag{11}$$

where (i) I_t, I_x, and I_y are derivatives of $I(x, y, t)$ with respect to time, spatial direction x and y, respectively, and (ii) α is the ratio of weights of the brightness constancy integral to that of spatial smoothness. This equation is solved numerically to estimate the values of u and v (Akemann et al., 2012).

Intermediate PC-MRI Synthesis

Given two input PC-MRI I_0 and I_1 and a time $t \in (0, 1)$, our purpose is to estimate the intermediate PC-MRI $\hat{I}$ at time $T = t$. Based on HS optical flow and inspired by intermediate video frame interpolation (Meyer et al., 2015; Jiang et al., 2018), we propose fusing the warped input PC-MRI at time $T = t$. Let $(u, v)_{t\to 0}$ and $(u, v)_{t\to 1}$ represent the optical flow from I_t to I_0 and I_t to I_1, respectively. We can synthesize the intermediate PC-MRI $\widehat{I_t}$ as follows

$$\hat{I}_t=\alpha_0\bigodot g\left(I_0,\ (u,v)_{t\to 0}\right)(1-\alpha_0)\bigodot g\left(I_0,\ (u,v)_{t\to 1}\right), \tag{12}$$

where $g(\cdot,\cdot)$ is a backward warping function, which can be executed using bilinear interpolation and is differentiable (Zhou et al., 2016). The parameter α_0 controls the contribution of the two input PC-MRI images, and depends on two factors: temporal consistency and occlusion reasoning (Jiang et al., 2018). The $\odot$ represents element-wise multiplication, implying content perception weighting of input PC-MRI. For temporal consistency, the closer the time step $T = t$ is to $T = 0$, the greater contribution of I_0 makes to $\hat{I}_t$; a similar property holds for I_1 (Jiang et al., 2018). On the other hand, considering the particularity of PC-MRI acquisition process, the occlusion question can be neglected. As a result, we can obtain the intermediate PC-MRI on consecutive frames based on Eq. (12) to produce a continuous velocity field for computing LAVD.

The pipeline for Optical flow-LAVD based identification of Lagrangian vortex ring consists of four steps, and these steps are presented in **Figure 2**. First, the HS optical flow computation on consecutive frames is carried out. Second, based on the HS optical flow, the intermediate PC-MRI can be synthesized to produce a continuous velocity field. Third, the segmentation of the interested cardiac chamber is performed. Finally, the LAVD is computed and used to detect the Lagrangian vortex core and region within the cardiac chamber.

RESULTS OF ANALYTICAL STUDIES

Optical Flow-LAVD Based Vortex Ring Identification and Analysis

The proposed algorithm successfully identifies large-scale Lagrangian vortex rings that appear in the RA and analyzes their changes and evolution during selected time frame indices from $N_t = 8$ *to* 18, As expressed in our previous research, vortex within the RA is formed and deformed during this period (Wong et al., 2009a). The variation of the Lagrangian vortex ring core and region can be visually examined by using the red circular markers as shown in **Figure 3**. The computation of the LAVD within the RA is based on Eq. (8), and the convexity deficiency of a closed curve in the plane is defined as the ratio of the area difference between the curve and its convex hull to the area enclosed by the curve (Haller et al., 2015). Then we can refer to our work in Yang et al. (2021) and visualized analysis, for the convexity deficiency threshold $d_{max} = 1$, to ensure the tubular characteristics in the heart (Yang et al., 2021). In addition, the volume of each Lagrangian vortex ring can be computed as the product of the area inside the delineation and the slice thickness, which is in line with an earlier study by Töger et al. (2012). **Figure 3** illustrates the temporal evolution of vortex volume within the RA of the healthy subject.

Horn-Schunck Optical Flow Based Intermediate PC-MRI Synthesis Analysis

Impact of Different Components on the Quality of PC-MRIs

For evaluation, we performed a number of ground-truth comparisons using the leave-some-out method (Meyer et al., 2015), i.e., the intermediate PC-MRIs are synthesized and compared to the original ones. We reported the Structural Similarity Index (SSIM) scores of predictions and ground-truth, as well as the interpolation errors (IE) (Meyer et al., 2015). To prevent noise and irrelevant content interference, we just computed SSIM and IE of the interested cardiac chamber.

We analyzed the impact of leaving out an increasing number of intermediate PC-MRI on decaying in image quality. The plot in **Figure 4A** visualizes the variation of IE of synthesized PC-MRI when skipping increasing frames. At the same time, we derived the SSIM and IE at different algorithm steps, as shown in **Table 1**. It can be seen that the optical flow computed before segmentation can obtain better intermediate images. Based on Eq. (11), we also carried out an experimental analysis of the influence of the main parameter α on the quality of reconstructed intermediate PC-MRI, as shown in **Figure 4B**.

Comparison With Other Interpolation Methods

We compared three different views including optical flow interpolation, phase-based interpolation, and linear interpolation to deal with the construction of the intermediate PC-MRI. The most popular methods for finding pixel correspondences across images are based on optical flow (Sun et al., 2010; Baker et al., 2011), while using image phase information directly to replace image brightness in the data term of standard optical flow formulations has been noticeable (Fleet and Jepson, 1990; Meyer et al., 2015). The phase-driven frame interpolation concept was applied to the discrete Fourier transform of an image, and it decomposes the input images into several oriented frequency bands $R_{\omega,\theta}$ by steerable pyramid filters (Meyer et al., 2015). Then, Linear interpolation in time and space has been adopted to produce a continuous velocity field based on PC-MR velocity data (Töger et al., 2012). We have detailed the comparison of SSIM and IE during the selected time frame indices from $N_t = 8$ *to* 18, as shown in **Figures 4B,C**. By comparing SSIM and IE, we find that the HS optical flow method has higher prediction quality, especially in the case of existence of a large-scale vortex. Hence, combined with HS optical flow based Intermediate PC-MRI synthesis to recover a more accurate continuous velocity field, the LAVD can describe precisely the evolution of Lagrangian vortex rings within the RA, to help medical experts enhance their understanding of the physiological functions of swirling blood flow.

Visual Analysis and the Experiment on Segmentation Dependence

We have carried out a visualization analysis of the difference between Optical flow-LAVD and linear interpolation-LAVD, as shown in **Figure 5**. The identification results of vortex rings within the RA based on different methods are represented by red and orange circular markers, respectively. In order to clearly reveal the distinction of the visual results, we selected time frame indices of large-scale vortex existent from $N_t = 8$ *to* 10. It is found that the Optical flow-LAVD can more accurately describe the complexity of the Lagrangian vortex ring boundary.

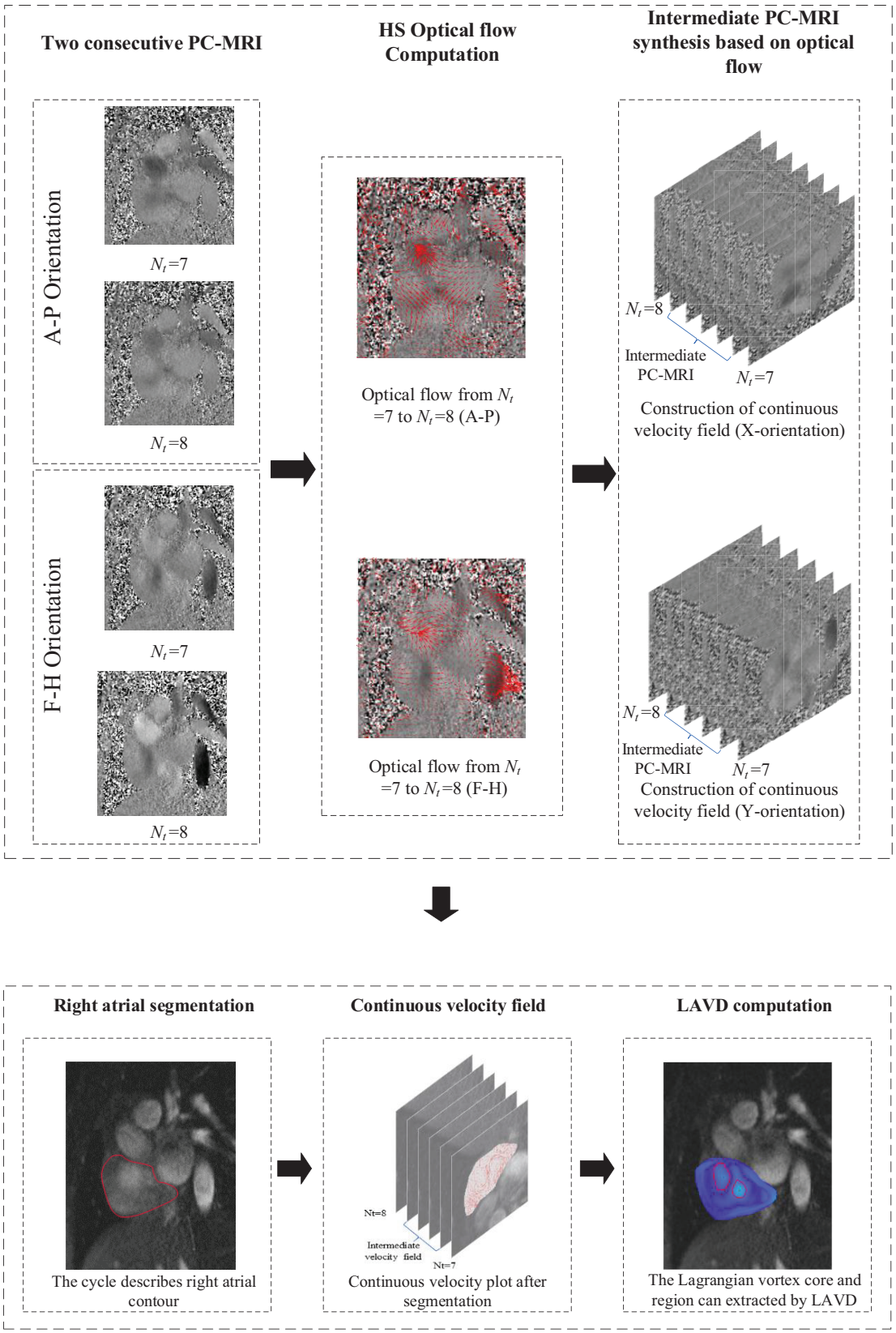

FIGURE 2 | The pipeline of the proposed Optical flow-LAVD based identification of Lagrangian vortex ring.

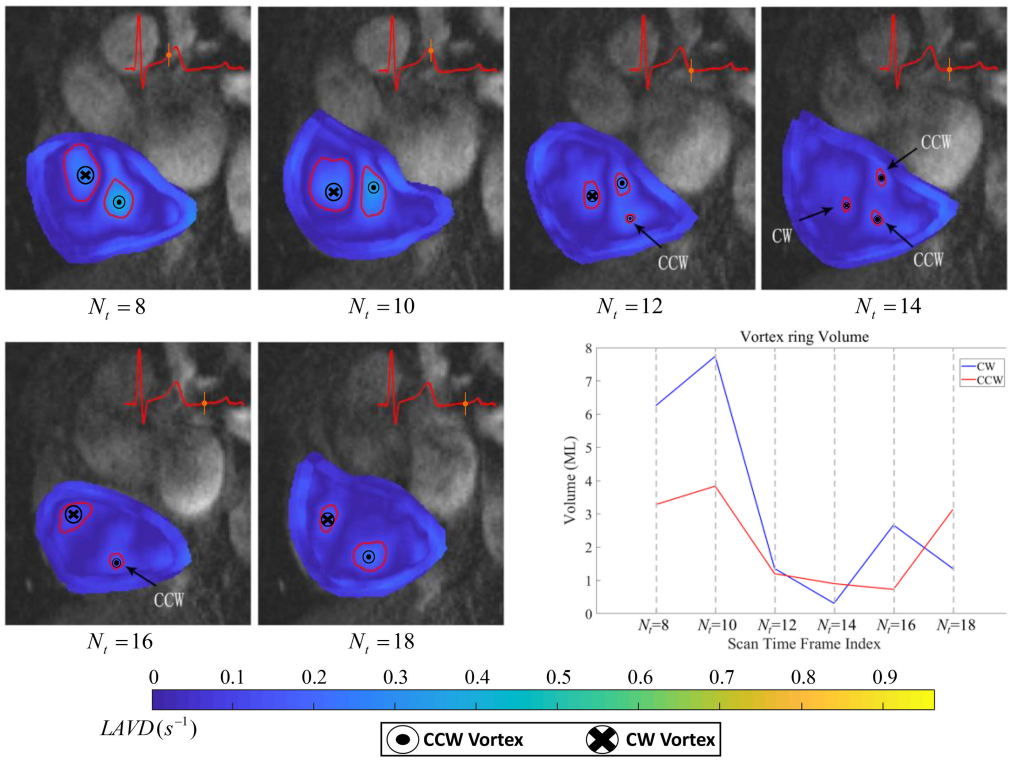

FIGURE 3 | Evolution of Lagrangian vortex rings of a healthy subject. From time frame $N_t = 8$ *to* 18, the blood is swirling in both the clockwise (CW) and counter-clockwise (CCW) directions simultaneously. The LAVD contour map is produced to indicate its strength. The diagram at the lower right shows the vortex volume measured at the level of the two opposite rotation vortex rings.

In order to assess the sensitivity of Optical flow-LAVD based vortex ring extraction using different segmentation masks, we have derived the Dice similarity coefficient (DSC) as

$$\frac{2TP}{TP + FP + FN}, \tag{13}$$

where the TP, FP, TN, and FN represent the number of true positives, false positives, true negatives, and false negatives, respectively. We applied two different masks to selected time frame indices from $N_t = 8$ *to* 18 and computed the DSC of the identification results of vortex rings under manual segmentation and automatic segmentation. **Table 2** provides the DSC and segmentation time to verify the robustness of the Optical flow-LAVD to different segmentation masks.

DISCUSSION

We have presented a novel method for the identification of Lagrangian vortex rings core and region within the RA from PC-MRI data to allow for quantitative vortex volume. In particular, we have demonstrated (i) the variation in Lagrangian vortex rings within the RA during the diastolic phase from time frame indices $N_t = 8$ *to* 18 of one cardiac cycle with 25 phases. (ii) the characteristics of the PC-MRI by constructing accurate continuous velocity fields, based on an image-optical flow algorithm for computing LAVD.

Lagrangian Vortex Rings Within RA Identification and Analysis

We have extracted the large-scare Lagrangian vortex rings that appear in the RA, and have analyzed their development and changes during selected time frame indices from $N_t = 8$ *to* 18, which is in accordance with the previous publications (Wong et al., 2009a,b, 2010). The development of the vortex rings core and region can be visually examined using red circular as shown in **Figure 3**. In addition, we superimposed the corresponding MR images onto these LAVD maps to give an indication of the location of the vortex features with respect to the chamber walls. In the beginning during time frame $N_t = 8$ *to* 10, two large-scale Lagrangian vortex rings exist in the chamber simultaneously, and we can note from **Figure 3** that one counter-clockwise (CCW) Lagrangian vortex ring exists in the atrium along with a second clockwise (CW) Lagrangian vortex ring approximately to the upper-left of it. At the same time, the consequences of LAVD based identification are asymmetric, subject to the asymmetry of the heart as a whole (Kilner et al., 2000). Then later during time frame $N_t = 12$ *to* 14, two typical vortex rings are partly dissipated, and they cannot remain strictly toroid and change over time. In particular, the CCW Lagrangian

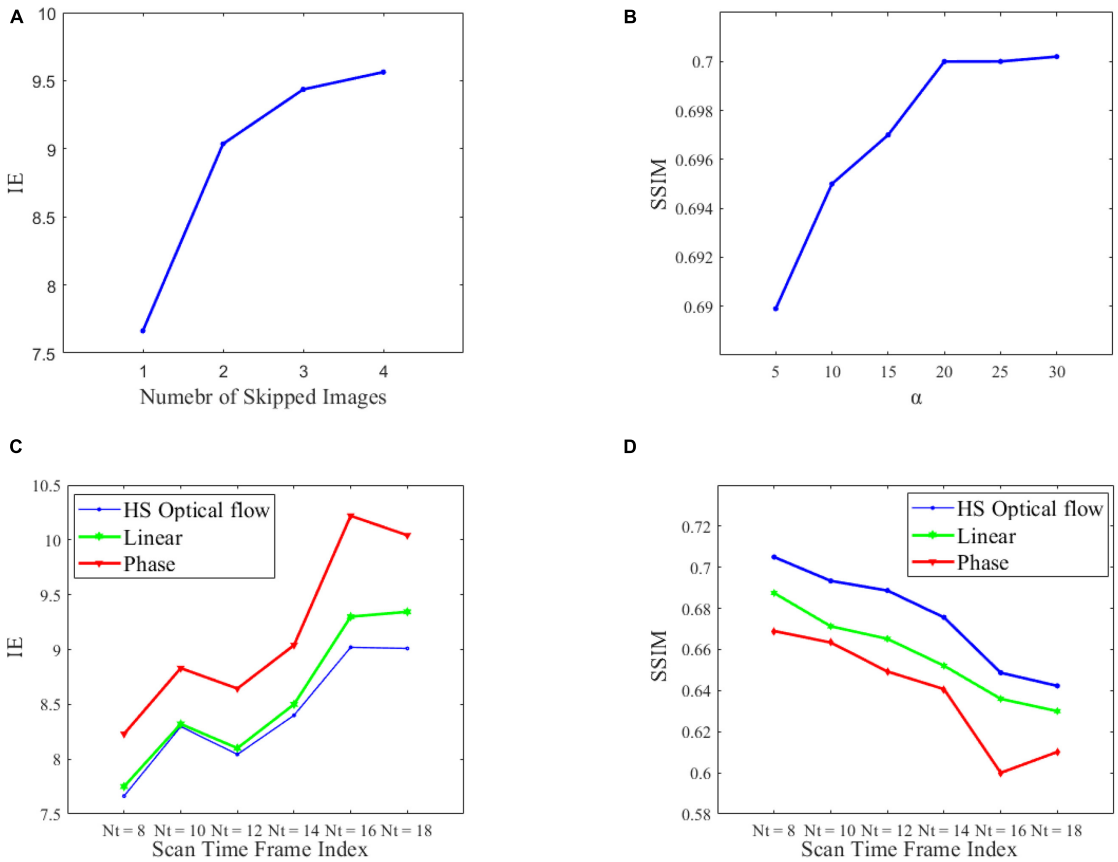

FIGURE 4 | Performance of the proposed algorithm. **(A)** Quality of interpolated PC-MRI vs. the number of skipped images. **(B)** The influence of parameter α on SSIM. **(C,D)** IE and SSIM performances during the selected time frame indices for optical flow interpolation, phase-based interpolation, and linear interpolation, to deal with the construction of the intermediate PC-MRI.

vortex ring decomposes into two vortex rings of different scales, one of which moves toward the chamber wall regions. Eventually during time frame $N_t = 16$ *to* 18, we identified two dominant vortex rings of opposite rotation to grow in scale until the CCW vortex ring becomes slightly larger than the CW one.

The relative rotation region variation of two vortex rings is demonstrated by plotting the vortex volume with respect to cardiac time frames, as shown in **Figure 3**. Toward the end-systole from $N_t = 8$ *to* 10, the flow slows down and a corresponding dilation of the RA induces the flow in the inferior and superior *vena cava* to accelerate (Kilner et al., 2000). We note that the volume of two vortex rings of opposite rotation is increased, and the volume of the CW vortex ring and CCW vortex ring grow from 6.26 *to* 7.74 *ml* and 3.28 *to* 3.84 *ml*, respectively. With the opening of the atrioventricular valves, the blood surges into the relaxed ventricle from $N_t = 12$ *to* 14 (Kilner et al., 2000). The volume of the two vortex rings is decreased, and declines from 1.36 *to* 0.31 *ml* and 1.22 *to* 0.90 *ml* (the volume sum of two CCW vortex rings), respectively. From time frame $N_t = 16$ *to* 18, the volume of CW and CCW vortex rings change successively and range from 2.66 *to* 1.35 *ml* and0.73 *to* 3.13 *ml*, respectively. The enlarged vortex rings can minimize stasis and thereby facilitate the flow of blood into the ventricle (Töger et al., 2012). After $N_t =$ 18, we do not extract the Lagrangian vortex ring within RA, as a large amount of blood had flowed into the ventricle and there was no strict toroid flow. we set the convexity deficiency threshold to 1 in order to ensure the tubular characteristics (Haller, 2016; Yang et al., 2021). In conclusion, based on the statistics of the volume plot, we can describe the Lagrangian vortex ring development in a quantitative manner. Lagrangian vortex rings are distinctive material curves that organize the blood flow (Günther and Theisel, 2018). They present steady swirling scale flow, and manifest the persistence of Lagrangian vortex rings within the heart, to enable understanding of the role of evolution of vortices in the blood flow. We have also visualized the stretching and diffusion of vortex rings, which give deeper insight into vortex dynamics, revealing how vortex rings are weakened or reinforced by the cardiac flow field.

TABLE 1 | Comparison in different segmentation order.

	IE	SSIM
Before-segmentation	8.52	0.55
After-segmentation	8.29	0.67

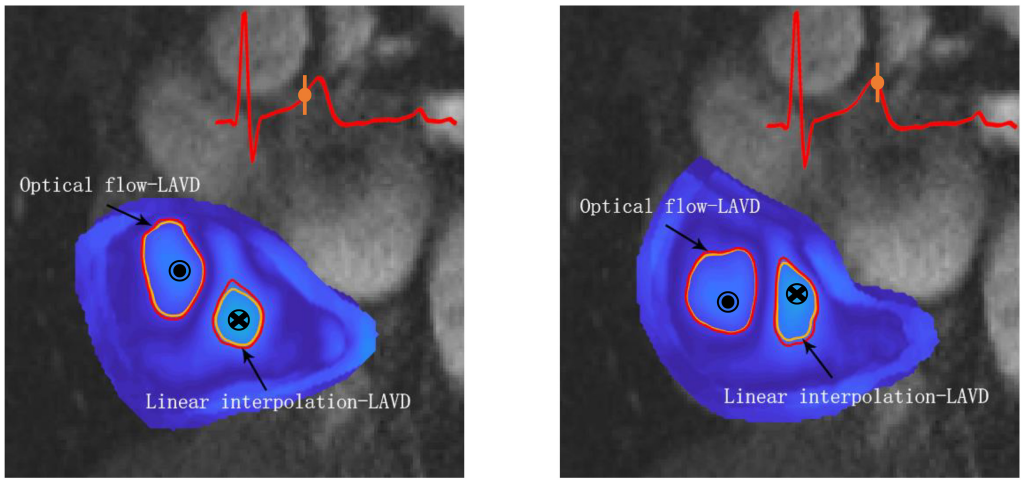

$N_t = 8$ $N_t = 10$

FIGURE 5 | The identification results of Lagrangian vortex rings based on Optical flow-LAVD (red) and linear interpolation-LAVD (orange).

Intermediate PC-MRI Synthesis Analysis

Impact of Different Components on the Quality of PC-MRIs

We first investigated whether leaving out an increasing number of intermediate PC-MRI decays the synthesis quality. We computed IE under four different conditions: skipping single, two, three, and four frames. **Figure 4A** shows the degradation in the quality of interpolated PC-MRI with increased motion between frames. In order to estimate it more reliably and accurately, we simply use two consecutive frames to construct a continuous velocity field. We have also investigated the contribution of segmentation in our method, as shown in **Table 2**. By applying the step of computing optical flow first and then segmentation, better interpolated PC-MRI can be acquired, which is caused by the variation of RA contours and globality of HS optical flow (Afrashteh et al., 2017). We further studied the influence of the main parameter α on the quality of interpolated PC-MRI. We can observe from **Figure 4B** that as the parameter α increases, the SSIM score improves. However, there is a specific threshold, such that over-sizing using larger α has little effect on reliability.

Comparison With Existing Interpolation Methods

We have compared the HS optical flow-based Intermediate PC-MRI synthesis method with other methods including linear interpolation (Töger et al., 2012) and phase-based interpolation (Meyer et al., 2015). They are derived from different understandings of images. The IE scores and SSIM scores on each selected time frame from three methods are shown in **Figures 4C,D**, and the overall evaluation is shown in **Table 3**. Our Optical flow-LAVD model achieves the best performance on selected time frame indices. Particularly, the HS optical flow can achieve the best IE and SSIM during the large-scale vortex existent periods from $Nt = 8$ *to* 10. In comparison, the quality of phase-based interpolated PC-MRI is slightly worse. This interpolation method captures phase information, but the irrelevant content and noise of PC-MRI have a negative effect. The variation in IE and SSIM during selected time frame indices is typically declining. This is due to larger pixel displacement and weakly turbulent flow pattern during the end of RA diastole period (Kheradvar et al., 2019).

Visual Analysis and Segmentation Dependence

Between the Optical flow-LAVD and linear interpolation-LAVD, visual analysis finds the differences in their Lagrangian vortex ring identification results. During the large-scale vortex existence period, the Optical flow-LAVD detected vortex ring region is wide and its boundary fits a complex ellipse, especially in the case of CW vortex rings shown in **Figure 5**. It can be found that the Optical flow-LAVD can more realistically describe the Lagrangian vortex rings formation. Furthermore, the computation of LAVD is an integral process. Two different vortex ring identification results boil down to the accumulation of

TABLE 2 | Comparison with different segment masks.

Method	DSC	Segmentation time (s)
Automatic segmentation	0.89	18
Manual segmentation	1	52

TABLE 3 | Comparisons with different interpolation methods.

	IE	SSIM
HS optical flow interpolation	**8.29**	**0.67**
Linear interpolation	8.56	0.65
Phased-based interpolation	9.17	0.62

Bold values highlight the highest scores.

numerical integration errors, which also indicates the importance of the high-performance interpolation method.

Regarding the vortex ring identification results under the manual segmentation as the reference condition, we compute the overlap of vortex regions under automatic segmentation and compare the segmentation time. The automatic segmentation masks are seen to yield poor agreement for Lagrangian vortex ring extraction, as shown in **Table 2**, which demonstrates the sensitivity of Optical flow-LAVD when using different segmentation approaches. While the LAVD is objective, we note that this measure is relative to its neighborhood, and its value-range depends on the neighborhood size (Günther and Theisel, 2018). Thus, the precision of automatic segmentation to achieve our algorithm speed-up is needed.

In summary, the HS optical flow-based interpolation method achieves the best results over the PC-MRI sequence, in generating a more accurate continuous velocity field. This is remarkable and interesting, Considering the characteristics of the PC-MRI, we combine the image-interpolation algorithm to compute the Lagrangian features of cardiovascular blood flow.

Limitations

There are several works that need to be improved in the proposed purposed method. Firstly, no reference standard exists for Lagrangian vortex rings within the cardiac chambers. However, the numerical simulation model we used is in excellent agreement with the model of Haller et al. (2015). There are no comparison experiments between healthy controls and patients. Nevertheless, the focus of this study is to provide a proof of concept of Optical flow-LAVD based vortex ring identification and, as discussed previously, combining optical flow can improve the accuracy of describing vortex evolution. In our following investigations, we will consider obtaining the synthetic data based on fluid dynamics simulations (Rispoli et al., 2015; Rajat et al., 2016)and diagnosis of additional pathological patients, in order to further validate the performance of our method, based on Optical Flow-LAVD. Vortices within the ventricular chambers reflect the pathophysiological link between the diastolic filling and systolic ejection, and present a better reproducibility because of their higher intensity field (Hong et al., 2013; Kheradvar et al., 2019). For that purpose, identification of vortices within the ventricular chambers by Optical flow-LAVD is to be the focus of our future work. Secondly, the blood flow in the heart is accompanied by the formation of vortex rings which dynamically occupy the 3D space of the heart chamber (Kräuter et al., 2020). The 3D vortex ring extraction is significant for a more accurate description of vortex formation (Wong et al., 2009a). In fact, the computation of LAVD to identify the 3D vortex ring in the heart has not been investigated, and remains a topic for our future research. Thirdly, we have strictly set the convexity deficiency threshold to ensure the tubular characteristics, leading to ignoring some vortices with a relative ring shape (Yang et al., 2021). So, future work is required to establish an adaptive method instead of setting threshold artificially. We also recognize that LAVD is relative to its neighborhood, and its value-range depends on the neighborhood size (Günther and Theisel, 2018). Thus, a high demand is placed on the method of high-precision segmentation of the heart chamber. Finally, we have used the HS optical flow-based interpolation method to achieve the best results over the PC-MRI sequence. However, the IE scores and SSIM scores on each selected time frame highlight the insufficiency of the interpolation model's capacity to deal with the challenging motion regions of the heart; the temporal sampling in medical image sequences are lower than that of natural scene videos (Guo et al., 2020; Samuel et al., 2020), and the computation of optical flow is expensive (Meyer et al., 2015; Samuel et al., 2017). Improving the optical flow-based interpolation performance, and decreasing the computation time are also key factors for our future research.

CONCLUSION

In this study, we have proposed a novel cardiac Lagrangian vortex rings identification method, based on a combination of LAVD and optical flow. We first estimate the optical flow between two consecutive PC-MRI, and the intermediate optical flow fields can be approximated by warping the procedure for constructing continuous velocity fields. We then compute LAVD by using the synthesized velocity field to accurately extract the Lagrangian vortex core and region within RA. The temporal evolution of Lagrangian vortex rings within RA is described for the first time; it is found that the optical flow-based interpolation method achieves the best results over the PC-MRI sequence. Our method provides a solution for the cardiac vortex ring formation analysis, and improves understanding of blood flow dynamics within the heart.

DATA AVAILABILITY STATEMENT

The raw data supporting the conclusions of this article will be made available by the authors, without undue reservation.

ETHICS STATEMENT

The studies involving human participants were reviewed and approved by the Royal Adelaide Hospital Committee and the Institutional Review Board. The patients/participants provided their written informed consent to participate in this study.

AUTHOR CONTRIBUTIONS

KY, SW, OS, HZ, DG, DY, and KW processed the data for analysis and performed the statistical analysis. All authors contributed to the study design, data interpretation, and writing of the report.

FUNDING

This work was funded by the National Natural Science Foundation of China (Grant Number 81771927).

REFERENCES

Afrashteh, N., Inayat, S., Mohsenvand, M., and Mohajerani, M. H. (2017). Optical-flow analysis toolbox for characterization of spatiotemporal dynamics in mesoscale optical imaging of brain activity. *Neuroimage* 153, 58–74. doi: 10.1016/j.neuroimage.2017.03.034

Akemann, W., Mutoh, H., Perron, A., Park, Y. K., Iwamoto, Y., and Knöpfel, T. (2012). Imaging neural circuit dynamics with a voltage-sensitive fluorescent protein. *J. Neurophysiol.* 108, 2323–2337. doi: 10.1152/jn.00452.2012

Baker, S., Scharstein, D., Lewis, J. P., Roth, S., Black, M. J., and Szeliski, R. (2011). A database and evaluation methodology for optical flow. *Int. J. Comput. Vis.* 92, 1–31. doi: 10.1007/s11263-010-0390-2

Dabiri, J. O., and Gharib, M. (2005). The role of optimal vortex formation in biological fluid transport. *Proc. Biol. Sci.* 272, 1557–1560. doi: 10.1098/rspb.2005.3109

Dyverfeldt, P., Bissell, M., Barker, A. J., Bolger, A. F., Carlhäll, C. J., Ebbers, T., et al. (2015). 4D flow cardiovascular magnetic resonance consensus statement. *Cardiovasc. Magn. Reson.* 17:72.

Elbaz, M. S. M., Calkoen, E. E., Westenberg, J. J. M., Lelieveldt, B. P. F., Wroest, A. A., and Geest, R. (2014). Vortex flow during early and late left ventricular filling in normal subjects: quantitative characterization using retrospectively-gated 4D flow cardiovascular magnetic resonance and three-dimensional vortex core analysis. *J. Cardiovasc. Magn. Reson.* 16:78.

Epps, B. (2017). "Review of vortex identification methods," in *Proceedings of the 55th AIAA Aerospace Sciences Meeting*, (Grapevine, TX), 989–1001.

Fleet, D. J., and Jepson, A. D. (1990). Computation of component image velocity from local phase information. *Int. J. Comput. Vis.* 5, 77–104. doi: 10.1007/bf00056772

Günther, T., and Theisel, H. (2018). The state of the art in vortex extraction. *Comput. Graph. Forum* 37, 149–173. doi: 10.1111/cgf.13319

Guo, Y. Y., Lie, B., Ahn, E., Feng, D., Wang, Q., and Kim, J. (2020). "A spatiotemporal volumetric interpolation network for 4D dynamic medical image," in *Proceedings of the 2020 IEEE/CVF Conference on Computer Vision and Pattern Recognition*, (Seattle, WA), 4725–4734.

Haller, G. (2016). Dynamic rotation and stretch tensors from a dynamic polar decomposition. *J. Mech. Phys. Solids* 86, 70–93. doi: 10.1016/j.jmps.2015.10.002

Haller, G., Hadjighasem, A., Farazmand, M., and Huhn, F. (2015). Defining coherent vortices objectively from the vorticity. *J. Fluid Mech.* 795, 136–173. doi: 10.1017/jfm.2016.151

Hong, G. R., Kim, M., Pedrizzetti, G., and Vannan, M. A. (2013). Current clinical application of intracardiac flow analysis using echocardiography. *J. Cardiovasc. Ultrasound* 21, 155–162. doi: 10.4250/jcu.2013.21.4.155

Horn, B. K., and Schunck, B. G. (1981). Determining optical flow. *Artif. Intell.* 17, 185–204.

Jiang, H. Z., Sun, D. Q., Jampani, V., Yang, M. H., Miller, E. L., and Kautz, J. (2018). "Super SloMo: high quality estimation of multiple intermediate frames for video interpolation," in *Proceedings of the 2018 IEEE/CVF Conference on Computer Vision and Pattern Recognition* (Salt Lake City, Hawaii: Hawaii), 9000–9008.

Katsanoulis, S., Farazmand, M., Serra, M., and Haller, G. (2017). Vortex boundaries as barriers to diffusive vorticity transport in two-dimensional flows. *Phys. Rev. Fluids* 5:24701.

Kheradvar, A., and Gharib, M. (2007). Influence of ventricular pressure drop on mitral annulus dynamics through the process of vortex ring formation. *Ann. Biomed. Eng.* 35, 2050–2064. doi: 10.1007/s10439-007-9382-y

Kheradvar, A., and Gharib, M. (2009). On mitral valve dynamics and its connection to early diastolic flow. *Ann. Biomed. Eng.* 37, 1–13. doi: 10.1007/s10439-008-9588-7

Kheradvar, A., Milano, M., and Gharib, M. (2007). Correlation between vortex ring formation and mitral annulus dynamics during ventricular rapid filling. *ASAIO J.* 53, 8–16. doi: 10.1097/01.mat.0000249870.44625.22

Kheradvar, A., Rickers, C., Morisawa, D., Kim, M., Hong, G. R., and Pedrizzetti, G. (2019). Diagnostic and prognostic significance of cardiovascular vortex formation. *J. Cardiol.* 74, 403–411. doi: 10.1016/j.jjcc.2019.05.005

Kilner, P. J., Yang, G. Z., Wilkes, A. J., Mohiaddin, R. H., Firmin, D. N., and Yacoub, M. H. (2000). Asymmetric redirection of flow through the heart. *Nature* 404, 759–761. doi: 10.1038/35008075

Kräuter, C., Reiter, U., Reiter, C., Nizhnikava, V., Masana, M., Schmidt, A., et al. (2020). Automated mitral valve vortex ring extraction from 4D-flow MRI. *Magn. Reson. Med.* 84, 3396–3408. doi: 10.1002/mrm.28361

Liu, T., and Shen, L. (2008). Fluid flow and optical flow. *J. Fluid Mech.* 614, 253–291. doi: 10.1017/s0022112008003273

Markl, M., Harloff, A., Bley, T. A., Zaitsev, M., Jung, B., Weigang, E., et al. (2007). Time-resolved 3D MR velocity mapping at 3T: improved navigator-gated assessment of vascular anatomy and blood flow. *Magn. Reson. Imaging* 25, 824–831. doi: 10.1002/jmri.20871

Meyer, S., Wang, O., Zimmer, H., Grosse, M., and Hornung, A. S. (2015). "Phase-based frame interpolation for video," in *Proceedings of the 2015 IEEE Conference on Computer Vision and Pattern Recognition*, (Boston, MA), 1410–1418.

Rajat, M., Seo, J. H., Vedula, V., Choi, Y. J., Liu, H., Huang, H. H., et al. (2016). Computational modeling of cardiac hemodynamics: current status and future outlook. *J. Comput. Phys.* 305, 1065–1082.

Rispoli, V. C., Nielsen, J. F., Nayak, K. S., and Carvalho, J. L. A. (2015). Computational fluid dynamics simulations of blood flow regularized by 3D phase contrast MRI. *BioMed. Eng. OnLine* 14:110.

Samuel, O. W., Asogbon, G. M., Sangaiah, A. K., Fang, P., and Li, G. (2017). An integrated decision support system based on ANN and Fuzzy_AHP for heart failure risk prediction. *Expert Syst. Appl.* 68, 163–172. doi: 10.1016/j.eswa.2016.10.020

Samuel, O. W., Yang, B., Geng, Y., Asogbon, M. G., Pirbhulal, S., Mzurikwao, D., et al. (2020). A new technique for the prediction of heart failure risk driven by hierarchical neighborhood component-based learning and adaptive multi-layer networks. *Future Gener. Comput. Syst.* 110, 781–794. doi: 10.1016/j.future.2019.10.034

Sengupta, P. P., Korinek, J., and Jahangir, A. (2006). Left ventricular structure and function: basic science for cardiac imaging. *J. Am. Coll. Cardiol.* 48, 1988–2001.

Sun, D., Roth, S., and Black, M. J. (2010). "Secrets of optical flow estimation and their principles," in *Proceedings of the 2010 IEEE Computer Society Conference on Computer Vision and Pattern Recognition*, (San Francisco, CA), 2432–2439.

Töger, J., Kanski, M., Carlsson, M., Kovacs, S. J., Söderlind, G., Arheden, H., et al. (2012). Vortex ring formation in the left ventricle of the heart: analysis by 4d flow mri and lagrangian coherent structures. *Ann. Biomed. Eng.* 40, 2652–2662. doi: 10.1007/s10439-012-0615-3

Wong, K. K. L., Kelso, R. M., Worthley, S. G., Sanders, P., Mazumdar, J., and Abbott, D. (2009a). Cardiac flow analysis applied to phase contrast magnetic resonance imaging of the heart. *Ann. Biomed. Eng.* 37, 1495–1515. doi: 10.1007/s10439-009-9709-y

Wong, K. K. L., Kelso, R. M., Worthley, S. G., Sanders, P., Mazumdar, J., and Abbott, D. (2009b). Theory and validation of magnetic resonance fluid motion estimation using intensity flow data. *PLoS One* 4:e4747. doi: 10.1371/journal.pone.0004747

Wong, K. K. L., Tu, J., Kelso, R. M., Worthley, S. G., Sanders, P., Mazumdar, J., et al. (2010). Cardiac flow component analysis. *Med. Eng. Phys.* 32, 174–188. doi: 10.1016/j.medengphy.2009.11.007

Wulff, J., Sevilla-Lara, L., and Black, M. J. (2017). "Optical flow in mostly rigid scenes," in *Proceedings of the 2017 IEEE Conference on Computer Vision and Pattern Recognition* (Salt Lake City, Hawaii: Hawaii), 6911–6920.

Xu, J., Ranftl, R., and Koltun, V. (2017). "Accurate optical flow via direct cost volume processing," in *Proceedings of the 2017 IEEE Conference on Computer Vision and Pattern Recognition* (Salt Lake City, Hawaii: Hawaii), 5807–5815.

Yang, K., Wu, S., Zhang, H., Ghista, D. N., Samuel, O. W., and Wong, K. K. L. (2021). Lagrangian-averaged vorticity deviation of spiraling blood flow in the heart during isovolumic contraction and ejection phases. *Med. Biol. Eng. Comput.* 59, 1417–1430. doi: 10.1007/s11517-021-02366-2

Yang, Z. H., and Melissa, A. G. (2015). "Comparing leading and trailing edge vortex circulation history with vortex identification and tracking methods," in *Proceedings of the 54th AIAA Aerospace Sciences Meeting*, (San Diego, CA), 2082–2092.

Zhou, T., Tulsiani, S., Sun, W., Malik, J., and Efros, A. A. (2016). "View synthesis by appearance flow," in *Computer Vision – European Conference on Computer Vision 2016. Lecture Notes in Computer Science*, Vol. 9908, eds B. Leibe, J. Matas, N. Sebe, and M. Welling (Cham: Springer), 286–301. doi: 10.1007/978-3-319-46493-0_18

Conflict of Interest: DG was employed by company University 2020 Foundation, Inc.

The remaining authors declare that the research was conducted in the absence of any commercial or financial relationships that could be construed as a potential conflict of interest.

Publisher's Note: All claims expressed in this article are solely those of the authors and do not necessarily represent those of their affiliated organizations, or those of the publisher, the editors and the reviewers. Any product that may be evaluated in this article, or claim that may be made by its manufacturer, is not guaranteed or endorsed by the publisher.

frontiers in Physiology

ORIGINAL RESEARCH
published: 22 September 2021
doi: 10.3389/fphys.2021.690453

A Phase Defect Framework for the Analysis of Cardiac Arrhythmia Patterns

Louise Arno[1], *Jan Quan*[1], *Nhan T. Nguyen*[1], *Maarten Vanmarcke*[1], *Elena G. Tolkacheva*[2] *and Hans Dierckx*[1]*

[1] KULeuven Campus KULAK, Department of Mathematics, Kortrijk, Belgium, [2] Biomedical Engineering Department, University of Minnesota, Minneapolis, MN, United States

During cardiac arrhythmias, dynamical patterns of electrical activation form and evolve, which are of interest to understand and cure heart rhythm disorders. The analysis of these patterns is commonly performed by calculating the local activation phase and searching for phase singularities (PSs), i.e., points around which all phases are present. Here we propose an alternative framework, which focuses on phase defect lines (PDLs) and surfaces (PDSs) as more general mechanisms, which include PSs as a specific case. The proposed framework enables two conceptual unifications: between the local activation time and phase description, and between conduction block lines and the central regions of linear-core rotors. A simple PDL detection method is proposed and applied to data from simulations and optical mapping experiments. Our analysis of ventricular tachycardia in rabbit hearts ($n = 6$) shows that nearly all detected PSs were found on PDLs, but the PDLs had a significantly longer lifespan than the detected PSs. Since the proposed framework revisits basic building blocks of cardiac activation patterns, it can become a useful tool for further theory development and experimental analysis.

Keywords: cardiac arrhythmia, spiral wave, self-organization, phase defect, non-linear analysis

OPEN ACCESS

Edited by:
Anmar Khadra,
McGill University, Canada

Reviewed by:
Gil Bub,
McGill University, Canada
Richard H. Clayton,
The University of Sheffield, United Kingdom

***Correspondence:**
Hans Dierckx
h.dierckx@kuleuven.be

Specialty section:
This article was submitted to Computational Physiology and Medicine, a section of the journal Frontiers in Physiology

Received: *02 April 2021*
Accepted: *19 August 2021*
Published: *22 September 2021*

Citation:
Arno L, Quan J, Nguyen NT, Vanmarcke M, Tolkacheva EG and Dierckx H (2021) A Phase Defect Framework for the Analysis of Cardiac Arrhythmia Patterns. Front. Physiol. 12:690453. doi: 10.3389/fphys.2021.690453

1. INTRODUCTION

About once per second, a wave of electrical depolarization travels through the heart, coordinating its mechanical contraction. The heart is a prime example of a dynamical system that can self-organize across different scales: changes in the flow of ions through the cell membrane affect the dynamics of the emergent pattern and may lead to life-threatening heart rhythm disorders. For more than a century, great efforts have been allocated to understand the different dynamical mechanisms of arrhythmia initiation and maintenance in the heart. It was found that electrical activity during cardiac arrhythmias may travel in a closed circuit within the cardiac wall, and thus re-excite the heart (Mines, 1913). Later on, Allessie et al. demonstrated with electrode recordings that re-excitation of the tissue by the wave itself was also possible without a central obstacle (Allessie et al., 1973). These rotating vortices, also called rotors, were later demonstrated using optical mapping techniques, both in ventricular tachycardia (Gray et al., 1995a) and ventricular fibrillation (Gray et al., 1998).

Gray et al. (1998) also developed the concept of phase analysis to identify structures in the excitation patterns in the heart. They considered two fields $V(\vec{r}, t)$ and $R(\vec{r}, t)$ of the system and

calculated the phase of a point of the medium as the polar angle in the (V, R)-plane, see **Figure 1**:

$$\phi_{\text{act}}(V, R) = \text{atan2}(R - R_*, V - V_*) + b. \quad (1)$$

An additive constant in Equation (1) is included here to fix the absolute phase, e.g., such that resting state corresponds to $\phi_{\text{act}} = 0$. To discriminate from an alternative phase definition below, we call this classical phase the "activation phase" and denote it as ϕ_{act}.

The application of phase analysis to cardiac electrical signals during arrhythmia showed that there are few points in the medium where all possible phases meet each other, such that the point itself has no well-defined phase, see Gray et al., 1998 and **Figure 1C**. Such point is now generally accepted to be a phase singularity (PS), and since then PSs have been widely used in the analysis of cardiac excitation patterns. In two dimensions (2D), PSs are associated with the rotor core, i.e., the regions around which electrical waves revolve tachycardia or fibrillation.

In three dimensions (3D), the set of PSs in the medium extend to a dynamical curve, the rotor filament. The rotor filament has been used in many modeling and theoretical studies, as it allows for easy visualization of the rotor dynamics (Wellner et al., 2002; Clayton et al., 2005; Verschelde et al., 2007; Dierckx et al., 2012).

To identify PSs in datasets, different methods have been developed (Fenton and Karma, 1998; Gray et al., 1998; Bray and Wikswo, 2003; Clayton et al., 2005; Kuklik et al., 2015, 2017). However, these methods that look for PSs have limitations when performing detections near conduction block lines, as illustrated in **Figure 2**. A first limitation of the classical PS concept is non-robustness of PS detection methods. **Figure 2A** shows an example of a simulation of a 2D sheet of cardiac tissue using the S1-S2 stimulation protocol. The second (S2) pulse undergoes unidirectional block in the wave of the S1 pulse, leading to the formation of a conduction block line (CBL), rendered in black. The region excited by the S2 stimulus grows, turning around the CBL endpoints, but no PSs are detected at its end. Later on, when the initial S2 region has repolarized, a large number of PSs is found at the CBL, even though there is no rotor core. Moreover, the precise number of PSs found depends on the algorithm used, as shown in the third and fourth panel of **Figure 2A**. In literature, other false positives of PS identification have been reported (Podziemski et al., 2018).

A second limitation of classical PS detection algorithms is related to rotors with so-called linear cores, i.e., rotors which have a CBL in the central region (core) around which they rotate, see **Figure 2B**. If one looks at the point where the wave front ends on the CBL, this is in the classical picture a PS, see **Figure 2B**. However, looking closer, only 3 phases are found in the neighborhood of this point: excitable tissue (ahead of the front, blue), recently excited tissue (behind the front, green), and refractory tissue (across the CBL, red). A point touching three phases is not necessarily a mathematical PS, as the latter should touch all phases (**Figure 5**).

If we represent the same linear core rotor in terms of the local activation time (LAT), as indicated in the rightmost panel of **Figure 2B**, an extended CBL is clearly seen, where isochrones of activation coincide. However, this extended CBL is not captured by the classical PS analysis.

A third limitation of the classical PS detection methods concerns the coincidence of PSs and CBLs. Podziemski et al. (2018) and our own optical mapping experiments of ventricular tachycardia in rabbits indicate that the PSs are generally localized at a CBL, see **Figure 2C**. When comparing different time frames, we moreover find that the PSs tend to jump between different locations on the CBL, while the CBL itself seems to persist longer in time.

The goal of this paper is to present a new framework for phase analysis, which will lead to identification of novel structures in the regions of conduction block: phase defect lines (PDLs) and phase defect surfaces (PDSs) instead of PSs and filaments. In the context of cardiac arrhythmia patterns, interpreting linear rotor cores as a phase defect was only done very recently by Tomii et al. (2021) and in our preprint to this manuscript (Arno et al., 2021). Within this paper, we additionally introduce a phase based on local activation time, which bridges the gap between the phase viewpoint and LAT viewpoint. We propose a simple PDL detection method and apply it to data from simulations

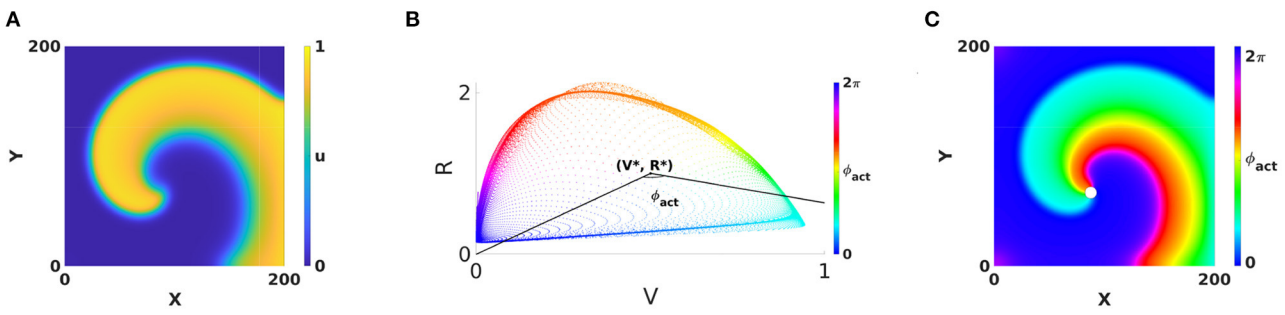

FIGURE 1 | Classical phase analysis of cardiac rotors. **(A)** Circular-core rotor with Aliev-Panfilov kinetics (Aliev and Panfilov, 1996), where in each point an activation variable u and a recovery variable v are defined. **(B)** Two observables of the system, $V = u$ and $R = v$ plotted against each other reveal a cycle corresponding to the action potential. The polar angle with respect to a point (V_*, R_*) situated within the cycle serves as a definition of activation phase. **(C)** Coloring the rotor using phase and a periodic colormap reveals a special point where all phases meet, the phase singularity (PS), see white dot. This point has $V = V_*$, $R = R_*$.

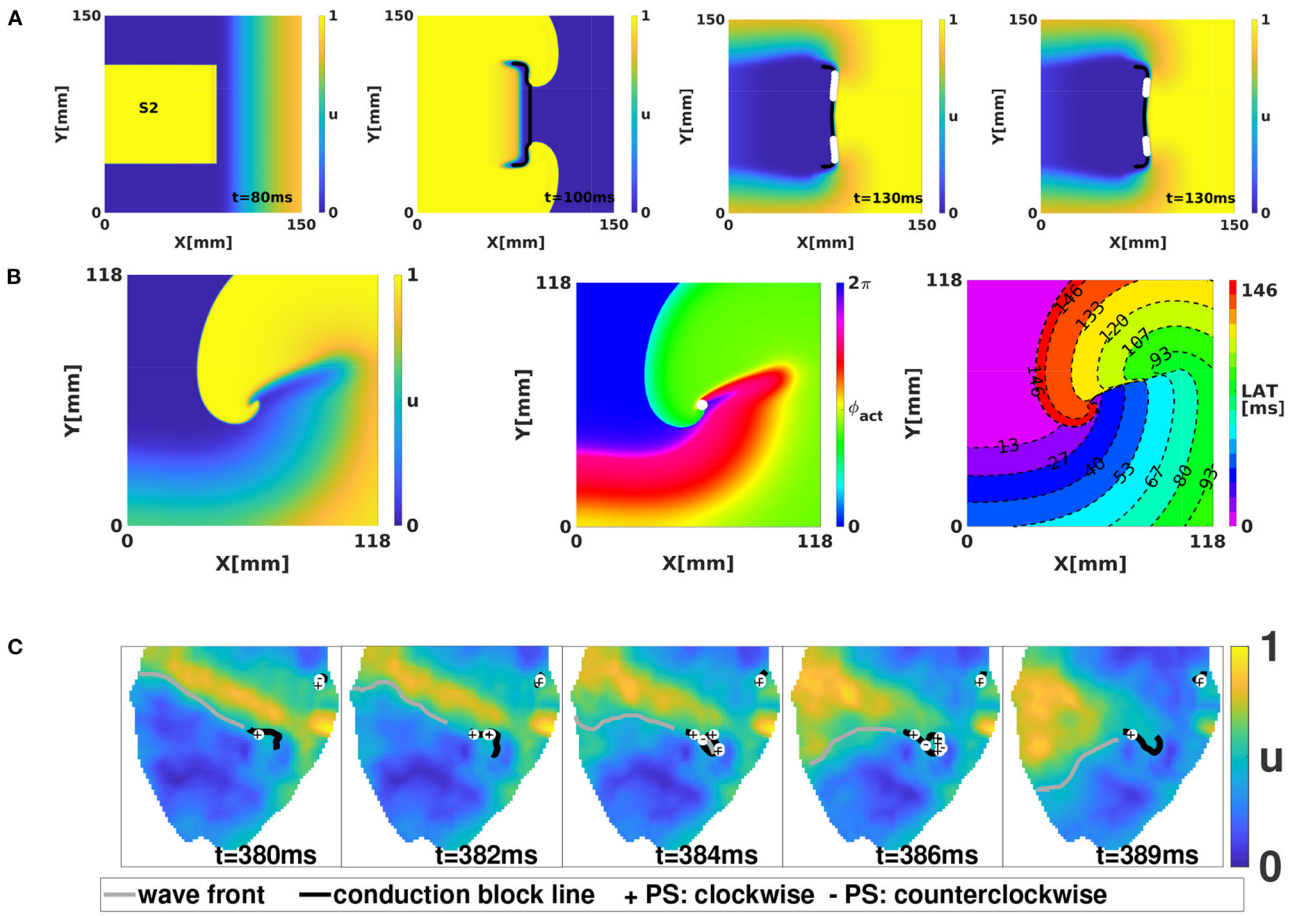

FIGURE 2 | Limitations of current PS detection algorithms. **(A)** Application of the S1-S2 stimulation protocol in the BOCF (Bueno-Orovio et al., 2008) model to initiate a rotor. White dots denoted detected PSs with either a 2×2 ring (third panel) or $2 \times 2 + 4 \times 4$ ring (fourth panel) using the method of Kuklik et al. (2017). Both methods identify multiple PS on the CBL (black line). **(B)** A linear-core rotor in the Fenton Karma model, from 3 perspectives: transmembrane voltage (left), activation phase (middle panel) with PS indicated (white) and LAT (right). **(C)** Optical mapping of rabbit hearts during ventricular tachycardia showing that detected PSs are all located on CBLs.

(in 2D and 3D) and optical mapping experiments. We draw conclusions from the analysis of our experiments and outline how future theory development can be initiated from the phase defect concept.

2. METHODS

2.1. Methods for Data Generation and PS and CBL Detection

2.1.1. Numerical Simulations

To illustrate our theoretical concepts, numerical simulations were performed in a cardiac monodomain model:

$$\partial_t \mathbf{u} = \Delta \mathbf{P} \mathbf{u} + \mathbf{F}(\mathbf{u}). \tag{2}$$

This partial differential equation states how a column matrix $\mathbf{u}(\vec{r}, t)$ of m state variables evolves in time. The constant matrix $\mathbf{P} = \mathrm{diag}(\mathrm{P}_{11}, 0, ...0)$ makes sure that only the transmembrane potential u_1 undergoes diffusion. Note that our analysis methods are applicable to excitation patterns in general and are not restricted to reaction-diffusion systems only.

In this work, we use the reaction-kinetics functions $\mathbf{F}(\mathbf{u})$ from Aliev and Panfilov (1996) (AP model, $m = 2$), Fenton and Karma (1998) (FK model, $m = 3$), and Bueno-Orovio et al. (2008) (BOCF model, $m = 4$). The equations are numerically integrated using the Euler method with the spatial resolution dx and time step dt as specified in **Table 1**. Only in the example with a biventricular geometry, uniaxial anisotropy was included: the Laplacian in (2) was replaced by $\partial_i(D^{ij}\partial_j)$ with $D^{ij} = D_1\delta^{ij} + (D_1 - D_2)e_f^i e_f^j$, with $D_1 = 1, D_2 = 1/5$ and $\vec{e}_f$ the local fiber orientation as measured by Hren and Stroink (1995).

The first and second state variables in these different models were used to calculate ϕ_{act}, see **Table 1** for definitions and threshold values.

TABLE 1 | Overview of mathematical models of cardiac excitation and parameters used in simulations throughout this work.

Kinetics	AP	FK	BOCF
References	Aliev and Panfilov, 1996	Fenton and Karma, 1998	Bueno-Orovio et al., 2008
Parameter set	Standard	MLRI(2D) and MBR(3D)	Epicardial (EPI)
Diffusion coefficient P_{11}	1	0.1 mm^2/ms	0.11 mm^2/ms
dx (2D)	0.5	0.262 mm	0.25 mm
dx (3D)	-	0.31 mm	0.5 mm
dt	0.0029	0.16 ms (2D) and 0.1 ms (3D)	0.1 ms
Domain size (2D)	200 × 200	118 × 118 mm	150 × 150 mm
Domain size (3D)	-	186 × 186 ×6.2 mm	168 × 208 ×231 mm
Variable used as V (V_*)	u (0.5)	u (0.5)	u (0.5)
Variable used as R (R_*)	v (1)	1-v (0.8)	1-v (0.2)
Δt for LAT	1	1.6 ms	5 ms
Δt_c for CBL detection	10	16 ms	45 ms
$\Delta\phi_{arr,crit}$ for CBL detection	0.7 rad	2 rad	0.5 rad
τ in ϕ_{arr}	20	70 ms	300 ms
Simulation used in	**Figures 1**, **8**, **10**	**Figures 2**, **5**, **6**, **8**, **11**	**Figures 2**, **4**, **7**, **9**, **12**

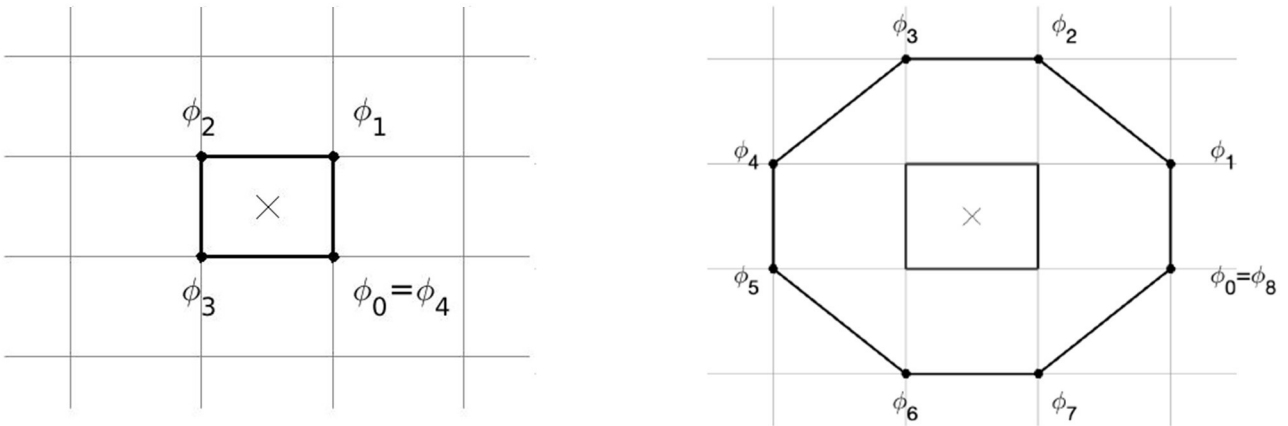

FIGURE 3 | Method of PS detection by Kuklik et al. (2017) as used in this paper. Phase differences are considered between pairs of points on a ring of 4 points (**Left**, 2 × 2 method) or 8 points (**Right**, 4 × 4 method), to assess whether a PS is present at the central location.

2.1.2. Optical Mapping Experiments

We applied our new framework to experimentally recorded movies of rotors in isolated Langendorff-perfused rabbit hearts ($n = 6$), as described by Kulkarni and Tolkacheva (2018). Optical movies corresponding to the fluorescence signal were recorded from the epicardial surfaces of the left or right ventricular surface of the heart (LV and RV) at 1,000 frames per second, with 14-bit, 80 x 80-pixel resolution cameras (Little Joe, RedShirt Imaging, SciMeasure) after a period of stabilization of approximately 30 min. Data processing was performed using a custom-made program in Matlab[1]. The background was removed by thresholding, and in each pixel the intensity was normalized against the minimal and maximal value of optical intensity attained in that pixel over the full recording. The characteristic timescale of activation was found as the inverse of the dominant frequency of activation was used to evaluate the Hilbert transform to obtain the activation phase ϕ_{act} (Bray and Wikswo, 2002).

2.1.3. Methods for PS and CBL Detection

PSs were detected using the method of Kuklik et al. (2017), see **Figure 3**. A ring of $N = 4$ or $N = 8$ pixels was considered around each grid cell of the medium, and the phase difference was computed between adjacent points on the ring. If exactly one of these phase differences was larger than π in absolute value, a PS was assigned to that grid element:

$$PS \text{ at } \vec{r}_0 \qquad \Leftrightarrow \#\{k|\ \left|\phi_k(\vec{r}_0) - \phi_{k-1}(\vec{r}_0)\right| > \pi\} = 1. \quad (3)$$

In the 2 × 2 method, only the 4 points around each grid cell are used; in the 2 × 2 + 4 × 4 method, a second ring of 8 pixels was used and a PS is assigned if both the small ring and large ring have one phase difference larger than π, see **Figure 3**.

[1]Matlab. version 9.9.0. (2020). The MathWorks Inc., Natick, Massachusetts.

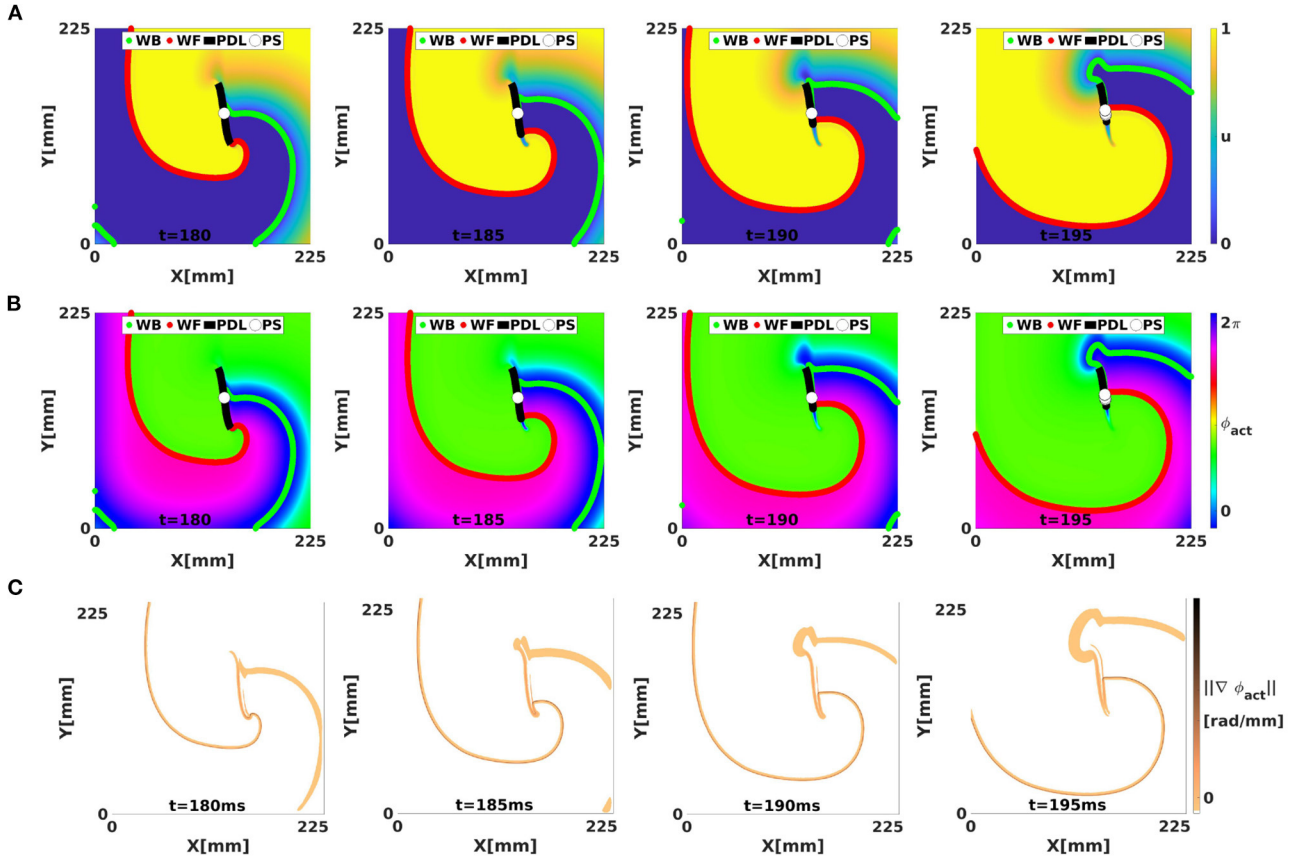

FIGURE 4 | Analysis of a simulated linear-core rotor (BOCF model) using activation phase, showing the WF, WB, classical PSs, and CBL/PDL at different times. The WF and WB were computed as points with $V = V_*$ with positive or negative dV/dt. The CBL/PDL was computed with Equation (4). **(A)** Transmembrane potential u. The classical PS is located near the position where the WF joins the PDL. At $t = 195$, several PSs are found near this intersection. **(B)** Same frames colored with the classical activation phase, showing sudden transitions at WF, WB, and PDL, see gradient of ϕ_{act} in **(C)**.

To localize CBLs, frames were recorded every Δt time units, and if in the new frame, V rose above V_*, this time was locally saved as the newest LAT. If an edge connecting two neighboring points of the grid had two LAT that differed by more than $\Delta t_c \approx dx/c$ (with c the plane wave velocity in the medium), the middle of that edge was considered to be part of a CBL:

$$\left.\begin{array}{l} |t_{\text{activation}}(\vec{r}_1) - t_{\text{activation}}(\vec{r}_2))| > \Delta t_c \\ \text{and } t_{\text{activation}}(\vec{r}_1) > 0 \\ \text{and } t_{\text{activation}}(\vec{r}_2) > 0 \end{array}\right\} \Rightarrow \frac{\vec{r}_1 + \vec{r}_2}{2} \in CBL. \tag{4}$$

Here, the first condition selects the union of the WF and the CBL. The threshold values Δt_c that we used with the different model kinetics are given in **Table 1**. The second and third condition are imposed to obtain CBLs only.

2.2. Theory

2.2.1. Introduction of Phase Defects

In many physical sciences, interfaces are found between regions of different phase, where they are known as domain walls or phase defects. In this sub-section, we demonstrate the existence of phase defects.

Figure 4 shows in each row the time evolution of a simulated linear-core rotor (at four different times). When applying classical phase analysis with ϕ_{act}, see **Figure 4B**, we note that there are several interfaces that connect excited (**Figure 4A**, yellow) to non-excited (**Figure 4A**, blue) areas. These interfaces can be shown by plotting the spatial gradient of ϕ_{act}, see **Figure 4C**. When taking the spatial gradient, it is important to disregard phase differences of 2π. We compute spatial derivatives of phase in the grid point with discrete position (i, j) as:

$$(\partial_x \phi)_{ij} \approx U(\phi_{i+1,j} - \phi_{i,j})/dx \tag{5}$$

with U the unwrap function, which adds an integer multiple of 2π to its argument, to bring the result closest to zero:

$$U(x) = min_{k\in\mathbb{Z}}[x + 2k\pi] = mod(x + \pi, 2\pi) - \pi. \tag{6}$$

In the linear-core rotor, we note different steep transitions between zones of approximately equal phase, and discriminate between them as follows. We denote by ϕ_1 a phase in the middle

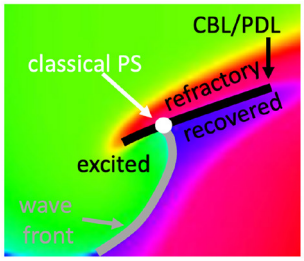

FIGURE 5 | Closer look at a linear-core rotor. At the location where classical methods detect a PS, three distinct phases come together: recovered, excited and refractory tissue. At either side of the CBL, two distinct phases are present: refractory vs. either excitable or recovered. Therefore, the CBL is a phase defect line (PDL).

of the upstroke (depolarization), and ϕ_2 a phase in the middle of the down stroke (repolarization). These values are found as

$$\phi_1 = mean\{\phi(\vec{r},t)|V(\vec{r},t) = V_* \text{ and } \frac{dV}{dt}(\vec{r},t) > 0\},$$
$$\phi_2 = mean\{\phi(\vec{r},t)|V(\vec{r},t) = V_* \text{ and } \frac{dV}{dt}(\vec{r},t) < 0\}. \quad (7)$$

Thereafter, the wave front (WF) and wave back (WB) can be defined as (with ♡ depicting the domain or cardiac tissue):

$$WF(t) = \{\vec{r} \in \heartsuit | \phi_{\text{act}}(\vec{r},t) = \phi_1\}, \quad (8)$$
$$WB(t) = \{\vec{r} \in \heartsuit | \phi_{\text{act}}(\vec{r},t) = \phi_2\}.$$

In the classical view, the only way to connect WF and WB is in a PS, where different phases ϕ_1 and ϕ_2 can meet.

However, if a wave hits unrecovered (refractory) tissue, unidirectional conduction block occurs and a CBL is formed. In that case, a third kind of interface is seen, in addition to WF and WB, see **Figure 5**. Since the tissue at either side of a CBL was activated at a different time, it also has different phase, see different colors across the black line in **Figure 5**. This observation implies that not only the end point of a wave front (the classical PS) is a special point, but that all points on a CBL have a non-trivial phase structure: they are situated on a region where phase suddenly transitions from one value to another, which we call a phase defect line (PDL).

Note that the PDL shown here persists in time until either both sides have fully recovered, or when one side of the line is re-excited again, while the other is not.

Figure 4C shows the norm of $\vec{\nabla}\phi_{\text{act}}$, which visualizes the domain walls between the different zones of similar phase; note that without further filtering, the transition zones consist of the union of WF, WB, and PDL.

2.2.2. An Alternative Phase Definition Based on LAT

We find it useful to discriminate WF and WB from CBLs, since the former are "natural" behavior in an excitable system, while conduction block can lead to the formation of abnormal patterns and arrhythmias and therefore, deserves to be detected separately. Therefore, we now introduce another definition of phase, which is only sensitive to CBLs.

As we described before, the classical definition of phase is not unique, as one could make various choices for the observables V and R, and their threshold values V_*, R_* can be also chosen at will, as long as they are located within the cycle in the (V,R)-plane.

The most important feature of the phase is its periodicity. For convenience, we choose the phase of the resting state to be phase equal to 0. Apart from that, there is need to let the phase correspond to the polar angle in one choice of (V,R)-coordinates: we can define new equivalent phases ϕ by a continuous mapping of ϕ_{act}:

$$\phi = h(\phi_{\text{act}}), \quad h(0) = 0, \quad h(2\pi) = 2\pi, \quad h'(\phi_{\text{act}}) > 0. \quad (9)$$

The last condition ensures that the transformation between the phases is invertible. In a mathematical sense, fixing a phase is nothing but introducing coordinates on the inertial manifold (dynamical attractor) on which the dynamics takes place. As with coordinates in the plane or on a surface, many choices are possible, and depending on the circumstances, some may be more appropriate than others.

To link the concept of LAT with phase, we propose to take the elapsed time

$$t_{\text{elapsed}}(\vec{r}) = t - t_{\text{activation}}(\vec{r}) \quad (10)$$

as the new phase, since in leading order (neglecting inhomogeneity, electrotonic effects and long-term memory), the state of a point will depend on the elapsed time since previous activation. However, $t_{\text{elapsed}} \in \mathbb{R}^+$, which is an unbound interval, such that t_{elapsed} itself is not a suitable replacement for ϕ_{act}. To this purpose, we apply a sigmoidal function to t_{elapsed}, in order to define an "arrival time phase":

$$\phi_{\text{arr}}(\vec{r},t) = 2\pi \tanh(3t_{\text{elapsed}}(\vec{r},t)/\tau). \quad (11)$$

Here, τ is a characteristic time constant of the medium, e.g., the mean action potential duration. **Figures 6A,B** show how ϕ_{arr} depends on both t and ϕ_{act} for FK reaction kinetics. From this, it can be seen that, to a good approximation, ϕ_{arr} is a reparameterization of ϕ_{act}. The new phase ϕ_{arr} is not constant in time, but gets update at the places where the wave front excites tissue, just like the updates in LAT. It relies on two parameters, which we chose manually for now: the timescale τ and the critical threshold V_* to consider tissue as excited, see definition (8).

Importantly, ϕ_{arr} unifies the classical phase description (since ϕ_{act} is a phase) with the LAT description (since it is defined based on LAT). When a linear-core rotor is plotted using ϕ_{arr}, as shown in **Figure 7**, we see that the WF and WB are not strongly emphasized anymore, since both occur near $\phi_{\text{arr}} = 0$ (omitting phase differences of 2π). Still visible as a spatial phase transition is the region of conduction block, or the PDL, see **Figure 6C**.

The "wave arrival time phase" ϕ_{arr} is thus a kind of hybrid between classical phase and the LAT viewpoint. For, the lines of equal phase will now correspond to the isochrones that commonly appear in medical literature and our **Figure 2B**. At

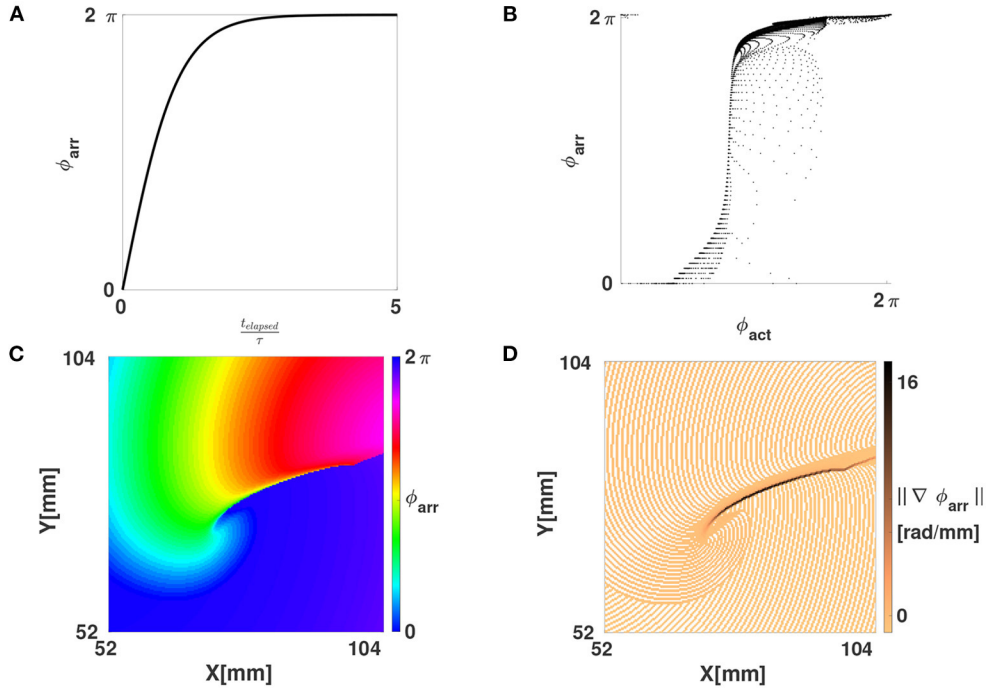

FIGURE 6 | Phase defects shown using the LAT-based phase ϕ_{arr}. **(A)** The function $\phi_{arr}(t_{elapsed})$ from Equation (11). **(B)** Scatter plot of ϕ_{arr} vs. ϕ_{act}, showing that one is a reparameterization of the other on the interval $[0, 2\pi]$. **(C)** Same linear-core rotor in the FK model as in **Figure 2B**, now shown with ϕ_{arr}. Note that WF and WB are no longer showing abrupt phase variations, these only happen at the PDL, i.e., the points where conduction block happened. **(D)** Magnitude of the gradient of ϕ_{arr}. Due to the discrete sampling of LAT, a staircase artefact in the gradient is seen (no smoothing was applied here).

a CBL, LAT changes discontinuously across the conduction block site, and this phase defect region now clearly exhibits a discontinuous phase. So, depending on the definition of phase used (ϕ_{act} or ϕ_{arr} or another one) the phase defect will be either a steep but continuous phase transition, or a true discontinuity in phase.

2.2.3. Interpretation of Phase Defects as Branch Cuts From Complex Analysis

Here, we demonstrate how phase defects can be interpreted as a branch cut from complex analysis (Arfken and Weber, 1995). For any non-zero complex number of the form $z = x + iy$ with $i^2 = -1$, the phase can be calculated using

$$\arg(z) = \text{atan2}(y, x). \tag{12}$$

Next, one can consider functions of a complex variable: $w = f(z)$ with both w and z complex numbers, e.g., $w = z^2$. To make a visual representation of the function value, one can draw colormaps of the phase $\arg(w)$, or show $\arg(w)$ as an XY-dependent elevation in a so-called Riemann surface; see **Figure 8**. In case of polynomial or rational functions, such phase map will reveal point singularities similarly to PSs found in circular-core spiral waves, see **Figure 8A**. When the phase of the simple function $w = f(z) = z$ is shown as a graph of (x, y) the phase surface resembles a helicoid. If one walks around the PS once in the XY-plane, the phase will change by 2π, but since phase is measured disregarding terms of 2π, one ends in the same state. This effect is more easily seen using a cyclic colormap in 2D, see **Figure 8A**. Close to the central axis of the helicoid, the height (phase) is undefined, which is typical for a PS.

In contrast to polynomial and rational functions, functions f which include roots, exhibit a discontinuity in their phase, also called "branch cut" in mathematics. In particular, for the function $w = f(z) = \sqrt{z^2 - 1}$, there is a line of discontinuous phase for (x, y) between $(-1, 0)$ and $(1, 0)$. This line is easily noticed in the representation as a color map as a sudden transition in color, see **Figure 8**. This situation is in our opinion very similar to the phase discontinuity in the linear-core rotor throughout this paper.

For, if one regards two neighboring points on both sides of a conduction block line at the rotor core, they will have distinct phases. There need not be a single point where all phases spatially converge (that is, a PS), as on both sides the phases can gradually change to take the same value at the points where the branch cut stops.

From this paragraph and **Figure 8** it is apparent that the PSs and PDLs are different topological structures. We argue in this paper that we and Tomii et al. (2021) are the first to note this difference in a cardiac electrophysiology context, and that discriminating between these different structures can be useful in theory development and applications.

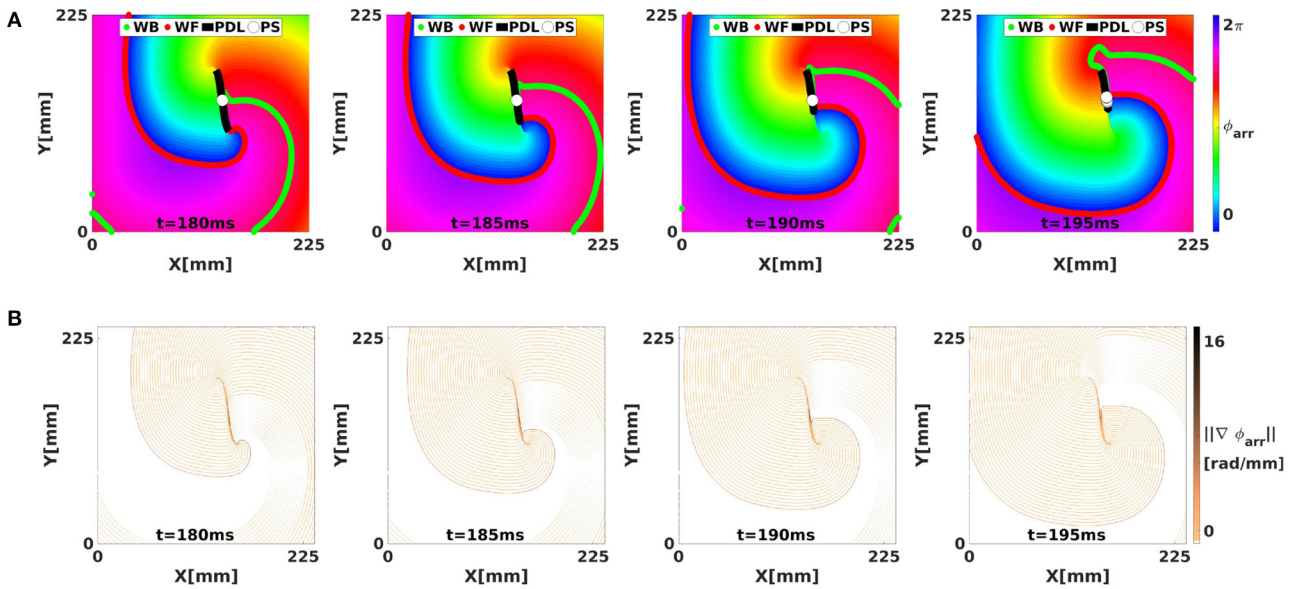

FIGURE 7 | Analysis of the simulated linear-core rotor from **Figure 4** using LAT phase. **(A)** With ϕ_{arr}, there are no sudden transitions in phase along the WF and WB, such that only CBLs are shown as phase defects, with large local phase gradient **(B)**.

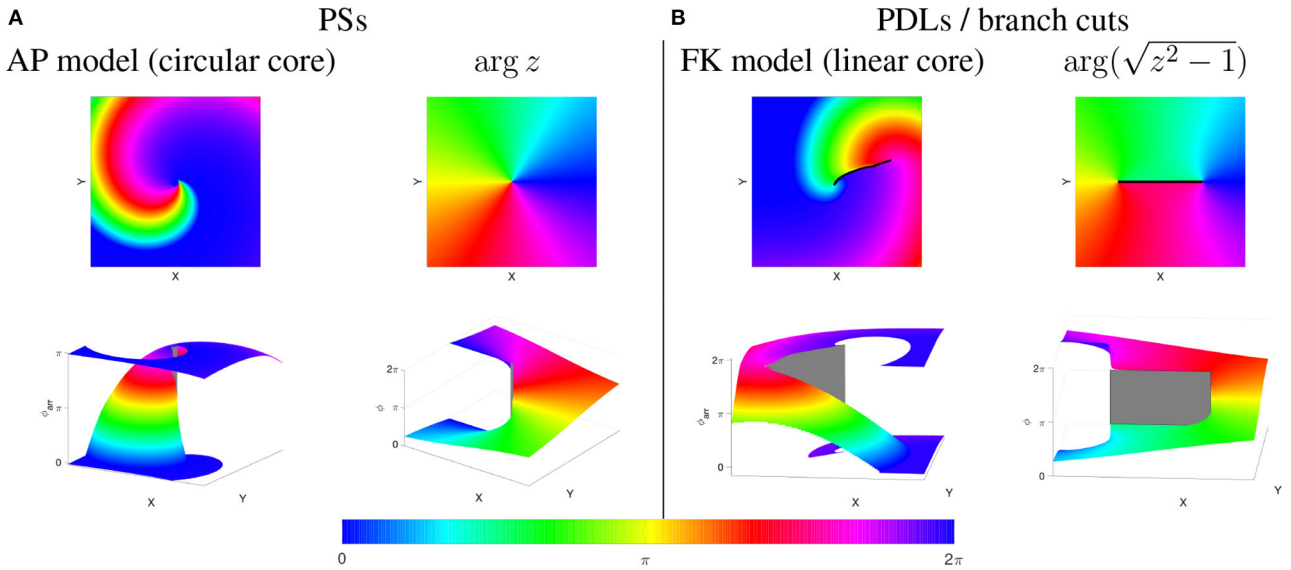

FIGURE 8 | PSs vs. PDLs in cardiac models and complex analysis. Phases are rendered in-plane (top row) and in 3D, as a Riemannian surface (bottom row). **(A)** Rigidly rotating spirals, as in the Aliev-Panfilov (AP) reaction-diffusion model (Aliev and Panfilov, 1996) correspond to a PS (gray), similar to the mathematical function $\phi(x, y) = \arg(z)$ shown to the right of it. **(B)** Linear-core cardiac models, e.g., (Fenton and Karma, 1998) exhibit a PDL or branch cut (black/gray), like the mathematical function $w = f(z) = \arg(\sqrt{z^2 - 1})$ shown to the right of it. Gray areas denote a jump in the phase over a quantity not equal to an integer multiple of 2π, i.e., a PDL (physics) or branch cut (mathematics).

2.3. Methods for Phase Defect Detection

The numerical identification of PDLs in cardiac excitation patterns can be performed using various methods. Based on a phase (either ϕ_{act} or ϕ_{arr}), one can assign a PDL to the midpoint of edges along which the phase gradient exceeds a predefined value, taking into account that phase differences of 2π are excluded:

$$|U(\phi(\vec{r}_1) - \phi(\vec{r}_2))| > \Delta\phi_{crit} \Rightarrow \frac{\vec{r}_1 + \vec{r}_2}{2} \in PDL. \quad (13)$$

However, if the LAT is known, this method approximates the more direct method of identifying a CBL, see Equation (4). A

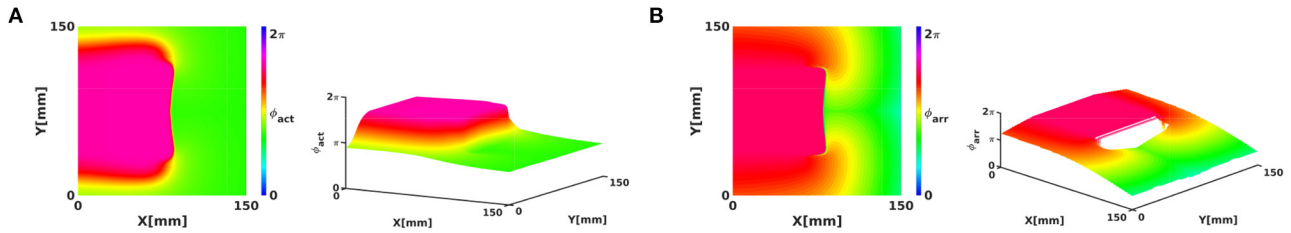

FIGURE 9 | Interpretation of a CBL as a phase defect clarifies why a PS detection finds PSs on it. **(A)** ϕ_{act}, rendered in 2D and 3D as a Riemannian surface. **(B)** ϕ_{arr}, rendered in 2D and 3D as a Riemannian surface. At the CBL/PDL, the phase surface has a cliff-like appearance.

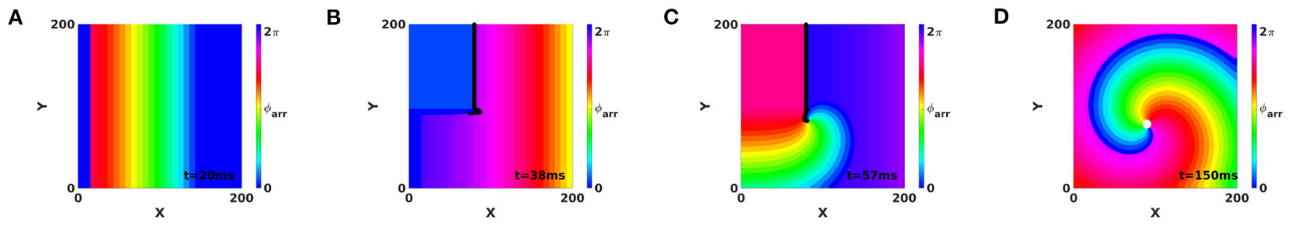

FIGURE 10 | Creation of a PS from a PDL using a S1-S2 protocol with AP kinetics, showing coexistence of PDL and PS in models that generate circular-core spirals. Snapshots **(A–D)** shown at times $t = 20$ ms, $t = 38$ ms, $t = 57$ ms, and $t = 150$ ms.

comparison between different manners to numerically compute PDLs will be deferred to another publication.

Below, we also compare the lifetime of PSs and PDLs in experimental recordings. To estimate PS lifetime, we calculated PSs at each time frame between 501 and 1,500 ms using the Hilbert transform of $V(t)$, followed by PS detection using $2 \times 2 + 4 \times 4$-method, which is considered as robust in literature (Kuklik et al., 2017). If a PS moved between two subsequent frames at most 1 pixel in the horizontal, vertical, or diagonal direction, while keeping its chirality, it was considered PS. Otherwise the PS was considered a new one.

A similar approach was taken for PDLs. PDLs in experiments were computed using Equation (13), with manually chosen threshold $\Delta\phi_{crit} = 2.22$. If the middle of an edge was on a PDL, both neighboring nodes of the Cartesian grid were considered to be part of the PDL. A PDL was assumed to persist in time if the PDL at the new time and at the old time had points which were not further than 1 pixel away from each other (in horizontal, vertical, or diagonal direction). PDLs were allowed to branch and merge, and the lifetime was computed as the earliest and latest time which were connected by this family of PDLs.

A PS was furthermore considered to lie on a PDL if its distance was less than 0.5 pixels from a point on the PDL. PDLs in **Figures 2C**, **13** were visually rendered using splines. The wave front was added to these figures using Equations (7)–(8), with $V_* = 0.5$.

3. RESULTS

Here we illustrate the appearance and relation between PSs and PDLs in simulations and an optical mapping experiment.

3.1. Numerical Results in Two Dimensions

3.1.1. Rendering of Cardiac Activation Phase Around a Conduction Block Line as Riemannian Surfaces

The CBLs presented in **Figure 2** are examples of PDLs: to this purpose, we redraw the rightmost panel of **Figure 2A** here using ϕ_{act} and ϕ_{arr}, rendered in 2D and 3D in **Figure 9**. Here, it can be seen that the suspected PSs in fact lie on the line where phase is nearly discontinuous.

We distinguish two cases here. If no rotor is attached to the phase defect, the Riemann surface looks like a sheet of paper with a cut in it and both edges shifted relative to each other, see **Figure 9**. If a rotor is attached to the phase defect, the Riemann surface looks like two rising slopes connecting two floors in a parking lot, see lower right panel in **Figure 8B**.

3.1.2. Coexistence of PS and PDL in the Same System

Here we demonstrate that PDLs can also exist in media that sustain spiral waves with PSs. This is illustrated in simulations where application of S1S2 pacing induces a PDL at the WB of the first stimulus, see **Figure 10**. Since AP reaction kinetics were used (Aliev and Panfilov, 1996), the PDL will disappear after both sides have reached full recovery, resulting in a PS at the core of the spiral wave, see **Figure 10D**. Hence, we conclude that PDLs and PSs can coexist in media supporting circular-core spiral waves, since the PDL is found at conduction block sites and PSs are found in the spiral wave core.

3.1.3. Absence of a PS at the Edge of a PDL

Although **Figure 10** shows a PS situated near the end of a PDL, this is certainly not always the case. Counter examples

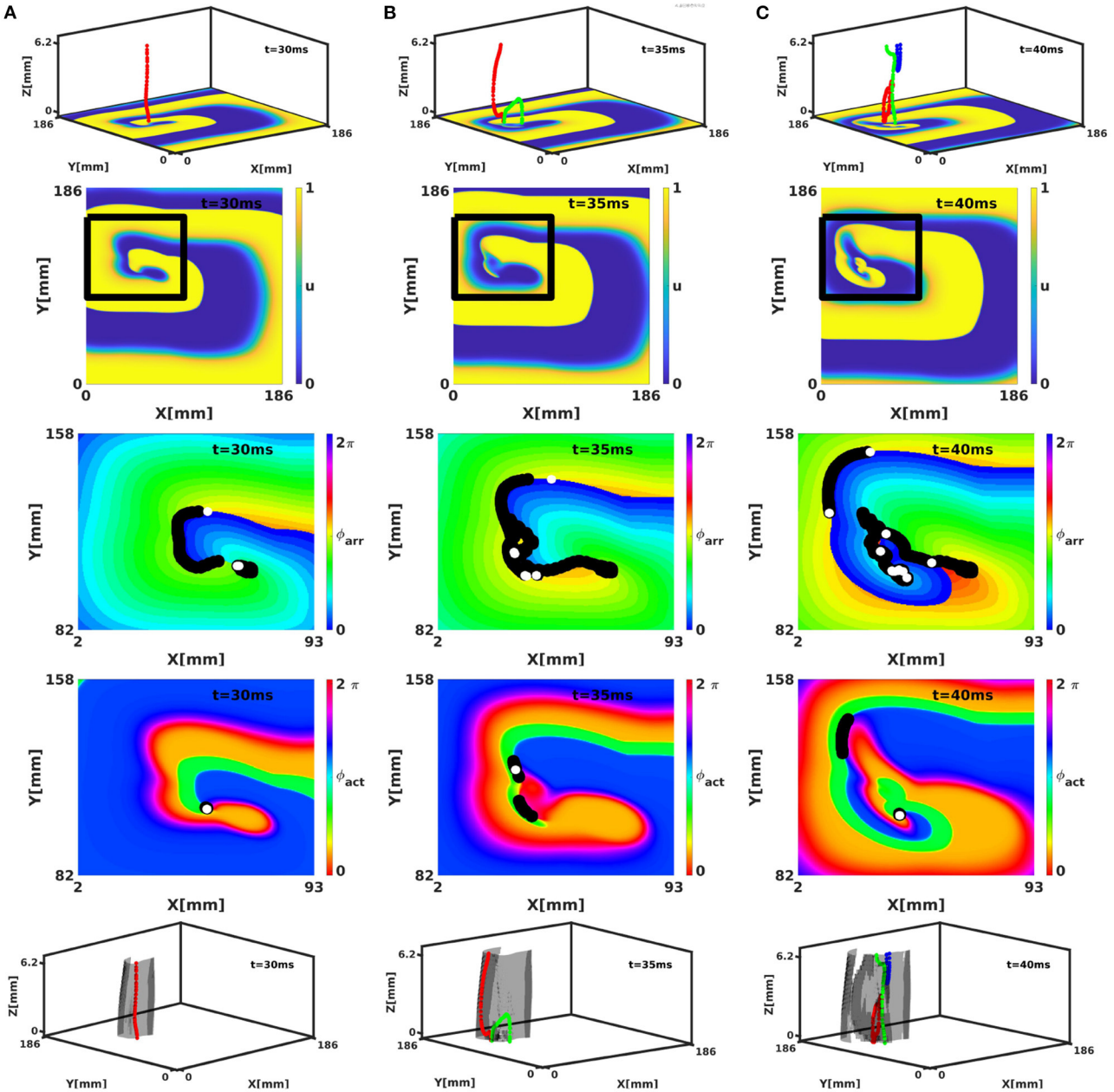

FIGURE 11 | Analysis of a break-up pattern in a 3D slab geometry with linear-core rotors and rotational anistropy in the FK model. Panels **(A–C)** show activity at times $t = 30$, 35, and 40 ms, respectively. The rows show respectively 3D activity with filaments (colors indicate different filaments), normalized transmembrane voltage on the bottom surface, and analysis of the surface patterns in terms of ϕ_{arr} and ϕ_{act} and 3D activity with filaments colored as above and PDSs indicated in gray. Note that several phase defects are observed, indicating conduction block near the spiral wave core.

of PSs located away from end points of a PDL can be seen in **Figures 2**, **4**.

The underlying mathematical reason is the following. At the edge of a PDL, the phase surface starts to be "torn," see **Figure 8B**. Still, at this point itself, the phase is well-defined. This situation is different from a PS, see **Figure 8A**, where the Riemann surface locally resembles a staircase surface and the phase itself cannot be determined.

3.1.4. Phase Defect Analysis of Scroll Wave Turbulence

The phase defect framework was illustrated above on simple examples, but is designed to analyse much more (complex) dynamics in excitation patterns. We conducted a 3D simulation in the FK model with rotational anisotropy-induced break-up, as detailed in Fenton and Karma (1998). **Figure 11** shows snapshots of the turbulent pattern on the bottom surface of the slab

(representing endo- or epicardial view in this geometrical model). Here, it can be seen that multiple PSs are detected on CBLs, that correspond to the core of cardiac rotors.

3.2. Numerical Results in Three Dimensions

In classical 3D theory, the PS extends to a dynamically varying curve called the rotor filament. With linear cores in the phase defect framework, the PDL will also extend in three dimensions, to form a phase defect surface (PDS). The bottom row of **Figure 11** shows the PDSs for the full 3D break-up patterns in the FK model. Here, it is seen that the PDLs that we identified on the myocardial surface extend to surfaces in three dimensions. From the surface recording (2D) already, it can be seen that these surfaces can branch and merge in time.

A second example of PDSs is shown in **Figure 12A**, where a scroll wave with linear core was initiated by setting initial conditions with unidirectional block in the left-ventricular and right-ventricular free wall and the intraventricular septum. When viewed in terms of phase defects, 3 PDSs are seen. The two PDSs on the left correspond to filaments, and the rightmost PDS is a CBL; no matching filament is seen in **Figure 12A**.

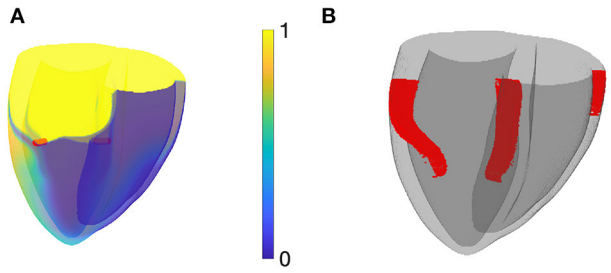

FIGURE 12 | Numerical simulation of rotors in the BOCF model in a biventricular human geometry. **(A)** Snapshot colored according to normalized transmembrane voltage, showing 2 classical rotor filaments in red. **(B)** Phase defect surfaces (PDSs) for the same snapshot. The two leftmost PDS bear a classical filament in them, the rightmost one (in the right-ventricular free wall) is a site of conduction block.

3.3. Analysis of Rotors From Isolated Rabbit Hearts

Electrical activity of a Langendorff-perfused rabbit heart was visualized during ventricular tachycardia via optical mapping experiments (Kulkarni and Tolkacheva, 2018) as detailed in section 2.1.2. The processed movies of the different experiments performed are accessible in the **Supplementary Material**, and various characteristics of rotors in these movies are summarized in **Table 2**.

A first important observation in **Figure 13** and **Table 2** is that in more than 99% of the cases where a PS was found, it was situated on a PDL. A typical sequence of the activation is presented in **Figure 13**. Here, a classical rotor can be recognized from the progression in time of a wave front (gray line) that starts in the top-right corner and circles counterclockwise around a line of conduction block that comprises the center of this rotor. Note that the PS detection algorithm finds a variable number of PSs on a PDL over time and therefore, the lifetime of the PSs are smaller than the mean PDL lifetime, as is shown in **Table 2**. In contrast, the mean lifetime of PSs was about 3 frames.

Second, two types of PDLs were observed: approximately two thirds of them were not associated with any PS during their lifetime and we recognize these as conduction block lines without a rotor attached to them. About one third of PDLs/CBLs had at least one PS on them during their lifetime, and these are therefore, at the rotor core.

A third observation is that no rotors in the observed ventricular tachycardia completed a full turn on the epicardial surface, confirming other results in literature; a representative example is shown in the rightmost panel of **Figure 13**. Prior to completing a full rotation, excitation is surfacing from deeper layers, leading to a full conduction block. After that, the excitation loops in the same sequence, leading to a nearly

TABLE 2 | PS and PDL properties observed via optical mapping experiments from $n = 6$ rabbit hearts using two cameras, such that the entire epicardial wall is imaged.

Exp ID	1	2	3	4	5	6	Average
# PS / frame	6.55	7.38	7.29	5.96	4.85	9.00	6.84
# PDL / frame	11.82	13.14	13.20	13.23	11.54	17.59	13.42
# PS not on a PDL / # PS	0.05	0.07	0.03	0.10	0.04	0.10	0.06
# PDL without a PS /frame	7.29	8.13	8.35	9.04	8.38	11.50	8.78
# new PS/frame	1.45	1.51	1.65	1.47	1.23	2.02	1.55
# new PDL/frame	0.41	0.46	0.42	0.43	0.36	0.66	0.46
Fraction of PS never on PDL	0.35%	0.07%	0.24%	0.61%	0.41%	0.40%	0.34%
Fraction of PDL never hosting PS	61%	60%	63%	64%	66%	64%	63%
Dominant frequency (Hz)	20.57	20.45	17.38	18.59	19.31	20.14	19.40
Dominant period (ms)	48.63	48.89	57.55	53.80	51.80	49.66	51.72
Mean PS lifespan (ms)	3.42	3.75	3.31	2.94	2.83	3.33	3.26
Mean PDL lifespan (ms)	15.22	15.14	16.39	15.25	13.96	12.50	14.74

Here, PSs were computed using the integral method using the "2 × 2 + 4 × 4" ring of points (Kuklik et al., 2017). Phase was computed for both PSs and PDLs with $V(t)$ the normalized optical intensity and $R(t)$ its Hilbert transform.

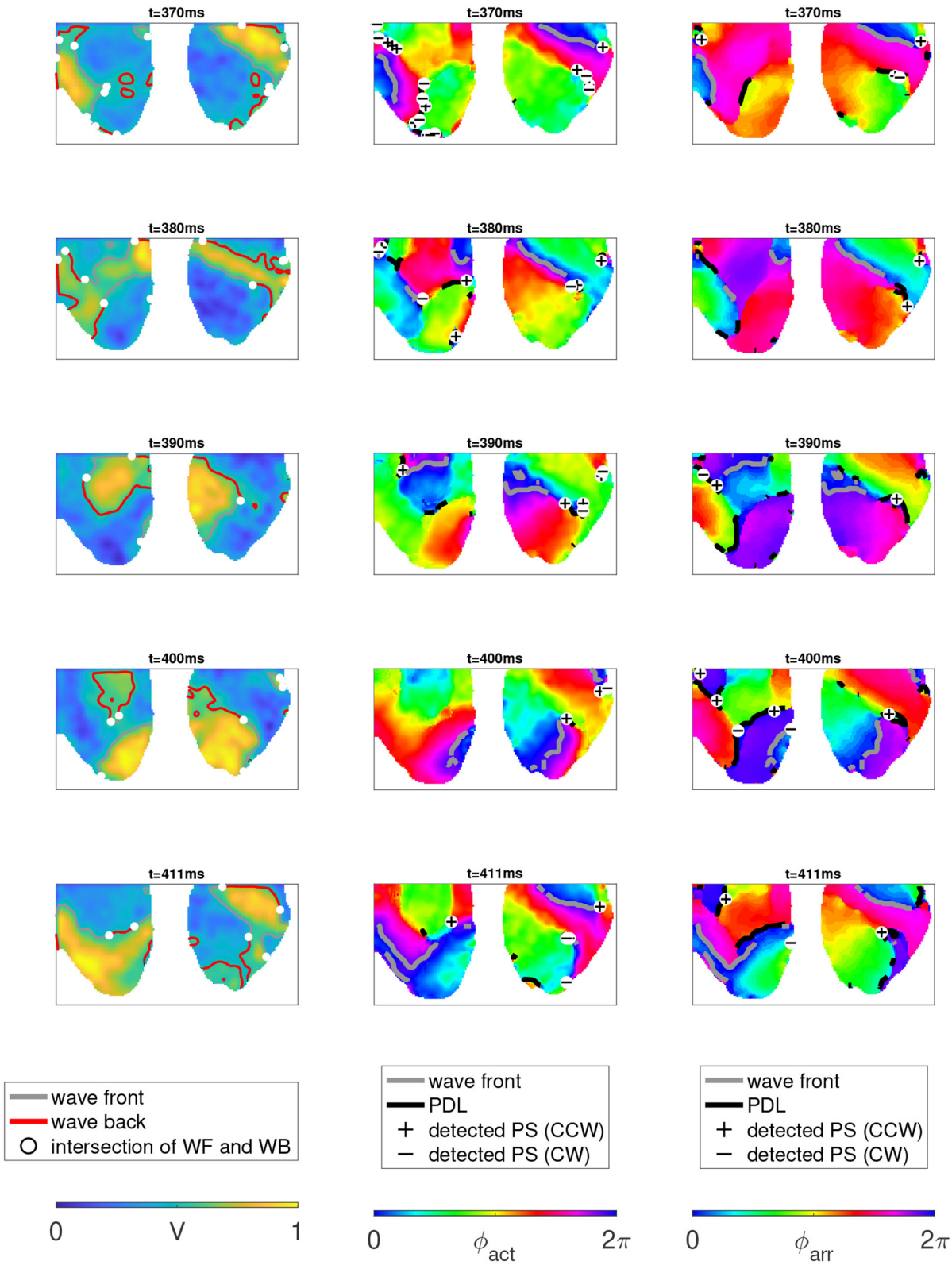

FIGURE 13 | Analysis of two-sided optical mapping data in rabbit hearts during ventricular tachycardia. **Left**: normalized optical intensity (transmembrane voltage) V, together with WF ($V^* = 0.5, \dot{V} > 0$) and wave back ($V^* = 0.5, \dot{V} < 0$). **Middle**: same data series, ϕ_{act} computed with R the Hilbert transform of V, with PSs and PDLs computed from ϕ_{act}. **Right**: colormap indicates ϕ_{arr}, computed with $\tau = 99$ ms, equal to the inverse dominant frequency. PSs and PDLs computed from ϕ_{arr} are also shown. PS detection was done using the $2 \times 2 + 4 \times 4$ method of Kuklik et al. (2017).

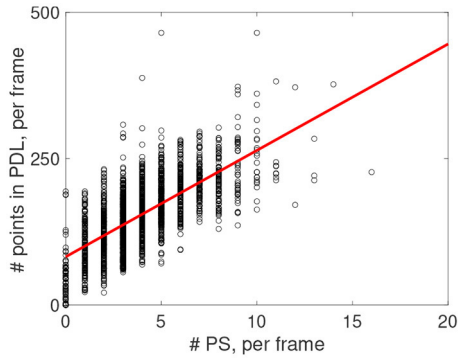

FIGURE 14 | Post-processing of rotors observed via optical mapping experiments from $n = 6$ rabbit hearts. Positive correlation (red line) between number of detected PS and number of points in the PDL for the experiment shown in **Figure 13**.

periodic ventricular tachycardia. Note that the fact that the rotor is not performing a full rotation on the epicardial surface is not reflected by the PS analysis, but becomes visible only in the PDL framework. We verified visually that this scenario was true for most re-entrant activity in the data.

Figure 14 shows that in every recorded frame the number of PSs correlates with the total length of PDLs in that frame (data from one experiment is shown, counting PSs observed with two cameras on both sides of the heart). The intersection of the trend line with the vertical axis at finite distance shows that even without PSs, PDLs are found, which we attribute to CBLs without a rotor connected to it.

4. DISCUSSION

In this manuscript, we proposed a topological framework for excitable systems that feature conduction block lines. We brought terminology from complex analysis (Riemann surfaces, branch cuts) to a cardiac electrophysiology context and demonstrated that the phase defect concept can describe more structures than the classical PS. Moreover, we introduced the arrival time phase, which allows to convert activation time measurements to phase, and thereby unifies the isochrone and phase description of cardiac tissue.

Our main findings are the following (1) the distribution of phase in our cardiac simulations and experiments is organized in regions with slow spatial variations of phase, separated from each other by localized interfaces, which we called phase defects; (2) that when arrival time phase is used, the only aberrant interfaces occur at CBLs; (3) at these PDLs, classical detection methods tend to localize PSs.

4.1. PDLs vs. PSs

The concept of extended PDLs can in our opinion explain some limitations associated with classical PS analysis that we presented in **Figure 2**. First, near the central region of a PDL, the phase changes abruptly, and if this phase difference exceeds π, these points on a PDL can be classified by traditional methods as PSs, see **Figure 2A**. One option is to filter the resulting PSs and remove closely spaced PSs, but another option suggested here is to recognize the structures as line defects rather than point defects of phase.

The observation that points on a PDL can be detected as PSs at once explains why PSs are often found on CBLs, as was seen in **Figure 2C**. Here, we conclude that in systems that form linear-core rotors (even short-lived) do not possess PSs, but only PDLs. Conversely, systems that sustain circular-core rotors can have PSs at the spiral core, and PDLs at conduction block lines.

In **Figure 2B**, we argued that a PS cannot capture the shape of a linear core. In contrast, a PDL can do so, as it is a line spanning the entire conduction block region.

Geometrically speaking, PDLs and PSs are related to each other: a PS can be seen as the limit of a PDL having length zero. Conversely, a PDL can also be regarded as some kind of extended PS. Hence, the PDL concept can be seen as a refinement of a PS. Therefore, we make the suggestion to adapt current phase analysis methods to accommodate for PDLs, which can potentially make analysis more robust and accurate.

4.2. Physiological Interpretation of Phase Defects

In analogy to the term "phase singularity" referring to spiral wave tips, we here suggested the term "phase defect line" (PDL) to refer to CBLs when their phase structure needs to be emphasized. PDLs are ubiquitous in other branches of physics, e.g., magnetism (Landau and Lifshitz, 1935), liquid crystals (Williams, 1963), and string theory (Vilenkin, 1985).

Our justification as to why PDLs exist in these systems is based on biological rather than mathematical arguments and essentially traces back to the arguments of Winfree (1974). Consider the activation cycle of an excitable cell, i.e., its action potential, as shown in **Figure 1B**. Now, if one expects a PS in the center of a vortex, one assumes that the cells can also be in a state that lies somewhere in the middle of the cycle in state space. However, this situation may be biologically impossible: electrophysiology processes during activation will push the cell along its activation cycle, not necessarily allowing it to occupy the middle state. In case of a PDL, the "forbidden" state does not need to be realized. Going back from state space to real space, the region with forbidden states is mapped to the PDL.

If one, however, models cardiac tissue in the continuum approximation using a diffusion term, the transmembrane potential becomes continuous, and if this potential is used as one of the observables (V, R) to infer phase, points in the "forbidden zone" of state space are actually realized by the smoothing effect, leading to a finite thickness of border between regions of different phase. Since this diffusive effect acts during one action potential with duration τ, we estimate the effective thickness of the phase defect line to be

$$d = \sqrt{D\tau} \tag{14}$$

with D the diffusion coefficient for transmembrane potential in the direction perpendicular to the PDL. For the BOCF model for human ventricle, one has $D = 1.171\,\mathrm{cm}^2/\mathrm{s}$ and $\tau =$

269 ms, leading to a PDL thickness of $d = 5.6$ mm if the PDL is perpendicular to the myofiber direction. With conduction velocity anisotropy ratio $c_1/c_2 \approx 2.5$, one finds $d = 14$ mm if the PDL is oriented parallel to the myofiber direction. These are rough estimates in a minimal monodomain model.

Thus, as with other interfaces between phases in nature, a boundary layer forms with a thickness related to fundamental constants of the problem. This boundary layer effect explains why the common PS detection methods usually do return a result, even in the region of conduction block. When the new framework is applied to a linear-core rotor, the classical spiral wave tip or PS is expected to be the point where a wave front ends on a PDL. However, this may depend on the precise tip structure, spatial resolution and PS detection method, see e.g., **Figure 4**.

4.3. Relation to Other Works

Between the submission of our preprint (Arno et al., 2021) and acceptance of this paper, a paper was published by Tomii et al. (2021), who also identify a phase discontinuity at the center of cardiac vortices, and compares it to a branch cut in complex analysis. This effect was demonstrated by Tomii et al. in numerical simulations only. They detected PDLs using

$$\cos(\phi(\vec{r}_1) - \phi(\vec{r}_2)) > A \Rightarrow \frac{\vec{r}_1 + \vec{r}_2}{2} \in PDL. \qquad (15)$$

This method is very similar to our Equation (13). However, our study goes further than their result, as we introduce arrival time phase to link the phase picture with LAT, we demonstrate the presence of PDLs in optical mapping experiments, and report about PDSs in 3D as well.

We are also aware that the concept itself of a CBL is not new at all, as conduction blocks are mentioned for more than a century in electrophysiology reports (Mines, 1913). In 3D, filaments have also been reported as being ribbon-like before (Efimov et al., 1999). However, these observations have not been thoroughly integrated in pattern analysis methods (which is usually based on PSs) or the dynamical systems approach to better understand arrhythmias (which has long considered circular-cores only).

Meanwhile, CBLs are routinely localized and visualized during clinical procedures, e.g., as the result of an ablation. A prime insight advocated in this manuscript, and by Tomii et al. (2021), is that the CBL itself is an extended line of abrupt change between two regions with different activation phase, and that this resembles more a mathematical branch cut than a PS. Further studies are recommended to see if the phase defect concept can help to solve some basic questions in the field, such as why rotors do not complete full turns in tissue, and which characteristics of the reaction kinetics determine the core shape.

4.4. Relevance of Phase Defects for Theory of Arrhythmias

The recognition that a PS may not be the best option to describe linear core rotors, is in our opinion opening up several paths for further analysis and insight in cardiac arrhythmia patterns.

First, by introducing the arrival time phase ϕ_{arr}, we have unified the LAT description with the phase description, which allows computing ϕ_{act}. Which phase to use in practice will depend on the availability of data and their quality. **Figure 6** furthermore shows that both phases can be converted into each other. Hence, activation phase can also be estimated from LAT, and arrival time phase from a single snapshot of V and R at a given time.

Second, this work was inspired by localizing the regions where an external stimulus can affect rotor dynamics. The relevant sensitivity function is here known as a "response function" (RF) (Biktasheva and Biktashev, 2003), and these have been computed recently also for meandering and linear-core rotors (Marcotte and Grigoriev, 2015; Dierckx et al., 2017). For circular-core rotors, it has been numerically demonstrated that the RF is located near the spiral wave tip, or its PS. So, rather than acting as a point particle, the rotor has a finite extent given by the spatial decay width of its RFs, with sensitivity localized near the spiral wave tip or PS, not at its instantaneous rotation center. For linear-core spirals, the PDL at their core indicates that the sensitivity is located around this zone of rapidly varying phase. More specifically, their RF was shown to be localized near the end points of the PDL (Dierckx et al., 2017) ("turning points"), suggesting that linear-core rotors resemble a localized particle that hops from turning point to turning point. That the sensitivity is lower in the middle part of the PDL can be understood from the conduction block interpretation: this block line cannot move much, as the tissue on one side is inexcitable. Hence, the PDL concept confirms insights from RF theory, and it can be hoped that combining both may open up ways to deepen the understanding of how point dynamics (local electrophysiology) affect the emerging patterns.

Third, it is yet unclear how essential structures such as WBs and CBLs move under the influence of external stimuli such as impeding waves or electrotonic currents from boundaries or 3D effects. To answer this question is a key step toward designing better methods to control wave patterns, e.g., as in defibrillation. The identification of the phase defect, with boundary layer, could allow in the near future to design a quantitative theory of their dynamics, in analogy to earlier successes on rotor filaments with circular cores (Keener, 1988) and excitation fronts (Kuramoto, 1980), which have lead to instability criteria for pattern formation in the heart (Biktashev et al., 1994; Dierckx et al., 2012).

Fourth, a consequence of this investigation is that describing fibrillation patterns using PSs only (Gray et al., 1995b; Gurevich and Grigoriev, 2019) may not be sufficient to fully understand the dynamics if conduction block occurs. Therefore, these studies could benefit from additional identification of PDLs, of which we made first steps in **Figures 11**, **13**.

Finally, our preliminary results on 3D dynamics in **Figure 11**, and **Figure 12** is a first step to extending the filament concept to the PDSs, like was done here to go from PSs to PDLs. In 2D, we here demonstrated that circular-core spiral waves are centered around a PS and linear-core meandering spirals rotate around a PDL. Since in 3D, the collection of classical PSs forms a filament curve, linear-core scroll waves extend to PDSs. Therefore, the study of the dynamics of meandering scroll waves can benefit

from its description in terms of phase defect surfaces. These surfaces, as shown in **Figures 11**, **12** have a ribbon shape (Efimov et al., 1999), but the meaning of the ribbon is different from the ribbon model for filaments (Echebarria et al., 2006), where the surface normal of the ribbon was purely related to scroll wave twist. In our framework, the width of the PDS (ribbon) is approximately equal to the length of the PDL in 2D. How dynamical concepts such as filament tension (Biktashev et al., 1994) and rigidity (Dierckx et al., 2012) generalize to PDSs is still an open problem. For the intermediate case of flower-like meander (Barkley et al., 1990), between the extremes of circular and linear cores, it still needs to be determined whether the phase structure is a PS, PDL or a different structure. Further analysis of complex 3D dynamics in the phase defect framework will be the topic of further investigation.

4.5. Interpretation of Experimental Results

Our analysis of rotors observed in isolated rabbit hearts during experiments shows in short two observations. First, that PSs on the epicardium were in this system always located on conduction block lines (PDLs). This observation is in line with older and more recent literature (Efimov et al., 1999; Podziemski et al., 2018). Second, the rotors were not performing more than one full rotation. To our knowledge, the question on why rotors are not performing multiple rotations in ventricular tissue is unresolved. The phase defect framework may be used to answer this question in a comprehensive manner, rather than resorting to numerical simulations only.

Another relevant question is whether the PS or PDL is the structure that governs the organization of cardiac arrhythmias. Here, we would answer that both are intricately related to each other: in systems with linear-core rotors, we think the PS only arises due to smoothing of the phase field and is therefore located at a specific spot on the PDL, often where it meets the wave front. Whether one should localize PSs or PDLs in experiments or clinical situation, depends on the application and desired accuracy.

4.6. Limitations and Outlook

The concept of PDLs was illustrated here in a very simple setting: we mostly considered single rotors or rotor creation in 2D. Our initial results in 3D (see **Figure 12**) and with break-up patterns (see **Figure 11**) show that there is rich dynamics present that can be further analyzed using the phase defect framework. We also did not consider alternans here, as in that case the inertial manifold in state space will be not a simple closed curve, and may require two or more phase parameters to describe those states. This effort will be undertaken in future work.

Also, we have described the framework in a general setting, without explicit attention to the reason why rotors form in the system. Future work could be directed to elucidate differences between rotors formed by dynamical breakup (e.g., in atrial fibrillation models) or by interaction with inhomogeneities of the medium.

In this paper, the phase defect concept was used only to describe the observed patterns, without yet looking into how the topology determines the evolution of the structures such as WFs, WBs, and PDLs. Still, we developed the phase defect framework with the aim of providing a comprehensive quantitative analysis of excitation patterns, in the line of previous works on circular-core rotors and filaments (Keener, 1988; Wellner et al., 2002; Verschelde et al., 2007; Dierckx et al., 2012). The PDL concept provides not only a terminology for it, but also a way forward: solutions will need to be stitched together at the PDL interface, to elucidate their dynamics, much like was done before for wave front dynamics (Keener, 1986).

In the optical mapping experiments, the mechanical uncoupler blebbastatin was used, which however also affects the physiology of the cardiac cells. Therefore, the phase defect structures that we observed could be different from real cardiac tissue where no such uncoupler is present.

Furthermore, we used simple methods to find PDLs and WFs in the experimental data. As a result of representing the PDL as a spline curve, it is seen in **Figure 13** that the wave fronts are not exactly touching the PDLs, while this is expected from theory. We will continue refining our numerical processing methods to make this image more consistent.

This study was also set in a fundamental science setting. Yet, it is inspired by the clinically relevant length and timescales: how do local dynamics self-organize in complex patterns with rotors and conduction block lines? In our opinion, contributions to the answer can be found from scrutinizing the patterns themselves, and building up a comprehensive understanding after the correct building blocks have been identified.

Finally, we suggest to try our methods to clinically relevant datasets, such as LAT maps derived from local electrograms. Existing algorithms could be tuned or extended, given that the classical PS was found in our simulations and experiments on a line of nearly discontinous phase.

4.7. Conclusion

In summary, the key ideas presented in this manuscript are:

1. Near conduction block lines, the phase of cardiac cells is close to discontinuous along a line, rather than along a point, as assumed in classical phase analysis;
2. Therefore, in excitable systems that have a forbidden zone in the inner region of their typical excursion (action potential) in state space, detected PSs are located at PDLs;
3. There is more than one definition of phase, and these different phases can be translated into each other depending on the goal and available data.

As a historical note, we find that the name of mathematician Bernhard Riemann is inscribed twice in our hearts: the heart is not only a Riemannian manifold due to anisotropy of wave propagation (Wellner et al., 2002; Verschelde et al., 2007; Young and Panfilov, 2010), but also features phase defect lines showing

non-trivial Riemannian surfaces that organize the electrical patterns during arrhythmias.

DATA AVAILABILITY STATEMENT

The raw data supporting the conclusions of this article will be made available by the authors, without undue reservation.

ETHICS STATEMENT

The animal study was reviewed and approved by use of data (no new experiments).

AUTHOR CONTRIBUTIONS

HD and ET conceived the study. ET conducted optical mapping experiments. HD and LA ran the numerical simulations and performed experimental data analysis together with JQ, NN, and MV. All authors contributed to manuscript writing and internal reviewing.

FUNDING

ET was supported by National Science Foundation DCSD Grant 1662250. HD received mobility funding from the FWO-Flanders, Grant K145019N. LA was supported by a KU Leuven FLOF grant.

ACKNOWLEDGMENTS

We thank Alexander V. Panfilov, A. M. Pertsov, and D.A. Pijnappels for helpful comments on the manuscript and L. Leenknegt and D. Kabus for proofreading. A pre-print of this article is available at the following link: https://arxiv.org/abs/2101.00315v1. The content of this manuscript is also available on Arxiv at https://arxiv.org/abs/2101.00315.

SUPPLEMENTARY MATERIAL

The Supplementary Material for this article can be found online at: https://www.frontiersin.org/articles/10.3389/fphys.2021.690453/full#supplementary-material

REFERENCES

Aliev, R., and Panfilov, A. (1996). A simple two-variable model of cardiac excitation. *Chaos Solitons Fractals* 7, 293–301. doi: 10.1016/0960-0779(95)00089-5

Allessie, M., Bonke, F., and Schopman, F. (1973). Circus movement in rabbit atrial muscle as a mechanism of tachycardia. *Circ. Res.* 33, 54–62. doi: 10.1161/01.RES.33.1.54

Arfken, G. B., and Weber, H. J. (1995). *Mathematical Methods for Physicists, 4th Edn*. San Diego, CA: Academic Press.

Arno, L., Quan, J., Vanmarcke, M., Nguyen, N., Tolkacheva, E., and Dierckx, H. (2021). Phase defect lines during cardiac arrhythmias: from theory to experiment. *arXiv [Preprint] arXiv*:2101.00315. Available online at: https://arxiv.org/abs/2101.00315v1

Barkley, D., Kness, M., and Tuckerman, L. (1990). Spiral-wave dynamics in a simple model of excitable media: the transition from simple to compound rotation. *Phys. Rev. A* 42, 2489–2492. doi: 10.1103/PhysRevA.42.2489

Biktashev, V., Holden, A., and Zhang, H. (1994). Tension of organizing filaments of scroll waves. *Philos. Trans. R. Soc. Lond. A* 347, 611–630. doi: 10.1098/rsta.1994.0070

Biktasheva, I., and Biktashev, V. (2003). Wave-particle dualism of spiral wave dynamics. *Phys. Rev. E* 67:026221. doi: 10.1103/PhysRevE.67.026221

Bray, M.-A., and Wikswo, J. (2002). Considerations in phase plane analysis for nonstationary reentrant cardiac behavior. *Phys. Rev. E* 65:051902. doi: 10.1103/PhysRevE.65.051902

Bray, M.-A., and Wikswo, J. (2003). Examination of optical depth effects on fluorescence imaging of cardiac propagation. *Biophys. J.* 85, 4134–4145. doi: 10.1016/S0006-3495(03)74825-5

Bueno-Orovio, A., Cherry, E., and Fenton, F. (2008). Minimal model for human ventricular action potentials in tissue. *J. Theor. Biol.* 253, 544–560. doi: 10.1016/j.jtbi.2008.03.029

Clayton, R., Zhuchkova, E., and Panfilov, A. (2005). Phase singularities and filaments: simplifying complexity in computational models of ventricular fibrillation. *Prog. Biophys. Mol. Biol.* 90, 378–398. doi: 10.1016/j.pbiomolbio.2005.06.011

Dierckx, H., Selsil, O., Verschelde, H., and Biktashev, V. (2012). Buckling of scroll waves. *Phys. Rev. Lett.* 109:174102. doi: 10.1103/PhysRevLett.109.174102

Dierckx, H., Verschelde, H., and Panfilov, A. (2017). Measurement and structure of spiral wave response functions. *Chaos* 27, 1–10. doi: 10.1063/1.4999606

Echebarria, B., Hakim, V., and Henry, H. (2006). Nonequilibrium ribbon model of twisted scroll waves. *Phys. Rev. Lett.* 96:098301. doi: 10.1103/PhysRevLett.96.098301

Efimov, I., Sidorov, V., Cheng, Y., and Wollenzier, B. (1999). Evidence of 3d scroll waves with ribbon-shaped filament as a mechanism of ventricular tachycardia in the isolated rabbit heart. *J. Cardiovasc. Electrophysiol.* 10, 1452–1462. doi: 10.1111/j.1540-8167.1999.tb00204.x

Fenton, F., and Karma, A. (1998). Vortex dynamics in three-dimensional continuous myocardium with fiber rotation: filament instability and fibrillation. *Chaos* 8, 20–47. doi: 10.1063/1.166311

Gray, R., Jalife, J., Panfilov, A., Baxter, W., Cabo, C., Davidenko, J., et al. (1995a). Mechanisms of cardiac fibrillation. *Science* 270, 1222–1223. doi: 10.1126/science.270.5239.1222

Gray, R., Jalife, J., Panfilov, A., Baxter, W., Cabo, C., and Pertsov, A. (1995b). Non-stationary vortex-like reentrant activity as a mechanism of polymorphic ventricular tachycardia in the isolated rabbit heart. *Circulation* 91, 2454–2469. doi: 10.1161/01.CIR.91.9.2454

Gray, R., Pertsov, A., and Jalife, J. (1998). Spatial and temporal organization during cardiac fibrillation. *Nature* 392, 75–78. doi: 10.1038/32164

Gurevich, D., and Grigoriev, R. (2019). Robust approach for rotor mapping in cardiac tissue. *Chaos* 29:053101. doi: 10.1063/1.5086936

Hren, R., and Stroink, G. (1995). Application of surface harmonic expansions for modeling human torso. *IEEE Trans. Biomed. Eng.* 42, 521–524. doi: 10.1109/10.376157

Keener, J. (1986). A geometrical theory for spiral waves in excitable media. *SIAM J. Appl. Math.* 46, 1039–1056. doi: 10.1137/0146062

Keener, J. (1988). The dynamics of three-dimensional scroll waves in excitable media. *Phys. D* 31, 269–276. doi: 10.1016/0167-2789(88)90080-2

Kuklik, P., Zeemering, S., Maesen, B., Maessen, J., Crijns, H., Verheule, S., et al. (2015). Reconstruction of instantaneous phase of unipolar atrial contact electrogram using a concept of sinusoidal recomposition and hilbert transform. *IEEE Trans. Biomed. Eng.* 62, 296–302. doi: 10.1109/TBME.2014.2350029

Kuklik, P., Zeemering, S., Van Hunnik, A., Maesen, B., Pison, L., Lau, D., et al. (2017). Identification of rotors during human atrial fibrillation using contact mapping and phase singularity detection: technical considerations. *IEEE Trans. Biomed. Eng.* 64, 310–318. doi: 10.1109/TBME.2016.2554660

Kulkarni, K., Lee, S. W., Kluck, R., and Tolkacheva, E. G. (2018). Real-time closed loop diastolic interval control prevents cardiacalternans in isolated whole rabbit hearts. *Ann. Biomed. Eng.* 46, 555–566. doi: 10.1007/s10439-018-1981-2

Kuramoto, K. (1980). Instability and turbulence of wave fronts in reaction-diffusion systems. *Prog. Theor. Phys*. 63, 1885–1903. doi: 10.1143/PTP.63.1885

Landau, L., and Lifshitz, E. (1935). On the theory of the dispersion of magnetic permeability in ferromagnetic bodies. *Phys. Z. Sowjetunion* 53, 153–164.

Marcotte, C. D., and Grigoriev, R. O. (2015). Unstable spiral waves and local Euclidean symmetry in a model of cardiac tissue. *Chaos* 25:063116. doi: 10.1063/1.4922596

Mines, G. (1913). On dynamics equilibrium in the heart. *J. Physiol*. 46, 349–382. doi: 10.1113/jphysiol.1913.sp001596

Podziemski, P., Zeemering, S., Kuklik, P., van Hunnik, A., Maesen, B., Maessen, J., et al. (2018). Rotors detected by phase analysis of filtered, epicardial atrial fibrillation electrograms colocalize with regions of conduction block. *Circ. Arrhythmia Electrophysiol*. 11:e005858. doi: 10.1161/CIRCEP.117.005858

Tomii, N., Yamazaki, M., Ashihara, T., Nakazawa, K., Shibata, N., Honjo, H., et al. (2021). Spatial phase discontinuity at the center of moving cardiac spiral waves. *Comput. Biol. Med*. 130:104217. doi: 10.1016/j.compbiomed.2021.104217

Verschelde, H., Dierckx, H., and Bernus, O. (2007). Covariant stringlike dynamics of scroll wave filaments in anisotropic cardiac tissue. *Phys. Rev. Lett*. 99:168104. doi: 10.1103/PhysRevLett.99.168104

Vilenkin, A. (1985). Cosmic strings and domain walls. *Phys. Rep*. 121, 263–315. doi: 10.1016/0370-1573(85)90033-X

Wellner, M., Berenfeld, O., Jalife, J., and Pertsov, A. (2002). Minimal principle for rotor filaments. *Proc. Natl. Acad. Sci. U.S.A*. 99, 8015–8018. doi: 10.1073/pnas.112026199

Williams, R. (1963). Domains in liquid crystals. *J. Chem. Phys*. 39, 384–388. doi: 10.1063/1.1734257

Winfree, A. T. (1974). Patterns of phase compromise in biological cycles. *J. Math. Biol*. 1, 73–93. doi: 10.1007/BF02339491

Young, R., and Panfilov, A. (2010). Anisotropy of wave propagation in the heart can be modeled by a riemannian electrophysiological metric. *Proc. Natl. Acad. Sci. U.S.A*. 107, 15063–15068. doi: 10.1073/pnas.1008837107

Conflict of Interest: The authors declare that the research was conducted in the absence of any commercial or financial relationships that could be construed as a potential conflict of interest.

frontiers in Physiology

ORIGINAL RESEARCH
published: 27 September 2021
doi: 10.3389/fphys.2021.734178

Long-Time Prediction of Arrhythmic Cardiac Action Potentials Using Recurrent Neural Networks and Reservoir Computing

Shahrokh Shahi[1]*, *Christopher D. Marcotte*[1], *Conner J. Herndon*[2], *Flavio H. Fenton*[2], *Yohannes Shiferaw*[3] *and Elizabeth M. Cherry*[1]

[1] School of Computational Science and Engineering, Georgia Institute of Technology, Atlanta, GA, United States, [2] School of Physics, Georgia Institute of Technology, Atlanta, GA, United States, [3] Department of Physics & Astronomy, California State University, Northridge, CA, United States

The electrical signals triggering the heart's contraction are governed by non-linear processes that can produce complex irregular activity, especially during or preceding the onset of cardiac arrhythmias. Forecasts of cardiac voltage time series in such conditions could allow new opportunities for intervention and control but would require efficient computation of highly accurate predictions. Although machine-learning (ML) approaches hold promise for delivering such results, non-linear time-series forecasting poses significant challenges. In this manuscript, we study the performance of two recurrent neural network (RNN) approaches along with echo state networks (ESNs) from the reservoir computing (RC) paradigm in predicting cardiac voltage data in terms of accuracy, efficiency, and robustness. We show that these ML time-series prediction methods can forecast synthetic and experimental cardiac action potentials for at least 15–20 beats with a high degree of accuracy, with ESNs typically two orders of magnitude faster than RNN approaches for the same network size.

Keywords: reservoir computing, recurrent neural network, echo state network, time series forecasting, cardiac action potential

OPEN ACCESS

Edited by:
Hans Dierckx,
KU Leuven Kulak, Belgium

Reviewed by:
Edward Joseph Vigmond,
Université de Bordeaux, France
Kunichika Tsumoto,
Kanazawa Medical University, Japan

***Correspondence:**
Shahrokh Shahi
shahi@gatech.edu

Specialty section:
This article was submitted to Computational Physiology and Medicine, a section of the journal Frontiers in Physiology

Received: *30 June 2021*
Accepted: *27 August 2021*
Published: *27 September 2021*

Citation:
Shahi S, Marcotte CD, Herndon CJ, Fenton FH, Shiferaw Y and Cherry EM (2021) Long-Time Prediction of Arrhythmic Cardiac Action Potentials Using Recurrent Neural Networks and Reservoir Computing. Front. Physiol. 12:734178. doi: 10.3389/fphys.2021.734178

1. INTRODUCTION

Cardiac electrical signals, known as action potentials, exhibit complex non-linear dynamics, including period-doubling bifurcations in their duration (Guevara et al., 1984; Watanabe et al., 2001) and amplitude (Chen et al., 2017), along with higher-order period-doublings (Gizzi et al., 2013) and chaotic behavior (Chialvo et al., 1990). Potentially life-threatening states like fibrillation often are preceded by such long-short oscillations in action potential duration or amplitude known as alternans in the medical literature (Nolasco and Dahlen, 1968; Pastore et al., 1999; Gizzi et al., 2013; Chen et al., 2017). A number of methods for control of cardiac alternans have been developed (Rappel et al., 1999; Christini et al., 2006; Berger et al., 2007; Garzón et al., 2009; Garzon et al., 2014; Kulkarni et al., 2018), and while some have been demonstrated in cardiac experimental preparations (Christini et al., 2006; Kulkarni et al., 2018), they have not yet found clinical application in part because of the limited length scales over which control can be accomplished (Echebarria and Karma, 2002; Garzon et al., 2014; Otani, 2017). An alternative

strategy focusing on preventing rather than controlling alternans could be more attractive clinically, but such an approach would require accurate prediction of when such dynamics would occur.

Data-driven approaches can be used to forecast systems like cardiac action potentials by inferring the dynamics from observed data represented as time series (Kutz, 2013). Along with conventional techniques for time-series modeling and forecasting like autoregression approaches (Stock and Watson, 2001; Ing, 2003) and dynamic mode decomposition (Schmid, 2010), machine-learning methods have become increasingly used for predicting dynamical system states (Kutz, 2013; Chattopadhyay et al., 2020; Dubois et al., 2020). Recent years have seen significant advances in the field of machine learning, especially deep learning techniques. Recurrent neural networks (RNNs) have been successfully employed in dynamical domains, as the recurrent connections in the network provide a notion of memory and allow them to naturally embed temporal information. However, RNNs are still trained using the computationally expensive technique of back-propagation through time and remain prone to vanishing and exploding gradient problems. Gated RNNs can help overcome some of these problems; for example, to overcome the vanishing gradient problem, gated RNNs take advantage of memory cell architecture and a gating mechanism allowing the network to select which information should be kept and which forgotten (Hochreiter and Schmidhuber, 1997). This process enables the network to learn the long-term dependencies in sequential temporal data. Two widely used gated RNN approaches include long short-term memory (LSTM) networks and gated recurrent units (GRUs).

An alternative approach for modeling and predicting dynamical systems is reservoir computing (RC) (Lukoševičius and Jaeger, 2009; Sun et al., 2020), where, in contrast to other RNN architectures, the training remains limited to the output layer and the remaining parameters are selected randomly. Despite this simplification compared to other RNN architectures, RC techniques, including the commonly used echo state network (ESN) approach (Jaeger, 2002; Lukoševičius, 2012), have been used successfully to provide accurate multi-step-ahead predictions in non-linear and chaotic time series with very low computational costs (Bianchi et al., 2017; Han et al., 2021). Variations of ESNs, including clustered ESNs, where the reservoir consists of multiple sparsely connected sub-reservoirs (Deng and Zhang, 2006; Junior et al., 2020), and hybrid ESNs, which include input from a mathematical model and are a type of physics-informed machine learning technique (Oh, 2020; Willard et al., 2020), have been shown to have good performance in some cases (Pathak et al., 2018; Doan et al., 2019).

In this work, we show that it is possible to accurately predict future sequences of cardiac action potentials from complex voltage activity obtained *in silico* and in *ex-vivo* experiments. We further compare the performance of several machine-learning techniques for a multi-step prediction of complex cardiac action potential time series. In particular, we consider the accuracy and computational efficiency of LSTMs and GRUs along with ESNs, including a clustered architecture and a physics-informed hybrid option, for different network sizes.

2. METHODS

Below we provide a brief overview of machine-learning-based time series forecasting methods, describe the datasets we use, and give the details of our specific implementations.

2.1. Time Series Forecasting Methods

In this section, we provide a brief summary of the machine-learning approaches we use to forecast cardiac action potential time series.

2.1.1. Gated Recurrent Neural Networks

Recurrent neural networks (RNN) were introduced as a special class of neural networks in which the recurrent connections allow information to persist in the network. However, they suffer from vanishing and exploding gradient problems, which limit their ability to learn long-term dependencies in temporal sequences. Gated RNNs like long short-term memory networks (LSTMs) were developed to remedy such problems. These networks employ memory cells and a gating mechanism to address exactly these issues. **Supplementary Figure 1A** illustrates the information flow in an LSTM cell. In an LSTM network, a hidden state h_t is calculated using a map formalism:

$$\begin{aligned} i_t &= \sigma(\boldsymbol{W_i} x_t + \boldsymbol{U_i} h_{t-1} + b_i), \\ f_t &= \sigma(\boldsymbol{W_f} x_t + \boldsymbol{U_f} h_{t-1} + b_f), \\ o_t &= \sigma(\boldsymbol{W_o} x_t + \boldsymbol{U_o} h_{t-1} + b_o), \\ \tilde{c_t} &= \tanh(\boldsymbol{W_c} x_t + \boldsymbol{U_c} h_{t-1} + b_c), \\ c_t &= f_t \odot c_{t-1} + i_t \odot \tilde{c_t}, \\ h_t &= \tanh(c_t) \odot o_t, \end{aligned} \tag{1}$$

where i_t, f_t, and o_t denote the input, forget, and output gates, at time t, respectively; x_t is the input vector; $\boldsymbol{W}$ and $\boldsymbol{U}$ are the weight matrices that along with biases b are adjusted during the learning process, c_t is the cell state (the internal memory of the LSTM unit), and $\tilde{c_t}$ is the cell input activation vector. In these equations, each σ function is sigmoidal and $\odot$ denotes Hadamard element-wise multiplication.

Gated recurrent units (GRUs) also were introduced to avoid vanishing and exploding gradient problems and share many similarities in architecture and performance with LSTM networks. The GRU memory cell can be considered as a simplification of an LSTM cell (see **Supplementary Figure 1B**). Compared to an LSTM memory cell, in a GRU unit, the input and forget gates are combined into a single update gate. This simplification considerably reduces the number of trainable weights and makes GRUs more computationally efficient; at the same time, the prediction does not experience a considerable deterioration in most cases and in some applications may even improve (Bianchi et al., 2017). The GRU equations are given by

$$\begin{aligned} z_t &= \sigma(\boldsymbol{W_z} x_t + \boldsymbol{U_z} h_{t-1} + b_z), \\ r_t &= \sigma(\boldsymbol{W_r} x_t + \boldsymbol{U_r} h_{t-1} + b_r), \\ \tilde{h_t} &= \tanh(\boldsymbol{W_h} x_t + \boldsymbol{U_h}(r_t \odot h_{t-1}) + b_h), \\ h_t &= (1 - z_t) \odot h_{t-1} + z_t \odot \tilde{h_t}, \end{aligned} \tag{2}$$

where z_t and r_t are update and reset gates, respectively, and $\tilde{h}_t$ is the candidate state. During the training process, the weight matrices $\boldsymbol{W}$ and $\boldsymbol{U}$ and the bias vector b are adjusted, thereby enabling the update and reset gates to select which information should be kept through time and which information is irrelevant for the problem and can be forgotten.

2.1.2. Echo State Networks

ESNs are a simple yet successful RNN architecture in which most of the network parameters are initialized randomly and remain untrained. **Supplementary Figures 2A,B** demonstrates the main components of an ESN. The hidden layer in an ESN is called the reservoir, which is a randomly initialized RNN.

The reservoir state h_t is updated according to

$$h_t = (1-\alpha)h_{t-1} + \alpha \tanh\left(\boldsymbol{W^{in}} x_t + \boldsymbol{W} h_{t-1}\right), \tag{3}$$

where $\boldsymbol{W^{in}}$ and $\boldsymbol{W}$ are the input weight and reservoir weight matrices, respectively; both are initialized randomly and remained untrained. We utilize an extension of the standard ESN formalism that includes a "leaky" update model, which explicitly includes a linear history term. The input signal is denoted by x_t and the constant parameter $\alpha \in [0, 1]$ is known as the leaking rate. The output of the network is calculated by the following equation:

$$y_t = f^{out}\left(\boldsymbol{W^{out}}\left[x_t; h_t\right]\right), \tag{4}$$

where f^{out} is the output layer activation function, which is chosen here as a unity function. The output weights $\boldsymbol{W^{out}}$ are obtained here by regularized least-square regression with Tikhonov regularization to avoid overfitting.

Since the initial success of reservoir computing techniques and ESNs, a variety of network topologies have been proposed in the literature, including clustered reservoirs and deep ESNs. The main components of the network are similar to the baseline ESN architecture except for the reservoir topology; for clustered ESNs, the randomized connections between neurons form a set of sub-reservoirs sparsely connected to each other. The network topology is schematically illustrated in **Supplementary Figures 2C,D** and the update and training equations are the same as those for the baseline ESN (Equations 3 and 4).

We also consider a hybrid ESN approach, which is a physics-informed machine learning approach in which a knowledge-based model is integrated into an ESN; the model and ESN operate simultaneously during the training and prediction. The architecture of this approach is presented in **Supplementary Figure 2E**. For our application, the network in this design is driven with three input signals: $u_1(t)$, the pacing stimulus exciting the network at prescribed intervals; $u_2(t) = V_{\mathrm{KB}}(t)$, the knowledge-based model providing the voltage dynamics of a cardiac cell; and $u_3(t) = V(t)$, the synthetic or experimental voltage measurements. The knowledge-based model can be a much simpler (typically imperfect) model that provides an approximation of the dynamical behavior of the system, such as the two-variable Mitchell-Schaeffer (Mitchell and Schaeffer, 2003) or three-variable Fenton-Karma (Fenton and Karma, 1998) model, to increase the predictive ability of the network. Consequently, the time evolution of the reservoir state h_t is given by the same Equation 3, where the input signal vector is formed as follow,

$$x_t = \left[(u_1(t); u_2(t); u_3(t)\right]. \tag{5}$$

Here we use the Corrado-Niederer update of the Mitchell-Schaeffer model (Corrado and Niederer, 2016) with $\tau_{in} = 0.3$ ms, $\tau_{out} = 6$ ms, $\tau_{open} = 120$ ms, $\tau_{close} = 150$ ms, and $v_{gate} = 0.13$.

2.2. Datasets

To evaluate and compare the performance of these approaches in forecasting cardiac action potential time series, the methods are applied to two synthetic datasets derived from cardiac cell models and to an experimental dataset. We describe the three datasets used below.

2.2.1. Fenton-Karma Model-Derived Dataset

As one dataset, we use a time series of randomly timed action potentials generated using the Fenton-Karma (FK) model (Fenton and Karma, 1998), which includes a voltage variable and two gating variables. The model uses the Beeler-Reuter fitting of the FK model (parameter set 3 in Fenton et al., 2002) and is paced with cycle lengths drawn from a normal distribution using a 2-ms square stimulus current with magnitude 0.4 for 100 beats. To ensure a wide range of action potential durations, the cycle length distribution is centered at 320 ms with a standard deviation of 50 ms. The differential equations of the model are solved using the forward Euler method with a fixed time step of 0.1 ms; this time series is coarsened to obtain the synthetic voltage dataset (see section 2.3.4). The voltage data is then coupled with the stimulus timing so that a multivariate dataset is used, as explained in section 2.3.5.

Figure 1A shows the voltage trace that together with the corresponding stimulus input form the FK dataset; **Figure 1B** shows the corresponding action potential duration (APD) values. Data selected for training are shown in blue and testing data are shown in black. Just over 80 action potentials are used for training and about 20 for testing. Because the cycle lengths used include values both above and below the bifurcation to alternans, the resulting APDs included in the dataset span a range of about 200 ms. **Figure 1C** shows a blowup of the shaded regions in **Figures 1A,B** to illustrate the irregular timing of stimuli and variation in voltage responses within the training data.

2.2.2. Noble Model-Derived Dataset

As a different type of model-derived dataset, we use the four-variable Noble model (Noble, 1962) for a Purkinje cell in the absence of external pacing. To provide variation in action potential timing and duration, the Noble model is coupled to the three-variable Lorenz model (Lorenz, 1963) in the chaotic regime ($\rho = 28$, $b = 8/3$, and $\sigma = 10$). Time is effectively rescaled in the Lorenz system by multiplying each of the three differential equations by a factor of 0.001. The anionic current conductance in the Noble model was set to be proportional to the z variable of the Lorenz model, thereby driving oscillations

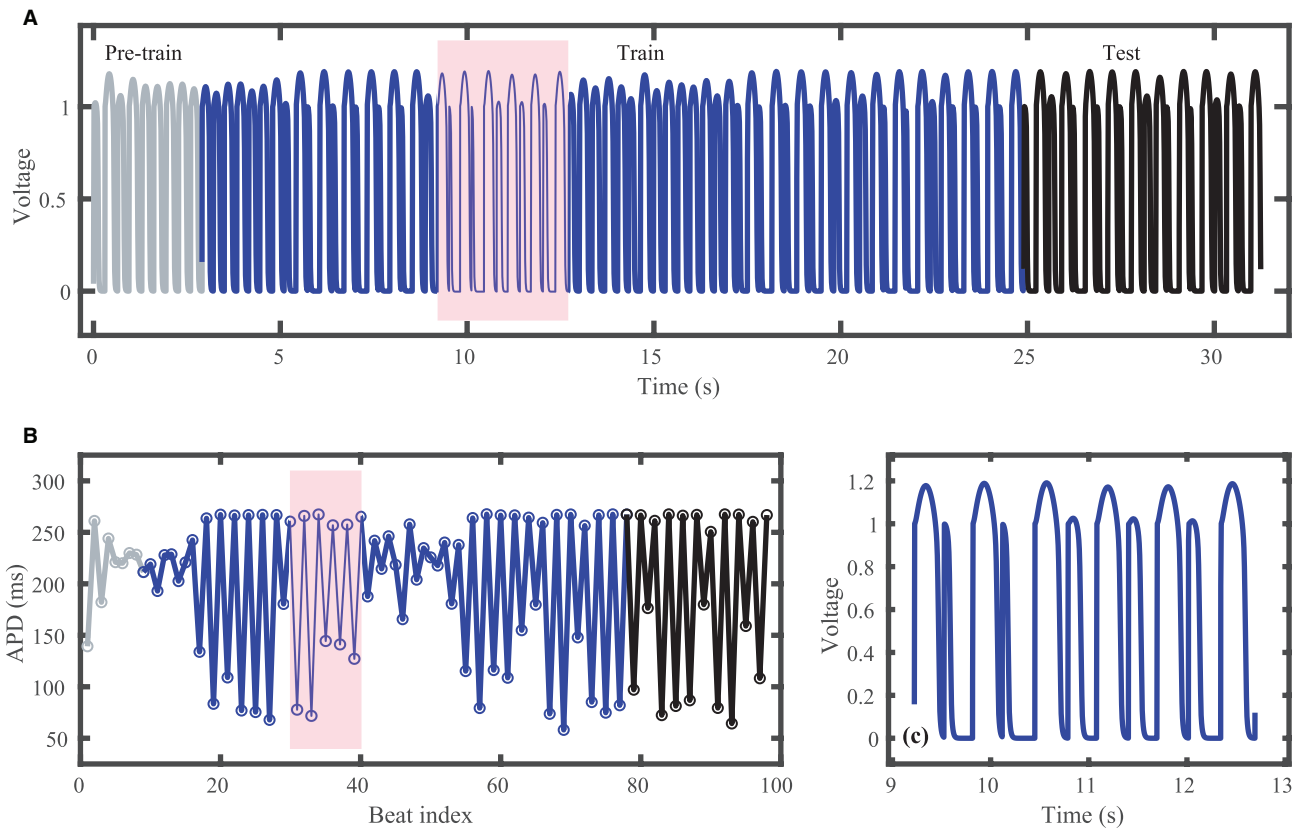

FIGURE 1 | Synthetic action potential time series generated by the Fenton-Karma (FK) model with randomly distributed cycle lengths. **(A)** Voltage time series including unused pre-training data (gray), training data (blue), and testing (prediction) data (black). **(B)** Corresponding APDs, following the same color scheme as **(A)**. **(C)** Zoomed in voltage trace corresponding to the shaded region in **(A,B)** showing the irregular action potential shapes and durations.

in the anionic current magnitude in concert with the Lorenz oscillations. Specifically, the conductance was set to 0 for $z = 0$ and to 0.2 for $z = 60$. This extension provides two important features of this dataset: first, the variation in cycle lengths is driven by a chaotic, rather than a random process, and second, there is no need for application of an external stimulus, as action potentials occur when the cell is quiescent and the Lorenz-driven current brings the voltage above the threshold for excitation. Therefore, in this case, only a univariate time series of voltage data is provided, with no external stimulus data. All other model parameters remain as specified in Noble (1962).

The Noble dataset voltage trace and action potentials are shown in **Figure 2**, with the training portion (around 65 action potentials) shown in blue and the testing portion (14 action potentials) in black. Because of the inclusion of the chaotic Lorenz model as a driving force, the Noble model-derived dataset demonstrates considerable variation in action potentials, with no consistent pattern. APDs vary between about 310 and 345 ms.

2.2.3. Experimental Dataset

The third dataset consists of irregular activity recorded from zebrafish hearts subjected to constant diastolic interval (DI) pacing (Cherry, 2017; Zlochiver et al., 2017); see **Figure 3**. All experimental procedures were approved by the office of Research Integrity Assurance of Georgia Tech under IACUC A100416. Zebrafish (*Danio rerio*) of either sex were anesthetized via cold water bath. Following anesthesia, hearts were quickly excised and immersed in Tyrode's solution (in mM: NaCl 124, KCl 4, $NaHCO_3$ 24, $NaH_2PO_4{\cdot}H_2O$ 0.9, $MgCl_2{\cdot}6H_2O$ 2, dextrose 5.5). Blebbistatin, used to stop contraction without major effects on electrophysiology (Fenton et al., 2008; Kappadan et al., 2020), was added to Tyrode's solution 20–30 min prior to data acquisition to help suppress heart motion. The heart was held in place by insect pins which attached the bulbus arteriosus to the bottom of a Sylgard-lined Petri dish. Stimulation was applied through AgCl bipolar electrodes placed on opposite sides of the heart close by to stimulate via electric field.

Intra- and extracellular voltages were acquired by two glass micropipettes containing 2.5 M KCl solution fastened into microelectrode holders (MEH3SFW, World Precision Instruments). Ag/AgCl half cells within the microelectrode holders sent signals to be buffered by pair of DC-powered preamplifiers (Electro 705, World Precision Instruments), which were connected together to output a differential measurement of transmembrane voltage. This transmembrane voltage was

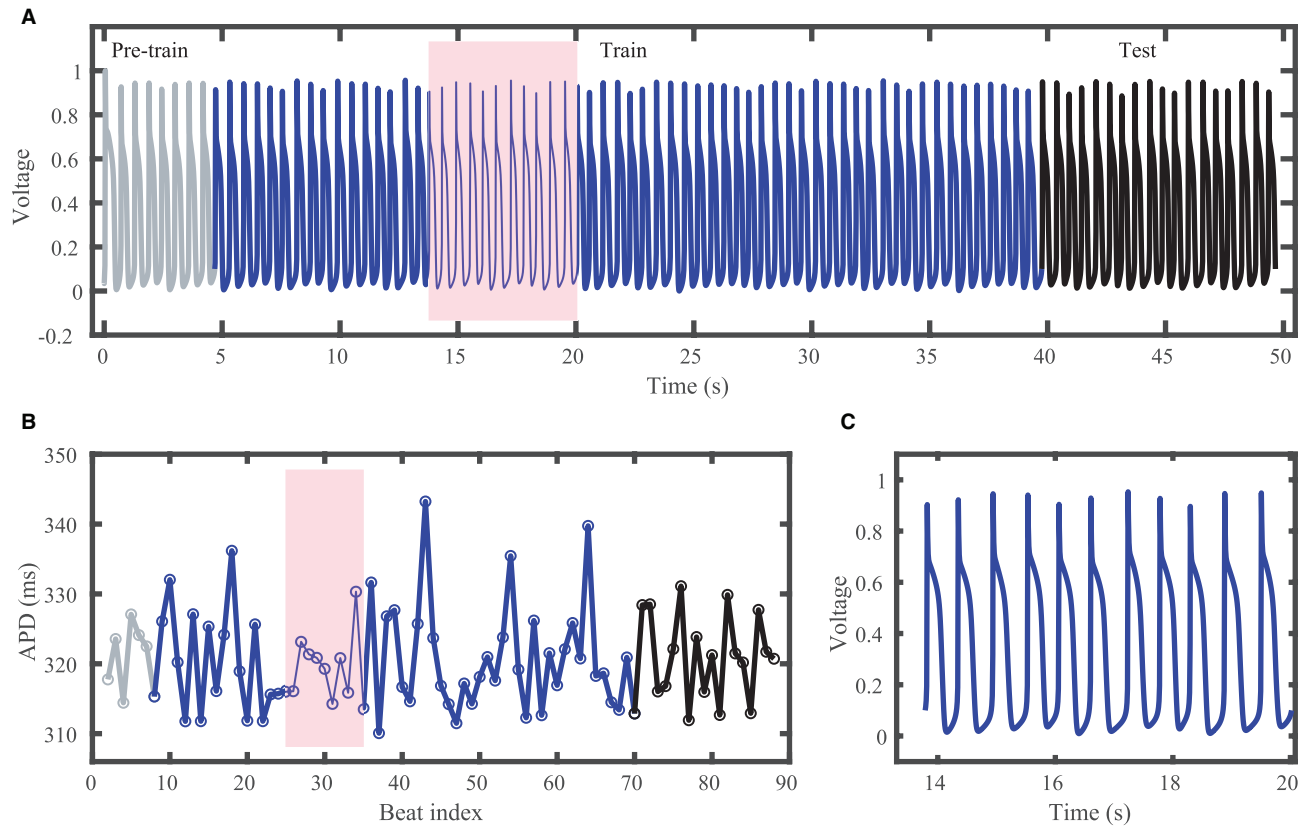

FIGURE 2 | Synthetic action potential time series generated by the Noble model driven by the chaotic Lorenz model. **(A)** Voltage time series including unused pre-training data (gray), training data (blue), and testing (prediction) data (black). **(B)** Corresponding APDs, following the same color scheme as **(A)**. **(C)** Zoomed in voltage trace corresponding to the shaded region in **(A,B)** showing the irregular action potential shapes and durations.

then split into two paths. One path led through a BNC breakout board (BNC-2110, National Instruments) to be read by a DAQ (PCIe-6341, National Instruments) and written to a file at 10,000 samples/s by a computer running a custom-built MATLAB script. Transmembrane voltage was also sent through a custom-built circuit that applied a gain and offset to the signals before being read by an Arduino Due. The Arduino Due then interpreted signals on-the-fly and determined when the heart should be stimulated to enforce a user-set DI, which was communicated to a current source stimulus isolator (Isostim A320, World Precision Instruments) that stimulated the heart.

Although constant-DI pacing can lead to stable and predictable APDs (Kulkarni et al., 2018), in our recordings APDs were highly variable despite the constant DI maintained. This high variability may result from the much smaller DIs used compared to the values used by Kulkarni et al. (2018), which were very close to the alternans bifurcation period. **Figure 3** shows the experimental dataset voltage trace and APDs, including over 100 training (blue) and over 20 testing (black) action potentials. Stimulus artifacts were removed using spline interpolation in a pre-processing step.

2.3. Implementation Details

All methods were implemented in MATLAB (R2020b) and were run on the same computer equipped with a 1.4 GHz Quad-Core Intel Core i5 processor and 8 GB of RAM, operating with macOS Big Sur (Version 11.4).

2.3.1. Hyperparameter Selection

The optimum values of various hyperparameters required for each method were tuned through an extensive grid search, the set of values for which are given in **Supplementary Table 1**. The ranges of the hyperparameter values used for the grid search and the number of values tested were chosen according to the results of initial experiments to generate reasonable results and also factor in the observed level of sensitivity of the employed approaches to each hyperparameter. Optimal hyperparameter values were obtained for each network size and dataset; see **Supplementary Tables 2–6**. Therefore, the results presented reflect the best attainable performance of each method for a given network size for each dataset.

2.3.2. Gated RNN Implementations

The LSTM and GRU networks are constructed using the MATLAB Deep Learning toolbox, where the network topologies

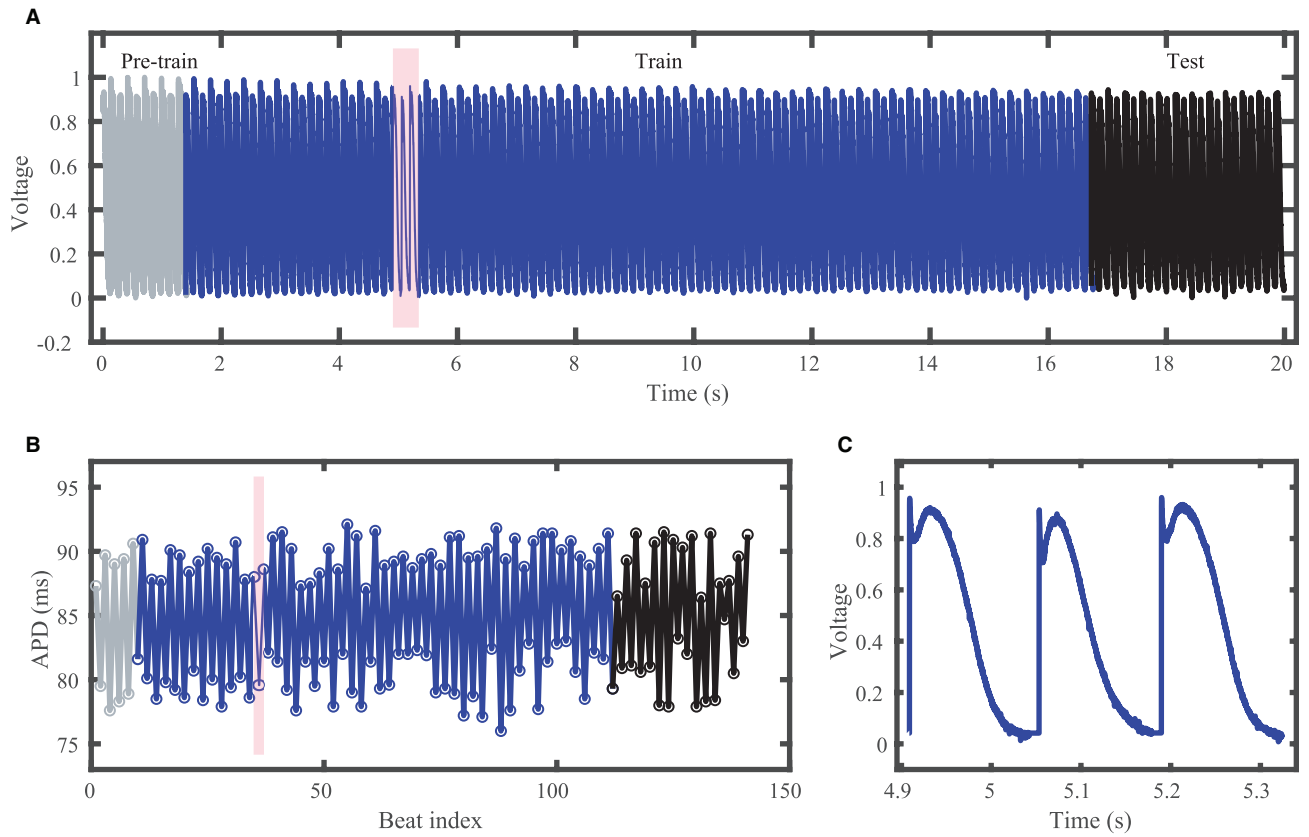

FIGURE 3 | Experimental zebrafish action potential time series featuring irregular alternans characterized by action potentials with irregular cycle lengths and durations. **(A)** Voltage time series including unused pre-training data (gray), training data (blue), and testing (prediction) data (black). **(B)** Corresponding APDs, following the same color scheme as **(A)**. **(C)** Zoomed in voltage trace corresponding to the shaded region in **(A,B)** showing the irregular action potential shapes and durations.

are specified by a graph of layers. To predict the action potential time series multiple steps into the future, a sequence-to-sequence regression LSTM architecture is employed that entails several main components. First, a sequential input layer is required to feed the input time series into the network. Then, an LSTM layer is used to learn the long-term dependencies between the time steps of the input sequential data. Finally, a fully connected layer connects the LSTM layer to a regression output layer to complete the design. The architecture of the GRU networks is the same as for the LSTM network except for employing a GRU layer instead of an LSTM layer. In addition to the single-layer architectures, multi-layer networks with multiple stacked gated layers are also tested in this work.

The main hyperparameters to configure in gated RNNs include the number of hidden layers and hidden units, the optimizer for the training network, and the hyperparameters related to the optimization solver, such as the maximum number of epochs, learning rate, learning rate drop factor, and regularization factor. Due to the high computational costs of gated RNNs, running an exhaustive grid search on all hyperparameters is not pragmatically feasible. Therefore, based on our initial experiments, some of these hyperparameters are set while the grid search determines the optimum values of those demonstrating a more significant role in the performance of the network. Accordingly, the Adam optimizer (Kingma and Ba, 2014) is employed for training the network with the MATLAB default training configurations and the maximum number of 30 epochs. Then, the grid search is employed to determine the optimum number of hidden layers and the initial learning rate (**Supplementary Tables 2**, **3**).

The trained network then can be used to predict the response of the system for the next time step. To forecast voltage values multiple steps ahead, a recursive approach is adopted in which at each time step, the response is predicted using the trained network and the network state is updated correspondingly. This predicted value is featured as the input for the next time step prediction. This procedure is repeated to predict the voltage response for the entire prediction horizon.

2.3.3. Echo State Network Implementations

The baseline ESN technique is implemented based on the original tutorial presented by Jaeger (2002) and the practical guide presented by Lukoševičius (2012). The reservoir graph is generated using the Erdős–Rényi algorithm (Bollobás, 2001), after which it is rescaled and updated to satisfy the echo state property of the network (Yildiz et al., 2012) ensuring that the

effect of initial conditions should vanish progressively and the reservoir state should asymptotically depend only on the input signals. The same procedure is conducted to construct the reservoirs in the clustered and hybrid ESNs. More specifically, in the hybrid ESN, the reservoir graph is generated with the same randomized approach, while in the clustered ESN, the sub-reservoir clusters are generated first, then connected to each other randomly, where an additional hyperparameter specifies the probability of the inter-cluster connections.

During the training of an ESN, the first initial steps of the network states are discarded to wash out the initial states and ensure the network dynamics are fully developed. Here, the first ten beats are considered as the transient phase and their corresponding state values are not used for training the networks.

Compared to the gated RNNs, the number of hyperparameters that play a more significant role in network performance in RC techniques is considerably higher, and the performance of the network highly depends on finding a good set of hyperparameters, including the number of neurons in the reservoir, connection probability used in the Erdős–Rényi graph generation step, reservoir spectral radius, input weight scale, leaking rate, and ridge regression regularization factor. Additionally, the number of clusters and the knowledge-based model are additional parameters to consider in clustered and hybrid ESNs, respectively. Although the size of the hyperparameter grid search space grows exponentially in RC techniques and is much higher compared to that of gated RNNs, because of the lower computational efforts required in ESN approaches, we obtained grid search results two times faster than for the gated RNNs.

Note that due to the random nature of ESNs and the intrinsic sensitivity of the network to the initial values of the parameters, the results for each network size are averaged over 10 experiments with different seed values for the random number generator.

2.3.4. Data Resampling

Although it is common to obtain data at a particular fixed time resolution, such a resolution often is not optimal; for example, it may contain so many points that it is difficult to obtain a good fit. More generally, an imbalanced distribution of data points in a time series can significantly deteriorate the performance of time-series prediction techniques. In such situations, a certain range of values are overrepresented compared to the rest of the time series, giving rise to a bias toward the values or behaviors that occur more frequently in the sequence. For example, in the case of an action potential time series, sampling that is uniform in time causes the upstroke phase, associated with the rapid depolarization of the cell membrane potential, to be underrepresented compared to the rest of the time series. Therefore, it is expected that prediction techniques may fail to correctly capture the upstroke phase in such cases and thus may produce a poor forecast overall. A common approach for tackling such issues is the use of resampling strategies (Moniz et al., 2017), which operate on the training dataset to make the distribution of the data points more balanced in terms of their information content.

In this work, we implement an under-sampling technique in which each data point is only included in the dataset if its voltage is sufficiently distinct from the last included data point, thereby ensuring more data points where the voltage changes rapidly. In this approach, two consecutive data points are considered distinct if the difference between the voltage values is greater than or equal to a threshold. If the threshold is set to zero, the dataset remains the same. In contrast, a very large threshold will result in great information loss and important features will be removed from the action potential time series. Therefore, the resampling threshold is also treated as a hyperparameter so that its optimum value is determined along with the other hyperparameters by the grid search. We also include a data point if the time since the last included data point exceeds a separate threshold, which is also treated as a hyperparameter, to ensure there is a sufficient density of points in portions of the action potential where the voltage changes slowly. **Supplementary Table 1** illustrates the possible values of the resampling thresholds used in the grid search. We found a significant increase in the predictive accuracy when using this resampling strategy and it is used for all results shown here.

2.3.5. Univariate vs. Multivariate Time Series Prediction

In practice, the action potential forecasting task entails predicting one variable (voltage) over time, resulting in a univariate time series. However, the input time series can be either a univariate or multivariate time series. The former occurs when the input data is assumed to be endogenous and is not driven by an external stimulus. The latter portrays cases in which cardiac cells are stimulated exogenously; in such a case, the pacing stimulus can also be introduced to the network along with the cardiac voltage signal. In this work, both scenarios are considered. Accordingly, the univariate input models are employed for forecasting the Noble dataset, where the auto-oscillatory nature of this model eliminates the requirements of applying an external stimulus. In contrast, both the FK dataset, which uses random stimulus timings, and the experimental dataset, which uses varying stimulus timings owing to the constant DIs but variable APDs, are used with multivariate time series prediction, which incorporates the pacing stimulus signal. In the case of the experimental data, the timing of applied stimuli is not directly available; thus, a pre-processing step is applied to detect the starting point of each beat in time and then a 2-ms stimulus current with a relative magnitude of 0.2 is used to generate the pacing stimulus signal. This process generates a stimulus current that is then resampled so that stimulus values are available for each resampled voltage data point. Our initial experiments demonstrate that the magnitude of the stimulus does not affect the quality of the predictions in this setup, but introducing the stimulus signal considerably improves the predictive ability in the first place.

Supplementary Figures 2A,C illustrate the architectures of the baseline and clustered ESNs, respectively, that are used for the univariate input case. To accommodate the pacing stimulus signal in multivariate input settings, these architectures are updated to include one more feature in the input layer (**Supplementary Figures 2B,D**). Introducing the stimulus

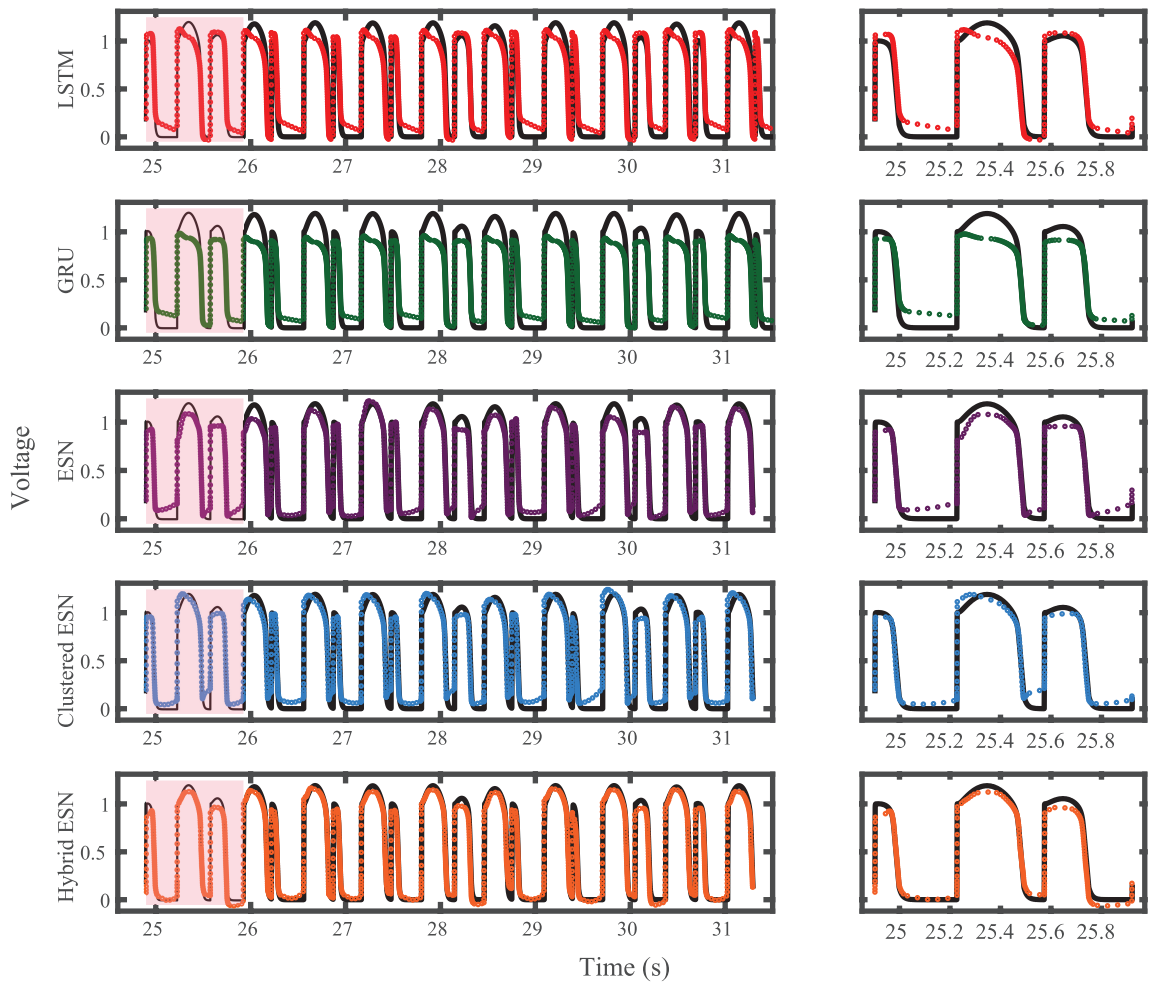

FIGURE 4 | FK dataset action potential prediction results obtained for the five methods using a fixed network size of 100 neurons. Test data are shown in black for reference and the predictions in color. **(Left)** All predicted APs. **(Right)** Zoomed view of the first three predicted APs.

information into the hybrid ESN approach is inevitable because in this architecture, the knowledge-based model should be synchronized with the input action potential time series to operate simultaneously. Therefore, the hybrid ESN is essentially developed for a multivariate input case (**Supplementary Figure 2E**). Accordingly, the pre-processing described step can be employed to extract the timing of the stimulus current. Similarly, in gated RNNs, the multivariate input case can be handled by adjusting the number of inputs in the sequential input layer.

2.3.6. Evaluation Metrics

To assess prediction accuracy, we use the root mean square error (RMSE) metric:

$$RMSE = \sqrt{\frac{1}{n}\sum_{i=1}^{n}\left(\hat{V}_i - V_i\right)^2}. \quad (6)$$

where V_i and $\hat{V}_i$ are the target and predicted outputs, respectively, and n denotes the length of the test dataset. Note that the voltage values of the Noble and experimental datasets have been linearly rescaled to be between zero and one. The FK model is already scaled so that its upstroke reaches a maximum of one; no further rescaling is performed. As discussed in section 2.3.4, in all cases, the dataset values used here are not uniformly spaced in time.

We also assess error by comparing action potential durations (APDs). We define an APD as the time interval over which the voltage during an action potential is continuously larger than the threshold value, which is selected as 0.3 for the synthetic datasets (FK and noble) and 0.35 for the experimental dataset.

3. RESULTS

3.1. FK Model-Derived Dataset

The FK model-derived dataset (hereafter referred to as the FK dataset), shown previously in **Figure 1**, includes irregularity in action potential shapes and durations through the use of cycle

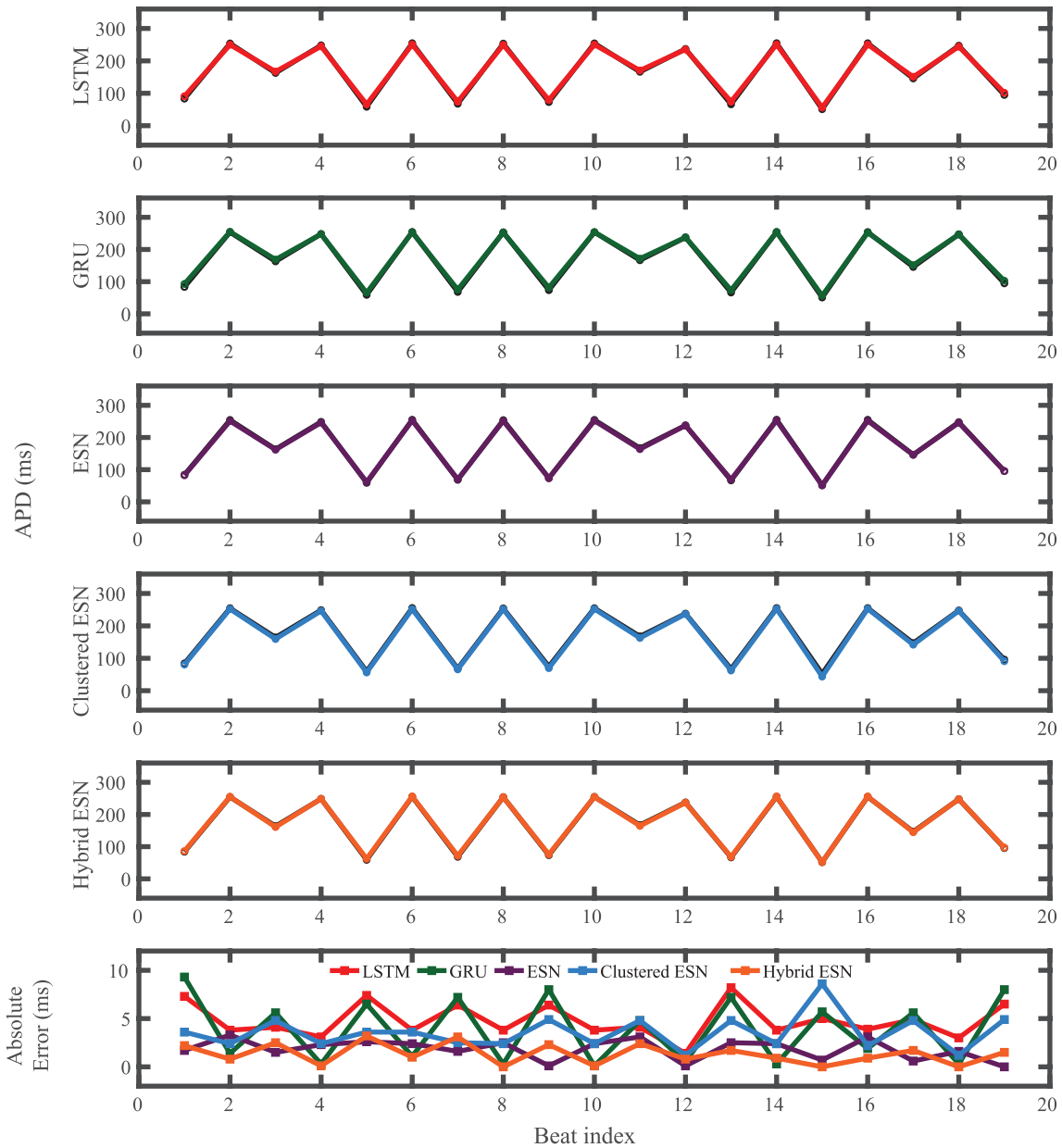

FIGURE 5 | FK dataset APD prediction results obtained for the five methods using a fixed network size of 100 neurons. APDs from data used for testing are shown in black for reference and predicted APDs are shown in color. Absolute error in APD prediction is shown in the bottom subplot, with color corresponding to prediction method.

lengths drawn from a normal distribution. **Figure 4** shows the 19 action potentials predicted by the five methods (LSTM, GRU, ESN, clustered ESN, and hybrid ESN) for a fixed network size of 100 hidden units. All five methods match the action potential upstrokes and downstrokes well. As a result, the predictions for APD by all methods have very low error (below 10 ms) across all 19 beats with no growth over time, as shown in detail in **Figure 5**, despite the irregular alternans present in the dataset. However, different methods exhibit different prediction accuracies for the plateau and rest phases of the action potentials. Specifically, the hybrid ESN does the best job of matching voltage values during these phases; the ESN approaches produce good results during the plateau but show depolarization preceding each action potential rather than remaining at a stable rest potential. The LSTM and GRU methods show the largest discrepancies, including plateau height mismatches and significant slowing in repolarization leading to elevated resting potentials.

Network size has a limited effect on overall accuracy as measured by RMSE. **Figure 6** shows that there is no clear trend in error as the network size is increased, except that the hybrid

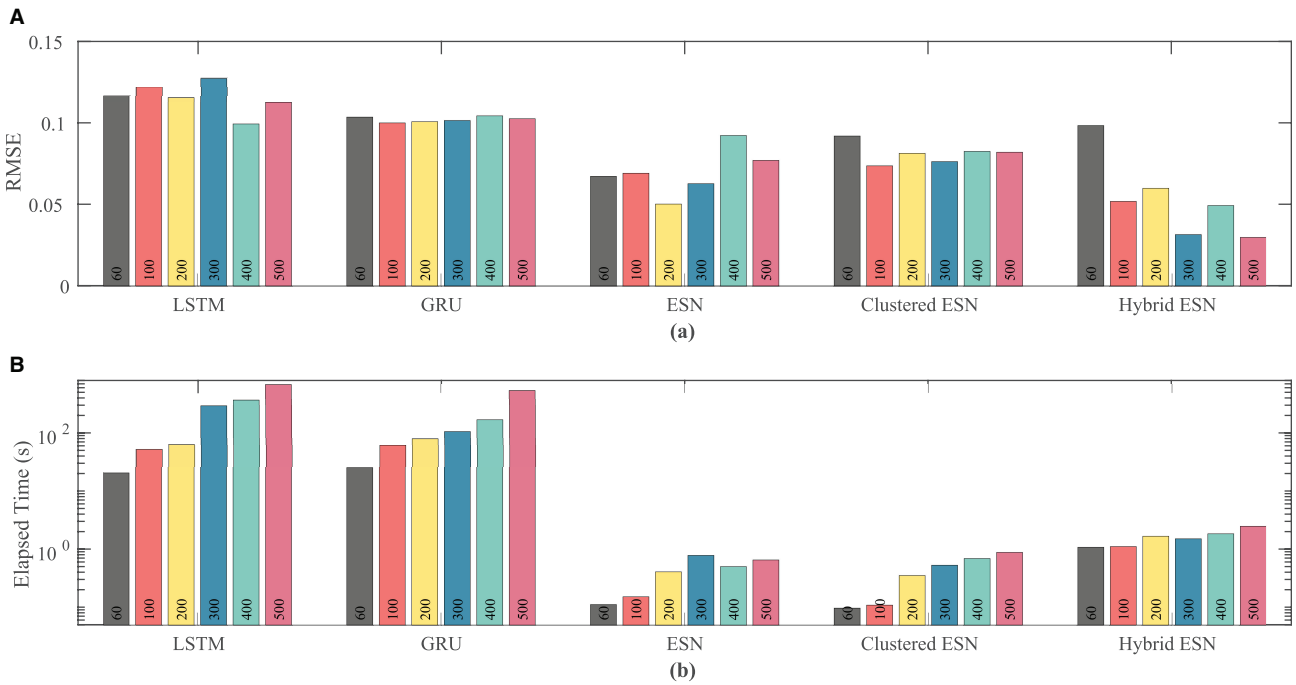

FIGURE 6 | Comparison of RMSE **(A)** and computational time **(B)** for each method and network size tested for the FK dataset.

ESN error is much lower for networks with at least 100 neurons. The hybrid ESN also has the lowest or near lowest error for all cases with at least 100 neurons, while the ESN and clustered ESN methods generally achieve slightly lower error than the LSTM and GRU methods.

The lower plot in **Figure 6** demonstrates that for a fixed network size the ESN and clustered ESNs accomplish the combination of training and prediction tasks much faster—by roughly two orders of magnitude—than the LSTM and GRU methods, with the hybrid ESN placing in between. These timing differences across the methods are maintained across all network sizes. However, within each individual method, the time for training and prediction increases with the number of neurons, except for the hybrid ESN method, for which such a trend is less clear.

3.2. Noble Model-Derived Dataset

The results of using the five methods to predict action potentials in the Noble dataset (shown in **Figure 2**) using a fixed network size of 100 can be seen in **Figure 7**, which shows the voltage traces, and in **Figure 8**, which shows the predicted APDs and absolute error in APD. The LSTM predictions generally achieve good agreement throughout the testing phase, with some discrepancies during the plateau and an overestimation of phase 4 depolarization. The GRU predictions are similar except that they repolarize less completely and consistently underestimate the peak upstroke voltage. The ESN and clustered ESN methods show improved accuracy with relatively minor discrepancies. In contrast, the hybrid ESN exhibits a very different action potential shape more in line with the capabilities of the knowledge-based model and consistently overestimates APD.

Figure 9 shows that the ESN and clustered ESNs achieve the lowest RMSE across different network sizes. The hybrid ESN and LSTM methods perform relatively well across most network sizes but produce larger RMSE values for some network sizes. GRUs have the highest error for most network sizes for this dataset. It is difficult to discern a clear trend in accuracy with increased network size; prediction method differences appear to have stronger effects.

As with the FK model, the RNN approaches consistently take longer than the ESN and clustered ESN approaches, with the hybrid ESN in between. For network sizes of at least 100 hidden units, the ESN and clustered ESN methods require about two orders of magnitude less computational time than the RNN methods. For all approaches, there is a modest increase in computational time for 100 or more hidden units as the network size increases, with the exception of the hybrid ESN, for which the computational time is approximately constant across all network sizes tested.

3.3. Experimental Dataset

For the experimental dataset, obtained from zebrafish paced using a constant-DI protocol and shown in **Figure 3**, all five methods are able to reconstruct most of the action potential features, as demonstrated in **Figure 10** with 100 hidden units. With each method, the discrepancies in predicted voltage values occur mostly during the portions of the action potentials with smaller voltage derivatives, the plateau and the rest phase. All methods underestimate the plateau height and fall short of repolarizing fully, with the hybrid ESN continuing to repolarize slowly throughout what should be the rest phase while the

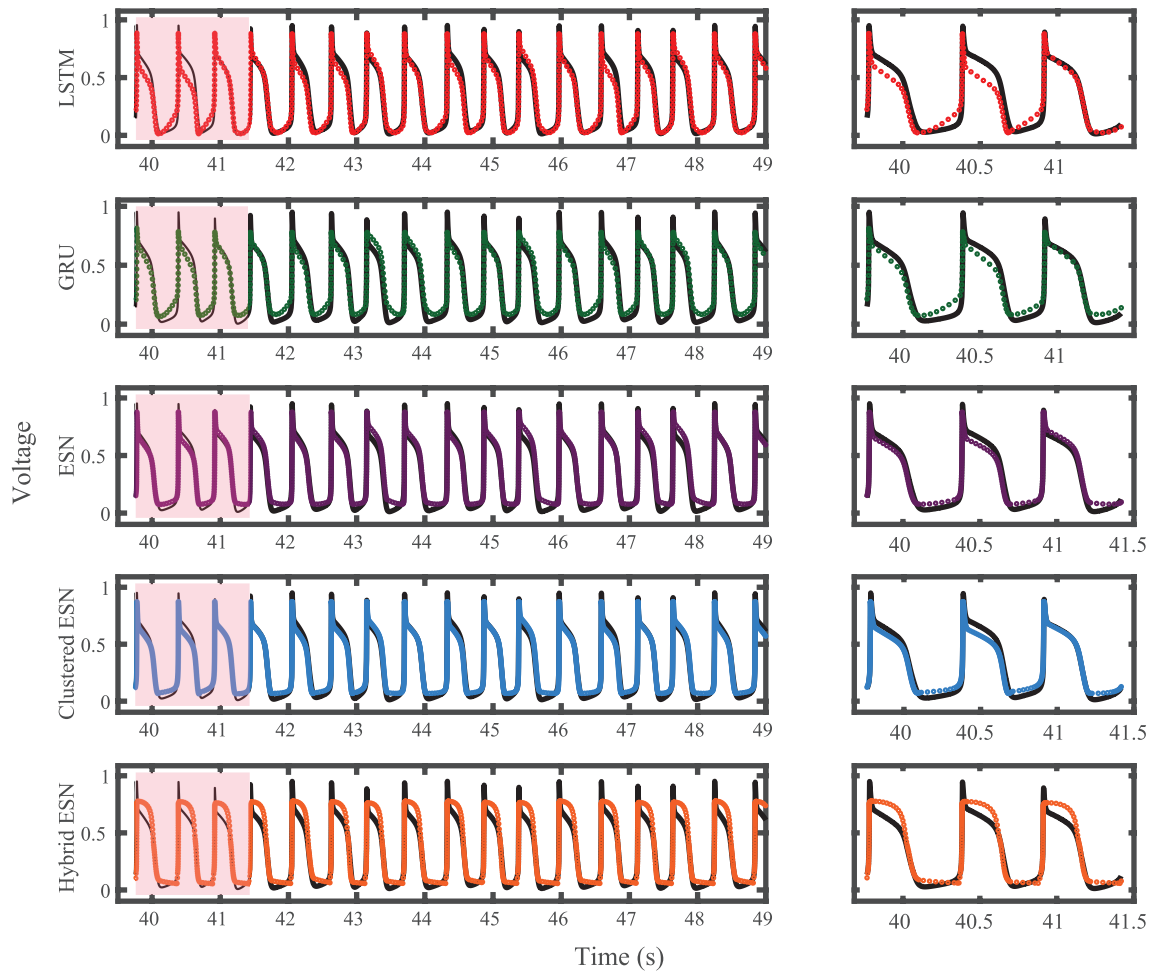

FIGURE 7 | Noble dataset action potential prediction results obtained for the five methods using a fixed network size of 100 neurons. Test data are shown in black for reference and the predictions in color. **(Left)** All predicted APs. **(Right)** Zoomed view of the first three predicted APs.

other methods produce depolarization during this phase. The performance does not vary significantly over the full prediction series, although some individual action potentials are not fit well. As shown in **Figure 11**, the largest APD differences from the true values occur for the hybrid ESN, with the clustered ESN yielding especially good results. The ESN and hybrid ESN consistently underestimate APD values, and the APD values predicted by the LSTM and GRU methods are generally less extreme than the true APDs (that is, the long APDs are predicted to be shorter and the short APDs are predicted to be longer).

As the number of neurons is changed, there is no clear effect on accuracy, except possibly for the hybrid ESN, which appears to have a slight trend toward lower RMSE with more neurons; see **Figure 12**. In contrast, the time required for training and prediction shows the same trend as for the other data sets, with the LSTM and GRU approaches requiring about two orders of magnitude more time for the same network size than the ESN and clustered ESN approaches, and the hybrid ESN in between. All the methods show a trend toward increasing time with increasing network size, except for the hybrid ESN, which as before appears insensitive to network size.

4. DISCUSSION

In this paper, we tested five different ML time series prediction methods, two based on RNNs and three based on a type of reservoir computing, to predict irregular voltage dynamics arising from random or chaotic effects for three cardiac datasets. We found that for clinically relevant intervals (1–3 s, or 6–19 beats at 160 ms) for the detection of cardiac arrhythmia in embedded devices (Madhavan and Friedman, 2013), we were able to predict voltage traces that closely match the true dynamics. We showed that for all datasets considered, all five prediction methods could produce accurate forecasts of both voltage and APD for around 15–20 action potentials (as long as was tested). With the exception of GRU predictions for the Noble dataset, RMSE values on the order of 0.1 normalized voltage units or lower could be attained for every combination of dataset and

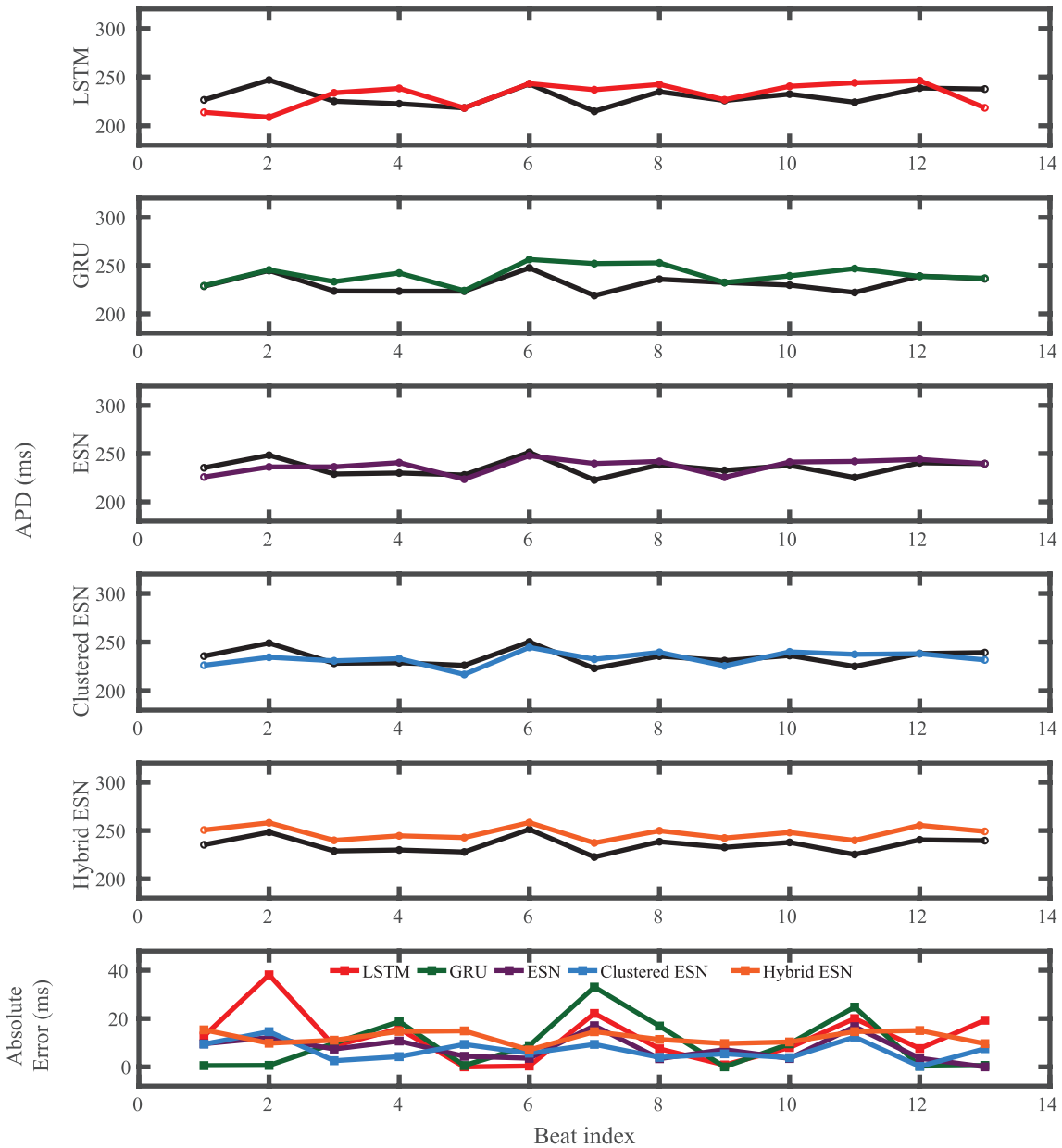

FIGURE 8 | Noble dataset APD prediction results obtained for the five methods using a fixed network size of 100 neurons. APDs from data used for testing are shown in black for reference and predicted APDs are shown in color. Absolute error in APD prediction is shown in the bottom subplot, with color corresponding to prediction method.

prediction method. APD errors were typically less than 5 ms for both the FK and experimental datasets, with larger typical errors of around 20 ms (sometimes more) for the Noble dataset. Over the measured interval, none of the methods exhibited any long-term trend in the APD error, indicating that the methods have seen sufficient training data to accurately model the real action potential response to stimulation and the associated APD distribution.

In addition, we demonstrated that the ESN approaches achieved lower error than the RNN approaches for the synthetic datasets and that the hybrid ESN achieved the best accuracy for the experimental dataset. Furthermore, the accuracy obtained, as measured by RMSE, was largely independent of network size. The time required for training and prediction typically was about two orders of magnitude lower for the ESN and clustered ESN architectures compared to the LSTM and GRU approaches, with the hybrid ESN timing in between. Computation time also generally grew with the network size, with the exception of the hybrid ESN, where computational time was essentially constant across all network sizes considered. We expect this insensitivity

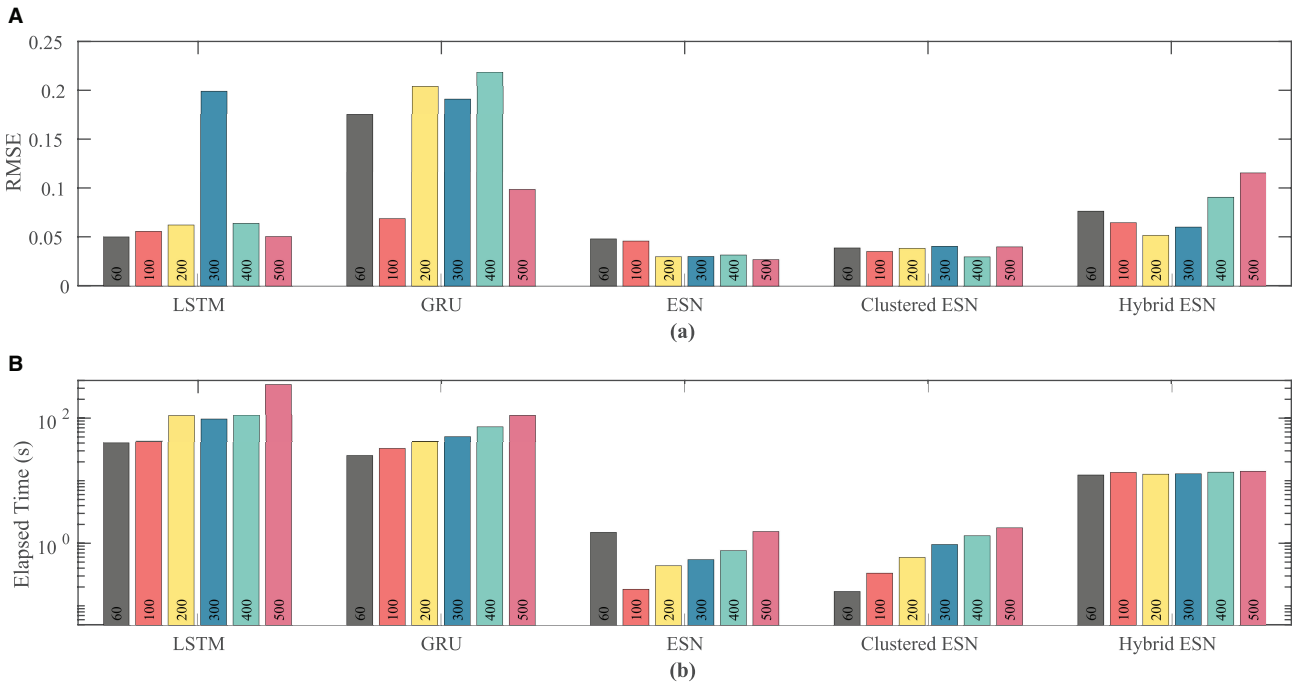

FIGURE 9 | Comparison of RMSE **(A)** and computational time **(B)** for each method and network size tested for the Noble dataset.

occurred because the time associated with solving the knowledge-based model (essentially a set of differential equations describing a cardiac cell), which is independent of network size, was more expensive than the cost of the ESN itself and thus dominated the total training and prediction time.

We investigated different types of dynamics, including those influenced by underlying randomness and chaos. We found the lowest RMSE values for the FK and experimental datasets and the highest RMSE values for the chaotically-driven Noble dataset. For the FK dataset, the hybrid ESN typically achieved the lowest error for all but the smallest network size, with the other ESN approaches achieving slightly less error than the LSTM and GRU methods. The Noble dataset elicited a particularly poor performance for the GRU method, with RMSE values typically three or four times larger than for the other methods; also, the hybrid ESN did not perform as well as the other ESNs. However, it is possible that use of a univariate time series in this case contributed to lower accuracy, rather than just the chaotic dynamics alone. For the experimental dataset, which likely has elements of both randomness and chaos, the hybrid ESN generally achieved the lowest error, with the other methods producing similar RMSE values. Overall, our results indicate that the ESN architecture provides better performance than LSTM and GRU approaches for the voltage forecasting task.

4.1. Effects of Algorithmic Choices

The action potential time series used in this work were highly imbalanced. In this study, although we found the need to downsample the original data for use with testing and training, we did not perform systematic studies regarding how to optimize this task. As a general observation, starting from the initial highly imbalanced time series, by increasing the sampling spacing and reducing the number of data points, the training and testing errors were reduced. However, the information loss caused by removing data points is the obvious side effect if the spacing becomes too large. Our choice of tying the time spacing to changes in voltage ensured good resolution during rapidly changing parts of action potentials, including the upstroke, but led to a lack of points during the rest and plateau phases, contributing to apparent errors during these times of slow changes in voltage. Further studies are required to investigate various spacing and resampling strategies to propose an optimal approach.

Although our results illustrate that ESNs provide the best prediction accuracy together with the lowest computational times in most cases for the methods and datasets considered, the ESN approach shows the most sensitivity to the hyperparameter and network parameter values. Our grid search results demonstrated a wide variability in the prediction performance obtained by various ESNs with very similar configurations. This motivates more study to improve the robustness of this approach. Among the three RC techniques used in this work, the hybrid ESN showed the least sensitivity to the hyperparameter values. We expect that the knowledge-based model promotes the predictive ability of the network by generating an approximate action potential, which the network perturbs to resolve the precise AP shape.

Incorporating the pacing stimulus into a multivariate input setup considerably improved the prediction performance of the network over using a univariate voltage input and extended the

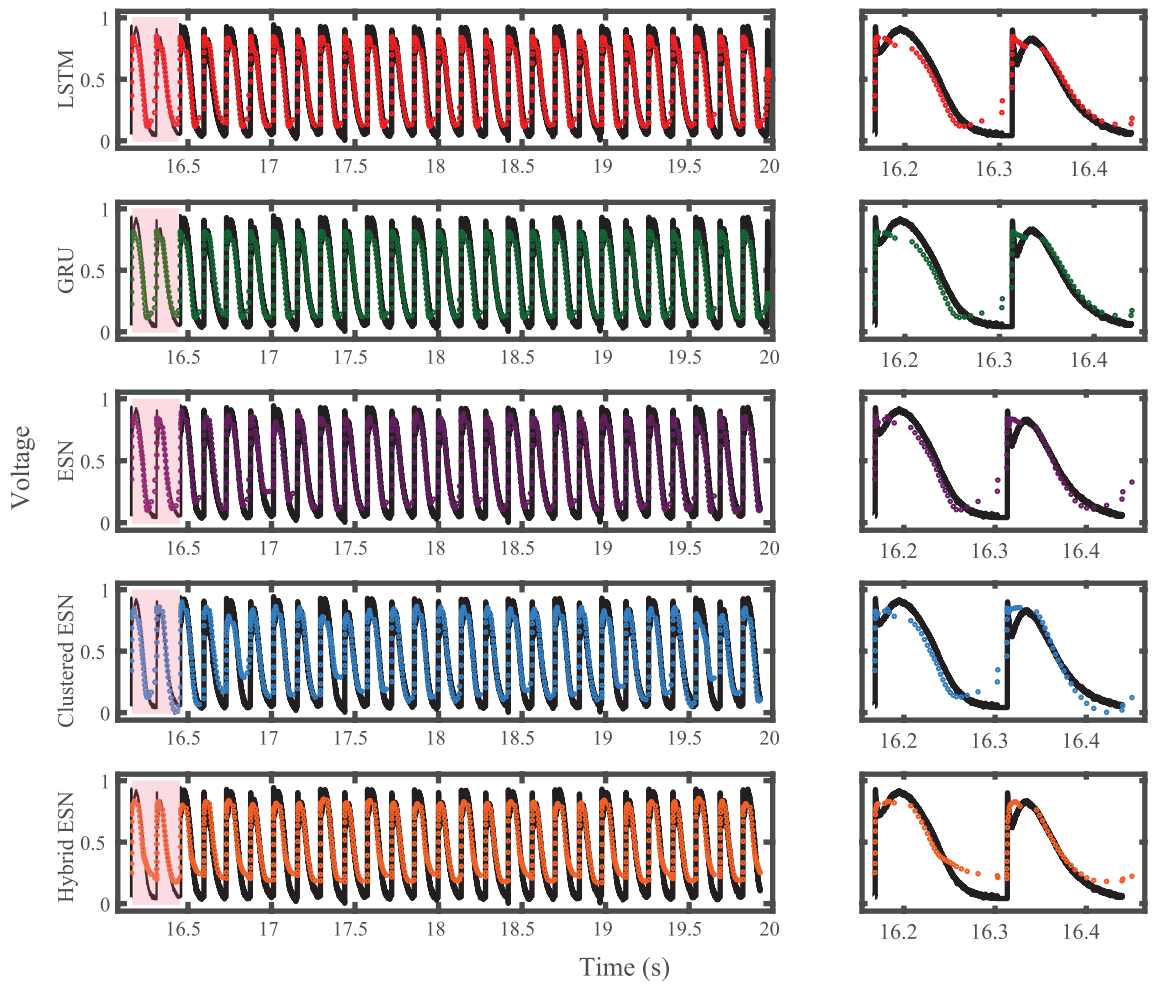

FIGURE 10 | Experimental dataset action potential prediction results obtained for the five methods using a fixed network size of 100 neurons. Test data are shown in black for reference and the predictions in color. **(Left)** All predicted APs. **(Right)** Zoomed view of the first two predicted APs.

forecasting horizon to a higher number of beats. In the absence of the stimulus information, depending on the dynamics of the system, the predictions remain accurate only for the first few beats after the training.

4.2. Limitations and Future Work

Our study contains a number of limitations. First, we studied a limited number of datasets. It is possible that different types of dynamics (e.g., more strongly chaotic) could lead to different results, and in particular experimental data from other sources could prove more difficult to predict. In addition, we did not study how much training data was needed to obtain good results. Furthermore, it remains an important open question how long the action potential predictions will remain accurate without deteriorating, although in this case we have found lower bounds.

We also considered a small number of time series prediction methods. There are many variations on these methods (Chandra et al., 2021; Han et al., 2021) and it is possible that performance improvements could be achieved. Even choosing different settings for the methods considered, such as a different number of clusters for the clustered ESNs, potentially could affect performance. There are also different types of prediction methods that we did not consider. For example, ESNs have been connected to vector autoregression (VAR) (Bollt, 2021), thereby motivating additional studies of VAR for prediction. It also would be interesting to study the accuracy of predictions of APD obtained by training on APD values only.

For the hybrid ESN, we only considered the use of one knowledge-based model, the Corrado-Niederer update of the Mitchell-Schaeffer model. It is possible that different model choices could affect the accuracy or computational time of the hybrid method; for example, an even simpler two-variable model like the FitzHugh-Nagumo model could potentially make the hybrid ESN approach more competitive with the other ESNs considered here, while a knowledge-based model that is matched to the data-generating model might present a near-trivial prediction task. Additionally, more complex cardiac cell models with detailed calcium dynamics may have an impact on

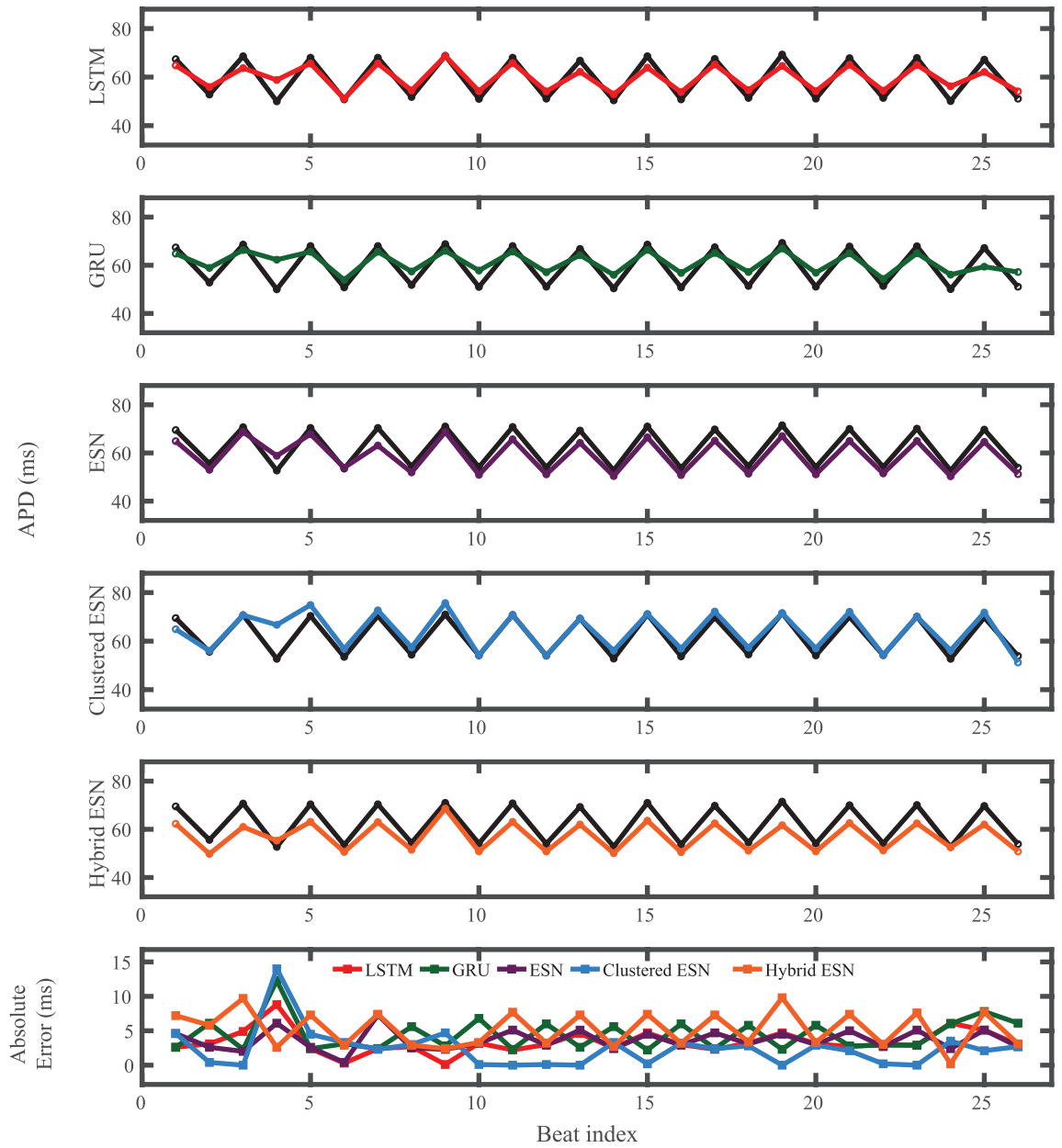

FIGURE 11 | Experimental dataset APD prediction results obtained for the five methods using a fixed network size of 100 neurons. APDs from data used for testing are shown in black for reference and predicted APDs are shown in color. Absolute error in APD prediction is shown in the bottom subplot, with color corresponding to prediction method.

long-term tissue memory. In practice, this long-term change in the cardiac cell may lessen the predictive power of the presented ML models over long time intervals.

We also note that there is a close connection between ML-based methods and data assimilation. In the cardiac case, Kalman filter-based methods including data assimilation have been used thus far for reconstruction (Muñoz and Otani, 2010, 2013; Hoffman et al., 2016; Hoffman and Cherry, 2020; Marcotte et al., 2021), but they also can be used for forecasting, as is more typical in data assimilation's original weather forecasting context (Hunt et al., 2007). It may be beneficial to pursue approaches that seek to merge data assimilation and machine learning for this task (Albers et al., 2018; Brajard et al., 2020; Gottwald and Reich, 2021).

Along with extensions of our present work to address the issues discussed above, in the future we intend to consider predicting cardiac voltage dynamics during the development of arrhythmias. We expect this goal may necessitate the use of spatially extended models of cardiac tissue as part of the prediction process, although handling the information from spatial neighbors requires very large networks that will pose new computational challenges. The combination

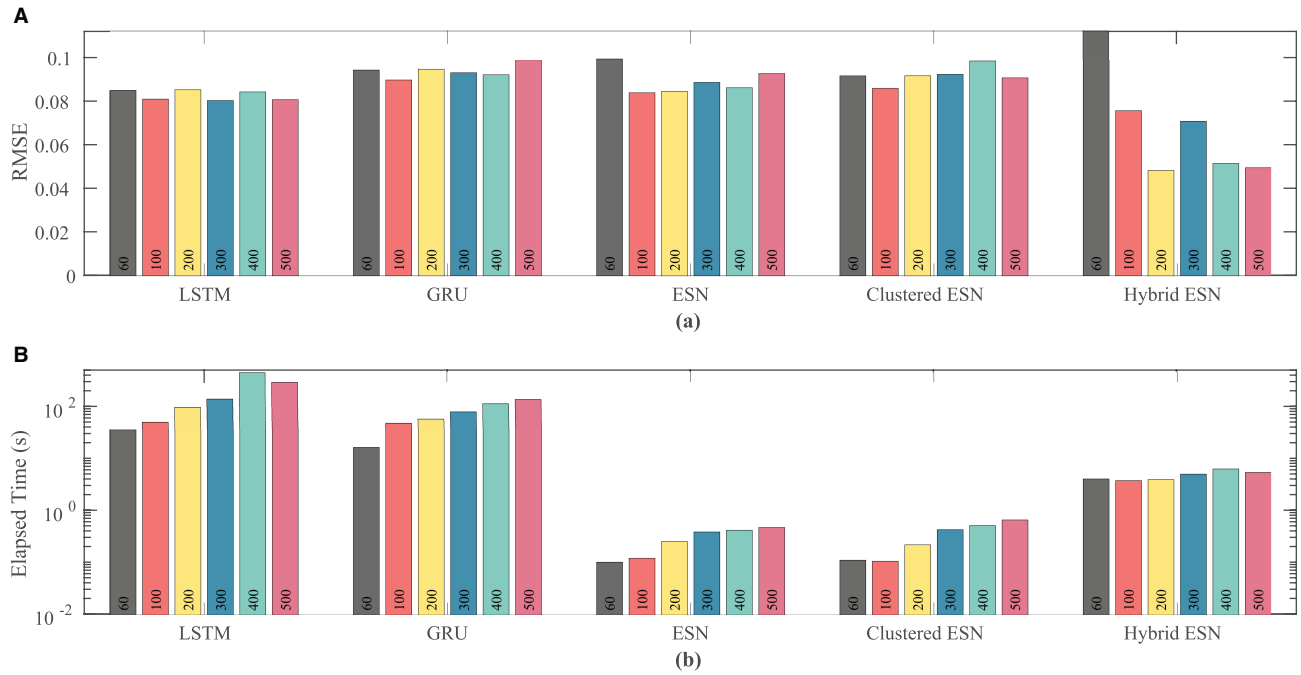

FIGURE 12 | Comparison of RMSE **(A)** and computational time **(B)** for each method and network size tested for the experimental dataset.

of ESNs and local states (Pathak et al., 2018; Zimmermann and Parlitz, 2018) or specialized deep-learning architectures (Herzog et al., 2018) may be useful in tackling such problems, but these methods remain computationally demanding and may require new approaches. In addition, we may need to carefully consider the types of dynamics included in the training data in order to accurately predict transitions between different types of dynamics, such as the transition from normal rhythm to tachycardia or the transition from tachycardia to fibrillation. Accurate prediction of such transitions may lead to advances in control designed to prevent the development of fatal arrhythmias.

DATA AVAILABILITY STATEMENT

The raw data supporting the conclusions of this article will be made available by the authors, without undue reservation.

ETHICS STATEMENT

The animal study was reviewed and approved by the Office of Research Integrity Assurance of Georgia Tech under IACUC A100416.

AUTHOR CONTRIBUTIONS

SS, FF, YS, and EC contributed to developing the study concept. SS, CM, and EC contributed to study design. SS and EC developed the synthetic datasets and analyzed and data. CH and FF obtained the experimental datasets. SS, FF, and EC wrote the manuscript. CM, CH, and YS critically revised the manuscript. All authors contributed to the article and approved the submitted version.

FUNDING

This study was supported in part by the National Science Foundation grants CMMI-2011280 (EC) and CMMI-1762553 (FF) and by the National Institutes of Health grant 1R01HL143450-01 (EC and FF).

SUPPLEMENTARY MATERIAL

The Supplementary Material for this article can be found online at: https://www.frontiersin.org/articles/10.3389/fphys.2021.734178/full#supplementary-material

REFERENCES

Albers, D. J., Levine, M. E., Stuart, A., Mamykina, L., Gluckman, B., and Hripcsak, G. (2018). Mechanistic machine learning: how data assimilation leverages physiologic knowledge using Bayesian inference to forecast the future, infer the present, and phenotype. *J. Am. Med. Informat. Association* 25, 1392–1401. doi: 10.1093/jamia/ocy106

Berger, C. M., Cain, J. W., Socolar, J. E. S., and Gauthier, D. J. (2007). Control of electrical alternans in simulations of paced myocardium

using extended time-delay autosynchronization. *Phys. Rev. E* 76:041917. doi: 10.1103/PhysRevE.76.041917

Bianchi, F. M., Maiorino, E., Kampffmeyer, M. C., Rizzi, A., and Jenssen, R. (2017). *Other Recurrent Neural Networks Models*. Cham: Springer International Publishing. doi: 10.1007/978-3-319-70338-1_4

Bollobás, B. (2001). "Random graphs," in *Cambridge Studies in Advanced Mathematics* (Cambridge: Cambridge University Press). doi: 10.1017/CBO9780511814068

Bollt, E. (2021). On explaining the surprising success of reservoir computing forecaster of chaos? the universal machine learning dynamical system with contrast to VAR and DMD. *Chaos* 31:013108. doi: 10.1063/5.0024890

Brajard, J., Carrassi, A., Bocquet, M., and Bertino, L. (2020). Combining data assimilation and machine learning to emulate a dynamical model from sparse and noisy observations: a case study with the Lorenz 96 model. *J. Comput. Sci.* 44:101171. doi: 10.1016/j.jocs.2020.101171

Chandra, R., Goyal, S., and Gupta, R. (2021). Evaluation of deep learning models for multi-step ahead time series prediction. *IEEE Access* 9, 83105–83123. doi: 10.1109/ACCESS.2021.3085085

Chattopadhyay, A., Hassanzadeh, P., and Subramanian, D. (2020). Data-driven predictions of a multiscale Lorenz 96 chaotic system using machine-learning methods: reservoir computing, artificial neural network, and long short-term memory network. *Nonlinear Process. Geophys.* 27, 373–389. doi: 10.5194/npg-27-373-2020

Chen, D. D., Gray, R. A., Uzelac, I., Herndon, C., and Fenton, F. H. (2017). Mechanism for amplitude alternans in electrocardiograms and the initiation of spatiotemporal chaos. *Phys. Rev. Lett.* 118:168101. doi: 10.1103/PhysRevLett.118.168101

Cherry, E. M. (2017). Distinguishing mechanisms for alternans in cardiac cells using constant-diastolic-interval pacing. *Chaos* 27:093902. doi: 10.1063/1.4999354

Chialvo, D. R., Gilmour, R. F. Jr., and Jalife, J. (1990). Low dimensional chaos in cardiac tissue. *Nature* 343, 653–657. doi: 10.1038/343653a0

Christini, D. J., Riccio, M. L., Culianu, C. A., Fox, J. J., Karma, A., Gilmour, J.r., et al. (2006). Control of electrical alternans in canine cardiac Purkinje fibers. *Phys. Rev. Lett.* 96:104101. doi: 10.1103/PhysRevLett.96.104101

Corrado, C., and Niederer, S. A. (2016). A two-variable model robust to pacemaker behaviour for the dynamics of the cardiac action potential. *Math. Biosci.* 281, 46–54. doi: 10.1016/j.mbs.2016.08.010

Deng, Z., and Zhang, Y. (2006). "Complex systems modeling using scale-free highly-clustered echo state network," in *Proceedings of the International Joint Conference on Neural Networks*, IJCNN 2006, part of the IEEE World Congress on Computational Intelligence (Vancouver, BC: IEEE), 3128–3135. doi: 10.1109/IJCNN.2006.247295

Doan, N. A. K., Polifke, W., and Magri, L. (2019). "Physics-informed echo state networks for chaotic systems forecasting," in *Computational Science - ICCS 2019. ICCS 2019. Lecture Notes in Computer Science*, Vol. 11539, eds J. M. F. Rodrigues, P. J. S. Cardoso, J. Monteiro, R. Lam, V. V. Krzhizhanovskaya, M. H. Lees, J. J. Dongarra, and P. M.A. Sloot (Cham: Springer International Publishing), 192–198.

Dubois, P., Gomez, T., Planckaert, L., and Perret, L. (2020). Data-driven predictions of the lorenz system. *Phys. D Nonlinear Phenomena* 408:132495. doi: 10.1016/j.physd.2020.132495

Echebarria, B., and Karma, A. (2002). Spatiotemporal control of cardiac alternans. *Chaos* 12, 923–930. doi: 10.1063/1.1501544

Fenton, F., and Karma, A. (1998). Vortex dynamics in three-dimensional continuous myocardium with fiber rotation: filament instability and fibrillation. *Chaos* 8, 20–47. doi: 10.1063/1.166311

Fenton, F. H., Cherry, E. M., Hastings, H. M., and Evans, S. J. (2002). Multiple mechanisms of spiral wave breakup in a model of cardiac electrical activity. *Chaos* 12, 852–892. doi: 10.1063/1.1504242

Fenton, F. H., Cherry, E. M., and Kornreich, B. G. (2008). Termination of equine atrial fibrillation by quinidine: an optical mapping study. *J. Vet. Cardiol.* 10, 87–103. doi: 10.1016/j.jvc.2008.10.002

Garzón, A., Grigoriev, R. O., and Fenton, F. H. (2009). Model-based control of cardiac alternans on a ring. *Phys. Rev. E* 80:021932. doi: 10.1103/PhysRevE.80.021932

Garzon, A., Grigoriev, R. O., and Fenton, F. H. (2014). Continuous-time control of alternans in long Purkinje fibers. *Chaos* 24:033124. doi: 10.1063/1.4893295

Gizzi, A., Cherry, E. M., Gilmour, R. F. Jr., Luther, S., Filippi, S., et al. (2013). Effects of pacing site and stimulation history on alternans dynamics and the development of complex spatiotemporal patterns in cardiac tissue. *Front. Cardiac Electrophysiol.* 4:71. doi: 10.3389/fphys.2013.00071

Gottwald, G. A., and Reich, S. (2021). Supervised learning from noisy observations: combining machine-learning techniques with data assimilation. *Phys. D Nonlinear Phenomena* 423:132911. doi: 10.1016/j.physd.2021.132911

Guevara, M. R., Ward, G., Shrier, A., and Glass, L. (1984). Electrical alternans and period-doubling bifurcations. *Comput. Cardiol.* 11, 167–170.

Han, Z., Zhao, J., Leung, H., Ma, K. F., and Wang, W. (2021). A review of deep learning models for time series prediction. *IEEE Sens. J.* 21, 7833–7848. doi: 10.1109/JSEN.2019.2923982

Herzog, S., Wörgötter, F., and Parlitz, U. (2018). Data-driven modeling and prediction of complex spatio-temporal dynamics in excitable media. *Front. Appl. Math. Stat.* 4:60. doi: 10.3389/fams.2018.00060

Hochreiter, S., and Schmidhuber, J. (1997). Long short-term memory. *Neural Comput.* 9, 1735–1780. doi: 10.1162/neco.1997.9.8.1735

Hoffman, M. J., and Cherry, E. M. (2020). Sensitivity of a data-assimilation system for reconstructing three-dimensional cardiac electrical dynamics. *Philos. Trans. R. Soc. A Math. Phys. Eng. Sci.* 378:20190388. doi: 10.1098/rsta.2019.0388

Hoffman, M. J., LaVigne, N. S., Scorse, S. T., Fenton, F. H., and Cherry, E. M. (2016). Reconstructing three-dimensional reentrant cardiac electrical wave dynamics using data assimilation. *Chaos* 26:013107. doi: 10.1063/1.4940238

Hunt, B. R., Kostelich, E. J., and Szunyogh, I. (2007). Efficient data assimilation for spatiotemporal chaos: a local ensemble transform Kalman filter. *Phys. D* 230, 112–126. doi: 10.1016/j.physd.2006.11.008

Ing, C.-K. (2003). Multistep prediction in autoregressive processes. *Econometr. Theory* 19, 254–279. doi: 10.1017/S0266466603192031

Jaeger, H. (2002). *Tutorial on Training Recurrent Neural Networks, Covering BPPT, RTRL, EKF and the "echo state network" Approach*. Bonn: GMD-Forschungszentrum Informationstechnik.

Junior, L. O., Stelzer, F., and Zhao, L. (2020). "Clustered echo state networks for signal observation and frequency filtering," in *Anais do VIII Symposium on Knowledge Discovery, Mining and Learning* (Porto Alegre: SBC), 25–32, doi: 10.5753/kdmile.2020.11955

Kappadan, V., Telele, S., Uzelac, I., Fenton, F., Parlitz, U., Luther, S., et al. (2020). High-resolution optical measurement of cardiac restitution, contraction, and fibrillation dynamics in beating vs. blebbistatin-uncoupled isolated rabbit hearts. *Front. Physiol.* 11:464. doi: 10.3389/fphys.2020.00464

Kingma, D. P., and Ba, J. (2014). ADAM: a method for stochastic optimization. *arXiv preprint arXiv:1412.6980*.

Kulkarni, K., Lee, S. W., Kluck, R., and Tolkacheva, E. G. (2018). Real-time closed loop diastolic interval control prevents cardiac alternans in isolated whole rabbit hearts. *Ann. Biomed. Eng.* 46, 555–566. doi: 10.1007/s10439-018-1981-2

Kutz, J. N. (2013). *Data-Driven Modeling & Scientific Computation: Methods for Complex Systems & Big Data*. New York, NY: Oxford University Press, Inc.

Lorenz, E. N. (1963). Deterministic non-periodic flow. *J. Atmos. Sci.* 20, 130–141. doi: 10.1175/1520-0469(1963)020<0130:DNF>2.0.CO;2

Lukoševičius, M. (2012). "A practical guide to applying echo state networks," in *Neural Networks: Tricks of the Trade: Second Edition*, eds G. Montavon, G. B. Orr, and K. R.Müller (Berlin; Heidelberg: Springer), 659–686. doi: 10.1007/978-3-642-35289-8_36

Lukoševičius, M., and Jaeger, H. (2009). Reservoir computing approaches to recurrent neural network training. *Comput. Sci. Rev.* 3, 127–149. doi: 10.1016/j.cosrev.2009.03.005

Madhavan, M., and Friedman, P. A. (2013). Optimal programming of implantable cardiac-defibrillators. *Circulation* 128, 659–672. doi: 10.1161/CIRCULATIONAHA.112.000542

Marcotte, C. D., Fenton, F. H., Hoffman, M. J., and Cherry, E. M. (2021). Robust data assimilation with noise: applications to cardiac dynamics. *Chaos* 31:013118. doi: 10.1063/5.0033539

Mitchell, C. C., and Schaeffer, D. G. (2003). A two-current model for the dynamics of cardiac membrane. *Bull. Math. Biol.* 65, 767–793. doi: 10.1016/S0092-8240(03)00041-7

Moniz, N., Branco, P., and Torgo, L. (2017). Resampling strategies for imbalanced time series forecasting. *Int. J. Data Sci. Anal.* 3, 161–181. doi: 10.1007/s41060-017-0044-3

Muñoz, L. M., and Otani, N. F. (2010). Enhanced computer modeling of cardiac action potential dynamics using experimental data-based feedback. *Comput. Cardiol.* 37, 837–840.

Muñoz, L. M., and Otani, N. F. (2013). "Kalman filter based estimation of ionic concentrations and gating variables in a cardiac myocyte model," in *Computing in Cardiology 2013* (Zaragoza), 53–56.

Noble, D. (1962). A modification of the Hodgkin-Huxley equations applicable to Purkinje fibre action and pace-maker potentials. *J. Physiol.* 160, 317–352. doi: 10.1113/jphysiol.1962.sp006849

Nolasco, J. B., and Dahlen, R. W. (1968). A graphic method for the study of alternation in cardiac action potentials. *J. Appl. Physiol.* 25, 191–196. doi: 10.1152/jappl.1968.25.2.191

Oh, D. K. (2020). Toward the fully physics-informed echo state network-an ode approximator based on recurrent artificial neurons. *arXiv preprint arXiv:2011.06769*.

Otani, N. F. (2017). Theory of the development of alternans in the heart during controlled diastolic interval pacing. *Chaos* 27:093935. doi: 10.1063/1.5003250

Pastore, J. M., Girouard, S. D., Laurita, K. R., Akar, F. G., and Rosenbaum, D. S. (1999). Mechanism linking t-wave alternans to the genesis of cardiac fibrillation. *Circulation* 99, 1385–1394. doi: 10.1161/01.CIR.99.10.1385

Pathak, J., Hunt, B., Girvan, M., Lu, Z., and Ott, E. (2018). Model-free prediction of large spatiotemporally chaotic systems from data: a reservoir computing approach. *Phys. Rev. Lett.* 120:024102. doi: 10.1103/PhysRevLett.120.024102

Rappel, W. J., Fenton, F., and Karma, A. (1999). Spatiotemporal control of wave instabilities in cardiac tissue. *Phys. Rev. Lett.* 83, 456–459. doi: 10.1103/PhysRevLett.83.456

Schmid, P. J. (2010). Dynamic mode decomposition of numerical and experimental data. *J. Fluid Mech.* 656, 5–28. doi: 10.1017/S0022112010001217

Stock, J. H., and Watson, M. W. (2001). Vector autoregressions. *J. Econ. Perspect.* 15, 101–115. doi: 10.1257/jep.15.4.101

Sun, C., Song, M., Hong, S., and Li, H. (2020). A review of designs and applications of echo state networks. *arXiv preprint arXiv:2012.02974*.

Watanabe, M. A., Fenton, F. H., Evans, S. J., Hastings, H. M., and Karma, A. (2001). Mechanisms for discordant alternans. *J. Cardiovasc. Electrophysiol.* 12, 196–206. doi: 10.1046/j.1540-8167.2001.00196.x

Willard, J., Jia, X., Xu, S., Steinbach, M., and Kumar, V. (2020). Integrating physics-based modeling with machine learning: a survey. *arXiv preprint arXiv:2003.04919*.

Yildiz, I. B., Jaeger, H., and Kiebel, S. J. (2012). Re-visiting the echo state property. *Neural Netw.* 35, 1–9. doi: 10.1016/j.neunet.2012.07.005

Zimmermann, R. S., and Parlitz, U. (2018). Observing spatio-temporal dynamics of excitable media using reservoir computing. *Chaos* 28:043118. doi: 10.1063/1.5022276

Zlochiver, S., Johnson, C., and Tolkacheva, E. G. (2017). Constant DI pacing suppresses cardiac alternans formation in numerical cable models. *Chaos* 27:093903. doi: 10.1063/1.4999355

Conflict of Interest: The authors declare that the research was conducted in the absence of any commercial or financial relationships that could be construed as a potential conflict of interest.

Publisher's Note: All claims expressed in this article are solely those of the authors and do not necessarily represent those of their affiliated organizations, or those of the publisher, the editors and the reviewers. Any product that may be evaluated in this article, or claim that may be made by its manufacturer, is not guaranteed or endorsed by the publisher.

frontiers in Physiology

ORIGINAL RESEARCH
published: 25 October 2021
doi: 10.3389/fphys.2021.731025

Cellular Size, Gap Junctions, and Sodium Channel Properties Govern Developmental Changes in Cardiac Conduction

Madison B. Nowak[1], *Rengasayee Veeraraghavan*[1,2], *Steven Poelzing*[3,4] *and Seth H. Weinberg*[1,2]*

[1] *Department of Biomedical Engineering, The Ohio State University, Columbus, OH, United States,* [2] *The Ohio State University Wexner Medical Center, Davis Heart and Lung Research Institute, Columbus, OH, United States,* [3] *Department of Biomedical Engineering and Mechanics, Virginia Polytechnic Institute and State University, Blacksburg, VA, United States,* [4] *Virginia Polytechnic Institute and State University, Fralin Biomedical Research Institute at Virginia Tech Carilion, Roanoke, VA, United States*

OPEN ACCESS

Edited by:
Elena Tolkacheva, University of Minnesota Twin Cities, United States

Reviewed by:
Rob Gourdie, Fralin Biomedical Research Institute, United States
Eleonora Grandi, University of California, Davis, United States

***Correspondence:**
Seth H. Weinberg
weinberg.147@osu.edu

Specialty section:
This article was submitted to Computational Physiology and Medicine, a section of the journal Frontiers in Physiology

Received: *25 June 2021*
Accepted: *28 September 2021*
Published: *25 October 2021*

Citation:
Nowak MB, Veeraraghavan R, Poelzing S and Weinberg SH (2021) Cellular Size, Gap Junctions, and Sodium Channel Properties Govern Developmental Changes in Cardiac Conduction. Front. Physiol. 12:731025. doi: 10.3389/fphys.2021.731025

Electrical conduction in cardiac ventricular tissue is regulated via sodium (Na^+) channels and gap junctions (GJs). We and others have recently shown that Na^+ channels preferentially localize at the site of cell-cell junctions, the intercalated disc (ID), in adult cardiac tissue, facilitating coupling via the formation of intercellular Na^+ nanodomains, also termed ephaptic coupling (EpC). Several properties governing EpC vary with age, including Na^+ channel and GJ expression and distribution and cell size. Prior work has shown that neonatal cardiomyocytes have immature IDs with Na^+ channels and GJs diffusively distributed throughout the sarcolemma, while adult cells have mature IDs with preferentially localized Na^+ channels and GJs. In this study, we perform an *in silico* investigation of key age-dependent properties to determine developmental regulation of cardiac conduction. Simulations predict that conduction velocity (CV) biphasically depends on cell size, depending on the strength of GJ coupling. Total cell Na^+ channel conductance is predictive of CV in cardiac tissue with high GJ coupling, but not correlated with CV for low GJ coupling. We find that ephaptic effects are greatest for larger cells with low GJ coupling typically associated with intermediate developmental stages. Finally, simulations illustrate how variability in cellular properties during different developmental stages can result in a range of possible CV values, with a narrow range for both neonatal and adult myocardium but a much wider range for an intermediate developmental stage. Thus, we find that developmental changes predict associated changes in cardiac conduction.

Keywords: cardiac electrophysiology, computational models, intercalated disc, development, cardiac conduction

1. INTRODUCTION

It is well-established that conduction in cardiac tissue is regulated by ionic currents and gap junction (GJ) coupling (Shaw and Rudy, 1997; Kucera et al., 2002). In ventricular tissue, the voltage-gated sodium (Na^+) channel, $Na_v1.5$, is primarily responsible for generating the depolarizing Na^+ current (I_{Na}), and connexin43 (Cx43) is the primary GJ protein, facilitating the passive

current flow between adjacent cells (Veeraraghavan et al., 2014), both of which mediate conduction. Altering either I_{Na} or GJ coupling can lead to changes in conduction and ultimately increase the risk of arrhythmias (Quan and Rudy, 1990; Shaw and Rudy, 1997; Rohr et al., 1998).

We (Veeraraghavan et al., 2015; Veeraraghavan and Gourdie, 2016; Mezache et al., 2020) and others (Kucera et al., 2002; Rhett et al., 2012; Agullo-Pascual et al., 2014; Leo-Macias et al., 2016) have shown that $Na_v1.5$ channels preferentially localize at the intercalated disc (ID), the area of cell-cell junctions in cardiac tissue. Multiple *in silico* studies have hypothesized that I_{Na} at the ID can be altered via Na^+ nanodomain signaling at the intercellular cleft space (Kucera et al., 2002; Sperelakis, 2002; Mori et al., 2008; Lin and Keener, 2010; Wei et al., 2016; Tveito et al., 2017; Weinberg, 2017; Hichri et al., 2018; Jæger et al., 2019; Wei and Tolkacheva, 2020). This, in turn, can modulate cell-cell coupling through a mechanism known as ephaptic coupling (EpC). In this paper we consider two primary effects of EpC: electrical field effects and Na^+ depletion in the intercellular cleft (i.e., the narrow extracellular space between electrically coupled cells at the ID). To elaborate briefly, EpC is governed by the following: Na^+ influx during the action potential upstroke in an "upstream" or pre-junctional depolarizing cell during a propagating electrical wave decreases the electrical potential within the intercellular cleft. This reduction of the potential within the intercellular cleft then depolarizes the "downstream" or post-junctional apposing cell from the extracellular, rather than the intracellular, side of the cell membrane. Additionally, Na^+ influx reduces the Na^+ concentration within the intercellular cleft, which governs the flux of the Na^+ channels at the ID in both cells. The width or volume of the intercellular cleft space is one of the key properties governing the magnitude of these effects. When the intercellular cleft is narrow, both the elevated transmembrane potential (V_m) and locally depleted Na^+ concentration within the intercellular cleft reduce the Na^+ current driving force and, therefore, the Na^+ current. This reduction in I_{Na} has been termed "self-attenuation" and has been shown to slow conduction velocity (CV) (Kucera et al., 2002; Sperelakis, 2002; George et al., 2016; Hichri et al., 2018).

Several key properties governing EpC and conduction overall are known to change during development: Cells in neonatal myocardium do not have fully formed IDs, and Na^+ channels and GJs are distributed diffusively throughout the sarcolemma (Fromaget et al., 1992; Vreeker et al., 2014). Consistent with reduced Na^+ channel expression, it has been shown that pediatric cardiomyocytes produce a reduced I_{Na}, compared to adult cardiomyocytes (Cai et al., 2011; Cordeiro et al., 2013). Cx43 is essentially undetectable until 23 weeks *in utero* and remain randomly distributed on the sarcolemma in neonatal cardiomyocytes (Peters et al., 1994; Hirschy et al., 2006; Vreeker et al., 2014; Swift et al., 2020). Vreeker et al. showed that Cx43 tends to relocate to the lateral membrane around 5 months postnatal and does not begin to preferentially localize at the ID until around 2.5–5 years old, with full preferential localization occurring at roughly 7 years of age (Vreeker et al., 2014). $Na_v1.5$ channels, however, reside on the lateral membrane in neonatal cardiomyocytes and begin to begin to preferentially localize at the ID around 5 months postnatal, much earlier than Cx43 (Harrell et al., 2007; Vreeker et al., 2014). Additionally, studies have shown that adult cardiomyocytes are larger than neonatal cardiomyocytes (Cordeiro et al., 2013; Vreeker et al., 2014; Swift et al., 2020). This is especially important given that cell size broadly influences all electrical activity in the cell by altering surface area, cell volume, membrane capacitance, ion channel expression, etc. (Kato et al., 1996; Spach et al., 2000).

We hypothesize that the developmental-associated increase in both Na^+ and GJ current will increase CV from the neonatal stage to the adult and that this regulation will be influenced by the relative strength of EpC at different developmental stages. In the paper, we perform a wide parameter investigation, varying age-associated parameters including gap junctional conductance (f_{gap}), cell size (S), Na^+ channel density (ρ_{Na}), and Na^+ channel ID localization (ID_{Na}) and measure CV in simulated cardiac tissue. To our knowledge, no studies have investigated the interdependence of these parameters on conduction within a health myocardium during development from neonatal to adult tissue. While one study investigated the changes on impulse conduction in the canine myocardium, it was limited to a comparison of 8 week old postnatal to adult purkinje fibers (Rosen et al., 1981). Thus, in our study, we investigate conduction through ventricular tissue in a range of developmental stages and conditions. We find that CV has a biphasic dependence on cell size, in a manner that depends on GJ coupling. In addition, we find that ephaptic effects play a larger role in conduction for larger cells with low GJ coupling. Interestingly, simulations predict that variability in cellular properties in intermediate developmental stage between neonatal cardiomyocytes and adult cardiomyocytes can lead to a wide range of possible CV values, but this range narrows to a normal range with adult tissue-associated parameters.

2. METHODS

Full details of the computational model are provided in **Supplementary Material**. Briefly, we simulate a 50-cell cable of guinea pig ventricular myocytes (Livshitz and Rudy, 2007) that incorporates a Markov chain model for the wild-type (WT) Na^+ channel (Clancy et al., 2002), shown in **Figure 1**. We note that a Markov chain formulation for I_{Na} was not necessary to reproduce our results, as prior studies have shown EpC effects are reproduced by Hodgkin-Huxley Na^+ channel models (Kucera et al., 2002; Weinberg, 2017; Moise et al., 2021), but rather is used to facilitate an appropriate comparison with our prior work simulating $Na_v1.5$ gain-of-function mutations (Nowak et al., 2021), which were also modeled with a Markov chain. As in our previous work (Greer-Short et al., 2017; Weinberg, 2017; Nowak et al., 2020, 2021) and work performed by others (Kucera et al., 2002), we account for non-uniform Na^+ subcellular localization by spatially discretizing each cell into two ID membrane patches at the ends of the cell and axial membrane patches along the length of the cell. The number of axial patches varied with the size of the cell, as described below, with each axial patch fixed in length ($L_p = 10\ \mu$m).

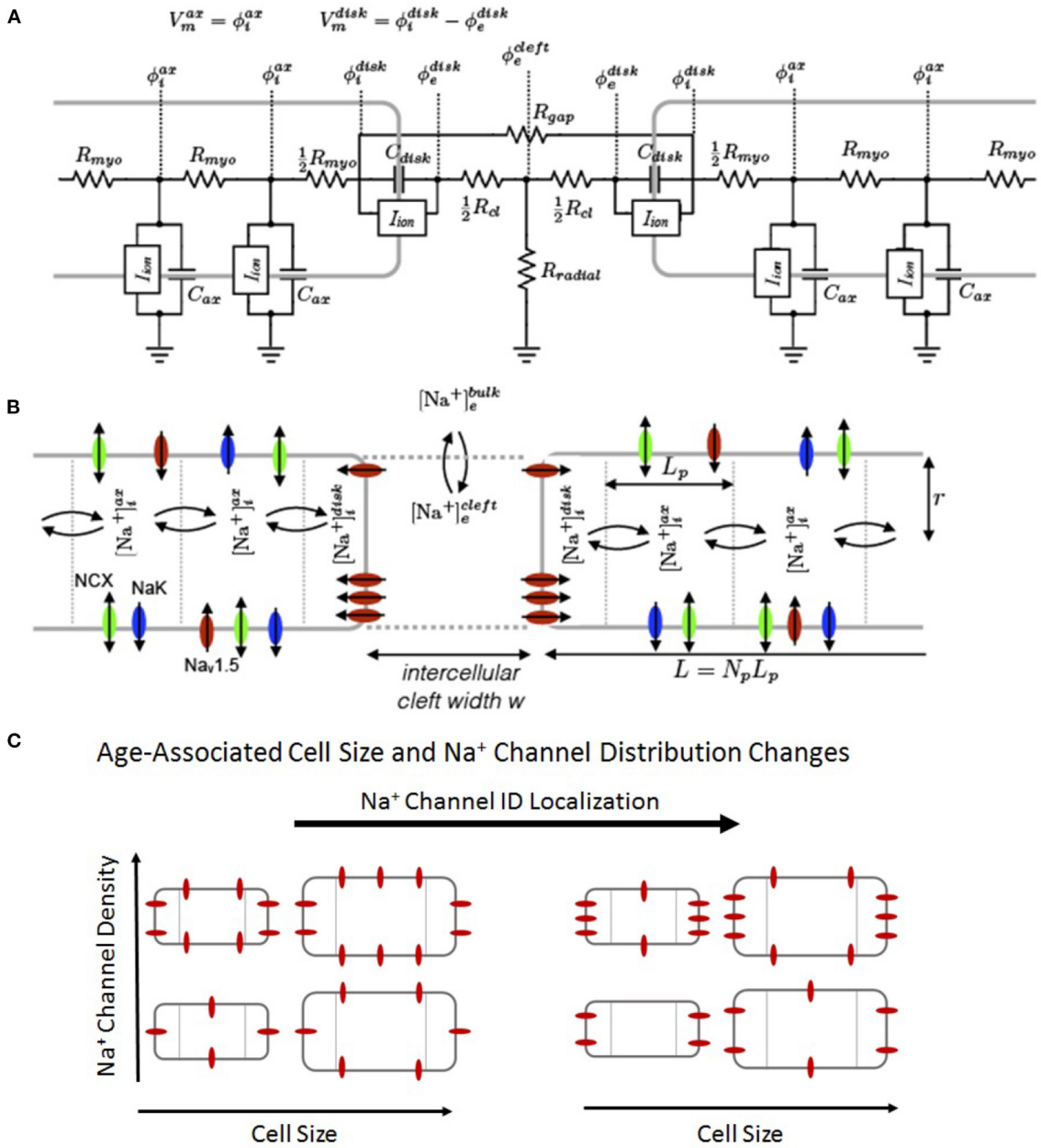

FIGURE 1 | Schematic of the computational model. **(A)** Electric circuit representation of coupled myocytes. Intracellular nodes are coupled via a myoplasmic resistance (R_{myo}). End nodes are coupled via a gap junctional resistance (R_{gap}). Extracellular potentials at the disc and intercellular cleft (ϕ_e^{disc} and ϕ_e^{cleft}, respectively) are governed by a T-shaped network of two axial resistances in the intercellular cleft (R_{cl}) and one radial resistance (R_{radial}). **(B)** Na^+concentration in diffusively coupled compartments, including intracellular Na^+in the axial and disc compartments ($[Na^+]_i^{ax}$ and $[Na^+]_i^{disc}$) and extracellular Na^+in the intercellular cleft and bulk spaces ($[Na^+]_e^{cleft}$ and $[Na^+]_e^{bulk}$). **(C)** Representation of age-associated change in model parameters, including changes in cell size (S), Na^+ channel density (ρ_{Na}), and Na^+channel ID localization (ID_{Na}).

Cells are coupled via GJs and EpC: gap junctional coupling is represented via gap junctional conductances coupling ID nodes of adjacent cells (g_{gap}, represented by resistor R_{gap} in the electrical circuit). EpC is represented by a T-shaped junction of two intercellular cleft resistances (R_{cl}) and a radial bulk (R_{radial}), which are proportional and inversely proportional to intercellular cleft width w, respectively. Intracellular nodes are coupled with a myoplasmic resistance (R_{myo}) (**Figure 1A**). The nominal value for g_{gap} is defined as $g_{gap}^0 = 1266\ nS$, and changes in GJ coupling are accounted for by adjusting the GJ scaling factor f_{gap} (between 0 and 1), such that $g_{gap} = f_{gap} g_{gap}^0$.

A wide range of macroscopic GJ conductance values have been measured experimentally, with values ranging from the low 10s of nanosiemens up to approximately 2,000 nS (Weingart, 1986; Wittenberg et al., 1986; White et al., 1990; Moreno et al., 1994; Kwak and Jongsma, 1996; Verheule et al., 1997; Kucera et al., 2002; Valiunas et al., 2002; Desplantez et al., 2007; McCain et al., 2012; Nielsen et al., 2012). While studies have shown increases in Cx43 expression with age, to our knowledge, no studies have quantified GJ conductances throughout development. Therefore, we performed simulations with GJ conductance spanning from the low to high end of physiological measurements and hypothesized that such a range is qualitatively similar to different developmental stages and consistent with Cx43 expression changes. Importantly, the values chosen were consistent with experimental measurements of conduction for neonatal and adult myocardium (Rosen et al., 1981; George et al., 2019; King et al., 2021). We note that age-associated changes in GJ localization are represented as changes in GJ coupling (i.e., changes in f_{gap}), as all GJs are located at cell ends in the one-dimensional tissue model.

We account for dynamic $[Na^+]$ in three spaces: (i) the ID ($[Na^+]_i^{disc}$), mediated by I_{Na}^{disc} and intracellular diffusion, (ii) the intercellular cleft ($[Na^+]_e^{cleft}$), with volume proportional to w and mediated by ID Na^+ current I_{Na}^{disc} and passive diffusion with the bulk extracellular space, and (iii) the axial intracellular space ($[Na^+]_i^{ax}$), mediated by axial Na^+ current I_{Na}^{ax} and intracellular diffusion. The cable was paced at one end with a specified basic cycle length (BCL). Unless otherwise stated, for all simulations, we utilize a $BCL = 500$ ms or a pacing rate of 2 Hz, which is normal pacing for the guinea pig model that is utilized for this study.

In addition to GJ coupling, we perform simulations in which we adjust several key age-associated properties: (1) We vary Na^+ channel localization at the ID (ID_{Na}) between 0.1 and 1, to account for Na^+ channel redistribution, where $ID_{Na} = 1$ represents 100% or all Na^+ channels localized at the ID. (2) We define and vary a cell size scaling factor (S) between 0.2 and 1 to account for cell size growth, where 100% cell size represents an adult cell. The cell geometry is assumed to be cylindrical, with radius r and length L, defined as $r = Sr_0$ and $L = n_pL_p$, where the nominal adult radius $r_0 = 11$ μm, the number of axial patches $n_p = Sn_p^0$, and the maximum axial membrane patches $n_p^0 = 10$. Note, we only consider values of S such that n_p is a whole number, and that nominal adult cell length $L_0 = n_p^0L_p = 100$ μm. Additionally, note that since S scales both cell length and radius, cell membrane surface area is scaled by S^2, e.g., $S = 0.4$ corresponds with surface area scaled by a factor of 0.16. (3) We also vary the Na^+ channel density (ρ_{Na}) between 0.2 and 1 to account for age-associated changes in Na^+ channel expression, where 100% ρ_{Na} represents full expression of Na^+ channels on the cell membrane. The total cellular Na^+ conductance is proportional to both ρ_{Na} and total cell surface area, such that we can define a normalized total Na^+ channel conductance ($G_{Na} = \rho_{Na}S^2$, also between 0 and 1), where the total Na^+ channel conductance (in physical units) is equal to G_{Na}, scaled by the nominal total Na^+ channel conductance ($G_{Na}^0 = 21.78$ mS/cm^2). Thus, for ρ_{Na} and S of 100%, total Na^+ channel conductance is G_{Na}^0. (4) Finally, we vary the intercellular cleft width (w) from 10 to 40 nm, consistent with intercellular cleft width ranges measured at the ID in our previous work (Veeraraghavan and Gourdie, 2016; Greer-Short et al., 2017; Nowak et al., 2020, 2021).

3. RESULTS

3.1. Ephaptic Effects Are Enhanced for Larger Cells With Low Gap Junctional Coupling

Motivated by findings that both GJ coupling (Peters et al., 1994; Hirschy et al., 2006; Vreeker et al., 2014; Swift et al., 2020) and cell size (Kato et al., 1996; Spach et al., 2000; Cordeiro et al., 2013; Vreeker et al., 2014) increase with age, we first investigate how changes in cell size and GJ coupling influence conduction. We first consider moderate localization of Na^+ channels at the ID ($ID_{Na} = 50\%$), high whole cell Na^+ channel density ($\rho_{Na} = 100\%$), and a nominal intercellular cleft width ($w = 20$ nm). In **Figure 2**, the time series for transmembrane voltage (V_m), pre- and post-junctional Na^+ current (I_{Na}^{pre} and I_{Na}^{post}, respectively), GJ current (I_{GJ}), and the cleft voltage (V_{cleft}) are shown during the action potential upstroke at the same spatial location within the cardiac tissue for varying cell size and GJ coupling.

For low GJ coupling (**Figure 2**, *left*), the slowed action potential upstroke for the large cell size indicates that conduction slows as cell size increases. For tissue with small cell size, a large pre-junctional current I_{Na}^{pre} rapidly activates the post-junctional current I_{Na}^{post} (**Figures 2B,C**, red), and the smaller membrane surface area results in a relatively larger GJ current density I_{GJ} (**Figure 2D**, red), compared with larger cell size. In contrast, for tissue with larger cell size, GJ current density is reduced (**Figure 2D**, purple), and further cleft hyperpolarization is enhanced, i.e., V_{cleft} is more negatively polarized (**Figure 2E**, purple). This enhanced EpC effect ultimately drives the self-attenuation mechanism, in which I_{Na}^{post} driving force is reduced. Collectively, these effects result in slower conduction for tissue with larger cell size.

For moderately low and moderately high GJ coupling (**Figure 2**, *center left* and *center right*), these EpC effects are reduced; however, cleft hyperpolarization is still enhanced for larger cell sizes (**Figures 2B–E**). For high GJ coupling (**Figure 2**, *right*), the faster action potential upstroke for large cell size indicates that conduction is enhanced as cell size increases. In this case, I_{GJ} is sufficiently large, such that the self-attenuation effects on post-junctional Na^+ current are counterbalanced, in a manner that conduction is faster for tissue with larger cell size. Additionally, for larger cell size, there are fewer cell-cell junctions in a given length of tissue, which also results in overall faster conduction.

3.2. Conduction Velocity Depends on Key Cellular and Tissue Properties

We next more broadly investigated the interdependence between cell size, whole cell Na^+ channel density (ρ_{Na}), Na^+ channel

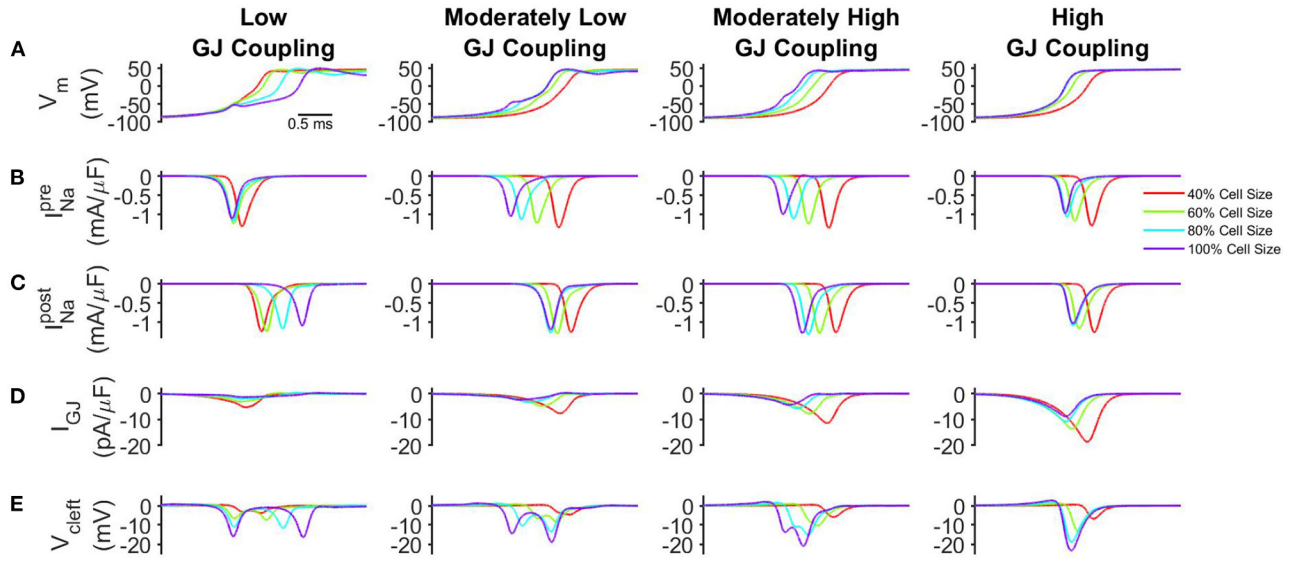

FIGURE 2 | Conduction velocity (CV) depends on cell size and GJ coupling. **(A)** Transmembrane voltage of the post-junctional node of the ID (V_m), **(B)** Na^+ current at the pre-junctional node of the ID (I_{Na}^{pre}), **(C)** Na^+ current at the post-junctional node of the ID (I_{Na}^{post}), **(D)** GJ current at the ID (I_{GJ}), and **(E)** cleft voltage (V_{cleft}) are shown in tissue for low (50.6 nS), moderately low (101 nS), moderately high (253 nS), and high (1,266 nS) GJ coupling. For clarity, traces are shown for the same spatial point of 1.2 mm from the pacing site. Parameters: ID_{Na}= 50%, ρ_{Na}= 100%, $w = 20\ nm$.

ID localization (ID_{Na}), and GJ coupling on CV (**Figure 3**). We consider a wide range of parameters to assess the age-associated changes on CV. For all cases investigated, as expected, CV consistently increases with both increasing GJ coupling and ρ_{Na}. For low GJ coupling (**Figure 3A**), as illustrated above, CV decreases as cell size increases, due to both the reduced GJ current density and the self-attenuation mechanism previously stated. Increased Na^+ channel preferential localization at the ID tends to moderately increase CV for larger cell sizes due to increased EpC, which increases conduction for low GJ coupling.

In contrast, for high GJ coupling (**Figure 3D**), CV increases as cell size increases due to fewer GJs per unit length, as described above. As ID_{Na} increases, CV decreases moderately, more so for larger cell sizes, again due to increased EpC, which decreases conduction for high GJ coupling. From low to high GJ coupling, the CV-cell size relationship transitions from decreasing to increasing, such that for moderate GJ coupling strengths, CV exhibits a biphasic relationship with cell size (**Figures 3B,C**). However, for most conditions, CV only moderately varies across the wide range of cell sizes, which suggests GJ and EpC effects that depend on cell size are fairly balanced for these conditions. Increased Na^+ channel ID localization has only small effects, tending to increase CV for the moderately low GJ coupling cases.

We indicate two key regions of interest: the neonatal regime and the adult regime. The neonatal regime is indicated by gray boxes and represents the range of parameters associated with neonatal myocardium: small cell size, low Na^+ channel ID localization, and low to moderately low GJ coupling (Peters et al., 1994; Kato et al., 1996; Spach et al., 2000; Vreeker et al., 2014). The adult regime is indicated by black boxes and represents the range of parameters associated with adult myocardium: large cell size, high preferential Na^+ channel localization at the ID, and moderately high to high GJ coupling. In the neonatal regimes, CV is slow, consistent with the reduced GJ coupling, and further is sensitive to changes in cell size. In contrast, in the adult regime, CV is faster, consistent with the higher GJ coupling, and additionally does not depend on cell size. In both regimes, CV is highly sensitive to changes in Na^+ channel density. Collectively, this suggests that developmental changes result in conduction that is more robust to changes in cell size. Additionally, in **Supplementary Material**, we perform a similar broad investigation for a bradycardic pacing rate (1 Hz, or BCL of 1,000 ms), and we found that CV has a nearly identical relationship with cell size, Na^+ channel density and localization, and GJ coupling under these conditions (**Supplementary Figure 1**), as compared with the normal pacing rate.

3.3. Conduction Velocity Is Correlated to Total Cell Na^+ Conductance and Gap Junctional Coupling

The previous analysis shows CV had a consistent positive dependence on Na^+ current density ρ_{Na}, yet the relationship between CV and cell size depends on GJ coupling. As the total cell Na^+ conductance (G_{Na}) depends on both cell size and Na^+ channel density, we next investigate how CV depends on G_{Na} for varying GJ coupling conditions (**Figure 4**). For all GJ coupling strengths, we find discrete vertical "columns" of points, which correspond to the same G_{Na} value (i.e., same ρ_{Na} and S) and different values of Na^+ channel localization (ID_{Na}). From these data, we observe that increased ID_{Na} typically

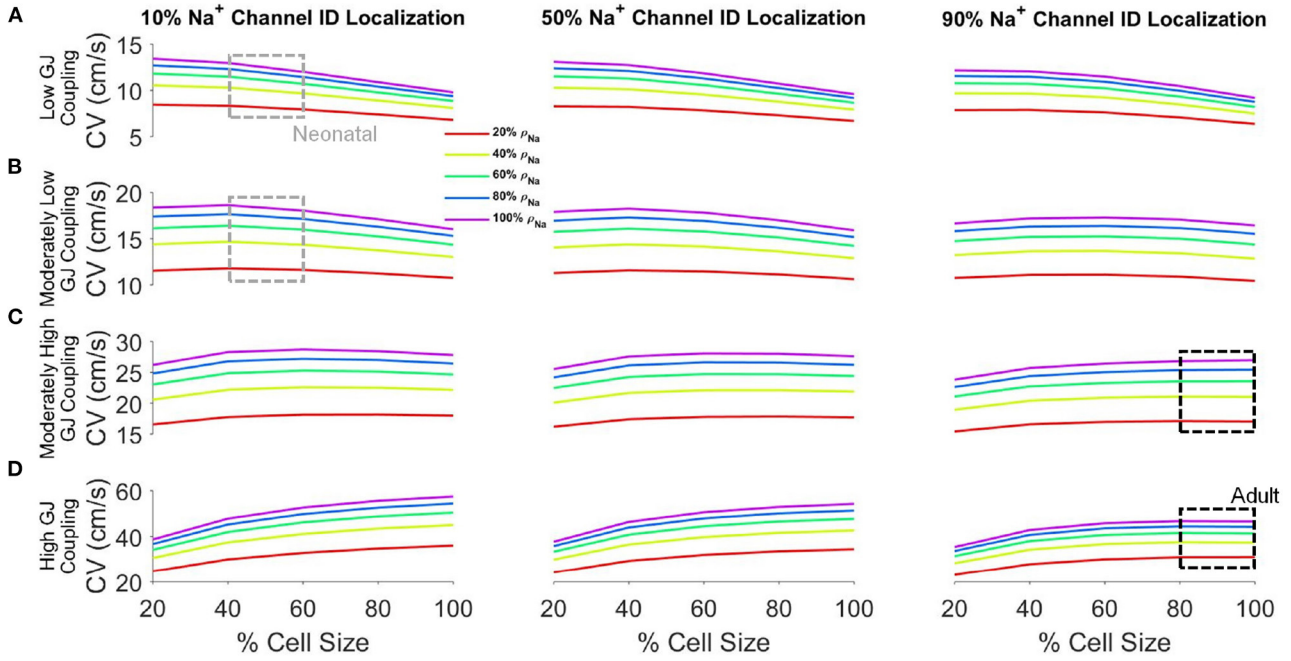

FIGURE 3 | Conduction velocity (CV) depends on key cellular and tissue properties. CV is shown as a function of cell size for different values of Na^+channel densities (ρ_{Na}) for low **(A)**, moderately low **(B)**, moderately high **(C)**, and high **(D)** GJ coupling and 10% (*left*), 50% (*middle*), and 90% (*right*) Na^+ channel ID localization (ID_{Na}). Parameters: Cleft width $w = 20$ *nm*. Parameter regimes associated with neonatal (gray boxes) and adult (black boxes) tissue are highlighted.

slows conduction, except for cases of moderately low GJ coupling and larger cell size. Additionally, we observe diagonal "bands" of points, which correspond with the same cell sizes and different ρ_{Na} values, which illustrate that CV increases with increasing ρ_{Na}, as in **Figure 2**.

With all of these dependencies within given "columns" or "bands," we also consider if there is a distinct relationship between CV and G_{Na} for a given GJ coupling strength. For low GJ coupling (**Figure 4A**), CV is overall very weakly correlated with G_{Na} (dashed black line), indicating that for these conditions, the total Na^+ channel conductance is not predictive of CV. However, as GJ coupling increases, the correlation between CV and G_{Na} increases and approaches 1 for high GJ coupling (**Figures 4B–D**), demonstrating a closer relationship between conduction and total Na^+ current conductance.

Prior work from us and others has shown that the intercellular width (w) is a critical parameter governing the strength of EpC effects and ultimately conduction (Kucera et al., 2002; Lin and Keener, 2010; Greer-Short et al., 2017; Nowak et al., 2020), so we next investigate how the correlation between CV and G_{Na} depends on w. In **Figure 5**, we plot the Pearson correlation coefficient r as a function of GJ coupling for different values of w. For all cleft widths, the correlation increases from near 0 to near 1 as GJ coupling increases, as in **Figure 4**. However, for narrow clefts (red), the correlation is less sensitive to changes in GJ coupling, such that the correlation coefficient is more positive for lower GJ coupling and less positive for higher GJ coupling, compared with wider clefts. These results are consistent with EpC playing a larger role governing conduction for lower GJ coupling, such that there is a stronger relationship between CV and G_{Na} for these conditions.

3.4. Conduction Velocity Depends on Developmental Stage

The above results illustrate the complex relationship between conduction and cellular/tissue properties known to alter with age and development. As previously discussed, neonatal tissues are associated with low Na^+ channel expression and ID localization and smaller cell size, while adult tissues have larger cells and high Na^+ channel expression and localization at the ID. We hypothesize that, during both disease and development, these properties remain variable in both time and between patients. For a final analysis, we investigate CV for conditions representing an age-associated progression, considering neonatal, intermediate developmental stages, and adult tissue (**Figure 6**). To account for variability, we consider a range of values for each of the key parameters investigated throughout this study: cell size, Na^+ channel density, and Na^+ channel localization at the ID. These parameters were varied over a 20% range. The minimum and maximum CV values over all parameter conditions for each stage were plotted (solid black lines), along with the average over the different parameter values (dashed black line). Due to lack of evidence of the precise order in which these parameters change throughout the developmental process, we consider different possible parameter conditions for the intermediate stages: uniform ρ_{Na} and ID_{Na} increase, staged S and ρ_{Na} increases, staged S and ID_{Na} increases, and staged ρ_{Na} and ID_{Na} increases ranging from neonatal to adult tissue parameter

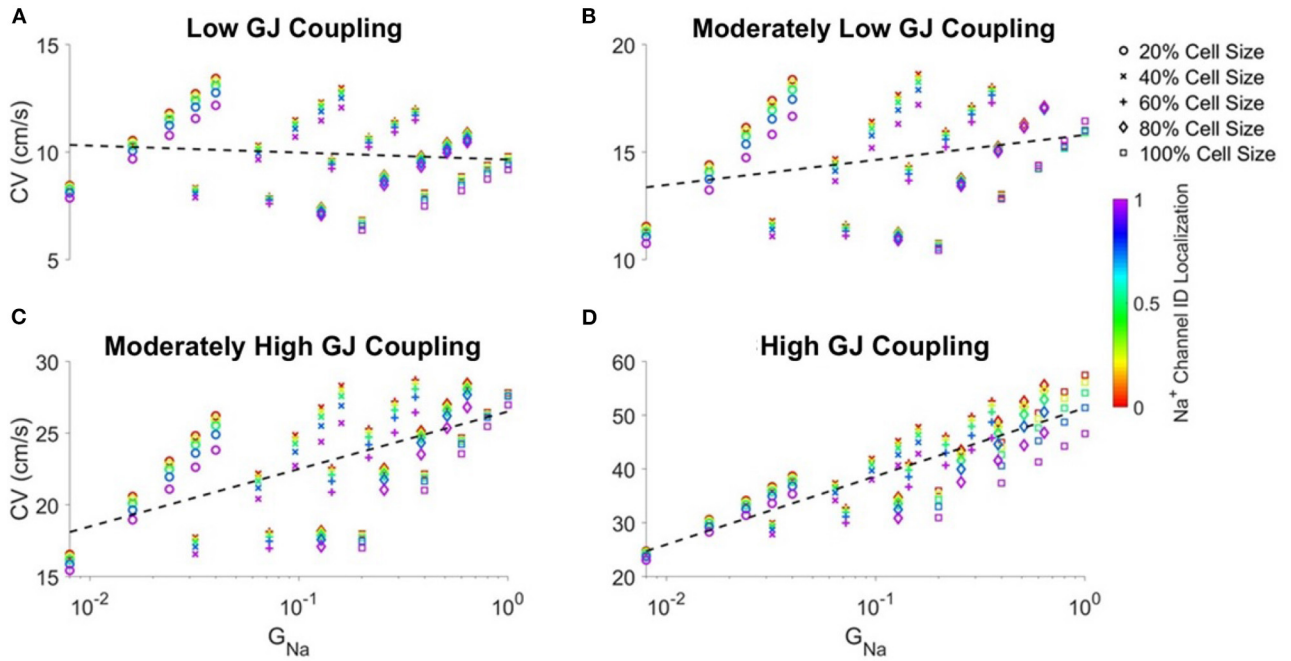

FIGURE 4 | Correlation between conduction velocity (CV) and total cell Na^+ conductance (G_{Na}) increases as gap junctional coupling increases. Conduction velocity (CV) is shown as a function of G_{Na} for different cell sizes and Na^+ channel ID localization for **(A)** low, **(B)** moderately low, **(C)** moderately high, and **(D)** high GJ coupling. Pearson correlation coefficients r for low ($r = -0.103$), moderately low ($r = 0.283$), moderately high ($r = 0.607$), high ($r = 0.865$) GJ coupling. Parameters: Cleft width $w = 20$ *nm*.

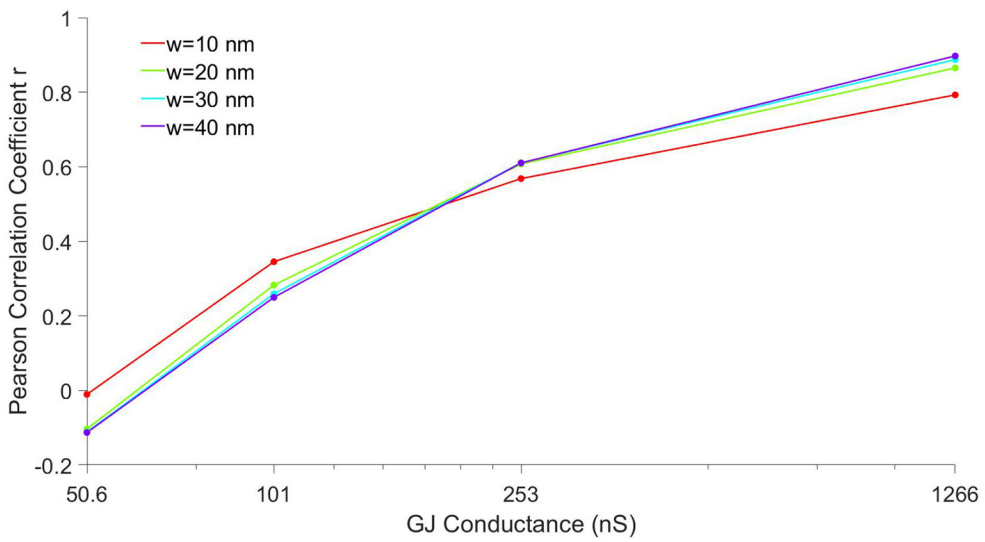

FIGURE 5 | Correlation between conduction velocity (CV) and total cell Na^+ conductance depends on gap junctional coupling. The Pearson correlation coefficient r between CV and total cell Na^+ conductance (G_{Na}) is shown as a function of GJ coupling conductance, for four different cleft width w values.

values. The parameter ranges for each developmental stage are listed in **Supplementary Table 2**.

For the neonatal stage, the range of CVs is small and conduction speeds are slow. For the first intermediate developmental stage, the CV range is moderately larger, but the conduction remains slow. However, for the second intermediate developmental stage, the CV range is dramatically increased, ranging from roughly 20 cm/s to over 50 cm/s, suggesting that conduction greatly increases and can approach adult myocardium values, but may be more variable during

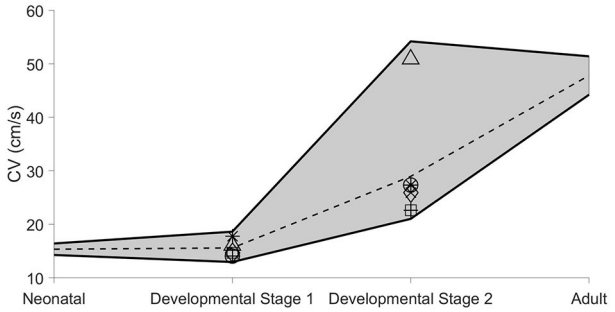

FIGURE 6 | Age-associated ranges of conduction velocity (CV). The range of CV values (see text for details) are shown as functions of age-dependent progression. Parameter ranges and markers for each stage are shown in **Supplementary Table 2**. The dashed line shown for each stage represents the average CV value over all conditions within the specified parameter ranges. Cleft width $w = 20$ *nm*.

this intermediate stage. For the adult stage, the range of CVs decreases, such that conduction is consistently within the normal faster propagation regime, suggesting robust conduction regardless of small changes in cellular and tissue properties.

4. DISCUSSION

In this study, we investigate the regulation of key age-dependent properties, specifically cell size, Na^+ channel density and localization, and GJ coupling, on cardiac conduction. We summarize our key findings: CV is consistently increased by increased Na^+ current density, across all conditions. However, simulations predict that CV biphasically depends on cell size, depending on the strength of GJ coupling. That is, CV increases with increasing cell size for high GJ coupling, yet decreases with increasing cell size for low GJ coupling. As a consequence, CV and total cell Na^+ channel conductance are well-correlated in cardiac tissue with high GJ coupling, but not correlated with CV for low GJ coupling. We predict that the role of EpC governing conduction changes during development, such that neonatal tissue is less sensitive to changes in EpC due to smaller Na^+ channel ID localization. We postulate that even though GJ coupling is low during this early stage, the small cell size and therefore small membrane capacitance is such that the lower Na^+ current density is still sufficient to maintain robust conduction in the myocardium. However, conduction is very slow during this stage due to the relatively high ratio of cell-cell junctions for a given length of tissue. These findings are consistent with Swift et al. (2020), who found slower atrioventricular conduction in neonatal and early postnatal rats, compared with adult rat myocardium.

As development progresses, model predictions are consistent with faster conduction. Further, simulations predict that a wide range of conduction velocities are possible during intermediate developmental stages due to variability in cellular/tissue properties and the relative timing of developmental changes. However, despite similar variability in parameter values, this variability in CV prediction narrows in adult tissue and is consistent with experimental measures (George et al., 2019; King et al., 2021). Interestingly, we see a larger influence of EpC effects in larger cell sizes with reduced GJ coupling, as would be the case in intermediate developmental stages and in adult myocardium for pathological conditions such heart failure (Smith et al., 1991; Peters et al., 1997; Yao et al., 2003; Akar et al., 2004; Poelzing and Rosenbaum, 2004), indicating a possible mechanism for maintained conduction during such transitional or diseased states. Additionally, this enhanced variability in conduction for intermediate developmental stages may be desirable, as this variability suggests an ability to adapt and modulate cardiac activity in response to developmental perturbations, which inherently vary significantly for different individuals.

Previous studies have investigated the properties of Na^+ channels and GJs and their roles in the developing heart. Work by Harrell et al. (2007) found that $Na_v1.5$ mRNA was significantly more up-regulated in adult mouse hearts than in neonatal hearts. Similarly, Cordeiro et al. (2013) find that both peak and late I_{Na} is significantly smaller in neonatal canine cardiomyocytes compared to that of adults, and Cai et al. (2011) found the same in human atrial cardiomyocytes. Vreeker et al. (2014) show that the GJ protein Cx43 transitions from diffusely distributed on the cardiomyocyte membrane to highly associated with mechanical junctions at the ID during development in human samples, as similarly shown in rat myocardium (Angst et al., 1997). In contrast, Peters et al. (1994) found that GJs and adherens junctions have a highly correlated distribution over postnatal development of the ventricle in human samples. Incorporating developmental changes in GJ distribution, Spach et al. (2000) previously simulated a neonatal cardiomyocyte with diffuse GJs and smaller size and found that conduction was slower in the neonatal tissue, compared with adult myocardium with GJs primarily localized at the ID and larger size.

While these studies are crucial in understanding cardiac development, to our knowledge, our study is the first to combine all these key developmental changes occurring in conjunction with each other, specifically cellular size, gap junctional conductance, and Na^+ channel expression and distribution. Thus, we find that ephaptic effects are more pronounced in larger cells with low GJ coupling. We also find that CV biphasically depends on cell size in a manner dependent on GJ coupling: CV is relatively fast for both low GJ coupling and small cell size and high GJ coupling and large cell size. Interestingly, we find that CV is correlated total Na^+ conductance for high GJ coupling. Finally, by incorporating previous data on developmental changes (Peters et al., 1994; Spach et al., 2000; Harrell et al., 2007; Cai et al., 2011; Cordeiro et al., 2013; Vreeker et al., 2014), we predict how the variability in the ranges for conduction change in conjunction with developmental stages.

Recently, we investigated the age-dependent manifestation of a long QT type 3 (LQT3)-associated gain-of-function mutation in $Na_v1.5$ (Nowak et al., 2021). LQT3, while relatively rare, has a high mortality, reaching 49% (Vignati, 2007), and critically patients tend to remain asymptomatic until well after puberty (Beaufort-Krol et al., 2005; Wilde et al., 2016; Kutyifa et al., 2018). Interestingly, in pediatric patients with LQT syndromes,

Na^+ channel blockers are commonly prescribed as a form of chronic management (Hanisch, 2001), and our results are consistent with the safety of this approach due to the weak dependence of conduction on overall total cell Na^+ channel conductance. In our study, we predicted that not only does the manifestation of arrhythmias depend on developmental stage, but that the sensitivity to changes in intercellular cleft width depended on these age-associated properties as well. Interestingly, Brugada syndrome (BrS), an inherited cardiac arrhythmia disorder caused a loss-of-function mutation in $Na_v1.5$, also often manifests later in life; the average first event occurs around 42 years old (Milman et al., 2017). Our study is consistent with this clinical manifestation, as simulations predict that in these early developmental stages with low GJ coupling, conduction is less sensitive to overall Na^+ conductance (**Figure 4**), due to the overall small cell sizes in neonatal tissue.

Finally, we acknowledge limitations of our study. To study developmental changes in Na^+ channel distribution, we incorporate this critical subcellular detail in the representation of cardiac tissue; however, our model is still a simplification of the complex cardiac tissue structure. Specifically, our model assumes a simplified cylindrical cell and uniform intercellular cleft, while the geometry of individual cells and the ID structure is known to be complex heterogeneous (Veeraraghavan et al., 2015). Future work will focus on investigating how ID structure changes in development and impacts conduction (Moise et al., 2021). Additionally, cardiac tissue is a three-dimensional structure, and our one-dimensional cable representation cannot fully represent all aspects of developmental changes, such as GJ localization along the lateral membrane. In a two- or three-dimensional tissue, GJ redistribution from the lateral membrane to the ID would also be expected to impact conduction heterogeneously dependent on the direction of wavefront propagation relative to the underlying tissue geometry, such that early developmental stages are associated with isotropic conduction while anisotropic conduction is associated with adult myocardium, consistent with previous work from Spach et al. (2000). Further, while we observe minimal differences in CV between normal and slow pacing rates, Entz et al. (2016) previously showed that CV slowing at faster pacing rates differed between longitudinal and transverse conduction, and further was regulated by extracellular ionic composition, suggesting that properties governing EpC may similarly modulate heart rate dependence. Additionally, expression of ion channels vary across individual patients, and these differences may impact conduction during development. Further, recent work from the Posnack lab has shown that several expression of several key ion channel and calcium handling proteins vary with developmental stage in rats (Swift et al., 2020). We are particularly interested in similar changes in human myocardium, and future work will incorporate such details as available and established in the literature.

DATA AVAILABILITY STATEMENT

The raw data supporting the conclusions of this article will be made available by the authors, without undue reservation.

AUTHOR CONTRIBUTIONS

MN performed computational studies and wrote the original manuscript draft. RV contributed to the manuscript draft. SP and SW designed simulations, provided funding, and contributed to the manuscript draft. All authors contributed to the article and approved the submitted version.

FUNDING

This study was supported by funding from the National Institutes of Health, grant numbers R01HL138003 (SW, SP), R01HL102298 (SP), and R01HL148736 (RV).

SUPPLEMENTARY MATERIAL

The Supplementary Material for this article can be found online at: https://www.frontiersin.org/articles/10.3389/fphys.2021.731025/full#supplementary-material

REFERENCES

Agullo-Pascual, E., Lin, X., Leo-Macias, A., Zhang, M., Liang, F.-X., Li, Z., et al. (2014). Super-resolution imaging reveals that loss of the c-terminus of connexin43 limits microtubule plus-end capture and nav1. 5 localization at the intercalated disc. *Cardiovasc. Res.* 104, 371–381. doi: 10.1093/cvr/cvu195

Akar, F. G., Spragg, D. D., Tunin, R. S., Kass, D. A., and Tomaselli, G. F. (2004). Mechanisms underlying conduction slowing and arrhythmogenesis in nonischemic dilated cardiomyopathy. *Circ. Res.* 95, 717–725. doi: 10.1161/01.RES.0000144125.61927.1c

Angst, B. D., Khan, L. U., Severs, N. J., Whitely, K., Rothery, S., Thompson, R. P., et al. (1997). Dissociated spatial patterning of gap junctions and cell adhesion junctions during postnatal differentiation of ventricular myocardium. *Circ. Res.* 80, 88–94. doi: 10.1161/01.RES.80.1.88

Beaufort-Krol, G. C., van den Berg, M. P., Wilde, A. A., van Tintelen, J. P., Viersma, J. W., Bezzina, C. R., et al. (2005). Developmental aspects of long QT syndrome type 3 and Brugada syndrome on the basis of a single SCN5A mutation in childhood. *J. Am. Coll. Cardiol.* 46, 331–337. doi: 10.1016/j.jacc.2005.03.066

Cai, B., Mu, X., Gong, D., Jiang, S., Li, J., Meng, Q., et al. (2011). Difference of sodium currents between pediatric and adult human atrial myocytes: evidence for developmental changes of sodium channels. *Int. J. Biol. Sci.* 7:708. doi: 10.7150/ijbs.7.708

Clancy, C. E., Tateyama, M., and Kass, R. S. (2002). Insights into the molecular mechanisms of bradycardia-triggered arrhythmias in long QT-3 syndrome. *J. Clin. Investig.* 110, 1251–1262. doi: 10.1172/JCI0215928

Cordeiro, J. M., Panama, B. K., Goodrow, R., Zygmunt, A. C., White, C., Treat, J. A., et al. (2013). Developmental changes in expression and biophysics of ion channels in the canine ventricle. *J. Mol. Cell. Cardiol.* 64, 79–89. doi: 10.1016/j.yjmcc.2013.09.001

Desplantez, T., Dupont, E., Severs, N. J., and Weingart, R. (2007). Gap junction channels and cardiac impulse propagation. *Journal of Membrane Biology* 218, 13–28. doi: 10.1007/s00232-007-9046-8

Entz, M. I., George, S. A., Zeitz, M. J., Raisch, T., Smyth, J. W., and Poelzing, S. (2016). Heart rate and extracellular sodium and potassium modulation of gap junction mediated conduction in guinea pigs. *Front. Physiol.* 7:16. doi: 10.3389/fphys.2016.00016

Fromaget, C., El Aoumari, A., and Gros, D. (1992). Distribution pattern of connexin 43, a gap junctional protein, during the differentiation of mouse heart myocytes. *Differentiation* 51, 9–20. doi: 10.1111/j.1432-0436.1992.tb00675.x

George, S. A., Bonakdar, M., Zeitz, M., Davalos, R. V., Smyth, J. W., and Poelzing, S. (2016). Extracellular sodium dependence of the conduction velocity-calcium relationship: evidence of ephaptic self-attenuation. *Am. J. Physiol. Heart Circ. Physiol*. 310, H1129–H1139. doi: 10.1152/ajpheart.00857.2015

George, S. A., Hoeker, G., Calhoun, P. J., Entz, M., Raisch, T. B., King, D. R., et al. (2019). Modulating cardiac conduction during metabolic ischemia with perfusate sodium and calcium in guinea pig hearts. *Am. J. Physiol. Heart Circ. Physiol*. 316, H849–H861. doi: 10.1152/ajpheart.00083.2018

Greer-Short, A., George, S. A., Poelzing, S., and Weinberg, S. H. (2017). Revealing the concealed nature of long-QT type 3 syndrome. *Circ. Arrhythmia Electrophysiol*. 10:e004400. doi: 10.1161/CIRCEP.116.004400

Hanisch, D. (2001). Pediatric arrhythmias. *J. Pediatr. Nurs*. 16, 351–362. doi: 10.1053/jpdn.2001.26571

Harrell, M. D., Harbi, S., Hoffman, J. F., Zavadil, J., and Coetzee, W. A. (2007). Large-scale analysis of ion channel gene expression in the mouse heart during perinatal development. *Physiol. Genomics* 28, 273–283. doi: 10.1152/physiolgenomics.00163.2006

Hichri, E., Abriel, H., and Kucera, J. P. (2018). Distribution of cardiac sodium channels in clusters potentiates ephaptic interactions in the intercalated disc. *J. Physiol*. 596, 563–589. doi: 10.1113/JP275351

Hirschy, A., Schatzmann, F., Ehler, E., and Perriard, J.-C. (2006). Establishment of cardiac cytoarchitecture in the developing mouse heart. *Dev. Biol*. 289, 430–441. doi: 10.1016/j.ydbio.2005.10.046

Jæger, K. H., Edwards, A. G., McCulloch, A., and Tveito, A. (2019). Properties of cardiac conduction in a cell-based computational model. *PLoS Comput. Biol*. 15:e1007042. doi: 10.1371/journal.pcbi.1007042

Kato, Y., Masumiya, H., Agata, N., Tanaka, H., and Shigenobu, K. (1996). Developmental changes in action potential and membrane currents in fetal, neonatal and adult guinea-pig ventricular myocytes. *J. Mol. Cell. Cardiol*. 28, 1515–1522. doi: 10.1006/jmcc.1996.0141

King, D. R., Entz, M., Blair, G. A., Crandell, I., Hanlon, A. L., Lin, J., et al. (2021). The conduction velocity-potassium relationship in the heart is modulated by sodium and calcium. *Pflügers Arch*. 473, 557–571. doi: 10.1007/s00424-021-02537-y

Kucera, J. P., Rohr, S., and Rudy, Y. (2002). Localization of sodium channels in intercalated disks modulates cardiac conduction. *Circ. Res*. 91, 1176–1182. doi: 10.1161/01.RES.0000046237.54156.0A

Kutyifa, V., Daimee, U. A., McNitt, S., Polonsky, B., Lowenstein, C., Cutter, K., et al. (2018). Clinical aspects of the three major genetic forms of long QT syndrome (LQT 1, LQT 2, LQT 3). *Ann. Noninvasive Electrocardiol*. 23:e12537. doi: 10.1111/anec.12537

Kwak, B. R., and Jongsma, H. J. (1996). Regulation of cardiac gap junction channel permeability and conductance by several phosphorylating conditions. *Mol. Cell. Biochem*. 157, 93–99. doi: 10.1007/978-1-4613-1275-8_11

Leo-Macias, A., Agullo-Pascual, E., Sanchez-Alonso, J. L., Keegan, S., Lin, X., Arcos, T., et al. (2016). Nanoscale visualization of functional adhesion/excitability nodes at the intercalated disc. *Nat. Commun*. 7, 1–12. doi: 10.1038/ncomms10919

Lin, J., and Keener, J. P. (2010). Modeling electrical activity of myocardial cells incorporating the effects of ephaptic coupling. *Proc. Natl. Acad. Sci. U.S.A*. 107, 20935–20940. doi: 10.1073/pnas.1010154107

Livshitz, L. M., and Rudy, Y. (2007). Regulation of Ca2+ and electrical alternans in cardiac myocytes: role of camkii and repolarizing currents. *Am. J. Physiol. Heart Circ. Physiol*. 292, H2854–H2866. doi: 10.1152/ajpheart.01347.2006

McCain, M. L., Desplantez, T., Geisse, N. A., Rothen-Rutishauser, B., Oberer, H., Parker, K. K., et al. (2012). Cell-to-cell coupling in engineered pairs of rat ventricular cardiomyocytes: relation between cx43 immunofluorescence and intercellular electrical conductance. *Am. J. Physiol. Heart Circ. Physiol*. 302, H443–H450. doi: 10.1152/ajpheart.01218.2010

Mezache, L., Struckman, H. L., Greer-Short, A., Baine, S., Györke, S., Radwański, P. B., et al. (2020). Vascular endothelial growth factor promotes atrial arrhythmias by inducing acute intercalated disk remodeling. *Sci. Rep*. 10, 1–14. doi: 10.1038/s41598-020-77562-5

Milman, A., Andorin, A., Gourraud, J.-B., Sacher, F., Mabo, P., Kim, S.-H., et al. (2017). Age of first arrhythmic event in brugada syndrome: data from the sabrus (survey on arrhythmic events in brugada syndrome) in 678 patients. *Circ. Arrhythmia Electrophysiol*. 10:e005222. doi: 10.1161/CIRCEP.117.005222

Moise, N., Struckman, H. L., Dagher, C., Veeraraghavan, R., and Weinberg, S. H. (2021). Intercalated disk nanoscale structure regulates cardiac conduction. *J. Gen. Physiol*. 153:e202112897. doi: 10.1085/jgp.202112897

Moreno, A., Rook, M., Fishman, G., and Spray, D. (1994). Gap junction channels: distinct voltage-sensitive and-insensitive conductance states. *Biophys. J*. 67, 113–119. doi: 10.1016/S0006-3495(94)80460-6

Mori, Y., Fishman, G. I., and Peskin, C. S. (2008). Ephaptic conduction in a cardiac strand model with 3d electrodiffusion. *Proc. Natl. Acad. Sci. U.S.A*. 105, 6463–6468. doi: 10.1073/pnas.0801089105

Nielsen, M. S., Nygaard Axelsen, L., Sorgen, P. L., Verma, V., Delmar, M., and Holstein-Rathlou, N.-H. (2012). Gap junctions. *Comprehens. Physiol*. 2, 1981–2035. doi: 10.1002/cphy.c110051

Nowak, M. B., Greer-Short, A., Wan, X., Wu, X., Deschênes, I., Weinberg, S. H., et al. (2020). Intercellular sodium regulates repolarization in cardiac tissue with sodium channel gain-of-function. *Biophys. J*. 118:2829–2843. doi: 10.1016/j.bpj.2020.04.014

Nowak, M. B., Poelzing, S., and Weinberg, S. H. (2021). Mechanisms underlying age-associated manifestation of cardiac sodium channel gain-of-function. *J. Mol. Cell. Cardiol*. 153, 60–71. doi: 10.1016/j.yjmcc.2020.12.008

Peters, N. S., Coromilas, J., Severs, N. J., and Wit, A. L. (1997). Disturbed connexin43 gap junction distribution correlates with the location of reentrant circuits in the epicardial border zone of healing canine infarcts that cause ventricular tachycardia. *Circulation* 95, 988–996. doi: 10.1161/01.CIR.95.4.988

Peters, N. S., Severs, N. J., Rothery, S. M., Lincoln, C., Yacoub, M. H., and Green, C. R. (1994). Spatiotemporal relation between gap junctions and fascia adherens junctions during postnatal development of human ventricular myocardium. *Circulation* 90, 713–725. doi: 10.1161/01.CIR.90.2.713

Poelzing, S., and Rosenbaum, D. S. (2004). Altered connexin43 expression produces arrhythmia substrate in heart failure. *Am. J. Physiol. Heart Circ. Physiol*. 287, H1762–H1770. doi: 10.1152/ajpheart.00346.2004

Quan, W., and Rudy, Y. (1990). Unidirectional block and reentry of cardiac excitation: a model study. *Circ. Res*. 66, 367–382. doi: 10.1161/01.RES.66.2.367

Rhett, J. M., Ongstad, E. L., Jourdan, J., and Gourdie, R. G. (2012). Cx43 associates with na v 1.5 in the cardiomyocyte perinexus. *J. Memb. Biol*. 245, 411–422. doi: 10.1007/s00232-012-9465-z

Rohr, S., Kucera, J. P., and Kléber, A. G. (1998). Slow conduction in cardiac tissue, I: effects of a reduction of excitability versus a reduction of electrical coupling on microconduction. *Circ. Res*. 83, 781–794. doi: 10.1161/01.RES.83.8.781

Rosen, M. R., Legato, M. J., and Weiss, R. M. (1981). Developmental changes in impulse conduction in the canine heart. *Am. J. Physiol. Heart Circ. Physiol*. 240, H546–H554. doi: 10.1152/ajpheart.1981.240.4.H546

Shaw, R. M., and Rudy, Y. (1997). Ionic mechanisms of propagation in cardiac tissue: roles of the sodium and l-type calcium currents during reduced excitability and decreased gap junction coupling. *Circ. Res*. 81, 727–741. doi: 10.1161/01.RES.81.5.727

Smith, J., Green, C., Peters, N., Rothery, S., and Severs, N. (1991). Altered patterns of gap junction distribution in ischemic heart disease. An immunohistochemical study of human myocardium using laser scanning confocal microscopy. *Am. J. Pathol*. 139:801.

Spach, M. S., Heidlage, J. F., Dolber, P. C., and Barr, R. C. (2000). Electrophysiological effects of remodeling cardiac gap junctions and cell size: experimental and model studies of normal cardiac growth. *Circ. Res*. 86, 302–311. doi: 10.1161/01.RES.86.3.302

Sperelakis, N. (2002). An electric field mechanism for transmission of excitation between myocardial cells. *Circ. Res*. 91, 985–987. doi: 10.1161/01.RES.0000045656.34731.6D

Swift, L. M., Burke, M., Guerrelli, D., Reilly, M., Ramadan, M., McCullough, D., et al. (2020). Age-dependent changes in electrophysiology and calcium handling: implications for pediatric cardiac research. *Am. J. Physiol. Heart Circ. Physiol*. 318, H354–H365. doi: 10.1152/ajpheart.00521.2019

Tveito, A., Jæger, K. H., Kuchta, M., Mardal, K.-A., and Rognes, M. E. (2017). A cell-based framework for numerical modeling of electrical conduction in cardiac tissue. *Front. Phys*. 5:48. doi: 10.3389/fphy.2017.00048

Valiunas, V., Beyer, E. C., and Brink, P. R. (2002). Cardiac gap junction channels show quantitative differences in selectivity. *Circ. Res*. 91, 104–111. doi: 10.1161/01.RES.0000025638.24255.AA

Veeraraghavan, R., and Gourdie, R. G. (2016). Stochastic optical reconstruction microscopy-based relative localization analysis (STORM-RLA) for quantitative nanoscale assessment of spatial protein organization. *Mol. Biol. Cell* 27, 3583–3590. doi: 10.1091/mbc.e16-02-0125

Veeraraghavan, R., Gourdie, R. G., and Poelzing, S. (2014). Mechanisms of cardiac conduction: a history of revisions. *Am. J. Physiol. Heart Circ. Physiol.* 306, H619–H627. doi: 10.1152/ajpheart.00760.2013

Veeraraghavan, R., Lin, J., Hoeker, G. S., Keener, J. P., Gourdie, R. G., and Poelzing, S. (2015). Sodium channels in the cx43 gap junction perinexus may constitute a cardiac ephapse: an experimental and modeling study. *Pflügers Arch.* 467, 2093–2105. doi: 10.1007/s00424-014-1675-z

Verheule, S., Van Kempen, M. J., Welscher, P. H., Kwak, B. R., and Jongsma, H. J. (1997). Characterization of gap junction channels in adult rabbit atrial and ventricular myocardium. *Circ. Res.* 80, 673–681. doi: 10.1161/01.RES.80.5.673

Vignati, G. (2007). Pediatric arrhythmias: which are the news? *J. Cardiovasc. Med.* 8, 62–66. doi: 10.2459/01.JCM.0000247438.12817.9e

Vreeker, A., Van Stuijvenberg, L., Hund, T. J., Mohler, P. J., Nikkels, P. G., and Van Veen, T. A. (2014). Assembly of the cardiac intercalated disk during pre-and postnatal development of the human heart. *PLoS ONE* 9:e94722. doi: 10.1371/journal.pone.0094722

Wei, N., Mori, Y., and Tolkacheva, E. G. (2016). The dual effect of ephaptic coupling on cardiac conduction with heterogeneous expression of connexin 43. *J. Theoret. Biol.* 397, 103–114. doi: 10.1016/j.jtbi.2016.02.029

Wei, N., and Tolkacheva, E. G. (2020). Interplay between ephaptic coupling and complex geometry of border zone during acute myocardial ischemia: effect on arrhythmogeneity. *Chaos* 30:033111. doi: 10.1063/1.5134447

Weinberg, S. (2017). Ephaptic coupling rescues conduction failure in weakly coupled cardiac tissue with voltage-gated gap junctions. *Chaos* 27:093908. doi: 10.1063/1.4999602

Weingart, R. (1986). Electrical properties of the nexal membrane studied in rat ventricular cell pairs. *J. Physiol.* 370, 267–284. doi: 10.1113/jphysiol.1986.sp015934

White, R. L., Doeller, J., Verselis, V., and Wittenberg, B. (1990). Gap junctional conductance between pairs of ventricular myocytes is modulated synergistically by H+ and Ca++. *J. Gen. Physiol.* 95, 1061–1075. doi: 10.1085/jgp.95.6.1061

Wilde, A. A., Moss, A. J., Kaufman, E. S., Shimizu, W., Peterson, D. R., Benhorin, J., et al. (2016). Clinical aspects of type 3 long-QT syndrome: an international multicenter study. *Circulation* 134, 872–882. doi: 10.1161/CIRCULATIONAHA.116.021823

Wittenberg, B. A., White, R., Ginzberg, R. D., and Spray, D. C. (1986). Effect of calcium on the dissociation of the mature rat heart into individual and paired myocytes: electrical properties of cell pairs. *Circ. Res.* 59, 143–150. doi: 10.1161/01.RES.59.2.143

Yao, J.-A., Hussain, W., Patel, P., Peters, N. S., Boyden, P. A., and Wit, A. L. (2003). Remodeling of gap junctional channel function in epicardial border zone of healing canine infarcts. *Circ. Res.* 92, 437–443. doi: 10.1161/01.RES.0000059301.81035.06

Conflict of Interest: The authors declare that the research was conducted in the absence of any commercial or financial relationships that could be construed as a potential conflict of interest.

Publisher's Note: All claims expressed in this article are solely those of the authors and do not necessarily represent those of their affiliated organizations, or those of the publisher, the editors and the reviewers. Any product that may be evaluated in this article, or claim that may be made by its manufacturer, is not guaranteed or endorsed by the publisher.

frontiers in Physiology

ORIGINAL RESEARCH
published: 24 November 2021
doi: 10.3389/fphys.2021.725218

Cardiac and Autonomic Dysfunctions Assessed Through Recurrence Quantitative Analysis of Electrocardiogram Signals and an Application to the 6-Hydroxydopamine Parkinson's Disease Animal Model

*Lucas Shinoda[1], Laís Damasceno[1], Leandro Freitas[1], Ruy Campos[2], Sergio Cravo[2], Carla A. Scorza[1], Fúlvio A. Scorza[1] and Jean Faber[1,3]**

[1] Neuroscience Division, Department of Neurology and Neurosurgery, Escola Paulista de Medicina, Federal University of São Paulo, São Paulo, Brazil, [2] Cardiovascular Division, Department of Physiology, Escola Paulista de Medicina, Federal University of São Paulo, São Paulo, Brazil, [3] Nucleus of Neuroengineering and Computation, Institute of Science and Technology, Federal University of São Paulo, São Paulo, Brazil

A classic method to evaluate autonomic dysfunction is through the evaluation of heart rate variability (HRV). HRV provides a series of coefficients, such as Standard Deviation of n-n intervals (SDNN) and Root Mean Square of Successive Differences (RMSSD), which have well-established physiological associations. However, using only electrocardiogram (ECG) signals, it is difficult to identify proper autonomic activity, and the standard techniques are not sensitive and robust enough to distinguish pure autonomic modulation in heart dynamics from cardiac dysfunctions. In this proof-of-concept study we propose the use of Poincaré mapping and Recurrence Quantification Analysis (RQA) to identify and characterize stochasticity and chaoticity dynamics in ECG recordings. By applying these non-linear techniques in the ECG signals recorded from a set of Parkinson's disease (PD) animal model 6-hydroxydopamine (6-OHDA), we showed that they present less variability in long time epochs and more stochasticity in short-time epochs, in their autonomic dynamics, when compared with those of the sham group. These results suggest that PD animal models present more "rigid heart rate" associated with "trembling ECG" and bradycardia, which are direct expressions of Parkinsonian symptoms. We also compared the RQA factors calculated from the ECG of animal models using four computational ECG signals under different noise and autonomic modulatory conditions, emulating the main ECG features of atrial fibrillation and QT-long syndrome.

Keywords: recurrence quantitative analysis, Poincaré map, Parkinson's disease, computational ECG model, 6-OHDA animal model, HRV (heart rate variability) and ECG-complexes, cardiac and autonomic dysfunctions

OPEN ACCESS

Edited by:
Xiaopeng Zhao,
The University of Tennessee, Knoxville, United States

Reviewed by:
Alireza Valizadeh,
Institute for Advanced Studies in Basic Sciences (IASBS), Iran
Marianna Meo,
EPD Solutions, A Philips Company, Netherlands

****Correspondence:***
Jean Faber
jean.faber@unifesp.br

Specialty section:
This article was submitted to Computational Physiology and Medicine, a section of the journal Frontiers in Physiology

Received: *15 June 2021*
Accepted: *08 October 2021*
Published: *24 November 2021*

Citation:
Shinoda L, Damasceno L, Freitas L, Campos R, Cravo S, Scorza CA, Scorza FA and Faber J (2021) Cardiac and Autonomic Dysfunctions Assessed Through Recurrence Quantitative Analysis of Electrocardiogram Signals and an Application to the 6-Hydroxydopamine Parkinson's Disease Animal Model. Front. Physiol. 12:725218. doi: 10.3389/fphys.2021.725218

INTRODUCTION

The autonomic nervous system (ANS) modulates cardiovascular function *via* two main pathways, the sympathetic (SNS) and parasympathetic (PNS) systems that play agonist-antagonist roles (Cannon, 1939). In general, SNS activation increases the heart rate and cardiac ventricle contractility, while the PNS mainly decreases heart rate, with faster local responses in the atrium transmitted *via* the vagus nerve (Hopkins and Armour, 1984; Shivkumar et al., 2016). Since autonomic balance modulates the heart rate (Sztajzel, 2004), the simplest way to analyze ANS activity is to measure heart rate variability (HRV) using ECG recordings. Traditional techniques quantify autonomic modulations searching for frequency characteristics, namely, low frequency (LF), high frequency (HF), and their ratio LF/HF ranges or temporal features, standard deviation of NN intervals (SDNN), and root mean square of successive R-R interval differences (RMSSD), on the ECG-*tachogram* along the time series constructed (most commonly) from the R-R peak time distances (RR: interbeat intervals between all successive heartbeats; NN: interbeat intervals from which artifacts have been removed) (Malliani et al., 1994; Montano et al., 2009; Akselrod et al., 2014). However, these techniques are limited and require assumptions that are difficult to verify, especially for small ECG samples, which make these quantifications unreliable (Mansier et al., 1996). Some studies have used non-linear techniques such as Poincaré Map (PM) (or First Return map) and Recurrence Quantification Analysis (RQA) to find other ANS and ECG characteristics associated with heart and ANS disorders (Kamen and Tonkin, 1995; Tulppo et al., 1997). These methods have already been applied to ANS dysfunction related to seizures and sudden death, revealing their capacity to characterize biosignals in a clinical context (Zbilut and Webber, 1992; Marwan et al., 2002; Marwan, 2003; Billeci et al., 2018; Khazaei et al., 2018).

To assess the autonomic dysfunction associated with heart rate dynamics, we propose a proof-of-concept study where we constructed a set of four artificial ECG patterns modeling the main ECG features related to the two most common autonomic-cardiac dysfunctions, atrial fibrillation (AF) and long-QT syndrome (QT), and two control ECG signals, a complete periodic regular ECG (DET) activity without noise, and an ECG pattern with high Gaussian noise (GN). The AF and long-QT syndrome patterns were chosen mainly because they are very prevalent in Parkinson's disease (PD) (Tysnes and Storstein, 2017).

Parkinson's disease is a neurodegenerative disorder characterized by decreased levels of dopamine in the *striatum* and *substantia nigra* (Stephen et al., 1988; Poewe et al., 2017). Although it is mainly characterized by motor manifestations, non-motor conditions often precede motor symptoms (Braak et al., 2003; Schapira et al., 2017). Autonomic dysfunction (AD) is diagnosed in 80% of patients with PD, and can be aggravated due to a denervation of autonomic pathways, causing orthostatic hypotension and cardiac autonomic imbalance (Orimo et al., 1999; Smit et al., 1999; Goldstein et al., 2000; Goldstein, 2006; Evatt et al., 2009; Velseboer et al., 2011; Schapira et al., 2017). In this way, finding a robust and sensitive quantitative technique that can perform a better characterization of possible electrophysiological biomarkers from ECG signals may represent a paradigm shift in the diagnosis and progression monitoring of this disease (van Dijk et al., 1993; Cersosimo and Benarroch, 2013).

Through the Poincaré map and RQA factors relative to the four artificial ECG patterns, we were able to characterize and identify the main non-linear ECG and HRV features associated with the AR and QT disorders (Rodrigues et al., 2019). We then applied the Poincaré map and RQA techniques on ECG recordings from a small set of animal models of Parkinson's disease, using the unilateral 6-hydroxydopamine (6-OHDA) model that, with lesions of the nigrostriatal pathway, produce similar motor impairments to those seen in PD and a sham group (Ungerstedt, 1968). By projecting their non-linear factors on the artificial ECG factors, we were able to compare them with the same non-linear features assessed in the ECG recordings of the PD animal models. This comparison produces a systematic protocol for better physiological interpretation and validation of these techniques considering the PD autonomic-heart dysfunction scenario.

MATERIALS AND METHODS

All experiments were approved by the Animal Care and Use Committee of the Federal University of São Paulo (protocol: CAAE 6463110417), and the analysis applied to biological signals was approved by the Ethics and Research Committee of the Federal University of São Paulo, under the protocol number CAAE 7299310719.

To study the possible effects associated with dysautonomia, we considered three different approaches: (i) PRQRST complex analysis focusing on the waveform characteristics, such as their amplitude variations; (ii) HRV analysis by evaluating the tachogram characteristics through their Poincaré Maps; and (iii) ECG signal analysis by evaluating their non-linear dynamics through RQA.

To perform the RQA analysis, we built four simple distinct artificial ECG signals (aECG), each with a predominant feature: (1) deterministic (DET), (2) atrial fibrillation (AF), (3) long QT syndrome (LQT), and (4) Gaussian noise (GN). We then calculated the low-frequency and high-frequency ratio (LF/HF) modulation from the R-R tachogram patterns of each aECG. Finally, we added white noise with different intensities to the R-R tachograms to simulate different degrees of dysautonomia most prevalent in PD.

Furthermore, we consider the application of these techniques to a set of ECG signals recorded from Wistar rats using the unilateral 6-hydroxidopamine (6-OHDA) model to mimic PD based on the Ungerstedt protocol (Ungerstedt, 1968). Two independent groups of rats were studied: the experimental group (6-OHDA, $n = 3$) and the control group (Sham, $n = 3$), which underwent the same surgical procedure as the 6-OHDA set, free of any drugs. We performed an exhaustive search in both sets of ECG signals looking for epochs where the standard ECG and HRV metrics could not distinguish 6-OHDA features from

Sham features, but RQA could. Finally, the ECG and HRV features described by the four aECG patterns, using different quantification techniques, were compared with ECG signals recorded from 6-OHDA and from sham animal models to identify similarities between 6-OHDA models with AF, LQT, DET, and GN, and establish a better signal interpretation.

Artificial Electrocardiogram Model

To correlate the information from RQA factors with PD conditions, we implement four distinct computational models of ECG (aECG), mimicking four special heart conditions that are most prevalent in PD. These artificial ECG signals were based on the McSharry model (Mcsharry et al., 2003), which in turn is based on the tachogram power spectrum and calculated from the R-R peak intervals of the aECG signals. The tachograms were built using a heart rate of 350 bpm with a standard deviation of 50 bpm to represent the standard dynamics of rat heartbeats.

By varying the low and high frequency ratio (LF/HF), the tachograms reflected the temporal distribution of the aECG complexes over time. In this way, by applying the inverse Fourier transform to the LF/HF, the power spectrum of the tachogram is extracted, and the (artificial) ECG signal is reconstructed by sequentially introducing a standard PQRST complex model. The standard PQRST complexes were adapted to fit the physiological patterns of a rat animal model (increasing HR and removing Q waves), since the standard PQRST complex was designed for human heart ECG (Mcsharry et al., 2003). Gaussian noise was added considering 1% of the amplitude of the aECG signals to describe more realistic patterns.

The aECG patterns were constructed to represent the following four conditions: (1) a regular, deterministic ECG signal (DET) without extra noise or any other effect to be used as a control; (2) atrial fibrillation ECG signal (AF), built by removing the P waves and replacing them with white noise along the PQ interval; (3) long QT syndrome (LQT), built by stretching the QT interval in time and decreasing its amplitude; and (4) a noisy ECG signal (NSE), created by introducing a high-level white noise pattern, with 100% amplitude on the DET aECG pattern. The aECGs (1) and (4) were used as control signals while the aECGs (2) and (3) were used to represent the heart dysfunction models described in the literature (Oka et al., 1997; Deguchi et al., 2002; Çanga et al., 2018). Finally, for each aECG model, four noise degrees were added to their corresponding tachograms, 0, 33, 66, and 99% of maximum amplitude, and four different modulation levels of the LF/HF ratio, given by 0, 0.5, 1, 1.5, to represent different autonomic balance effects on heart dynamics. Using the McSharry model (Mcsharry et al., 2003) we adopted:

(1) DET signal was the default model: angles θ_i (degree) [P: −70, Q: −15, R: 0, S: 15, T: 100]; a_i [P: 1.2, Q: −5, R: 30, S: −7.5, T: 0.75]; b_i [P: 0.25, Q: 0.1, R: 0.1, S:0.1, T: 0.4];
(2) LQT signal (long QT waves—it did not emulate arrythmia): θ_i [P: −70, Q: −15, R: 0, S: 15, T: 100]; a_i [P: 1.2, Q: −5, R: 30, S: −7.5, T: 0.75]; b_i [P: 0.25, Q: 0.1, R: 0.1, S: 0.1, T: 0.6];
(3) AF signal (low P-wave peak): θ_i [P: −70, Q: −15, R: 0, S: 15, T: 100]; a_i [P: 0.2, Q: −5, R: 30, S: −7.5, T: 0.75]; b_i [P: 0.125, Q: 0.1, R: 0.1, S:0.1, T: 0.4];
(4) NSE signal = (100% of gaussian noise) × DET;

Rat Electrocardiogram

Rat ECG signals were registered from a 6-hydroxydopamine (6-OHDA) animal model based on the procedure described by Ungerstedt (1968). This model is based on the degradation of dopamine neurons in the substantia nigra, mimicking the PD condition. The sham control group received the same surgical procedure, but without the addition of 6-OHDA in the brain.

We used a total of six Wistar rats, $n = 3$ 6-OHDA and $n = 3$ sham, weighing 230–300 g from the experimental animal center of the Federal University of São Paulo—UNIFESP, maintained at a temperature of 21° ± 2°C, and light and dark cycle of 12 h with free access to food and water (for more details see Rodrigues et al., 2019).

All ECG data were recorded using PowerLab 8/35 (Adinstruments, Australia) and recorded at a sampling rate of 1,000 Hz for 60 min on day 14. The process and visualization methods were performed using MATLAB™ software and a computer with 8 GB RAM, Intel® Core™ i7-6700 processor, 3.4 GHz.

To perform the analysis, all ECG signals were recorded for approximately 2 h. Due to animal movements and environmental interference, we opted for a conservative selection epoch, considering 15 window samples of 20 s sparsely (Acharya et al., 2006).

Electrocardiogram Waveform Analysis

The waveform analysis applied to the PQRST complexes was based on Quiroga Spike Sorting (Quiroga, 2012). In this technique, the main signal changes for a specific event are searched via principal component analysis (PCA) decomposition. In this approach, the PCA features correspond to the associated time window of each PQRST complex, aligned through the R-peaks as a reference, with an interval of 18 ms for both sides. If their waveforms covariate along the ECG complexes, clusters will appear, emphasizing differences and similarities.

Standard Heart Rate Variability Features

To evaluate differences in the autonomic balance activity in each ECG group, two main features of the heart rate variability (HRV) were calculated from their tachograms, namely, standard deviation of NN intervals (which are the standard deviation of normal intervals of RR, disregarding ectopic beat, known as SDNN) and root mean square of successive differences (RMSSD). The SDNN describes the autonomic balance for long periods of time, whereas RMSSD provides autonomic balance data for short periods of time (Shaffer and Ginsberg, 2017) (see **Figures 1A,B**).

Poincaré Map (First Return Map)

We also evaluated the autonomic balance using Poincaré Maps, which consists of scatter plots given by past R-R intervals (RR_{t-1}) against present R-R intervals (RR_t) (Brennan et al., 2001). Through Poincaré maps, it is possible to characterize the tachograms according to their scatter patterns (Woo et al., 1992). This is done qualitatively by studying cluster shapes and quantitatively using the deviations SD2 and SD1, which represent the major axis and the minor axis of an ellipse, respectively (see **Figure 1C**). The standard deviation

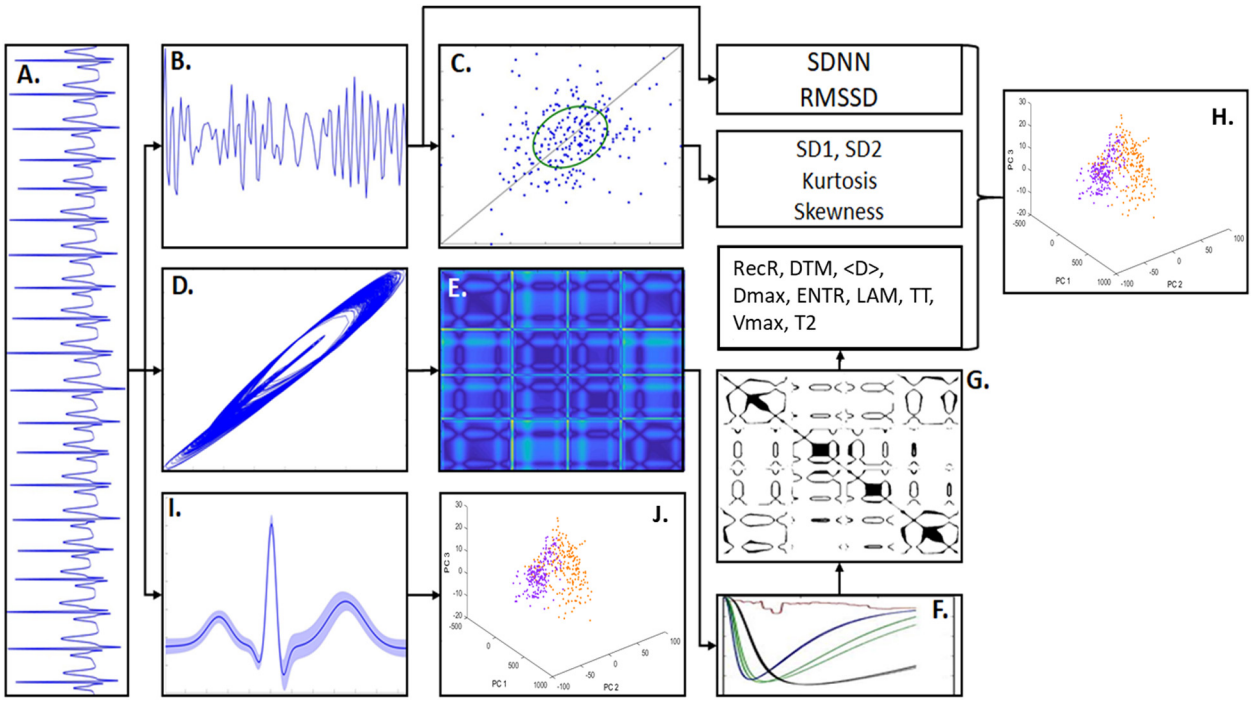

FIGURE 1 | Methodology scheme. **(A)** An example of artificial ECG pattern. By quantifying the R-R intervals from the ECG signals it was built the correspondent tachogram time-series consisted of R-R sequences. **(B)** From the ECG tachogram it was quantified two temporal features, standard deviation of n-n intervals (SDNN) and root mean square of successive differences (RMSSD) and built the Poincaré Map (PM). **(C)** The PM represents the scatter of points from the tachogram-space with the axis (RR_n, $RR_{n+\tau}$). The phase spaces of the ECG signals were also constructed, given by the coordinates (X_t, $X_{t+\tau}$, $X_{t+2\tau}$), which shows the signal trajectory seen in **(D)**. In **(E)** is shown the distance matrix, representing the Euclidian distance of each sample-point in relation to all other points in the phase-space. **(F)** Shows the recurrence quantification analysis (RQA) characteristics that allowed to select an epsilon threshold. **(G)** Shows an example of Recurrence Plot from the distance matrix given an epsilon. The RQA factors calculated in this work were: recurrence rate (RecR), determinism (DTM), mean diagonal length (<D>), maximum diagonal length (Dmax), Shannon entropy (ENTR), Trapping Time (TT), laminarity (LAM), maximum vertical length (Vmax), and time type 2 (T2). **(H)** Principal component analysis (PCA) calculated from the RQA factors highlights the differences between PD model and sham groups. **(I)** ECG waveform samples (PQRST complexes) extracted from the ECG patterns (considering its mean and SD). **(J)** PCA calculated from the ECG waveforms highlights the main differences in the signal morphology.

SD2 quantifies the point distribution across the line of identity (LOI), and the standard deviation SD1 quantifies the point distribution across the line perpendicular to the LOI. Both are directly associated with ECG beat-to-beat interval distribution (Brennan et al., 2001) and autonomic balance. SD1 is strongly correlated with LF, which represents parasympathetic modulation (Shaffer and Ginsberg, 2017).

Recurrence Quantification Analysis

To evaluate the non-linear ECG features, we applied RQA. RQA is a technique applicable to any type of time series that allows access to time series characteristics that standard techniques cannot (Eckmann et al., 1995). Through RQA coefficients, it is possible to categorize a signal according to its level of stochasticity, chaoticity, and determinism, which can help to understand the type of physical coupling under its dynamics (Marwan et al., 2002). RQA is based on signal phase-space reconstruction, defined by

$$X : X(x_0, x_1, x_2, \ \ldots \ , \ x_{\tau_{m-1}}; x_1, x_2, x_3, \ \ldots \ , \ x_m; x_0, x_1, x_2, \ \ldots \ , \ x_m) \quad (1)$$

where τ is a parameter time delay, and the dimension m is a dimensionality parameter. Any time series can be described through its phase space in a two-dimensional matrix, representing the distances from every sample point. Additionally, a threshold ε must be defined, limiting which higher values are defined as recurrences, creating a recurrence plot (RP), defined by:

$$RP\left(i,j\right) = H\left(\varepsilon - DM(i,j)\right), \ \begin{cases} H > 0 \ \Rightarrow RP\left(i,j\right) = 1 \\ H < 0 \ \Rightarrow RP\left(i,j\right) = 0 \end{cases} \quad (2)$$

where H(.) is the Heaviside step function and DM(.) is the distance matrix that contains all point-to-point Euclidian distances in the phase space (Marwan et al., 2007) (**Figures 1D,E**).

All parameters, τ and m and ε, were calculated individually for each signal, following the statistical characteristics of each one. After, using the Sturges Formula to optimize the histogram bins, the mutual information was determined (Sturges, 1926). Thus, for each signal, the chosen value of τ was the one that maximize the time-lag of 10 window samples of 20 s and that minimize the mutual information lower than 1/e (Kantz and Schreiber, 1997;

Marwan and Webber, 2015). The dimension m was calculated using the False Nearest Neighbors (FNN) technique, considering the 10 window samples with the predefined tau. Following previous studies, the chosen value of m corresponded to the first dimension that present a FNN less than 0.1 (Fraser and Swinney, 1986; Zbilut and Webber, 1992; Marwan, 2003). Finally, the value of ε is based on the maximum phase-space diameter percentage, using the Euclidian distance, as described in Marwan et al. (2007). That is, we chose heuristically ε = 9%, from an interval of 1–15% of the maximum diameter associated with the phase space, given a value of τ and m that maximized the differences between the groups of interest. Additionally, the values in $DM(i,j)$ were normalized by the maximum diameter of the phase space describing all data at the same scale (see **Figures 1F,G**).

To quantify the ECG signal recurrences, we chose nine RQA coefficients calculated on the dot structure patterns displayed by the recurrent plots (RPs) (Marwan et al., 2007). Only structures with more than three dots were considered as a proper recurrence, minimizing spurious effects. All the coefficients are based on the percentage of dots, horizontal dot-line structures, and diagonal dot-line structures on RPs, where each one provides information associated with time recurrences and trajectories according to the degree of stochasticity, chaoticity, or determinism (Zbilut and Webber, 1992; Gao, 1999; Marwan et al., 2002, 2007; Marwan, 2003). The nine coefficients used in this study are defined as follows:

Recurrence rate (RecR) quantifies the density of recurrences. This indicates the regularity of signal recurrences in the signal. Therefore, it is associated with the determinism.

$$RecR(\varepsilon, N) = \frac{1}{N^2 - N} \sum_{i \neq j=1}^{N} RP_{i,j}^{m,\varepsilon} \tag{3}$$

where ε is the threshold, N is the total number of elements in RP, and $RP_{i,j}^{m,\varepsilon}$ are the RP i,j-elements, calculated using Equation (1), according to the threshold ε and embedded in dimension m.

DTM quantifies the density of recurrence time intervals. This indicates the regularity in the signal. It is defined by:

$$DTM = \frac{\sum_{d=d_{min}}^{N} d\ P_d(d)}{\sum_{d=d_{min}}^{N} d\ RP_{i,j}} \tag{4}$$

where $P_d(.)$ is the probability of finding a diagonal with length d, calculated from a histogram, and d_{min} is the minimum acceptable distance value (defined as three dots).

The average diagonal length ($<D>$) quantifies the weighted average length of time recurrence. This indicates divergence of the space-phase trajectory; therefore, it is associated with stochasticity.

$$< D > = \frac{\sum_{d=d_{min}}^{N} d\ P_d\left(d\right)}{\sum_{d=d_{min}}^{N} P_d(d)} \tag{5}$$

The maximum diagonal length (Dmax) quantifies the maximum length of a time recurrence. When inverted, it indicates the exponential divergence of the phase-space trajectory.

$$D_{max} = \max(d) \tag{6}$$

The Shannon entropy (ENTR) quantifies the complexity of interval recurrences. This indicates the stochasticity and chaoticity of the signal:

$$ENTR = -\sum_{d=d_{min}}^{N} P_d\left(d\right) \ln P_d(d) \tag{7}$$

where $P_d(.)$ is the probability of obtaining the diagonal with length d in the diagonal length of the RP, and $ln(.)$ is the natural logarithm of $P_d\left(d\right)$.

Laminarity (LAM) quantifies the percentage of fixed events in each time interval of recurrences. Since it evaluates the relative number of laminar events, it is associated with chaoticity:

$$LAM = \frac{\sum_{v=v_{min}}^{N} vP_v(v)}{\sum_{v=1}^{N} vP_v(v)} \tag{8}$$

where v is the length of the vertical line, and v_{min} is the minimum length of the vertical line.

Trapping Time (TT) quantifies the mean value of fixed events in each time interval of recurrence. This indicates fine-scale irregularity; therefore, it is associated with determinism and stochasticity.

$$TT = \frac{\sum_{v=v_{min}}^{N} vP_v\left(v\right)}{\sum_{v=v_{min}}^{N} P_v\left(v\right)} \tag{9}$$

The maximum vertical length (Vmax) quantifies the maximum vertical length, whose meaning remains unclear, but it can be related to states with low variability, being locked at a single event:

$$V_{max} = \max(v) \tag{10}$$

Time Type Two (T2) quantifies the average time necessary for a given event to return to its origin point (arbitrarily close to ε) in the phase space. This indicates signal dispersion and, therefore, is associated with stochasticity and chaoticity.

$$T_k^{(2)} = < j_{k+1} - j_k >, \text{ with } \mathcal{R}_i = \{x_{j1}, x_{j2}, \ldots \mid R_{i,jk} = 1\},\ \forall i, j, k \tag{11}$$

Statistics

We applied the Kolmogorov-Smirnov normality test to all sample data, and because samples could not be considered from a normal distribution, non-parametric tests were used (Massey, 2017). Group differences were assessed using cluster analysis and the Kruskal-Wallis test, followed by the Tukey-Kramer *post hoc* test (Kramer, 1956). For two-sample comparisons, we used the Mann-Whitney test. A multifactorial analysis, clustergram, was applied to choose which RQA metrics would be optimal to distinguish both groups. For this analysis, the Euclidean distance was used to quantify the similarities among the RQA coefficients considering each condition (6-OHDA and sham). The significance level for all statistical analyses was established when $p < \alpha$, where α = 5%, represented in figures by the symbol "*". All analyses were performed using the MATLAB® software (v. R2016a).

Principal Components for Clustering Analysis

To highlight the global covariations and similarity effects from the different analyses (RQA on aECG and RQA on ECG animal models) considering the four different conditions LQT, AFR, NSE, and DET, when subjected to different noise levels and different LF/HF ratios, we performed a principal component analysis (PCA). For PCA, one matrix of 84 rows and 10 columns comprising four matrices of 41 rows (representing all 41 signal epochs of 60 s) and 10 columns (representing all RQA factors): one for LQT condition (41 × 10), another for AF condition (41 × 10), another for the NSE condition (41 × 10), and one for the DET condition (41 × 10), each column representing an RQA factor was measured. Therefore, these RQA factors were considered as PCA features and aECG conditions (LQT, AFR, NSE, and DET) as trial effects. This method was repeated for each noise level and LF/HF conditions (**Figure 1H**).

For all PCA spaces analyzed here, we use only the first two components, PC1 and PC2 (**Figures 1I,J**), since they were able to explain more than 80% of the data covariances (**Figure 2F** uses three PCs only for a better visualization).

Finally, all RQA data from the animal models were projected onto the RQA space previously obtained from the aECG conditions through the PCA approach. Once an ECG pattern was projected onto the aECG PCA space, the Euclidean distance was calculated considering each centroid cluster related to each aECG cluster, including the sham group.

RESULTS

To show the possible differences using traditional coefficients (such as SDRMS) and RQA, we first evaluated the dynamics associated with the four artificial ECG patterns by varying the percentage of noise on their HRV with four different LF/HF ratios. This reveals how the traditional techniques are unstable under different conjugation of noise and LF/HF imbalance. By applying RQA to these aECG signals, we were able to identify and quantify non-linear features associated with each cardio/autonomic condition. In our results, the RQA technique has shown to be more robust and sensitive for detecting autonomic dysfunction under different noises conjugated with LF/HF imbalances on the aECG signals. We were able to evaluate HRV and heart dynamics simultaneously with a better resolution across different temporal scales and under different autonomic-heart conditions.

Artificial Electrocardiogram

Figure 3A exhibits the electrographic traces related to the four aECG signals, namely, AF, LQT, DET, and NSE. From their PQRST-complexes, using R-peak as reference to centralize them, they were superposed, and then their confidence interval was calculated (**Figure 3B**). By using PCA, we were able to separate each group according to their waveform patterns (**Figure 3C**). This result suggests that their waveforms contain distinct information associated with each heart condition. However, despite this distinguishability, this technique does not provide access to the dynamics of the autonomic system.

To provide a complementary perspective on ANS dynamics, we also applied Poincaré maps to the aECGs to evaluate their behavior and their relationship to the different LF/HF ratios and noise intensities. **Figure 4A** shows how Poincaré maps of aECG conditions (*xy*-axis) vary according to their level of noise (ellipses on *z*-axis). This shows that the higher the magnitude of noise applied to the tachograms, the greater the data dispersion. **Figure 4B** shows the sensitivity of the standard HRV coefficients (SDNN, RMSSD, SD1, and SD2) under different noise levels. Once again, higher values of noise applied to tachograms yielded higher values of HRV coefficients, except for the NSE group, which exhibited a parabolic fluctuation but with indistinct values among the coefficients. **Figure 4C** shows the opposite effect, focusing on how Poincaré Maps vary, for each aECG condition (*xy*-axis) as a function of LF/HF modulations (*z*-axis). Now, the variation in LF/HF modulations produces subtle restrictions on the ellipsis-shaped limits. **Figure 4D** shows how HRV coefficients vary as a function of LF/HF modulations.

Figure 5A shows all phase-spaces associated with the aECG patterns considering different regimes of noise and HRV LF/HF ratios. LQT (blue) has lower amplitude variation than other groups, decreasing its structure size in comparison to the other groups. For almost all cases, AF and DET presented the same information, distinguishing only in their P-wave structure, which is more visible in DET than AF.

From **Figure 5B**, it is possible to see that when noise and LF/HF increase, there are more irregular diagonal dot structures on the RPs. In this regime, all four conditions (DET, LQT, AFR, and NSE) present larger and longer periods of recurrence, and still exhibit a trend. The RP vertical line structures are also influenced by noise and modulation, meaning that the ECG signals increase spurious recurrences. When the LF/HF modulation increases, the diagonal structure sizes become irregular owing to the fluctuation of the instantaneous heart rate. These changes represent irregularities in ECG events that reflect variations in HRV. Conversely, when noise increases, the periods of the diagonal structures of the RP are irregular but different from the LF/HF modulations, and the ECG events do not exhibit a trend. This reflects the irregularities of the ECG PQRST complexes, which decrease the recurrences and shorten the rectangles in RP.

Figure 5C shows four distinct clusters for almost all regimes of noise and LF/HF ratios. This means that RQA non-linear features, which represent aECG recurrence over time, are more significant than complex morphological changes in autonomic dysfunction. It is also possible to see that the increase in noise level yields an increase in the cluster size, mixing them.

Application of Recurrence Quantification Analysis to the Electrocardiogram of Parkinson's Disease Animal Models

To show the reliability of RQA to real ECG signals, we applied it to a set of ECGs recorded from animal models of PD

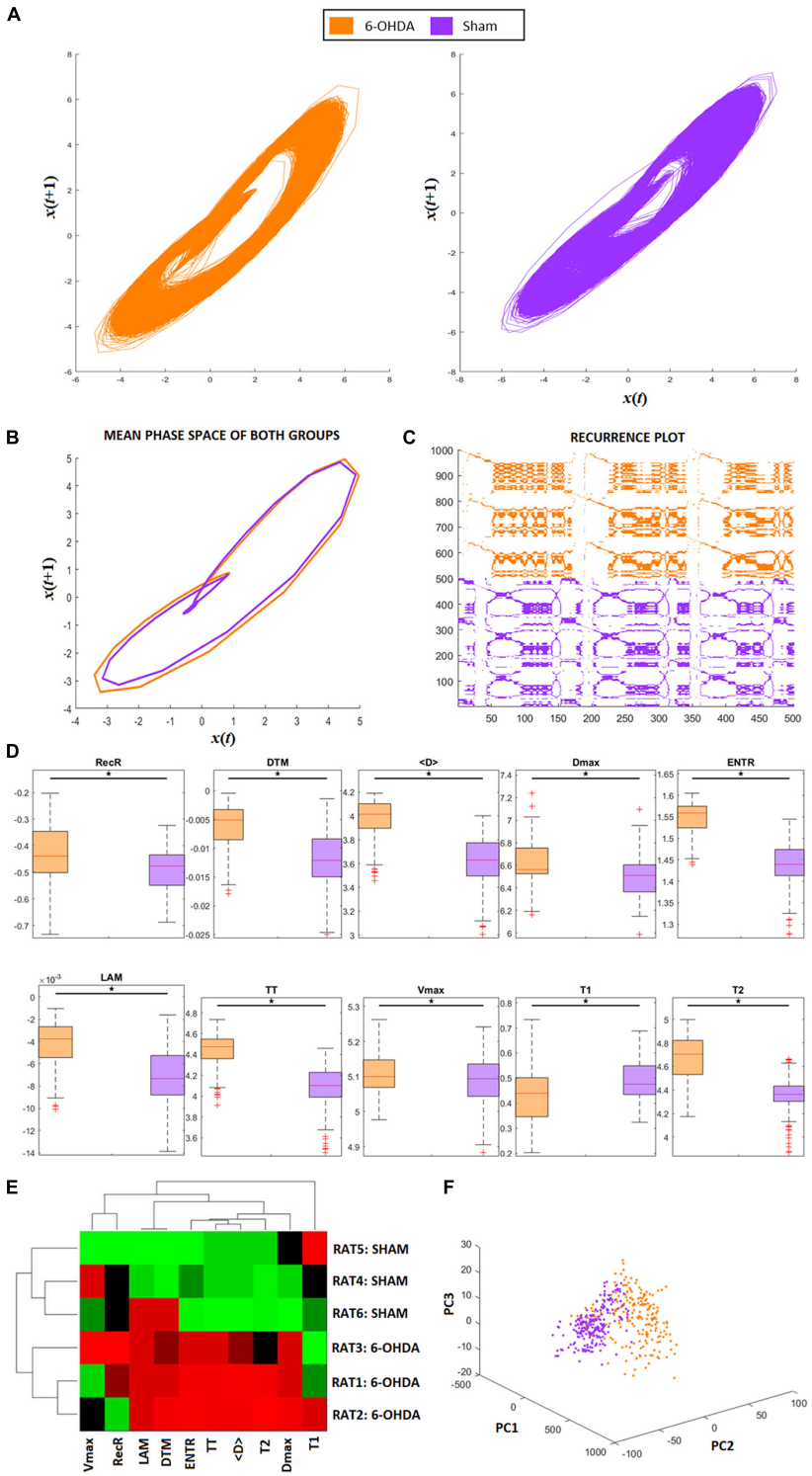

FIGURE 2 | RQA from animal model ECG recordings. **(A)** Phase space trajectories of ECG signals. **(B)** Phase-space mean trajectories related to both groups. **(C)** RP from the ECG signals of both groups. The 6-hydroxydopamine (6-OHDA) signals are more recurrent than ECG from the sham group. **(D)** Statistical comparison between each RQA factor from 6-OHDA and sham groups. All factors are revealed to be statistically different (exhibited in logarithm scale). **(E)** Clustergram of RQA factors using Euclidian distance as the metric of similarity. Each group presents its own set of RQA coefficient, forming two different clusters, 6-OHDA are rats 1–3, and sham are rats 4–6. In this case, Time type 2 (T2), Shannon entropy (ENTR), Trapping Time (TT), mean diagonal length (<D>), and maximum diagonal length (Dmax) are the main coefficients to distinguish one group from the other. **(F)** Principal Component Analysis from RQA factors also reveal that both groups differ from each other, with two distinct clusters with minimal overlap between them.

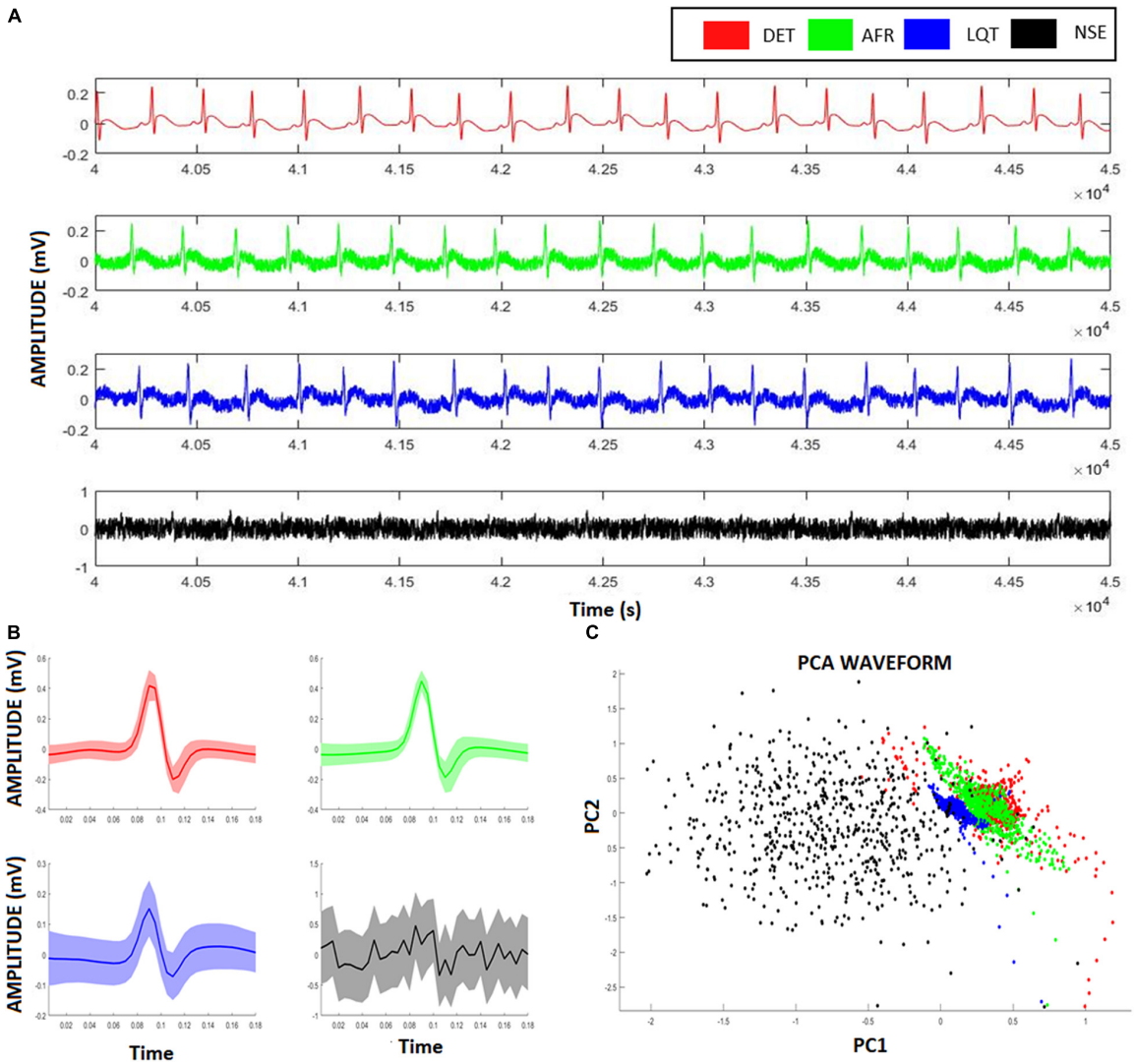

FIGURE 3 | Artificial ECG patterns. **(A)** Red signals represent the deterministic aECG, the green signal represents the atrial fibrillation (AF) pattern relative to the aECGs, the blue signal represents the long-QT (LQT) syndrome pattern relative to the aECGs, the black signal represents a deterministic aECG signal embedded of high noise (NSE). **(B)** The correspondent PQRST-complexes from each aECG model, showing their average and confidence interval. **(C)** Scatter-plot relative to the two first scores from a Principal Component Analysis (PCA) considering all four ECG-complexes shown in **(B).** Despite the clusters formed from different groups overlaps each other, it is still possible to identify and distinguish the groups from their ECG-waveforms.

(6-OHDA) and compared their non-linear features with a sham group and with the four artificial ECG signals. By comparing the RQA coefficients from the real and artificial signals, we were able to distinguish PD ECG features from sham ECG features more effectively than by using ECG waveforms and traditional HRV factors.

Figure 6A shows two representative ECG signals recorded from a 6-OHDA animal model (orange) and from a SHAM animal (lilac). **Figures 6B,C** show the ECG-complex waveforms for both groups and their PCA, respectively, highlighting the differences between ECG waveforms from the 6-OHDA and sham groups. It is possible to identify two clusters with an overlap, indicating that PCA was not able to detect statistical differences between the ECG complex shapes from 6-OHDA and SHAM groups. **Figure 6D** displays the clusters from Poincaré mapping associated with the ECG-tachograms from both groups. It shows that the 6-OHDA group has a denser cluster than Sham group, but both present a central dispersion tendency onto the identity line. This effect occurs since their window samples are presented R-R intervals do not exhibit drastic variations over time (such as arrhythmia). Their averages are mainly stationary, yielding this similarity with the main diagonal. These differences were detected through the SD1 and SD2 coefficients, and SDNN and RMSSD, which are different for both groups (**Figure 6E**). It also shows that for all HRV factors, 6-OHDA groups exhibit significant lower values, indicating that both groups are different in their HRV variability but not necessarily in their ECG complex waveforms.

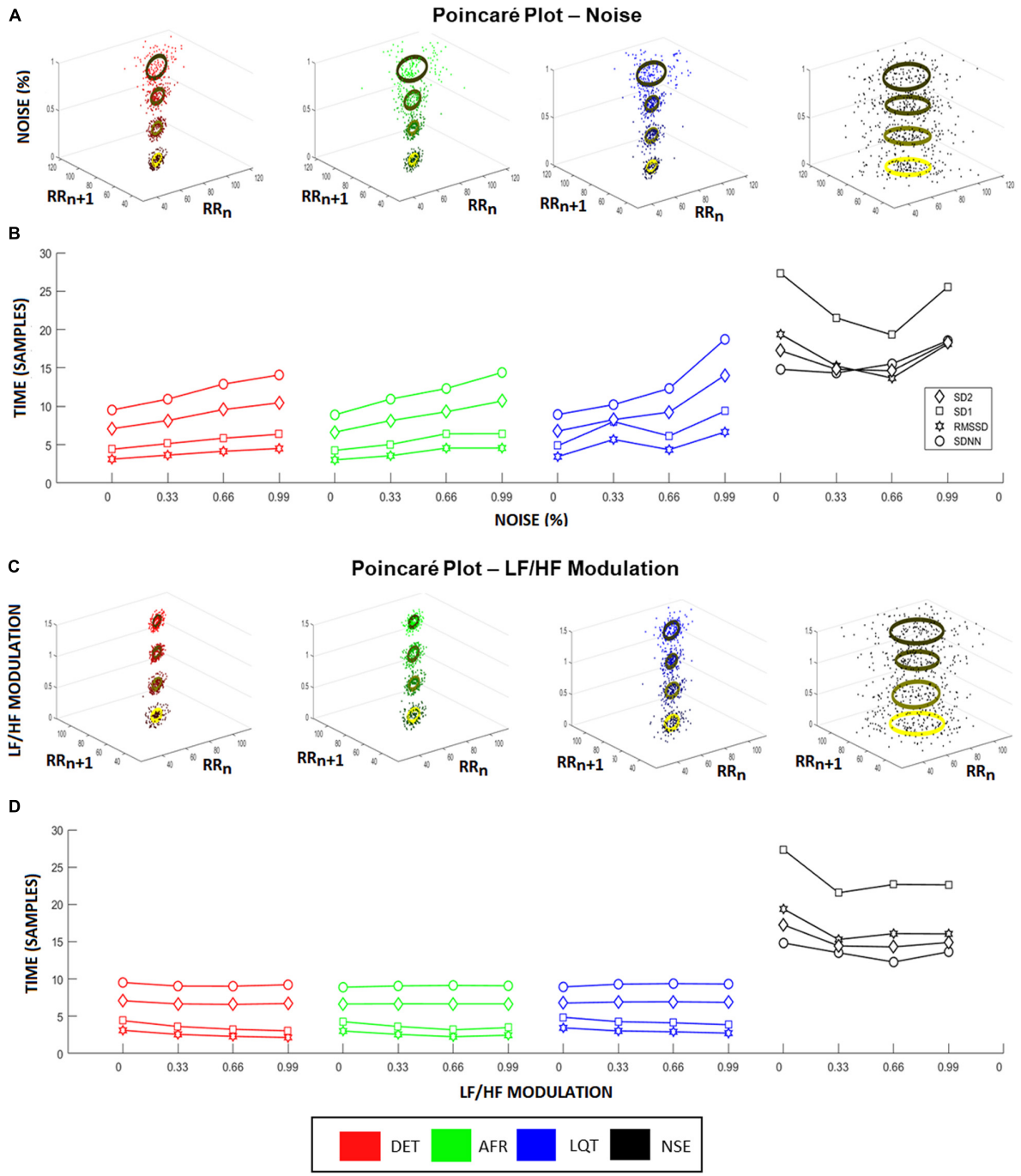

FIGURE 4 | Heart rate variability (HRV) coefficients from aECG signals. **(A)** Higher noise levels spread the Poincaré Maps, raising both, SD1 and SD2, for all groups except noisy ECG signal (NSE). This raise is highlighted in **(B)**, where it represents the changes in HRV characteristics according to different noise levels. In this situation, all coefficients raise linearly according to the increasing of noise levels, where RMSSD showed to be the more sensitive coefficient. **(C)** Changes in Poincaré plot according to LF/HF modulation is observed. In this picture, the colors represent the different intensities of LF/HF modulations. Higher LF/HF values produce higher radius values of Poincaré Map ellipses, emphasizing the differences between SD1 and SD2 coefficients for every group. **(D)** It shows the HRV coefficient values variating according to different LF/HF ratio values. Long-time coefficients, SDNN and SD2, become stable as short-time coefficients, SD1 and RMSSD, decrease their values.

For these groups, these classic HRV features were already enough to detect the effects of PD on HRV patterns. However, since we cannot properly distinguish their ECG features, the possible effects from isolated cardiac dysfunction could be masked. By applying RQA we can calculate other ECG features that highlight differences that the standard techniques cannot. As

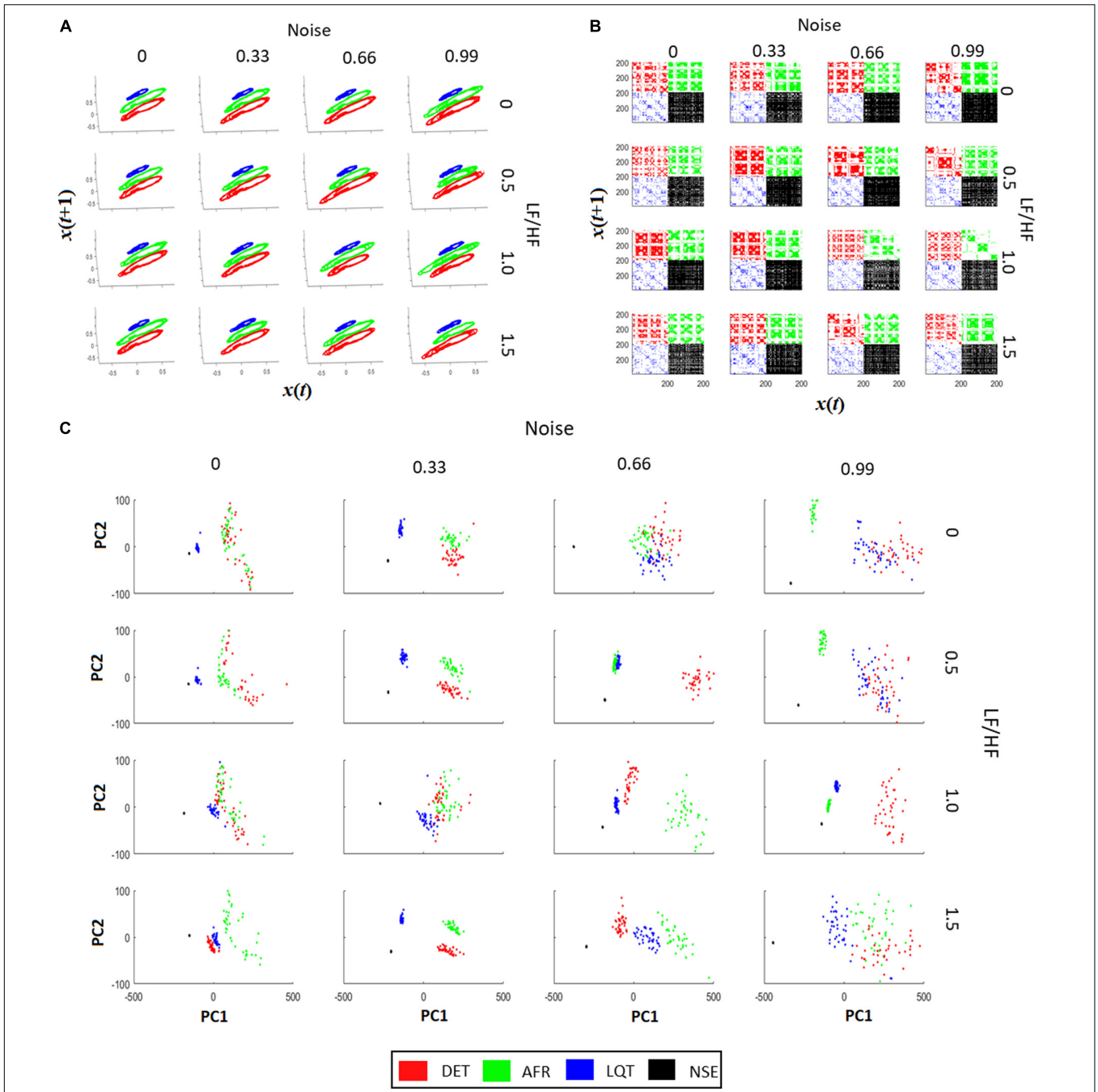

FIGURE 5 | Recurrence quantification analysis (RQA) characteristics of aECG signals. **(A)** The signal recurrences of each group in each condition. Higher values of LF/HF increase the variability of ECG in the phase-space trajectories. **(B)** Each recurrent plot (RP) of each group are different. The changes happen not only on individual dots, but also on the dot-lines and diagonal dot-structures, changing the main characteristics gather from RPs. By increasing the intensity of noise in the tachograms, it turns the RP pattern less periodic, affecting the main structures related to trajectory recurrences in RPs. The LF/HF modulation turns the dot-structures less regular, also affecting the value of dot-structures related to recurrences. **(C)** PCA projections using RQA coefficients (RR, DTM, <D>, Vmax, ENT, TT, T2) for each aECG condition. In most cases it is possible to differentiate each cluster from each group. The raise of LF/HF modulation changes the clusters from Long QT syndrome (LQT) and atrial fibrillation (AF), and the raise of noise, let the RQA features less condensed, making it more difficult to differentiate AF from LQT.

we will show, they are more sensible and robust under noise and LF/HF modulations.

Figure 2A shows the phase-space of the signal embedded dimension for both groups (6-OHDA and SHAM), highlighting their recurrences in time. It is possible to see that the SHAM group has more variance along cycles than 6-OHDA group. The mean recurrences relative to each group can be seen in **Figure 2B**. Even though the ECG recordings have complex

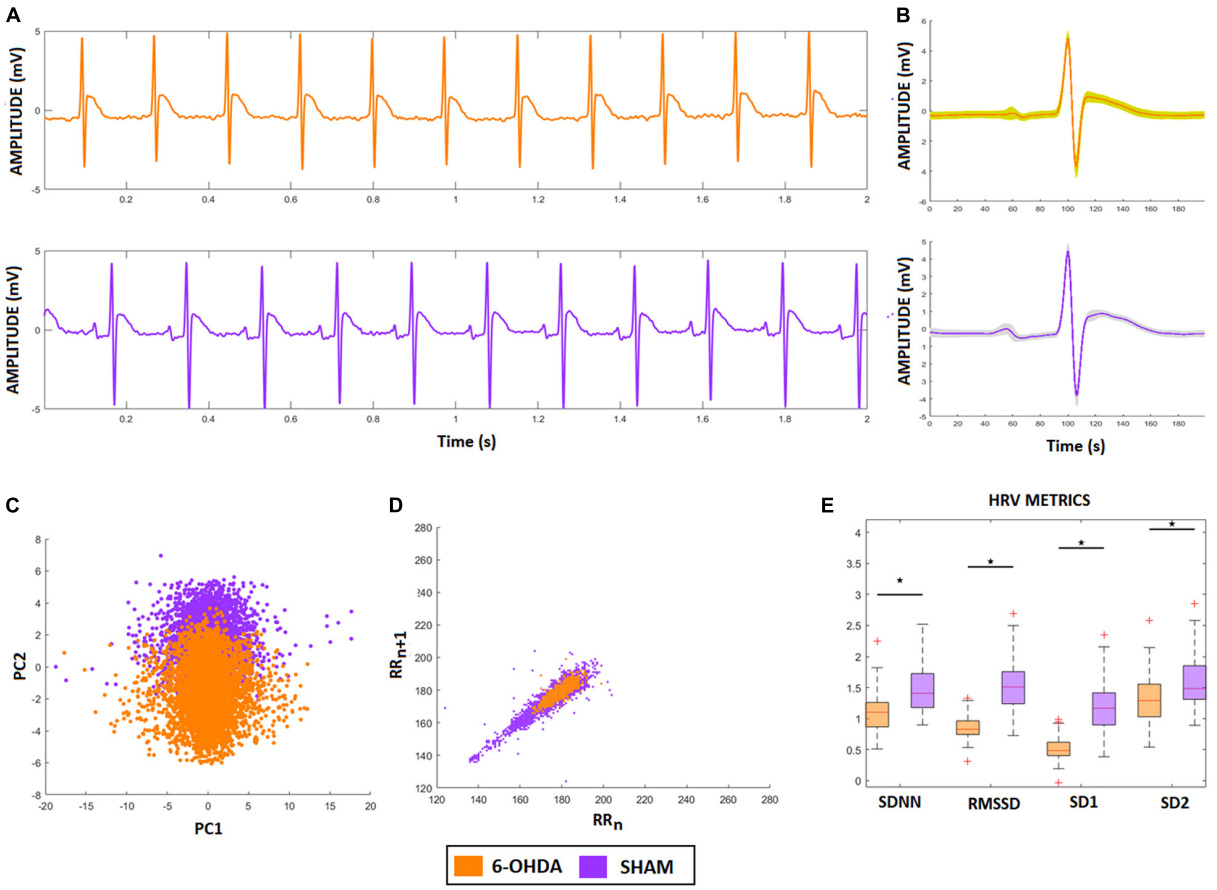

FIGURE 6 | ECG and HRV standard features from animal model. **(A)** ECG signals from both animal models, 6-OHDA in orange and Sham in lilac. **(B)** Morphologic differences of PQRST-complexes. **(C)** Principal Component Analysis of PQRST complex, it is possible to see two clusters, one in orange and one in lilac. **(D)** Poincaré plot of both ECG recordings, showing that 6-OHDA group has a denser cluster. **(E)** HRV coefficients for each group, all characteristics presented significative difference ($\rho < 0.05$), by comparing 6-OHDA with Sham groups.

morphological changes (as shown in **Figures 6A,B**), their amplitude changes do not affect the recurrences, meaning that their single event diameters in the phase-space are not different on average, with minor changes along QRS complexes. A representative RP for both groups is exhibited in **Figure 2C**, where it is shown that 6-OHDA ECG recordings are more recursive than sham ECG recordings. These recurrences are evaluated through the RP diagonal lines that reflect the recurrences of their PQRST complexes, and through the RP vertical lines that reflect large-scale temporal recurrences.

In **Figure 2D**, we can compare each RQA factor, all of which reveal significant differences between the 6-OHDA and sham groups. Except for factor T1, group 6-OHDA exhibited higher values. Considering all RQA factors, we conclude that the 6-OHDA group presents signals that are less stochastic and less chaotic than those of the sham group.

The results are presented in **Figure 2E** corroborate the statistical pairwise comparisons shown in **Figure 2D**, considering a clustergram analysis for both animal groups and all RQA factors as markers. It can be seen that seven RQA factors can distinguish both groups, in this case: LAM, DET, T2, ENTR, TT, $< D >$, and Dmax. These factors indicate that the main changes in 6-OHDA ECG signals in comparison with SHAM are more relevant in their level of periodicity (LAM, TT, T2) and in their waveforms (DET, ENTR, $< D >$, and Dmax), as shown in **Figure 2D**. That is, the 6-OHDA group PQRST complex events stay for longer periods of time in a single event than the SHAM group, and it takes more time to return to a single event. This feature can express bradycardia and lower variability in RR intervals. Furthermore, the 6-OHDA amplitude values tended to remain stable over time, with lower variability in signal amplitude.

In **Figure 2F**, we see the PCA analysis using RQA factors as PCA features. It is possible to completely distinguish 6-OHDA from the sham group using RQA factors, corroborating previous results. In contrast to **Figure 6C**, which considers only waveforms, RQA factors simultaneously capture ECG features and HRV.

These analyses show how RQA can be used to detect other statistical signal features related to comorbidities that standard techniques cannot detect, mainly under noise and LF/HF modulations.

Recurrence Quantification Analysis Cluster Analysis: Artificial Electrocardiogram vs. Electrocardiogram

To quantify possible similarities between real ECG features with aECG features, we projected the RQA factors related to 6-OHDA and sham groups onto the PCA space constructed by the four RQA factors calculated from aECG (DET, AFR, LQT, and NSE). Additionally, the Euclidean distance was calculated between each of the five centroid clusters (DET, AFR, LQT, NSE, and sham), using the 6-OHDA centroid cluster as the main reference. These metrics were chosen since we wanted only to quantify the proximal clusters, and the physiological features attributed to the aECG were simplified in comparison to the real ECG. By adopting more rigorous metrics of similarity, we were not able to evaluate the cluster correspondences.

From **Figure 7A**, it is possible to see that additional external noise on signals yields dispersion, making it difficult to distinguish which group is nearest to 6-OHDA. **Figure 7B** shows how the distance values from the 6-OHDA cluster vary according to each noise and LF/HF modulation. It can be seen that the 6-OHDA RQA factors stay nearest to the AFR for higher LF/HF values and nearest to DET for lower LF/HF values. This indicates that the 6-OHDA ECG patterns exhibit AFR features. **Figure 7C** shows the ECG recordings corresponding to the last square values shown in **Figure 7B**, with 99% noise and 1.5 of LF/HF modulation. **Figure 7D** shows the ECG recordings corresponding to the second square of **Figure 7B**, with 99% noise and 0.5 of LF/HF modulation.

DISCUSSION

In this work, we propose a proof-of-concept study showing that using only linear properties of ECG recordings may be insufficient to describe integrally cardiac-autonomic dysfunctions. Instead, we use the RQA technique that intrinsically incorporates temporal event recurrences at different time scales, which can consider heart and autonomic conditions simultaneously. Through a simplified computational model, we were able to build two cardiac/autonomic conditions (and two other controls) that commonly can be detected on the morphology of ECG-complexes and on their HRV, mainly in PD. In sequence, we calculated the standard temporal HRV factors SDNN and RMSSD, SD1, and SD2 coefficients, and applied PCA to their corresponding waveforms to search for different physiological ECG patterns. However, neither PCA nor HRV factors were able to properly distinguish the variations associated with each condition (especially, atrial fibrillation and long-QT syndrome). By varying the noise intensity and autonomic LF/HF ratio associated with their tachograms, we could compare the sensitivity and robustness of the standard HRV factors.

We verified that all HRV characteristics increased linearly as noise intensity increased (**Figure 4C**), indicating that HRV factors can be disrupted by environmental noise, outliers, or misdetections. The same effect was observed within Poincaré plots, whereas the intensity of noise increased the scattering as well (**Figure 4A**). However, even with these effects, none of the coefficients was sensitive enough to properly detect noise and LF/HF modulations. The SDNN and SD2 factors, for instance, remained stable for every LF/HF value, and RMSSD and SD1 decreased their values only slightly. These results could be due to the short term of aECG signals since they were simulated only for 5 min (Shaffer et al., 2014). However, this means that, at least, these coefficients always require long ECG recordings to operate properly.

RQA was more sensitive and robust in detecting non-linear features related to each of the four conditions expressed on their aECGs. We calculated nine RQA factors associated with the four aECG conditions: DET, AF, LQT, and NSE (**Figure 5A**). We verified that as the noise intensity increased, the RPs also increased their number of dot structures, and the number of spurious correlations increased (correlations of dot length lower than three; **Figure 5B**). We can see that the periodicity of the ECG signals is strongly modulated by the LF/HF ratio changes (**Figure 5C**). As the LF/HF ratio increases, the RPs lose vertical dot structures, indicating an increase in stochasticity (Garfinkel et al., 1997; Schauerte et al., 2001; Chen et al., 2014). It is important to mention that a healthy heart does not exhibit a purely deterministic dynamic. In fact, it presents stochasticity given by internal and external factors, and non-periodicity is reported, as chaotic dynamics, which makes the RQA a better technique to evaluate it (Braak et al., 2007; Pyatigorskaya et al., 2016; Çanga et al., 2018).

When we analyzed the RQA factors (RecR, DET, LAM, TREND, T2, ENTR, TT, $< D >$, and D_{max}) as PCA variables, we were able to explain all the covariations associated with each specific group under all different noise and HF/LF modulations (**Figure 5C**). This indicates that RQA metrics are not only more sensitive for detecting noise and autonomic modulations on short-time ECG recordings, but can also explain HRV conditions more accurately.

Application: Electrocardiogram From Animal Models of Parkinson's Disease

By applying PCA to the ECG complex waveforms recorded from animal models, we verified that they were not able to completely distinguish 6-OHDA from the SHAM groups (**Figure 7E**). This lack of difference in ECG signals gave rise to two questions: (i) Are RQA and/or Poincaré Map factors capable of differentiating each one of these conditions?, and (ii) How do HRV features influence each condition?

To answer these questions, we first analyzed different features related to heart rate variability (HRV) time series considering each ECG pattern, associated with 6-OHDA and sham groups, looking for distinct sympathetic (SNS) and parasympathetic (PNS) activities. Using Poincaré Maps and standard factors (SDNN and RMSSD), we verified that the 6-OHDA group had lower HRV coefficients than the sham group (**Figures 6D,E**). This result can also be verified through the smaller cluster of 6-OHDA group in the Poincaré map (**Figure 6D**), which comes from the low variance of R-R time sizes, which is associated with its higher average value (cluster centroid) in comparison to the SHAM group. Therefore, the 6-OHDA group had longer RR intervals,

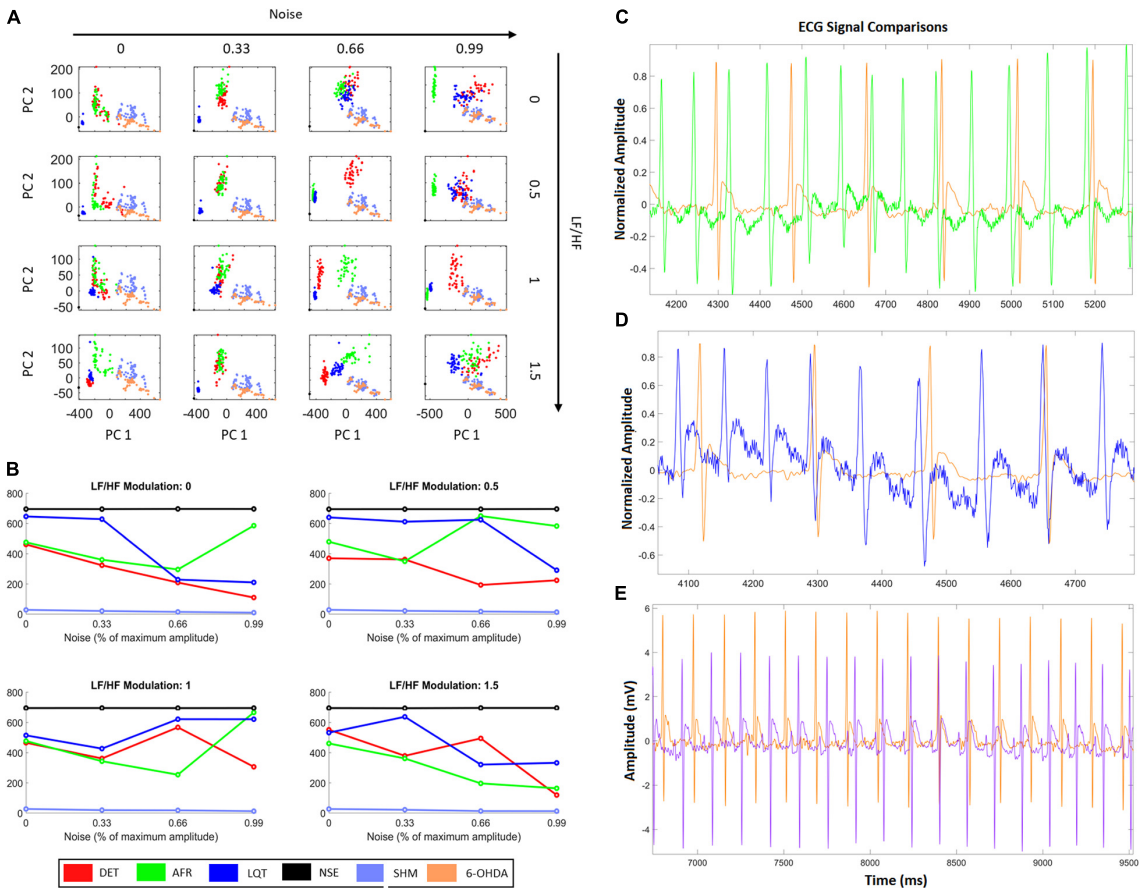

FIGURE 7 | HRV characteristics combined with RQA metrics from aECG and ECG animal models. **(A)** Projections of RQA factors calculated from the animal ECGs onto the principal components space constructed from the RQA factors calculated from the four aECG patterns. **(B)** The distances calculated from all centroid clusters in relation to the 6-OHDA centroid cluster, considering the different conditions in terms of HRV modulation and noise intensity. The closest cluster (related to real ECGs) are the cluster from DET aECG pattern for all conditions of HRV and noise. There is an alternation of the distance values, that occurs mainly for high levels of noise, where atrial fibrillation (AF) and Long-QT Syndrome (LQT) change their centroid values. It indicates that high noises in tachograms could interfere in standard metrics. **(C)** Comparison of AF to 6-OHDA for LF/HF modulation equal to 1.5 and noise equal to 99%. Both signals look similar, where their centroid cluster distances exhibit the lowest distance values. **(D)** It shows an example of LQT aECG pattern considering a noise intensity equal to 99% and LF/HF modulation equal to 0, compared with 6-OHDA ECG signal. The proximity of P-waves and T-waves suggests all signals exhibit only QRS-complexes and one bi-event defined by the union of P and T waves. **(E)** Differences between 6-OHDA and Sham ECGs.

indicating bradycardia and decreased sensitivity to fast responses to external stimuli (Pursiainen et al., 2002; Imrich et al., 2008). According to the literature, one possible explanation for this low HRV activity in PD is a lack of sympathetic activity response (Goldstein et al., 2000).

In terms of RQA, the ECG recordings from the 6-OHDA group were more recursive than the ECG signal from the sham group, since its RecR and DTM factors were higher than those of the sham group. This result indicates that the 6-OHDA group had a lower ECG amplitude variability over time, with more recurrent events. This can be checked through its phase space (**Figure 2A**) and Poincaré map (**Figure 6D**). These effects could be physiologically interpreted mainly by: (*i*) low concentrations of Ca^{+2} in conductive heart cells (Kramer, 1956); (*ii*) myocardial changes that lead to atrial fibrillation and yield a periodicity increase of specific events along the ECG signals (Hong et al., 2019); and (iii) heart sympathetic denervation, which decreases HRV and produces regular and periodic ECG (Orimo et al., 1999; Goldstein et al., 2000).

The higher values of $< D >$ in 6-OHDA ECGs compared with sham indicates that their signals present higher self-similarity, which is also revealed by their event periodicities. This RQA factor indicates that the ECG signals have small perturbations across time, with one major divergence found in the QRS complex. Additionally, higher values of Dmax, TT, LAM, and T2 in 6-OHDA signals compared to sham signals indicate that their ECG events are more recurrent over time. That is, given an ECG-reference, such as R-pick, the way it appears along the signal in time is more regular and similar to the previous ones. While Dmax and LAM coefficients exhibit a more deterministic dynamic, hinting at a low autonomic modulation (in both the PNS and SNS branches), TT and T2 coefficients indicate that ECG events are more alike and longer. Long events come from low amplitude changes and represent more "rigid R-R intervals," corroborating Poincaré maps (Marwan et al., 2002; Marwan, 2003, 2006). Furthermore, a decrease in heart rate tends to increase the periodicity of the signal, which can be promoted by PD bradycardia (Buob et al., 2010).

Higher values of ENTR indicate that the system itself has some variation in amplitude and is more complex. In this way, the values of ENTR for 6-OHDA ECG recordings are the first indication of greater chaoticity than those of sham signals, in the sense that they have some physical constraints that modulate its activity. This chaoticity is also justified by considering the values of Dmax and TT of 6-OHDA (Wolf et al., 1991; Shibata et al., 2009). One possible origin of this physical constraint is the potential fluctuations due to atrial fibrillation (AF), caused by the decomposition of P-waves into many short waves (Goldstein, 2006).

The coefficients Vmax and T1, despite presenting a significant difference, did not help to discriminate the PD condition, using 6-OHDA models, from sham as revealed by the Clustergram analysis (**Figure 2E**). Using the seven RQA factors indicated by the Clustergram ($< D >$, D_{max} ENTR, TT, LAM, DTM, and T2) as PCA features, this result can be corroborated. Furthermore, **Figure 2F** shows that by using the factors, the differences between both groups are optimized and clarified, indicating once again that RQA coefficients explain the variations between both groups.

Considering all RQA coefficients together, we can conclude that ECG signals from 6-OHDA animal models exhibit higher irregularity in their morphology over time, including higher variation in its amplitude, but lower variation in its R-R intervals. This result is probably a consequence of the effect of Parkinson's disease on autonomic control, which promotes a self-paced rhythm with a strong interference of the parasympathetic path that decreases HRV (Shaffer and Ginsberg, 2017). This excessive regularity makes the heart less flexible to changes, which may be one of the causes of orthostatic hypotension (Smit et al., 1999; Velseboer et al., 2011). Although RQA exhibited pairwise statistical differences, when applied to 6-OHDA and SHAM groups, it was still missing a proper physiological interpretation associated with a more global and integrated analysis of these factors, mainly for specific heart and autonomic conditions related to PD, such as atrial fibrillation and long Q-T.

Finally, we projected all RQA factors calculated from the ECG animal models, 6-OHDA and SHAM, onto the RQA PCA space calculated from the four artificial ECG conditions (DET, AF, LQT, and NS). With these projections, we quantify which of the four artificial conditions the 6-OHDA group would statistically resemble. In this way, by evaluating the centroid distances from each aECG condition to the 6-OHDA conditions, we saw that the sham cluster was the nearest group and the NSE cluster was the furthest. Furthermore, for high noise intensity (0.99), independent of the autonomic frequency ratio, the DET and AF clusters were the closest clusters. This result is expected because aECG models are limited and real ECG signals have complex components (beyond noise and modulation) that differentiate both from all aECG patterns.

Nevertheless, by looking at AF and LQT clusters (green and blue), we see how their distances to 6-OHDA vary according to different noise levels and autonomic modulations. For all LF/HF ratios, the LQT clusters became closer to 6-OHDA for a higher level of noise. This effect can occur because of the addition of noise to the aECG tachograms, which may superpose T- and P-waves, as shown in **Figures 5A**, **6C–E**. Conversely, AF clusters are closer to the 6-OHDA clusters for high values of LF/HF modulation. This can be seen by comparing their ECG morphologies, as shown in **Figures 6C–E**. Both signals, aECG AF and ECG 6-OHDA, present no P-waves. This increases the R-R intervals, which are expressed by the large vertical lines in their RP (**Figures 4B**, **6C**).

Although the metrics and model features under this quantification were simplified (for human beings all parameters used to construct the aECG must be readjusted), these results suggest that 6-OHDA signals could be correlated with AF signals, indicating a possible tendency of this pathology in PD (van Dijk et al., 1993; Velseboer et al., 2011). Additionally, these results also suggest that LF/HF modulation could lead to misinterpretations due to changes in the morphology of ECG signals, making it difficult to distinguish all groups from low noise values. The main differences between groups were found for intermediate values of LF/HF modulation, where the main changes in all groups occurred, making it easier to pinpoint the cluster condition closest to the 6-OHDA group. A previous study has already indicated that AF is possibly related to autonomic imbalance, especially when one of the branches is highly activated in relation to others (Marwan, 2003).

It is important to note that the addition of noise in the aECG tachograms may modify their aECG morphologies, which may be a limitation of the model. Furthermore, any alteration of heart calcium flux may also lead to an alteration in the myocardial dynamics itself (Ren et al., 2004). These changes also affect heart waveform dynamics, thereby promoting a possible misinterpretation of HRV factors. Therefore, despite showing that RQA factors are more sensitive to ECG and tachogram dynamics, it is still necessary to know if there are well-defined signatures associated with ECG changes caused by a lack of autonomic modulation or by a lack of myocardial response. Both causes can be interpreted as dysautonomia, and the source of the autonomic imbalance (Shibata et al., 2009; Buob et al., 2010) is not obvious from the ECG. However, we emphasize that this issue is a general limitation for HRV analysis that uses only ECG signals, and through RQA factors, it is possible to assess not only "static pictures" of the ECG signals or global coefficients (as averages and deviations along time) but also a reflection of the recurrences and periodicities of the signals (Shaffer and Ginsberg, 2017).

In summary, the artificial ECG patterns associated with RQA factors can be a new approach to help understanding the complex dynamics found in real ECGs. Here, despite the simplifications, the RQA factors suggested that the 6-OHDA group can present atrial fibrillation (AF) mainly for high values of LF/HF ratios. It also pointed out that 6-OHDA ECG recordings exhibit high variations in baseline and temporal regular events. These features have been associated with reduced cerebral blood flow and, recently, a high risk of sudden death from epilepsy (Billeci et al., 2018; Khazaei et al., 2018).

This proof-of-concept study indicates that by applying RQA technique on ECG signals from PD of animal models, they present lower variability in periodicity (RR intervals) but higher complexity in their baseline (amplitude). This means that the 6-OHDA ECG signals exhibit more deterministic event intervals but more stochastic traces. Most likely, these characteristics

suggest a lack of autonomic modulation. We interpret it as an "uncalibrated ANS" where both branches work together, but the relationship between them is no longer cooperative, producing an unbalanced heart dynamic. Although the application study was limited due to the small animal samples, we believe this work opens a new direction for the application of RQA to ECG signals. RQA is a very promising technique to advance new studies of heart-brain dynamics to elucidate other heart or autonomic changes in PD patients.

DATA AVAILABILITY STATEMENT

The raw data supporting the conclusions of this article will be made available by the authors, without undue reservation. Requests should be made to to jean.faber@unifesp.br.

ETHICS STATEMENT

All the experiments were approved by the Animal Care and Use Committee of Ethics of the Federal University of São Paulo (protocol: CAAE 6463110417), and the analysis applied on biological signals were approved by the Ethics and Research Committee of the Federal University of São Paulo, under the protocol number: CAAE 7299310719.

AUTHOR CONTRIBUTIONS

LS, LD, LF, FS, and JF contributed to investigation. LS, SC, and JF contributed to methodology. SC, CS, and FS contributed to conceptualization. LS contributed to data curation, formal analysis, and visualization. FS and JF contributed to validation, project administration, supervision, and contributed to funding acquisition. LD and LF contributed to resources. LS and JF contributed to software. LS and RC contributed to writing—original draft preparation. LS, LD, LF, RC, CS, FS, and JF contributed to writing—review. All authors contributed to the article and approved the submitted version.

FUNDING

This study was financed in part by the Coordenação de Aperfeiçoamento de Pessoal de Nível Superior - Brasil (CAPES) - Finance Code 001 and by Conselho Nacional de Desenvolvimento Científico e Tecnológico (CNPq), No. 442563-2016/7.

ACKNOWLEDGMENTS

We would like to thank Esper Cavalheiro for reviewing the manuscript.

REFERENCES

Acharya, U. R., Joseph, K. P., Kannathal, N., Lim, C. M., and Suri, J. S. (2006). Heart rate variability: a review. *Med. Biol. Eng. Comp.* 44, 1031–1051.

Akselrod, S., Gordon, D., Ubel, F., Shannon, D., Berger, A., and Cohen, R. (2014). Power spectrum analysis of heart rate fluctuation: a quantitative probe of beat-to-beat cardiovascular control. *Science* 213, 220–222.

Billeci, L., Marino, D., Insana, L., Vatti, G., and Varanini, M. (2018). Patient-specific seizure prediction based on heart rate variability and recurrence quantification analysis. *PLoS One* 13:e0204339. doi: 10.1371/journal.pone.0204339

Braak, H., del Tredici, K., Rüb, U., de Vos, R. A. I., Jansen Steur, E. N. H., and Braak, E. (2003). Staging of brain pathology related to sporadic Parkinson's disease. *Neurobiol. Aging* 24, 197–211. doi: 10.1016/S0197-4580(02)00065-9

Braak, H., Sastre, M., Bohl, J. R. E., Vos, R. A. I., and del Tredici, K. (2007). Parkinson's disease: lesions in dorsal horn layer I, involvement of parasympathetic and sympathetic pre- and postganglionic neurons. *Acta Neuropathol.* 113, 421–429. doi: 10.1007/s00401-007-0193-x

Brennan, M., Palaniswami, M., and Kamen, P. (2001). Do existing measures of Poincareé plot geometry reflect nonlinear features of heart rate variability? *IEEE Trans. Biomed. Eng.* 48, 1342–1347. doi: 10.1109/10.959330

Buob, A., Winter, H., Kindermann, M., Becker, G., Möller, J. C., Oertel, W. H., et al. (2010). Parasympathetic but not sympathetic cardiac dysfunction at early stages of Parkinson's disease. *Clin. Res. Cardiol.* 99, 701–706. doi: 10.1007/s00392-010-0170-6

Çanga, Y., Emre, A., Yüksel, G. A., Karataş, M. B., Yelgeç, N. S., Gürkan, U., et al. (2018). Assessment of atrial conduction times in patients with newly diagnosed Parkinson's disease. *Parkinson's Dis.* 2018:2916905. doi: 10.1155/2018/2916905

Cannon, W. B. (1939). *The Wisdom of the Body*. New York, NY: W.W. Norton & Company, Inc.

Cersosimo, M. G., and Benarroch, E. E. (2013). Central control of autonomic function and involvement in neurodegenerative disorders. *Handb. Clin. Neurol.* 117, 45–57. doi: 10.1016/B978-0-444-53491-0.00005-5

Chen, P. S., Chen, L. S., Fishbein, M. C., Lin, S. F., and Nattel, S. (2014). Role of the autonomic nervous system in atrial fibrillation: pathophysiology and therapy. *Circulation Res.* 114, 1500–1515. doi: 10.1161/CIRCRESAHA.114.303772

Deguchi, K., Sasaki, I., Tsukaguchi, M., Kamoda, M., Touge, T., Takeuchi, H., et al. (2002). Abnormalities of rate-corrected QT intervals in Parkinson's disease - a comparison with multiple system atrophy and progressive supranuclear palsy. *J. Neurol. Sci.* 199, 31–37. doi: 10.1016/S0022-510X(02)00079-5

Eckmann, J. P., Oliffson Kamphorst, O., and Ruelle, D. (1995). Recurrence plots of dynamical systems. *World Sci. Ser. Nonlinear Sci. Series A* 16, 441–446. doi: 10.1209/0295-5075/4/9/004

Evatt, M. L., Chaudhuri, K. R., Chou, K. L., Cubo, E., Hinson, V., Kompoliti, K., et al. (2009). Dysautonomia rating scales in Parkinson's disease: *Sialorrhea, dysphagia*, and constipation - Critique and recommendations by movement disorders task force on rating scales for Parkinson's disease. *Movement Disorders* 24, 635–646. doi: 10.1002/mds.22260

Fraser, A. M., and Swinney, H. L. (1986). Independent coordinates for strange attractors from mutual information. *Phys. Rev. A* 33, 1134–1140.

Gao, J. B. (1999). Recurrence time statistics for chaotic systems and their applications. *Phys. Rev. Lett.* 83, 3178–3181. doi: 10.1103/PhysRevLett.83.3178

Garfinkel, A., Chen, P. S., Walter, D. O., Karagueuzian, H. S., Kogan, B., Evans, S. J., et al. (1997). Quasiperiodicity and chaos in cardiac fibrillation. *J. Clin. Invest.* 99, 305–314. doi: 10.1172/JCI119159

Goldstein, D. S. (2006). Orthostatic hypotension as an early finding in Parkinson's disease. *Clin. Autonomic Res.* 16, 46–54. doi: 10.1007/s10286-006-0317-8

Goldstein, D. S., Holmes, C., Li, S.-T., Bruce, S., and Verhagen Metman, L. (2000). Cardiac sympathetic denervation in Parkinson's disease background: in Parkinson's disease, orthostatic hypotension can. *Ann. Int. Med.* 133, 338–347.

Hong, C. T., Chan, L., Wu, D., Chen, W. T., and Chien, L. N. (2019). Association between Parkinson's disease and atrial fibrillation: a population-based study. *Front. Neurol.* 10:22. doi: 10.3389/fneur.2019.00022

Hopkins, D. A., and Armour, J. A. (1984). Localization of sympathetic postganglionic and parasympathetic preganglionic neurons which innervate different regions of the dog heart. *J. Comp. Neurol.* 229, 186–198.

Imrich, R., Eldadah, B. A., Bentho, O., Pechnik, S., Sharabi, Y., Holmes, C., et al. (2008). Attenuated pre-ejection period response to tyramine in patients with cardiac sympathetic denervation. *Ann. N. Y. Acad. Sci.* 1148, 486–489. doi: 10.1196/annals.1410.066

Kamen, P. W., and Tonkin, A. M. (1995). Application of the Poincaré plot to heart rate variability: a new measure of functional status in heart failure. *Australian New Zealand J. Med.* 25, 18–26. doi: 10.1111/j.1445-5994.1995.tb00573.x

Kantz, H., and Schreiber, T. (1997). *Nonlinear Time Series Analysis*. Cambridge: University Press.

Khazaei, M., Raeisi, K., Goshvarpour, A., and Ahmadzadeh, M. (2018). Early detection of sudden cardiac death using nonlinear analysis of heart rate variability. *Biocybernetics Biomed. Eng.* 38, 931–940. doi: 10.1016/j.bbe.2018.06.003

Kramer, C. Y. (1956). Extension of multiple range tests to group means with unequal numbers of replications. *Biometrics* 12, 307–310.

Malliani, A., Lombardi, F., and Pagani, M. (1994). Power spectrum analysis of heart rate variability: a tool to explore neural regulatory mechanisms. *Br. Heart J.* 71:1.

Mansier, P., Clairambault, J., Charlotte, N., Médigue, C., Vermeiren, C., LePape, G., et al. (1996). Linear and non-linear analyses of heart rate variability: a minireview. *Cardiovas. Res.* 31, 371–379. doi: 10.1016/0008-6363(96)00009-0

Marwan, N. (2003). *Encounters with Neighbours: Current Developments of Concepts Based on Recurrence Plots and their Applications*. PhD thesis, Potsdam: Institute for Physics, University of Potsdam.

Marwan, N. (2006). *Encouters with Neighbours - Current Developments of Concepts Based on Recurrence Plots and their Applications*. Dissertation thesis, Potsdam: Institute for Physics, University of Potsdam.

Marwan, N., Carmen Romano, M., Thiel, M., and Kurths, J. (2007). Recurrence plots for the analysis of complex systems. *Phys. Rep.* 438, 237–329. doi: 10.1016/j.physrep.2006.11.001

Marwan, N., and Webber, C. L. (2015). *Recurrence Quantification Analysis: Theory and Best Practices*. London: Springer.

Marwan, N., Wessel, N., Meyerfeldt, U., Schirdewan, A., and Kurths, J. (2002). Recurrence-plot-based measures of complexity and their application to heart-rate-variability data. *Phys. Rev. E - Statist. Phys. Plasmas Fluids Related Interdisciplinary Top.* 66, 1–16. doi: 10.1103/PhysRevE.66.026702

Massey, F. J. Jr. (2017). The kolmogorov-smirnov test for goodness of fit. *J. Am. Stat. Assoc.* 46, 68–78.

Mcsharry, P. E., Clifford, G. D., Tarassenko, L., and Smith, L. A. (2003). Electrocardiogram Signals. *IEEE Trans. Biomed. Eng.* 50, 289–294. doi: 10.1109/TBME.2003.808805

Montano, N., Porta, A., Cogliati, C., Costantino, G., Tobaldini, E., Casali, K. R., et al. (2009). Heart rate variability explored in the frequency domain: a tool to investigate the link between heart and behavior. *Neurosci. Biobehav. Rev.* 33, 71–80. doi: 10.1016/j.neubiorev.2008.07.006

Oka, H., Mochio, S., Sato, H., and Katayama, K. (1997). Prolongation of QTc interval in patients with parkinson's disease. *Eur. Neurol.* 37, 186–189. doi: 10.1159/000117432

Orimo, S., Ozawa, E., Nakade, S., Sugimoto, T., and Mizusawa, H. (1999). I-metaiodobenzylguanidine myocardial scintigraphy in Parkinson ' s disease. *J. Neurol. Neurosurg. Psychiatry* 67, 189–194.

Poewe, W., Seppi, K., Tanner, C. M., Halliday, G. M., Brundin, P., Volkmann, J., et al. (2017). Parkinson's disease. *Nat. Rev. Dis. Primers* 3:17013. doi: 10.1038/nrdp.2017.13

Pursiainen, V., Haapaniemi, T. H., Korpelainen, J. T., Huikuri, H. V., Sotaniemi, K. A., and Myllylä, V. (2002). Circadian heart rate variability in Parkinson's disease. *J. Neurol.* 249, 1535–1540. doi: 10.1007/s00415-002-0884-0

Pyatigorskaya, N., Mongin, M., Valabregue, R., Yahia-Cherif, L., Ewenczyk, C., Poupon, C., et al. (2016). Medulla oblongata damage and cardiac autonomic dysfunction in Parkinson's disease. *Neurology* 87, 2540–2545.

Quiroga, R. Q. (2012). Spike sorting. *Curr. Biol.* 22, R45–R46. doi: 10.1002/9781118628522.ch8

Ren, J., Porter, J. E., Wold, L. E., Aberle, N. S., Muralikrishnan, D., and Haselton, J. R. (2004). Depressed contractile function and adrenergic responsiveness of cardiac myocytes in an experimental model of Parkinson's disease, the MPTP-treated mouse. *Neurobiol. Aging* 25, 131–138. doi: 10.1016/S0197-4580(03)00035-6

Rodrigues, L. D., Oliveira, L. F., Shinoda, L., Scorza, C. A., Faber, J., Ferraz, H. B., et al. (2019). Cardiovascular alterations in rats with Parkinsonism induced by 6-OHDA and treated with Domperidone. *Sci. Rep.* 9:8965.

Schapira, A. H. V., Chaudhuri, K. R., and Jenner, P. (2017). Non-motor features of Parkinson's disease. *Nat. Rev. Neurosci.* 18, 435–450. doi: 10.1038/nrn.2017.62

Schauerte, P., Scherlag, B. J., Patterson, E., Scherlag, M. A., Matsudaria, K., Nakagawa, H., et al. (2001). Focal atrial fibrillation: experimental evidence for a pathophysiologic role of the autonomic nervous system. *J. Cardiovas. Electrophysiol.* 12, 592–599. doi: 10.1046/j.1540-8167.2001.00592.x

Shaffer, F., and Ginsberg, J. P. (2017). An overview of heart rate variability metrics and norms. *Front. Public Health* 5:258. doi: 10.3389/fpubh.2017.00258

Shaffer, F., McCraty, R., and Zerr, C. L. (2014). A healthy heart is not a metronome: an integrative review of the heart's anatomy and heart rate variability. *Front. Psychol.* 5:1040. doi: 10.3389/fpsyg.2014.01040

Shibata, M., Morita, Y., Shimizu, T., Takahashi, K., and Suzuki, N. (2009). Cardiac parasympathetic dysfunction concurrent with cardiac sympathetic denervation in Parkinson's disease. *J. Neurol. Sci.* 276, 79–83. doi: 10.1016/j.jns.2008.09.005

Shivkumar, K., Ajijola, O. A., Anand, I., Armour, J. A., Chen, P. S., Esler, M., et al. (2016). Clinical neurocardiology defining the value of neuroscience-based cardiovascular therapeutics. *J. Physiol.* 594, 3911–3954. doi: 10.1113/JP271870

Smit, A. A. J., Wieling, W., Opfer-Gehrking, T. L., van Emmerik-Levelt, H. M., and Low, P. A. (1999). Patients' choice of portable folding chairs to reduce symptoms of orthostatic hypotension. *Clin. Autonomic Res.* 9, 341–344. doi: 10.1007/BF02318381

Stephen, J. K., Kathleen, S., and Oleh, H. (1988). Uneven pattern of dopamine loss in the striatum of patients with idiopathic Parkinson's disease. *New England J. Med.* 318, 876–880.

Sturges, H. A. (1926). The choice of a class interval. *J. Am. Statist. Assoc.* 21, 65–66.

Sztajzel, J. (2004). Heart rate variability: a noninvasive electrocardiographic method to measure the autonomic nervous system. *Swiss Med. Weekly* 134, 514–522. doi: 10.1006/pupt.2000.0250

Tulppo, M. P., Mäkikallio, T. H., Seppänen, T., Laukkanen, R. T., and Huikuri, H. V. (1997). Vagal modulation of heart rate during exercise: effects of age and physical fitness. *Scand. Cardiovas. J. Suppl.* 31:12.

Tysnes, O. B., and Storstein, A. (2017). Epidemiology of Parkinson's disease. *J. Neural Transm. (Vienna)* 124, 901–905. doi: 10.1007/s00702-017-1686-y

Ungerstedt, U. (1968). 6-Hydroxy-Dopamine induced degeneration of central monoamine neurons. *Eur. J. Pharmacol.* 5, 107–110. doi: 10.1016/0014-2999(68)90164-7

van Dijk, J. G., Haan, J., Zwinderman, K., Kremer, B., van Hilten, B. J., and Roos, R. A. C. (1993). Autonomic nervous system dysfunction in Parkinson's disease: relationships with age, medication, duration, and severity. *J. Neurol. Neurosurg. Psychiatry* 56, 1090–1095. doi: 10.1136/jnnp.56.10.1090

Velseboer, D. C., de Haan, R. J., Wieling, W., Goldstein, D. S., and de Bie, R. M. A. (2011). Prevalence of orthostatic hypotension in Parkinson's disease: a systematic review and meta-analysis. *Parkinsonism Related Disorders* 17, 724–729. doi: 10.1016/j.parkreldis.2011.04.016

Wolf, P. A., Abbott, R. D., and Kannel, W. B. (1991). Atrial fibrillation as an independent risk factor for stroke: the framingham study. *Stroke* 22, 983–988. doi: 10.1161/01.STR.22.8.983

Woo, M. A., Stevenson, W. G., Moser, D. K., Trelease, R. B., and Harper, R. M. (1992). Patterns of beat-to-beat heart rate variability in advanced heart failure. *Am. Heart J.* 123, 704–710. doi: 10.1016/0002-8703(92)90510-3

Zbilut, J. P., and Webber, C. L. (1992). Embeddings and delays as derived from quantification of recurrence plots. *Phys. Lett. A* 171, 199–203. doi: 10.1016/0375-9601(92)90426-M

Conflict of Interest: The authors declare that the research was conducted in the absence of any commercial or financial relationships that could be construed as a potential conflict of interest.

frontiers in Physiology

ORIGINAL RESEARCH
published: 14 December 2021
doi: 10.3389/fphys.2021.753282

Machine Learning Prediction of Cardiac Resynchronisation Therapy Response From Combination of Clinical and Model-Driven Data

*Svyatoslav Khamzin[1], Arsenii Dokuchaev[1], Anastasia Bazhutina[1,2], Tatiana Chumarnaya[1], Stepan Zubarev[3], Tamara Lyubimtseva[3], Viktoria Lebedeva[3], Dmitry Lebedev[3], Viatcheslav Gurev[4] and Olga Solovyova[1,2]**

[1] Institute of Immunology and Physiology Ural Branch of the Russian Academy of Sciences, Yekaterinburg, Russia, [2] Ural Federal University, Yekaterinburg, Russia, [3] Almazov National Medical Research Centre, Saint Petersburg, Russia, [4] IBM Research, Yorktown, NY, United States

OPEN ACCESS

Edited by:
Hans Dierckx,
KU Leuven Kulak, Belgium

Reviewed by:
Steven Pogwizd,
University of Alabama at Birmingham, United States
Jan Christoph,
University of California, San Francisco, United States

***Correspondence:**
Olga Solovyova
o.solovyova@iip.uran.ru

Specialty section:
This article was submitted to Cardiac Electrophysiology, a section of the journal Frontiers in Physiology

Received: 04 August 2021
Accepted: 22 November 2021
Published: 14 December 2021

Citation:
Khamzin S, Dokuchaev A, Bazhutina A, Chumarnaya T, Zubarev S, Lyubimtseva T, Lebedeva V, Lebedev D, Gurev V and Solovyova O (2021) Machine Learning Prediction of Cardiac Resynchronisation Therapy Response From Combination of Clinical and Model-Driven Data. Front. Physiol. 12:753282. doi: 10.3389/fphys.2021.753282

Background: Up to 30–50% of chronic heart failure patients who underwent cardiac resynchronization therapy (CRT) do not respond to the treatment. Therefore, patient stratification for CRT and optimization of CRT device settings remain a challenge.

Objective: The main goal of our study is to develop a predictive model of CRT outcome using a combination of clinical data recorded in patients before CRT and simulations of the response to biventricular (BiV) pacing in personalized computational models of the cardiac electrophysiology.

Materials and Methods: Retrospective data from 57 patients who underwent CRT device implantation was utilized. Positive response to CRT was defined by a 10% increase in the left ventricular ejection fraction in a year after implantation. For each patient, an anatomical model of the heart and torso was reconstructed from MRI and CT images and tailored to ECG recorded in the participant. The models were used to compute ventricular activation time, ECG duration and electrical dyssynchrony indices during intrinsic rhythm and BiV pacing from the sites of implanted leads. For building a predictive model of CRT response, we used clinical data recorded before CRT device implantation together with model-derived biomarkers of ventricular excitation in the left bundle branch block mode of activation and under BiV stimulation. Several Machine Learning (ML) classifiers and feature selection algorithms were tested on the hybrid dataset, and the quality of predictors was assessed using the area under receiver operating curve (ROC AUC). The classifiers on the hybrid data were compared with ML models built on clinical data only.

Results: The best ML classifier utilizing a hybrid set of clinical and model-driven data demonstrated ROC AUC of 0.82, an accuracy of 0.82, sensitivity of 0.85, and specificity of 0.78, improving quality over that of ML predictors built on clinical data from much larger datasets by more than 0.1. Distance from the LV pacing site to the post-infarction

zone and ventricular activation characteristics under BiV pacing were shown as the most relevant model-driven features for CRT response classification.

Conclusion: Our results suggest that combination of clinical and model-driven data increases the accuracy of classification models for CRT outcomes.

Keywords: cardiac resynchronization therapy, machine learning, cardiac modeling, electrophysiology, prediction, heart failure, hybrid approach

1. INTRODUCTION

Cardiac resynchronization therapy (CRT) is one of the most effective non-pharmacological therapies for patients with chronic heart failure (CHF). It enhances the pumping function increasing the left-ventricular (LV) ejection fraction (EF), promotes reversed cardiac remodeling, and improves patients' quality of life (Abraham et al., 2002; Bristow et al., 2004). Nevertheless, 30–50% of candidates for CRT have no significant improvement after implantation (Vernooy et al., 2014), which points to the importance of clarifying the criteria for patient selection and optimizing the implantation procedure itself.

Lack of response to CRT is a multifactorial problem associated with variability in individual characteristics, disease patterns, and treatment (Mullens et al., 2009). Combined assessment of multiple factors and individual patient characteristics can improve prediction of response to CRT. With increasing availability of electronic databases, Machine Learning (ML) provides an opportunity to perform such assessment, improving patient selection for therapy (Krittanawong et al., 2017; Lopez-Jimenez et al., 2020). Recent studies using ML techniques have achieved impressive results in preoperative clinical data analysis for selecting patients for CRT. Predictive models have been developed to estimate mortality or hospitalization risks from the baseline clinical parameters (Kalscheur et al., 2018; Tokodi et al., 2020, 2021), to assess improvements in EF based on baseline indices and analysis of medical records (Hu et al., 2019) and to stratify patients by an unsupervised learning approach implementing ECG traces (Cikes et al., 2019) and electrocardiography (Feeny et al., 2020). In a recent study (Feeny et al., 2019), Feeny and co-authors using supervised ML approaches selected 9 clinical features (QRS morphology, QRS duration, New York Heart Association CHF classification, LV EF and end-diastolic diameter (EDD), sex, ischemic cardiomyopathy, atrial fibrillation, and epicardial LV lead) that were sufficient to predict patient improvement with fairly high accuracy.

In addition to advances in ML approaches, significant progress has been made in computer modeling of the heart (Auricchio and Prinzen, 2017; Lee et al., 2018). Recent work has shown that patient-specific computer models based on 12-channel ECG and cardiac anatomy measurements are able to reproduce ventricular activation (Potse et al., 2014; Lee et al., 2019; Lopez-Perez et al., 2019; Camps et al., 2021). Moreover, such models may be used to simulate the effect of CRT and study dyssynchrony characteristics (Villongco et al., 2016; Lee et al., 2019).

In recent modeling studies, a combination of cardiac imaging data, personalized models and ML techniques has demonstrated greater accuracy in predicting the propensity for life threatening cardiac arrhythmia in patients with coronary artery disease and cardiac sarcoidosis as compared with current guidelines for ICD implantation (Sung et al., 2020; Shade et al., 2021). Similar hybrid approaches have been used to predict arrhythmia recurrence after pulmonary vein ablation and to target successive ablation procedures in patients with atrial fibrillation (Shade et al., 2020). Our study is another facet demonstrating the relevance of using personalized models as a tool for patient stratification and clinical decision-making.

In this retrospective proof-of-concept study we have developed a new technique to predict CRT response prior to the procedure. First, we developed personalized electrophysiological models simulating ventricular activation and body-surface ECG at the intrinsic activation pattern under left bundle branch block (LBBB) and at BiV pacing mimicking the results of CRT implantation. Then, we used preoperative clinical data along with features derived from clinical image analysis and personalized model simulations to create a supervised multivariable classifier predicting the probability of patient improvement. To the best of our knowledge this has been done for the first time.

The main hypothesis of our study is that personalized model simulations are able to improve ML classification accuracy as compared with pre-operative clinical data alone. Indeed, if the coronary sinus anatomy is available for a patient (which is possible to derive from CT data), one can predict an accessible area for pacing electrode installation and use this area in a personalized ventricular model to simulate BiV pacing. Thus, simulations performed prior to clinical intervention can be used to directly assess the effects of BiV pacing on ventricular activation time, ECG biomarkers and electrical dyssynchrony indices (subject, of course, to the accuracy of model approximation) and hence to estimate whether the goal of the CRT procedure—synchronization of ventricular activation in a particular patient—can be achieved. Importantly, such data can not be derived from pre-operative clinical data itself. Simulated BiV features can be used for patient classification (estimation of CRT response probability) along with other available clinical data and simulated LBBB features.

The study focuses on the following research aims: to assess the contribution of simulated indices derived from personalized modeling to the accuracy of ML predictive models; and to define important clinical and model-derived features in the hybrid dataset for CRT response prediction.

For the first time, we used a hybrid combination of clinical data and model-derived data on ventricular geometry and electrical activation at both intrinsic LBBB pattern and BiV pacing for the development of ML classifier of CRT response. Here, simulated ECG and electrical dyssynchrony features at BiV pacing were selected among the most significant features by means of feature importance algorithms used for classifier development. The ML classifiers on the hybrid dataset outperformed classifiers built upon the clinical data.

2. METHODS

The schematic outline of the research pipeline, including patient cohort selection, clinical indices' acquisition, electrophysiological modeling, feature selection, and machine learning model training, is illustrated in **Figure 1**.

2.1. Clinical Data

2.1.1. Study Population

In this retrospective non-randomized single-center observational study, we enrolled 57 CHF patients on optimal drug treatment who underwent CRT device implantation at Almazov National Medical Research Centre from August 2016 to August 2019. Participants signed approved inform consent. The study protocol was approved by the Institutional Ethical Committee.

The criteria for inclusion into the study were:

1. age over 18;
2. functional class (FC) II-IV of CHF according to the classification of the New York Heart Association (NYHA) at the outpatient stage of treatment;
3. LV EF $\leq$ 35% (Simpson);
4. QRS duration (QRSd) more than 120 ms;
5. sinus rhythm, left bundle branch block (LBBB);
6. optimal drug therapy.

The exclusion criteria were:

1. acute myocardial infarction, transient ischemic attack, acute cerebrovascular accident less than 3 months before the start of the study;
2. patients who were scheduled to undergo myocardial revascularization or heart transplantation during the observation period;
3. congenital and acquired defects, as well as heart tumors, LV aneurysm, if scheduled for surgery during the observation period;
4. active inflammatory and autoimmune diseases of the myocardium;
5. thyrotoxicosis at the time of inclusion in the study;
6. anemic syndrome: blood hemoglobin level less than 90 g/l;
7. diseases limiting life expectancy to less than 1 year.

2.1.2. Data Collection

Patients were evaluated before CRT device implantation and during the follow-up period of 12 months after implantation. Patients underwent investigation according to standard pro forma with some additional research methods appropriate for this study.

Standard research methods include:

- clinical examination (complaints, medical history, and physical examination)-before CRT and 1 year after CRT;
- general blood test, biochemical blood test (glucose, potassium, sodium, creatinine, urea, total bilirubin and its fractions, total cholesterol, total protein, AST, and ALT), general urinalysis-before CRT;
- 12-lead ECG-before and 1 year after CRT; ECG monitoring during CRT device programming and during the entire observation period;
- echocardiographic studies before and 1 year after CRT to assess LV reverse remodeling;
- stress tests to exclude/confirm coronary artery disease: stress echocardiography, bicycle ergometry or treadmill test, where clinically indicated;
- coronary angiography, where clinically indicated.

Additional research methods include:

- ECG recording in intrinsic rhythm and under BiV pacing, while programming the CRT device within 7 days after implantation.
- Electrocardiographic imaging using an Amycard system (Amycard, EP Solutions SA, Yverdon, Switzerland). Prior to ECG imaging, a maximum of 224 unipolar body surface mapping electrodes were placed on the patient's torso, followed by computed tomography (CT) imaging of the heart and thorax (Somatom Definition 128, Siemens Healthcare, Germany). Subsequently, the electrodes were connected to the model 01C multichannel electrophysiology laboratory system (Amycard) for continuous ECG recordings during the pacing protocol. CT data were imported into Wave program version 2.14 (Amycard software) to reconstruct 3-dimensional geometry of the torso and heart. Finally, epi/endo ventricle models were manually built with marked active poles of RV and LV leads for bi-ventricular pacing simulations.
- MRI (MAGNETOM Trio A Tim 3 T, Siemens AG or INGENIA 1.5 T, Philips) with contrast (Gadovist or Magnevist) before CRT to detect structural damage of the myocardium.
- Tissue Doppler echocardiography to record ventricle mechanical dyssynchrony. Analysis of interventricular dyssynchrony (IVD) and intraventricular dyssynchrony in the LV (LVD) was performed using biomarkers suggested by Yu et al. (2009). IVD was assessed by the time difference between the start of systolic flows into the aorta and the pulmonary trunk as measured by a pulse-wave Doppler, a value of less than 40 ms was taken as an IVD normal value. LVD was assessed using two biomarkers: dyssynchrony index defined as the temporal difference between the maximal and minimal peak systolic velocities between 12 LV segments (Tsmax–Ts min, 105 ms was taken as threshold normal value), and standard deviation in the peak systolic velocities for 12 LV segments (SD–12, 34 ms was taken as cutoff value). To determine the peak systolic velocities, the technique of color tissue Doppler ultrasonography was used.

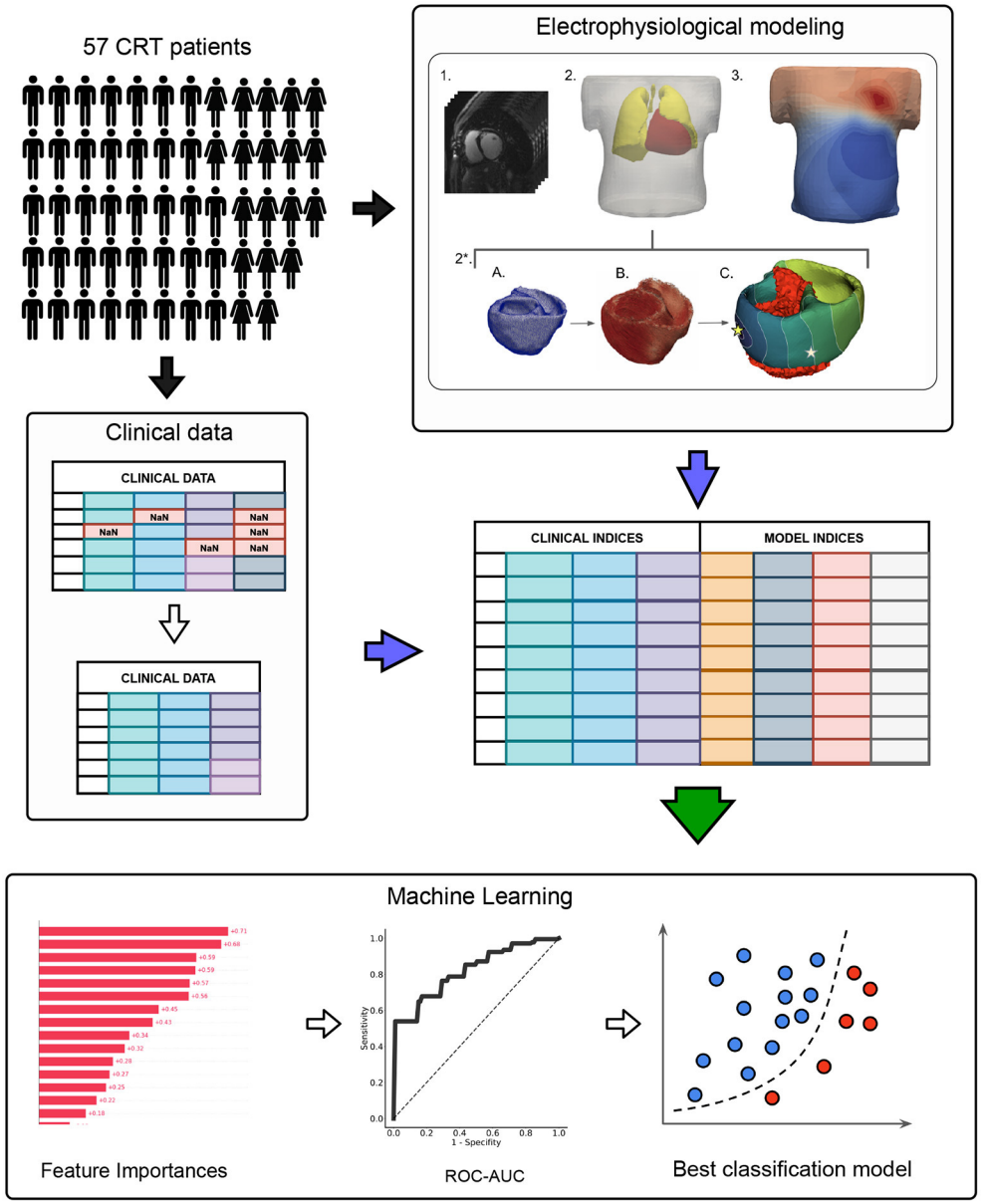

FIGURE 1 | The schematic outline of the data analysis and machine learning pipeline. The pipeline included three major steps: I. CRT patient cohort assembling II. Preprocessing of clinical data and electrophysiological (EP) modeling III. Machine learning model development. In the clinical data preprocessing stage: features with missing values were excluded, non-categorical data were normalized by subtracting mean and dividing by standard deviation, collinear features were removed from the dataset by threshold > 0.85. EP modeling stage included: 1. CT data processing; 2. Segmentation of finite element meshes of the torso and lungs. 2*. Personalization of the heart model: a) Heart segmentation; b) Assignment of myocardial fibers (Bayer et al., 2012); c) Infarction scar/fibrosis assignment, pacing protocol selection (LBBB or BiV) and activation map calculation (stars indicate pacing sites), the infarction area is marked in red. 3. Calculation of torso potential map and ECG signals deriving.

Baseline clinical data for the patients' cohort is presented in **Supplementary Table S1**.

2.2. Personalized Ventricular Models of Electrophysiology

Patient-specific models were generated for each of the 57 cases. Semi-automatic CT segmentation approach helped to extract torso, lungs and ventricles (**Figure 1** EP modeling, items 1–2). Finite-element meshes were smoothed, refined and merged. Average edge length was 15 mm for torso, 10 mm for lungs and 4 mm for heart.

Then, the LV myocardial tissue in the patient ventricular model was further annotated as either normal tissue or disease-induced remodeling area according to the expert's MRI

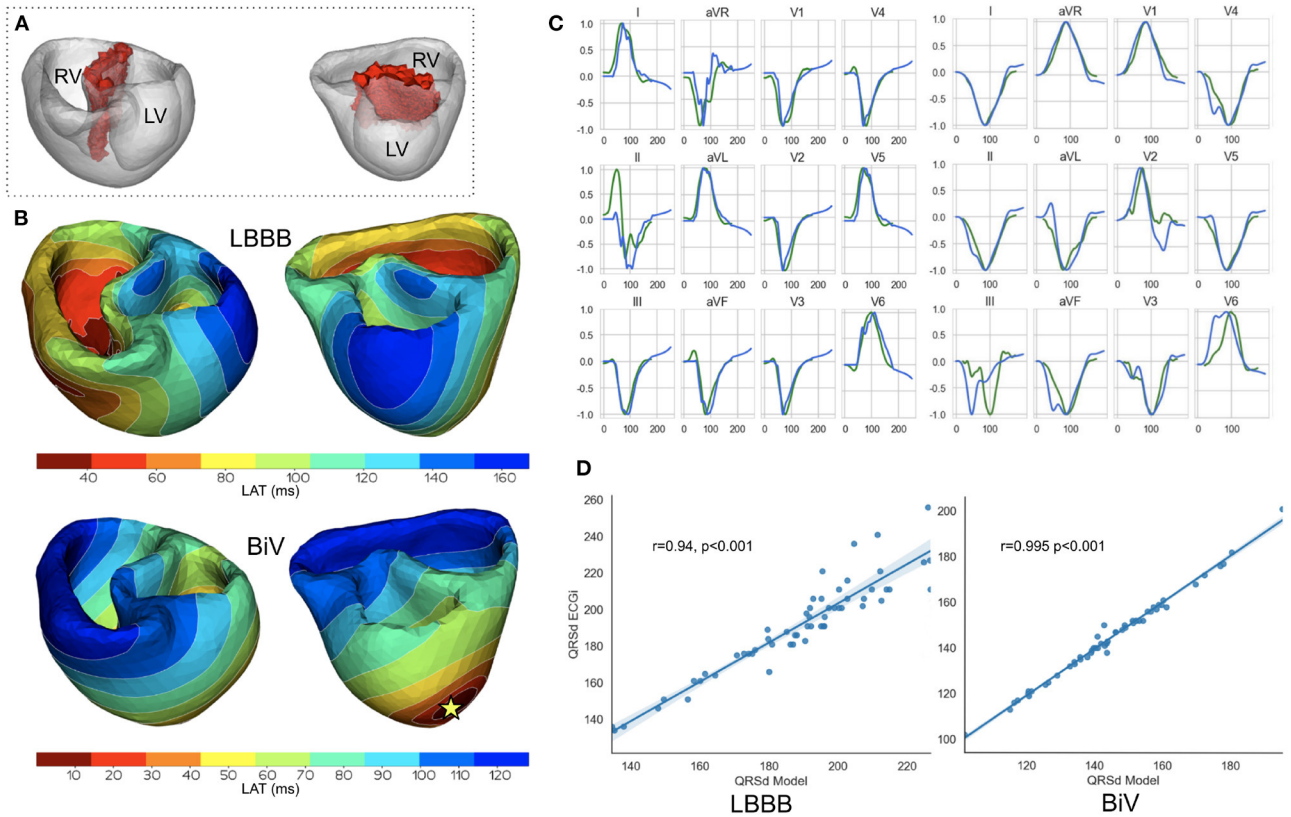

FIGURE 2 | Model validation. Example of a personalized ventricular model for patient #11. **(A)** Area of fibrosis in the interventricular septum (red zone). **(B)** Comparison of model activation maps for LBBB (top) and BiV pacing (bottom). Star indicates LV pacing site for BiV pacing stimulation. The RV stimulating electrode was located in the apex of the surface. **(C)** Calculated ECG signals (QRS complexes) for LBBB on the left and BiV pacing on the right. Green line-signals recorded in the clinic. Blue line-simulated signals. The amplitude of the QRS signals is normalized to the maximum values of the signals. **(D)** Scatter plots showing correlations of QRS complex duration for 57 patients. Dots denote individual patients. The blue line is the regression line, Pearson correlation coefficient for LBBB is 0.94 ($p < 0.001$) for BiV pacing is 0.99 ($p < 0.001$).

examination report from the patient's medical history. The annotation was made as a schematic map of myocardial damage (fibrosis/scar remodeling) using the conventional 17-segment American Heart Association (AHA) model of the LV (Cerqueira et al., 2002), split into three layers, endocardial, mid-myocardial and epicardial, in which damaged regions were highlighted. Each personalized LV geometry computational model was also segmented into 17 x 3 regions (17 segments and 3 layers) according to the AHA scheme. The described areas of scar/fibrosis were labeled on a 17-segment LV AHA model. The scar regions were then simulated as an inexcitable area, and fibrosis regions were associated with a low myocardial conductivity parameter. **Supplementary Figure S1** an example of personalized ventricular model with assigned fibrosis/scars. We also demonstrate a diagram with scar/fibrosis distribution between the segments and the relative volume of the infarct/fibrosis in every segment of AHA LV model (**Supplementary Figure S4**).

The Infarct/fibrosis volume was calculated according to the computational model. The relative volume vs. the myocardial volume was also determined. The compact scar regions were then simulated as an non-excitable area, therefore such zones were excluded from model calculations. Fibrosis regions were assigned a low constant conductivity value (1% of normal conductivity). **Figure 2A** shows a ventricular geometry model for patient #11 with a zone of intramural fibrosis (red) located in the septum (AHA segments 2,3,8,9).

For every patient-specific ventricular model, the electrical activity in the myocardium and ECG on the body-surface were simulated in several steps. We used an Eikonal model (Keener, 1991) to calculate the activation time at each point of the ventricular mesh. An Eikonal model is widely used to simulate the cardiac activation map as one of the fastest methods (Franzone and Guerri, 1993; Pullan et al., 2006; Pezzuto et al., 2017; Camps et al., 2021). To assign fiber direction at every point of the myocardium, a rule-based approach was used (Bayer et al., 2012). Cardiac tissue was simulated as an anisotropic medium with a conductivity ratio of 4:1 along vs. across the myocardial fibers providing the conduction velocity ratio 2:1 in the fiber and in the transverse direction, respectively. A global value of the conductivity along the fibers was set for the entire myocardial tissue

and fitted against the clinical data as described in the next section.

The QRS complexes in 12-lead ECG on the body surface were computed from the activation time maps simulated by an Eikonal model using the approach for fast phenomenological cardiac models proposed by Pezzuto et al. (2017). In this approach, a predefined cellular action potential is assigned to each model element at corresponding activation time. The potential from the myocardium is transformed on the body surface by utilizing a pseudo-bidomain approach (Bishop and Plank, 2011). To generate action potentials in cardiomyocytes, we employed a widely used cellular ionic model TNNP (ten Tusscher, 2006) for human ventricular cardiomyocytes. We defined the locations of 12-lead ECG electrodes on the torso surface and used simulated QRS complexes of ECG signals for the analysis (**Figure 1** EP modeling, items 2-3). Using this approach for ECG calculation, we achieved a high correlation between simulated and experimental QRS durations for our personalized ventricular models (see **Figure 2**).

2.2.1. Simulation of LBBB Activation Pattern and BiV Pacing

We calculated model-driven indices with reference to two types of ventricular pacing: LBBB activation pattern and BiV pacing.

For LBBB activation, RV sub-endocardial surface was annotated and a Purkinje network was generated using standard parameters from a Costabal model (Sahli Costabal et al., 2016). The right bundle branch was set at about 40 mm length, originating on the intraventricular septum, reaching the RV apex, and then splitting into the Purkinje fiber system of RV (Dobrzynski et al., 2013). His system was isolated from the working myocardium and connected to it only at the ends of the Purkinje fibers through Purkinje-myocardial junction points (PMJs). We set the stimulation time in each PMJ according to the distance to the origin node divided by the conduction velocity in the His-Purkinje system, which we assumed to be 3 mm/ms (Ono et al., 2009).

We used a simulated LBBB ventricular activation map to define an area on late activation time (LAT) in every patient model. LAT zone is frequently considered as a target area for LV electrode installation for the best ventricular synchronization at BIV pacing (Stephansen et al., 2018; Zubarev et al., 2019; Lahiri et al., 2020). We used the distance from LV active pole to LAT zone as one of the model-derived features for training CRT response classifiers.

The location of BiV pacing sites were derived from CT images. Active poles of RV and LV leads were annotated manually in Wave program version 2.14 (Amycard software). For BiV pacing simulations, we set a zero time delay between the RV and LV pacing sites as programmed in patients.

The activation time at the stimulation points for LBBB and BiV mode of activation was considered as a boundary condition for solving the Eikonal equation.

2.2.2. Personalization of the Electrophysiological Models

Patient-specific ventricular models in both LBBB and BiV pacing protocols were fitted to reproduce individual data from recorded ECG with the ventricular pacing mode switched off (intrinsic rhythm with LBBB) and switched on (BiV pacing).

For each patient-specific model, we assumed a uniform conductivity in the myocardial tissue in the entire ventricles and solved an optimization problem to find a global conductivity parameter minimizing the discrepancy between simulated and clinical data recorded in the patient in either LBBB or BiV stimulation protocol independently. The post-infarction scar regions were excluded from the model tissue, and a low conductivity of 1% of normal value was assigned to the fibrotic tissue regions when solving the optimization problem. The global conductivity parameter was fitted to minimize the difference between the means of simulated and clinically measured QRSd from the 12-lead ECG recorded in the patient. We used L-BFGS-B algorithm built into SciPy.minimize routine to handle optimization in the model.

Figures 2B,C shows the personalization results for patient #11 with intramural fibrosis located in the septum (AHA segments 2, 3, 8, 9 depicted in red in **Figure 2A**). Although the model parameters were fitted to minimize the difference between the means of simulated and clinical QRSd, the morphology of the simulated QRS complexes corresponded well with clinical ones (see **Figure 2C**, blue lines show model signals, green lines show recorded clinical signals). The scatter plots in **Figure 2D** demonstrate high correlations between simulated and clinical QRSd for both LBBB and BiV modes. The higher correlation coefficient for BiV pacing is explained by precise positioning of the pacing sites derived from CT imaging data, while for LBBB we used a synthetic model of ventricular activation that does not reflect the morpho-anatomical characteristics of the RV conduction system in a particular patient.

2.2.3. Model-Derived Biomarkers of Myocardial Damage, Pacing Site Location, and Myocardial Electrical Activity

Our patient-specific models allowed us to identify several clinically important features affecting ventricular activation. The first group of model-derived indices are based on CT and MRI data coupled with electrophysiology model simulations. Using a digital ventricular model, we were able to define the volume of post-infarction scar and non-ischemic fibrosis and their size relative to the myocardial tissue volume. Knowing RV and LV active poles positions, we measured distance between them (DLvRv). Furthermore, distances from LV pacing site to the infarct/fibrosis area (DLvInfarct) and to the area of LAT (DLvLATZ) under intrinsic rhythm were calculated. When calculating distance biomarkers (see DLvLATZ, DLvLesion and DLvRv in **Supplementary Table S1**), we solved an isotropic Eikonal equation as a simple method to define the distance from a certain point on the ventricular surface to the border of a specific area. The latter distances mimic distances that can be directly measured from CT or MRI data using a ruler.

The second group of model-derived indices was calculated in LBBB and BiV mode of myocardial activation. We simulated the time activation map for both chambers and 12-lead ECG and calculated the following biomarkers derived from the time-dependent signals for further analysis of CRT response: total ventricular activation time (TAT), maximum QRS complex

TABLE 1 | Model biomarkers.

Index	Definition	Explanation
TAT, ms	$TAT = AT_{max} - AT_{min}$	Total ventricular activation time, AT_{min} (ms) - activation start time, AT_{max} (ms) - late activation time.
QRSd, ms	$QRSd = max(T_S - T_Q)$	Maximum QRS complex duration in all leads - difference in the Q-S peaks time on the ECG signal.
AT_{RVLV}, ms	$AT_{RVLV} = ATmax_{LV} - ATmax_{RV}$	Interventricular dyssynchrony index - the difference between the time of late activation of LV and RV.
mAT_{STLV}	$mAT_{STLV} = \frac{LVlat_{mean} - ST_{mean}}{TAT}$	LV activation dyssynchrony index, where $LVlat_{mean}$ (ms)- average activation time of LV free wall, ST_{mean} - average activation time of septum.
$IntAV_{STLV}$, ms	$IntAV_{STLV} = \int \lvert \frac{AV_{LAT}(t)}{V_{LAT}} - \frac{AV_{ST}(t)}{V_{ST}} \rvert dt$	Integral index of LV activation dyssynchrony, $AV_{ST}(t)$ - fraction of myocardial volume activated in septum at time t, $AV_{LAT}(t)$ - fraction of myocardial volume activated in free wall at time t, V_{LAT} - free wall volume, V_{ST} - septum volume.

duration, difference between the total LV and RV activation times (AT_{LVRV}), relative difference between the mean activation times of LV free wall and septum (mAT_{STLV}), integral index of LV free wall and septum myocardial volume activation ($IntAV_{STLV}$). The last three indices characterizing inter- and intraventricular electrical dyssynchrony of myocardial activation were used in work of Villongco et al. (2016).

These simulated features were used as predictions of the effects of BiV pacing on ventricular electrical synchronization. **Table 1** presents a complete list of the simulated characteristics with related definitions and formulas. The average values of all model-derived indices for our enrolled cohort are shown in **Supplementary Table S1**.

Below, changes in feature values under BiV pacing against the LBBB baseline are expressed in relative units. For clinical characteristics, ΔX_{CRT} = (X_{CRT}-X_{LBBB})/X_{LBBB}, where X_{LBBB} and X_{CRT} are feature values before and after CRT device implantation, respectively. For simulated indices, ΔX_{BiV} = (X_{BiV}-X_{LBBB})/X_{LBBB}, where X_{LBBB} and X_{BiV} are feature values in the LBBB activation mode and BiV pacing. For the indices that are initially showed in relative units, e.g., EF and mAT_{STLV}, the response to pacing is expressed as an absolute increment in the LBBB value: ΔEF_{CRT} = EF_{CRT}-EF_{LBBB}, and $\Delta mAT_{STLV\,BiV}$ = $mAT_{STLV\,BiV}$-$mAT_{STLV\,LBBB}$.

For some features, we also used normalized characteristics, i.e., the ratio of the value to the myocardial tissue volume (MTV). Note, MTV should not be confused with the volume of the cavity inside the ventricle. We can evaluate MTV using a digital model of the ventricular geometry based on CT images. When using such normalization, the volume of the preserved myocardium only is taken into account, without allowing for the infarct area. Since the scar tissue is not excited and does not contract, it is excluded from the volume of the active ventricular myocardium. Normalized features give a characteristic's values per unit volume of the myocardium (analogous to the values per mass unit of the myocardium). For instance, TAT/MTV indirectly reflects a reciprocal value of the average velocity of myocardium activation in the ventricles.

2.3. A Predictive Model of Response to CRT Based on Preoperative Clinical Data and Electrophysiology Model Simulations

For classifier development, we applied several supervised machine learning (ML) approaches to identify an optimal set of features and learning algorithm combination showing the best performance characteristics on hybrid data for our patient cohort. The hybrid dataset for building the classifier contained clinical and model-derived features as described above. At the preprocessing step, features with missing values were excluded. Non-categorical data were normalized by subtracting the mean and dividing by standard deviation. Collinear features were also removed from the dataset by threshold > 0.85.

Several criteria for CRT response definition were used for classification. The primary criterion for responders was more than 10% increase in LV EF (EF10) (Feeny et al., 2019). The following criteria were also considered: a reduction in ESV $>$ 15% (ESV15, see Foley et al., 2009; Park et al., 2012); a 5 and 15% increase in LV EF (Feeny et al., 2019), and combined EF10 and ESV15.

We evaluated several classification algorithms: logistic regression (LR), linear discriminant analysis (LDA), support vector machine (SVM) with linear kernel, random forest (RF) classifier; each evaluated in combination with three different feature sets obtained by feature selection methods. The following algorithms were used for feature selection: random forest mean decrease accuracy (MDA), univariate statistical testing (UST, two-sample *t*-test for continuous variables and chi-squared test for categorical variables), and L1-based feature selection (L1, based on weights of LR). Features were selected in a cross-validation loop for each subset. The top 8 features chosen by the algorithms were used to construct the classifiers.

Feature selection and training of classification algorithms was done using a Leave-One-Out cross-validation loop. Within the loop, the ML classifier score for each test fold (hear each consisting of just one observation) was calculated. These ML scores were combined into one set to build the receiver operating characteristic (ROC) curve and to calculate the area under the ROC curve (AUC). The highest-performing combination of the classifier with feature selecting algorithm was chosen to develop the final classifier.

In addition, we used repeated stratified five-fold cross-validation with 1,000 iteration in order to be confident in assessing the quality of the classifier. We quantified the classification performance of each feature set–algorithm combination with ROC AUC across all folds and iterations. The classifier with the highest ROC AUC was selected as the final classifier for our hybrid dataset.

2.3.1. Software

Cardiac electrophysiology was modeled with the help of software written at the Institute of Immunology and Physiology UB RAS

based on FENICS library (for solving PDE problems) (Logg and Wells, 2010) and VTK (for working with meshes). For the machine learning pipeline (see **Figure 1**): classifier development, statistical modeling, feature selection, cross validation, and ROC-AUC calculation we used the sklearn library.

2.3.2. Statistics

Detailed analysis was performed using the IBM SPSS Statistics 23.0.0.0 software package (USA). For qualitative data, the frequency and percentage of total patients in the cohort were calculated. Quantitative data are presented as mean ± standard deviation. Comparisons between two dependent groups were made using Wilcoxon's test for quantitative data and McNimar's test for qualitative data. Nonparametric Friedman's two-way ANOVA was applied to compare related groups. Comparison between two independent groups was carried out using the Mann-Whitney test for quantitative data and Pearson's chi-square test for qualitative data. Feature dependence was assessed using the Spearman rank correlation test. The critical level of statistical significance was taken equal to 0.05.

3. RESULTS

3.1. Responders vs. Nonresponders: Analysis of Clinical Data Before and After CRT Device Implantation and Model Simulations in LBBB and BiV Pacing

We found an average positive response to BiV pacing in all clinical indicators and corresponding simulated indexes of the CRT outcome in the entire patient cohort (a summary of statistics for clinical data, CT/MRI derived data and model-driven biomarkers is presented in Section S.1, **Supplementary Table S1**). High variability of the effects of BIV pacing on biomarkers in both the clinical and simulated data suggest a significantly nonuniform output among the patients. Therefore, the patients were classified into two groups of responders and nonresponders to the therapy.

We have used several conventional criteria to classify responders and nonresponders to CRT in the patient cohort based on clinical data on the post-operative LV reversed remodeling. Primary classification was defined by a higher than 10% increase in the LV EF for responders (ΔEF_{CRT} >10% referred hereafter as EF10 criterion). This criterion was used in clinical studies, and allowed us to compare qualitatively the results of our predictive models for CRT response with the findings reported recently by Feeny et al. (2019). Surprisingly, the 10% cutoff for EF improvement in responders is close to the average EF increase of 9 ± 8% observed in our patient cohort. Classification results based on other CRT response definitions are described in the **Supplementary Materials** and discussed in the section 4.

Table 2 summarizes the clinical and model-derived variables in the groups with or without LV EF improvement according to the EF10 criterion. In our patient cohort, 23 (40%) patients demonstrated an improved EF (referred to as CRT responders) and 34 (60%) patients were classified as nonresponders. The ratio seems biased toward nonrespondents, but we have intentionally raised the LV EF improvement threshold in order to be more confident in predicting true positive responses. Average EF is raised in both groups, and the increase is significantly higher in the responders vs. nonresponders (17 ± 5% vs. 3 ± 5%, respectively). The EF improvement after CRT is accompanied by a prominent ESV reduction by 47 ± 19% in the responder group against an insignificant diminishing by 9 ± 37% in nonresponders. Similarly, a much higher average EDV reduction is seen in the responders due to LV postoperative reverse remodeling after CRT. Although the average QRSd is decreased, no statistical significance between the groups was found. No difference in the CRT effect on the mechanical dyssynchrony indices was found as well.

In consistency with the clinical data, the model simulations revealed a decrease in both TAT and QRSd under BiV pacing in each of the two sub-populations of models (**Figure 3**). The electrical dyssynchrony indices also reveal a prominent decrease in the groups, with the highest reduction in the inter-ventricular dyssynchrony index AT_{RVLV} (**Figure 3**). Meanwhile, no difference in the relative decrease in the indexes between the responder and nonresponder groups was observed (**Table 2**).

Analyzing CT/MRI derived geometry indexes, we figured out no difference in the relative volume of infarct/fibrosis in LV myocardial tissue between the groups (**Table 2**). At the same time, we found a shorter distance from the LV pacing site to the damaged zone in the nonresponder group (28 ± 27 mm in nonresponders vs. 45 ± 28 mm in responders), suggesting less effective pacing of the normal tissue in nonresponders. Interlead spacing does not statistically differ between groups. No difference in the distance from LV pacing site to the LAT area in LBBB activation mode was found as well.

It is of note that most of the individual biomarkers in the intrinsic LBBB activation pattern derived from either clinical, or CT/MRI, or simulated data do not show a significant difference in the distribution between the responder and nonresponder groups. This means that no one single index could be considered as a diagnostic feature for preoperative classification (**Table 2**).

Among the pre-operative clinical data, two features, i.e., LV EF_{LBBB} and the inter-ventricular mechanical dyssynchrony index IVD_{LBBB}, displayed differences between the groups classified according to the EF10 criterion. Here, LV EF demonstrated a bit higher average value along with a bit lower value of IVD in the nonresponders than in responders. This is consistent with a low negative correlation between EF_{LBBB} before and ΔEF_{CRT} after implantation ($r = -0.48$, $p = 0.031$, see **Supplementary Figure S7**). However, high EF variation in each group comparable with the difference between the group averages did not allow us to find a valid threshold separating the groups. The average accuracy of the Logistic Regression classification with One-Leave-Out cross-validation based on EF_{LBBB} was only 0.62 with rather low values of both sensitivity at 0.69 and specificity at 0.55. A low positive correlation was also found between IDV_{LBBB} and ΔEF_{CRT} ($r = 0.32$, $p = 0.029$), suggesting its possible predictive power for CRT response. However, we did not have IDV and other mechanical dyssynchrony indices for all

TABLE 2 | Clinical, imaging, model data and predictive model scores for responders and nonresponders defined by EF10 criterion.

	Patient cohort *n* = 57					
Variable	**Responders *n* = 23 (40%)**			**Nonresponders *n* = 34 (60%)**		
			Clinical data			
Gender (male/female)		15/8			23/11	
Age, year		64 ± 6			63 ± 7	
BMI		27 ± 5			30 ± 5#	
IHD/DCM		14 (61%)/9(49%)			22 (65%)/12(35%)	
History of AF		4 (17%)			8 (24%)	
	LBBB	**CRT**	**Δ, %**	**LBBB**	**CRT**	**Δ, %**
FC CHF :		Decrease in FC 17 (70%)			Decrease in FC 15 (44%)	
I	0 (0%)	7 (30%)*	7	0 (0%)	3 (9%)	3
II	12 (52%)	12 (52%)	0	12 (35%)	19 (56%)**	7
III	11(48%)	2 (8%)*	–9	22 (65%)	4 (12%)**	–18
QRSd, ms	192 ± 20	143 ± 14**	–25 ± 11	190 ± 26	145 ± 21**	–22 ± 16
			Echocardiography data			
EDV, ml	301 ± 69	196 ± 68**	–33 ± 22	290 ± 106	263 ± 138##	–7 ± 33##
ESV, ml	231 ± 59	119 ± 48**	–47 ± 19	207 ± 87	185 ± 118*##	–9 ± 37##
EDD, mm	74 ± 8	62 ± 10**	–16 ± 10	73 ± 7	69 ± 9 **##	–5 ± 8 ##
ESD, mm	64 ± 9	48 ± 13**	–26 ± 17	62 ± 9	57 ± 10 **##	–7 ± 13##
EF, %	23 ± 5	40 ± 6**	17 ± 5	29 ± 6##	32 ± 7**##	3 ± 5##
IVD, ms ($n = 34$)	76 ± 17	46 ± 22**	–38 ± 29	63 ± 19##	33 ± 14**	–44 ± 27
ΔTs, ms ($n = 34$)	82 ± 35	76 ± 34*	–20 ± 39	87 ± 44	58 ± 33*	–12 ± 78
SD12, ms ($n = 34$)	31 ± 14	27 ± 12	–20 ± 40	33 ± 16	23 ± 12**	–15 ± 74
			CT/MRI data			
MTV,ml		332 ± 142			377 ± 143	
InfarctV, ml		45 ± 39			54 ± 39	
InfarctV/MTV		0.14 ± 0.08			0.16 ± 0.13	
DLvRv,mm		108 ± 23			105 ± 25	
DLvLATZ,mm		44 ± 16			58 ± 27	
DLvInfarct,mm		45 ± 28			28 ± 27#	
			Model data			
	LBBB	**BiV**	**Δ, %**	**LBBB**	**BiV**	**Δ,%**
TAT, ms	269 ± 109	141 ± 31**	–45 ± 18	246 ± 130	138 ± 46**	–45 ± 24
QRSd, ms	192 ± 21	143 ± 14**	–30 ± 12	187 ± 24	152 ± 28**	–22 ± 20
AT_{RVLV}, ms	103 ± 65	26 ± 26**	–75 ± 21	95 ± 79	20 ± 21**	–76 ± 27
$IntAV_{STLV}$, ms	101 ± 57	34 ± 15**	–51 ± 36	106 ± 59	33 ± 16**	–53 ± 52
mAT_{STLV}	0.36 ± 0.10	0.29 ± 0.14	–6 ± 20	0.36 ± 0.09	0.27 ± 0.13**	–9 ± 17
			Predictive model scores			
Score by Feeny et al. (2019)		0.63 ± 0.20			0.55 ± 0.23	
MLCD score (EF10)		0.47 ± 0.23			0.37 ± 0.24	
MLHD score (EF10)		0.58 ± 0.25			0.29 ± 0.22##	

Mean ± SD.

**$p < 0.05$, **$p < 0.01$ LBBB vs. CRT or LBBB vs. BiV. Comparisons between two dependent groups were made using Wilcoxon's test for quantitative data and McNimar's test for qualitative data.*

#$p < 0.05$, ##$p < 0.01$ Responders vs Nonresponders. Comparison between two independent groups was carried out using the Mann-Whitney test for quantitative data and Pearson's chi-square test for qualitative data.

Δ - Average change in indicator $\Delta X = X$ CRT - X LBBB / XLBBB or $\Delta X = X$BiV - X LBBB / X LBBB. Δ is calculated as the absolute difference for normalized values (EF and mAT_{STLV}) and FC.

BMI, Body mass index; IHD, Ischemic heart disease; DCM, Dilated cardiomyopathy; AF, Atrial Fibrillation; FC CHF, functional class of congestive heart failure; IVD, interventricular dyssynchrony; ΔTs, maximum temporary difference in peak systolic velocities between 12 LV segments; SD12, standard deviation of the peak systolic velocities of 12 LV segments; MTV, myocardial tissue volume; LAT, late activation time; TAT, total ventricular activation time; QRSd, maximal duration of QRS complex on 12 leads; AT_{RVLV}, difference of total LV and RV activation time; $IntAV_{STLV}$, integral index of LV free wall and septum myocardial activation dyssynchrony; mAT_{STLV}, difference between mean activation time of LV free wall and septum; MLCD score (EF10), ML score on the clinical data for EF10 criterion; MLHD score (EF10), ML score on the hybrid data for EF10 criterion.

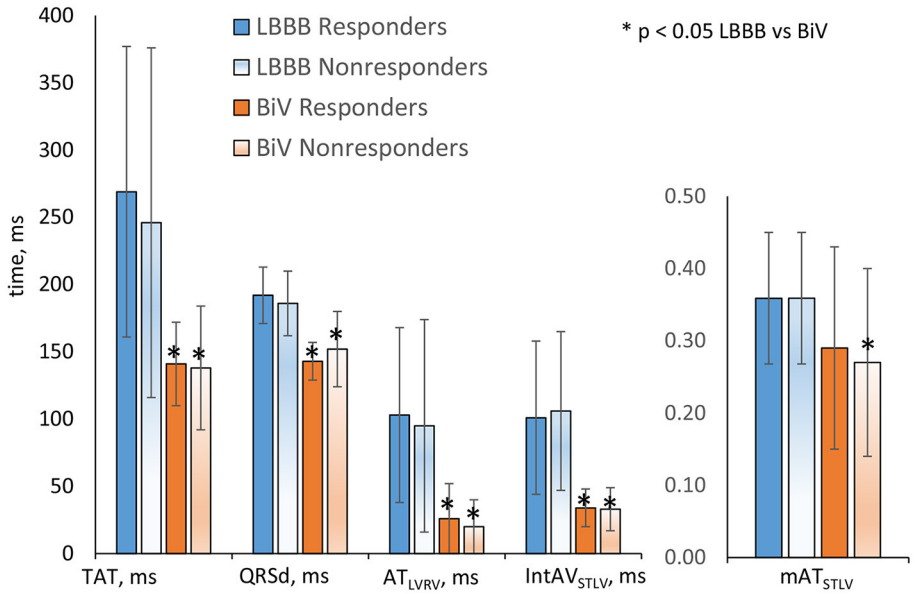

FIGURE 3 | Simulation features in the LBBB activation mode and under BiV pacing for responders and nonresponders. Bar indicates mean. Error bar is SD. Comparisons between two dependent groups (LBBB vs. BiV) were made using Wilcoxon'stest. No difference in the indexes between the responder and nonresponder groups was observed. *$p < 0.05$ LBBB vs. BiV.

57 patients in our cohort and, therefore, decided against using them in further analysis (see section 5).

Although in this proof-of-the-concept study some data used for model building were recorded after operation, we consider all CT/MRI and model-derived features as potentially pre-operative because all of them can actually be assessed before operation (see also section 5. on this issue). Among the data derived from CT/MRI, we found only the distance between the LV pacing site and the area of myocardial damage showing a significant difference between the responders and nonresponders (**Table 2**). However, this index did not show a significant correlation with either ΔEF_{CRT} (see **Supplementary Figure S7**) as well.

In consistency with the absence of difference between clinical QRSd in responders and nonresponders, none of the simulated electrophysiological biomarkers showed any significant difference between groups both in the LBBB mode of activation and under BiV pacing either (**Figure 3** and **Table 2**), which also did not allow them to be considered as individual classifying features.

Our dataset analysis suggested a hypothesis that the only combination of the clinical and MRI/CT derived biomarkers that can be evaluated before operation together with predictions on the BiV response simulated using a personalized ventricular model may increase the predictive power of such a hybrid dataset for patient classification.

3.2. Predictive Models of CRT Response Built on Hybrid Dataset of Clinical Data Before Operation and Personalized Model Simulations at LBBB and BiV Pacing

We used the hybrid input dataset containing 57 data entries with features derived from clinical data recorded prior to operation, CT/MRT derived data and simulated features calculated using personalized models of ventricular excitation in LBBB and BiV pacing activation modes for every patient from our cohort as described in the previous sections. The complete list of features fed to the feature selection algorithms when developing CRT response classifiers is shown in **Figure 4** (right) in descending order of the feature importance. We trained supervised classifiers using an EF10 criterion ($\Delta EF > 10\%$) of CRT response. To choose the best classifier, we compared 4 different classification models (classifiers) with Leave-One-Out and five-fold cross-validation and 3 different feature selection methods inside a cross-validation loop. A summary of the model ROC AUC used to characterize the quality of the trained models is shown in **Table 3**. It is seen that average ROC AUC vary from a smallest value of 0.7 to the best one of 0.82 obtained for SVM and LDA classifiers with Univariate approach for feature selection.

Figure 4 (left) shows a ROC curve for the best SVM classifier trained for the EF10 response criterion. **Table 4** summarizes the classifier characteristics. The best SVM classifier for CRT response demonstrates a high accuracy of 0.82, sensitivity of 0.85, and specificity of 0.78.

ML scores generated by the best SVM classifier correlate with post-operational improvement in the EF ($r = 0.46$, $p < 0.001$, see **Figure 5**). Moreover, the distributions of the average scores in the responder and nonresponder groups in our patient cohort significantly differ between each other with a significantly higher average score in the responder vs. nonresponder group (0.58 ± 0.25 vs. 0.29 ± 0.22, $p < 0{,}01$, see **Figure 6** and **Table 2**). A corresponding score threshold of 0.46 was defined for the responders in our patient cohort for the best classifier according to the EF10 response definition.

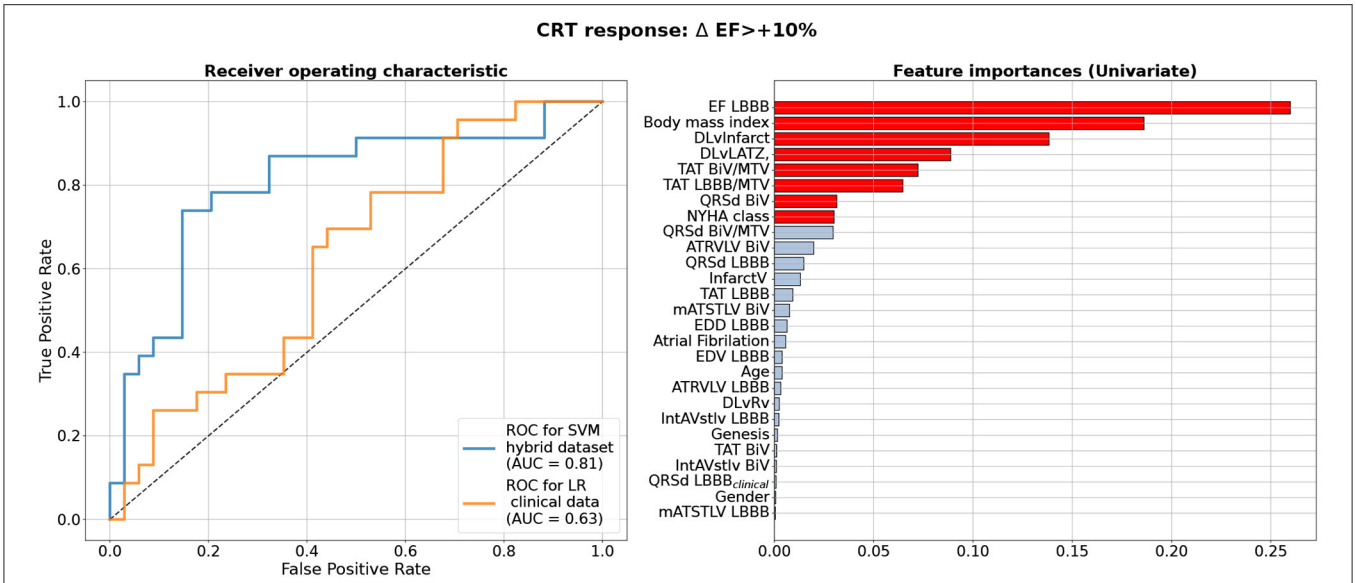

FIGURE 4 | Best Machine Learning Classifiers for CRT response prediction from the hybrid dataset of clinical and model-drived data for 57 patients. Left panel shows receiver operating characteristic (ROC) curves for the best classifiers based on the ΔEF > 10% criterion of CRT response. Blue line shows ROC curve for Support Vector Machine Classifier (SVM) using Leave-One-Out cross-validation on hybrid dataset. Yellow line shows a ROC curve with corresponding ROC AUC for a Logistic Regression(LR) model trained on the data subset containing clinical features as suggested in Feeny et al. (2019). Values of the area under the ROC curve (ROC AUC) for the models are shown on the panel. Right panel shows clinical and model-drived feature list in descending order of importance ranged using Univariate feature selection approach for the best classifier.

TABLE 3 | Comparison of ROC AUC for different Machine Learning classifiers using leave-one-out and five-fold cross-validation and different feature selection algorithms for EF10 criterion of CRT response.

Classifier	Leave-one-out			Five-fold		
	Feature selection method			Feature selection method		
	L1	MDA	Univariate	L1	MDA	Univariate
Logistic regression	0.76	0.78	0.80	0.74 ± 0.15	0.76 ± 0.14	0.80 ± 0.14
Linear discriminant analysis	0.73	0.76	0.82	0.71 ± 0.15	0.76 ± 0.15	0.80 ± 0.14
Support vector machine	0.70	0.73	**0.82**	0.72 ± 0.15	0.75 ± 0.15	**0.80 ± 0.14**
Random forest	0.73	0.72	0.73	0.72 ± 0.16	0.70 ± 0.16	0.72 ± 0.16

L1, Logistic Regression feature selection; MDA, Mean Decrease Accuracy; Univariate, Univariate statistical testing: two-sample t-test for continuous variables and chi-squared test for categorical variables. Bold text indicates the best classifier.

Figure 4 (right) shows a ranged list of feature importances selected by the SVM classifier trained on the entire dataset for the EF10 CRT response criterion. Eight most important features colored in red were selected for the final classifier. The pre-operative EF_{LBBB} showed the highest importance among other inputs, which is in line with our findings on the correlation between ΔEF_{CRT} and EF_{LBBB}. The other two of the three clinical features contributing to the CRT response were BMI and NYHA stage. Therefore, the majority of the selected features were indices derived from CT/MRI and simulated features in the LBBB and BiV modes of activation. In particular, the distance between the LV pacing site and the infarct/fibrosis area was the third in the feature importance range, and a combination of TAT/MTV_{LBBB}, TAT/MTV_{BiV} and $QRSd_{BiV}$ showed the highest importance among simulated features. Corresponding coefficients at the input variables in the terms of the best LR classifier are given in **Supplementary Table S2**.

The yellow line in **Figure 4** (left panel) shows the ROC curve for an LR classifier trained on the clinical data only according to the EF10 criterion. The sub-set of clinical features used here for CRT response prediction was the same as selected in the article by Feeny et al. (2019) for their best LR classifier (see the complete feature list and corresponding coefficients at the input variables

TABLE 4 | Performance of the classifiers on hybrid vs. clinical data.

SVM on hybrid dataset				
$\Delta EF > +10\%$, cutoff = 0.46				
		Responder	**Non-responder**	
Model responder		18	5	
Model Non-responder		5	29	
Accuracy	Sensitivity	Specificity	ppv	npv
0.82	0.85	0.78	0.78	0.85
LR on hybrid dataset				
$\Delta EF > +10\%$, cutoff = 0.46				
		Responder	**Non-responder**	
Model Responder		15	8	
Model Non-responder		7	27	
Accuracy	Sensitivity	Specificity	ppv	npv
0.74	0.65	0.79	0.68	0.77
LR on clinical dataset				
$\Delta EF > +10\%$, cutoff = 0.51				
		Responder	**Non-responder**	
Model Responder		8	12	
Model Non-responder		15	22	
Accuracy	Sensitivity	Specificity	ppv	npv
0.53	0.65	0.35	0.40	0.59
Response score by Feeny et al. (2019)				
$\Delta EF > +10\%$, cutoff = 0.62				
		Responder	**Non-responder**	
Model Responder		13	15	
Model Non-responder		10	19	
Accuracy	Sensitivity	Specificity	ppv	npv
0.56	0.56	0.57	0.46	0.65

SVM, Support Vector Machine; LR, Logistic Regression; ppv, positive predictive value; npv, negative predictive value.

in **Supplementary Table S2**). The average ROC AUC for this predictive model appears to be 0.63 for our patient cohort, with an average accuracy of 0.53, sensitivity of 0.65, and specificity of 0.35 (**Table 4**), which are much lower than the characteristics of the ML model trained on the hybrid input dataset containing a combination of clinical and model-driven features. Note that this AUC is close to the AUC value of 0.62 we obtained for the LR classifier trained on EF_{LBBB} only, suggesting that the rest of the clinical information does not contribute essentially to the model predictions.

We compared also the accuracy of EF10 improvement predictions from our ML classifier on the hybrid data with the accuracy of predictions based on our patients' clinical features fed into a "ML score calculator" presented in Feeny et al. (2019) (**Table 4**). This predictor showed an accuracy of 0.56, sensitivity of 0.56, and specificity of 0.57 on our 57 patient dataset, which are similar with the performance of the LR classifier trained on the clinical data, but much lower that the performance of our ML classifiers on hybrid data.

Figure 6 shows average ML scores generated by the classifier on the hybrid data for the entire patient cohort and for the responder and nonresponder groups according to the EF10 definition in comparison with the ML scores predicted by the LR classifier trained on the clinical data from our patient cohort and those from the calculator by Feeny et al. (2019). The average ML score from Feeny et al. (2019) on the entire patient cohort is seen to be higher than our ML scores, explaining lower rates of true positive and true negative predictions from the calculator on our patient cohort. Moreover, the only classifier on hybrid data generates significantly higher ML scores in the responder vs. nonresponder group, suggesting its higher predictive performance. In contrast, the average ML scores did not differ between responders and nonresponders according for the LR classifier on the clinical data (0.47 ± 0.23 vs. 0.37 ± 0.24, $p = 0.111$) and for the Feeny's calculator from Feeny et al. (2019) (0.63 ± 0.20 vs. 0.55 ± 0.23, $p = 0.213$) in our patient cohort (see also **Table 2**).

These results clearly highlight the significance of model-driven features for CRT response prediction.

4. DISCUSSION

The researchers sought ways to predict CRT response for ensuring more effective patient stratification and different

outcome end-points for improving state, increasing survival period and preventing adverse effects (Lahiri et al., 2020). Despite of intensive research performed in the field, the fraction of patients with low response to the therapy remains as high as 30–50% depending on which criteria are used for assessing CRT outcome. New artificial intellegence and ML based approaches to data analysis have been extensively used in attempts to increase the accuracy of patient differentiation (Kalscheur et al., 2018; Feeny et al., 2019, 2020; Tokodi et al., 2021). Computational models based on clinical data are also employed to identify mechanisms responsible for the poor efficacy and develop approaches improving CRT outcomes (Lumens et al., 2015; Huntjens et al., 2018; Lee et al., 2018; Isotani et al., 2020). Recently, a new trend has emerged in this research area, which uses a combination of clinical and model data together with ML for solving challenging medical problems (Aronis et al., 2021; Heijman et al., 2021). As far as we know, there have been no reports of *in-silico* studies involving a hybrid approach to predict CRT response in a cohort that would combine a dataset of patient-specific features derived from clinical measurements and simulations on personalized ventricular models.

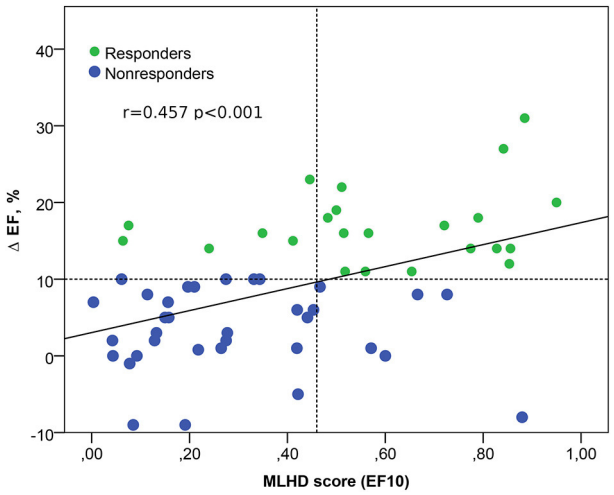

FIGURE 5 | Relation between the ML score on the hybrid data (MLHD score) for EF10 criterion and the post-operational change in the EF. Solid line - regression line Δ EF = 3 + 14 MLHD score; horizontal dotted line shows a 10% threshold for LV EF improvement; vertical dotted line is a MLHD score cutoff of 0.46 for responders; r is the Spearman correlation coefficient; p is the significance for the group difference.

4.1. Improvement of Classification Models Built on Hybrid Data vs. Predictors on Clinical Data

In this study, we combined the MR/CT-imaging and model derived features with pre-operative clinical data used conventionally to characterize patient's state in a hybrid dataset for building predictive models of CRT response in the patients by ML techniques. A sub-set of simulated features containing TAT, QRSd and three electrical dyssynchrony indices generated by every of 57 patient-specific electrophysiology models under LBBB and BIV pacing was used as an input to ML algorithms. The personalized models were also used to define LAT zone in the LV under LBBB mode of activation and to calculate the distances between the pacing sites, and from the LV pacing site to the LAT zone and to the LV infarct/fibrosis area, which were also used as input features for ML classifiers. The basic hypothesis of our study was that model-driven simulations of the response to BiV pacing may essentially enhance the predictive power of the hybrid dataset for CRT response evaluation.

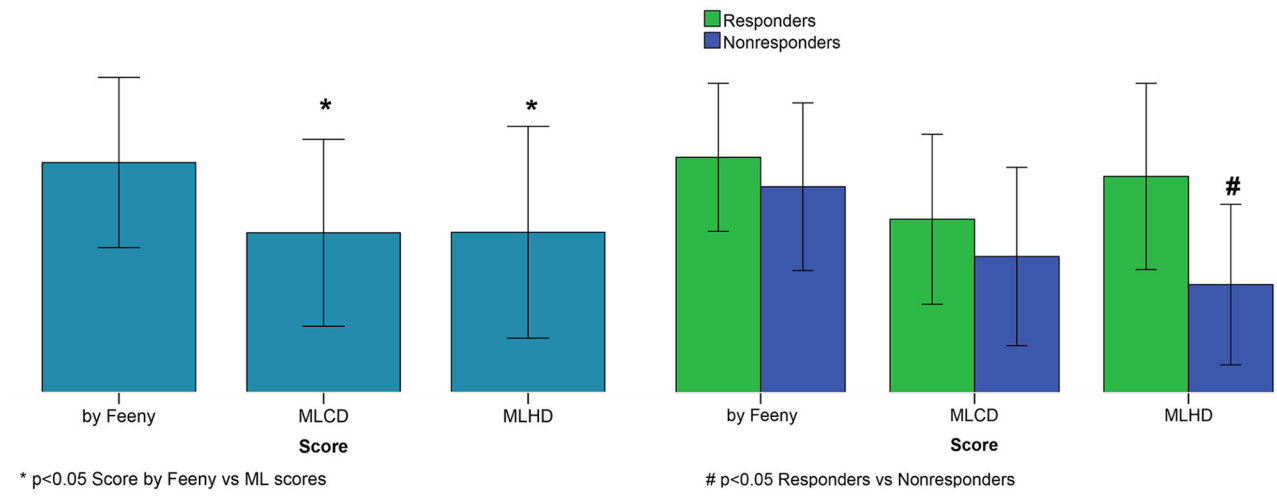

FIGURE 6 | CRT response scores. Left panel: Average scores. Right panel: Average scores for responders and nonresponders. Score by Feeny et al. (2019); MLCD–ML score on the clinical data for EF10 criterion; MLHD-ML score on the hybrid data for EF10 criterion. Bar indicates mean. Error bar is SD. Nonparametric Friedman's two-way ANOVA was used to compare related groups (Score by Feeny vs. ML scores). Comparison between two independent groups (responders vs. nonresponders) was performed using the Mann-Whitney test.

Despite the rather small size of the dataset used for ML classifier development (57 entries in the entire dataset), we were able to obtain ML classification models achieving high accuracy in predicting the response to CRT (see **Figure 4** and **Table 3**). The ROC AUC value for the best SVM classifier is as high as 0.82 for $\Delta EF > 10\%$ cutoff for responders.

The most significant result of our study is that our best classification models built on the hybrid dataset outperformed the ML classifier trained on the pre-operative clinical data only (see **Figure 4** and **Table 4**). In the latter, we used a subset from the same 57 patient dataset containing 9 clinical features for each patient. The features were selected in recent study by Feeny et al. (2019) as most important for training the best LR model based on the clinical data from a thousand of patients. So, we used the same clinical features to train similar LR classifier on the data from our patient cohort. The best model built on the clinical data demonstrated a ROC AUC of 0.63, and the accuracy, sensitivity and specificity much lower than those for the classifiers built on the hybrid dataset (see **Figure 4** and **Table 4**). Then we used the same 9 clinical features for every 57 patients as a testing dataset to fed to the ML score calculator provided by Feeny ea (see the **Supplementary Materials** in Feeny et al., 2019). It showed an accuracy of 0.56 for our patient cohort. The performance of the ML score calculator tested on the clinical data from our 57 patients is similar with the performance of the LR classifier we trained on the same data. Both classifiers showed lower performance as compared with the classifiers trained on the hybrid data from the same 57 patients. Moreover, our hybrid data classifier outperformed classifiers reported in Feeny et al. (2019) (see **Table 3** ibidem), which were trained on different sets of clinical data from about thousand of patients. Note, the clinical data classifiers on a large dataset demonstrated higher metrics than those built on 57 clinical data inputs. This supports our expectation of further improvement of the hybrid data classifier with data-set extension. Therefore, we may conclude that our ML classifiers built on the combination of clinical and model-derived features significantly improve CRT prediction quality with higher accuracy, sensitivity and specificity.

In addition, we compared the average ML CRT response scores in the responder and non-responder groups provided by the best SVM classifier on hybrid data, the LR classifier on the clinical data and that provided by the ML score calculator from Feeny et al. (2019) (see **Figure 6**). Noteworthy, for the SVM classifier based on the hybrid data, we found a significantly higher average score in the responders vs. nonresponders confirming the predictive power of the ML model. In contrast, the average ML scores predicted by the LR classifier on the clinical data and calculator from Feeny et al. (2019) did not differ between responders and nonresponders in our patient cohort (see **Table 2**).

Therefore, our results clearly show significant advantages ensured by the use of hybrid data combining clinical data with simulated features from personalized electrophysiology models for building ML predictive models of CRT response.

4.2. Feature Selection for Classification Models From Hybrid Data

During classifier development, we tested several feature selection methods for different classifiers and different numbers of features to define the final model with best characteristics (see **Figure 4**). Note that we did not predetermine input features for classifiers based on prior analysis. Instead, the features were automatically selected inside the cross-validation loop as described in section 2. The final feature lists selected for the best predictive models contain 8 inputs. Importantly, the most important feature set contained fewer clinical features compared with model-derived ones. In consistency with ESC guidelines on the significance of pre-operative baseline LV EF_{LBBB} for CRT response, it was selected as the most important feature for the classification model based on the EF10 definition (see **Figure 4**). Interestingly, BMI was selected at the second position in the feature chart. The latter result is in line with study by Hsu et al. (2012), who demonstrated that BMI < 30 kg/m^2 predicted LV EF super-response.

We also tested the importance of model-driven characteristics extracted from the CT/MRI data coupled with model simulations. In our study, LV myocardial damage volume (both absolute and relative to the survival myocardium volume) did not reveal high importance by itself, but the distance from the LV pacing site to the infarct/fibrosis area was selected as the third most important feature for classifiers (see **Figure 4**). We found no significant correlations between this distance and the post-operative values of LV EF improvement ΔEF_{CRT} or ESV reduction ΔESV_{CRT} (see **Supplementary Figure S7**). However, the role of the distance from the LV pacing site to the infarct/fibrosis area in CRT response prediction was supported by a positive correlation between the ML score and the distance ($r = 0.445$, $p = 0.001$). As expected, much higher average distance in the responder vs. nonresponder group (45 ± 28 vs. 28 ± 27 mm, $p = 0.02$, see **Table 2**) was found.

Our findings are consistent with the results of clinical studies which assessed the significance of myocardial infarct size for CRT response. The extent of scar core and gray zone was automatically quantified using cardiac MRI analysis (Nguyên et al., 2018a). The highest percentage of CRT response was observed in patients with low focal scar values and high QRS area before operation. Such area was calculated using vector-cardiography. In study by Marsan et al. (2009) MRI was performed in candidates to derive LV mechanical dyssynchrony and the extent of scar tissue to predict CRT response. Higher LV dyssynchronies were strongly associated with echocardiographic response to CRT, while the total extent of scar correlates with non-response. Importantly, a univariable logistic regression analysis showed that the presence of a match between the LV lead position and a transmural scar was also significantly associated with non-response to CRT. The location of scar in the posterolateral region of the LV, which is empirically thought to be a target site for LV lead implantation, was associated with lower response rates following CRT (Chalil et al., 2007). In study by Pezel et al. (2021), no difference was found in presence and extent of scar between CRT responders and non-responders. However, in non-responders, the LV lead

was more often over an akinetic/dyskinetic area suggesting the presence of tissue lesions, a fibrotic area, or an area with myocardial thickness < 6 mm.

As seen in **Figure 4**, the distance from the LV pacing site to LAT zone was selected as a 4-th feature in the importance list for EF10 definition of CRT response. Accordingly, we revealed a low negative correlation between the distance and ML classification score ($r = -0.263$, $p = 0.048$) suggesting its possible role in CRT response prediction. This was a bit surprising, as no difference in this feature was found between the responders and non-responders (see **Table 2**), as well as no correlation with LV EF improvement in our patient cohort ($r < 0.25, p > 0.05$). However, selection of this distance as an important feature for ML classifier is in line with clinical studies, where the LAT zone was considered as a target area for LV lead deployment (Chumarnaya et al., 2017; Stephansen et al., 2018; Zubarev et al., 2019; Lahiri et al., 2020). In particular, consistent with clinical data, our results indicate that optimal electrode deployment should be guided by a kind of minimum-maximum optimization with respect to the distances from LAT and disease-induced remodeling area, respectively. Preoperative model-based prediction of such optimal pacing site location seems extremely valuable.

Although ventricular mechanical dyssynchrony was considered with respect to CRT improvements (Duckett et al., 2011; Heydari et al., 2012; Stankovic et al., 2014; Chumarnaya et al., 2017), we did not use mechanical dyssynchrony indices in developing our classifiers because not every patient had these features indicated in the retrospective dataset. We did not find a correlation between the ML response scores generated from the selected hybrid data and the mechanical dyssynchrony indices measured in 34 patients at the baseline ($r < 0.25$, $p > 0.05$ for IVD, Tsmax-Tsmin, SD12). This was not consistent with a correlation between the IVD index and postoperative ΔEF in the patient cohort ($r = 0.32$, $p = 0.029$), and a significant difference in the average IDV indices between responders and nonresponders defined by LV EF improvement (75 ± 17 vs. 63 ± 19, $p = 0.013$, see **Table 2**). These controversial findings did not allow us to disprove the possible importance of mechanical dyssynchrony indices for ML response prediction, and this hypothesis should be further evaluated on a dataset of bigger size.

It is especially remarkable that each classification model included simulated characteristics of myocardial activation and ECG from the personalized electrophysiology models under LBBB and BiV pacing selected among the most important features. Our best SVM classifier for the EF10 response definition selected three simulated features TAT/MTV under LBBB and BiV pacing, and QRSd under BIV pacing among the 8 most important ones for EF improvement prediction (see **Figure 4**). In particular, two of the three features TAT/MTV and QRSd under BIV pacing correlated with EF improvement ($r = 0.27$ and $r = -0.31$, $p < 0.05$, see **Supplementary Figure S7**), supporting their importance for ML predictions. Note, the *in-silico* indices of electrical dyssynchrony assessed in our study were not selected as important for ML classifiers. These indices were previously suggested by Villongco et al. (2016), who demonstrated a correlation between the post-operational ESV reduction and the change in the mAT_{STLV} index of inter-ventricular dyssynchrony under BiV pacing against the LBBB baseline on data from 8 patients. In study by Lumens et al. (2015), a combination of clinical data and personalized models of cardiac mechanics and hemodynamics also demonstrated significant role of inter-ventricular electrical dissynchrony in predicting CRT response defined by an improved LV hemodynamic performance assessed via increase in the maximal derivative of LV pressure (dP/dtmax). In contrast, we found no significant correlations between any of the simulated indices of electrical dyssynchrony and echocardiographic CRT response in our cohort ($r < 0.25$, $p > 0.05$). The role of such simulated indices needs further analysis to be performed on a dataset of bigger size.

4.3. Hybrid Dataset Size and Cross-Validation

It is noteworthy that the ML classifiers we developed to predict LV EF improvement can be considered as powerful, especially taking into account the database size of less than 60 entries. In several studies, the ROC AUC was shown to improve significantly with increasing the dataset size from tens to thousands of entries (Feeny et al., 2019). These results allow us to expect further substantial improvement of the quality of the ML classifiers with further increasing the training dataset size. Poor reproducibility of ML results is known as a frequent problem with classifiers developed on small samples. In our case, the restrictive size of the dataset did not allow us to divide data into a conventional 80% training sub-set and 20% testing sub-set, so we had to use 57 Leave-One-Out combinations of data for classifier training.

To confirm the good quality of our classifiers, we tested also a widely-used repeated stratified five-fold cross-validation method with over 1,000 iterations. In this approach we chose 1,000 combinations of 45 training samples from our dataset to train classifiers and the rest 12 samples to test the models. The statistics of the ROC AUC for the five-fold cross-validation approach is shown in **Table 3** (right column) in comparison with that of Leave-One-Out cross-validation (left column). It is seen that average ROC AUCs at five-fold cross-validation are slightly lower than those generated with the Leave-One-Out approach but the latter values fall in the confidence interval of ROC AUC distributions shown by five-fold cross-validation on our dataset. Results demonstrate stability of the ML classifiers we built on our hybrid dataset and confirm the robustness of the ML predictions.

When developing our classifiers, we noticed that the list of features in the cross-validation loop was not steady. This was mainly due to the small sample size. However, even taking this factor into account, we obtained a high accuracy of the constructed classifiers. Testing the SVM classifier for EF10 with a smaller number of features, we found that even for 5 features, the classifier showed the same accuracy as for 8 features (for other criteria of CRT response we observed a lower accuracy with reduced input data dimension). This suggests that with any further increase in the dimension, the classifier cannot converge to optimal solution. Therefore, adding more features to such a small size dataset does not make classifiers more accurate. We

hope that with an increase in the size of dataset, the accuracy of the classifiers will additionally increase due to a more stable feature selection.

4.4. Classifiers for Various Definitions of CRT Response

We used different CRT response definitions to build ML classifiers for our hybrid dataset. Unfortunately, no consensus has been achieved on how to define "response" to CRT Foley et al. (2009), making it difficult to compare different clinical trials and modeling studies. CRT response definition by markers of LV reverse remodeling following device implantation is widely used, and a more than 15% reduction in LV end-systolic volume ($\Delta ESV < -15\%$) is the most widely accepted criterion (Park et al., 2012). In consistency with that, an optimal cutoff value for ΔESV was defined at 13.5% (sensitivity = 0.719, specificity = 0.719) for a 1-Year hierarchical clinical composite end point in patients who underwent CRT (Uhm et al., 2019). Our earlier 278 patients' study by Chumarnaya et al. (2021) revealed a 9% cutoff value for ESV reduction for responders. Surprisingly, in our patient cohort, the grouping by either 10% or 15% cutoff for ESV reduction for responders was the same. Therefore, we used the latter definition (ESV15) to determine a positive response to CRT.

A summary of the statistics for the hybrid dataset labeled according to the ESV15 definition of CRT response is presented in **Supplementary Table S3**. ML classifiers with leave-one-out cross-validation on the hybrid data showed a high performance with best ROC AUC of 0.74 (see **Supplementary Figure S9**), and an accuracy of 0.70, sensitivity of 0.87, specificity of 0.37, ppv of 0.73 and npv of 0.58. See also the classifier characteristics for five-fold cross-validation in **Supplementary Table S5**. The ML scores generated by the best classifier built on the ESV15 criterion correlated with post-operational reduction in ESV ($r = -0.27$, $p = 0.039$, see **Supplementary Figure S10**).

The results are slightly less powerful as compared with classifiers built on the EF10 criterion. The latter showed higher ROC AUCs, similar sensitivity, but higher specificity as compared to ESV15 (see **Figure 4** and **Supplementary Figure S9**, **Table 3** and **Supplementary Table S5**). The ML scores based on ESV15 labeling are higher as compared with EF10 scores (0.69 ± 0.18 vs. 0.40 ± 0.35, $p < 0.01$, respectively) tending to overestimate predictions for the negative response. Note that for both CRT response criteria the average scores are significantly higher in responders vs. nonresponders, indicating good predictive quality of the ML classifiers.

Surprisingly, the sub-sets of 8 most important features selected for classifiers on different response criteria almost did not intersect. For the ESV15 criterion, the pre-operative EDV_{LBBB} showed the primary importance among other inputs in consistency with its correlation with ΔESV_{CRT} ($r = -0.36$, $p < 0.05$). Another clinical feature selected for classification was IHD/DCM index reflecting the etiology of CHF in patients (see **Supplementary Figure S9**). The rest of the selected features were indices derived from CT/MRI data and simulated features in LBBB and BiV modes of activation. Similar to EF10, the distance from the LV pacing site to infarct/fibrosis zone was the third in the feature importance range, and simulated TAT/MTV_{LBBB} was selected for both ESV15 and EF10 criteria together with other model-derived features different between the criteria (see **Figure 4** and **Supplementary Figure S9**).

Unexpectedly, we were not able to generate a predictive model for ESV15 criterion from the clinical feature sub-set suggested in Feeny et al. (2019) with ROC AUC > 0.5 on the dataset for our patient cohort. When we calculated ML scores using the calculator from Feeny et al. (2019) for our responders and nonresponders defined by ESV15 criterion, the average ML scores did not differ between the groups, while the ML scores based on the hybrid data were significantly different (see **Supplementary Table S3**). These findings also point to the power of model-driven data in CRT response prediction.

We also compared the accuracy of ML classifiers built on the hybrid dataset for CRT response defined by 5, 10, 15% LV EF improvement and by coupled EF10 and ESV15 criteria (see **Supplementary Tables S4, S5** in the Materials). For every response definition, our best classifiers demonstrate improved performance as compared with all clinical and ML predictors reported in Feeny et al. (2019). Note again that our hybrid data classifiers were trained on a dataset of much smaller size than previously published (Feeny et al., 2019). Like in Feeny et al. (2019), for different ΔEF criteria an average accuracy of the predictive models increases with the cutoff for the LV EF improvement for CRT responders. However, the sensitivity and predictive positive value of the models tend to decrease with increasing the ΔEF cutoff, while both the specificity and predictive negative value increase. Thus, ML scores tend to underestimate the probability of a super-response. The best balance between sensitivity and specificity was shown for the $\Delta LV\ EF > 10\%$ definition of CRT response which also demonstrates the best ROC AUC among other criteria, thus supporting the choice of this criterion for response evaluation in patients.

4.5. Principal Coordinate Analysis and Unsupervised ML Clustering for CRT Response Prediction

The supervised multi-variable classifiers we discussed in the previous sections were built using feature selection approaches where input values are intrinsic functional characteristics of the processes. Often, in ML algorithms principal component analysis (PCA) is used for data dimension reduction, which allows more objective exclusion of collinearity between the input features. We tested the PCA in combination with Logistic Regression using different numbers of PCs for classifier development. We evaluated ROC AUCs using from 2 to 10 PCs, and obtained the best ROC AUC of 0.70 for 5 PCs (**Supplementary Figure S8**, left panel) with explainable variance of 0.58. This ROC AUC is much lower than the best values demonstrated by other ML classifiers we developed using row feature values.

As we showed in the previous section, classification results depend on the positive CRT response definition used for data labeling. Another ML approach is unsupervised ML

data clustering based on their similarity without the help of class labels. We performed clustering by K-means, used in recent studies for CRT response evaluation (Cikes et al., 2019; Feeny et al., 2020). Using K-means clustering on the two first PCs, we differentiated our dataset into 2 clusters (see **Supplementary Figure S8**, right panel). However, mean ΔEF_{CRT} were not significantly different between the groups (8.0 ± 8.6% vs. 10.7 ± 8.3%, $p = 0.27$), similar to no difference in mean ΔESV_{CRT} (−20 ± 38% vs. −34 ± 31%, $p = 0.15$). Moreover, distribution between the two clusters of CRT responders and non-responders defined by the EF10 criterion shows random assignment to the groups (see **Supplementary Figure S8**, right panel). These findings suggest that unsupervised learning on a small dataset does not allow one to reliably differentiate pre-operational data into groups clearly associated with CRT response characteristics. In contrast, the supervised ML algorithms we developed provided valuable predictions of CRT response showing the potential of model-derived features.

5. LIMITATIONS

There are several limitations in our study that have to be overcome to make our approach actually usable in clinic. First, ventricular geometry in our personalized models was derived from CT images obtained after CRT device implantation, not before it. This was essential for this proof-of-concept study because it allowed us to define the precise location of pacing electrodes and to fit our models to both LBBB and BiV ECG data for the same ventricular geometry thus demonstrating the potential of our models for reproducing real clinical data. Despite supposed difference in the ventricular geometry our simulated ECGs in the LBBB mode had a high correlation with pre-operative clinical ECGs ($r = 0.84$, $p < 0.05$), thus demonstrating the effect of ventricular geometry as being secondary. Of course, the reverse remodeling of the ventricles after CRT may affect the difference in model simulations before and after operation. That is why we primarily focused on the CRT response definition based on the EF improvement which has low-to-moderate correlation with ventricular remodeling in our patient cohort. The main idea of using model-derived biomarkers for CRT response prediction was the possibility to assess the primary effect of ventricular synchronization itself on the electrophysiological characteristics of activation, where changes in the geometry seem less important.

The second limitation is that we used here a simplified Eikonal equation allowing us to reproduce the QRS complex of an ECG but not an entire ECG signal. Moreover, we used a simplified approach to tailor the model to personalized data focusing on the mean QRSd from 12-lead ECG as a target for the parameter identification problem. Then we used the maximal QRSd as a model biomarker for building a classificator. The QRS morphology may provide much more information for tailoring personalized electrophysiology models and then for CRT response predictions. A recent study of Camps et al. (2021) showed a way toward more accurate personalization of the activation processes in ventricles based on the QRS signals recorded in patients, which may be usefull for model improvement. Feeny et al. (2020) also demonstrated the power of the entire ECG signal for ML predictions of CRT response, suggesting that the use of the entire simulated ECG under BiV pacing may further improve ML predictors. In future studies, we will use more adequate mono-domain models to reproduce both activation and repolarisation of myocardium, and will assess the contribution of entire ECG signals to the accuracy of CRT predictive models.

Next, we have shown high importance of the distance from the LV pacing site to the myocardial damage area in ML predictions. In this study, we did not have access to raw MRI data from patients to be able to derive accurate information on post-infarction scar or fibrosis morphology. We used only textual descriptions of the infarct zone location with a segment accuracy within a 17-segment AHA LV model from an expert who evaluated MRI data in patients. There are great examples of using detailed morphology of myocardial remodeling area in personalized cardiac models for predicting the risk of cardiac arrhythmia and patient stratification (Lopez-Perez et al., 2019). We think more objective information on the scar and fibrosis morphology may improve predictive models of CRT response as well.

In this study, for CRT response prediction we used simulated characteristics of ventricular activation and ECG derived from electrophysiological models. The use of the model features characterizing ventricular excitation is justified by the essence of the therapy, which ensures electrical synchronization of ventricular activation, and the success of this synchronization determines the outcome of the operation. However, the goal of CRT implantation is the synchronization of ventricular contraction and subsequent improvement in the mechanical performance of the ventricles. This opens up a further direction for studies using electromechanical models of cardiac activity which are being developed in modeling community including our group (Sugiura et al., 2012; Chabiniok et al., 2016; Isotani et al., 2020) and which are able to predict directly EF, dP/dtmax changes and other mechanical biomarkers of CRT response. Such models were already used for clinical data analysis in CRT patients by several groups (Sermesant et al., 2012; Okada et al., 2017; Lee et al., 2018; Isotani et al., 2020), demonstrating the power of such simulations for CRT response predictions. In particular, we believe that reduced mechanical models using regression or ML approaches to reproduce the behavior of complex 3D models such as developed with our participation (Di Achille et al., 2018) would be the best choice in terms of possible clinical application of model simulations.

In this study, the precise RV/LV pacing lead location was determined from the post-operative CT scans for the patients. Thus, the same pacing sites were used in our BiV model simulations to exclude the effects of uncertainty in lead position on the ML prediction results. This was the first step in the validation of our new technique suggesting its high potential in CRT response prediction. In real practice, however, patient selection should be done before the clinical procedure. The main advantage of using personalized computational models

is the possibility to compute characteristics of ventricular activation from any accessible pacing sites. Indeed, if the coronary sinus anatomy is appropriate (which is possible to derive from CT data), one can predict an accessible area for pacing electrode installation. Hence, this area could be included in a personalized ventricular model to simulate BiV pacing. Moreover, RV/LV electrode locations can be varied throughout the ventricle surfaces. Thus, simulations performed prior to clinical intervention can be used to directly assess the effects of BiV pacing on ventricular activation time, ECG biomarkers and electrical dyssynchrony indices from various pacing sites. Also, it might be helpful during selection the best possible electrode location optimizing ventricular synchronization (or any other optimized function) from model simulations. To sum up, the next step of our approach development is the prediction of pacing lead location prior to interventions by using features extracted from the results of the simulations of BiV pacing.

A number of clinical and simulation studies paid great attention to the possibility to target pacing lead implantation (Bakos et al., 2014; Nguyên et al., 2018b; Sieniewicz et al., 2018). Different criteria for optimal electrode location were discussed in the literature, including optimization of electrical synchronization characteristics, e.g., maximal narrowing of QRSd, or minimization of interventricular dyssynchrony; maximal proximity to the late activation zone or late contraction zone; avoiding the match with infarct zone; or maximizing the mechanical performance characteristics, e.g., dP/dtmax (Bakos et al., 2014; Nguyên et al., 2018a; Isotani et al., 2020; Albatat et al., 2021). The use of simulations from personalized models in CRT response prediction opens the possibility to re-evaluate these hypotheses and suggest a new strategy for implantation planning with allowing for model-based prediction of optimal location for pacing electrodes. We are going to test this hypothesis in a future prospective study.

The long-term goal of CRT is to reduce morbidity and mortality in heart failure patients with reduced left ventricular function and intraventricular conduction delay. Several studies tested ML approaches for predicting outcomes after CRT in terms of patient survival and frequency of adverse events in the longer term after operation (Kalscheur et al., 2018; Tokodi et al., 2020). We had no sufficient data to perform such analysis using simulated data, and this could be another new direction of future studies.

Last but not least, in this study we had a limited data sample from 57 patients. Of course, this number is quite small for ML algorithms operating on thousands of entries with a possibility to use separate subsets for training and testing. However, our predictive models based on hybrid data from clinic and computational models of cardiac activity have demonstrated high performance with accuracy much higher than that demonstrated by predictors developed on clinical data from a thousand of patients. We used feature selection within the cross-validation loop to eliminate any bias factors. The performance of the best classifier was also higher than that of available classifiers based on clinical data (which are based on much larger datasets). In addition, in this study we used simple models that do not tend to overfit on small datasets. Also, we didn't do any hyperparameter search, as a result of which the models could be overfit. We believe that feature selection in the cross-validation loop will be more stable on a larger dataset. This inspires hope that a larger dataset and more informative data from time-dependent simulated signals may further improve CRT response predictions.

6. CONCLUSIONS

We have developed a new technology combing personalized heart modeling and supervised ML techniques to predict CHF patient improvement under CRT. We constructed 57 multimodal image-based personalized models of ventricular geometry and myocardial damage area. The models were used to simulate ventricular activation and ECG on the patient torso at LBBB and BiV pacing. Supervised ML algorithms used features extracted from the results of the simulations combined with additional clinical indices and MRI/CT derived features.

Despite a limited dataset, we have developed several high-performing ML classifiers from the hybrid dataset. The best SVM classifier showed an accuracy of 0.82, sensitivity of 0.85, and specificity of 0.78. The classifier on hybrid data outperformed ML predictors built on clinical data only.

The majority of the most relevant features selected from the hybrid dataset for the ML classifiers were model-driven indices, suggesting their great power for CRT response prediction. Distance from the LV pacing site to the infarct/fibrosis area and features extracted from simulations under BiV pacing were shown as the most important features for patient classification.

The novel proposed approach has great potential clinical implications suggesting patient care improvement. With an ML classifier on hybrid data created and thoroughly validated, one would be to assess with a high degree of accuracy the likelihood of improvement in a particular patient's condition prior to a CRT procedure. In this way, ML scores would be computed for the patient using personalized model simulations for BIV pacing (or other type of stimulation) from various accessible pacing site locations. The range of generated ML scores would classify this patient as a potential responder or nonresponder to the therapy, thus supporting individual selection for it. At the same time, the best pacing site location predicted from the model simulation results and corresponding ML scores could further be used to guide electrode deployment during CRT procedure optimizing the patient output. This technology would be especially effective in the merging of detailed multimodal imaging data on the ventricular geometry and structure of myocardial damage (infarct, fibrosis, inflammation, adipose), coronary sinus anatomy, His-Purkinje conduction system and information on cellular remodeling in the myocardial tissue.

DATA AVAILABILITY STATEMENT

The raw data supporting the conclusions of this article will be made available by the authors, without undue reservation.

ETHICS STATEMENT

The studies involving human participants were reviewed and approved by Institutional Ethical Committee of Almazov National Medical Research Centre. The patients/participants provided their written informed consent to participate in this study.

AUTHOR CONTRIBUTIONS

OS, SK, TC, AD, and AB participated in conceptualization and designing of the study, data collection, and preprocessing. SK implemented the Eikonal and pseudobidomain models, implemented machine learning models and analyzed the data, interpreted the results and was a major contributor to performed study. SZ, AB, and AD contributed in CT images segmentation and anatomical models construction. AD developed Purkinje system model and performed computational simulations for LBBB. AB was a major contributor to the anatomical model preprocessing and enhancement, infarction assignment, and performed computational simulations for BiV pacing. SZ, TL, VL, DL, and TC participated in clinical data collection and preprocessing. TC contributed in clinical data analysis, result interpretation, providing descriptive statistics. VG contributed in designing of the machine learning study. OS made a major contribution to the conceptualization and designing of the study, supervised all stages of study execution and was a major contributor to writing the manuscript. All authors contributed to manuscript preparation and approved the final version of the manuscript.

FUNDING

This work was supported by Russian Science Foundation grant no. 19-14-00134.

SUPPLEMENTARY MATERIAL

The Supplementary Material for this article can be found online at: https://www.frontiersin.org/articles/10.3389/fphys.2021.753282/full#supplementary-material

REFERENCES

Abraham, W. T., Fisher, W. G., Smith, A. L., Delurgio, D. B., Leon, A. R., Loh, E., et al. (2002). Cardiac resynchronization in chronic heart failure. *N. Engl. J. Med.* 346, 1845–1853. doi: 10.1056/NEJMoa013168

Albatat, M., Arevalo, H., Bergsland, J., Strøm, V., Balasingham, I., and Odland, H. H. (2021). Optimal pacing sites in cardiac resynchronization by left ventricular activation front analysis. *Comput. Biol. Med.* 128:104159. doi: 10.1016/j.compbiomed.2020.104159

Aronis, K. N., Prakosa, A., Bergamaschi, T., Berger, R. D., Boyle, P. M., Chrispin, J., et al. (2021). Characterization of the electrophysiologic remodeling of patients with ischemic cardiomyopathy by clinical measurements and computer simulations coupled with machine learning. *Front. Physiol.* 12:684149. doi: 10.3389/fphys.2021.684149

Auricchio, A., and Prinzen, F. W. (2017). Enhancing response in the cardiac resynchronization therapy patient: the 3B perspective—bench, bits, and bedside. *JACC Clin. Electrophysiol.* 3, 1203–1219. doi: 10.1016/j.jacep.2017.08.005

Bakos, Z., Markstad, H., Ostenfeld, E., Carlsson, M., Roijer, A., and Borgquist, R. (2014). Combined preoperative information using a bullseye plot from speckle tracking echocardiography, cardiac CT scan, and MRI scan: Targeted left ventricular lead implantation in patients receiving cardiac resynchronization therapy. *Eur. Heart J. Cardiovasc. Imaging* 15, 523–531. doi: 10.1093/ehjci/jet233

Bayer, J. D., Blake, R. C., Plank, G., and Trayanova, N. A. (2012). A novel rule-based algorithm for assigning myocardial fiber orientation to computational heart models. *Ann. Biomed. Eng.* 40, 2243–2254. doi: 10.1007/s10439-012-0593-5

Bishop, M. J., and Plank, G. (2011). Bidomain ECG simulations using an augmented monodomain model for the cardiac source. *IEEE Trans. Biomed. Eng.* 58, 2297–2307. doi: 10.1109/TBME.2011.2148718

Bristow, M. R., Saxon, L. A., Boehmer, J., Krueger, S., Kass, D. A., De Marco, T., et al. (2004). Cardiac-resynchronization therapy with or without an implantable defibrillator in advanced chronic heart failure. *N. Engl. J. Med.* 350, 2140–2150. doi: 10.1056/NEJMoa032423

Camps, J., Lawson, B., Drovandi, C., Minchole, A., Wang, Z. J., Grau, V., et al. (2021). Inference of ventricular activation properties from non-invasive electrocardiography. *Med. Image Anal.* 73:102143. doi: 10.1016/j.media.2021.102143

Cerqueira, M. D., Weissman, N. J., Dilsizian, V., Jacobs, A. K., Kaul, S., Laskey, W. K., et al. (2002). Standardized myocardial sementation and nomenclature for tomographic imaging of the heart: a statement for healthcare professionals from the cardiac imaging committee of the council on clinical cardiology of the american heart association. *Circulation* 105, 539–542. doi: 10.1161/hc0402.102975

Chabiniok, R., Wang, V. Y., Hadjicharalambous, M., Asner, L., Lee, J., Sermesant, M., et al. (2016). Multiphysics and multiscale modelling, data–model fusion and integration of organ physiology in the clinic: ventricular cardiac mechanics. *Interface Focus* 6:20150083. doi: 10.1098/rsfs.2015.0083

Chalil, S., Foley, P. W., Muyhaldeen, S. A., Patel, K. C., Yousef, Z. R., Smith, R. E., et al. (2007). Late gadolinium enhancement-cardiovascular magnetic resonance as a predictor of response to cardiac resynchronization therapy in patients with ischaemic cardiomyopathy. *Europace* 9, 1031–1037. doi: 10.1093/europace/eum133

Chumarnaya, T., Lyubimtseva, T., Solodushkin, S., Lebedeva, V., Lebedev, D., and Solovyova, O. (2021). Evaluation of the effectiveness of cardiac resynchronization therapy in the long-term postoperative period. *Russian J. Cardiol. Accepted*. doi: 10.15829/1560-4071-2021-4531

Chumarnaya, T., Trifanova, M., Lyubimtseva, T., Lebedeva, V., Poroshin, I., Trukshina, M., et al. (2017). Impact of inter-ventricular lead distance on cardiac resynchronization therapy outcomes. *Comput. Cardiol.* 44, 1–4. doi: 10.22489/CinC.2017.290-106

Cikes, M., Sanchez-Martinez, S., Claggett, B., Duchateau, N., Piella, G., Butakoff, C., et al. (2019). Machine learning-based phenogrouping in heart failure to identify responders to cardiac resynchronization therapy. *Eur. J. Heart Fail.* 21, 74–85. doi: 10.1002/ejhf.1333

Di Achille, P., Harouni, A., Khamzin, S., Solovyova, O., Rice, J. J., and Gurev, V. (2018). Gaussian process regressions for inverse problems and parameter searches in models of ventricular mechanics. *Front. Physiol.* 9:1002. doi: 10.3389/fphys.2018.01002

Dobrzynski, H., Anderson, R. H., Atkinson, A., Borbas, Z., D'Souza, A., Fraser, J. F., et al. (2013). Structure, function and clinical relevance of the cardiac conduction system, including the atrioventricular ring and outflow tract tissues. *Pharmacol. Ther.* 139, 260–288. doi: 10.1016/j.pharmthera.2013.04.010

Duckett, S. G., Ginks, M., Shetty, A. K., Bostock, J., Gill, J. S., Hamid, S., et al. (2011). Invasive acute hemodynamic response to guide left ventricular lead implantation predicts chronic remodeling in patients undergoing cardiac resynchronization therapy. *J. Am. Coll Cardiol.* 58, 1128–1136. doi: 10.1016/j.jacc.2011.04.042

Feeny, A. K., Rickard, J., Patel, D., Toro, S., Trulock, K. M., Park, C. J., et al. (2019). Machine learning prediction of response to cardiac resynchronization therapy. *Circ. Arrhythm. Electrophysiol.* 12:e007316. doi: 10.1161/CIRCEP.119.007316

Feeny, A. K., Rickard, J., Trulock, K. M., Patel, D., Toro, S., Moennich, L. A., et al. (2020). Machine learning of 12-lead qrs waveforms to identify cardiac resynchronization therapy patients with differential outcomes. *Circ. Arrhythm. Electrophysiol.* 13:e008210. doi: 10.1161/CIRCEP.119.008210

Foley, P. W., Leyva, F., and Frenneaux, M. P. (2009). What is treatment success in cardiac resynchronization therapy? *Europace* 11(Suppl. 5):v58–v65. doi: 10.1093/europace/eup308

Franzone, P. C., and Guerri, L. (1993). Spreading of excitation in 3-d models of the anisotropic cardiac tissue. i. validation of the eikonal model. *Math. Biosci.* 113, 145–209. doi: 10.1016/0025-5564(93)90001-Q

Heijman, J., Sutanto, H., Crijns, H. J. G. M., Nattel, S., and Trayanova, N. A. (2021). Computational models of atrial fibrillation: achievements, challenges, and perspectives for improving clinical care. *Cardiovasc. Res.* 117, 1682–1699. doi: 10.1093/cvr/cvab138

Heydari, B., Jerosch-Herold, M., and Kwong, R. Y. (2012). Imaging for planning of cardiac resynchronization therapy. *JACC Cardiovasc. Imaging* 5, 93–110. doi: 10.1016/j.jcmg.2011.11.006

Hsu, J. C., Solomon, S. D., Bourgoun, M., McNitt, S., Goldenberg, I., Klein, H., et al. (2012). Predictors of super-response to cardiac resynchronization therapy and associated improvement in clinical outcome: the MADIT-CRT (multicenter automatic defibrillator implantation trial with cardiac resynchronization therapy) study. *J. Am. Coll. Cardiol.* 59, 2366–2373. doi: 10.1016/j.jacc.2012.01.065

Hu, S.-Y., Santus, E., Forsyth, A. W., Malhotra, D., Haimson, J., Chatterjee, N. A., et al. (2019). Can machine learning improve patient selection for cardiac resynchronization therapy? *PLoS ONE* 14:e0222397. doi: 10.1371/journal.pone.0222397

Huntjens, P. R., Ploux, S., Strik, M., Walmsley, J., Ritter, P., Haissaguerre, M., et al. (2018). Electrical substrates driving response to cardiac resynchronization therapy: a combined clinical-computational evaluation. *Circ. Arrhythm. Electrophysiol.* 11:e005647. doi: 10.1161/CIRCEP.117.005647

Isotani, A., Yoneda, K., Iwamura, T., Watanabe, M., ichi Okada, J., Washio, T., et al. (2020). Patient-specific heart simulation can identify non-responders to cardiac resynchronization therapy. *Heart Vessels.* 35, 1135–1147. doi: 10.1007/s00380-020-01577-1

Kalscheur, M. M., Kipp, R. T., Tattersall, M. C., Mei, C., Buhr, K. A., Demets, D. L., et al. (2018). Machine learning algorithm predicts cardiac resynchronization therapy outcomes: lessons from the COMPANION trial. *Circ. Arrhythm. Electrophysiol.* 11:e005499. doi: 10.1161/CIRCEP.117.005499

Keener, J. P. (1991). An eikonal-curvature equation for action potential propagation in myocardium. *J. Math. Biol.* 29, 629–651. doi: 10.1007/BF00163916

Krittanawong, C., Zhang, H., Wang, Z., Aydar, M., and Kitai, T. (2017). Artificial intelligence in precision cardiovascular medicine. *J. Am. Coll. Cardiol.* 69, 2657–2664. doi: 10.1016/j.jacc.2017.03.571

Lahiri, A., Chahadi, F. K., Ganesan, A. N., and McGavigan, A. D. (2020). Characteristics that predict response after cardiac resynchronization therapy. *Curr. Cardiovasc. Risk Rep.* 14, 1–10. doi: 10.1007/s12170-020-00640-w

Lee, A., Nguyen, U., Razeghi, O., Gould, J., Sidhu, B., Sieniewicz, B., et al. (2019). A rule-based method for predicting the electrical activation of the heart with cardiac resynchronization therapy from non-invasive clinical data. *Med. Image Anal.* 57, 197–213. doi: 10.1016/j.media.2019.06.017

Lee, A. W. C., Mendonca Costa, C., Strocchi, M., Rinaldi, C. A., and Niederer, S. A. (2018). Computational modeling for cardiac resynchronization therapy. *J. Cardiovasc. Transl. Res.* 11, 92–108. doi: 10.1007/s12265-017-9779-4

Logg, A., and Wells, G. N. (2010). Dolfin: automated finite element computing. *ACM Trans. Math. Softw.* 37, 1–18. doi: 10.1145/1731022.1731030

Lopez-Jimenez, F., Attia, Z., Arruda-Olson, A. M., Carter, R., Chareonthaitawee, P., Jouni, H., et al. (2020). Artificial intelligence in cardiology: present and future. *Mayo Clin. Proc.* 95, 1015–1039. doi: 10.1016/j.mayocp.2020.01.038

Lopez-Perez, A., Sebastian, R., Izquierdo, M., Ruiz, R., Bishop, M., and Ferrero, J. M. (2019). Personalized cardiac computational models: from clinical data to simulation of infarct-related ventricular tachycardia. *Front. Physiol.* 10:580. doi: 10.3389/fphys.2019.00580

Lumens, J., Tayal, B., Walmsley, J., Delgado-Montero, A., Huntjens, P. R., Schwartzman, D., et al. (2015). Differentiating electromechanical from non-electrical substrates of mechanical discoordination to identify responders to cardiac resynchronization therapy. *Circ. Cardiovasc. Imaging* 8:e003744. doi: 10.1161/CIRCIMAGING.115.003744

Marsan, N. A., Westenberg, J. J., Ypenburg, C., van Bommel, R. J., Roes, S., Delgado, V., et al. (2009). Magnetic resonance imaging and response to cardiac resynchronization therapy: relative merits of left ventricular dyssynchrony and scar tissue. *Eur. Heart J.* 30, 2360–2367. doi: 10.1093/eurheartj/ehp280

Mullens, W., Grimm, R. A., Verga, T., Dresing, T., Starling, R. C., Wilkoff, B. L., et al. (2009). Insights from a cardiac resynchronization optimization clinic as part of a heart failure disease management program. *J. Am. Coll. Cardiol.* 53, 765–773. doi: 10.1016/j.jacc.2008.11.024

Nguyên, U. C., Claridge, S., Vernooy, K., Engels, E. B., Razavi, R., Rinaldi, C. A., et al. (2018a). Relationship between vectorcardiographic QRSarea, myocardial scar quantification, and response to cardiac resynchronization therapy. *J. Electrocardiol.* 51, 457–463. doi: 10.1016/j.jelectrocard.2018.01.009

Nguyên, U. C., Cluitmans, M. J., Luermans, J. G., Strik, M., de Vos, C. B., Kietselaer, B. L., et al. (2018b). Visualisation of coronary venous anatomy by computed tomography angiography prior to cardiac resynchronisation therapy implantation. *Neth. Heart J.* 26, 433–444. doi: 10.1007/s12471-018-1132-2

Okada, J., i., Washio, T., Nakagawa, M., Watanabe, M., Kadooka, Y., et al. (2017). Multi-scale, tailor-made heart simulation can predict the effect of cardiac resynchronization therapy. *J. Mol. Cell. Cardiol.* 108, 17–23. doi: 10.1016/j.yjmcc.2017.05.006

Ono, N., Yamaguchi, T., Ishikawa, H., Arakawa, M., Takahashi, N., Saikawa, T., et al. (2009). Morphological varieties of the Purkinje fiber network in mammalian hearts, as revealed by light and electron microscopy. *Arch. Histol. Cytol.* 72, 139–149. doi: 10.1679/aohc.72.139

Park, M. Y., Altman, R. K., Orencole, M., Kumar, P., Parks, K. A., Heist, K. E., et al. (2012). Characteristics of responders to cardiac resynchronization therapy: the impact of echocardiographic left ventricular volume. *Clin. Cardiol.* 35, 779–780. doi: 10.1002/clc.22043

Pezel, T., Mika, D., Logeart, D., Cohen-Solal, A., Beauvais, F., Henry, P., et al. (2021). Characterization of non-response to cardiac resynchronization therapy by post-procedural computed tomography. *Pacing Clin. Electrophysiol.* 44, 135–144. doi: 10.1111/pace.14134

Pezzuto, S., Kal'avský, P., Potse, M., Prinzen, F. W., Auricchio, A., and Krause, R. (2017). Evaluation of a rapid anisotropic model for ecg simulation. *Front. Physiol.* 8:265. doi: 10.3389/fphys.2017.00265

Potse, M., Krause, D., Kroon, W., Murzilli, R., Muzzarelli, S., Regoli, F., et al. (2014). Patient-specific modelling of cardiac electrophysiology in heart-failure patients. *Europace* 16(Suppl_4):iv56–iv61. doi: 10.1093/europace/euu257

Pullan, A. J., Tomlinson, K. A., and Hunter, P. J. (2006). A finite element method for an eikonal equation model of myocardial excitation wavefront propagation. *SIAM J. Appl. Math.* 63, 324–350. doi: 10.1137/S0036139901389513

Sahli Costabal, F., Hurtado, D. E., and Kuhl, E. (2016). Generating Purkinje networks in the human heart. *J. Biomech.* 49, 2455–2465. doi: 10.1016/j.jbiomech.2015.12.025

Sermesant, M., Chabiniok, R., Chinchapatnam, P., Mansi, T., Billet, F., Moireau, P., et al. (2012). Patient-specific electromechanical models of the heart for the prediction of pacing acute effects in CRT: a preliminary clinical validation. *Med. Image Anal.* 16, 201–215. doi: 10.1016/j.media.2011.07.003

Shade, J. K., Cartoski, M. J., Nikolov, P., Prakosa, A., Doshi, A., Binka, E., et al. (2020). Ventricular arrhythmia risk prediction in repaired tetralogy of fallot using personalized computational cardiac models. *Heart Rhythm.* 17, 408–414. doi: 10.1016/j.hrthm.2019.10.002

Shade, J. K., Prakosa, A., Popescu, D. M., Yu, R., Okada, D. R., Chrispin, J., et al. (2021). Predicting risk of sudden cardiac death in patients with cardiac sarcoidosis using multimodality imaging and personalized heart modeling in a multivariable classifier. *Sci. Adv.* 7, 8020–8048. doi: 10.1126/sciadv.abi8020

Sieniewicz, B. J., Gould, J., Porter, B., Sidhu, B. S., Behar, J. M., Claridge, S., et al. (2018). Optimal site selection and image fusion guidance technology to facilitate cardiac resynchronization therapy. *Expert. Rev. Med. Devices* 15, 555–570. doi: 10.1080/17434440.2018.1502084

Stankovic, I., Aarones, M., Smith, H. J., Vörös, G., Kongsgaard, E., Neskovic, A. N., et al. (2014). Dynamic relationship of left-ventricular dyssynchrony and

contractile reserve in patients undergoing cardiac resynchronization therapy. *Eur. Heart J.* 35, 48–55. doi: 10.1093/eurheartj/eht294

Stephansen, C., Sommer, A., Kronborg, M. B., Jensen, J. M., Bouchelouche, K., and Nielsen, J. C. (2018). Electrically guided versus imaging-guided implant of the left ventricular lead in cardiac resynchronization therapy: a study protocol for a double-blinded randomized controlled clinical trial (ElectroCRT). *Trials* 19:600. doi: 10.1186/s13063-018-2930-y

Sugiura, S., Washio, T., Hatano, A., Okada, J., Watanabe, H., and Hisada, T. (2012). Multi-scale simulations of cardiac electrophysiology and mechanics using the University of Tokyo heart simulator. *Prog. Biophys. Mol. Biol.* 110, 380–389. doi: 10.1016/j.pbiomolbio.2012.07.001

Sung, E., Prakosa, A., Aronis, K. N., Zhou, S., Zimmerman, S. L., Tandri, H., et al. (2020). Personalized digital-heart technology for ventricular tachycardia ablation targeting in hearts with infiltrating adiposity. *Circ. Arrhythm. Electrophysiol.* 13:e008912. doi: 10.1161/CIRCEP.120.008912

ten Tusscher, K. H. W. J. (2006). Alternans and spiral breakup in a human ventricular tissue model. *AJPHeart Circ. Physiol.* 291, H1088–H1100. doi: 10.1152/ajpheart.00109.2006

Tokodi, M., Behon, A., Merkel, E. D., Kovács, A., Tősér, Z., Sárkány, A., et al. (2021). Sex-specific patterns of mortality predictors among patients undergoing cardiac resynchronization therapy: a machine learning approach. *Front. Cardiovasc. Med.* 8:87. doi: 10.3389/fcvm.2021.611055

Tokodi, M., Schwertner, W. R., Kovács, A., Tősér, Z., Staub, L., Sárkány, A., et al. (2020). Machine learning-based mortality prediction of patients undergoing cardiac resynchronization therapy: the SEMMELWEIS-CRT score. *Eur. Heart J.* 41, 1747–1756. doi: 10.1093/eurheartj/ehz902

Uhm, J. S., Oh, J., Cho, I. J., Park, M., Kim, I. S., Jin, M. N., et al. (2019). Left ventricular end-systolic volume can predict 1-year hierarchical clinical composite end point in patients with cardiac resynchronization therapy. *Yonsei Med. J.* 60, 48–55. doi: 10.3349/ymj.2019.60.1.48

Vernooy, K., van Deursen, C. J. M., Strik, M., and Prinzen, F. W. (2014). Strategies to improve cardiac resynchronization therapy. *Nat. Rev. Cardiol.* 11, 481–493. doi: 10.1038/nrcardio.2014.67

Villongco, C. T., Krummen, D. E., Omens, J. H., and McCulloch, A. D. (2016). Non-invasive, model-based measures of ventricular electrical dyssynchrony for predicting CRT outcomes. *Europace* 18(Suppl_4):iv104–iv112. doi: 10.1093/europace/euw356

Yu, C. M., Bax, J. J., and Gorcsan, J. (2009). Critical appraisal of methods to assess mechanical dyssynchrony. *Curr. Opin. Cardiol.* 24, 18–28. doi: 10.1097/HCO.0b013e32831bc34e

Zubarev, S., Chmelevsky, M., Potyagaylo, D., Budanova, M., Trukshina, M., Rud, S., et al. (2019). "Noninvasive electrocardiographic imaging with magnetic resonance tomography in candidates for cardiac resynchronization therapy," in *Computing in Cardiology, 2019-September* (Singapore: IEEE).

Conflict of Interest: VG was employed by IBM Research.

The remaining authors declare that the research was conducted in the absence of any commercial or financial relationships that could be construed as a potential conflict of interest.

Publisher's Note: All claims expressed in this article are solely those of the authors and do not necessarily represent those of their affiliated organizations, or those of the publisher, the editors and the reviewers. Any product that may be evaluated in this article, or claim that may be made by its manufacturer, is not guaranteed or endorsed by the publisher.

frontiers in Physiology

ORIGINAL RESEARCH
published: 17 December 2021
doi: 10.3389/fphys.2021.782176

Rotor Localization and Phase Mapping of Cardiac Excitation Waves Using Deep Neural Networks

Jan Lebert[1], *Namita Ravi*[1,2], *Flavio H. Fenton*[3] *and Jan Christoph*[1]*

[1] Cardiovascular Research Institute, University of California, San Francisco, San Francisco, CA, United States, [2] Yale School of Medicine, Yale University, New Haven, CT, United States, [3] School of Physics, Georgia Institute of Technology, Atlanta, GA, United States

The analysis of electrical impulse phenomena in cardiac muscle tissue is important for the diagnosis of heart rhythm disorders and other cardiac pathophysiology. Cardiac mapping techniques acquire local temporal measurements and combine them to visualize the spread of electrophysiological wave phenomena across the heart surface. However, low spatial resolution, sparse measurement locations, noise and other artifacts make it challenging to accurately visualize spatio-temporal activity. For instance, electro-anatomical catheter mapping is severely limited by the sparsity of the measurements, and optical mapping is prone to noise and motion artifacts. In the past, several approaches have been proposed to create more reliable maps from noisy or sparse mapping data. Here, we demonstrate that deep learning can be used to compute phase maps and detect phase singularities in optical mapping videos of ventricular fibrillation, as well as in very noisy, low-resolution and extremely sparse simulated data of reentrant wave chaos mimicking catheter mapping data. The self-supervised deep learning approach is fundamentally different from classical phase mapping techniques. Rather than encoding a phase signal from time-series data, a deep neural network instead learns to directly associate phase maps and the positions of phase singularities with short spatio-temporal sequences of electrical data. We tested several neural network architectures, based on a convolutional neural network (CNN) with an encoding and decoding structure, to predict phase maps or rotor core positions either directly or indirectly via the prediction of phase maps and a subsequent classical calculation of phase singularities. Predictions can be performed across different data, with models being trained on one species and then successfully applied to another, or being trained solely on simulated data and then applied to experimental data. Neural networks provide a promising alternative to conventional phase mapping and rotor core localization methods. Future uses may include the analysis of optical mapping studies in basic cardiovascular research, as well as the mapping of atrial fibrillation in the clinical setting.

Keywords: atrial fibrillation, cardiac electrophysiology, spiral waves, phase singularity, catheter mapping, optical mapping, neural networks, artificial intelligence

OPEN ACCESS

Edited by:
Elena Tolkacheva, University of Minnesota Twin Cities, United States

Reviewed by:
Caroline Helen Roney, King's College London, United Kingdom
Maria S. Guillem, Universitat Politècnica de València, Spain

***Correspondence:**
Jan Christoph
jan.christoph@ucsf.edu

Specialty section:
This article was submitted to Cardiac Electrophysiology, a section of the journal Frontiers in Physiology

Received: *23 September 2021*
Accepted: *11 November 2021*
Published: *17 December 2021*

Citation:
Lebert J, Ravi N, Fenton FH and Christoph J (2021) Rotor Localization and Phase Mapping of Cardiac Excitation Waves Using Deep Neural Networks. Front. Physiol. 12:782176. doi: 10.3389/fphys.2021.782176

1. INTRODUCTION

Cardiac muscle cells constantly oscillate between an "excited" and a "resting" electrical state, allowing us to assign a phase ϕ to the state of each cell during this cycle. Cardiac mapping techniques, such as catheter electrode mapping or voltage-sensitive optical mapping, measure the spread of electrical impulses across the heart surface and visualize the spatio-temporal evolution of electrical activity. These visualizations are frequently depicted as phase maps $\phi(\vec{x}, t)$, which uniquely represent the time course of the action potential in each location of the tissue and express the synchronicity of the activation in both space and time. Phase maps are particularly suited to characterize the spatio-temporal disorganization of the electrical wave dynamics underlying cardiac fibrillation (Winfree, 1989; Gray et al., 1998; Witkowski et al., 1998; Nash et al., 2006; Umapathy et al., 2010; Christoph et al., 2018). During fibrillation, the heart's electrophysiology degenerates into a dynamic state driven by chaotic wave phenomena, which propagate rapidly through the heart muscle and cause irregular, asynchronous contractions. These inherently three-dimensional wave phenomena can be observed on the heart's surface using optical mapping, where they often take the shape of rapidly rotating spiral vortex waves or "rotors". Phase maps depict these rotors as pinwheel patterns, with each pinwheel consisting of lines of equal phase that merge at the rotational center of the vortex wave. The topological defect at the vortex's core is referred to as a phase singularity. During ventricular fibrillation, phase singularities move across the heart surface, interact with each other, and undergo pairwise creation and annihilation. Phase singularities provide a means to automatically localize and track reentrant vortex waves through the heart muscle. They can be used to track wavebreaks (Liu et al., 2003; Zaitsev et al., 2003), or interactions of vortex cores with the underlying substrate (Valderrabano et al., 2003), to simplify the visualization of three-dimensional scroll wave dynamics (Fenton and Karma, 1998; Clayton et al., 2006), and to measure fluctuations in the complexity of the dynamics (Zaritski et al., 2004). In short, phase singularities are an elegant way to characterize high-frequency arrhythmias that involve reentrant vortex waves, such as ventricular fibrillation (VF) or atrial fibrillation (AF) (Nattel et al., 2017).

Various methods have been proposed to compute phase maps and phase singularities (PS). These methods have been applied to both simulations of VF (Fenton and Karma, 1998; Bray et al., 2001; Clayton et al., 2006) and AF (Hwang et al., 2016; Rodrigo et al., 2017), as well as experimental data, including electrode recordings of human VF (Nash et al., 2006; Umapathy et al., 2010) and human AF (Kuklik et al., 2015; Podziemski et al., 2018; Abad et al., 2021) optical maps of the transmembrane potential during VF (Gray et al., 1998; Iyer and Gray, 2001; Bray and Wikswo, 2002; Rogers, 2004; Christoph et al., 2018) and AF (Yamazaki et al., 2012; Guillem et al., 2016) in isolated hearts, optical maps of action potential spiral waves in cardiac cell cultures (Bursac et al., 2004; Entcheva and Bien, 2006; Munoz et al., 2007; Umapathy et al., 2010; You et al., 2017), and time-varying 3D maps of mechanical strain waves measured during VF in isolated hearts using ultrasound (Christoph et al., 2018). However, phase maps and PS are prone to measurement artifacts and deficits caused by inadequate processing of the measurement data, particularly when the data is noisy or sparse (King et al., 2017; Kuklik et al., 2017; Rodrigo et al., 2017; Roney et al., 2017, 2019; You et al., 2017). Noise and motion artifacts are a frequent issue when analyzing optical mapping recordings (Zou et al., 2002; Christoph and Luther, 2018). Electrode mapping, used in both basic research and the clinical setting, is limited by low spatial resolution, or sparsity, even with the use of multi-electrode arrays and 64-lead basket catheters.

Mapping fibrillatory wave phenomena at low resolutions can lead to misrepresentation of the underlying dynamics. For example, low resolution phase mapping has been shown to create false positive detections of PS (King et al., 2017; Kuklik et al., 2017; Roney et al., 2017, 2019; You et al., 2017), contributing to much uncertainty in the imaging-based diagnosis of AF, a field in which rotors remain a highly controversial concept (Aronis et al., 2017; Nattel et al., 2017; Schotten et al., 2020). Mapping of AF would greatly benefit from computational methods, which could account for low spatial resolution and produce reliable visualizations of electrical phenomena from sparse and noisy spatio-temporal electrical signals.

In this study, we demonstrate that deep convolutional neural networks (CNNs) can be used to compute phase maps and phase singularities from short spatio-temporal sequences of electrical excitation wave patterns, even if these patterns are very sparse and very noisy. We use variations of two-stage encoder-decoder CNNs with an encoding stage, a latent space, and a decoding stage (see **Figure 2**). The neural network associates electrical excitation wave patterns with phase maps and phase singularity (PS) positions during a training procedure. After training, it is subsequently able to translate electrical excitation wave patterns into phase maps and PS when applied to new, previously unseen data. We tested two versions of the neural network with an integrated convolutional long short-term memory (LSTM) module in the latent space of the original encoder-decoder architecture and a U-Net architecture with skip-connections. Regardless of the particular architecture, the network was able to predict phase maps and PS in both experimental and synthetic data robustly and with high accuracy. When presented with sparse electrical data from a short temporal sequence of only 1–5 snapshots of electrical activity, the network maintained a robust accuracy level, even in the presence of strong noise. The approach may supersede more classical approaches due to its efficiency, its robustness against noise, and its ability to inter- and extrapolate missing measurement data with only minimal spatial and temporal information.

1.1. Phase Mapping and Phase Singularity Detection Techniques

Phase maps and phase singularities (PS) have been used to characterize cardiac fibrillation for over 30 years (Winfree, 1989), and various methods were introduced to compute PS either directly or indirectly (see **Figure 1C**). In computer simulations,

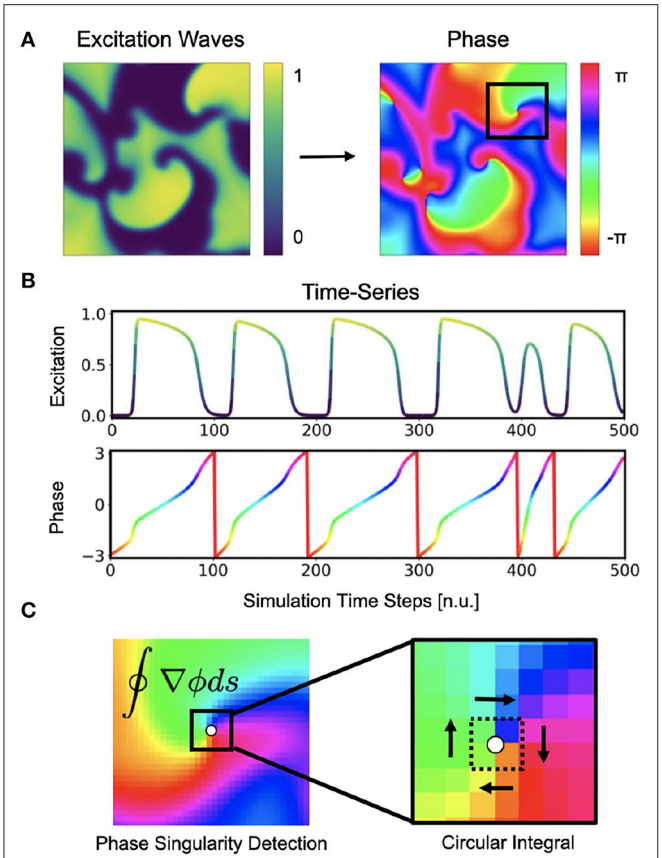

FIGURE 1 | Cardiac electrical excitation wave pattern and conversion into corresponding phase map for the localization of rotor core positions or phase singularities (PS). **(A)** Simulated electric spiral wave chaos pattern represented by transmembrane potential $V \in [0, 1]$ (n.u., normalized units) and corresponding phase pattern with phase angle $\phi \in [-\pi, \pi]$. **(B)** Time-series data showing a series of action potentials $V(t)$ and their representation as a phase signal $\phi(t)$ computed using the Hilbert transform. **(C)** Classical phase singularity (PS) developed by Iyer and Gray (2001) using a circular integral (2×2 kernel) for the localization of spiral cores. Here the method is used to generate PS training data for deep learning-based PS detection (see **Figure 2**). Detailed field of view of region highlighted by black box in **(A)**.

the computation of a phase state or PS is straight-forward as the dynamic variables from the equations describing the local electrical state are readily available in the simulation and can be used to define a phase angle instantaneously (Krinsky et al., 1992). For instance, with V and r for electrical excitation and refraction, respectively, see Equations (4)–(5), the phase angle can be defined as $\phi = \arctan2(V, r)$ (see also **Figure 3A**). Likewise, level-set methods using isocontour lines of two dynamic variables, such as V and r, can be used to locate PS directly as the intersection points of these isocontours (Barkley et al., 1990). However, with experimental data, there is typically only one measured variable, such as the transmembrane voltage or an electrogram, and it is accordingly not possible to define a phase without additional temporal information. With experimental data, it becomes necessary to construct a phase signal $\phi(t)$ from a single measured time-series $V(t)$ using techniques such as (i) delay embedding (Gray et al., 1998):

$$\phi(t) = \arctan2(V(t), V(t+\tau))) \quad (1)$$

with an embedding delay τ, typically defined as ∼1/4 of the average cycle length or the first zero-crossing of the auto-correlation function, or (ii) the Hilbert transform $\mathcal{H}(t)$, which generates the complex analytical signal of a periodic signal from which in turn the phase

$$\phi(t) = \mathrm{Re}(\mathcal{H}(t)) \quad (2)$$

can be derived (Bray and Wikswo, 2002). The most intuitive approach to compute a time-dependent phase signal $\phi(t)$ of a sequence of action potentials is to detect the upstrokes of two subsequent action potentials and to define a piecewise linear continuous function $\phi_L(t)$, which linearly interpolates the phase angle from $-\pi$ to π between the two upstrokes. The Hilbert transform generates a phase signal $\phi_{\mathcal{H}}(t)$ which is very similar to the linearly interpolated phase signal $\phi_L(t)$ (see **Figure 1B**).

Phase singularities can then be calculated (see **Figure 1C**), by using the circular line integral method developed by Iyer and Gray (2001) summing the gradient of the phase along a closed circular path s around a point $\vec{x} = (x, y)$ in the phase plane:

$$\oint \nabla\phi(x, y; t)\mathrm{d}s = \pm 2\pi \quad (3)$$

If the circular path is sufficiently small (typically around 2×2 pixels), the integral yields $\pm 2\pi$ when the line integral encloses a phase singularity (the sign indicates chirality), or 0 if it does not enclose a phase singularity. As the line integral method calculates the spatial gradient of the phase, it is very sensitive to noise and requires continuous and smooth phase maps. Therefore, much prior work has focused on improving the robustness of phase mapping and PS detection methods under more realistic conditions, e.g. with noise or other artifacts that typically occur with, for instance, contact electrode measurements. Zou et al. (2002) further refined the line integral method using convolutions and image analysis. Kuklik et al. (2015) introduced sinusoidal recomposition to remove undesired high-frequency components during the computation of phase signals using the Hilbert transform. In contrast to the line integration method, Tomii et al. (2016) proposed computing the phase variance to locate PS. Similarly, Lee et al. (2016) introduced a so-called "location-centric" method to locate PS, the method only requiring temporal information about the voltage at the core. Li et al. (2018) introduced a Jacobian-determinant method using delay embedding for identifying PS also without explicitly computing a phase. Marcotte and Grigoriev (2017) and Gurevich et al. introduced level-set methods to compute PS in noisy conditions and demonstrated the robustness of the approach with VF optical mapping data (Gurevich et al., 2017; Gurevich and Grigoriev, 2019). Vandersickel et al. (2019) proposed to use graph theory to detect rotors and focal patterns from arbitrarily positioned measurement sites. Mulimani et al. (2020) used CNNs to detect the core regions of simulated spiral waves using a CNN-based classification approach and discriminating

sub-regions containing spiral wave tips from areas exhibiting other dynamics, and consequently generated low-resolution heat maps indicating the likely and approximate core regions of spiral waves. Very similarly, Alhusseini et al. (2020) used CNNs to classify and discriminate rotational and non-rotational tiles in maps of AF acquired with basket catheter electrode mapping. Lastly, Li et al. (2020) provided a comparison of 4 different PS detection algorithms applied to AF and found that results can vary significantly.

2. METHODS

We developed a two-stage deep convolutional neural network (CNN) with encoder and decoder architecture and trained the network with pairs of two-dimensional maps showing electrical excitation wave patterns and corresponding "ground truth" phase maps and phase singularity (PS) locations. The training was performed with both simulation data and experimental data, which was obtained in voltage-sensitive optical mapping experiments in two different species during ventricular fibrillation (VF). After training, the network was applied to new data and used to predict phase maps or the positions of PS from "unseen" excitation wave patterns.

2.1. Neural Network Architecture

The architecture of our neural networks comprises an encoding stage, a latent space, and a decoding stage (see **Figure 2**). The neural networks are designed to translate an arbitrary two-dimensional electrical excitation wave pattern or a short sequence of two-dimensional excitation wave patterns into either a corresponding two-dimensional phase map, or predict the positions of phase singular points (PS) in the electrical maps. We developed three phase map prediction neural network models M1, M2, and M3, and two different PS prediction neural network models M1A and M1B which are based on M1. The three phase map prediction models are a basic encoder-decoder CNN version M1, an LSTM-version M2 and a U-Net version M3, see below for details. The difference between models M1A and M1B is mainly the associated loss function and the encoding of the ground truth PS. M1A uses a pixel-wise cross-entropy loss which does not account for the distance between predicted PS locations and ground truth PS locations unless they overlap, whereas M1B uses a loss function based on the distance between predicted and ground truth PS locations.

The phase map prediction neural networks are trained with excitation wave patterns as input and a two-dimensional trigonometric encoding of the phase map as target (see **Figure 3A**). The trigonometric encoding eliminates the discontinuity of a linear encoding of the cyclic phase ϕ by encoding the value onto a two-dimensional unit circle: $\phi \rightarrow (\cos(\phi), \sin(\phi)) =: (c, s)$. Therefore, the two phase mapping CNNs have a two-dimensional layer with two channels as output, which are estimates of the sine $\hat{s}$ and cosine $\hat{c}$ of the phase angle ϕ. The predicted phase $\hat{\phi}$ is decoded as $\hat{\phi} := \arctan2(\hat{s}, \hat{c})$. We use the hyperbolic tangent function as activation function in the last layer of the phase mapping CNNs to ensure that $\hat{c}, \hat{s} \in [-1, 1]$. All models are based on a convolutional encoder-decoder architecture (see **Figure 2**). However, whereas model

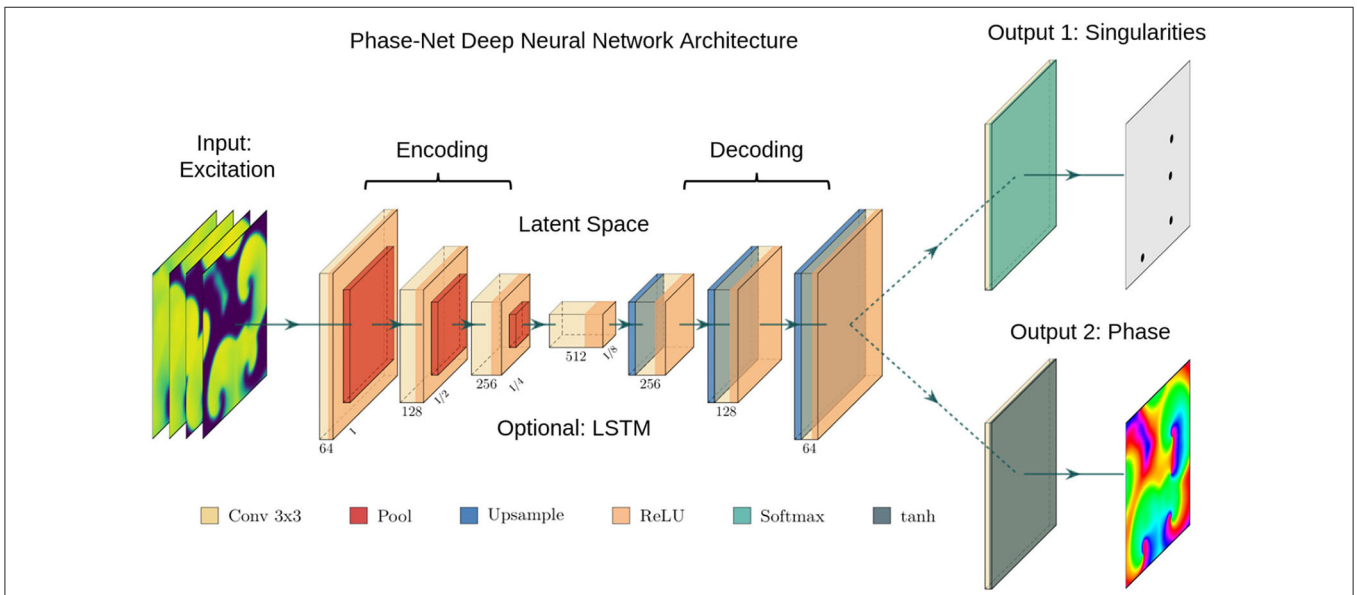

FIGURE 2 | Deep convolutional neural network (CNN) with encoding stage, latent space and decoding stage for the computation of either phase maps or phase singularities (PS) from spatio-temporal maps of electrical excitation. Excitation, phase and PS data is used to train the two neural network, which accordingly learns to translate a short sequence of excitation maps into a corresponding phase map or PS locations. After training, the networks can predict phase maps and PS positions from arbitrary unseen excitation data. We used either (i) a plain convolutional encoder-decoder network architecture, (ii) a U-Net variant, or (iii) a variant with a long short-term memory (LSTM) neural network module integrated into the latent space. The phase values are trigonometrically encoded as *x*- and *y*-components (see also **Figure 3**).

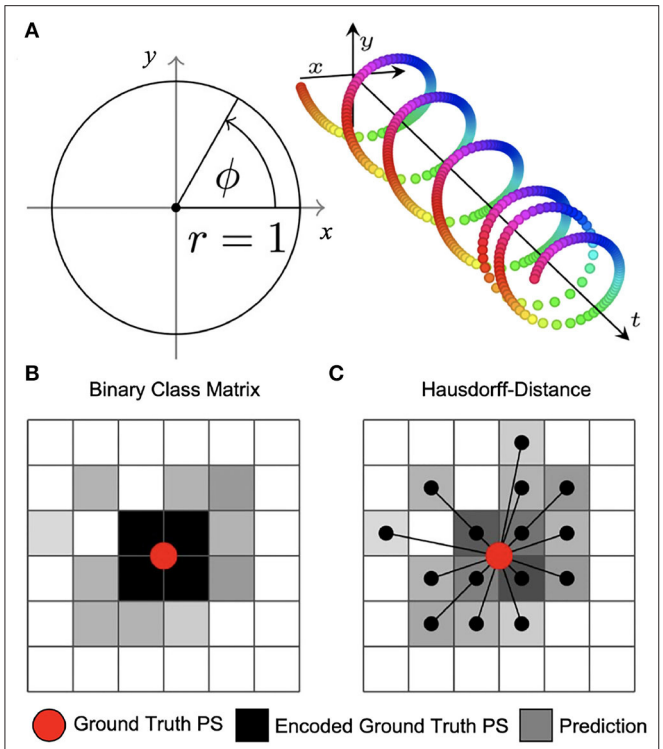

FIGURE 3 | Encoding of phase and phase singularities (PS) for deep learning. **(A)** Instead of estimating the phase angle $\hat{\phi}$ directly, the phase prediction network produces two numbers $\hat{c}, \hat{s} \in [-1, 1]$ for each pixel as output. During training, these are compared against the trigonometric encoding of the phase angle $\phi \rightarrow (\cos(\phi), \sin(\phi))$. We define the predicted phase as $\hat{\phi} := \arctan2(\hat{s}, \hat{c})$. **(B)** Binary class matrix-encoding (or "one-hot" encoding) of PS positions. The loss function (categorical cross-entropy) measures the difference between target PS (red) encoded as a 2×2 kernel (black) and predicted PS given as pixels (gray) with subsequent thresholding. Information about the distance between ground truth and predicted PS is not available to the minimization process during training. **(C)** Coordinate-based encoding of PS positions. The loss function is based on the weighted Hausdorff-distance between ground truth PS coordinates and predicted PS positions given as pixel positions.

M1 uses a two-dimensional convolutional layer in the latent space, the latent space of model M2 is a two-dimensional convolutional long short-term memory (LSTM) neural network layer (Hochreiter and Schmidhuber, 1997; Shi et al., 2015), and model M3 is based on the generic convolutional architecture of model M1, but includes long skip connections at each maxpooling/upsampling step, similar to U-Net (Ronneberger et al., 2015). In all models the encoder- and decoder-stage consist of three two-dimensional convolutional layers, each followed by a batch normalization layer (Ioffe and Szegedy, 2015), rectified linear unit (ReLU) activation layer (Nair and Hinton, 2010), and a maxpooling or upsampling layer. The convolutional layers use 64, 128, and 256 kernels in the encoding stage, 512 kernels in the latent space, and 256, 128, and 64 kernels in the decoder stage. The phase prediction models use the mean squared error as loss function.

The two PS prediction neural networks M1A and M1B are trained with excitation wave patterns as input and either (i) a dense binary class matrix representation of PS positions or (ii) coordinates of PS positions as target, respectively (see **Figures 3B,C**). The ground truth PS are located—by construction (see **Figure 1C**)—in the center of a 2×2 kernel. With model M1A we set 1 as target for all four neighboring pixels of a PS and 0 for all other pixels. While it is possible to train directly on such an encoding with a binary cross-entropy loss function, we achieved better accuracies when using a categorical encoding of the target image as a 128×128×2 class matrix, where in the first channel all non-PS pixels are valued 1 and in the second channel all 2×2 PS pixels are 1 and 0 otherwise. Accordingly, model M1A uses two output layers with a softmax activation function, and categorical cross-entropy as a loss function during training. Note that the loss corresponds to a pixel-wise loss, which does not take into account distances between ground-truth and approximated PS positions. With model M1B the target PS are encoded directly as a list of two-dimensional (x, y)-coordinates of PS positions and the loss function uses a weighted Hausdorff-distance with the parameter $\alpha = -3$ between the target PS and predicted pixel distributions approximating PS positions, which was introduced by Ribera et al. (2019) for the deep learning-based localization of objects (see illustration in **Figure 3C**). Note that the loss function includes information about spatial distances between ground-truth and approximated PS during training. Model M1B comprises one output layer with a sigmoid activation function and we used a threshold of 0.5 to obtain a binary PS prediction image. For both models M1A and M1B the predicted PS positions are computed as sub-pixel precise PS locations from the center of each connected object in the binary PS prediction image. Two pixels are connected (belong to the same object), if both are 1 and when their edges or corners are adjacent.

All network models analyze either a single, static two-dimensional excitation wave pattern or a short sequence of up to 10 excitation wave patterns as input. The patterns consist of consecutive snapshots of the activity sampled at the current time step t and at equidistant time intervals at previous time steps, see also section 2.2. Note that, if we refer to "video images / frames / excitation patterns" or "samples," each of these samples may refer to a single or a short series of $2 - 10$ two-dimensional excitation patterns. For model M1 and M3 the excitation wave patterns are represented as input channels, while for model M2 each temporal excitation wave pattern is processed separately in the neural network as the LSTM is a recurrent neural network. All neural network models were implemented in Tensorflow (Abadi et al., 2015) version 2.6.0.

2.2. Training Data Generation

We generated synthetic training data using a phenomenological computer model of cardiac electrophysiology (Aliev and Panfilov, 1996). In short, non-linear waves of electrical excitation and refractoriness were modeled using partial differential equations and an Euler finite differences numerical

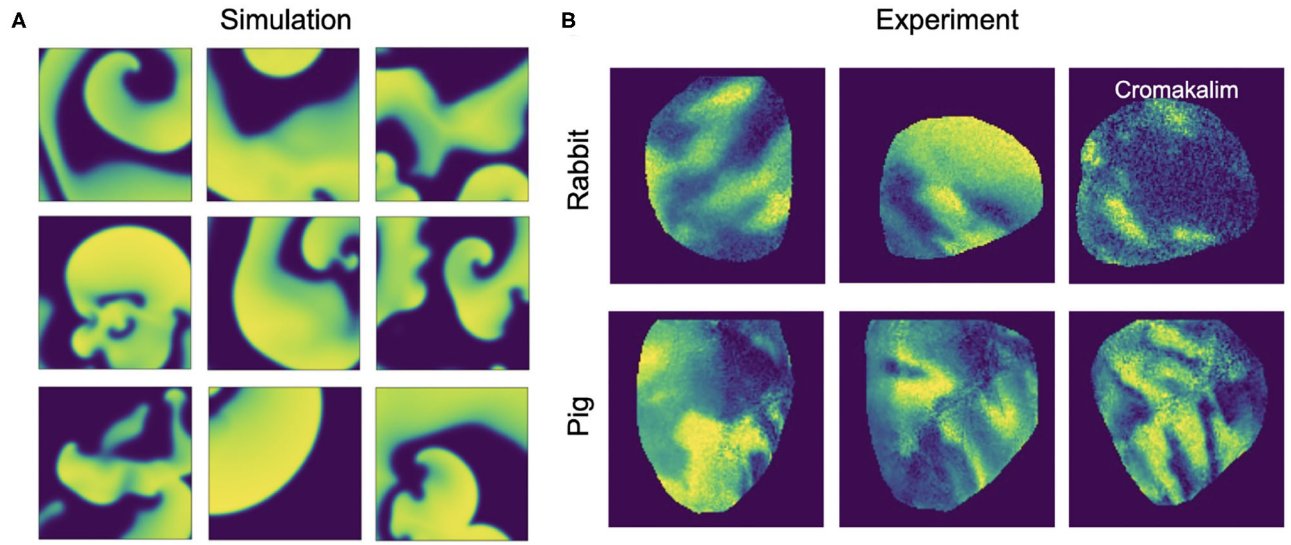

FIGURE 4 | Simulated and experimental training data. Each training dataset includes 20,000 samples. **(A)** Random snapshots of simulated electrical spiral wave chaos. The dynamics are diverse and include both chaotic and laminar episodes with both spiral and plane waves and include longer and shorter wavelengths and faster and slower conduction speeds, respectively. The simulated training data was further noisified and/or sparsified (see **Figures 5B**, **10A**). **(B)** Experimental training data generated in voltage-sensitive optical mapping experiments during ventricular fibrillation (VF) in rabbit (top) and pig (bottom) hearts. The rabbit data contains about 50% VF episodes with Cromakalim and 50% without. Therefore, both datasets include shorter and longer action potential wavelengths, as well as faster and slower and more and less complex dynamics, respectively.

integration scheme:

$$\frac{\partial V}{\partial t} = \nabla^2 V - kV(V-a)(V-1) - Vr \tag{4}$$

$$\frac{\partial r}{\partial t} = \epsilon(V,r)(kV(a+1-V) - r) \tag{5}$$

Here, V and r are dimensionless, normalized dynamic variables for electrical excitation (voltage) and refractoriness, respectively. Together with the isotropic diffusive term $\nabla^2 V = \nabla \cdot (D\nabla V)$ with the diffusion constant $D = 1.0$ in Equation (4), the model produces non-linear waves of electrical excitation and the term $\epsilon(V,r) = \epsilon_0 + \mu_1 r/(V+\mu_2)$ in Equation (5) and electrical parameters k, a, ϵ_0, μ_1, and μ_2 influence properties of the excitation waves. The size of the two-dimensional simulation domain was 200×200 cells/pixels. The parameters were set to $a = 0.09$, $k = 8.2$, $\epsilon_0 = 0.01$, $\mu_1 = 0.07$, $\mu_2 = 0.3$ and spiral wave chaos was initiated by applying a series of point stimulations in random locations. With the chosen parameters the dynamics exhibit both chaotic spiral wave and more laminar wave dynamics with strong fluctuations in the complexity of the wave patterns (see **Figures 4A**, **9F** and **Supplementary Videos 2, 4**). We generated 20 episodes with a series of 2,500 snapshots of the dynamics in each episode. **Figure 1A** shows an example of such a snapshot. The 2,500 snapshots show about 25 spiral wave rotations. Correspondingly, one spiral rotation is resolved by about 100 snapshots. Note that in the simulation the dynamics are resolved at a 10× higher temporal resolution than in the series of snapshots, because we stored a snapshot only in every 10th simulation time step. In total, we obtained 50,000 snapshots, from which we then created 20,000 training samples (see **Figure 4A**), where one training sample comprises a short sequence of snapshots with up to 10 images of the excitation. Within the sequence, the first snapshot, denoted with t_0, corresponds to the snapshot at time t in the video. The training is performed with the corresponding ground truth phase maps and PS obtained at this time step t and, correspondingly, the network also predicts a phase map or PS at time t. The other snapshots in each sample correspond to snapshots showing the dynamics at previous time steps t_{-1}, t_{-2} etc., where $t_{-i} = t_0 - i \cdot \tau$ with $i = 1, \ldots, N_t$ and N_t is the number of snapshots in the sample and τ is the temporal sampling distance between the frames over parts of the previous period. The parameters N_t and τ are discussed in more detail in section 3.5 and in **Figure 13**. The training samples were shuffled in time, while the temporal sequence within each sample was kept in its original order. We generated test data for evaluation that was not used during training by simulating 5,000 snapshots separately using the same electrical parameters and generating samples with the same parameters N_t and τ for testing purposes. We computed ground truth phase maps from the original series of excitation snapshots before shuffling using the Hilbert transform (Bray and Wikswo, 2002) and computed ground truth PS using the Iyer and Gray (2001) line integral method, as shown in **Figures 1B,C**. To simulate noisy excitation wave data, we added noise to the training data (see **Figure 5**). The Gaussian white noise was added to the individual pixels independently in each frame and independently over time ($\sigma = 0.1, 0.2, \ldots, 0.8$ states the standard deviation of the noise). Each excitation snapshot was optionally additionally sparsified by setting masked excitation values to 0.

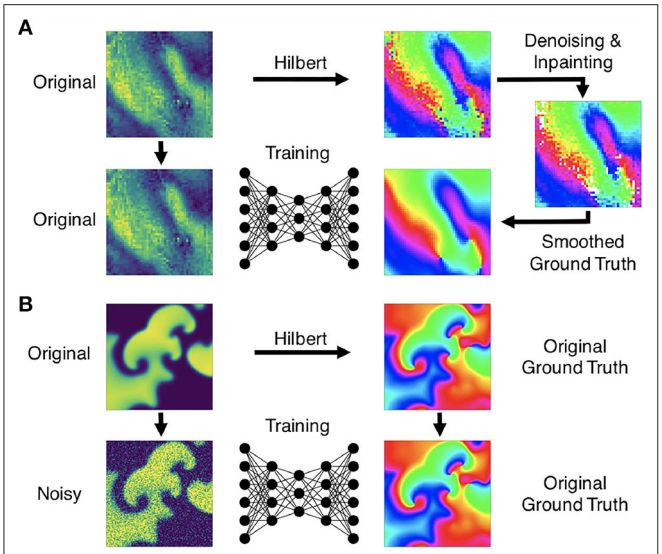

FIGURE 5 | Preprocessing of data for training of deep learning algorithm for computation of phase maps and phase singularities. **(A)** Preprocessing of noisy optical mapping data: computation of noisy phase maps from raw noisy optical maps using the Hilbert transform. Subsequent denoising using outlier removal, inpainting and smoothing to obtain ground truth phase maps for training. **(B)** Preprocessing of simulation data: computation of ground truth phase maps directly from smooth simulated excitation wave patterns and training with noisy (or sparsified) excitation data.

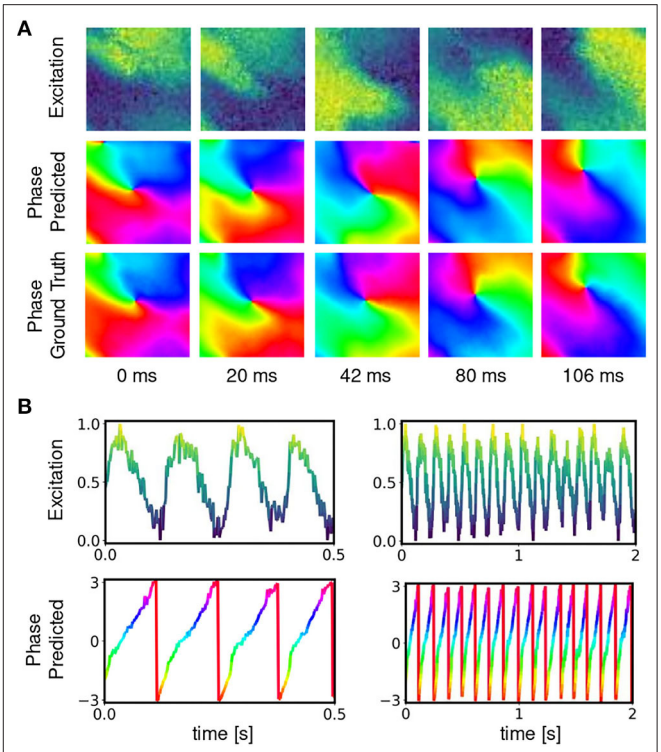

FIGURE 6 | Deep neural network-based prediction of phase maps from optical maps measured using voltage-sensitive fluorescent dye Di-4-ANEPPS during ventricular fibrillation on surface of isolated heart. **(A)** Optical maps of transmembrane voltage showing counter-clock-wise rotating action potential spiral vortex wave (normalized units [0,1], pixel-wise normalization, yellow: depolarized tissue, blue: refractory tissue). Comparison of predicted (top) and ground truth (bottom) phase maps with high qualitative and quantitative agreement. The phase prediction accuracy is 97% ± 6% and the predicted and ground truth phase maps are hard to distinguish. The data was not seen by the network during training. **(B)** Exemplary time-series from a single pixel showing transmembrane voltage $V(t)$ and predicted phase $\hat{\phi}(t)$, respectively.

We generated experimental training data using high-speed video data obtained in optical mapping experiments with voltage-sensitive fluorescent dyes (Di-4-ANEPPS). Imaging was performed during VF in isolated rabbit ($N = 2$) and porcine ($N = 5$) hearts at acquisition speeds of 500 fps, respectively, using a Teledyne Photometrics Evolve camera (128×128 pixels). The rabbit data included 6 recordings with 4 different views and more than 25,000 video frames in total. The pig data included 10 recordings with 8 different views and more than 100,000 video frames in total. About half of the rabbit data shows VF episodes with the potassium channel opener Cromakalim, which typically reduces the action potential duration and accelerates VF dynamics. The raw optical mapping videos were pixel-wise normalized in time using a sliding-window normalization (window size 100–120 frames). We used the Hilbert transform to compute phase maps of the pixel-wise normalized optical maps, the phase maps were subsequently denoised and smoothed, see **Figure 5A** and section 2.5, to obtain ground truth phase maps. These ground truth phase maps were then used to compute ground truth PS using the circular integral method as with the simulation data. 20,000 samples of the pixel-wise normalized noisy versions of the voltage-sensitive optical maps (without spatio-temporal smoothing), ground truth phase maps, and PS were used as training dataset for each species. The test datasets consisted of 5,000 samples, which were derived from 1-2 separate recordings, which were left out of the training dataset. Each training or test sample corresponds to a short series (10 frames) of voltage-sensitive optical maps showing action potential wave dynamics in analogy to the simulation data. The experimental samples were masked with masks outlining the shape of the heart. Pixels outside of the mask were set to 0. The same masks were also applied to simulated data (see **Supplementary Video 2**).

2.3. Training Procedure

Using the experimental and simulated data described in section 2.2, we generated training datasets consisting of corresponding two-dimensional electrical excitation wave data and phase maps as well as (x, y) positions of PS in these maps. The simulated data was resized from 200×200 pixels to 128×128 pixels to match the size of the experimental data. All predictions were performed on a separate dataset, which was not part of the training. The predictions in **Figures 6–15** were only performed on "unseen" data, which the neural network was not exposed to during training. A fraction of 5% of the samples of the training datasets were used for validation during training. The networks were trained with a batch size of 32 using the Adam (Kingma and Ba, 2015) optimizer with a learning rate of 0.001. All models were typically trained for 10 to 15

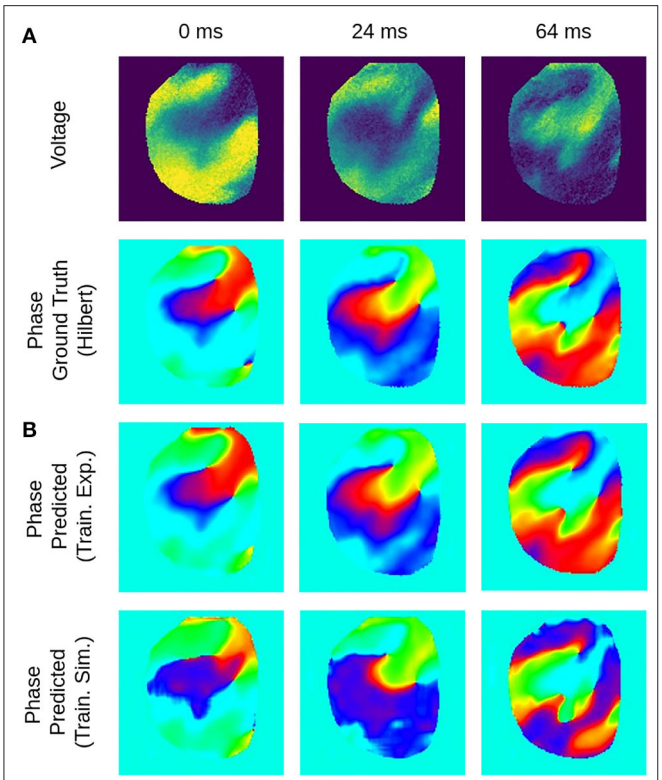

FIGURE 7 | Deep learning-based phase mapping of VF in rabbit heart with neural network trained on either experimental or simulation data. **(A)** Voltage-sensitive normalized optical maps showing action potential vortex waves during VF on rabbit heart and corresponding ground-truth phase maps computed using the Hilbert transform. **(B)** Prediction of phase maps using neural network model M1 trained with either rabbit optical mapping data (top, data not seen during training) or solely simulated data (bottom) of excitation spiral wave chaos (noise $\sigma = 0$) as shown in **Figure 4A** but masked as in **Figure 4B**. The phase prediction accuracy is $97 \pm 6\%$ and $94 \pm 11\%$ when training is performed with experimental or simulation data, respectively, see also **Figure 8** for a comparison of prediction accuracies when training across different species.

epochs on data including 20,000 frames or samples, if not stated otherwise.

2.4. Phase Mapping and Rotor Localization Accuracy

The phase prediction accuracy was determined by calculating the angular accuracy, $1 - \langle|\Delta\phi|\rangle/\pi$, where $|\Delta\phi|$ is the minimum absolute angle difference between the predicted phase $\hat{\phi}_i(x, y)$ and the ground truth phase $\phi_i(x, y)$. The average absolute angle difference

$$\langle|\Delta\phi|\rangle = \frac{1}{N \cdot N_{\text{pixels}}} \sum_{i,x,y} |\Delta\phi_i(x, y)| \tag{6}$$

is evaluated over all N_{pixels} pixels (x, y) in all N test samples i. All uncertainties of the phase prediction accuracies stated throughout this study correspond to the standard deviation of the angular accuracy over all N_{pixels} pixels in all N samples in the entire testing dataset. The PS prediction accuracy was evaluated with the precision, recall, and F-score based on the number of true positive *tp*, false positive *fp* and false negative *fn* PS predictions, as well as the mean absolute error of the number of predicted PS and the mean average Hausdorff distance. A true positive estimated PS position is counted if any estimated PS location is within at most r pixels from the ground truth PS. A false positive is counted if no ground truth PS is located within a distance of r from the estimated PS position. A false negative is counted if a ground truth PS does not have any estimated PS within a distance of at most r. We chose $r = 3$ pixels, see also **Figure 9E**. We note that this definition is biased in favor of the prediction when two PS are predicted within r pixels of a single ground truth PS, as both predicted PS will be counted as true positive. However, by construction of the prediction method (see **Figure 3** and section 2.1) this case occurs only very rarely. E.g., for none of the models presented in **Table 1** did this situation occur for more than 15 PS out of a total of $\sim$ 17,000 predicted PS. The bias in favor of the model is thus negligible for the precision, recall and F-score. Precision is $tp/(tp + fp)$, the proportion of estimated PS locations that are close enough to a ground truth PS location. Recall is $tp/(tp + fn)$, the proportion of the true phase singularities the neural network is able to detect. The F-score is the harmonic mean of precision and recall:

$$\text{F-score} = 2 \cdot \frac{\text{Precision} \cdot \text{Recall}}{\text{Precision} + \text{Recall}} \tag{7}$$

Additionally, we compute the mean absolute error (MAE) of the number of predicted PS

$$\text{MAE} = \frac{1}{N} \sum_{i=1}^{N} \left|\hat{n}_i - n_i\right| \tag{8}$$

where N is the number of dataset samples, n_i is the number of ground truth PS in the i-th sample, and $\hat{n}_i$ is the number of predicted PS for the sample. The average Hausdorff distance d_{AHD} measures the distance between two point sets X and Y:

$$d_{\text{AHD}}(X, Y) = \frac{1}{2}\left(\frac{1}{|X|}\sum_{\vec{x}\in X}\min_{\vec{y}\in Y}\|\vec{x} - \vec{y}\| + \frac{1}{|Y|}\sum_{\vec{y}\in Y}\min_{\vec{x}\in X}\|\vec{x} - \vec{y}\|\right) \tag{9}$$

where $|X|$ and $|Y|$ are the number of points in X and Y, respectively and $\|\cdot\|$ is the Euclidean distance. We report the mean average Hausdorff distance for PS predictions

$$\text{MAHD} = \frac{1}{N} \sum_{i=1}^{N} d_{\text{AHD}}(S_i, \hat{S}_i) \tag{10}$$

where S_i is the set of ground truth PS and $\hat{S}_i$ is the set of predicted PS for sample i. If either S_i or $\hat{S}_i$ is empty and the other set is not empty we set $d_{\text{AHD}}(S_i, \hat{S}_i)$ to the image diagonal in pixels.

2.5. Smoothing and Interpolation

To be able to compare the CNN-based phase predictions shown in **Figure 10B** with results obtained with a reference method, we reconstructed or enhanced the noisy and/or sparse phase maps shown in **Figure 10C** using kernel-based spatio-temporal outlier filter, inpainting and smoothing techniques. The filtering techniques were also applied to experimental data (see **Figure 5A**) and section 2.2. The filtering is performed on trigonometrically encoded phase values, where each real-valued phase value in the video is converted into its complex decomposition:

$$\phi(x, y; t) \rightarrow \cos\phi(x, y; t) + i \cdot \sin\phi(x, y; t) \tag{11}$$

Spatio-temporal kernels are then used to average the complex phase values in space and over time in small disk-shaped sub-regions $\mathcal{S}_{d,\Delta t}$ with diameter d and with $\Delta t = 3$ at times $t-1$, t and $t+1$. In order to remove outliers in the experimental data and the noisy simulated data, the Kuramoto order parameter $r(x, y; t)$ (Kuramoto, 1984) was computed in every pixel at every time step:

$$r \cdot e^{\phi} = \frac{1}{N} \sum_{i}^{N} e^{i\phi_j} \tag{12}$$

where $j = 1, \ldots, N$ is the number of complex phase values within each kernel with diameter $d = 5$ pixels and $\Delta t = 3$. Phase values were considered outliers if $r < 0.9$ and accordingly removed, as shown in **Figure 5A**. Missing phase values were replaced with phase values averaged from surrounding phase values within the spatio-temporal kernel, given that at least 30% of the entries within the kernel were non-missing or valid phase entries. The process was repeated until the entire video was filled with valid phase entries. Lastly, the denoised, inpainted phase maps were smoothed averaging all phase values within a small spatio-temporal kernel typically with $d = 7$ and $\Delta t = 3$, if not stated otherwise. In **Figure 10**, the noisy data was processed using the outlier and smoothing filters, the low resolution data was smoothed with $d = 11$ pixels, the 8×8 large and small grid data was inpainted 7 times with $d = 11$ pixels, and the sparse grid data was inpainted 10 times with $d = 19$ pixels, all with $\Delta t = 3$. With the sparse data the denoising was performed after inpainting and before smoothing.

3. RESULTS

We found that deep encoding-decoding convolutional neural networks (CNNs) can be used to compute phase maps and phase singularities (PS) from a short sequence of excitation wave patterns. The prediction of phase maps can be performed robustly and accurately ($\sim 90 - 99\%$) with both experimental and simulated data, even with extremely noisy or sparse patterns (see **Figures 6–13** and **Supplementary Videos 1**, **4–7**). Phase predictions remained accurate across different species, with models being trained on one species and then being successfully applied to another. Additionally, models that were trained solely on simulation data of VF could be applied to experimental data, see **Figures 7**, **8**. PS can be predicted either directly from excitation wave patterns or indirectly by first predicting phase maps from excitation wave patterns and then computing PS in the predicted phase maps. While in principle both direct and indirect PS prediction methods can determine the positions of PS very precisely (F-scores of ∼97%, see **Table 1**), direct PS predictions are very sensitive to noise and sparsity. Indirect PS predictions are far more robust. Accordingly, with the indirect PS prediction method we were able to locate PS in optical mapping recordings of VF sufficiently reliably and accurately, whereas with the direct PS prediction method this task was more challenging and produced only moderately successful results (see **Table 2**).

Figures 6, **7** and **Supplementary Video 1** show predictions of phase maps when the neural network analyzes voltage-sensitive optical mapping videos showing action potential spiral vortex waves during ventricular fibrillation (VF) on the surface of rabbit and porcine hearts. **Figure 6A** shows raw pixel-wise normalized optical maps with a counter-clock-wise rotating action potential spiral vortex wave on the ventricular surface of an isolated pig heart (close-up, 48×48 pixels cutout from original video image). The action potential rotor performs one rotation in about 110 ms. The phase maps in the second and third row in **Figure 6A** show the predicted phase maps $\hat{\phi}$ obtained with model M1 and ground truth phase maps ϕ, respectively. The action potential rotor is characterized by a pinwheel pattern in the phase maps, and the rotational core or PS is indicated by lines of equal phase which merge at the center of the pinwheel pattern. Predicted and ground truth phase maps are visually almost indistinguishable and exhibit only minor differences. The data was not seen by the neural network previously during training. The predicted phase maps are smooth even though the optical maps showing the action potential wave patterns are noisy. The neural network is able to predict more complicated wave patterns with multiple rotors or phase singularities (see **Figure 7** and **Supplementary Videos 1**, **3**). The upper row in **Figure 7B** shows phase map predictions of an action potential figure-of-eight reentry pattern on the ventricular surface of a rabbit heart during VF. The predicted and ground truth phase maps shown in **Figure 7A** can only be distinguished from each other upon close inspection. Analyzing a short sequence of 10 optical maps, the neural network provides phase map predictions which are very accurate and sufficiently smooth in both space and over time, and the predictions can be retrieved in real-time at an acquisition speed of 500 fps. **Figure 6B** shows an optical trace of a series of action potentials and the corresponding time-series of the predicted phase, which was obtained from the sequence of predicted phase maps in **Figure 6A** using model M1. Even though each phase map was predicted independently at each time step, the time-course of the predicted phase signal $\hat{\phi}(t)$ is relatively smooth, see **Supplementary Videos 1**, **4–7** for an impression of the temporal smoothness of the predictions. On average, the accuracy of the phase prediction with model architecture M1 is $97\% \pm 8\%$ or $98\% \pm 6\%$ in terms of angular accuracy, if the model was trained on pig data and is evaluated on pig data or, alternatively, trained on rabbit data and evaluated on rabbit data (evaluation on $\sim$ 5,000 frames that were not part of the training data), respectively. We did not find a

significant difference in the accuracy between models M1, the LSTM model M2, or the U-Net model M3. For instance, when trained and evaluated on pig data, the angular accuracy for the phase prediction was 96.5% ± 7.9% for M1, 96.1% ± 8.1% for M2, and 96.7% ± 7.8% for model M3.

3.1. Phase Prediction Across Species and Dynamical Regimes

We found that phase prediction models that were trained on pig optical mapping data can also be applied to rabbit optical mapping data and achieve equally high phase prediction accuracies on the data (96.5% ± 7.9% vs. 97.0% ± 7.5%), see **Figure 8**. With such cross-species training, we observed higher accuracies when training from one species to another than vice versa (Rabbit→Pig: 93.4% ± 12.2% vs. Pig→Rabbit: 97.0% ± 7.5%). This is presumably due to differences in the training data (more hearts, more diverse views in one species than the other). Surprisingly, we found that even models that were solely trained with simulation data, as shown in **Figure 4A**, can be used to predict phase maps of VF optical mapping data and that these models achieve acceptable results, see lower row in **Figures 7B**, **8** (the simulation data was randomly masked with masks which were used with the experimental data (see **Supplementary Video 2**), all values outside the mask were set to 0). This demonstrates that the model can be applied to significantly different data than the data it was trained on. This also hints at the model generalizing and learning to associate phase maps with spatio-temporal dark-bright patterns in general rather than memorizing the particular wave dynamics. Note that the simulation data only includes two-dimensional wave dynamics, whereas the experimental data corresponds to three-dimensional wave dynamics which are observed on the surface. To our surprise, we found that models trained on simulation data without noise performed better on optical mapping data than when they were trained on simulation data with noise. The network performed equally well across the different dynamical regimes in the simulated data, which includes episodes with both more laminar and more chaotic spiral wave dynamics with longer and shorter wavelengths (see **Figure 4**). Lastly, **Figure 8** shows that a neural network that was trained on a mixture of pig, rabbit and simulation data provides consistently high phase prediction accuracies of 96 − 98% across all three datasets. Taken together, these results demonstrate that the phase prediction neural network can be applied to a wide range of VF dynamics with various wave lengths and frequencies. Note that the rabbit data contains VF episodes with and without Cromakalim, which modulates the dynamics significantly. While it was not possible to create sufficiently large rabbit training datasets to determine the performance during cross-training (without Cromakalim → with Cromakalim or vice versa), we did not notice a significant change in accuracy when evaluating the performance of a general rabbit model on sub-data types (without Cromakalim vs. with Cromakalim). The analysis was performed with model M1.

FIGURE 8 | Phase prediction accuracies for neural network models trained on either pig, rabbit or simulation data, or a mixture of all data, cf. **Figure 4** and **Supplementary Video 2**. Prediction across species or from simulation to experiment with models trained on either one species and applied to another species or on simulation data and applied to rabbit or pig optical mapping data. All models were applied to test data consisting of 5,000 samples from experimental recordings or simulations, respectively. The prediction is most accurate when trained on the same data (Pig→Pig 97% ± 8%; Rabbit→Rabbit 98% ± 6%; Simulation→Simulation 99% ± 4%). Nevertheless, the models appear to generalize as prediction across species is possible and achieves accuracies above 90% (Pig→Rabbit 97% ± 8%, Rabbit→Pig 93% ± 13%). The pig training data is more diverse than the rabbit training data (more hearts and different views), which yields higher accuracies when predicting from pig to rabbit than vice versa. A model that was trained solely on simulation data can also be used to predict phase maps from experimental data (e.g., Simulation→Rabbit 95% ± 10%).

3.2. Phase Singularity Prediction

We found that the prediction of phase singularities (PS) from electrical excitation wave patterns was less accurate and less robust than predicting phase maps. This was especially true with challenging data, such as optical mapping recordings, or noisy and sparsified simulation data. Here, we compare three different neural network models M1, M1A, and M1B. Model M1 predicts PS indirectly by first predicting phase maps and subsequently calculating PS positions using the line integral technique. Models M1A and M1B both predict PS directly, where M1A uses a pixel-wise loss function and M1B uses a distance-based loss function during training, see section 2.1. Both models have different drawbacks: model M1A was better than M1B on simulation data both without and with noise (see **Table 1**), while M1B performs slightly better on optical mapping recordings than M1A (see **Table 2** and **Supplementary Video 3**). Model M1A is very conservative on challenging data, it occasionally produces false positives but mostly misses many true PS. Model M1B, on the other hand, is not as precise as M1A, and predicts more PS and produces more false detections. Overall, the indirect PS prediction using model M1 shows a far better performance than both direct methods with models M1A and M1B.

Figure 9 shows the PS predictions on simulated spiral wave chaos data. **Figures 9A,C** show predicted PS (black) and ground truth (white) PS superimposed onto the corresponding electrical excitation wave maps (PS were predicted with model M1A). The maps demonstrate that both predicted and ground truth PS describe equally well the tips of spiral waves. However, with noise, one of the six PS was not detected by the neural network

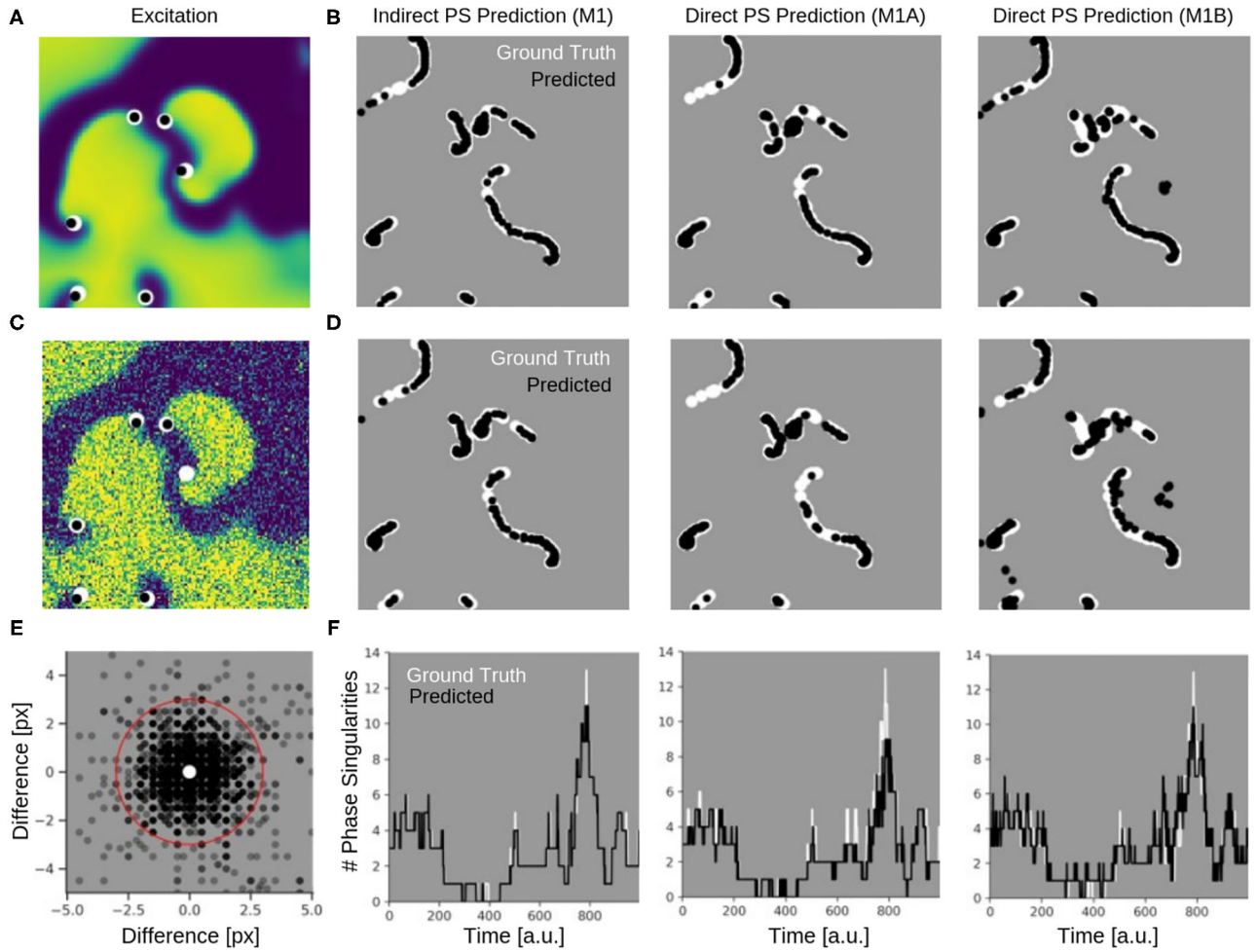

FIGURE 9 | Phase singularities (PS) predicted for neural networks M1 (indirect PS prediction, computing of PS from phase prediction), M1A (pixel-wise cross-entropy loss), and M1B (weighted Hausdorff distance loss) from simulated maps of electrical excitation. White: ground-truth or true PS. Black: predicted PS. A quantitative evaluation of the predicted PS is shown in **Table 1**. **(A)** Electrical spiral wave chaos without noise with PS superimposed indicating positions of spiral wave tips for model M1A. **(B)** Trajectories of ground truth (white) and predicted (black) PS without noise over 60 simulation time steps for the models M1, M1A, and M1B. **(C)** Electrical spiral wave chaos with noise ($\sigma = 0.3$) with PS superimposed indicating positions of spiral wave tips. **(D)** Trajectories of ground truth and predicted PS with noise. Increase in false negative predictions with noise. Model M1B also produces false positive detections. **(E)** Spatial mismatch of predicted PS (black) and ground truth PS (white, center) for model M1A. All predicted PS not within 3 pixels (red circle) from true PS are false positives. **(F)** Number of PS over time predicted with models M1, M1A, M1B from electrical spiral wave chaos with noise ($\sigma = 0.3$).

(false negative detection). **Figures 9B,D** show the trajectories of the predicted (black) and ground truth (white) PS over a short time span (60 simulation time steps), without and with noise ($\sigma = 0.3$), respectively, predicted indirectly with model M1 and directly with the models M1A and M1B. The predictions were obtained from a short sequence of $N_t = 5$ excitation frames (c.f. **Figure 13A**). The trajectories co-align and demonstrate that PS are mostly predicted in locations where true PS are located. However, model M1B produces false positives even without noise. Moreover, all PS prediction models miss a portion of ground truth PS, and we counted these mispredictions as false negatives. **Figure 9E** shows the spatial distribution of mismatches between predicted and ground truth PS for model M1A with noise $\sigma = 0.3$, where the positions of the predicted PS are plotted relative to the position of the ground truth PS at the center. All predicted PS which lie outside a radius of 3 pixels (red circle) from the ground truth PS are counted as false positives. The sub-pixel resolution accuracy of PS is a result of our method: we calculated PS positions from a series of pixels in the PS prediction image, see section 2.1. **Table 1** shows the evaluation of the PS prediction for all three models without and with noise in terms of precision, recall, F-score, MAE and MAHD on the test data consisting of 5,000 samples with 17,360 ground truth PS in total. Without noise model M1A is slightly better or equal to the indirect model M1 (e.g., F-score of 96.8 vs. 96.5 %), while model M1B is significantly worse in all measures (F-score 86.5 %). With noise however, the recall is significantly reduced for model M1A (85.9 vs. 96.4 %, F-score 91.2 %), as the number of false negative

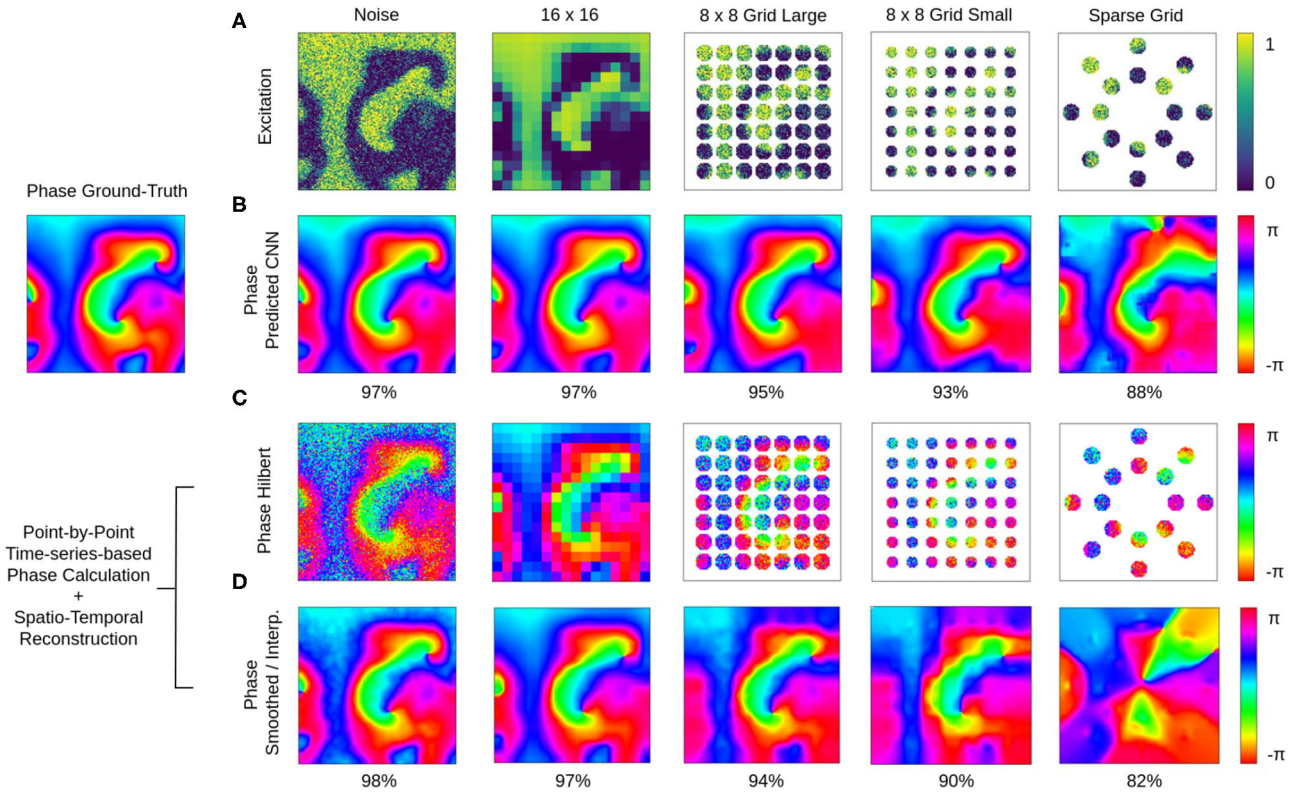

FIGURE 10 | Deep learning-based prediction of phase maps from noisy and/or sparse electrical excitation wave patterns. Left: Corresponding ground-truth phase map $\phi(x, y)$ calculated from original electrical excitation wave pattern (at $t = 415$) without noise or sparsification via the Hilbert transform, as shown in **Figures 11A,B**. **(A)** Excitation wave patterns with noise ($\sigma = 0.3$), low resolution (no-noise excitation pattern down-sampled with averaging to 16×16 pixel then up-sampled to 128×128 pixel), 8×8 grid of large round electrodes or fiber optics (15 pixel diameter, 43% coverage, $\sigma = 0.3$), 8×8 grid with small round electrodes or fiber optics (11 pixel diameter, 21% coverage, $\sigma = 0.3$) and a sparse star-shaped / ring-shaped grid of large round electrodes or fiber optics (15 pixel diameter, 16% coverage, $\sigma = 0.3$). **(B)** Corresponding predicted phase maps $\hat{\phi}(x, y)$ with 96.8% ± 3.2%, 96.8% ± 3.4%, 94.6% ± 7.4%, 93.1% ± 9.1%, and 87.8% ± 15.4% angular accuracies from left to right, respectively. Except with the sparse grid, the predicted phase maps $\hat{\phi}$ are hard to distinguish from the true phase map ϕ. The data was not seen by the network during training. Phase maps $\hat{\phi}(x, y, t_p)$ were predicted from a short spatio-temporal sequence of 5 electrical excitation wave maps $V(x, y, t = t_1, t_2, t_3, t_4, t_5)$. **(C)** Phase maps of the noisy, low resolution and sparse excitation wave patterns calculated via the Hilbert transform. **(D)** Smoothed and/or interpolated versions of the phase maps shown in **(C)** with 97.7% ± 2.9%, 96.9% ± 5.2%, 93.9% ± 10.3%, 90.1% ± 13.1%, and 81.9% ± 21.0% angular accuracies from left to right, respectively. Kernel-based phase smoothing and interpolation methods described in section 2.5. Note that the phase maps were calculated from video data and not from just 5 snapshots like in **(B)**.

predictions increases and the number of true positive predictions decreases (see **Figure 9D**). The number of false negatives does not increase, however, and the precision stays the same without and with noise with model M1A. This indicates that the model is rather conservative, insofar as when the difficulty for the model to predict PS locations increases it rather misses true PS instead of predicting false positives. This can also be seen in **Figure 9F**, which shows the number of predicted (black) and ground truth (white) PS over time for $\sigma = 0.3$.

While the indirect PS predictions obtained with model M1 follow the ground truth PS closely, the direct PS predictions obtained with models M1A and M1B follow the trend overall but at times deviate considerably from the ground truth. Model M1A consistently underestimates the number of PS, whereas model M1B both under- and overestimates PS. **Supplementary Video 5** shows the PS predictions with model M1A for different simulated electrical excitation wave patterns without and with noise as well as with sparsification. The conservatism of model M1A is caused by its pixel-wise loss function, which does not account for the distance between predicted PS locations and true PS positions unless the pixels overlap. The loss function is used during training to calculate an error value for every pixel of the predicted image of probable PS locations. As the likelihood of a pixel containing a PS is very small, there is a class imbalance (number of pixels with vs. without PS) for all pixel-wise loss functions and the network is biased toward not predicting a PS for challenging cases. Model M1B, on the other hand, uses a loss function which is directly based on the distance between predicted and ground truth PS locations. **Table 1** shows however, that model M1B is significantly less accurate for all measures than models M1 and M1A both with and without noise. **Figures 9B,D** show that M1B predicts false positives both without and with noise. In contrast, the indirect PS prediction with model M1 produces very few false positives, and the recall as well as the precision decrease only

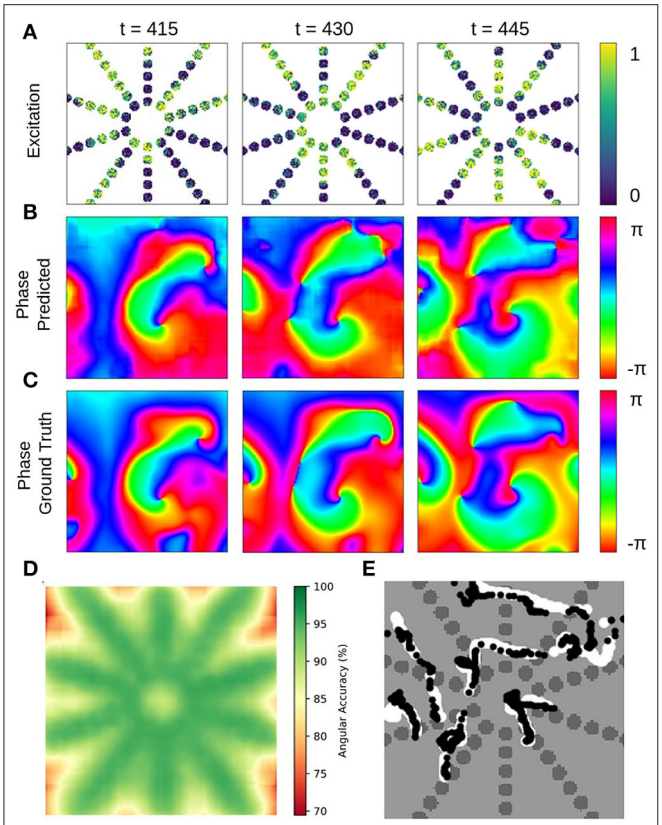

FIGURE 11 | Deep learning-based prediction of phase maps and rotor cores or phase singularities (PS) from sparse electrical excitation wave pattern mimicking multi-electrode catheter or optical fiber recordings. **(A)** Sparse excitation wave pattern with noise ($\sigma = 0.3$, 17% coverage). **(B)** Phase map $\hat{\phi}(x, y)$ predicted by neural network analyzing data in **(A)**. **(C)** Ground-truth phase map $\phi(x, y)$ obtained with complete, non-sparse, non-noisy data. **(D)** Spatially resolved angular accuracy (temporal average in each pixel) shows that accuracy decreases between electrodes. **(E)** Trajectories of ground truth PS (white) and predicted PS (black) using indirect prediction with model M1 (shown over 100 simulation time steps) (see also **Supplementary Video 8**).

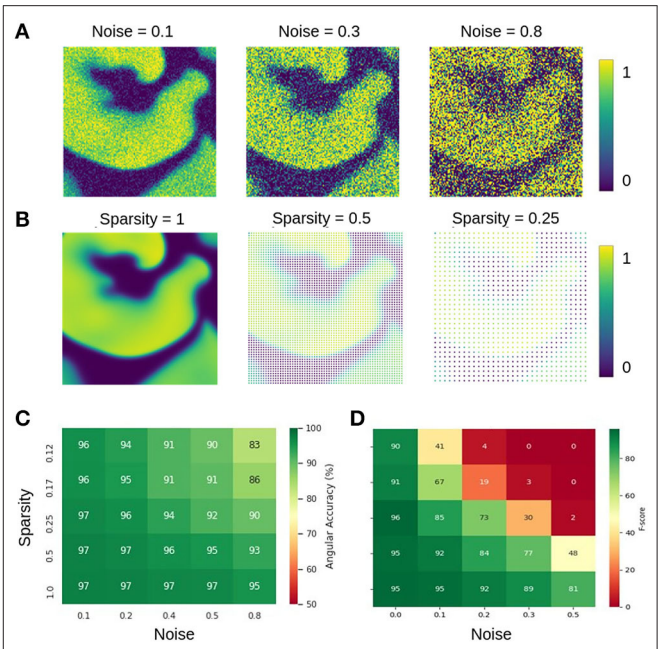

FIGURE 12 | Prediction accuracies with noisy and sparse data. **(A)** Noisy simulated electrical excitation wave patterns with noise levels of $\sigma = 0.1, 0.3, 0.8$. **(B)** Sparse simulated electrical excitation wave patterns with sparsity levels of $\xi = 1, 0.5, 0.25$. With $\xi = 0.25$ all pixels except every 4th pixel are set to 0 (no signal). **(C)** High phase prediction accuracies across broad range of noise and sparsity levels with model M1 (here shown with $N_t = 5$ sampled images, which are $\tau = 5$ simulation time steps apart, c.f. **Figure 13**). **(D)** PS prediction accuracy obtained with model M1A is more sensitive to noise and sparsity. The direct PS prediction fails when data is both very noisy and/or sparse.

moderately with the addition of noise resulting in an F-score of 94.6 %. With regard to the direct PS prediction it is important to point out that the PS locations are determined by weighting multiple pixels, which surround the true PS and indicate probable PS positions (see **Figure 3C**). With model M1B this position estimation is especially problematic because a lot more pixels indicate the PS than with model M1A. Accordingly, two nearby PS are often not sufficiently resolved in the prediction image and cannot be separated, which then produces a false positive detection between two true PS. We tested different methods designed to extract individual PS positions as proposed by Ribera et al. (2019), but did not observe an improvement of the PS prediction performance with model M1B.

Table 2 and **Supplementary Video 3** show PS predicted by the same models when trained and evaluated on rabbit optical mapping data (see also **Figure 4**). The indirect PS prediction with model M1 (F-score of 80.1 %) is far more robust than and superior to the direct PS prediction with experimental data. We found that these indirectly predicted PS matched the dynamics of the true PS computed from rabbit optical mapping data very well (see video). The direct prediction model M1A performs poorly (F-score of 11.8 %), as it misses most true PS (recall 11.8 %). However, it appears to predict some false positives mainly at the medium boundaries (see video). Model M1B achieves a significantly better F-score than model M1A of 42.5 % on the optical mapping data, as it does not suffer from the conservatism exhibited by model M1A. However, overall, the performance of model M1B is still poor on optical mapping data.

3.3. Prediction of Phase Maps From Noisy, Low-Resolution or Sparse Excitation Wave Maps

The phase prediction neural network can predict phase maps even from very noisy, low-resolution and/or very sparse electrical excitation wave maps. **Figures 10**, **11** and **Supplementary Videos 4**, **6** show phase predictions obtained with model M1 with various simulated noisy, low-resolution or sparse excitation wave patterns, which are very generic simulations of imaging scenarios with low-resolution or low signal-to-noise sensors, multi-electrode arrays or (catheter) mapping electrodes, fiber optics or other similar sensors. **Figure 10A** shows exemplary snapshots of the excitation videos that were analyzed: (1) a noisy ($\sigma = 0.3$) excitation pattern with

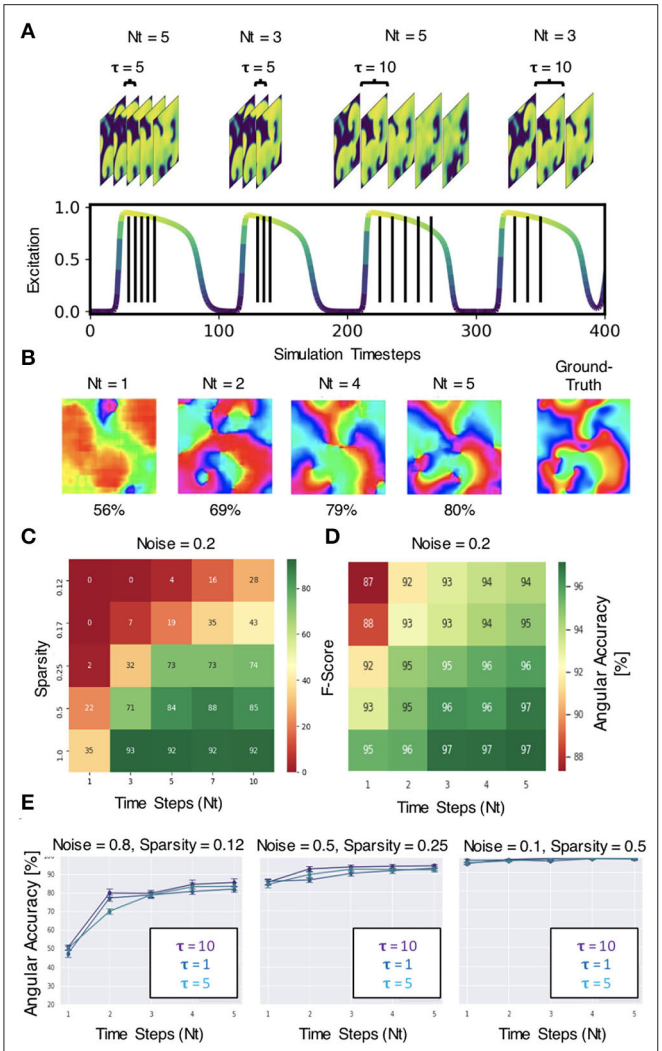

FIGURE 13 | Spatio-temporal sampling of excitation wave dynamics. **(A)** Schematic drawing illustrating number of sampled frames N_t and sampling distance τ between the frames with $N_t = 3$, $N_t = 5$ and $\tau = 5$, $\tau = 10$, respectively, shown relative to action potential duration (action potential duration $\sim 75 - 80$ time steps, cycle length or period ~ 100 time steps). **(B)** Analyzing longer temporal sequences with $N_t = 5$ frames increases prediction accuracy, here shown for very noisy ($\sigma = 0.8$) and sparse data ($\xi = 0.125$ or 16×16 non-zero data points), c.f. **Figures 12A–C**. In this example, the sampled excitation snapshots are $\tau = 5$ simulation time steps apart. **(C)** PS prediction accuracy (F-score) over number of samples N_t and sparsity ξ. More samples increase accuracy (here shown for noise $\sigma = 0.2$). **(D)** Phase prediction accuracy (angular accuracy) over number of samples N_t and sparsity ξ. More samples increase accuracy (here shown for noise $\sigma = 0.2$). **(E)** Phase prediction accuracy is not (significantly) affected by variation of sampling distance τ (all curves overlap, here shown with $\tau = 1, 5, 10$).

128×128 pixels resolution, (2) a low-resolution version of the same pattern that was derived by down-sampling the original non-noisy excitation pattern to 16×16 pixels resolution and then up-sampling the pattern without interpolation to 128×128 pixels resolution, (3) a 8×8 grid of large round electrodes or fiber optics 16 pixels apart with a diameter of 15 pixels each, the grid covering 43% of the area (with noise $\sigma = 0.3$), (4) a 8×8 grid with small round electrodes or fiber optics 16 pixels apart with a diameter of 11 pixels each, the grid covering 21% of the area (with noise $\sigma = 0.3$), and (5) a sparse star-shaped / ring-shaped grid of large round electrodes or fiber optics with a diameter of 15 pixels each, the grid covering 16% of the area (with noise $\sigma = 0.3$). **Figure 10A** shows the corresponding predicted phase maps $\hat{\phi}$ predicted using the neural network model M1. The predicted phase maps $\hat{\phi}$ are visually nearly indistinguishable from the ground truth phase map ϕ shown as a reference on the left. The phase maps were predicted with angular accuracies of 96.8%±3.2, 96.8% ± 3.4, 94.6% ± 7.4, 93.1% ± 9.1, and 87.8% ± 15.4% from left to right, respectively. The maps illustrate that the deep-learning-based phase prediction can suppress noise, enhance spatial resolution, and interpolate missing data and recover phase maps even when it only sees a fraction of the electrical data, as shown in the last example and in **Figure 11**.

The ground truth phase map ϕ in **Figure 10** was computed from the original electrical excitation wave pattern without noise ($\sigma = 0.0$) using the Hilbert transform, computing in each pixel (x, y) individually a phase signal from time-series data $V(t)_{x,y} \rightarrow \phi(t)_{x,y}$ as shown in **Figure 1**. The phase maps shown in **Figure 10C** were equally computed pixel-by-pixel using the Hilbert transform, but were computed directly from the noisy, low-resolution or sparse electrical excitation data shown in **Figure 10A**. The phase maps accordingly include the same features, e.g., they include noise or remain sparse. The phase maps shown in **Figure 10D** were reconstructed from the noisy, low-resolution or sparse phase maps in **Figure 10C** using spatio-temporal inpainting and smoothing techniques, as described in section 2.5. They serve as a reference and allow the comparison of the deep learning with another interpolation method. While the reconstructed phase maps in **Figure 10D** also provide sufficiently accurate reconstructions with noise, low-resolution and low sparsity, with further increasing sparsity the reference method fails to produce accurate results and is outperformed by the deep learning-based phase prediction. Note that, even though the accuracy of both approaches are equally or comparably high, the reconstructed phase maps in **Figure 10D** contain noise or distortions, while the deep learning-based approach in **Figure 10B** produces consistently very smooth phase maps.

The neural network's ability to interpolate and reconstruct phase maps allows the tracking of PS between sensors even when they are relatively far apart (see **Figure 11** and **Supplementary Video 8**). **Figures 11A–C** show a sparse, star-shaped electrode/sensor configuration measuring an excitation wave pattern, and the resulting predicted and ground truth phase maps with this configuration, respectively. The predicted phase maps resolve the rotor dynamics very well, particularly toward the center where the electrode density is higher (average angular accuracy for entire field of view: $\sim$ 91%). The average angular accuracy (temporal average in each pixel) resolved in space in **Figure 11D** indicates that the phase prediction accuracy remains sufficiently high between the electrodes toward the center. Accordingly, **Figure 11E** shows how the predicted PS (black) represent the ground truth PS (white) sufficiently well and follow their trajectories between and across electrodes (shown over 100 simulation time steps). The total area of the sensor/electrodes covers only 17% of the entire 2D simulation domain.

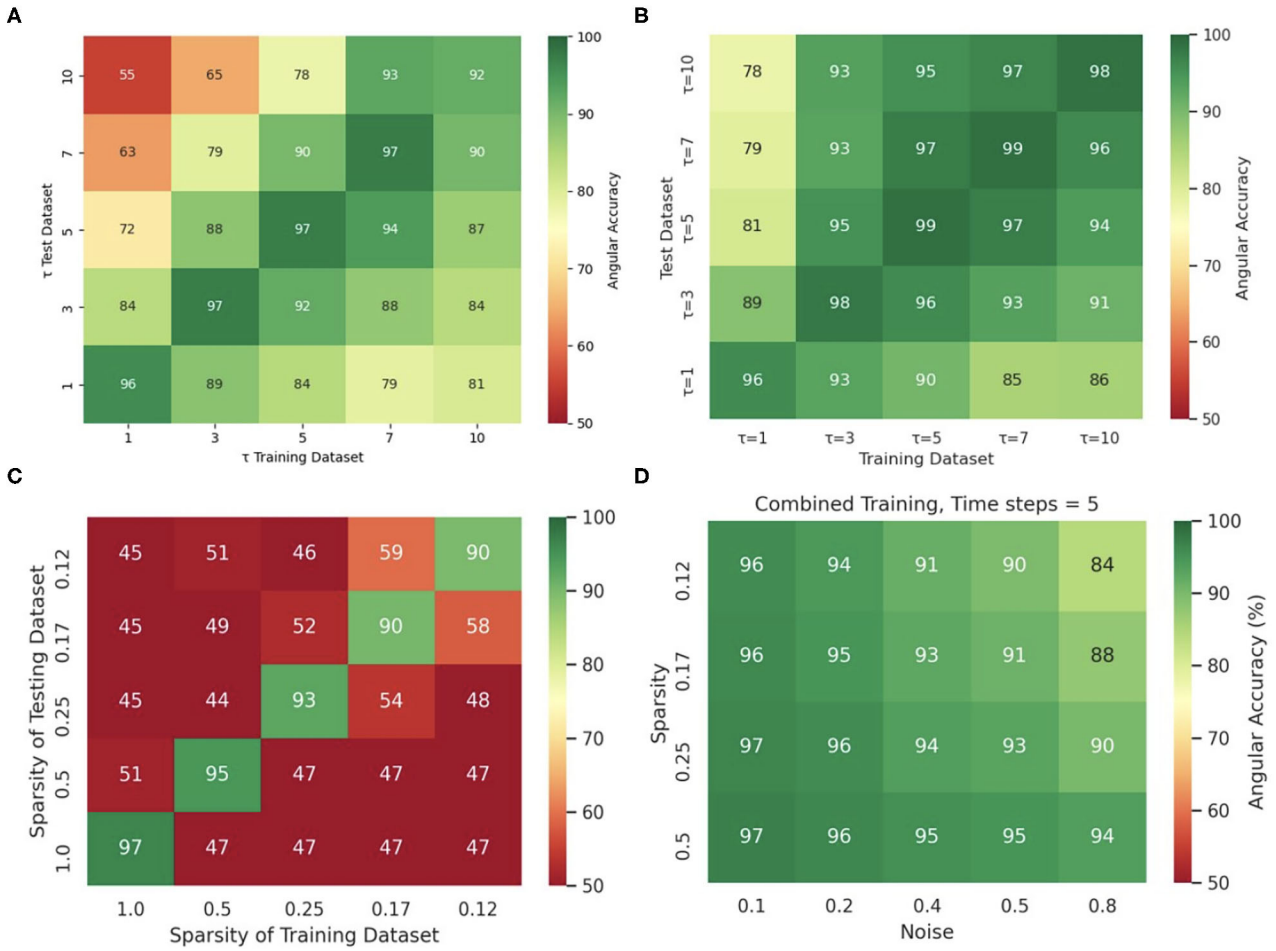

FIGURE 14 | Diverse and augmented training data increases robustness of deep-learning-based phase prediction. **(A)** The phase prediction accuracy decreases if a model that was trained with a specific sampling distance τ is applied to data that was sampled with a different sampling distance. **(B)** Data augmentation (randomly masking the data as shown in the right panel in **Supplementary Video 2**) minimizes the effect in **(A)**. **(C)** Phase prediction fails when neural network is trained on data with one specific sparsity (see also **Figure 12B**), and is then applied to data with different sparsity (off diagonal). **(D)** Phase prediction stays accurate across all noise levels and sparsities when training data also includes all noise and sparsity levels. Note that, by contrast, in **Figure 12C** the accuracy map was created by training separate models individually with each noise and sparsity combination. All results obtained with simulation data and neural network model M1.

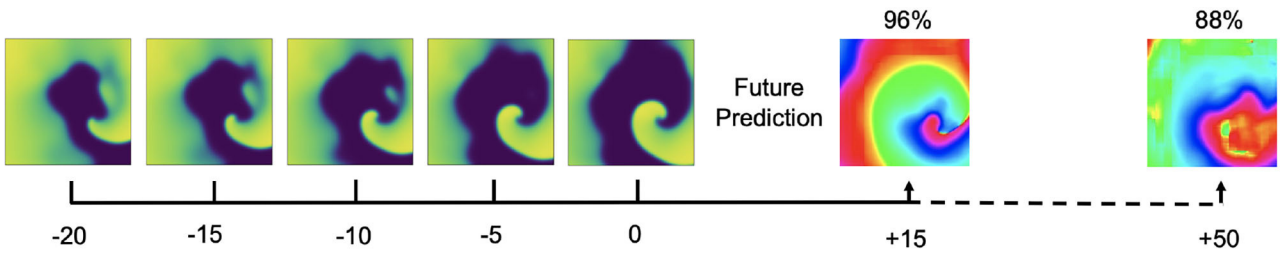

FIGURE 15 | Prediction of phase maps in future time steps with simulated electrical spiral wave chaos. Phase prediction accuracies of 98% and 88% predicting 15 and 50 simulation time steps into the future, respectively, analyzing $N_t = 5$ excitation wave frames at $t = 0,-5,-10,-15,-20$. The average rotational period of the spiral waves are about 100 simulation time steps.

3.4. Extreme Sparsity and Noise

The data shown in **Figure 12** characterizes the phase and PS prediction performance with extreme noise and sparsity in more detail. **Figure 12A** shows maps with simulated electrical excitation wave patterns with noise levels of $\sigma = 0.1$, 0.3, 0.8, and **Figure 12B** shows the same simulated electrical excitation

TABLE 1 | Evaluation of phase singularity (PS) prediction on simulated electrical spiral wave chaos without ($\sigma = 0$) and with noise ($\sigma = 0.3$) for the different models M1, M1A, M1B.

Model	**M1**		**M1A**		**M1B**	
Noise	$\sigma = 0$	$\sigma = 0.3$	$\sigma = 0$	$\sigma = 0.3$	$\sigma = 0$	$\sigma = 0.3$
Precision	97.2 %	96.2 %	97.2 %	97.2 %	86.7 %	82.1 %
Recall	95.7 %	93.1 %	96.4 %	85.9 %	86.4 %	84.3 %
F-score	96.5 %	94.6 %	96.8 %	91.2 %	86.5 %	83.1 %
MAE	0.2	0.2	0.2	0.5	0.4	0.5
MAHD	2.3 px	3.1 px	2.0 px	5.0 px	4.0 px	6.6 px
MAHD*	1.4 px	1.8 px	1.4 px	3.1 px	2.4 px	3.6 px

*PS predictions were performed from 5 excitation frames and are shown in **Figure 9**. MAE is the mean absolute error of the number of predicted PS, MAHD is the mean average Hausdorff distance. The test dataset contains 5,000 frames with 17,360 PS in total, however 420 frames contain no ground truth PS. If the model predicts any PS for a frame which contains no ground truth PS—or if no PS are predicted for a sample which does contain ground truth PS—we assign a maximum average Hausdorff distance (181 px) for the computation of the MAHD. This skews the MAHD significantly. Accordingly, MAHD* is the MAHD when we ignore these samples.*

TABLE 2 | PS prediction with models M1 (indirect from phase), M1A (pixel-wise loss), and M1B (distance-based loss) when trained and evaluated on rabbit optical mapping data using a radius of $r = 6$ px for computation of precision, recall, and F-score.

Model	**Precision (%)**	**Recall (%)**	**F-score (%)**	**MAE**	**MAHD**
M1	82.9	77.5	80.1	0.7	11.6
M1A	41.9	11.8	18.4	2.2	113.6
M1B	40.4	44.9	42.5	1.4	24.8

***Supplementary Video 3** shows the predicted PS for all three models. The indirect PS estimation (M1) is far more accurate than the direct PS prediction (M1A and M1B).*

wave patterns without noise but sparsified with sparsity levels of $\xi = 1.0, 0.5, 0.25$. The excitation images were sparsified by setting all pixels except every n-th pixel in x- and y-direction to 0 (no signal). Accordingly, a sparsity level of $\xi = 0.25$ corresponds to setting every pixel but every 4th pixel to 0, for instance. **Figures 12C,D** show the prediction accuracies obtained with different combinations of noise and sparsity for the phase prediction with model M1 (angular accuracy) and for the PS prediction with model M1A (F-score), respectively. The individual prediction accuracies were obtained when training was performed with each specific combination of σ and ξ. The map in **Figure 12C** shows that the phase prediction with model M1 is highly accurate and remains above 90% angular accuracy over a wide range of noise and sparsity levels. In particular, with non-sparse data ($\xi = 1.0$), the angular accuracy stays above 95% with noise levels of up to $\sigma = 0.8$, which corresponds to the noise level shown on the right in **Figure 12A**. With $\xi = 0.125$ sparsification, the information in the image is reduced to $16\times16 = 256$ non-zero pixels instead of $128\times128 = 16,384$ pixels. Therefore, the neural network can analyze only less than 2% of the image. Despite this reduction, the network provides accuracies of 94–97% with noise levels of $\sigma = 0.1$–0.2 (and at least 90% with noise levels of up to $\sigma = 0.5$). While the phase prediction is accurate over a broad range of noise and sparsity levels, **Figure 12D** shows that the direct prediction of PS using model M1A is less accurate and robust against noise or sparsity. The F-score stays above 90 % only at low noise or sparsity levels and deteriorates quickly when both increase (e.g., sparsity $\xi = 0.25$ and noise $\sigma = 0.3$). The F-score even drops entirely to 0 % in extremely noisy and sparse regimes. The systematic analysis in **Figure 12D** confirms the impression given in **Figures 9C,D** that the predicted PS trajectories frequently contain false detections when predicted directly. The angular accuracies and F-scores were computed over the testing dataset with 5,000 frames. The data shows that even though noise and sparsity impair the phase prediction accuracy, overall the phase predictions remain, in contrast to the PS prediction, robust and sufficiently accurate in the presence of strong noise and with extreme sparsity. Autoencoder neural networks have excellent denoising capabilities and are very effective at interpolating image data (Vincent et al., 2008; Gondara, 2016), and this property can be observed at work in **Figures 6**, **10**–**12**.

3.5. Spatio-Temporal Sampling Over Spiral Wave's Period Increases Prediction Accuracy

The neural network does not require very much information to be able to predict phase maps or phase singularities (PS). A short sequence of $N_t = 5$–10 excitation wave patterns is sufficient in most situations to make accurate predictions, even with extreme noise and/or sparsity, as shown in **Figure 12**. The results in **Figures 6**–**12** were obtained with either $N_t = 5$ or $N_t = 10$ excitation frames with simulated or experimental data, respectively. The number of sampled frames N_t and the sampling distance τ, which corresponds to the temporal offset between the samples (see sketch in **Figure 13A**), are the two main parameters determining the phase and PS prediction accuracy.

Regarding the number of sampled frames N_t, we found that the predictions become more accurate when sampling the activity with more frames, but the accuracy does not improve significantly further with more than $5 - 10$ frames. Analyzing a short spatio-temporal sequence ($N_t = 4, 5, \ldots, 10$) rather than just a single, static ($N_t = 1$) excitation wave pattern or a few ($N_t = 2, 3$) excitation wave patterns does not only increase the accuracy, but also improves the prediction robustness and ensures that the neural network is able to make predictions at

all in difficult environments with high noise or sparsity (see **Figures 13B–D**). **Figure 13B** shows how the prediction fails entirely if the network only analyzes 1 frame, but becomes progressively better with each frame and finally succeeds to produce satisfactory phase predictions (80%) when it analyzes a short sequence of $N_t = 2, 4, 5$ frames. In this example, the phase map was predicted from a very noisy ($\sigma = 0.8$) and very sparse ($\xi = 0.125$) excitation pattern. The data demonstrates that the neural network is able to compensate information that is lacking in space with additional information it retrieves over time. The multi-frame analysis can also slightly improve the neural network's prediction accuracy when it already achieves high accuracies in less extreme conditions. **Figure 13C** shows that the F-score increases from 22% to about 85% when using $N_t = 1, 3, 5, 7, 10$ frames for the direct PS prediction with model M1A. **Figure 13D** shows that the angular accuracy increases slightly from 93% to 97% when using $N_t = 1,2,3,4,5$ frames for the phase prediction with model M1 with low sparsity ($\xi = 0.5$) and low noise ($\sigma = 0.2$). The PS prediction benefits more from the multi-frame analysis as it is more sensitive to noise and sparsity.

Regarding the sampling distance τ, we made the following observations: (1) With experimental data, we were able to mix the rabbit, pig and simulation data and even though τ was not perfectly adjusted to all of the different dominant frequencies of the wave dynamics or imaging speeds, the network was able to produce accurate predictions across all data (see **Figure 8**). We chose a sampling distance of $\tau = 12$ ms for both the rabbit and pig data, resulting in an effective framerate of 83 fps. With $N_t = 10$ the series of sampled frames covered 75–140% of the cycle length or dominant period of the VF dynamics (about 90–170 ms). The phase prediction failed with the experimental data when we used shorter sampling times $T_\tau = \tau \cdot N_t$, which covered only a smaller fraction of the cycle length (e.g., 15%). (2) With the simulation data shown in **Figure 4A**, the sampling distance τ did not affect the phase prediction accuracy at all, and we achieved high accuracies even with short sampling times T_τ (e.g., 5% with $N_t = 5$ and $\tau = 1$). **Figure 13E** shows that the angular accuracy does not change significantly when the sampling distance is varied ($\tau = 1$, $\tau = 5$, or $\tau = 10$ with $N_t = 5$ frames, shown for 3 different noise and sparsity levels). With these parameters, the dynamics are sampled over 5, 25, or 50 simulation time steps, which corresponds to about 5, 25, or 50% of the average cycle length or dominant period of the spiral wave dynamics of about 100 simulation time steps, respectively.

3.6. Training Data Diversity Increases Robustness Against Varying Imaging Parameters

Training the neural network with more diverse data broadens the distribution of data it can analyze and will prevent eventual overfitting to a particular feature in a dataset. The network's insensitivity to the sampling distance τ with the simulation data, as discussed in section 3.5 and shown in **Figure 13E**, is an indication for overfitting when training and predicting solely on simulation data, because the same model trained with and applied to optical mapping data is unable to produce correct predictions with short τ. The different behavior with simulation and experimental data suggests that the network specializes with the simulation data in memorizing the dynamics based on instantaneous features (moving wavefronts etc.). However, this approach fails with experimental data, in which case it only succeeds if it is provided information that was sampled over a significant portion or the entire period of the reentry pattern. Interestingly, we also made the following observation: **Figure 14C** shows that the phase prediction accuracy drops if training was performed on the simulation data with just one specific sampling distance τ_{train} and the network is then applied to data that was sampled with a different sampling distance $\tau \neq \tau_{train}$. Importantly, the analysis was performed on the simulation data without data augmentation, as shown in **Figure 4A** (with $\sigma = 0$, $\xi = 1$). However, **Figure 4D** shows that if the same simulation data is augmented with the masks shown in **Figure 4B**, see also **Supplementary Video 2**, then the network performs better and achieves higher accuracies at other sampling distances τ even though it was not trained on these τ values. For instance, if the network was trained with $\tau_{train} = 5$ and achieves an accuracy of 99% at $\tau = 5$, it still achieves an accuracy of 96–97% with $\tau = 3$ or $\tau = 7$ just because the input data was augmented and includes other features (arbitrary masked regions) than just the wave dynamics on a square simulation domain. These findings are consistent with the finding that a single τ could be used with a mix of experimental and simulated data, as described in section 3.1.

Similarly, **Figure 14C** shows that if the neural network is trained solely with a particular sparsification, for instance with $\xi = 0.25$, then it excels at performing predictions with $\xi = 0.25$, but fails with different sparsifications. Accordingly, the phase prediction only succeeds when the sparsity of the testing dataset matches the sparsity during training (along the diagonal), and fails when the sparsities in the training and testing datasets are different (off the diagonal). However, this issue can be resolved by training the network with data that includes all sparsifications (here $\xi = 1.0, 0.5, 0.25, 0.17, 0.125$). **Figure 14D** shows that the same neural network can be applied to arbitrary noise and sparsification levels and will consistently yield phase prediction accuracies above 90% when the training was performed with data that contained all noise and sparsification levels. By contrast, in **Figure 12C** the training was performed individually with each specific combination of noise and sparsification. The broader training in **Figure 14D** makes the network more robust and yields just as high phase prediction accuracies as with each individual specialized training in **Figure 12C**.

The anecdotal findings in **Figures 8**, **14** are representative of a very general property of neural networks and data driven approaches. Similar observations would be made with other parameters, such as noise, blurring or arbitrary sparsification patterns and we made very similar observations in a previous study (Christoph and Lebert, 2020) with an architecturally very similar neural network.

3.7. Predicting Future Phase Maps or PS Positions

It is possible to predict phase maps and PS positions in future time steps, but only within the immediate future. **Figure 15** shows predictions of phase maps with simulated spiral wave chaos, which the neural network M1 predicted 15 and 50 simulation time steps into the future. The network analyzed $N_t = 5$ excitation wave frames at $t = 0,-5,-10,-15,-20$ to make each phase prediction and achieved 97.6% ± 2.5, 96.0% ± 3.4, 95.5% ± 4.1, and 87.7% ± 17.6% angular prediction accuracy 5, 10, 15, and 50 simulation time steps into the future, respectively. As the average cycle length or rotational period of the activity is about 100 simulation time steps, this corresponds to about half a rotation within which the prediction yet achieves satisfactory accuracies and about 1/5 of a rotation within which the prediction achieves very good accuracies.

4. DISCUSSION

We demonstrate that deep neural networks can be used to compute phase maps and locate the position of phase singularities (PS) when analyzing cardiac excitation wave dynamics. PS can be predicted by deep neural networks either directly from excitation wave patterns or indirectly by predicting first phase maps from the excitation wave patterns and then calculating PS in the predicted phase maps using classical techniques (e.g., the circular line integral method, shown in **Figure 1C**). This latter step is possible because the predicted phase maps are smooth. We found that the direct PS prediction was less robust than the prediction of phase maps, particularly with challenging data, and, accordingly, we only succeeded to reliably predict PS positions in experimental data with the indirect method. Predictions of phase maps and PS can be performed almost instantaneously from a short temporal sequence consisting of 1–10 snapshots of cardiac excitation waves. We successfully applied this deep learning-based rotor localization and phase mapping technique to both simulated and *ex-vivo* optical mapping data of ventricular fibrillation (VF), and we expect that the technique can also be applied to catheter mapping data of cardiac arrhythmias in clinical patients.

A critical issue in the use of neural networks lies in ensuring that the networks "generalize". Neural networks are known to perform very well when applied to data that is very similar to, or "within the distribution," of the training data, but their accuracy and robustness can quickly deteriorate when applied to other, less similar "out-of-distribution" data. Our results demonstrate that our deep learning-based phase mapping algorithm can be developed in one species and then applied to another species. We even show that the phase mapping algorithm can be developed with synthetic data generated in computer simulations and then applied to experimental data. This latter observation is particularly noteworthy in that the simulation data used to train the network was 2D, whereas the experimental data to which it was applied were surface observations of 3D dynamics. These findings suggest that the algorithm is able to learn the relevant correlation between patterns in a specific distribution of data, and then extrapolate this mapping to differently distributed data that is well outside of the training distribution. From our results it appears that the deep learning algorithm learns to associate phase patterns with a broad class of excitable spatio-temporal activity, and understands the more generalized phase mapping problem, independent of physiological parameters or species-dependent wave dynamics.

Based on these findings, we anticipate that it will be possible to develop a similar deep learning-based phase mapping approach for clinical mapping of arrhythmias in human patients. Neural networks can in principle analyze any data, and they will likely be able to predict phase maps from extracellular field potential or electrogram measurements, just as they are able to predict phase maps from optical measurements of the cellular transmembrane potential. Because neural networks excel at detecting hidden patterns in data, "ignoring" noise, interpolating missing data, and enhancing spatial resolution, all of which they can do simultaneously, they are ideally suited for the analysis of catheter mapping data of atrial fibrillation. The application of such a deep learning-based algorithm would not only be restricted just to phase mapping, but could in principle also be extended to map any other characterizing feature of arrhythmias (e.g., activation or conduction velocity maps). As our results indicate, neural networks would be able to integrate sparse data acquired with multi-electrode basket catheters, given that they are trained with adequate high-resolution imaging data, which could be generated *ex vivo* or in computer simulations. Ultimately, deep-learning has great potential to alleviate some of the shortcomings of catheter mapping, which are largely associated with limited spatial resolution and interpolation artifacts (Martinez-Mateu et al., 2018; Van Nieuwenhuyse et al., 2021), that in turn can lead to misrepresentations of rotor dynamics and fibrillatory wave patterns during atrial fibrillation.

Other advantages of our technique are (i) that it can compute phase maps and PS in real-time with data that was acquired over a brief interval and (ii) that it can obviate pre-processing of the raw data (e.g., spatio-temporal smoothing and outlier removal). The predictions do not require the collection of long time-series, can be performed within one rotational period of the wave dynamics (see **Figure 13A**), and can be calculated in real-time at 500–1,000 fps using GPU hardware (at 128×128 pixels resolution). Predictions can furthermore be performed into the immediate future, enabling predictions of PS positions within about the next 1/4 rotation of reentrant wave dynamics (see **Figure 15**). The latter aspect ii) makes the technique ideal for the processing of very noisy video data or data containing artifacts, such as motion artifacts. This could also make it an attractive phase mapping approach in other fields beyond cardiovascular research, for instance, when studying the dynamics of excitation waves and topological defects in other biological systems (Huang et al., 2010; Taniguchi et al., 2013; Tan et al., 2020; Liu et al., 2021). We expect that deep learning-based phase mapping can be applied to various forms of data. However, it should be noted that each application may require its own specialized training dataset and specific deep learning algorithm, despite the ability of these algorithms to generalize. The routine use

of the technique across many different laboratories will likely only be achieved with much larger and more diverse training datasets (including various species and experimental conditions). Further, neural networks are not a filtering technique *per se*, and will only be able to perform a particular task (e.g., denoising) if they are trained on adequate data. In future applications it will be crucial that training data includes the features, which are necessary for the neural network to learn the desired tasks. While we provided a proof-of-concept, we also acknowledge that there is still potential for improving the phase mapping and direct PS prediction overall, especially for use with experimental data. We found that the direct PS prediction was more sensitive to challenging data than the prediction of phase maps, especially with optical mapping data or noisy and sparsified simulation data. We anticipate that better direct PS predictions or even higher phase mapping accuracies could be achieved with both more and better training data and more advanced neural network architectures. We aim to address these issues in future research.

5. CONCLUSIONS

We demonstrated that convolutional neural networks can be used to predict phase maps and rotor core positions or phase singularities (PS) of reentrant cardiac excitation wave dynamics in both voltage-sensitive optical maps of ventricular fibrillation and simulated data mimicking low-resolution and/or sparse multi-electrode mapping data. The predictions can be made almost instantaneously, robustly and with accuracies of about 95%, and can be performed even in the presence of strong noise and highly sparse or incomplete data. Neural networks used for phase mapping of cardiac excitation waves are able to analyze data obtained in one species, even if they were trained on a different species, and can predict phase maps and PS with experimental data, even if they were trained solely with simulated data of electrical spiral wave chaos. In the future, our approach could be used in electro-anatomic mapping applications for the diagnosis of atrial fibrillation.

DATA AVAILABILITY STATEMENT

The raw data and source code supporting the conclusions of this article will be made available by the authors upon reasonable request.

ETHICS STATEMENT

All experiments conformed to the current Guide for Care and Use of Laboratory Animals, published by the National Institutes of Health (NIH Publication No. 85-23, revised 1996) and were approved by the Office of Research and Integrity Assurance at Georgia Institute of Technology.

AUTHOR CONTRIBUTIONS

JL and JC conceived the research and implemented the algorithms. JL, NR, and JC conducted the data analysis and designed the figures. FHF performed the experiments and provided the experimental data. JL, FHF, and JC discussed the results and wrote the manuscript. All authors contributed to the article and approved the submitted version.

FUNDING

This research was funded by the University of California, San Francisco. NR was a research Fellow supported by the Sarnoff Cardiovascular Research Foundation. FHF acknowledges support from NSF 2037894 and NIH 1R01HL143450.

SUPPLEMENTARY MATERIAL

The Supplementary Material for this article can be found online at: https://www.frontiersin.org/articles/10.3389/fphys.2021.782176/full#supplementary-material

Supplementary Video 1 | Neural network predictions of phase maps from voltage-sensitive optical mapping video data. The recording shows action potential spiral vortex waves during ventricular fibrillation on the left ventricular surface of a porcine heart, see also **Figure 6**. The pixel-wise normalized transmembrane voltage is shown on the left (yellow: depolarized, blue: repolarized tissue). Center: smoothed ground truth phase map, which was obtained from the noisy optical maps using the Hilbert transform, see **Figure 5A** and section 2.2. Right: phase map predicted by the neural network.

Supplementary Video 2 | Comparison of the neural network input images for the prediction of a single phase map for the pig, rabbit, and simulation datasets used in **Figures 7**, **8**. The video shows the $N_t = 10$ images given as input to the neural network to predict a single phase map for each type of dataset.

Supplementary Video 3 | PS prediction for rabbit optical mapping data using neural network models M1 **(left)**, M1A **(middle)**, M1B **(right)**. The PS for model M1 are predicted indirectly by first predicting phase maps then computing PS in the phase maps using the circular line integration method.

Supplementary Video 4 | Phase maps predicted by the neural network from (sparse) simulated electrical excitation wave maps without and with noise ($\sigma = 0.3$). **Left**: electric excitation wave maps uses as network input ($N_t = 5$). **Center**: ground truth or true phase. **Right**: neural network output.

Supplementary Video 5 | Phase singularities (PS) predicted by the neural network M1A from (sparse) simulated electrical spiral wave chaos without and with noise ($\sigma = 0.2$) for $N_t = 5$. **Left:** ground truth electrical excitation, **Center**: network input, **Right**: predicted PS (black) and true PS (white) superimposed onto the corresponding electrical excitation wave maps.

Supplementary Video 6 | Phase maps predicted by the neural network from (sparse) simulated electrical excitation wave maps without and with noise ($\sigma = 0.3$) for $N_t = 5$.

Supplementary Video 7 | Neural network prediction of a single phase map. The 5 noisy and sparse electrical wave frames given as input to the neural network, as well as the predicted phase map and the true phase map are shown.

Supplementary Video 8 | PS prediction using model M1 for the sparse and noisy excitation patterns shown in **Figure 11**. The predicted PS are shown in red, the ground truth in white. **Left**: The sparse excitation wave pattern with noise used as neural network input. **Right**: Ground truth excitation with sparsification shown in black.

REFERENCES

Abad, R., Collart, O., Ganesan, P., Rogers, A. J., Alhusseini, M. I., Rodrigo, M., et al. (2021). Three dimensional reconstruction to visualize atrial fibrillation activation patterns on curved atrial geometry. *PLoS ONE* 16 e0249873. doi: 10.1371/journal.pone.0249873

Abadi, M., Agarwal, A., Barham, P., Brevdo, E., Chen, Z., Citro, C., et al. (2015). *TensorFlow: Large-Scale Machine Learning on Heterogeneous Systems*. Available online at: tensorflow.org.

Alhusseini, M. I., Abuzaid, F., Rogers, A. J., Zaman, J. A., Baykaner, T., Clopton, P., et al. (2020). Machine learning to classify intracardiac electrical patterns during atrial fibrillation. *Circ. Arrhythmia Electrophysiol.* 13:e008160. doi: 10.1161/CIRCEP.119.008160

Aliev, R. R., and Panfilov, A. V. (1996). A simple two-variable model of cardiac excitation. *Chaos Solitons Fractals* 7, 293–301. doi: 10.1016/0960-0779(95)00089-5

Aronis, K. N., Berger, R. D., and Ashikaga, H. (2017). Rotors. *Circ Arrhythmia Electrophysiol.* 10:e005634. doi: 10.1161/CIRCEP.117.005634

Barkley, D., Kness, M., and Tuckerman, L. S. (1990). Spiral-wave dynamics in a simple model of excitable media: the transition from simple to compound rotation. *Phys. Rev. A* 42, 2489–2492. doi: 10.1103/PhysRevA.42.2489

Bray, M.-A., Lin, S.-F., Aliev, R. R., Roth, B. J., and Wikwso, J. P. Jr. (2001). Experimental and theoretical analysis of phase singularity dynamics in cardiac tissue. *J. Cardiovasc. Electrophysiol.* 12, 716–722. doi: 10.1046/j.1540-8167.2001.00716.x

Bray, M.-A., and Wikswo, J. P. (2002). Considerations in phase plane analysis for nonstationary reentrant cardiac behavior. *Phys. Rev. E* 65:051902. doi: 10.1103/PhysRevE.65.051902

Bursac, N., Aguel, F., and Tung, L. (2004). Multiarm spirals in a two-dimensional cardiac substrate. *Proc. Natl. Acad. Sci. U.S.A.* 101, 15530–15534. doi: 10.1073/pnas.0400984101

Christoph, J., Chebbok, M., Richter, C., Schröder-Schetelig, J., Bittihn, P., Stein, S., et al. (2018). Electromechanical vortex filaments during cardiac fibrillation. *Nature* 555, 667–672. doi: 10.1038/nature26001

Christoph, J., and Lebert, J. (2020). Inverse mechano-electrical reconstruction of cardiac excitation wave patterns from mechanical deformation using deep learning. *Chaos Interdiscipl J Nonlinear Sci.* 30:123134. doi: 10.1063/5.0023751

Christoph, J., and Luther, S. (2018). Marker-free tracking for motion artifact compensation and deformation measurements in optical mapping videos of contracting hearts. *Front. Physiol.* 9:1483. doi: 10.3389/fphys.2018.01483

Clayton, R., Zhuchkova, E., and Panfilov, A. (2006). Phase singularities and filaments: Simplifying complexity in computational models of ventricular fibrillation. *Prog. Biophys. Mol. Biol.* 90, 378–398. doi: 10.1016/j.pbiomolbio.2005.06.011

Entcheva, E., and Bien, H. (2006). Macroscopic optical mapping of excitation in cardiac cell networks with ultra-high spatiotemporal resolution. *Prog. Biophys. Mol. Biol.* 92, 232–257. doi: 10.1016/j.pbiomolbio.2005.10.003

Fenton, F., and Karma, A. (1998). Vortex dynamics in three-dimensional continuous myocardium with fiber rotation: filament instability and fibrillation. *Chaos Interdiscipl. J. Nonlinear Sci.* 8, 20–47. doi: 10.1063/1.166311

Gondara, L. (2016). Medical image denoising using convolutional denoising autoencoders. *arXiv preprint arXiv:1608.04667v04662*. doi: 10.1109/ICDMW.2016.0041

Gray, R. A., Pertsov, A. M., and Jalife, J. (1998). Spatial and temporal organization during cardiac fibrillation. *Nature* 392, 75–78. doi: 10.1038/32164

Guillem, M. S., Climent, A. M., Rodrigo, M., Fernandez-Aviles, F., Atienza, F., and Berenfeld, O. (2016). Presence and stability of rotors in atrial fibrillation: evidence and therapeutic implications. *Cardiovasc. Res.* 109, 480–492. doi: 10.1093/cvr/cvw011

Gurevich, D. R., and Grigoriev, R. O. (2019). Robust approach for rotor mapping in cardiac tissue. *Chaos Interdiscipl. J. Nonlinear Sci.* 29:053101. doi: 10.1063/1.5086936

Gurevich, D. R., Herndon, C., Uzelac, I., Fenton, F. H., and Grigoriev, R. O. (2017). "Level-set method for robust analysis of optical mapping recordings of fibrillation," in *2017 Computing in Cardiology (CinC)* (Rennes), 1–4. doi: 10.22489/CinC.2017.197-427

Hochreiter, S., and Schmidhuber, J. (1997). Long short-term memory. *Neural Comput.* 9, 1735–1780. doi: 10.1162/neco.1997.9.8.1735

Huang, X., Xu, W., Liang, J., Takagaki, K., Gao, X., and young Wu, J. (2010). Spiral wave dynamics in neocortex. *Neuron* 68, 978–990. doi: 10.1016/j.neuron.2010.11.007

Hwang, M., Song, J.-S., Lee, Y.-S., Li, C., Shim, E. B., and Pak, H.-N. (2016). Electrophysiological rotor ablation in *in-silico* modeling of atrial fibrillation: comparisons with dominant frequency, shannon entropy, and phase singularity. *PLoS ONE* 11:e0149695. doi: 10.1371/journal.pone.0149695

Ioffe, S., and Szegedy, C. (2015). "Batch normalization: Accelerating deep network training by reducing internal covariate shift," in *Proceedings of the 32nd International Conference on Machine Learning*, eds F. Bach and D. Blei (Lille: PMLR), 448–456.

Iyer, A. N., and Gray, R. A. (2001). An experimentalist's approach to accurate localization of phase singularities during reentry. *Ann. Biomed. Eng.* 29, 47–59. doi: 10.1114/1.1335538

King, B., Porta-Sanchez, A., Masse, S., Zamiri, N., Balasundaram, K., Kusha, M., et al. (2017). Effect of spatial resolution and filtering on mapping cardiac fibrillation. *Heart Rhythm* 14, 608–615. doi: 10.1016/j.hrthm.2017.01.023

Kingma, D. P., and Ba, J. (2015). Adam: a method for stochastic optimization. *arXiv [Preprint]*. arXiv:1412.6980

Krinsky, V. I., Efimov, I. R., and Jalife, J. (1992). Vortices with linear cores in excitable media. *Proc. R. Soc. Lond. Ser. A Math. Phys. Sci.* 437, 645–655. doi: 10.1098/rspa.1992.0084

Kuklik, P., Zeemering, S., Maesen, B., Maessen, J., Crijns, H. J., Verheule, S., et al. (2015). Reconstruction of instantaneous phase of unipolar atrial contact electrogram using a concept of sinusoidal recomposition and hilbert transform. *IEEE Trans. Biomed. Eng.* 62, 296–302. doi: 10.1109/TBME.2014.2350029

Kuklik, P., Zeemering, S., van Hunnik, A., Maesen, B., Pison, L., Lau, D. H., et al. (2017). Identification of rotors during human atrial fibrillation using contact mapping and phase singularity detection: technical considerations. *IEEE Trans. Biomed. Eng.* 64, 310–318. doi: 10.1109/TBME.2016.2554660

Kuramoto, Y. (1984). *Chemical Oscillations, Waves, and Turbulence*. Berlin; Heidelberg: Springer. doi: 10.1007/978-3-642-69689-3

Lee, Y.-S., Song, J.-S., Hwang, M., Lim, B., Joung, B., and Pak, H.-N. (2016). A new efficient method for detecting phase singularity in cardiac fibrillation. *PLoS ONE* 11:e0167567. doi: 10.1371/journal.pone.0167567

Li, T.-C., Pan, D.-B., Zhou, K., Jiang, R., Jiang, C., Zheng, B., et al. (2018). Jacobian-determinant method of identifying phase singularity during reentry. *Phys. Rev. E* 98:062405. doi: 10.1103/PhysRevE.98.062405

Li, X., Almeida, T. P., Dastagir, N., Guillem, M. S., Salinet, J., Chu, G. S., et al. (2020). Standardizing single-frame phase singularity identification algorithms and parameters in phase mapping during human atrial fibrillation. *Front. Physiol.* 11:869. doi: 10.3389/fphys.2020.00869

Liu, J., Totz, J. F., Miller, P. W., Hastewell, A. D., Chao, Y.-C., Dunkel, J., et al. (2021). Topological braiding and virtual particles on the cell membrane. *Proc. Natl. Acad. Sci. U.S.A.* 118. doi: 10.1073/pnas.2104191118

Liu, Y.-B., Peter, A., Lamp, S. T., Weiss, J. N., Chen, P.-S., and Lin, S.-F. (2003). Spatiotemporal correlation between phase singularities and wavebreaks during ventricular fibrillation. *J. Cardiovasc. Electrophysiol.* 14, 1103–1109. doi: 10.1046/j.1540-8167.2003.03218.x

Marcotte, C. D., and Grigoriev, R. O. (2017). Dynamical mechanism of atrial fibrillation: a topological approach. *Chaos Interdiscipl. J. Nonlinear Sci.* 27:093936. doi: 10.1063/1.5003259

Martinez-Mateu, L., Romero, L., Ferrer-Albero, A., Sebastian, R., Rodriguez Matas, J. F., Jalife, J., et al. (2018). Factors affecting basket catheter detection of real and phantom rotors in the atria: a computational study. *PLoS Comput. Biol.* 14:e1006017. doi: 10.1371/journal.pcbi.1006017

Mulimani, M. K., Alageshan, J. K., and Pandit, R. (2020). Deep-learning-assisted detection and termination of spiral and broken-spiral waves in mathematical models for cardiac tissue. *Phys. Rev. Res.* 2:023155. doi: 10.1103/PhysRevResearch.2.023155

Munoz, V., Grzeda, K. R., Desplantez, T., Pandit, S. V., Mironov, S., Taffet, S. M., et al. (2007). Adenoviral expression of I_KS contributes to wavebreak and fibrillatory conduction in neonatal rat ventricular cardiomyocyte monolayers. *Circ. Res.* 101, 475–483. doi: 10.1161/CIRCRESAHA.107.149617

Nair, V., and Hinton, G. E. (2010). "Rectified linear units improve restricted Boltzmann machines," in *ICML'10* (Madison, WI: Omni Press), 807–814.

Nash, M. P., Mourad, A., Clayton, R. H., Sutton, P. M., Bradley, C. P., Hayward, M., et al. (2006). Evidence for multiple mechanisms in human ventricular fibrillation. *Circulation* 114, 536–542. doi: 10.1161/CIRCULATIONAHA.105.602870

Nattel, S., Xiong, F., and Aguilar, M. (2017). Demystifying rotors and their place in clinical translation of atrial fibrillation mechanisms. *Nat. Rev. Cardiol.* 14, 509–520. doi: 10.1038/nrcardio.2017.37

Podziemski, P., Zeemering, S., Kuklik, P., van Hunnik, A., Maesen, B., Maessen, J., et al. (2018). Rotors detected by phase analysis of filtered, epicardial atrial fibrillation electrograms colocalize with regions of conduction block. *Circ Arrhythmia Electrophysiol.* 11:e005858. doi: 10.1161/CIRCEP.117.005858

Ribera, J., Guera, D., Chen, Y., and Delp, E. J. (2019). "Locating objects without bounding boxes,' in *2019 IEEE/CVF Conference on Computer Vision and Pattern Recognition (CVPR)* (Long Beach, CA). doi: 10.1109/cvpr.2019.00664

Rodrigo, M., Climent, A. M., Liberos, A., Fernandez-Aviles, F., Berenfeld, O., Atienza, F., et al. (2017). Technical considerations on phase mapping for identification of atrial reentrant activity in direct- and inverse-computed electrograms. *Circ. Arrhythmia Electrophysiol.* 10:e005008. doi: 10.1161/CIRCEP.117.005008

Rogers, J. (2004). Combined phase singularity and wavefront analysis for optical maps of ventricular fibrillation. *IEEE Trans. Biomed. Eng.* 51, 56–65. doi: 10.1109/TBME.2003.820341

Roney, C., Wit, A. L., and Peters, N. (2019). Challenges associated with interpreting mechanisms of AF. *Arrhythmia Electrophysiol. Rev.* 8, 273–284. doi: 10.15420/aer.2019.08

Roney, C. H., Cantwell, C. D., Bayer, J. D., Qureshi, N. A., Lim, P. B., Tweedy, J. H., et al. (2017). Spatial resolution requirements for accurate identification of drivers of atrial fibrillation. *Circ. Arrhythmia Electrophysiol.* 10:e004899. doi: 10.1161/CIRCEP.116.004899

Ronneberger, O., Fischer, P., and Brox, T. (2015). "U-Net: convolutional networks for biomedical image segmentation," in *Lecture Notesin Computer Science*, eds N. Navab, J. Hornegger, W. M. Wells, and A. F. Frangi (Cham: Springer International Publishing), 234–241. doi: 10.1007/978-3-319-24574-4_28

Schotten, U., Lee, S., Zeemering, S., and Waldo, A. L. (2020). Paradigm shifts in electrophysiological mechanisms of atrial fibrillation. *Europace* 23(Suppl_2), ii9–ii13. doi: 10.1093/europace/euaa384

Shi, X., Chen, Z., Wang, H., Yeung, D., Wong, W., and Woo, W. (2015). "Convolutional LSTM network: a machine learning approach for precipitation nowcasting," in *Annual Conference on Neural Information Processing Systems 2015*, eds C. Cortes, N. D. Lawrence, D. D. Lee, M. Sugiyama, and R. Garnett (Montreal, QC), 802–810.

Tan, T., Liu, J., Miller, P., Tekant, M., Dunkel, J., and Fakhri, N. (2020). Topological turbulence in the membrane of a living cell. *Nat. Phys.* 16, 657–662. doi: 10.1038/s41567-020-0841-9

Taniguchi, D., Ishihara, S., Oonuki, T., Honda-Kitahara, M., Kaneko, K., and Sawai, S. (2013). Phase geometries of two-dimensional excitable waves govern self-organized morphodynamics of amoeboid cells. *Proc. Natl. Acad. Sci. U.S.A.* 110, 5016–5021. doi: 10.1073/pnas.1218025110

Tomii, N., Yamazaki, M., Arafune, T., Honjo, H., Shibata, N., and Sakuma, I. (2016). Detection algorithm of phase singularity using phase variance analysis for epicardial optical mapping data. *IEEE Trans. Biomed. Eng.* 63, 1795–1803. doi: 10.1109/TBME.2015.2502726

Umapathy, K., Nair, K., Masse, S., Krishnan, S., Rogers, J., Nash, M. P., et al. (2010). Phase mapping of cardiac fibrillation. *Circ. Arrhythmia Electrophysiol.* 3, 105–114. doi: 10.1161/CIRCEP.110.853804

Valderrabano, M., Chen, P.-S., and Lin, S.-F. (2003). Spatial distribution of phase singularities in ventricular fibrillation. *Circulation* 108, 354–359. doi: 10.1161/01.CIR.0000080322.67408.B4

Van Nieuwenhuyse, E., Martinez-Mateu, L., Saiz, J., Panfilov, A. V., and Vandersickel, N. (2021). Directed graph mapping exceeds phase mapping in discriminating true and false rotors detected with a basket catheter in a complex *in-silico* excitation pattern. *Comput. Biol. Med.* 133:104381. doi: 10.1016/j.compbiomed.2021.104381

Vandersickel, N., Van Nieuwenhuyse, E., Van Cleemput, N., Goedgebeur, J., El Haddad, M., De Neve, J., et al. (2019). Directed networks as a novel way to describe and analyze cardiac excitation: directed graph mapping. *Front. Physiol.* 10:1138. doi: 10.3389/fphys.2019.01138

Vincent, P., Larochelle, H., Bengio, Y., and Manzagol, P.-A. (2008). *Extracting and Composing Robust Features with Denoising Autoencoders*. Helsinki: Association for Computing Machinery. doi: 10.1145/1390156.1390294

Winfree, A. T. (1989). Electrical instability in cardiac muscle: phase singularities and rotors. *J. Theoret. Biol.* 138, 353–405. doi: 10.1016/S0022-5193(89)80200-0

Witkowski, F. X., Leon, L. J., Penkoske, P. A., Giles, W. R., Spano, M. L., Ditto, W. L., et al. (1998). Spatiotemporal evolution of ventricular fibrillation. *Nature* 392, 78–82. doi: 10.1038/32170

Yamazaki, M., Mironov, S., Taravant, C., Brec, J., Vaquero, L. M., Bandaru, K., et al. (2012). Heterogeneous atrial wall thickness and stretch promote scroll waves anchoring during atrial fibrillation. *Cardiovasc. Res.* 94, 48–57. doi: 10.1093/cvr/cvr357

You, M. J., Langfield, P., Campanari, L., Dobbs, M., Shrier, A., and Glass, L. (2017). Demonstration of cardiac rotor and source mapping techniques in embryonic chick monolayers. *Chaos Interdiscipl. J. Nonlinear Sci.* 27:093938. doi: 10.1063/1.5001459

Zaitsev, A. V., Guha, P. K., Sarmast, F., Kolli, A., Berenfeld, O., Pertsov, A. M., et al. (2003). Wavebreak formation during ventricular fibrillation in the isolated, regionally ischemic pig heart. *Circ. Res.* 92, 546–553. doi: 10.1161/01.RES.0000061917.23107.F7

Zaritski, R., Mironov, S. F., and Pertsov, A. M. (2004). Intermittent self-organization of scroll wave turbulence in three-dimensional excitable media. *Phys. Rev. Lett.* 23:168302. doi: 10.1103/PhysRevLett.92.168302

Zou, R., Kneller, J., Leon, L. J., and Nattel, S. (2002). Development of a computer algorithm for the detection of phase singularities and initial application to analyze simulations of atrial fibrillation. *Chaos Interdiscipl. J. Nonlinear Sci.* 12, 764–778. doi: 10.1063/1.1497505

Conflict of Interest: The authors declare that the research was conducted in the absence of any commercial or financial relationships that could be construed as a potential conflict of interest.

frontiers in Physiology

ORIGINAL RESEARCH
published: 20 January 2022
doi: 10.3389/fphys.2021.767190

Similarity Score for the Identification of Active Sites in Patients With Atrial Fibrillation

*Vasanth Ravikumar[1], Sanket Thakare[2], Xiangzhen Kong[1], Henri Roukoz[3] and Elena G. Tolkacheva[2]**

[1] Department of Electrical and Computer Engineering, University of Minnesota, Minneapolis, MN, United States, [2] Department of Biomedical Engineering, University of Minnesota, Minneapolis, MN, United States, [3] Division of Cardiology, Department of Medicine, University of Minnesota, Minneapolis, MN, United States

OPEN ACCESS

Edited by:
T. Alexander Quinn, Dalhousie University, Canada

Reviewed by:
Tamas Szili-Torok, Erasmus University Medical Center, Netherlands
Larisa G. Tereshchenko, Oregon Health & Science University, United States
Felipe Atienza, Gregorio Marañón Hospital, Spain
Damian Redfearn, Queen's University, Canada

***Correspondence:**
Elena G. Tolkacheva
talkacal@umn.edu

Specialty section:
This article was submitted to Cardiac Electrophysiology, a section of the journal Frontiers in Physiology

Received: *30 August 2021*
Accepted: *24 November 2021*
Published: *20 January 2022*

Citation:
Ravikumar V, Thakare S, Kong X, Roukoz H and Tolkacheva EG (2022) Similarity Score for the Identification of Active Sites in Patients With Atrial Fibrillation. Front. Physiol. 12:767190. doi: 10.3389/fphys.2021.767190

Background: Atrial fibrillation (AF) is the most common cardiac arrhythmia and precursor to other cardiac diseases. Catheter ablation is associated with limited success rates in patients with persistent AF. Currently, existing mapping systems fail to identify critical target sites for ablation. Recently, we proposed and validated several individual techniques, such as dominant frequency (DF), multiscale frequency (MSF), kurtosis (Kt), and multiscale entropy (MSE), to identify active sites of arrhythmias using simulated intracardiac electrograms (iEGMs). However, the individual performances of these techniques to identify arrhythmogenic substrates are not reliable.

Objective: This study aimed to develop a similarity score using various iEGM analysis techniques to more accurately identify the spatial location of active sites of arrhythmia in patients with AF.

Methods: Clinical bipolar iEGMs were obtained from patients with AF who underwent either successful (m = 4) or unsuccessful (m = 4) catheter ablation. A similarity score (0–3) was developed via the earth mover's distance (EMD) approach based on a combination of DF, MSF, MSE, and Kt techniques.

Results: Individual techniques successfully discriminated between successful and unsuccessful AF ablation patients but were not reliable in identifying active spatial sites of AF. However, the proposed similarity score was able to pinpoint the spatial sites with high values (active AF sites) that were observed only in patients with unsuccessful AF termination, suggesting that these active sites were missed during the ablation procedure.

Conclusion: Arrhythmogenic substrates with abnormal electrical activity are identified in patients with unsuccessful AF termination after catheter ablation, suggesting clinical efficacy of similarity score.

Keywords: atrial fibrillation, ablation, signal processing, earth mover's distance (EMD), similarity score

INTRODUCTION

According to an estimate in 2014, 2.7–6.1 million people in the United States are afflicted by atrial fibrillation (AF). AF is the most common type of supraventricular arrhythmia in the United States and is associated with an increased risk of stroke (Go et al., 2001; Miyasaka et al., 2006). AF is characterized by the chaotic electrical activity in the atria (Munger et al., 2014). Furthermore, the prevalence of AF has been projected to increase to nearly 12.1 million people by 2050 (Miyasaka et al., 2006; Colilla et al., 2013). These reasons make AF a significant public health concern and underpin the need to develop more efficient treatment techniques.

Compared with antiarrhythmic drug therapy, catheter ablation improves AF symptoms and quality of life and reduces AF recurrence (Wazni et al., 2005; Jaïs et al., 2008; Wilber et al., 2010). Pulmonary vein (PV) isolation, the most commonly used catheter ablation approach, alone can be used as a strategy for catheter ablation in patients with paroxysmal AF (Sawhney et al., 2009; Ouyang et al., 2010; Chao et al., 2012). However, in the case of persistent and long-standing AF, electrical initiation of AF may arise outside the PV regions, which play an essential role in arrhythmogenesis and maintenance of AF (Elayi et al., 2010). Hence, it is important to identify AF ablation targets outside the PV regions for the improved success of catheter-based ablation therapy.

Several approaches, such as local activation maps, phase maps, and dominant frequency (DF) maps (Pandit and Jalife, 2013), are commonly used to identify ablation target sites. In our laboratory, we developed several novel techniques to identify active sites of AF, especially outside the PV regions, both in the frequency-domain [multiscale frequency (MSF) (Arunachalam et al., 2016b)] and time-domain [multiscale entropy (MSE) (Arunachalam et al., 2018) and kurtosis (Kt) (Arunachalam et al., 2016a)]. All novel techniques have been validated using optical mapping studies of *ex vivo* rabbit hearts and have been established to accurately identify the active sites or arrhythmias, such as pivot point of rotors in experiments where rotors have been visually observed (Annoni et al., 2018). These techniques were shown to be accurate under some clinical limitations, such as reduced signal time duration and decreased spatial resolution. It was also demonstrated that the novel techniques could differentiate between the intracardiac electrograms (iEGMs) recorded from patients with successful and unsuccessful AF ablation (Ravikumar et al., 2021). However, the use of individual approaches fails to robustly identify electrically active spatial sites for ablation (Ravikumar et al., 2021), and therefore, efforts on developing combinatory approaches to identify the active AF sites are needed.

In this study, we aimed to develop a similarity score by combining the various iEGM analysis approaches (DF, MSF, MSE, and Kt) based on an earth mover's distance (EMD) method. We further demonstrated that this similarity score can identify active spatial sites of AF in patients with unsuccessful AF termination, while no active sites of AF were present in patients with successful AF termination.

MATERIALS AND METHODS

Patient Population and Clinical Intracardiac Electrograms Data

All the patients (m = 8) had persistent AF and underwent PV isolation (PVI) during ablation therapy. Successful PVI was defined as the elimination or dissociation of all PV potentials recorded. Complete isolation of PVs was achieved in all cases. In patients whose rhythms were reorganized to atrial tachycardia (AT) or atrial flutter, mapping and ablation of the tachycardia were performed to restore sinus rhythm. In this study, successful AF termination was defined as the acute termination of the AF during PVI or after conversion into organized AT or atrial flutter before conversion into sinus rhythm, either spontaneous or with ablating the residual AT. In patients with unsuccessful AF termination, a further cardioversion procedure was performed to terminate AF, and therefore, unsuccessful AF termination was defined in patients who underwent cardioversion to restore sinus rhythm. The baseline characteristics of all patients are listed in **Supplementary Table 1**.

Clinically recorded bipolar iEGMs (BiEGMs) were obtained from the left atrium (LA) from m = 8 patients, with prior approval under the Institutional Review Board (IRB: STUDY00003128) of the University of Minnesota. All experiments were performed as per relevant guidelines and regulations, and the consent of the patient was obtained before obtaining the data. Simultaneous iEGM collection was carried out using the CARTO (Biosense Webster, Irvine, CA, United States) system, which has a sensor position accuracy of 0.8 mm and 5°. BiEGMs were recorded with a sample rate of 977 Hz and a duration of 5–15 s at different spatial sites (N = 16–24) in each patient, using high-resolution PentaRay catheters (Biosense Webster, Irvine, CA, United States). A spatial site was defined as the unique placement of the PentaRay catheter in the atria so that 10 BiEGMs were recorded and individually analyzed from each spatial site. Furthermore, the distribution of the metrics obtained from 10 BiEGMs in each site for the various approaches was compared using the EMD. Notably, 160–240 BiEGMs were recorded before the PVI ablation procedure.

Three independent reviews were performed to identify the noisy, low amplitude, and contact loss signals. BiEGMs with extremely low amplitude, high noise corruption, loss of contact, and low signal-to-noise ratio were removed, and only the good signals were used for the retrospective analysis. BiEGMs were then filtered with a third-order IIR Butterworth band-pass filter 3–15 Hz to maintain the frequency components of the recorded signals in the physiological range.

Similarity Score Based on Earth Mover's Distance Method

To develop a similarity score, four different approaches that were previously used in the literature for the BiEGM analysis, namely, MSF (Arunachalam et al., 2016b), MSE (Arunachalam et al., 2018), DF (Sanders et al., 2005), and Kt (Arunachalam et al., 2016a), were used. More details of these techniques are provided in **Supplementary Table 2**. We have chosen these

techniques for the initial development of similarity scores since they represent different characteristics of the BiEGM signals such as frequency, information content, and amplitude-based statistics. In this study, we have not examined the contribution of each individual approach to the outcomes of similarity score and therefore assigned equal weights to each approach. Furthermore, the similarity score can be optimized based on various weighted contributions from a different signal processing approaches.

The similarity score is based on the EMD approach (Rubner et al., 2000) and compares the performance of pairs of different individual techniques at various spatial sites in the atria of the patient. A high similarity score indicates that the individual techniques identified the same spatial site as the active site of AF.

The EMD is used to evaluate the similarity between two multidimensional distributions and is based on a solution to the well-known transportation problem (Rubner et al., 2000). First, let $\boldsymbol{P} = \{p_{n,1}, p_{n,2}, \ldots, p_{n,J}\}$ and $\boldsymbol{Q} = \{q_{n,1}, q_{n,2}, \ldots, q_{n,J}\}$ be the distributions of values from two different approaches for $J = 10$ BiEGMs, respectively, recorded at each site n. Second, we defined the Euclidean distance-vector, containing the distance between $\boldsymbol{P}$ and $\boldsymbol{Q}$ elements. Then, at each spatial site n, we calculated EMD_n (**P**, **Q**) as follows:

$$EMD_n\,(\boldsymbol{P}, \boldsymbol{Q}) \;=\; \frac{\sum_{i=1}^{J}\sum_{j=1}^{J} f_{ij} d_{ij}}{\sum_{i=1}^{J}\sum_{j=1}^{J} f_{ij}} \qquad (1)$$

where $n = [1, 2, \ldots, N]$ is spatial sites, f_{ij} is the flow rate between elements p_{n_i} and q_{n_j}, and d_{ij} is the distance between elements p_{n_i} and q_{n_j}. For example, using our recorded data from patient 1, we have $N = 18$ sites. Therefore, we obtained 18 values of EMD_n(**P**, **Q**). The value of EMD = 0.2 was considered as a threshold for similarity, i.e., if two approaches have EMD < 0.2 (Ravikumar et al., 2018), they are similar, i.e., they have a strong correlation. The threshold was selected based on the minimal distances between the distributions. Furthermore, this threshold indicates that matches have a similarity greater than 0.8 on a scale of 0–1 for the minimal distances between the distributions to be satisfied.

The EMD values were calculated for all approaches, and the following pairs were calculated for all the patients at each spatial site: (1) DF vs. MSF, (2) DF vs. MSE, (3) MSF vs. MSE, (4) DF vs. Kt, (5) MSF vs. Kt, and (6) MSE vs. Kt. Then, at each spatial site, the number of pairs satisfying the threshold requirements for the EMD similarity index (EMD < 0.2) was computed, ranging from 0 (no pair is above the threshold) to 6 (all pairs are above the threshold). Finally, a *similarity score* of 0–3 was assigned to each spatial site in every patient reflecting the number of pairs above the threshold: 0 (no pairs), 1 (1–2 pairs), 2 (3–4 pairs), and 3 (5–6 pairs). A high *similarity score* of 3 indicates that all four methods identify this specific spatial location as a potential site for AF abnormal activity and subsequent ablation.

Three-Dimensional Reconstruction Using VIEgram

A custom VIEgram software (Thakare et al., 2020) was used to demonstrate the three-dimensional (3D) visualization of individual approaches using BiEGMs collected from patients with AF. A custom-built Python script was used for data extraction, while data processing and 3D mapping were performed using custom-built MATLAB (MathWorks, Natick, MA, United States) scripts. The 3D images were constructed by superimposing the individual measures on a 3D mesh of the LA, and the individual approaches were correlated using the EMD approach.

Statistical Analysis

All the statistical analyses were performed using the MATLAB (MathWorks, Natick, MA, United States) software. A statistical Wilcoxon rank-sum test was performed for significance testing to determine whether the individual techniques can differentiate between the iEGMs recorded from patients with successful and unsuccessful AF termination, with $p < 0.05$ being considered as statistically significant. For categorical variables expressed as number and percentage, a Fisher's exact test was performed.

RESULTS

First, we aimed to demonstrate whether individual techniques (MSF, MSE, DF, and Kt) can discriminate between patients with successful and unsuccessful AF termination when applied to BiEGMs. In **Figure 1**, the box plots of the MSF, MSE, DF, and Kt values are shown for all patients with successful ($m = 4$) and unsuccessful ($m = 4$) AF termination. Notably, all the methods show statistical significance ($p < 0.05$) between the two groups of patients, suggesting the successful discrimination based on all BiEGMs.

To further demonstrate the performance of the BiEGM analysis approaches in identifying active sites of AF, the 3D visualization of individual approaches was performed using the custom-made VIEgram software. **Figures 2**, **3** show the representative examples of 3D maps of DF, MSF, MSE, and Kt obtained via VIEgram software for patients with unsuccessful and successful AF termination, respectively. The atria are visualized to show the left superior PV (LSPV) and the left inferior PV (LIPV). The corresponding example of a BiEGM signal from a single electrode (#) is also shown along with the individual DF, MSF, MSE, and Kt values from this recording. Notably, the visual inspection of spatial similarity between all four approaches does not suggest any correlation between the techniques both in a patient with unsuccessful and successful AF termination. Therefore, individual approaches alone cannot correctly identify the active sites of AF that should only be present in patients with unsuccessful AF termination.

To improve the performance of the various BiEGM analysis techniques for the identification of active AF sites, a similarity score was developed based on EMD to quantify the correlation between various pairs of the techniques at each spatial site. In **Figures 4**, **5**, the representative examples of the EMD values calculated for different pairs of approaches at different spatial sites are shown for patients with unsuccessful and successful AF termination, respectively. The gray shaded area indicates the regions with EMD < 0.2, where all pairs are strongly correlated, and therefore, the similarity score is high. As indicated

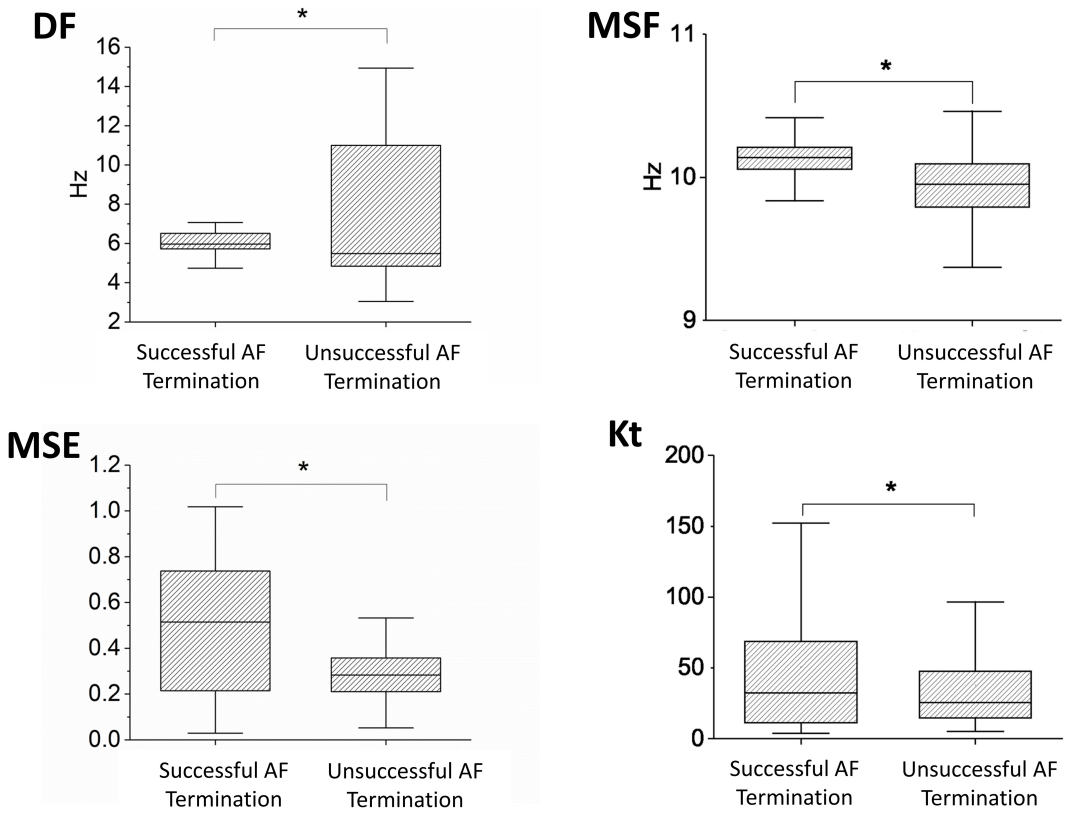

FIGURE 1 | Performance of the different approaches, such as dominant frequency (DF), multiscale frequency (MSF), multiscale entropy (MSE), and kurtosis (Kt), that were applied to the bipolar intracardiac electrogram (BiEGM) analysis from patients with successful (m = 4) and unsuccessful (m = 4) atrial fibrillation (AF) termination. Asterisk indicates statistical significance with $p < 0.05$.

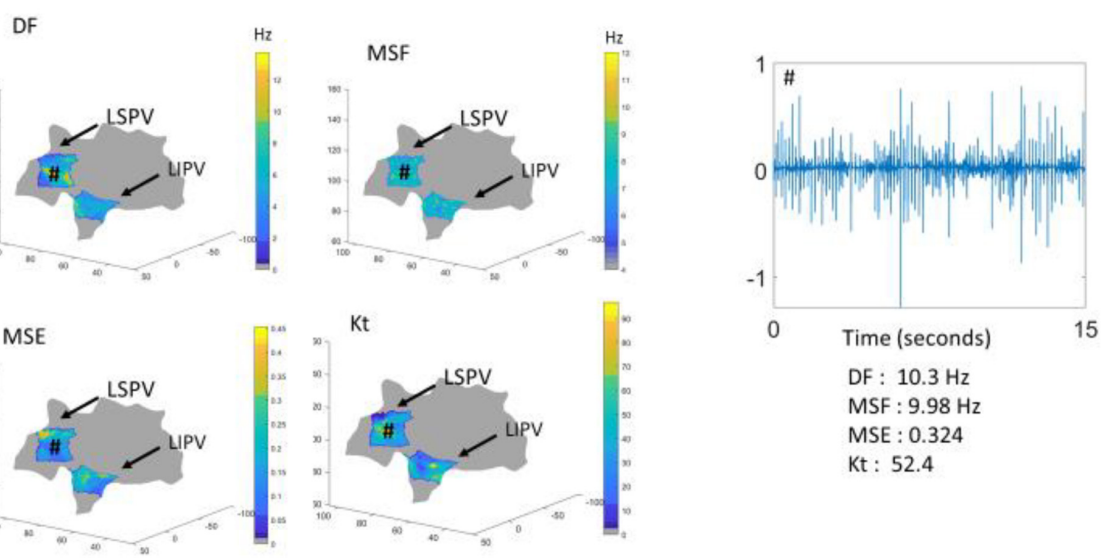

FIGURE 2 | The three-dimensional (3D) visualization of the individual approaches (DF, MSF, MSE, and Kt) generated using VIEgram software for a specific unsuccessful AF termination patient P1. Sample of BiEGM recorded from the left superior pulmonary vein (LSPV) (#) is shown along with individual DF, MSF, MSE, and Kt values.

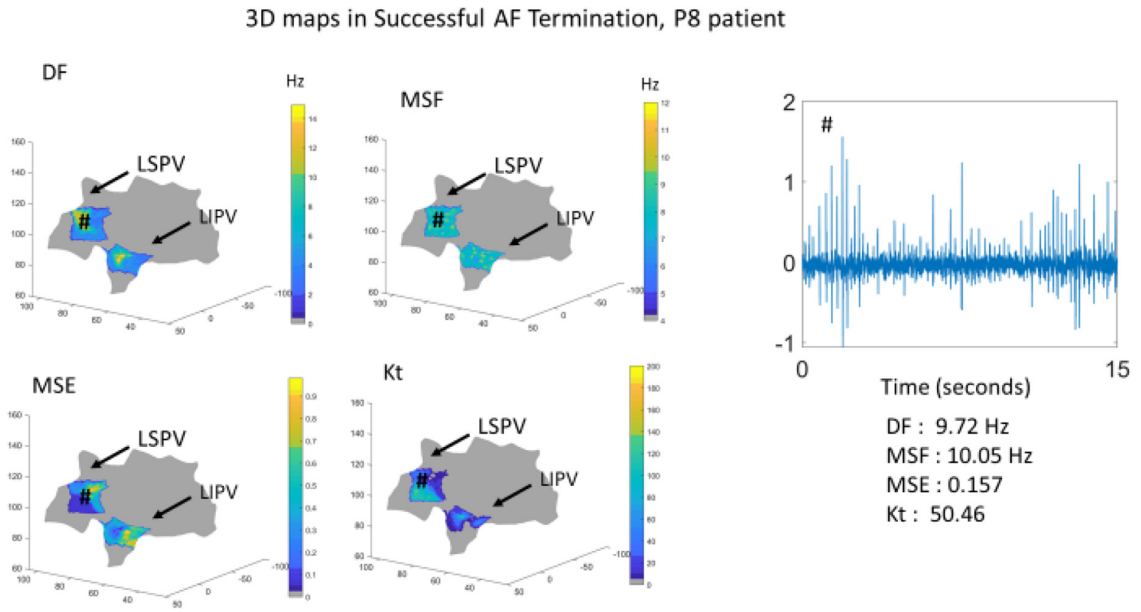

FIGURE 3 | The 3D visualization of the individual approaches (DF, MSF, MSE, and Kt) generated using VIEgram software for a specific successful AF termination patient P8. Sample of BiEGM recorded from LSPV (#) is shown along with individual DF, MSF, MSE, and Kt values.

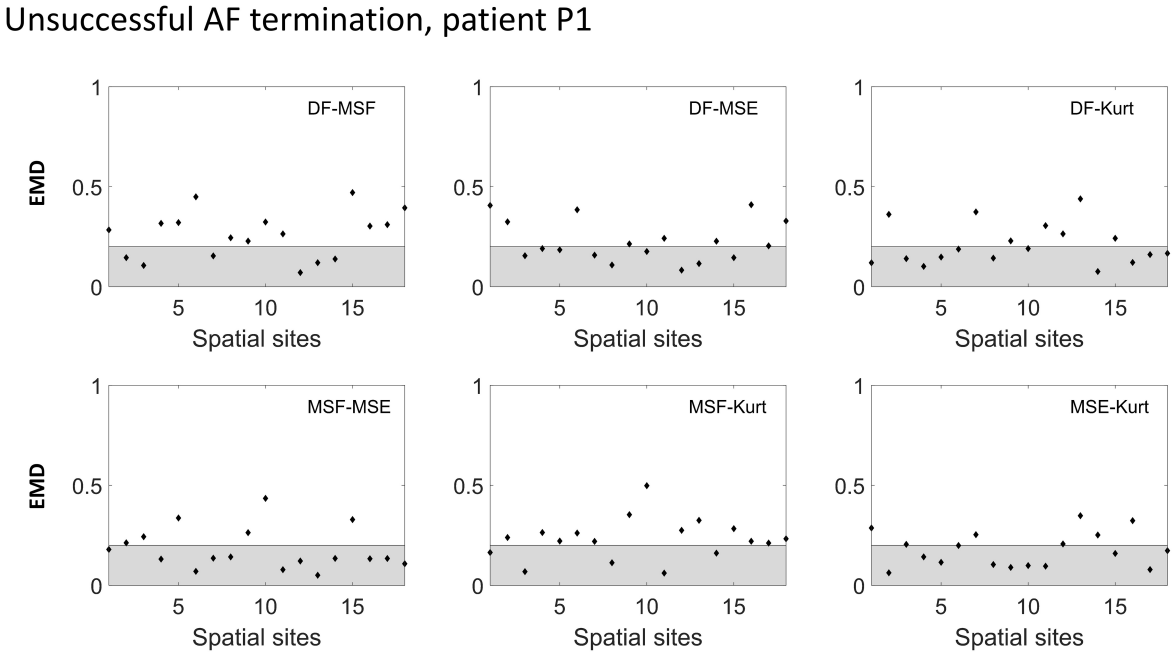

FIGURE 4 | Earth mover's distance (EMD) values calculated for the different pairs of approaches (DF, MSF, MSE, and Kt) in an unsuccessful AF termination patient P1. The gray area indicates the region where the correlation between the pairs is high (EMD < 0.2).

in **Figures 4**, **5**, different techniques have a different degree of correlation with each other, and the degree of correlation is also different depending on the spatial site. We hypothesized that the spatial sites in which at least 5 pairs of the techniques are correlated, i.e., with a high similarity score of 3, might be associated with active AF sites.

The correlation data from **Figures 4**, **5** are summarized in **Table 1** (patient P1 with unsuccessful AF termination) and **Table 2** (patient P8 with successful AF termination), respectively, where the EMD values below (orange) and above (gray) the threshold (EMD = 0.2) are shown for all the spatial sites. Notably, in patient P1 with unsuccessful AF termination, there are three

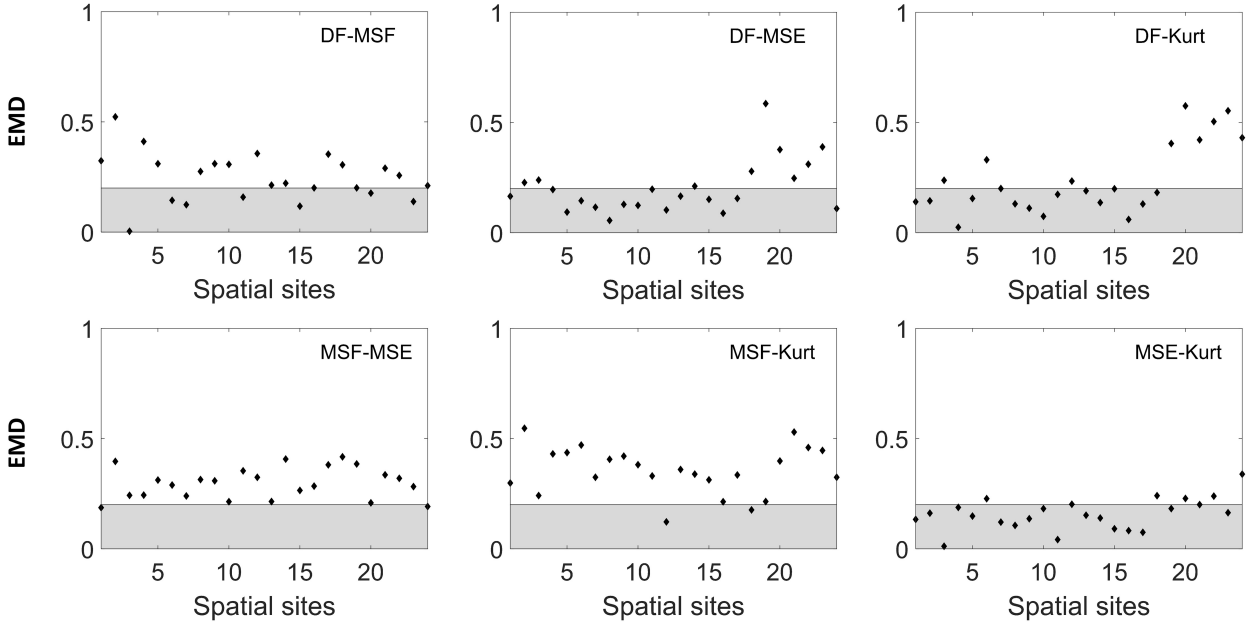

FIGURE 5 | Earth mover's distance (EMD) values calculated for the different pairs of approaches (DF, MSF, MSE, and Kt) in a successful AF termination patient P8. The gray area indicates the region where the correlation between the pairs is high (EMD < 0.2).

spatial sites (# 3, 8, and 14, red color) in which the similarity score is high (=3). Such a high similarity score indicates that at least 5 pairs of different approaches are correlated in these sites, suggesting the presence of active AF drivers, which most probably were not properly targeted during the AF ablation procedure. However, the absence of such red sites with a high similarity score in a patient with successful AF termination (**Table 2**) was noted, indicating that all active sites were appropriately targeted during the AF ablation procedure. Similar tables for all remaining patients are present in **Supplementary Tables 3–8**.

In **Figures 6**, **7**, the similarity scores for different spatial sites are shown for all patients with unsuccessful ($m = 4$) and successful ($m = 4$) AF termination, respectively. Notably, the spatial sites with high similarity scores (=3, red) are only identified in patients with unsuccessful AF termination, suggesting that these sites can be the active AF sites and potential AF ablation targets. The sites were distributed among the different regions of the heart, namely, LA appendage, lateral wall, roof wall, posterior wall, inferior wall, septal wall, LSPV, and LIPV.

DISCUSSION

Some recent studies indicated that a PV isolation alone could be a strategy for catheter ablation in patients with paroxysmal AF, while recurrence is not fully prevented (Sawhney et al., 2009; Ouyang et al., 2010; Chao et al., 2012). However, other studies suggested the need for mapping-specific ablation therapy in patients with persistent AF when active AF sites are outside of the PV regions (Barbhayia et al., 2015; Seitz et al., 2017). For instance, it has been shown that EGM dispersion occurs in the vicinity of AF drivers, and this dispersion is present both near and outside the PV regions. Therefore, it is important to develop new techniques for identifying AF substrates outside the vicinity of the PV regions and potentially improving the success rates of the catheter ablation procedure. Several studies demonstrated the successful identification of AF driver by the phase mapping of simultaneous recordings using a basket catheter (Narayan et al., 2012) and a noninvasive array of body surface electrodes (Haissaguerre et al., 2013). It was also demonstrated in the study by Roney et al. (2017) that spatial resolution is essential in identifying the AF reentrant activity. But the reported success rates using these guided strategies for patients with persistent AF remained inconclusive and ranged from 19 to 77% (Narayan et al., 2014; Miller et al., 2017; Mohanty et al., 2018).

Recently, our laboratory developed and validated the novel iEGM analysis techniques, such as MSF (Arunachalam et al., 2016b), MSE (Arunachalam et al., 2018), and Kt (Arunachalam et al., 2016a), to identify the sites with abnormal AF activity that can be a potential target for AF ablation. Furthermore, we demonstrated the feasibility of these techniques in identifying the active sites of arrhythmia under clinical limitations, with acceptable levels of specificities and sensitivities using numerically simulated iEGMs (Ravikumar et al., 2021). Multiple other studies have analyzed other signal processing-based ablation techniques (Lin et al., 2010; Okumura et al., 2011; Kumagai et al., 2013; Atienza et al., 2014) built on the DF- and PVI-based strategies. This study shows that the performance of

TABLE 1 | Earth mover's distance (EMD) correlation between different pairs of approaches for various spatial sites of a representative patient P1 with unsuccessful atrial fibrillation (AF) termination (from **Figures 1**, **3**).

Spatial Sites	1	2	3	4	5	6	7	8	9	10	11	12	13	14	15	16	17	18
Pairs																		
DF-MSF																		
MSE-Kurt																		
MSF-MSE																		
DF-MSE																		
MSF-Kurt																		
DF-Kurt																		

EMD < 0.2
EMD > 0.2

High/low correlation with respect to the threshold value of EMD = 0.2 is indicated by the orange/gray color. Red spatial sites indicate active AF sites with a similarity score >3, indicating that at least 5 pairs are highly correlated.

TABLE 2 | Earth mover's distance correlation between different pairs of approaches for various spatial sites of a representative patient P8 with successful AF termination (from **Figures 2**, **4**).

Spatial Sites	1	2	3	4	5	6	7	8	9	10	11	12	13	14	15	16	17	18	19	20	21	22	23	24
Pairs																								
DF-MSF																								
MSE-Kurt																								
MSF-MSE																								
DF-MSE																								
MSF-Kurt																								
DF-Kurt																								

EMD < 0.2
EMD > 0.2

High/low correlation with respect to the threshold value of EMD = 0.2 is indicated by the orange/gray color. Red spatial sites indicate active AF sites with a similarity score >3, indicating that at least 5 pairs are highly correlated.

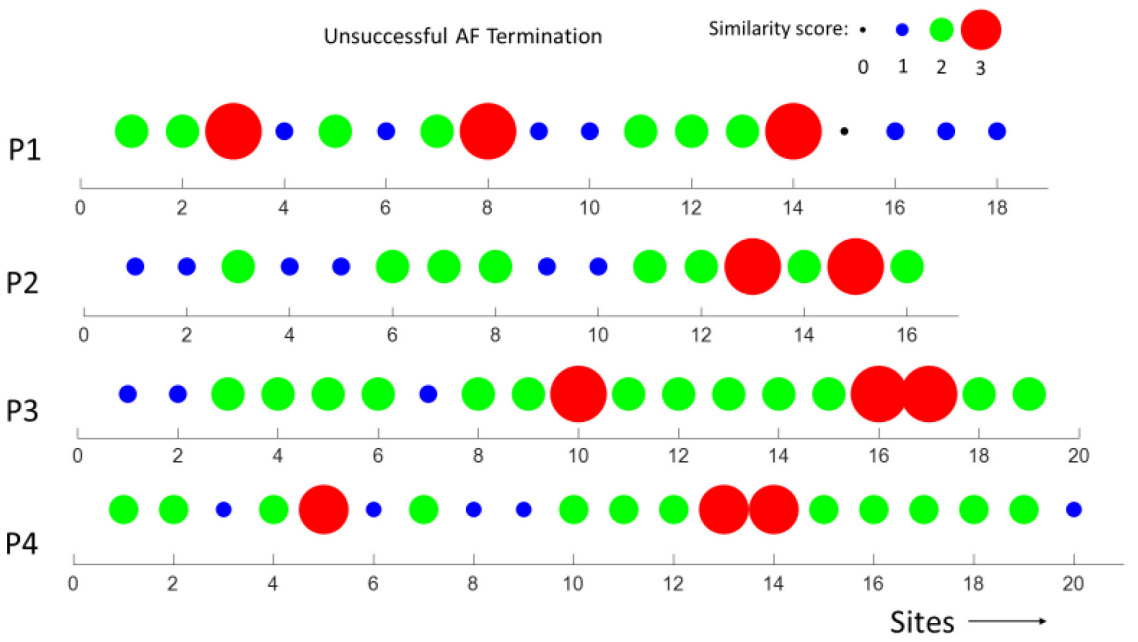

FIGURE 6 | Similarity scores calculated at different spatial sites in $m = 4$ patients with unsuccessful AF termination. Notably, the presence of several spatial sites (potential active AF sites) with a high similarity score (3, red) in all the patients.

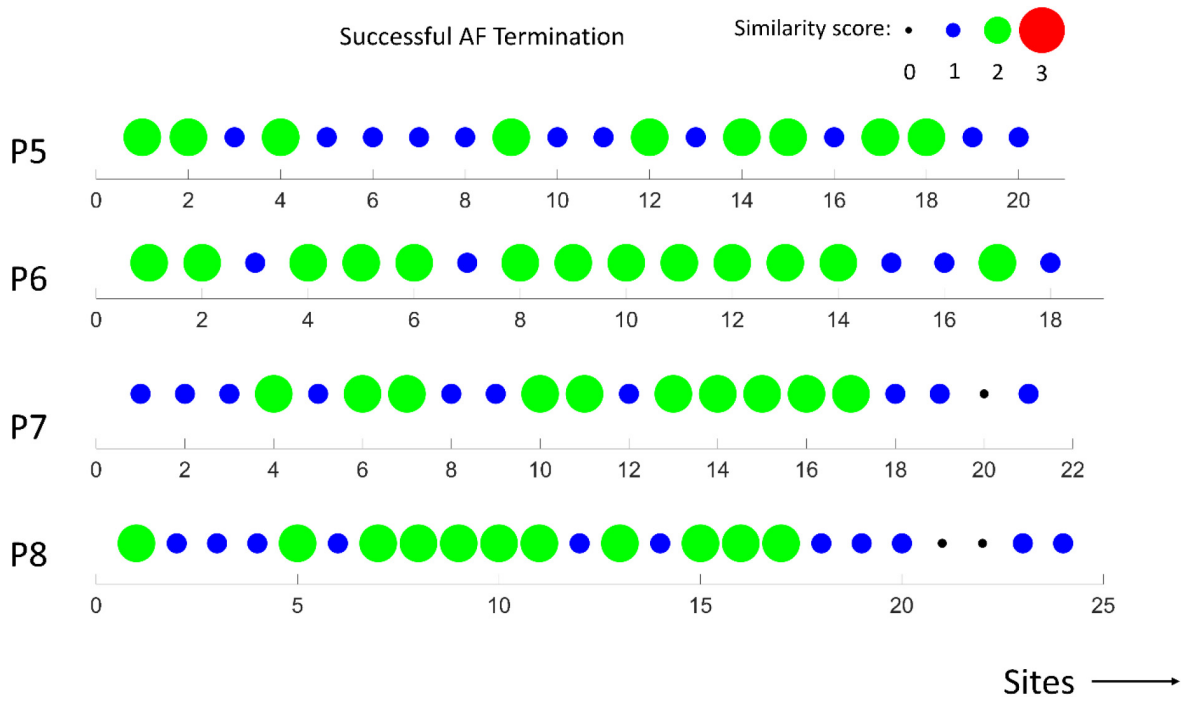

FIGURE 7 | Similarity scores calculated at different spatial sites in m = 4 patients with successful AF termination. Notably, the absence of active AF sites with a high similarity score (3).

individual techniques alone is insufficient in identifying the active AF spatial sites (**Figures 1**, **2**). To overcome this, we developed a similarity score that can help identify the active AF spatial sites by a combination of multiple methods.

We developed a similarity score that can bring together various signal processing approaches and successfully identify active AF sites based on the correlation between all the approaches. In this study, we demonstrated the performance of the similarity score based on four approaches, namely, MSF, MSE, DF, and Kt, to identify abnormal electrical sites in patients with unsuccessful AF termination. However, the similarity score might be extended and optimized by incorporating other iEGM analysis approaches and/or by combining a different number of approaches.

In this study, we have used a custom 3D visualization software previously developed (VIEgram) to perform a visual inspection of clinically recorded iEGMs and implement the previously developed novel iEGM analysis techniques (DF, MSF, MSE, and Kt). The recorded sites were distributed in these anatomical regions of the atria, LA appendage, lateral wall, roof wall, posterior wall, inferior wall, septal wall, LSPV, and LIPV. It was observed that the use of these individual approaches fails to robustly identify spatial sites for ablation; the 3D representations of individual methods among the same patients are visually not similar in the distribution of the metrics, thus increasing the difficulty and time consumed to interpret the different approaches at the same time, especially in patients with unsuccessful AF termination. To overcome this, in this study, we have developed a similarity score that combines all the individual approaches to provide the identification of the active AF site.

Limitations

There are several limitations to our study. First, we have performed only a retrospective analysis of the BiEGMs recorded from a small cohort of patients (m = 8) with persistent AF, using a newly developed similarity score. While there is a clear difference in similarity scores between patients with successful and unsuccessful AF ablation, we could only suggest that this method pointed out the active sites of AF. However, to directly demonstrate that these active sites are, in fact, affecting AF ablation outcomes, a prospective study in a cohort of larger patients has to be designed.

Successful AF ablation is defined as the absence of recurrence in AF episodes longer than 30 s in the long-term follow-ups ranging from 3 months to 1 year (Calkins et al., 2007), i.e., the recurrence of the first AF episode, or any atrial tachyarrhythmia post-ablation is perceived as a failure. In this study, the primary procedural endpoint for a successful termination was the termination of AF without electrical cardioversion. The successful termination of AF was defined as the conversion of AF into sinus rhythm by ablation and without electrical cardioversion. The acute success of the procedure was considered as the endpoint in this study. The long-term success of the ablation procedure was not the primary focus of this study but rather the acute success of the ablation procedure in the termination of the AF rhythms.

In this retrospective study, the BiEGMs were only from the LA and were distributed in the following anatomical regions of the atria: LA appendage, lateral wall, roof wall, posterior wall, inferior wall, septal wall, LSPV, and LIPV. However, the exact location of the spatial sites could not be identified due to the limitation of the data. All the approaches used in this study identify the AF activity present on the endocardial surfaces but do not identify intramural abnormal electrical activities. In the future, a prospective clinical study needs to be performed to validate the performance of the proposed similarity score and improve and add more approaches to make it more robust.

In this study, we have not examined the contribution of each feature but assigned equal weights. In the future, we need to determine the contribution of the various methods individually, also add more methods, and then optimize their contributions toward a final similarity score through a weighted sum approach. A larger data will be needed for this approach.

In this study, all the iEGMs were between the durations of 5–15 s. We have shown previously that the individual approaches are robust under reduced time durations (Annoni et al., 2018; Arunachalam et al., 2018), and therefore, we did not expect any significant impact of different time series duration of our results. With respect to spatial samples, the EMD is applied to the measures from the individual approaches at each spatial site and, therefore, will have no significant impact on the scores. In this study, the influence of the duration of the iEGM recordings on the similarity score was not studied.

CONCLUSION

In this retrospective study, we investigated the performance of individual BiEGM analysis approaches (DF, MSF, Kt, and MSE) and newly developed similarity scores to identify potential, abnormal, electrically active sites in patients with previously unsuccessful AF termination. The major findings of this study are as follows: (1) individual approaches can discriminate between patients with successful and unsuccessful AF termination but fail to robustly identify spatial sites with active AF drivers, (2) a novel EMD-based similarity score was developed and validated to identify the active AF sites in patients with unsuccessful AF termination, and (3) there was no single common region in the atria associated with active AF sites in patients with unsuccessful AF termination, thus indicating the need for patient-specific mapping and ablation therapy.

DATA AVAILABILITY STATEMENT

The raw data supporting the conclusions of this article will be made available by the authors, without undue reservation.

ETHICS STATEMENT

The studies involving human participants were reviewed and approved by the University of Minnesota's Institutional Review Board (IRB: STUDY00003128). The patients provided written informed consent for ablation and data collection for research purposes.

AUTHOR CONTRIBUTIONS

EGT, HR, and VR contributed to conceptualization. EGT and VR contributed to methodology. VR, ST, and XK contributed to software and scripts. VR contributed to validation and writing – original draft preparation. VR and ST contributed to formal analysis. VR, ST, XK, HR, and EGT contributed to writing – review and editing. ET contributed to supervision, project administration, and funding acquisition. All authors contributed to the article and approved the submitted version.

FUNDING

This study was funded by UMN MNP #21.30 (EGT) and National Institute of Health R01 HL104025 and R01 HL106592.

SUPPLEMENTARY MATERIAL

The Supplementary Material for this article can be found online at: https://www.frontiersin.org/articles/10.3389/fphys.2021.767190/full#supplementary-material

REFERENCES

Annoni, E. M., Arunachalam, S. P., Kapa, S., Mulpuru, S. K., Friedman, P. A., and Tolkacheva, E. G. (2018). Novel quantitative analytical approaches for rotor identification and associated implications for mapping. *IEEE Trans. Biomed. Eng.* 65, 273–281. doi: 10.1109/TBME.2017.2763460

Arunachalam, S. P., Annoni, E. M., Mulpuru, S. K., Friedman, P. A., and Tolkacheva, E. G. (2016a). "Kurtosis as a statistical approach to identify the pivot point of the rotor," in *Proceedings of the Annual International Conference of the IEEE Engineering in Medicine and Biology Society*, Piscataway: IEEE. 497–500. doi: 10.1109/EMBC.2016.7590748

Arunachalam, S. P., Annoni, E. M., Mulpuru, S. K., Friedman, P. A., and Tolkacheva, E. G. (2016b). Novel multiscale frequency approach to identify the pivot point of the Rotor [1]. *J. Med. Device.* 10:020948. doi: 10.1115/1.4033148

Arunachalam, S. P., Kapa, S., Mulpuru, S. K., Friedman, P. A., and Tolkacheva, E. G. (2018). Improved multiscale entropy technique with nearest-neighbor moving-average kernel for nonlinear and nonstationary short-time biomedical signal analysis. *J. Healthc. Eng.* 2018:8632436.

Atienza, F., Almendral, J., Ormaetxe, J. M., Moya, A., Martínez-Alday, J. D., Hernández-Madrid, A., et al. (2014). Comparison of radiofrequency catheter ablation of drivers and circumferential pulmonary vein isolation in atrial fibrillation: a noninferiority randomized multicenter RADAR-AF Trial. *J. Am. Coll. Cardiol.* 64, 2455–2467. doi: 10.1016/J.JACC.2014.09.053

Barbhayia, C. R., Kumar, S., and Michaud, G. F. (2015). Mapping atrial fibrillation: 2015 update. *J. Atr. Fibrillation* 8:1227. doi: 10.4022/JAFIB.1227

Calkins, H., Brugada, J., Packer, D. L., Cappato, R., Chen, S.-A., Crijns, H. J. G., et al. (2007). HRS/EHRA/ECAS expert consensus statement on catheter and surgical ablation of atrial fibrillation: recommendations for personnel, policy, procedures and Follow-UpA report of the Heart Rhythm Society (HRS) task force on catheter and surgical ablation of atrial fibrillation developed

in partnership with the european heart rhythm association (ehra) and the european cardiac arrhythmia society (ECAS); in collaboration with the American College of Cardiology (ACC), American Heart Association (AHA). *Europace.* 9, 335–379. doi: 10.1093/EUROPACE/EUM120

Chao, T. F., Tsao, H. M., Lin, Y. J., Tsai, C. F., Lin, W. S., Chang, S. L., et al. (2012). Clinical outcome of catheter ablation in patients with nonparoxysmal atrial fibrillation results of 3-year follow-up. *Circ. Arrhyth. Electrophysiol.* 5, 514–520. doi: 10.1161/CIRCEP.111.968032

Colilla, S., Crow, A., Petkun, W., Singer, D. E., Simon, T., and Liu, X. (2013). Estimates of current and future incidence and prevalence of atrial fibrillation in the U.S. adult population. *Am. J. Cardiol.* 112, 1142–1147.

Elayi, C. S., Di Biase, L., Barrett, C., Ching, C. K., Aly, M., Al Lucciola, M., et al. (2010). Atrial fibrillation termination as a procedural endpoint during ablation in long-standing persistent atrial fibrillation. *Hear. Rhythm* 7, 1216–1223. doi: 10.1016/J.HRTHM.2010.01.038

Go, A. S., Hylek, E. M., Phillips, K. A., Chang, Y., Henault, L. E., Selby, J. V., et al. (2001). Prevalence of diagnosed atrial fibrillation in adults. *Jama* 285:2370. doi: 10.1001/jama.285.18.2370

Haissaguerre, M., Hocini, M., Shah, A. J., Derval, N., Sacher, F., Jais, P., et al. (2013). Noninvasive panoramic mapping of human atrial fibrillation mechanisms: a feasibility report. *J. Cardiovasc. Electrophysiol.* 24, 711–717. doi: 10.1111/jce.12075

Jaïs, P., Cauchemez, B., Macle, L., Daoud, E., Khairy, P., Subbiah, R., et al. (2008). Catheter ablation versus antiarrhythmic drugs for atrial fibrillation: The A4 study. *Circulation* 118, 2498–2505. doi: 10.1161/CIRCULATIONAHA.108.772582

Kumagai, K., Sakamoto, T., Nakamura, K., Nishiuchi, S., Hayano, M., Hayashi, T., et al. (2013). Combined dominant frequency and complex fractionated atrial electrogram ablation after circumferential pulmonary vein isolation of atrial fibrillation. *J. Cardiovasc. Electrophysiol.* 24, 975–983. doi: 10.1111/JCE.12166

Lin, Y. J., Tsao, H. M., Chang, S. L., Lo, L. W., Hu, Y. F., Chang, C. J., et al. (2010). Role of high dominant frequency sites in nonparoxysmal atrial fibrillation patients: insights from high-density frequency and fractionation mapping. *Hear. Rhythm* 7, 1255–1262. doi: 10.1016/J.HRTHM.2010.06.019

Miller, J. M., Kalra, V., Das, M. K., Jain, R., Garlie, J. B., Brewster, J. A., et al. (2017). Clinical benefit of ablating localized sources for human atrial fibrillation: the indiana university FIRM registry. *J. Am. Coll. Cardiol.* 69, 1247–1256. doi: 10.1016/j.jacc.2016.11.079

Miyasaka, Y., Barnes, M. E., Gersh, B. J., Cha, S. S., Bailey, K. R., Abhayaratna, W. P., et al. (2006). Secular trends in incidence of atrial fibrillation in Olmsted County. Minnesota, 1980 to 2000, and implications on the projections for future prevalence. *Circulation* 114, 119–125. doi: 10.1161/CIRCULATIONAHA.105.595140

Mohanty, S., Mohanty, P., Trivedi, C., Gianni, C., Della Rocca, D. G., Di Biase, L., et al. (2018). Long-term outcome of pulmonary vein isolation with and without focal impulse and rotor modulation mapping: Insights from a meta-analysis. *Circ. Arrhythmia Electrophysiol.* 11:5789. doi: 10.1161/CIRCEP.117.005789

Munger, T. M., Wu, L. Q., Shen, W. K. (2014). Atrial fibrillation. *J. Biomed. Res.* 28, 1–17. doi: 10.7555/JBR.28.20130191

Narayan, S. M., Baykaner, T., Clopton, P., Schricker, A., Lalani, G. G., Krummen, D. E., et al. (2014). Ablation of rotor and focal sources reduces late recurrence of atrial fibrillation compared with trigger ablation alone: extended follow-up of the CONFIRM trial (conventional ablation for atrial fibrillation with or without focal impulse and rotor modulation). *J. Am. Coll. Cardiol.* 63, 1761–1768. doi: 10.1016/j.jacc.2014.02.543

Narayan, S. M., Krummen, D. E., Shivkumar, K., Clopton, P., Rappel, W. J., and Miller, J. M. (2012). Treatment of atrial fibrillation by the ablation of localized sources: CONFIRM (conventional ablation for atrial fibrillation with or without focal impulse and rotor modulation) trial. *J. Am. Coll. Cardiol.* 60, 628–636. doi: 10.1016/j.jacc.2012.05.022

Okumura, Y., Watanabe, I., Kofune, M., Nagashima, K., Sonoda, K., Mano, H., et al. (2011). Characteristics and distribution of complex fractionated atrial electrograms and the dominant frequency during atrial fibrillation: relationship to the response and outcome of circumferential pulmonary vein isolation. *J. Interv. Card. Electrophysiol.* 343, 267–275. doi: 10.1007/S10840-011-9637-2

Ouyang, F., Tilz, R., Chun, J., Schmidt, B., Wissner, E., Zerm, T., et al. (2010). Long-term results of catheter ablation in paroxysmal atrial fibrillation: Lessons from a 5-year follow-up. *Circulation* 122, 2368–2377. doi: 10.1161/CIRCULATIONAHA.110.946806

Pandit, S. V., and Jalife, J. (2013). Rotors and the dynamics of cardiac fibrillation. *Circ. Res.* 112, 849–862. doi: 10.1161/CIRCRESAHA.111.300158

Ravikumar, V., Annoni, E. M., Mulpuru, S. K., Roukoz, H., and Tolkacheva, E. G. (2018). "Evaluation of multiscale frequency approach for visualizing rotors in patients with atrial fibrillation," in *Proceedings of the Annual International Conference of the IEEE Engineering in Medicine and Biology Society*, Piscataway: IEEE. 5986–5989. doi: 10.1109/EMBC.2018.8513684

Ravikumar, V., Annoni, E., Parthiban, P., Zlochiver, S., Roukoz, H., Mulpuru, S. K., et al. (2021). Novel mapping techniques for rotor core detection using simulated intracardiac electrograms. *J. Cardiovasc. Electrophysiol.* 32, 1268–1280. doi: 10.1111/JCE.14948

Roney, C. H., Cantwell, C. D., Bayer, J. D., Qureshi, N. A., Lim, P. B., Tweedy, J. H., et al. (2017). Spatial resolution requirements for accurate identification of drivers of atrial fibrillation. *Circ. Arrhythmia Electrophysiol.* 10:4899. doi: 10.1161/CIRCEP.116.004899

Rubner, Y., Tomasi, C., and Guibas, L. J. (2000). The earth mover's distance as a metric for image retrieval. *Int. J. Comput. Vis.* 402, 99–121. doi: 10.1023/A:1026543900054

Sanders, P., Berenfeld, O., Hocini, M., Jaïs, P., Vaidyanathan, R., Hsu, L. F., et al. (2005). Spectral analysis identifies sites of high-frequency activity maintaining atrial fibrillation in humans. *Circulation* 112, 789–797. doi: 10.1161/CIRCULATIONAHA.104.517011

Sawhney, N., Anousheh, R., Chen, W. C., Narayan, S., and Feld, G. K. (2009). Five-Year outcomes after segmental pulmonary vein isolation for paroxysmal atrial fibrillation. *Am. J. Cardiol.* 104, 366–372. doi: 10.1016/J.AMJCARD.2009.03.044

Seitz, J., Bars, C., Théodore, G., Beurtheret, S., Lellouche, N., Bremondy, M., et al. (2017). AF ablation guided by spatiotemporal electrogram dispersion without pulmonary vein isolation: a wholly patient-tailored approach. *J. Am. Coll. Cardiol.* 69, 303–321. doi: 10.1016/J.JACC.2016.10.065

Thakare, S., Mulpuru, S. K., Roukoz, H., and Tolkacheva, E. G. (2020). "VIEgram - Analysis and Visualization of Intracardiac Electrograms on Patient-Specific 3D Atria Model," in *Proceedings of the Annual International Conference of the IEEE Engineering in Medicine and Biology Society,* Piscataway: IEEE, 2606–2609. doi: 10.1109/EMBC44109.2020.9175917

Wazni, O. M., Marrouche, N. F., Martin, D. O., Verma, A., Bhargava, M., Saliba, W., et al. (2005). Radiofrequency ablation vs antiarrhythmic drugs as first-line treatment of symptomatic atrial fibrillation: a randomized trial. *JAMA* 293, 2634–2640. doi: 10.1001/JAMA.293.21.2634

Wilber, D. J., Pappone, C., Neuzil, P., De Paola, A., Marchlinski, F., Natale, A., et al. (2010). Comparison of antiarrhythmic drug therapy and radiofrequency catheter ablation in patients with paroxysmal atrial fibrillation: a randomized controlled trial. *JAMA* 303, 333–340. doi: 10.1001/JAMA.2009.2029

Conflict of Interest: The authors declare that the research was conducted in the absence of any commercial or financial relationships that could be construed as a potential conflict of interest.

frontiers in Physiology

ORIGINAL RESEARCH
published: 15 February 2022
doi: 10.3389/fphys.2022.733706

Novel Analysis Method for Beating Cells Videomicroscopy Data: Functional Characterization of Culture Samples

Jonathan Béland[1,2], *James Elber Duverger*[1,3] *and Philippe Comtois*[1,2,3]*

[1] Research Centre, Montreal Heart Institute, Montreal, QC, Canada, [2] Department of Pharmacology and Physiology, Université de Montréal, Montreal, QC, Canada, [3] Institute of Biomedical Engineering, Université de Montréal, Montreal, QC, Canada

Cell culture of cardiac tissue analog is becoming increasingly interesting for regenerative medicine (cell therapy and tissue engineering) and is widely used for high throughput cardiotoxicity. As a cost-effective approach to rapidly discard new compounds with high toxicity risks, cardiotoxicity evaluation is firstly done *in vitro* requiring cells/tissue with physiological/pathological characteristics (close to *in vivo* properties). Studying multicellular electrophysiological and contractile properties is needed to assess drug effects. Techniques favoring process automation which could help in simplifying screening drug candidates are thus of central importance. A lot of effort has been made to ameliorate *in vitro* models including several *in vitro* platforms for engineering neonatal rat cardiac tissues. However, most of the initial evaluation is done by studying the rate of activity. In this study, we present new approaches that use the videomicroscopy video of monolayer activity to study contractile properties of beating cells in culture. Two new variables are proposed which are linked to the contraction dynamics and are dependent on the rhythm of activity. Methods for evaluation of regional synchronicity within the image field of view are also presented that can rapidly determine regions with abnormal activity or heterogeneity in contraction dynamics.

Keywords: imaging analysis, contractile activity, cardiomyocyte monolayer, non-linear analysis, heterogeneity, spatial-temporal activity

OPEN ACCESS

Edited by:
Elena Tolkacheva, University of Minnesota Twin Cities, United States

Reviewed by:
Vijay Rajagopal, The University of Melbourne, Australia
Seth H. Weinberg, The Ohio State University, United States

***Correspondence:**
Philippe Comtois
philippe.comtois@umontreal.ca

Specialty section:
This article was submitted to Computational Physiology and Medicine, a section of the journal Frontiers in Physiology

Received: *30 June 2021*
Accepted: *06 January 2022*
Published: *15 February 2022*

Citation:
Béland J, Duverger JE and Comtois P (2022) Novel Analysis Method for Beating Cells Videomicroscopy Data: Functional Characterization of Culture Samples. Front. Physiol. 13:733706. doi: 10.3389/fphys.2022.733706

INTRODUCTION

Cell culture of cardiac tissue analog is becoming increasingly interesting for regenerative medicine [conditioning of pre-injected stem cell-derived cardiomyocytes (Pillekamp et al., 2012; Hazeltine et al., 2014) and tissue engineering (Vunjak-Novakovic et al., 2011; Lu et al., 2013; Nunes et al., 2013; Wendel et al., 2013; Zhang et al., 2013)] and widely used for high throughput cardiotoxicity evaluation (Dick et al., 2010; Navarrete et al., 2013). Cardiotoxicity is a leading cause of market withdrawal for drugs (Stevens and Baker, 2009; Ferri et al., 2013) some because of inducing cardiac dysfunction. Many drugs demonstrate cardiotoxicity due to chronic exposure to anthracyclines such as doxorubicin (Menna et al., 2008) which are cytotoxic cancer drugs (Schimmel et al., 2004; Yeh et al., 2004). Chronic cardiotoxicity is usually evaluated in animal models including adult rodents (Alderton et al., 1992; Desai et al., 2013) or canine (Herman et al., 1983), over periods

of months of exposition. As a cost reduction approach to rapidly discard new compounds with high toxicity, cardiotoxicity evaluation is done *in vitro* with neonatal rat ventricular myocyte cultures and ultimately with human stem cell-derived cardiomyocyte. *In vitro*, spontaneous activity and contraction can be influenced when cardiomyocytes are grown on different surfaces (Engler et al., 2008). As such, studies typically do not extend beyond 10 days (Shirhatti et al., 1986; Dorr et al., 1988), limiting their relevance as models for chronic exposure. It has been suggested that biologically softer material could favor more rhythmic activity (Hazeltine et al., 2014) although it may be material dependent (Boudreau-Beland et al., 2015). Traditional *in vitro* systems also do not recapitulate the native tissue architecture or extracellular microenvironment of the heart, both of which are known to regulate myocyte phenotype (Feinberg et al., 2012; Sheehy et al., 2012). Furthermore, studies with animals and animal-derived cells are not always relevant to humans due to species-dependent differences (Sham et al., 1995), indicating a need to develop *in vitro* systems that are compatible with human-derived cardiac myocytes (Zhang et al., 2009). A lot of effort have been made to ameliorate *in vitro* models including several *in vitro* platforms for engineering neonatal rat cardiac tissues with simultaneous quantification of contractile function in response to variables such as tissue architecture (Grosberg et al., 2011; Feinberg et al., 2012), mechanical stretch (McCain et al., 2013), electrical stimulation (Chiu et al., 2011), or gelatin hydrogels developed as muscular thin film substrates (McCain et al., 2014).

Studying multicellular electrophysiological and contractile properties is needed to assess drug effects and techniques that can favor the automation of the process helping in simplifying the screening process. Techniques for imaging contractile activity has been developed for decades including approaches to measure spontaneous rhythms in culture (Rohr, 1990) to study the rate and stability of activity (Boudreau-Beland et al., 2015). Less costly and more easily distributed imaging chip-scale lensless wide-field-of-view microscopy imaging technique have been proposed which can render microscopy images of growing or confluent cell cultures (Zheng et al., 2011). Long-term culture of engineered animal and human cardiac tissues coupled to less invasive data recording on activity and contractility to better predict adverse or functional effects of drugs on the heart is highly desirable.

In this study, we present new approaches that use the videomicroscopy video to study contractile properties of beating cells in culture. Two new variables are proposed which are linked to the contraction dynamics and are dependent on the rhythms of activity. Methods for evaluation of regional synchronicity within the imagined field of view are also presented that can swiftly determine regions with abnormal activity or heterogeneity in contraction dynamics.

MATERIALS AND METHODS

Cardiomyocyte Isolation Procedure

All animal-handling procedures were concordant with the Canadian Council on Animal Care guidelines and were approved by the institutional Animal Research Ethics Committee. Isolation was performed according to the protocol of the neonatal cardiomyocyte isolation kit from Worthington. In summary, 1–3 days old rats (Sprague-Dawley, Charles River) were sacrificed by decapitation. Beating hearts were removed from the rats and immediately put in cold Ca^{2+} and Mg^{2+}-free Hank's Balanced Salt Solution. The ventricular muscle was selected by excision and the tissue was minced on ice into 1–3 mm^3 pieces. The mixture was subjected to purified enzymatic digestion (trypsin and collagenase). Isolated cells (enriched cardiomyocytes) were counted and seeded at a density of 10^6 cells/mL in the seeding area of the membrane pre-coated with 0.2% porcine-derived gelatin (G1890, Sigma) and 0.00125% fibronectin solution (F1141, Sigma). Cells were grown for 24 h in DMEM (319-050-CL, Wisent) with 5% fetal bovine serum (FBS, SH30396.03, Thermo Fisher Scientific Co., Ltd.) and 1% penicillin/streptomycin (450-201-EL, Wisent). Cardiomyocytes were then FBS starved with 1% penicillin/streptomycin in DMEM 24 h prior to the experiments. For the set of experiments used to study the effects of electrically pacing the cardiomyocytes at different pacing cycle length (PCL), the cells were washed and the medium changed to fresh DMEM without FBS just prior to record the activity (thus not being starved for 24 h prior to the experiments).

β-Adrenergic Stimulation

Acute effects of the β-adrenergic agonist, isoproterenol (ISO, I6504, Sigma-Aldrich) was studied by videomicroscopy with final concentration of 100 nmol/L at 1 min after injection.

Videomicroscopy Recording

Phase contrast videos of neonatal cardiomyocytes were acquired after 48 h post seeding *in vitro* with a Dalsa HM640 camera ($N_y = 640 \times N_x = 480$ pixels) at rates of 30, 50, or 100 frame per second (fps) coupled to an inverted Nikon optical microscope (10× magnification). The field of view (FOV) covered by the camera was 0.44 mm by 0.33 mm.

Mathematical Models of Cardiomyocyte Electrophysiology and Contraction

The Morotti et al. (2014) model of mouse ventricular myocyte modified to integrate the Negroni et al. (2015) model of myofilament contraction as used by Surdo et al. (2017)[1] was simulated at PCL ranging from 200 to 1,000 ms to study the effects of period of activity. To account for the duration of transient solution when starting from the resting steady-state, simulation output at 30 and 60 s are considered in this study. The Negroni et al. (2015) of rabbit ventricular myocyte was also simulated at different PCL for a 30 s duration of simulation. A modified version of the rabbit model was also studied where two parameters of the myofilament section were multiplied by a factor of 5: Yb (binding rate of Ca^{2+}) and f (transition rate between the 1st and 2nd state of the troponin system). The parameter Yv (part of the detachment function) was scaled down by a factor of 5.

[1] https://somapp.ucdmc.ucdavis.edu/Pharmacology/bers/

The models were numerically integrated in Matlab (R2008, MathWorks Inc., Natick, MA) using the variable-step, variable-order solver based on the numerical differentiation formulas of orders 1–5 for stiff system (ode15s). Relative error tolerance was set to 10^{-5}.

Statistical Analysis

All statistical analyses have been done in R (version 3.1.3). Linear regression was used to test for variable dependency on period of activity. The analysis of covariance (ANCOVA) was used to compare group and covariate effects. Means were compared with Student's *t*-test.

ANALYSIS APPROACH AND RESULTS

Studying the Global Contraction Characteristics

The proposed initial approach is using the raw video signal and calculating for each pixel the difference between frames separated by a delay corresponding to a defined frame interval.

Let $M(t)$ be the global camera frame recorded at time t. The composite signal ΔS is calculated using the following Equation:

$$\Delta S\,(t) = \frac{1}{N_x N_y} \sum_{j=1}^{N_y} \sum_{i=1}^{N_x} \left| \frac{M_{i,j}\,(t) - M_{i,j}\,(t-\tau)}{\tau} \right|, \qquad (1)$$

where τ is a discrete time delay (or number of frames for delay multiplied by the time between frames $\Delta t = 1/\text{fps}$), N_y and N_x are, respectively, the number of horizontal and vertical pixels such that i and j are the pixels coordinates along the horizontal and vertical axis. An example of the composite signal ΔS for a spontaneously beating sample is shown in **Figure 1** for different delay ($\tau = 1,4$, and 8 multiplied by Δt). The shortest delay $\tau = \Delta t$ corresponding to a frame-by-frame difference shows the highest noise level (**Figure 1A**) while increasing τ to $4\Delta t$ (**Figure 1B**) and $8\Delta t$ (**Figure 1C**) decreased the amplitude difference between the high and low amplitude peaks.

Link Between Videomicroscopy Signal and Cellular Contraction

In silico data and analysis reveal that the composite signal ΔS calculated from Eq. (1) can be interpreted as follow. The absolute derivative of the time-dependent cell length calculated from simulated sarcomere length (SL) obtained from the simulation is given by:

$$dSL_{abs}\,(t) = \left| \frac{dSL}{dt} \right| \qquad (2)$$

where SL is the sarcomere length. The change in SL calculated with the Surdo et al. (2017) model paced at a PCL of 500 ms is presented in **Figure 2A**. The time derivative of this contraction signal is depicted in **Figure 2B** which shows the initial contraction (negative derivative) followed by the positive relaxation signal. As shown in **Figure 2C**, there is a clear similarity between the rectified derivative given by Eq. (2) and the videomicroscopy signal obtained with Eq. (1) as shown in **Figures 1A**, **3A** (highlighted in the inset of panel A).

Two specific measures are proposed that are presented in **Figure 2D** which corresponds to the amplitude ratio between the contraction and relaxation peaks ($\text{Ratio}_{C/R}$) and the time between the contraction and relaxation peaks (Δ_{R-C}). The effects of the PCL on contraction signal and specific measures are shown in **Figure 2D** which highlights the sensitivity of the measures on rhythm and calcium dynamics. Decreasing the PCL from 500 to 220 ms lead to a decrease of 6% of Δ_{R-C} and of 33% of $\text{Ratio}_{C/R}$.

Automatic discrimination between contraction and relaxation peaks is important in the perspective of user-friendliness and for the approach to have a clear potential in a high throughput screening/testing system. The approach is based on the observations of experimental data showing differences in amplitude and rate of decrease around the peaks between the contraction and relaxation. Starting from a ΔS signal as shown in **Figure 3A**, three conditions are being used to detect and validate classification of the peaks: 1- there is alternance between contraction and relaxation peaks, 2- clusters are usually separated in the variable space given by the time difference between peaks ($\Delta t_{markers}$) and amplitude of the peaks (ΔS_{peaks}) as depicted in **Figure 3B**, 3- experimental data has sharpest peaks for contraction and widest peaks for relaxation resulting in more rapid amplitude loss around the maximum ΔS peak amplitude. The last condition can be easily evaluated by taking the amplitude for 1 sample (first sample before and after the position of the peak) and 2 samples (second sample before and after the peak) around the peak divided by the peak amplitude (Ratio_{drop}: the ratios given by the value of the first and second samples around the peak divided by the value of the signal for the peak define). As such, Ratio_{drop} serves to evaluate how fast the amplitude decreases around the peak distinguishing fast changes (narrow contraction peaks)_and slower changes (wide relaxation peaks). The obtained data are presented in **Figure 3C** where a lower average Ratio_{drop} is found for the contraction peaks (left circles; 0.77 ± 0.03 and 0.40 ± 0.06 n.u.) compared to the relaxation peaks (right dots; 0.92 ± 0.02 and 0.78 ± 0.04 n.u.). Using the second neighboring points (what we labeled drop by two samples) helps separating the contraction and relaxation groups of points (the red points behind more clearly separated as a function of Ratio_{drop}).

Changes in Contraction Measures

An example of an analyzed acquisition is presented in **Figure 4**. The signal ΔS is shown in **Figure 4A** with detected peaks (red circles) and resulting classification highlighted for contraction (red dotted lines) and relaxation peaks (red dashed lines). The resulting series of spontaneous activity shows a constant period T (**Figure 4B**: 0.64 ± 0.01 s) almost no variation in Δ_{R-C} (**Figure 4C**: 0.22 ± 0.01 s). However, $\text{Ratio}_{C/R}$ shows greater variability between samples (**Figure 4C**: 1.89 ± 0.06 n.u.) mainly due to variations in the maximum amplitude of the contraction peaks as seen on the signal in **Figure 4A**.

A set of 8 samples data obtained at PCL ranging from min. 500 to max. 2,000 ms are presented in **Figure 5** (each color corresponding to a given cell culture sample except for

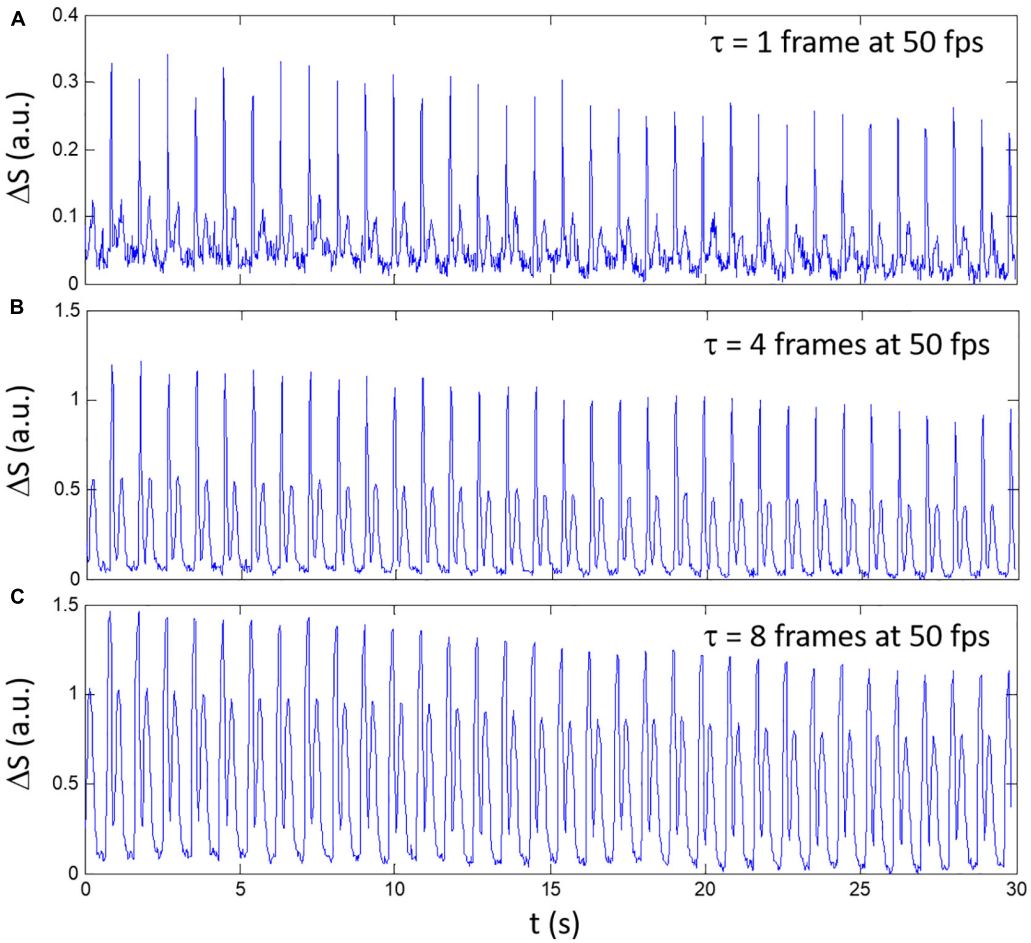

FIGURE 1 | An example of composite signals ΔS obtained with different delay between frames for a spontaneously beating sample. **(A)** $\tau = 1$ frame, **(B)** $\tau = 4$ frames, and **(C)** $\tau = 8$ frames. The video was recorded at 50 fps.

the black line that corresponds to the mean value of the samples). $<\Delta_{R-C}>$ (**Figure 5A**) is the lowest for shortest cycle length and is augmenting with PCL increasing except for one sample. The average curve (black line) shows a slight biphasic shape with intermediate PCL values being slightly higher than for the highest PCL (6/8 samples clearly showing a biphasic shape).

Data for $<\text{Ratio}_{C/R}>$ are presented in **Figure 5B**. The lowest value is usually found for lower PCL and is increasing with PCL increasing (7/8 samples). There is again a tendency for a biphasic shape of the curves which is more visible for the average curve (black line).

Comparison With Simulation Data

Long-term simulations of the Surdo et al. (2017) mouse ventricular model ionic model have been done for a comparison purpose with the experimental data. Simulation results for $<\Delta_{R-C}>$ are shown in **Figure 6A**. The general shape of the curves differs between the experiments and simulations. Similar to experimental data, simulated $<\Delta_{R-C}>$ is the lowest for shortest cycle length and is augmenting with PCL increasing for shortest PCL. There is, however, a particular biphasic shape (more like a narrow peak) as the maximum value is found around 240–245 ms before rapidly decreasing followed by a slow increase with PCL increasing. This narrow peak comes from the morphology of the |dSL/dt| relaxation phase which has a double hump shape. The peak in the $<\Delta_{R-C}>$ as a function of PCL comes from a change from the first hump to be higher to the second bump thus resulting from an added delay in the marker for relaxation (∼0.02 s). The maximum (experiments: 0.54 s; simulation: 0.21 s) and range (experiments: 0.14 s; simulation: 0.05 s) of $<\Delta_{R-C}>$ is also less than in experiments. We compared the results for two duration of simulation (30 and 60 s of simulation for different constant PCL) to highlight the possible transient behavior of the model. The rate main difference between shorter (30 s) and longer (60 s) simulations are a higher $<\Delta_{R-C}>$ right after the peak resulting in a slower increase with increasing PCL for PCL > 300 ms.

Simulated data for $<\text{Ratio}_{C/R}>$ are presented in **Figure 6B**. Similar to experimental data, the lowest value is found for lower PCL and is increasing with PCL increasing. There is a clear biphasic shape of the curve that seems also to be found in some experimental samples in **Figure 5B**. The highest values

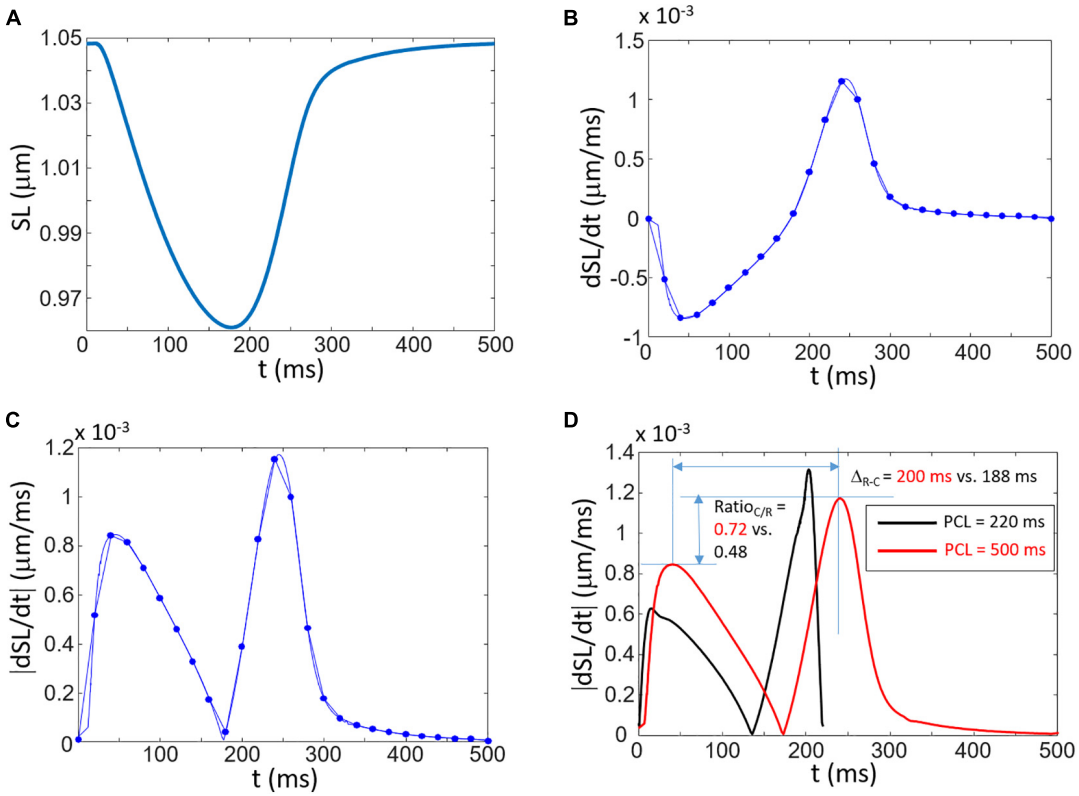

FIGURE 2 | Simulation of contraction and the link to the composite signal ΔS. **(A)** Shortening of the sarcomere length (SL) as a function of time. **(B)** The time derivative of SL. The dots correspond to the derivative calculated with a sub-sample signal corresponding to 50 samples/s ($\Delta t = 0.02$ s). **(C)** Rectified signal of **(B)** showing double peaks corresponding to the contraction and relaxation phases. **(D)** Explanation of two specific measures ($\Delta_{R\text{-}C}$ and $\text{Ratio}_{C/R}$) obtained from simulations at two difference PCL (black curve: PCL = 220 ms; red curve: PCL = 500 ms). A shorter PCL leads to a decreased $\Delta_{R\text{-}C}$ and decreased $\text{Ratio}_{C/R}$.

in simulated $<\text{Ratio}_{C/R}>$ is found near PCL = ∼375 ms. The biphasic shape comes from the difference in rate of change between the contraction and relaxation peaks with increasing PCL. Starting at PCL = 360 ms, the rate of increase in the amplitude of the relaxation peak as a function of increasing PCL is greater than the rate of increase of the contraction peak. As such, the Ratio_C/R for PCL > 360 ms is decreasing with PCL increasing. There is, however, a decrease in highest $<\text{Ratio}_{C/R}>$ for longer simulations (60 s compared to 30 s) indicating that it is, at least in part, linked to transient behavior of the model. More importantly is the range of values which differs from the experimental data. $<\text{Ratio}_{C/R}>$ is always less than one for simulated data with the mouse model while experimental data are mostly greater than one (except for some cases at lowest PCL). The differences are important because value lower than one means that the rate of relaxation is faster than the rate of contraction.

The differences between the experimental and simulated data lead us to test if it was because of the ionic model. Thus, the rabbit ventricular model by Negroni et al. (2015) was simulated with normal parameter values (ctl) and with two contraction parameters (modified, see "Materials and Methods" section for details). The change in parameters (between ctl and modified models) did not significantly impact the action potential duration when paced at 500 ms as shown in **Supplementary Figure 1A**. While the ctl model has a relaxation rate higher than the contraction rate (black curve in **Supplementary Figure 1C**) resulting in a $\text{Ratio}_{C/R} < 1$, the modified model (green curve) shows a faster contraction than relaxation ($\text{Ratio}_{C/R} > 1$). A visual comparison of the curves clearly shows that the modified model has longer Δ_{R-C} compared to the ctl model. $<\Delta_{R-C}>$ and $<\text{Ratio}_{C/R}>$ as a function of PCL for the Negroni et al. (2015) model can be found in **Supplementary Figures 2A,B**, respectively. The ctl rabbit ventricular model shows an increase in $<\Delta_{R-C}>$ compared to Morotti et al. mouse model (maximum value around 0.25 s vs. ∼0.21 s). Interestingly, simulating the modified Negroni et al. (2015) rabbit model resulted in even longer $<\Delta_{R-C}>$ (∼0.35 s) getting closer to the experimental values. While $<\text{Ratio}_{C/R}>$ for the ctl Negroni et al. (2015) rabbit ventricular model is always less than 1 the modified version resulted in $<\text{Ratio}_{C/R}>>$ over almost all the PCL range.

Average Values of Samples in Spontaneous Activity

A set of samples ($n = 29$) has been analyzed. For each video of 30 s duration, the average values <T>, $<\Delta_{R-C}>$,

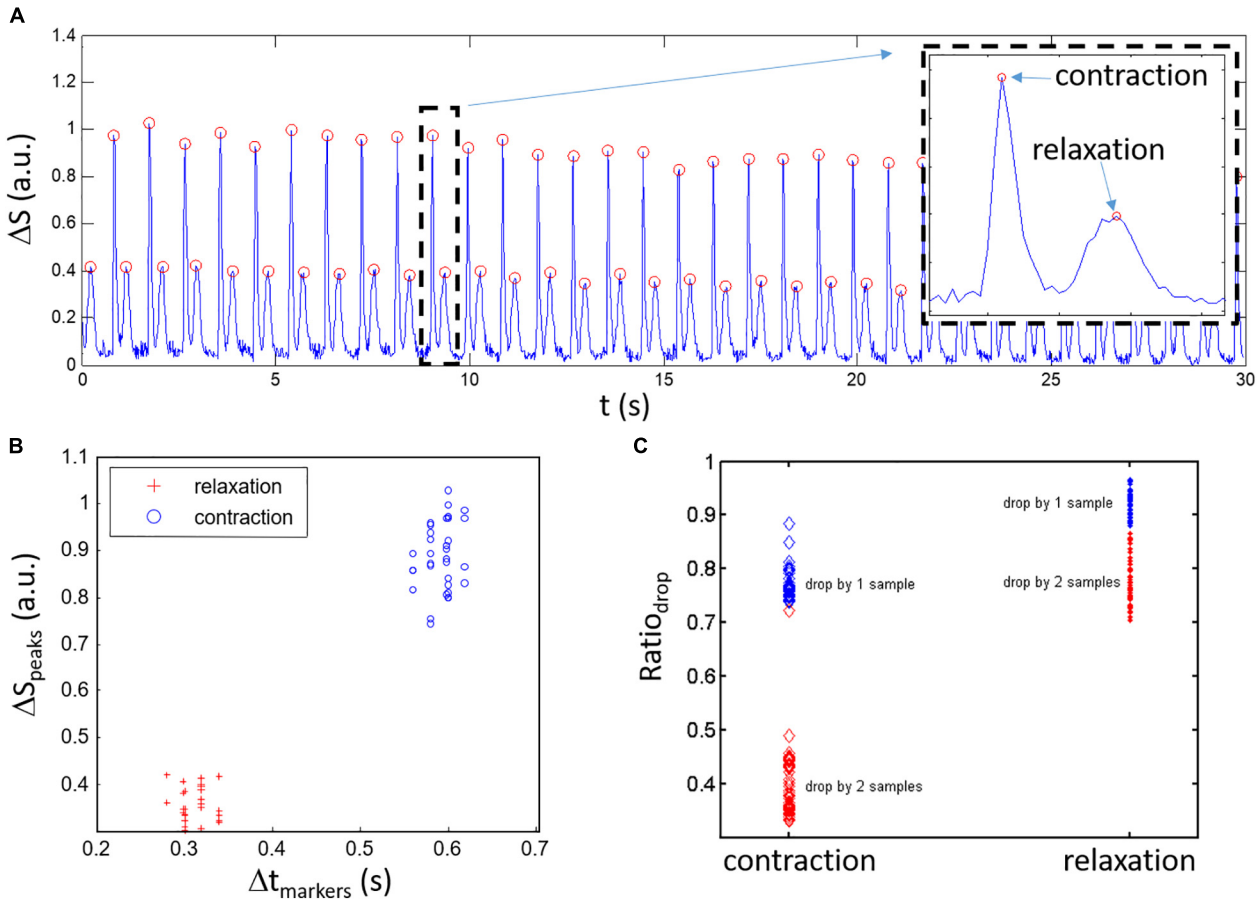

FIGURE 3 | Classification of ΔS peaks for a spontaneously beating sample. **(A)** An example of composite signal ΔS with detected peaks (red circles) showing alternation between high amplitude and low amplitude peaks. Inset: blow up of the activity within the dashed black rectangle which highlights the high amplitude contraction peaks followed by the lower amplitude relaxation peak like the derivative of the simulated contraction model. **(B)** Contraction and relaxation clusters are relatively well separated when viewed in the space with *x*-axis being the time between markers and *y*-axis being the peak amplitude (ΔS_{peaks}). **(C)** Estimation of the change in ΔS around the peaks given by the Ratio_{drop} (amplitude of 1st and 2nd samples around the peaks divided by the peak amplitude). Lower ratio Ratio_{drop} is linked to faster change in Δ*S* around the peaks for the contraction peaks compared to the relaxation.

and $<\text{Ratio}_{C/R}>$ were calculated as the average of the temporal values obtained from the signal analysis of individual acquisition. A clear monotone increase in $<\Delta_{R-C}>$ with increasing <T> is found as depicted in **Figure 7A** with ∼40% change between the minimum and maximum values. The linear regression ($p < 0.001$) has a slope of 0.072 s/s (represented as a red line) and intercept of 0.166 s. As expected, the variability is greater for $<\text{Ratio}_{C/R}>$ but a trend to an increasing ratio as <T> augments is found. However, the variation with the period is less with ∼23% change between the minimum and maximum values in the dataset (see **Figure 7B**). The fitted regression line ($p < 0.005$, red line on the panel) has a slope of 0.276 s^{-1} and an intercept of 1.93.

Influence of β–Adrenergic Stimulation on $<\Delta_{R-C}>$ and $<\text{Ratio}_{C/R}>$

The variation in the contraction measures that can be evaluated by our videomicroscopy approach has been tested with isoproterenol (ISO), a β–adrenergic agonist. Results are presented in **Figure 8**. As expected, the period of activity is significantly decreased with ISO compared to CTL (0.9 ± 0.6 s vs. 1.9 ± 2.4 s in CTL, $p < 0.05$). Similar variation of $<\Delta_{R-C}>$ is found between CTL and ISO groups as a function of <T> although <T> is in average smaller with ISO as expected (**Figure 8A**). Interestingly the $<\text{Ratio}_{C/R}>$ showed statistically significant <T> and group effects with $p < 0.001$. The slope of the linear regression being larger for the ISO group compared to CTL (0.146 for CTL vs. 0.490 for ISO).

Could the Proposed Measures, Δ_{R-C} and $\text{Ratio}_{C/R}$, Be Useful for Cardiotoxicity Testing?

In order to see if Δ_{R-C} and $\text{Ratio}_{C/R}$ may be interesting to evaluate cardiotoxicity, we used the change in sarcomere length data presented in **Figure 5B** in the study by Timolati et al. (2009) comparing the rat ventricular cardiomyocyte

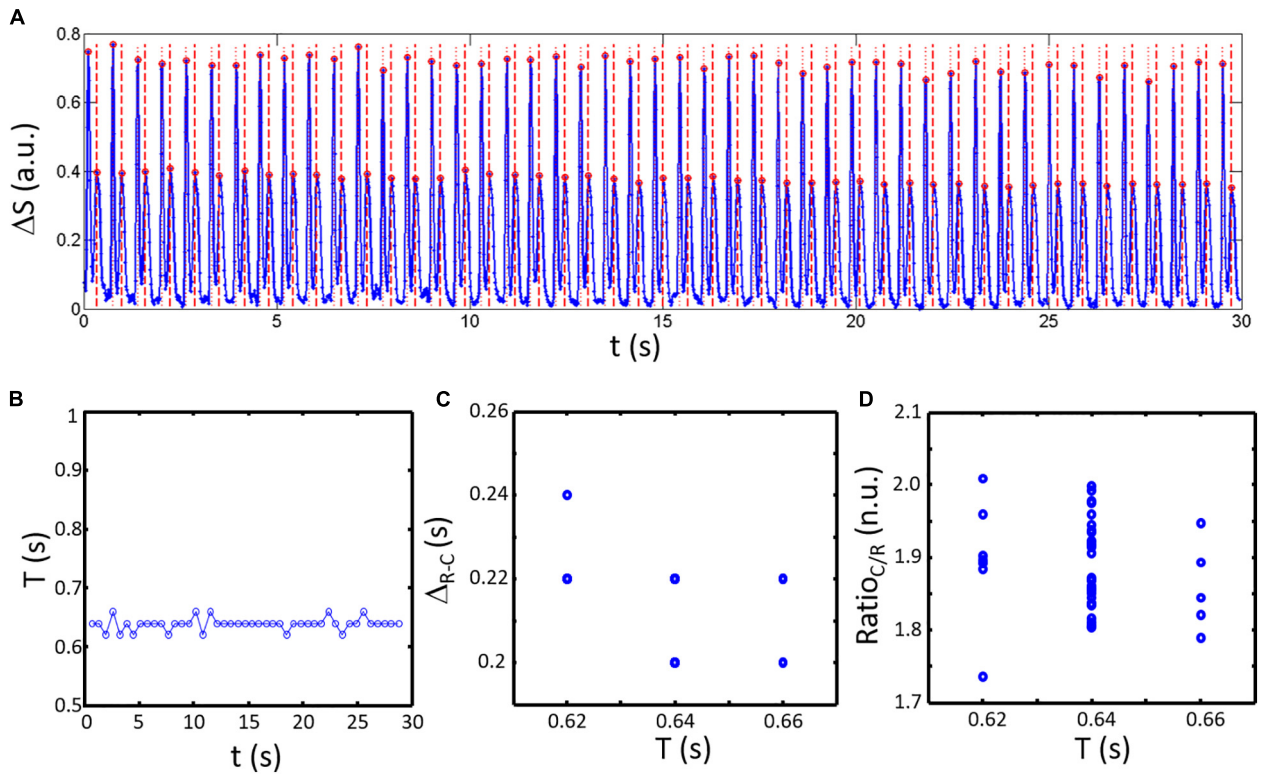

FIGURE 4 | Temporal variation in spontaneous activity obtained by analysis of ΔS with 50 fps. **(A)** The composite signal obtained for a representative sample (blue line). Detected peaks are highlighted by red circles. Post classification results are shown by dotted red lines (contraction peaks) and dashed red lines (relaxation peaks). **(B)** The period of activity given the time difference between contraction peaks shows a constant period of activity equal to the pacing cycle length (PCL). **(C)** Calculated $\Delta_{R\text{-}C}$ as a function of the period of activity (corresponding here to the time elapse since the last contraction) is only varying by ± one sample. **(D)** $\text{Ratio}_{C/R}$ is more varying compared to $\Delta_{R\text{-}C}$.

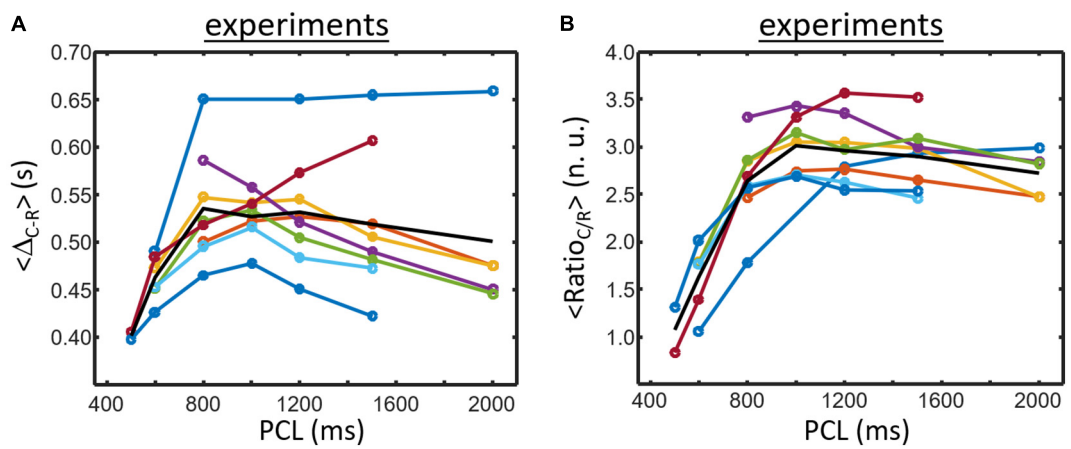

FIGURE 5 | Experimental data obtained for 8 samples electrically paced at different PCL. Each colored line corresponds to a sample results except for the black line that represent the mean of the 8 culture samples. **(A)** $\Delta_{R\text{-}C}$ is generally increasing for small PCL. The average curve (black line) exhibits a biphasic morphology which initially increases followed by a small decrease for large PCL (5/8 samples have similar morphology). **(B)** $\text{Ratio}_{C/R}$ usually starts low and is increasing when PCL increases. A biphasic pattern is also found for $\text{Ratio}_{C/R}$ (7/8 samples) and is also seen for the average curve (black line).

contraction paced with a period of 500 ms in control and treated with 1 μmol/L of doxorubicin for 48 h. The data was digitized and sampled with 10 ms between samples (shown in **Supplementary Figure 3**). Using the same approach as depicted in **Figure 2** for the Surdo et al. (2017) ionic model, we calculated the mean of the last two contractions (skipping

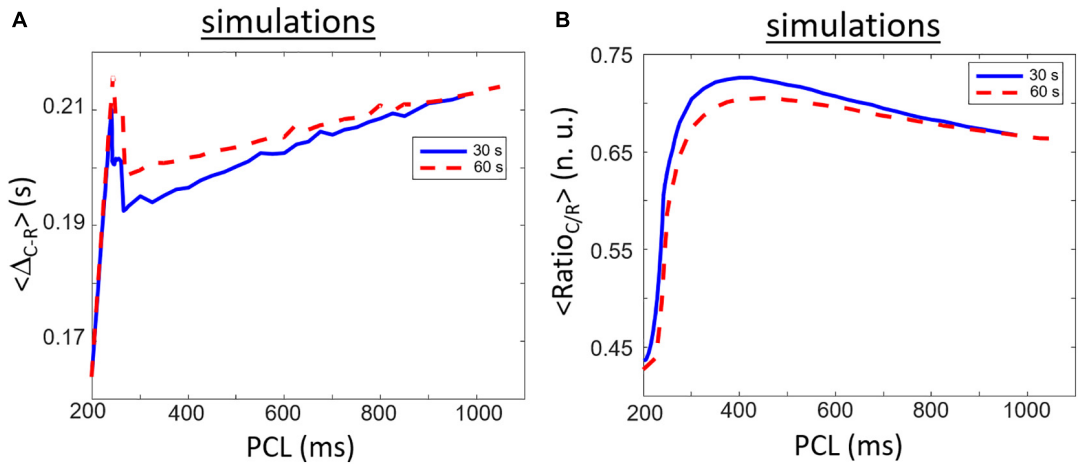

FIGURE 6 | Similar to **Figure 5** but for simulation results obtained after 30 (blue line) and 60 s (red line) of simulation. **(A)** Rapidly increasing $\Delta_{R\text{-}C}$ for short PCL increase followed be a rapid decrease and a long and slow increase when increasing the PCL. **(B)** $\text{Ratio}_{C/R}$ shows a clear biphasic waveform starting with a small value for short PCL which rapidly increases to a maximum value for PCL around 420 ms followed by a slower decrease while PCL increases. The maximum value of $\text{Ratio}_{C/R}$ is smaller at 60 s compared to 30 s indicating the part of the biphasic shape is due to transient dynamics.

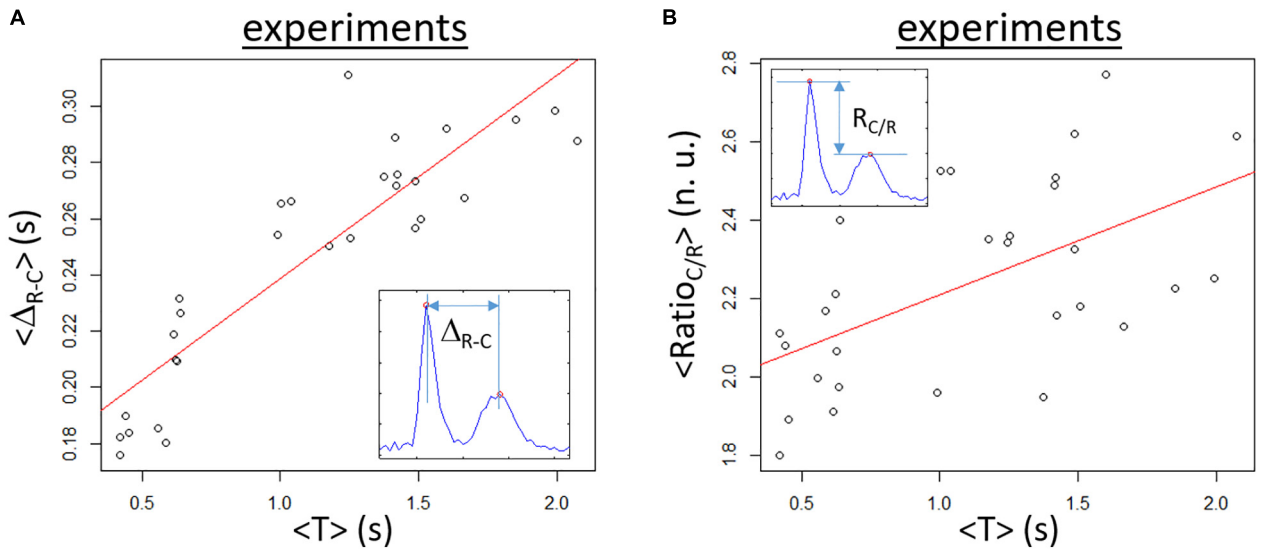

FIGURE 7 | Experimental data obtained for samples in spontaneous rhythm. **(A)** Mean temporal $\Delta_{R\text{-}C}$ ($<\Delta_{R\text{-}C}>$) is increasing when the mean T ($<T>$) is augmenting. The red line corresponds to the linear regression fit (slope of 0.072, $p < 0.001$, corr. = 0.89). **(B)** Mean $\text{Ratio}_{C/R}$ ($<\text{Ratio}_{C/R}>$) as a function of $<T>$ showing a slight augmentation with increasing $<T>$. The linear regression line (red line) has a slope of 0.276 ($p < 0.01$, corr = 0.56).

the first one) yielding $\Delta_{R-C} = 0.11$ s in control compared to 0.07 s for the doxorubicin-treated cardiomyocyte. $\text{Ratio}_{C/R}$ was increased in cardiomyocyte treated with doxorubicin (1.3 in control vs. 1.5 for the doxorubicin-treated cardiomyocyte). Although this result is very limited, it points to the interest of the measures in detecting contraction changes and evaluating cardiotoxicity.

From Global to Regional Analysis

All the previous analyses presented in this study are based on a global composite signal calculated using the entire FOV. The same approach can be used for sub-regions of the FOV by calculating a composite signal for each section. We present here two additional approaches aiming to study spatial-temporal differences in videomicroscopy signals.

Finding Areas With Non-correlating Activity in Spontaneous Activity

The first approach is based on determining how local signal correlates with the global composite signal. The first step is to split the image in contiguous regions of $N_{sub,x}$ and $N_{sub,y}$ pixels. The local composite signals are calculated over all sub-regions of

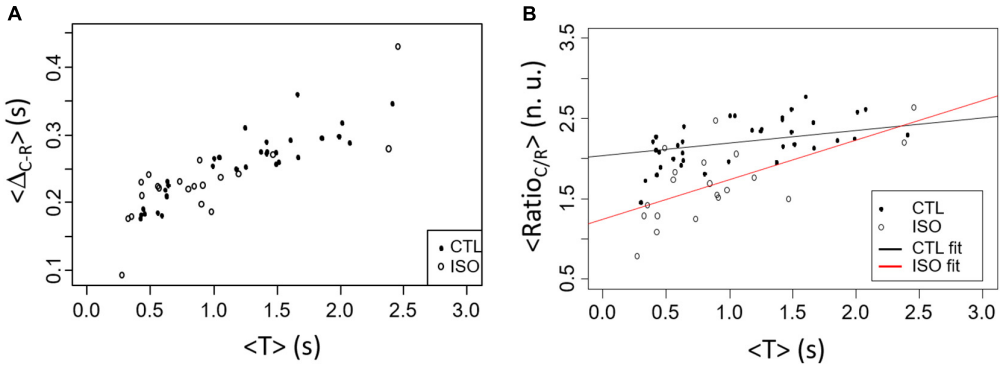

FIGURE 8 | Comparison between CTL (black points) and ISO (white circles) contraction results in spontaneous rhythm. **(A)** $<\Delta_{R\text{-}C}>$ as a function of <T> does not shows dissimilarity between groups. **(B)** $<\text{Ratio}_{C/R}>$ as a function of <T> differs between CTL and ISO with both a significant <T> and treatment effects (CTL vs. ISO).

$N_{sub,x}$ and $N_{sub,y}$ pixels from the total FOV with Eq. (3) (similar to Eq. 1).

$$\Delta S_{x',y'}(t) = \frac{1}{N_{sub,y}N_{sub,x}} \sum_{u=1}^{N_{sub,y}} \sum_{v=1}^{N_{sub,x}} \left| \frac{M_{u+N_{sub,y}(y'-1),v+N_{sub,x}(x'-1)}(t) - M_{u+N_{sub,y}(y'-1),v+N_{sub,x}(x'-1)}(t-\tau)}{\tau} \right| \quad (3)$$

where $N_{sub,y} = N_{sub,x} = 10$, $M(t)$ is the movie frame at time t, u and v are the local coordinate within each sub-region of the FOV and x' and y' are the new position within the segmented FOV (such that $x' = 1$, $y' = 1$ is the first pixel of the new video calculated from on the individual signals of the pixels $y = 1$–10 and $x = 1$–10 from the original video).

The energy (E) of the local composite signals is calculated using:

$$E_{x',y'} = \frac{1}{N_t - \tau} \sum_{t=\tau}^{N_t} \left(\frac{d\Delta S_{x',y'}(t)}{dt} \right)^2 \quad (4)$$

where N_t is the number of frames of the original video. An example of the spatial distribution of $\log(E_{x',y'})$ is displayed in **Figure 9A** and the corresponding histogram can be found in **Figure 9B**. High energy regions of the FOV are selected using a thresholding approach.

The correlation coefficient (CC) and lag between the global signal $\Delta S(t)$ and local composite signals $\Delta S_{x',y'}(t)$ are calculated. An example of the resulting map of coefficients and lag are respectively depicted in **Figures 9C,D** after keeping pixels with $\log(E) > 6$. In this example, most of the relevant section of the FOV have a correlation coefficient greater than 0.8 and a lag of 0 s which indicates that the local activity is highly similar between these regions and the global activity. However, some regions show lower correlation including regions with a correlation value of less than 0.4 (regions labeled sub 1 and 2 in **Figure 9C**). Interestingly, these regions have also non-zero lags. Using a thresholding approach on the correlation coefficient map, two corresponding clusters of low correlation with high energy can be detected and the average signal from these clusters are shown in **Figure 9E**. The signals in both sub 1 and 2 regions (red line) have strong peaks usually not occurring simultaneously with the global composite signal (blue dotted line). Please note that lower amplitude peaks are also found in this signals that correlate with the global activity.

Digging Deeper in Acquisitions With Complex Global Signal

Conditions that alter the development and function of cultured monolayers can affect the spatial-temporal activity. Confluent monolayers usually show consistent and relatively stationary signal with the common contraction/relaxation peaks as shown in **Figure 3A**. However, more complex global composite signals can be found such as multiple peak complexes as can be seen in the example shown in **Figure 10A**.

To investigate the causes of these complex patterns, a thresholding on the energy was done as previously showed [map of $\log(E)$ is shown in **Figure 10Bi** after thresholding with $\log(E) > 4$]. The method is based on cross correlation between two time series shifted relatively in time (the time shift being the lag). Calculation of the correlation coefficient with the global composite signals does not highlight important regions with low coefficient (**Figure 10Bii**). However, calculating the correlation coefficient and lag between cluster signals [from the average $\Delta S_{x',y'}(t)$ of each cluster] results in the matrix plot shown in **Figures 10C** (correlation coefficient) and D (lag). Both panels show a clear difference in correlation and lag between cluster 5 and the others (labeling of the clusters can be found on the map showing the correlation coefficient between cluster 5 and others in **Figure 10Biii**).

The causes of the correlation differences can be investigated by further studying the differences in the cluster $\Delta S_{x',y'}(t)$ signals represented by a grayscale in **Figure 10E**. A closer look at the maps shows that synchronization between cluster 5 and the others varies over time with almost simultaneous activity within the orange dashed rectangle (which has a corresponding normal

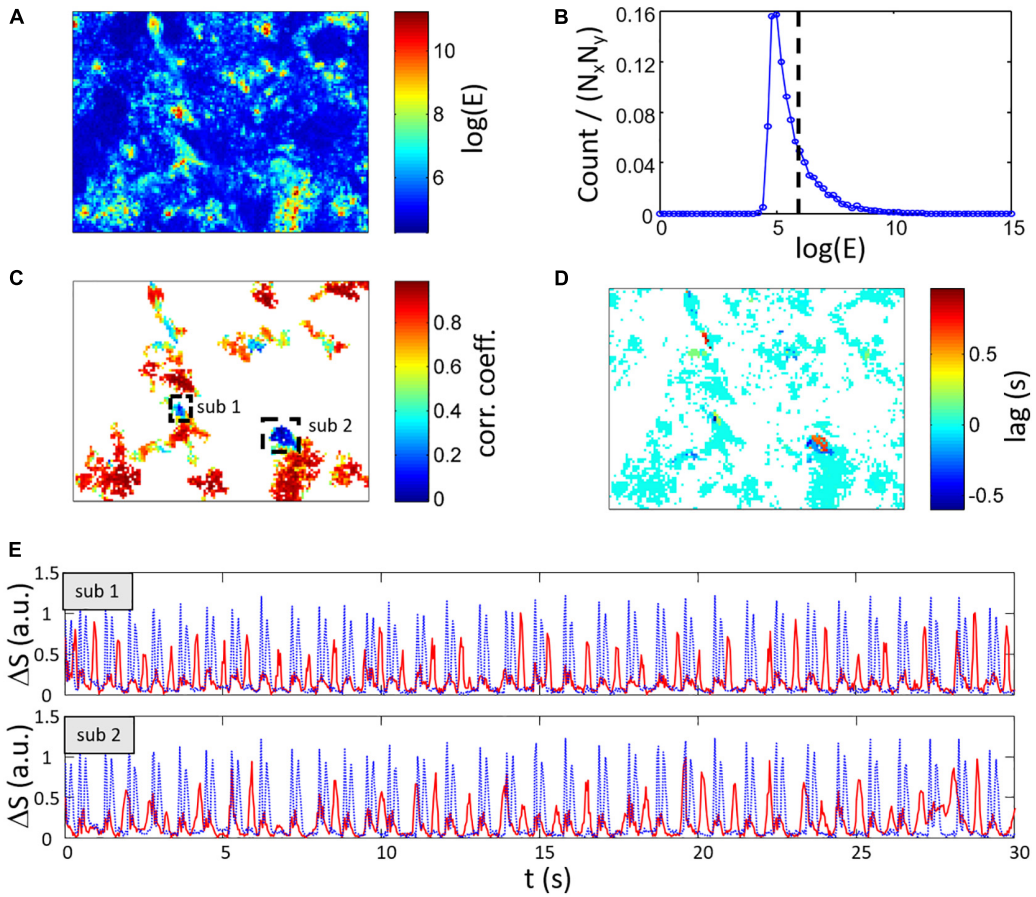

FIGURE 9 | Estimation of heterogeneous spontaneous contraction rhythms within the FOV. **(A)** Map of log(E) with the energy E calculated from Eq. (4) showing area with no contraction signal in blue. **(B)** Histogram of log(E) with the dashed line representing the threshold [log(E) > 6] use to select high energy signal regions. **(C)** Maximum correlation coefficient and **(D)** lag between local $\Delta S_{x',y'}(t)$ and global $\Delta S(t)$ for regions having log(E) > 6. Two low CC regions labeled sub 1 and sub 2 are highlighted. Most of the regions show high CC with 0 s lag. **(E)** Signal from region sub 1 (top axes) and sub 2 (bottom axes) showing the low CC (shown as red lines vs. global ΔS as dotted blue lines) and global ΔS.

double peak feature in the global signal shown by the blue line). However, the complex multi-peaks section encompassed within the red dashed rectangle corresponds to an earlier contraction in cluster 5 (with delays between cluster 4 and 5 of 100 and 160 ms for the 2nd and 3rd beats in the rectangle). The non-stationary aspect of the global signal can thus be understood by a change in timing of cluster 5 activity in respect to other clusters where the abnormal added peaks are found when a long delay between cluster contractions occurs. Depending on signal quality, the contraction/relaxation analysis approach presented in the first part of this article could be done on cluster signals to extract and compare temporal activity variations.

DISCUSSION AND CONCLUSION

In this study, we proposed novel approaches to study beating dynamics in cell culture. To our knowledge, the main contractility analysis method described herein the first to study the contractility characteristics based on monolayer videomicroscopy data. Indeed, previous methods focused mainly on period/frequency of activity (Rohr, 1990; Kim et al., 2011). Based on a simple composite signal calculated as the variation in pixels intensity, two main variables can be determined: the time difference and the ratio between the contraction and relaxation peaks. These new variables could be interesting to determine toxic effects on cardiomyocytes more importantly regarding heart failure risk. Both variables showed to be dependent on the period of activity (either paced as shown in **Figure 5** or spontaneously beating as in **Figure 7**). A note that a direct comparison between the spontaneously beating data and paced data cannot be done as being two different sets of experiments with different FBS-starved prior to experiments.

Comparison with simulation results show qualitative similarities between simulation and experimental data. However, there are quantitative differences on both variables of interest as, for example, $\text{Ratio}_{C/R}$ is less than one in the simulations but not in experiments. A recent study clearly showed that the rate of contraction is faster than the rate of relaxation (which

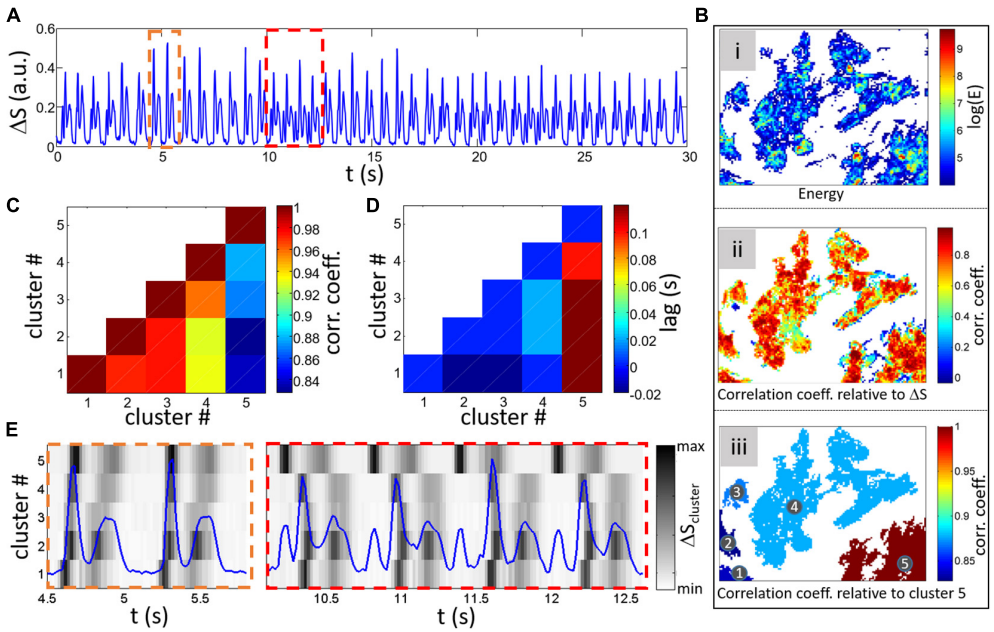

FIGURE 10 | Analysis of a different global ΔS for a different sample with complex activity. **(A)** Example of a non-stationary global signal with time intervals where multiple peaks (different to the contraction/relaxation peaks usually found). Two intervals are highlighted by dashed rectangles with the orange one showing the normal double peak signal and the red rectangle with multiple peaks. **(Bi)** Map of log(E) after thresholding [log(E) > 4]. **(Bii)** CC between individual cluster signals and global Δ*S*. **(Biii)** Labeled separated clusters with colorscale representing the CC between cluster 5 and other clusters. **(C)** Matrix of CC between clusters (Pillekamp et al., 2012; Lu et al., 2013; Wendel et al., 2013; Zhang et al., 2013; Hazeltine et al., 2014) with diagonal equal to 1 and **(D)** lag for maximum CC. Minimum CC and maximum lag are found between cluster 5 and all 4 other clusters. **(E)** Cluster Δ*S* signals for the 5 within the two intervals highlighted by rectangles in **(A)** is shown by a grayscale (peaks are darker and lower values whiter). The global Δ*S* is plotted in blue on top for comparison.

would lead to $\text{Ratio}_{C/R} > 1$) for both atrial and ventricular adult rat cardiomyocytes (Nollet et al., 2020). Visual inspection of published mouse cardiomyocyte shortening seems to also point to a $\text{Ratio}_{C/R} > 1$ (Lim et al., 2000). There is of course a correlation between the calcium dynamic and contraction characteristics. An interesting example has been published by del Monte et al. (1999) in their study on contractile function in isolated cardiomyocytes from failing human hearts. Failing heart cardiomyocytes are known to have decreased expression and function of SERCA2. The data presented show that the contraction is much slower than relaxation when looking at the cell shortening. As such, we expect to have a RatioC/R less than 1. Overexpression of SERCA2 yielded reverted the cell shortening to a cell shortening similar to the non-failing cardiomyocyte. The mathematical modeling in our study assumed an isotonic contraction while a confluent monolayer should probably be a mixed condition between isometric (on a stiff cell culture substrate) and isotonic on the free top side of the cells. The study by Rodriguez et al. (2011) clearly showed that even isolated (not being a monolayer), the velocity of contraction measured from displacement of an elastic post show a fastest contraction compared to relaxation. It is interesting to note that the force of contraction of an isolated but attached neonatal rat cardiomyocytes is heterogeneous with the highest forces being found at the periphery of the cell and lowest at the center (where the nucleus is found). As such, it is highly probable that the formation monolayer, by having cardiomyocytes constraining each other, would have an impact of the proposed measures. Thus, although there may still be differences between monolayers vs. isolated cells, it is likely that it is not the cause for the contraction rate being smaller than the relaxation rate in the simulations resulting in a $\text{Ratio}_{C/R}$ smaller than 1. Also, it is highly probable that differences between culture conditions (substrate rigidity, microstructure for cardiomyocyte alignment, mechanical and electrical stimulation) known for influencing cardiomyocyte function would also influence the contraction function and thus, possibly change the measures in some way. The exact link between the contraction waveform and the actual change in contraction measures obtained from the composite signal requires further investigation.

It is interesting and promising to see that the proposed measures is dependent on the rate of activity. We have shown that adrenergic stimulation (with isoproterenol) which is well known for its isotropic effect results in a change in $\text{Ratio}_{C/R}$ confirming that the proposed measures are of interest to evaluate contraction changes by pharmacological agents. Although it remains to be tested experimentally, analysis of previously published contraction changes induced by doxorubicin resulted in variations of both $\text{Ratio}_{C/R}$ and Δ_{R-C}. The last two proposed approaches (**Figures 9**, **10**) are interesting to evaluate the homogeneity of the monolayer activity and, in case of heterogeneous dynamics, quantify the correlation between monolayer areas. Conditions inducing partial electrical decoupling could be detected.

The proposed approaches may be also interesting in limiting impact on the beating cells as proposed previously (Kim et al., 2011; Pushkarsky et al., 2014) which remains to be evaluated. Light impact on cellular process can be decreased by limiting exposure and careful selection of wavelength bands to favor contrast but it is believed to be minimal (Rohr, 1990). Although extension to lens-free CMOS imaging remains to be tested, our method can be adjusted to cover various scales of field of view. The limited time resolution due to the relatively low frame per second from a reasonably priced sensor could be a limitation. However, even a slow frame rate of 30 fps (as used for the CTL vs. ISO experiments) showed a significant difference in the proposed contraction measures. Recent development in imaging technology and communication hardware with off-the-shelf USB 3.0 or MIPI CSI-2 cameras open the way to greater than 100 fps simple sensor solution. Even the Raspberry Pi camera module can now easily allow up to 90 fps with VGA resolution (640 × 480 pixels) opening the way to simple low-cost high throughput parallel screening.

The proposed alternative methods described here that aim to study heterogeneity in contraction signal are interesting as they can estimate cell culture characteristics impossible to study directly with classical methods (Rohr, 1990; Kim et al., 2011). Here, detection of localized abnormal activity (compared to the global activity) could also be a measure of cell/tissue sample deterioration. Moreover, the change in synchronization between regions, an important variable that can be link to intercellular coupling and be a factor favoring arrhythmia, can be evaluated. As such, actual application of these approaches and evaluation of their relevance as appropriate biomarker of new drug cardiotoxicity could be of great interest.

DATA AVAILABILITY STATEMENT

The raw data supporting the conclusions of this article will be made available by the authors, without undue reservation.

ETHICS STATEMENT

The animal study was reviewed and approved by the Montreal Heart Institute Animal Research Ethics Committee, Montreal Heart Institute.

AUTHOR CONTRIBUTIONS

JB collected the data. JB and PC helped design the initial phase of the study, did experimental data analysis and interpretation, and drafted the article. JD and PC did mathematical modeling data collection, analysis, and interpretation. JB, JD, and PC gave final approval of the version to be published.

FUNDING

This work was supported by the Montreal Heart Institute Foundation, the Natural Sciences and Engineering Research Council of Canada and by the Réseau ThéCell du Fonds de Recherche du Québec – Santé (FRQS).

ACKNOWLEDGMENTS

We are grateful to Jonathan Ledoux for the helpful discussions and to the reviewers for there suggestions.

SUPPLEMENTARY MATERIAL

The Supplementary Material for this article can be found online at: https://www.frontiersin.org/articles/10.3389/fphys.2022.733706/full#supplementary-material

REFERENCES

Alderton, P. M., Gross, J., and Green, M. D. (1992). Comparative study of doxorubicin, mitoxantrone, and epirubicin in combination with ICRF-187 (ADR-529) in a chronic cardiotoxicity animal model. *Cancer Res.* 52, 194–201.

Boudreau-Beland, J., Duverger, J. E., Petitjean, E., Maguy, A., Ledoux, J., and Comtois, P. (2015). Spatiotemporal stability of neonatal rat cardiomyocyte monolayers spontaneous activity is dependent on the culture substrate. *PLoS One* 10:e0127977. doi: 10.1371/journal.pone.0127977

Chiu, L. L., Iyer, R. K., King, J. P., and Radisic, M. (2011). Biphasic electrical field stimulation aids in tissue engineering of multicell-type cardiac organoids. *Tissue Eng. Part A* 17, 1465–1477. doi: 10.1089/ten.tea.2007.0244

del Monte, F., Harding, S. E., Schmidt, U., Matsui, T., Kang, Z. B., Dec, G. W., et al. (1999). Restoration of contractile function in isolated cardiomyocytes from failing human hearts by gene transfer of SERCA2a. *Circulation* 100, 2308–2311. doi: 10.1161/01.cir.100.23.2308

Desai, V. G., Herman, E. H., Moland, C. L., Branham, W. S., Lewis, S. M., Davis, K. J., et al. (2013). Development of doxorubicin-induced chronic cardiotoxicity in the B6C3F1 mouse model. *Toxicol. Appl. Pharmacol.* 266, 109–121. doi: 10.1016/j.taap.2012.10.025

Dick, E., Rajamohan, D., Ronksley, J., and Denning, C. (2010). Evaluating the utility of cardiomyocytes from human pluripotent stem cells for drug screening. *Biochem. Soc. Trans.* 38, 1037–1045. doi: 10.1042/BST0381037

Dorr, R. T., Bozak, K. A., Shipp, N. G., Hendrix, M., Alberts, D. S., and Ahmann, F. (1988). *In vitro* rat myocyte cardiotoxicity model for antitumor antibiotics using adenosine triphosphate/protein ratios. *Cancer Res.* 48, 5222–5227.

Engler, A. J., Carag-Krieger, C., Johnson, C. P., Raab, M., Tang, H. Y., Speicher, D. W., et al. (2008). Embryonic cardiomyocytes beat best on a matrix with heart-like elasticity: scar-like rigidity inhibits beating. *J. Cell Sci.* 121(Pt 22), 3794–3802. doi: 10.1242/jcs.029678

Feinberg, A. W., Alford, P. W., Jin, H., Ripplinger, C. M., Werdich, A. A., Sheehy, S. P., et al. (2012). Controlling the contractile strength of engineered cardiac muscle by hierarchal tissue architecture. *Biomaterials* 33, 5732–5741. doi: 10.1016/j.biomaterials.2012.04.043

Ferri, N., Siegl, P., Corsini, A., Herrmann, J., Lerman, A., and Benghozi, R. (2013). Drug attrition during pre-clinical and clinical development: understanding and managing drug-induced cardiotoxicity. *Pharmacol. Ther.* 138, 470–484. doi: 10.1016/j.pharmthera.2013.03.005

Grosberg, A., Alford, P. W., McCain, M. L., and Parker, K. K. (2011). Ensembles of engineered cardiac tissues for physiological and pharmacological study: heart on a chip. *Lab Chip* 11, 4165–4173. doi: 10.1039/c1lc20557a

Hazeltine, L. B., Badur, M. G., Lian, X., Das, A., Han, W., and Palecek, S. P. (2014). Temporal impact of substrate mechanics on differentiation of human embryonic stem cells to cardiomyocytes. *Acta Biomater.* 10, 604–612. doi: 10.1016/j.actbio.2013.10.033

Herman, E. H., Rahman, A., Ferrans, V. J., Vick, J. A., and Schein, P. S. (1983). Prevention of chronic doxorubicin cardiotoxicity in beagles by liposomal encapsulation. *Cancer Res.* 43, 5427–5432.

Kim, S. B., Bae, H., Cha, J. M., Moon, S. J., Dokmeci, M. R., Cropek, D. M., et al. (2011). A cell-based biosensor for real-time detection of cardiotoxicity using lensfree imaging. *Lab Chip* 11, 1801–1807. doi: 10.1039/c1lc20098d

Lim, C. C., Apstein, C. S., Colucci, W. S., and Liao, R. (2000). Impaired cell shortening and relengthening with increased pacing frequency are intrinsic to the senescent mouse cardiomyocyte. *J. Mol. Cell. Cardiol.* 32, 2075–2082. doi: 10.1006/jmcc.2000.1239

Lu, T. Y., Lin, B., Kim, J., Sullivan, M., Tobita, K., Salama, G., et al. (2013). Repopulation of decellularized mouse heart with human induced pluripotent stem cell-derived cardiovascular progenitor cells. *Nat. Commun.* 4:2307. doi: 10.1038/ncomms3307

McCain, M. L., Agarwal, A., Nesmith, H. W., Nesmith, A. P., and Parker, K. K. (2014). Micromolded gelatin hydrogels for extended culture of engineered cardiac tissues. *Biomaterials* 35, 5462–5471. doi: 10.1016/j.biomaterials.2014.03.052

McCain, M. L., Sheehy, S. P., Grosberg, A., Goss, J. A., and Parker, K. K. (2013). Recapitulating maladaptive, multiscale remodeling of failing myocardium on a chip. *Proc. Natl. Acad. Sci. U.S.A.* 110, 9770–9775. doi: 10.1073/pnas.1304913110

Menna, P., Salvatorelli, E., and Minotti, G. (2008). Cardiotoxicity of antitumor drugs. *Chem. Res. Toxicol.* 21, 978–989.

Morotti, S., Edwards, A. G., McCulloch, A. D., Bers, D. M., and Grandi, E. (2014). A novel computational model of mouse myocyte electrophysiology to assess the synergy between Na + loading and CaMKII. *J. Physiol.* 592, 1181–1197. doi: 10.1113/jphysiol.2013.266676

Navarrete, E. G., Liang, P., Lan, F., Sanchez-Freire, V., Simmons, C., Gong, T., et al. (2013). Screening drug-induced arrhythmia events using human induced pluripotent stem cell-derived cardiomyocytes and low-impedance microelectrode arrays. *Circulation* 128(11 Suppl. 1), S3–S13. doi: 10.1161/CIRCULATIONAHA.112.000570

Negroni, J. A., Morotti, S., Lascano, E. C., Gomes, A. V., Grandi, E., Puglisi, J. L., et al. (2015). beta-adrenergic effects on cardiac myofilaments and contraction in an integrated rabbit ventricular myocyte model. *J. Mol. Cell. Cardiol.* 81, 162–175. doi: 10.1016/j.yjmcc.2015.02.014

Nollet, E. E., Manders, E. M., Goebel, M., Jansen, V., Brockmann, C., Osinga, J., et al. (2020). Large-scale contractility measurements reveal large atrioventricular and subtle interventricular differences in cultured unloaded rat cardiomyocytes. *Front. Physiol.* 11:815. doi: 10.3389/fphys.2020.00815

Nunes, S. S., Miklas, J. W., Liu, J., Aschar-Sobbi, R., Xiao, Y., Zhang, B., et al. (2013). Biowire: a platform for maturation of human pluripotent stem cell-derived cardiomyocytes. *Nat. Methods* 10, 781–787.

Pillekamp, F., Haustein, M., Khalil, M., Emmelheinz, M., Nazzal, R., Adelmann, R., et al. (2012). Contractile properties of early human embryonic stem cell-derived cardiomyocytes: beta-adrenergic stimulation induces positive chronotropy and lusitropy but not inotropy. *Stem Cells Dev.* 21, 2111–2121. doi: 10.1089/scd.2011.0312

Pushkarsky, I., Liu, Y., Weaver, W., Su, T. W., Mudanyali, O., Ozcan, A., et al. (2014). Automated single-cell motility analysis on a chip using lensfree microscopy. *Sci. Rep.* 4:4717. doi: 10.1038/srep04717

Rodriguez, A. G., Han, S. J., Regnier, M., and Sniadecki, N. J. (2011). Substrate stiffness increases twitch power of neonatal cardiomyocytes in correlation with changes in myofibril structure and intracellular calcium. *Biophys. J.* 101, 2455–2464. doi: 10.1016/j.bpj.2011.09.057

Rohr, S. (1990). A computerized device for long-term measurements of the contraction frequency of cultured rat heart cells under stable incubating conditions. *Pflugers Arch.* 416, 201–206. doi: 10.1007/BF00370243

Schimmel, K. J., Richel, D. J., van den Brink, R. B., and Guchelaar, H. J. (2004). Cardiotoxicity of cytotoxic drugs. *Cancer Treat. Rev.* 30, 181–191.

Sham, J. S., Hatem, S. N., and Morad, M. (1995). Species differences in the activity of the Na(+)-Ca2 + exchanger in mammalian cardiac myocytes. *J. Physiol.* 488(Pt 3), 623–631. doi: 10.1113/jphysiol.1995.sp020995

Sheehy, S. P., Grosberg, A., and Parker, K. K. (2012). The contribution of cellular mechanotransduction to cardiomyocyte form and function. *Biomech. Model. Mechanobiol.* 11, 1227–1239. doi: 10.1007/s10237-012-0419-2

Shirhatti, V., George, M., Chenery, R., and Krishna, G. (1986). Structural requirements for inducing cardiotoxicity by anthracycline antibiotics: studies with neonatal rat cardiac myocytes in culture. *Toxicol. Appl. Pharmacol.* 84, 173–191. doi: 10.1016/0041-008x(86)90425-4

Stevens, J. L., and Baker, T. K. (2009). The future of drug safety testing: expanding the view and narrowing the focus. *Drug Discov. Today* 14, 162–167. doi: 10.1016/j.drudis.2008.11.009

Surdo, N. C., Berrera, M., Koschinski, A., Brescia, M., Machado, M. R., Carr, C., et al. (2017). FRET biosensor uncovers cAMP nano-domains at beta-adrenergic targets that dictate precise tuning of cardiac contractility. *Nat. Commun.* 8:15031. doi: 10.1038/ncomms15031

Timolati, F., Anliker, T., Groppalli, V., Perriard, J. C., Eppenberger, H. M., Suter, T. M., et al. (2009). The role of cell death and myofibrillar damage in contractile dysfunction of long-term cultured adult cardiomyocytes exposed to doxorubicin. *Cytotechnology* 61, 25–36. doi: 10.1007/s10616-009-9238-4

Vunjak-Novakovic, G., Lui, K. O., Tandon, N., and Chien, K. R. (2011). Bioengineering heart muscle: a paradigm for regenerative medicine. *Annu. Rev. Biomed. Eng.* 13, 245–267. doi: 10.1146/annurev-bioeng-071910-124701

Wendel, J. S., Ye, L., Zhang, P., Tranquillo, R. T., and Zhang, J. (2013). Functional consequences of a tissue-engineered myocardial patch for cardiac repair in a rat infarct model. *Tissue Eng. Part A* 20, 1325–1335. doi: 10.1089/ten.TEA.2013.0312

Yeh, E. T., Tong, A. T., Lenihan, D. J., Yusuf, S. W., Swafford, J., Champion, C., et al. (2004). Cardiovascular complications of cancer therapy: diagnosis, pathogenesis, and management. *Circulation* 109, 3122–3131. doi: 10.1161/01.cir.0000133187.74800.b9

Zhang, D., Shadrin, I. Y., Lam, J., Xian, H. Q., Snodgrass, H. R., and Bursac, N. (2013). Tissue-engineered cardiac patch for advanced functional maturation of human ESC-derived cardiomyocytes. *Biomaterials* 34, 5813–5820. doi: 10.1016/j.biomaterials.2013.04.026

Zhang, J., Wilson, G. F., Soerens, A. G., Koonce, C. H., Yu, J., Palecek, S. P., et al. (2009). Functional cardiomyocytes derived from human induced pluripotent stem cells. *Circ. Res.* 104, e30–e41.

Zheng, G., Lee, S. A., Antebi, Y., Elowitz, M. B., and Yang, C. (2011). The ePetri dish, an on-chip cell imaging platform based on subpixel perspective sweeping microscopy (SPSM). *Proc. Natl. Acad. Sci. U.S.A.* 108, 16889–16894. doi: 10.1073/pnas.1110681108

Conflict of Interest: The authors declare that the research was conducted in the absence of any commercial or financial relationships that could be construed as a potential conflict of interest.

frontiers | Frontiers in Physiology

BRIEF RESEARCH REPORT
published: 06 April 2022
doi: 10.3389/fphys.2022.805161

Automated Object Detection in Experimental Data Using Combination of Unsupervised and Supervised Methods

*Yiran Wu, Zhen Wang, Crystal M. Ripplinger and Daisuke Sato**

Department of Pharmacology, University of California, Davis, Davis, CA, United States

Deep neural networks (DNN) have shown their success through computer vision tasks such as object detection, classification, and segmentation of image data including clinical and biological data. However, supervised DNNs require a large volume of labeled data to train and great effort to tune hyperparameters. The goal of this study is to segment cardiac images in movie data into objects of interest and a noisy background. This task is one of the essential tasks before statistical analysis of the images. Otherwise, the statistical values such as means, medians, and standard deviations can be erroneous. In this study, we show that the combination of unsupervised and supervised machine learning can automatize this process and find objects of interest accurately. We used the fact that typical clinical/biological data contain only limited kinds of objects. We solve this problem at the pixel level. For example, if there is only one object in an image, there are two types of pixels: object pixels and background pixels. We can expect object pixels and background pixels are quite different and they can be grouped using unsupervised clustering methods. In this study, we used the *k*-means clustering method. After finding object pixels and background pixels using unsupervised clustering methods, we used these pixels as training data for supervised learning. In this study, we used logistic regression and support vector machine. The combination of the unsupervised method and the supervised method can find objects of interest and segment images accurately without predefined thresholds or manually labeled data.

Keywords: machine learning, unsupervised learning, *k*-means clustering, support vector machine, object detection, image processing, artificial intelligence, cardiac images

OPEN ACCESS

Edited by:
Elena Tolkacheva, University of Minnesota Twin Cities, United States

Reviewed by:
Yuan Feng, Shanghai Jiao Tong University, China
Giuseppe Baselli, Politecnico di Milano, Italy

***Correspondence:**
Daisuke Sato
dsato@ucdavis.edu

Specialty section:
This article was submitted to Computational Physiology and Medicine, a section of the journal Frontiers in Physiology

Received: *01 November 2021*
Accepted: *23 February 2022*
Published: *06 April 2022*

Citation:
Wu Y, Wang Z, Ripplinger CM and Sato D (2022) Automated Object Detection in Experimental Data Using Combination of Unsupervised and Supervised Methods. Front. Physiol. 13:805161. doi: 10.3389/fphys.2022.805161

INTRODUCTION

Cardiac cells and tissue have complex shapes. In addition, muscle contraction changes their shapes over time. When we analyze experimental data such as calcium concentration in the cell or membrane potential in tissue, it is necessary to segment out objects of interest from their background. If data contain signals from the outside of objects of interest, statistical values such as means, medians, and standard deviations can be erroneous.

If there are only a few images, it is possible to do it manually. However, for example, movie data contain many frames. In this case, it is desirable to automatize the process. There have been

many ways to do it automatically, at least partially. One way is to use a thresholding method if the background is less noisy and contrast between objects of interest and the background is relatively high (Gonzalez and Woods, 2018). However, it is often difficult to choose an appropriate threshold value, especially when the image data contain noisy or weak signal parts. Another way is to use the center of the object, which is confident, instead of using the whole object. However, the center and the fringe may have different signals and the signals from the fringe might be important.

More recently, machine learning, such as deep neural networks (DNNs), has been greatly improved, especially for image processing. DNNs have shown their success through computer vision tasks such as object detection, classification, and segmentation of image data including clinical and biological data. However, supervised DNNs require a large volume of labeled data to train DNNs and tuning of hyperparameters. For example, without segmentation maps as training data, convolution neural networks such as U-net (Ronneberger et al., 2015; Zhou et al., 2018; Khened et al., 2019) cannot be applied to the problem. In addition, we use various tools and materials in research experiments. This means we have to re-tune and re-train the model as we change the experimental settings. The goal of this study is to segment out objects of interest from the background automatically.

In this study, we show that the combination of unsupervised learning and supervised learning can automatize this process and find objects of interest accurately. Instead of DNNs, we used simple machine learning methods that require little time to train and have short inference time. As we show later, we can expect signals from object pixels and signals from background pixels are quite different and thus they can be grouped using unsupervised clustering methods. On the other hand, supervised learning methods often give better results. We proposed a combined method that possesses advantages of these two methods. Here, we used the unsupervised method to extract training data and the supervised method for prediction to find objects of interest accurately without the need for manually labeled data.

METHODS

Experimental Data Sets

In this study, we used movie data of action potential wave propagation in the heart. Each movie contains one heart object close to the center of the frame. Cardiac tissue was loaded with a fluorescent indicator (RH237), which changes the recorded fluorescence with changes in membrane potential. The goal here is to segment images into the heart and background in these movies. Data were collected at 1 kHz. Each movie consists of 1,024 frames (= 1,024 ms), while each frame is a 100 $px \times 100\ px$ 8 bit-grayscale image (**Figure 1A**). Pixel values were normalized between 0 and 1. This was done for each pixel. 0 was assigned to the minimum value of the pixel over time (not the minimum value of the entire movie). Similarly, 1 was assigned to the maximum value of the pixel over time. One data point consists of n frames. n is arbitrary. In this study, we chose n to be 32, 128, 256, 512, and 1,024. For example, when we acquire boundaries of objects for the first frame with $n = 512$, we use from frame 1 to frame 512. Each data point is classified individually. Then, using the result, we create a mask to hide the background for the first frame. Similarly, for the n-th frame, we use from frame n to frame $n+511$. In general, the larger n gives better classification performance. On the other hand, the smaller n gives better motion tracking performance. In this study, since the image contains 10,000 pixels, there are 10,000 data points to be classified.

k-Means Clustering

We first used one of the classical unsupervised methods called k-means clustering (Forgey, 1965; MacQueen, 1967; Hartigan and Wong, 1979). k-means clustering is originally used for signal processing that groups x data points into k clusters. Cardiac cells loaded with a fluorescent indicator show action potential signals and thus we expect the signals from the heart tissue would be different from those from the background in the data space (**Figure 1B**). We note that the dimension of the data space represented in **Figure 1B** is two. The dimension of data space in this study is n. We sampled pixels from heart tissue and background and plotted the change in values of these pixels over time (**Figure 2**). **Figures 2A–D** show representative signals from the heart tissues while **Figures 2E–H** show representative signals from the background. These panels demonstrate the distinct signal patterns in the object of interest and the background areas. In this study, we use the similarity of time-series data.

Manually Selected Training Data

In addition to unsupervised machine learning, we also used supervised machine learning which requires training datasets. We manually selected the heart areas from around the center of the heart and non-heart areas from around the four corners. Note that we only selected the regions far from the boundaries to assure the selected pixels belong to these classes. Since in our movies the heart/non-heart area do not change radically over time, our selection of the first frame could be applied to the whole 1,024 frames. The detail of the process is as follows:

1. Draw five polygons, corresponding to the central heart areas and four corner non-heart areas, avoiding the marginal areas.
2. Identify the pixel location circled by these polygons, and extract pixel values from the selected areas of 1,024 frames, respectively.
3. Append heart/non-heart labels (0, 1) to the two types of extracted values to create a dataset of shape (m, 1,025) (1,024 frames + 1 label), where m is the number of selected pixels.

We labeled 5,500 heart and 900 non-heart pixels, that is $m = 6{,}400$. Our training and validation sets are split with a ratio of 8:1 for both heart and non-heart pixels.

Logistic Regression

In this study, we used logistic regression and support vector machine (SVM) as supervised learning methods. Logistic

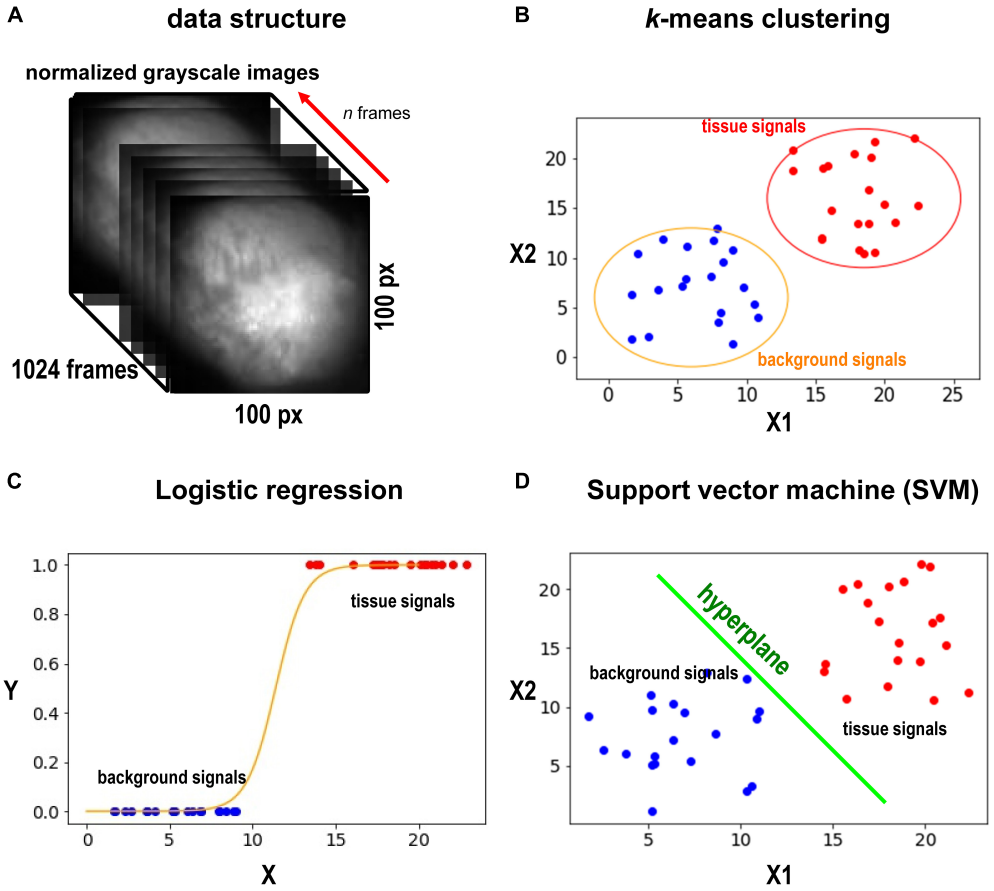

FIGURE 1 | Data sets and methods. **(A)** Grayscale image of the heart. The heart is located in the center of the image. We select *d* frames, and each pixel would have d values (*d*-dimensional vector) from the frames. **(B)** The schematic illustration of the k-means method. Here only two axes are shown. In our case, we compute in *d*-dimensional space. k-means is an unsupervised method, and no training is required. **(C)** The schematic illustration of SVM. SVM will find the best hyperplane to split the data. SVM requires training. **(D)** The schematic illustration of the logistic regression. the logistic regression will fit sigmoid function to the data points and find a middle point ($y = 0.5$) to split the points to the two classes (tissue and background). The logistic regression classifier requires training. We note that **(B–D)** are only for illustration. The actual dimension of the data in this study is *n*.

regression is one of the simplest yet effective classification methods (Pregibon, 1981; Peng et al., 2002), which models the probability of a solid outcome using logistic function. For a binary logistic regression model, the outcome would be 1/0, true/false, while in our case, it would be heart/background (**Figure 1C**). In terms of solving the problem, let X be the input pixel value and Y be the label, logistic regression defines a relation of $f(X) = \text{Sigmoid}(m^*X + c)$ (m and c are weights and bias), where $\text{Sigmoid}(t) = 1/[1+ \exp(-t)]$. The goal is to minimize $[Y\text{-}f(X)]^2$. The procedure is as follows:

1. Using the manually selected training data with dimension (6,400, 1,025) from 2.3, select *n* frames ($0 < n <= 1{,}024$) to prepare a new dataset with new dimension (6,400, n+1), including the label.
2. Train the logistic regression model with the selected data. Predict any single frame with input shape (10,000, *n*), and the output shape of (10,000, 1) can be reshaped to *100 px* × *100 px* to get the mask.

Support Vector Machine

We also used SVM as another example of supervised machine leaning. SVM is a robust classification model (Suykens and Vandewalle, 1999). SVM constructs a hyperplane in the data space to split the data points into the two classes (**Figure 1D**). While we are choosing the hyperplane, we want to maximize the minimal distance between the classes. When we draw a hyperplane to split the two classes, each class would have a point that have the minimal distance to the plane, and what SVM tries to do is to maximize this distance. We used the linear kernel for all the cases. The procedure is similar to logistic regression in section "Logistic Regression," except we train SVM in step 2.

Combined Method of *k*-Means Clustering and Support Vector Machine

As we will show in the "Results" section, SVM gives the most stable and accurate results within these three methods (*k*-means clustering, logistic regression, SVM). However, SVM requires manually labeled training data. On the other hand, with

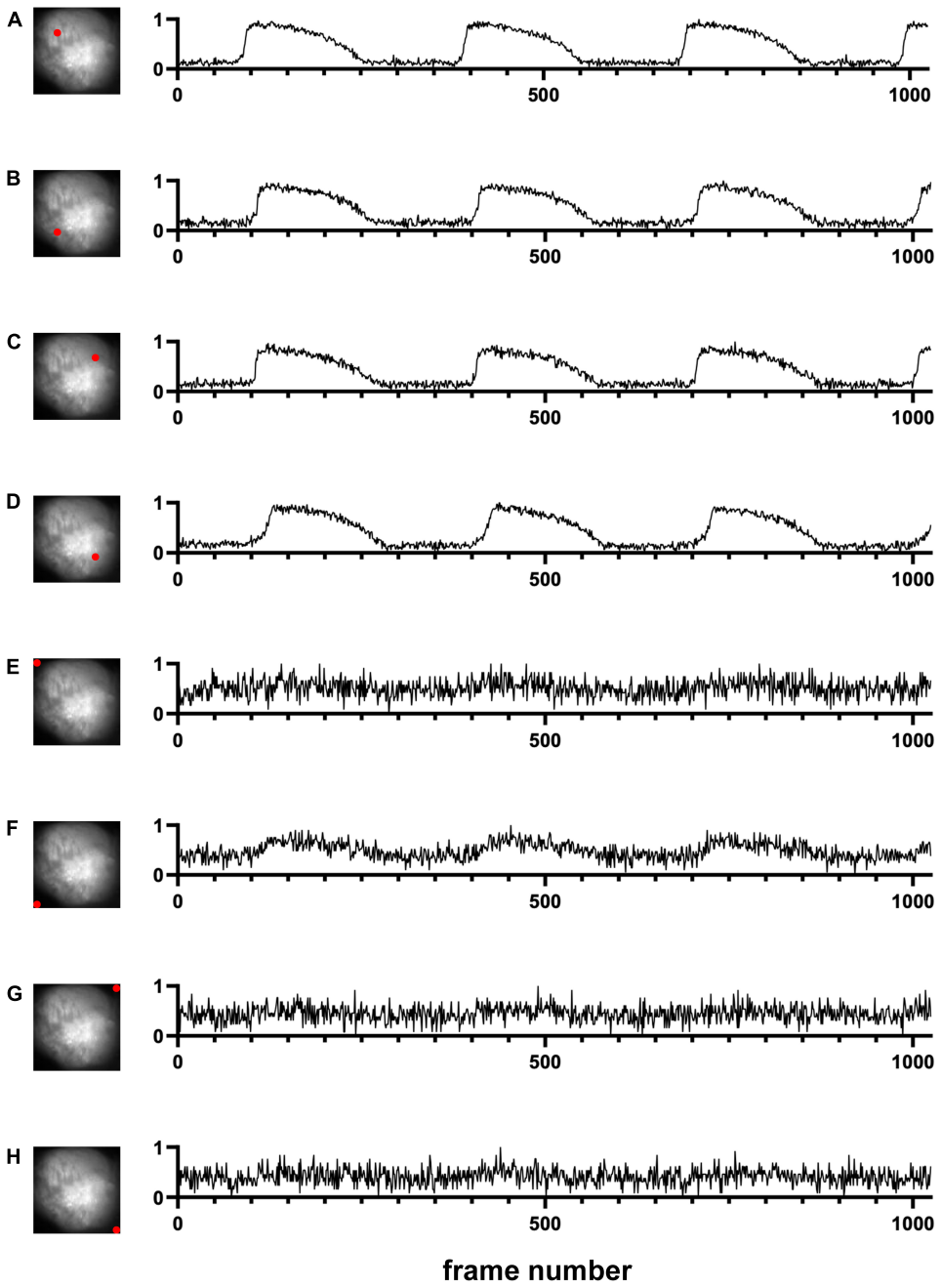

FIGURE 2 | Signals in time domain (Dataset No. 1). **(A–D)** Representative data from four pixel locations from cardiac tissue. **(E–H)** Representative data from four pixel locations from the background. For each plot, the x-axis represents the time, and the y-axis represents the change in values of one pixel location over time. Due to normalization, noise in background pixels is normally amplified **(E–H)**.

unsupervised machine learning, *k*-means does not work as well as SVM, but it does not require training data. Thus, it is natural to combine these two methods for one that performs well while does not need labeled training data. We first modify *k*-means to retrieve data points for training, and then applied SVM using those training data.

We first randomly choose a center for each cluster for *k*-means clustering, and then assign each data point to the nearest cluster. In our case, we have two clusters: heart tissue pixels and background (non-heart) pixels. Since we are using *k*-means to prepare data for training, we want to avoid the marginal areas and select the confident areas, just like when we select manually. We proposed *Distance Discount Factor* to help selecting the confident areas in *k* -means clustering.

Distance Discount Factor in k-means clustering is as follows. Let a data point A have a distance D_1 to Center 1 and D_2 to Center

2. We compare D_1 and D_2 to decide to which cluster A belongs. During this step, we multiply distance D_1 with a discount factor $\gamma \in (0, 1]$ to make D_1 smaller, that points are more likely to be assigned to Center 1 with the discounted distances. Despite the discount factor, there would still be points assigned to Center 2 with $D_2 < \gamma D_1$. These points would be viewed as stubborn points; they are so close to Center 2 that they cling to that center even after we posed a discount to D_1. Then these stubborn points would be the confident points that belong to this cluster, which would be extracted and labeled as training data. Despite we designed γ here to be in range $(0, 1]$ for convenience, a more loose range would be $\gamma \in (0, \infty)$. Since we have inequity "$D_2 < \gamma D_1$," multiply one side by γ would be the same to multiply another side by $1/\gamma$.

The basic algorithm of *k*-means clustering is not changed with the discount factor. At each iteration of *k*-means clustering, the discount factor would be applied when comparing distances of each point to the two centroids, which is basically a metric to decide how the points would be assigned to each centroid. With discount factor = 1, this is just the original k-means since the distances would not be changed, while with discount factor = 0, all points would be assigned to one cluster, since we assign points to the nearest centroid but distances of all points to this cluster are multiplied by 0.

The procedure of the combined method is as follows:

Input: A movie consisting of 1,024 frames, while each frame is a *100 px* × *100 px* 8 bit-grayscale image. Thus, there are 10,000 (× 1,024) data points.

1. Run k-means with the distance discount factor twice (one for the tissue and one for the background) on these data points to find confident heart tissue points (**Figure 4B**) and confident background points (**Figure 4C**), substituting the step where we manually select data. With these confident points we form a dataset of $m \times 1{,}024$ and corresponding labels of $m \times 1$ (let m be the number of confident points). Note that the discount factor needs to be tuned with visual observation only once for a specific task, in our experiments we tuned the discount factor with grid search on Dataset No.1 and it can be used for other datasets.
2. Set n to be the number of frames we extract. To segment the i th frame (n, $i \in [1, 1, 024]$; $n + i - 1 <= 1{,}024$), we extract frame $i \sim$ frame $n + i - 1$ and form a training dataset of $m \times (n + 1)$, with "$+ 1$" representing the labels.
3. Fit SVM (or other supervised methods) to this labeled dataset to get a classifier. Then for the i th frame, we use this classifier to classify each of the 10,000 pixels and get segments.

Noise Reduction With Modified Median Filter

We sometimes observed dotted noise in regions where signals are obscure. At the final stage, we applied a modified median filter to reduce noise specifically in masks (with only 0s and 1s) (**Supplementary Figure 6**). This function is similar to original median filter, but it is more flexible and is tailored for masks.

After classification, each pixel in the mask has a value of either 1 (heart pixel) or 0 (non-heart pixel). For each pixel location, we check whether its neighbor's value is the same as itself. We count these occurrences to determine whether to change its value. For example, assuming a pixel A has a value 1, we count the 3 × 3 neighbor pixels surrounding A. With a threshold of 3, if more than 3 pixels in the grid have the value of 1, we kept A unchanged. Otherwise, we change A to 0 since its neighbor's counts does not satisfy the threshold.

We make the function more flexible by enabling it to be applied to only one value. That is, if we set remove heart to false, the counting grid will not be applied if the pixel has a value 1 (heart pixel). Then the 1 s in the mask remain intact, while the 0 s can be changed to 1 if it does not satisfy the filter threshold.

Code Availability

Codes are written in Python and MATLAB and are available from GitHub[1].

RESULTS

In this study, we detected the heart in the experimental image data using unsupervised and supervised machine learning methods. We used *k*-means clustering as an unsupervised method, and logistic regression and SVM as supervised methods.

Figure 3 shows comparison of results between these three methods. *k*-means clustering worked better as the number of frames increased. On the other hand, logistic regression worked well when the number of frames was small. SVM worked well regardless of the number of frames.

Although SVM gave the most stable results among them, it requires training to use it. For **Figure 3**, we manually selected the training data as described in section "Methods." As the next step, we considered to prepare training data using unsupervised learning. **Figure 4A** is the original image data. We applied the *k*-means clustering with the distance discount factor and picked the heart pixels (**Figure 4B**) and non-heart pixels (**Figure 4C**). Using training data picked by the *k*-means clustering, we trained the SVM and classified heart and non-heart pixels. **Figure 4D** is the detected heart. **Figure 4E** shows the detected heart using manually picked training data for comparison. Here, we used 1,024 frames. We also varied the number of frames and tested the combined method (**Supplementary Figure 1**). **Supplementary Figures 2–5** shows all the results and comparisons between the combined method and SVM using manually selected training data. In all the cases, both results are very similar.

We also combined *k*-means clustering and logistic regression. However, in this case, the results were worse than the combined method of *k*-means clustering and SVM. **Supplementary Table 1** shows all the cases we did in this study.

SVM has a validation accuracy of 0.999 for all frames on both manually selected data and *k*-means selected data. Logistic regression has a validation accuracy of 0.999 for 128 and 256 frames, 0.59 for 512 frames, 0.5 for 1,024 frames. We calculated

[1]https://github.com/DSatoLab/Automated-Object-Detection-with-AI

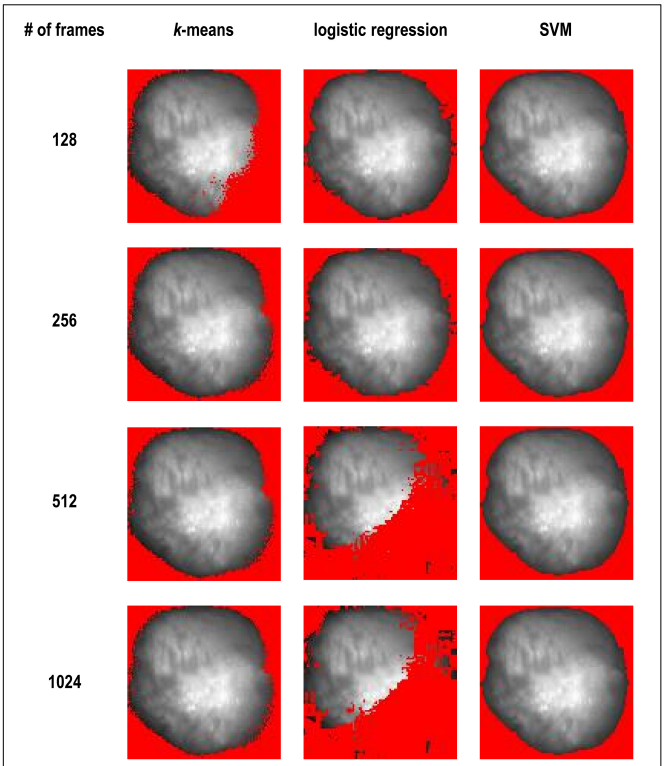

FIGURE 3 | K-means vs. logistic regression vs. SVM and with 128, 256, 512, and 1,024 frames (Dataset No. 1). The detected background was masked with red and only the heart area is shown.

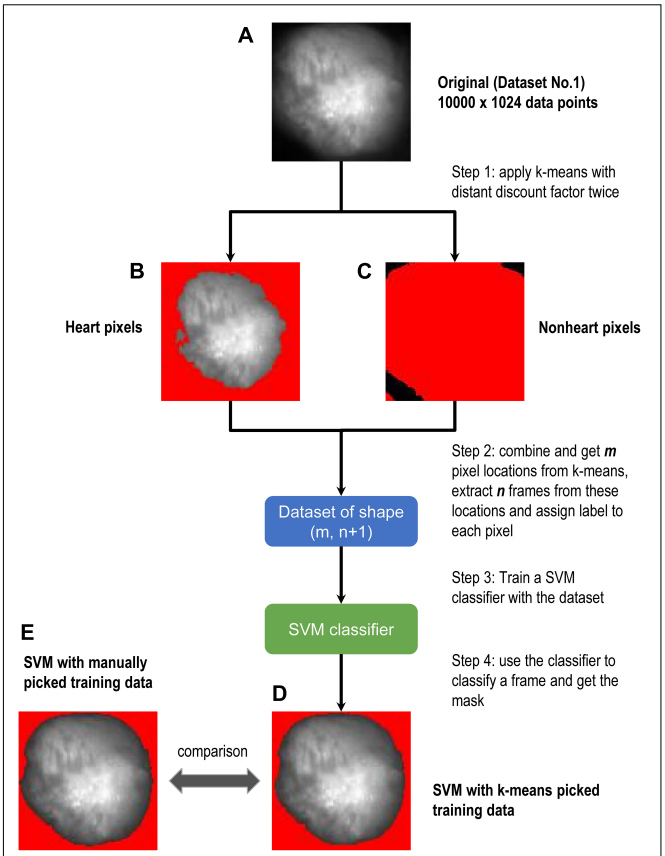

FIGURE 4 | Flow chart of combined method. **(A–E)** Are all from Dataset No.1. *k*-means was used to get the training data at the first step. Border zones were excluded from the training data. We chose data close to the centroids. The non-red area in **(B)** is heart and the non-red area in **(C)** is non-heart part. Then theses selected areas were labeled with 0 and 1 s to train SVM. **(D,E)** Are the results of the SVM model, where SVM of **(D)** is trained by k-means picked data and **(E)** is trained by manually picked data.

the ratio r = (the number of heart pixels)/(total number of pixels) with different methods (**Supplementary Table 1**). To get a clearer insight into the change of ratio with respect to the change in frames, we calculated the standard deviation (STD) of the heart ratios from each method (**Supplementary Table 1**). We expect STD would measure the consistency of each method, that is how the ratio is varied with different number of frames. Our results show SVM is much more consistent (lower STD) than logistic regression with either manually labeled data or *k*-means extracted data. Both methods have a lower STD with *k*-means extracted data than that with manually selected data.

Moving Objects and Boundaries

This algorithm can be applied to the moving objects and can track moving boundaries. **Supplementary Movie 1** shows the result when tissue is rotating. **Supplementary Movie 2** shows the result when tissue is shrinking. We also tested this algorithm using calcium transient data along with contraction by Huebsch et al. (2015). In these examples, we chose smaller frame number (n = 32). In all the cases, we could track moving boundaries accurately.

DISCUSSION

In this paper, we proposed the combined method of unsupervised machine learning and supervised machine learning to automatize the process of object detection mainly focusing on the cardiac movie data. We used the fact that most experimental data contain only a few objects and signals from the background are quite different from those of the objects of interest.

Unsupervised methods and supervised methods have their own advantages and combined unsupervised and supervised methods have been used in several areas. For example, Richard et al. (2007) used combined unsupervised and supervised methods for segmentation of radiophonic audio streams. Guo et al. (2015) used them to automatize lesion detection on MRI scans. In this study, we solved the problem of the heart tissue segmentation in grayscale movies. We formulated the problem from the per-pixel level instead of the per-image level. The advantages of the per-pixel view are: 1. Each pixel would be classified and thus the precision of the boundaries would be high. 2. The problem could be viewed as a simple binary classification problem. In one frame of the movie, the 100 × 100 pixels are viewed as 10,000 datapoints, which are reasonably enough for training of the model, and all we need is to classify them as heart or non-heart pixel and form a mask.

Many segmentation methods have been proposed to find objects in an image (Gonzalez and Woods, 2018). However, most of them are for a single image. In this study, we used multiple frames in the movie data to segment out objects of interest. In other words, we do not use spatial similarity. Instead, we use temporal similarity. This makes the algorithm robust for noise. In fact, due to normalization of signals over time, even if the noise levels are the same in the tissue pixels and the background pixels, the noise signals would be amplified in the background pixels (**Figures 2A–D** vs. **Figures 2E–H**). Thus, even during diastole, we can classify the tissue pixels and the background pixels.

In this study, we compared various methods. We first used unsupervised and supervised methods individually (**Figure 3**). We found that unsupervised learning like *k*-means clustering works in most cases, especially when the number of frames is large. *k*-means clustering does not require labeled data or predefined thresholds. However, in some cases, it could not identify the heart properly. *k*-means fails to segment the images when the number of frames is small (**Figure 3**, 128 frames), but it worked with more than 256 frames. Since change in the signal is small with a smaller number of frames, clustering cannot distinguish these pixels and background pixels where zero signal plus noise. With more data points, change in the signal from heart tissue becomes larger and the classification results became better with 256 frames or more. In other words, the model becomes more robust with higher dimensional data.

SVM performed better than logistic regression and *k*-means clustering. SVM worked with all the number of frames and the results are quite stable (**Figure 3**), but it requires labeled data to train. Thus, we combined the advantages of *k*-means clustering and SVM.

To choose reliable training data sets, we developed the distance discount factor strategy. The distance discount factor can be between 0 and 1. If the distance discount factor is 1, it is the same as the original k-means clustering. As the distance discount factor becomes smaller, we will find smaller subsets of points close to the centroids. Using this algorithm, we can find more reliable locations of centroids and exclude outlier data points as well as data points near the boundaries.

In this study, we chose the distance discount factor manually so that there would be a reasonable number of training data. But it is easy to automatize the process if the target number of training data is given.

Our results showed that the combined method performed well while it does not require any manual labeling. We confirmed that the combined method has similar results comparing to SVM with manually labeled data in almost all cases (**Supplementary Figures 2–5**). We also tested this method with a smaller number of frames (32 frames) (**Supplementary Figure 7**). Thirty-two frames are equal to 32 ms as the data acquisition rate is 1 Hz. In 32 ms, the motion of the heart is limited. Thus, when this method works, we can track the motion of the heart (**Supplementary Movies 1, 2**).

We imagine that logistic regression would have a better fit for classification problem due to nature of sigmoid function. From the results, logistic regression worked with 128 and 256 frames but failed with 512 and 1,024 frames (**Figure 3**). We tested with several numbers of frames and found that the effectiveness of the method decreases gradually as the number of frames (i.e., dimension of the data) increases. Regression methods loss its generality with higher dimensional data, as they are unable to draw an unregular line or shapes between the two classes in high dimensional spaces.

Our current task required labels only for one object and thus there were two classes. It is easy to extend the algorithm to increase the number of objects. If there are two types of objects in an image, there are three types of pixels. For a more complicated scenario, the cost of labeling becomes large. In this paper, we experimented with grayscale video data, and we combined *k*-means clustering with SVM to separate background noise from object of interest accurately. There are many other unsupervised and supervised methods. In future studies, we will try other combinations of unsupervised and supervised methods for more complicated scenarios.

DATA AVAILABILITY STATEMENT

The datasets presented in this study can be found in online repositories. The names of the repository/repositories and accession number(s) can be found below: https://github.com/DSatoLab/Automated-Object-Detection-with-AI.

AUTHOR CONTRIBUTIONS

All authors listed have made a substantial, direct, and intellectual contribution to the work, and approved it for publication.

FUNDING

This work was supported by the National Institutes of Health grants R00-HL111334 (DS), R01-HL149349 (DS), P01-HL141084 (DS), R01-HL121059 (DS), R01-HL111600 (CR), and Amazon AWS Cloud Credits for Research (DS).

SUPPLEMENTARY MATERIAL

The Supplementary Material for this article can be found online at: https://www.frontiersin.org/articles/10.3389/fphys.2022.805161/full#supplementary-material

Supplementary Figure 1 | Comparison between trained SVM using data from K-Means and manually selected data (Dataset No. 1).

Supplementary Figure 2 | Results of the combined method (Dataset No. 1) with 128 Frames.

Supplementary Figure 3 | Results of the combined method (Dataset No. 2) with 128 Frames.

Supplementary Figure 4 | Results of the combined method (Dataset No. 3) with 128 Frames.

Supplementary Figure 5 | Results of the combined method (Dataset No. 4) with 128 Frames.

Supplementary Figure 6 | Comparison between k-means and smoothed k-means with 128, 256, 512, and 1,024 frames (Dataset No. 1). The detected background is masked with red and only the heart area is shown.

Supplementary Figure 7 | Results of the combined method (Dataset No. 1) with 32 Frames.

Supplementary Table 1 | Ratio of Predicted Heart Pixels with different frames (Dataset No. 1). Ratio the number of heart pixels predicted by each method and different number of frames (Total of 10,000 pixels). STD is the standard deviation of each method (each row) to see the variation of each method with different number of frames. k-means used unlabeled data; Logistic regression and SVM used manually selected data to train; Combined SVM and combined logistic regression used labeled data from k-means clustering.

Supplementary Movie 1 | The result of the combined method when tissue was rotated 180 degrees over 1 s. The detected background is masked with red and only the heart area is shown. $n = 32$.

Supplementary Movie 2 | The result of the combined method when tissue was shrunk over one second. The detected background is masked with red and only the heart area is shown. $n = 32$.

REFERENCES

Forgey, E. (1965). Cluster analysis of multivariate data: efficiency vs. interpretability of classification. *Biometrics* 21, 768–769.

Gonzalez, R. C., and Woods, R. E. (2018). *Digital Image Processing*. London: Pearson.

Guo, D., Fridriksson, J., Fillmore, P., Rorden, C., Yu, H., Zheng, K., et al. (2015). Automated lesion detection on MRI scans using combined unsupervised and supervised methods. *BMC Med. Imaging* 15:50. doi: 10.1186/s12880-015-0092-x

Hartigan, J. A., and Wong, M. A. (1979). Algorithm AS 136: a K-means clustering algorithm. *J. R. Stat. Soc. Ser. C (Applied Statistics)* 28, 100–108. doi: 10.2307/2346830

Huebsch, N., Loskill, P., Mandegar, M. A., Marks, N. C., Sheehan, A. S., Ma, Z., et al. (2015). Automated video-based analysis of contractility and calcium flux in human-induced pluripotent stem cell-derived cardiomyocytes cultured over different spatial scales. *Tissue Eng. Part C Methods* 21, 467–479. doi: 10.1089/ten.TEC.2014.0283

Khened, M., Kollerathu, V. A., and Krishnamurthi, G. (2019). Fully convolutional multi-scale residual DenseNets for cardiac segmentation and automated cardiac diagnosis using ensemble of classifiers. *Med. Image Anal.* 51, 21–45. doi: 10.1016/j.media.2018.10.004

MacQueen, J. (1967). "Some methods for classification and analysis of multivariate observations," in *Proceedings of the 5th Berkeley Symposium on Mathematical Statistics and Probability* (Oakland, CA), 281–297.

Peng, C.-Y. J., Lee, K. L., and Ingersoll, G. M. (2002). An introduction to logistic regression analysis and reporting. *J. Educ. Res.* 96, 3–14. doi: 10.1080/00220670209598786

Pregibon, D. (1981). Logistic regression diagnostics. *Ann. Stat.* 9:720.

Richard, G., Ramona, M., and Essid, S. (2007). "Combined supervised and unsupervised approaches for automatic segmentation of radiophonic audio streams," in *Proceedings of the 2007 IEEE International Conference on Acoustics, Speech and Signal Processing – ICASSP '07, II-461-II-464* (Honolulu, HI).

Ronneberger, O., Fischer, P., and Brox, T. (2015). "U-Net: convolutional networks for biomedical image segmentation," in *Medical Image Computing and Computer–Assisted Intervention – MICCAI 2015. MICCAI 2015. Lecture Notes in Computer Science*, Vol. 9351, eds N. Navab, J. Hornegger, W. Wells, and A. Frangi (Cham: Springer), 234–241.

Suykens, J. A. K., and Vandewalle, J. (1999). Least squares support vector machine classifiers. *Neural Process. Lett.* 9, 293–300. doi: 10.1023/A:1018628609742

Zhou, Z., Rahman Siddiquee, M. M., Tajbakhsh, N., and Liang, J. (2018). "UNet++: a nested U-Net architecture for medical image segmentation," in *Deep Learning in Medical Image Analysis and Multimodal Learning for Clinical Decision Support. DLMIA 2018, ML-CDS 2018. Lecture Notes in Computer Science*, Vol. 11045, ed. D. Stoyanov (Cham: Springer), 3–11. doi: 10.1007/978-3-030-00889-5_1

Conflict of Interest: The authors declare that the research was conducted in the absence of any commercial or financial relationships that could be construed as a potential conflict of interest.

Publisher's Note: All claims expressed in this article are solely those of the authors and do not necessarily represent those of their affiliated organizations, or those of the publisher, the editors and the reviewers. Any product that may be evaluated in this article, or claim that may be made by its manufacturer, is not guaranteed or endorsed by the publisher.

frontiers | Frontiers in Physiology

TYPE Original Research
PUBLISHED 23 January 2023
DOI 10.3389/fphys.2023.734356

OPEN ACCESS

EDITED BY
Xiaopeng Zhao,
The University of Tennessee, Knoxville, United States

REVIEWED BY
Jan E. Azarov,
Komi Scientific Center (RAS), Russia
Bum-Rak Choi,
Warren Alpert Medical School of Brown University, United States

*CORRESPONDENCE
Richard D. Walton,
richard.walton@ihu-liryc.fr

SPECIALTY SECTION
This article was submitted to Cardiac Electrophysiology, a section of the journal Frontiers in Physiology

RECEIVED 01 July 2021
ACCEPTED 09 January 2023
PUBLISHED 23 January 2023

CITATION
Ramlugun GS, Kulkarni K, Pallares-Lupon N, Boukens BJ, Efimov IR, Vigmond EJ, Bernus O and Walton RD (2023), A comprehensive framework for evaluation of high pacing frequency and arrhythmic optical mapping signals. *Front. Physiol.* 14:734356. doi: 10.3389/fphys.2023.734356

A comprehensive framework for evaluation of high pacing frequency and arrhythmic optical mapping signals

Girish S. Ramlugun[1,2], Kanchan Kulkarni[1,2], Nestor Pallares-Lupon[1,2], Bastiaan J. Boukens[3,4], Igor R. Efimov[5,6,7], Edward J. Vigmond[1,8], Olivier Bernus[1,2] and Richard D. Walton[1,2]*

[1]IHU-Liryc, Fondation Bordeaux Université, Pessac-Bordeaux, France, [2]Univ. Bordeaux, Inserm, Centre de Recherche Cardio-Thoracique, Bordeaux, France, [3]Department of Physiology, Cardiovascular Research Institute Maastricht, University Maastricht, Maastricht, Netherlands, [4]Department of Medical Biology, Amsterdam Cardiovascular Sciences, Amsterdam University Medical Center, University of Amsterdam, Amsterdam, Netherlands, [5]Department of Biomedical Engineering, The George Washington University, Washington, DC, United States, [6]Department of Biomedical Engineering, Northwestern University, Chicago, IL, United States, [7]Department of Medicine, Northwestern University, Chicago, IL, United States, [8]Univ. Bordeaux, Centre National de la Recherche Scientifique (CNRS), Institut de Mathématiques de Bordeaux, UMR5251, Bordeaux, France

Introduction: High pacing frequency or irregular activity due to arrhythmia produces complex optical mapping signals and challenges for processing. The objective is to establish an automated activation time-based analytical framework applicable to optical mapping images of complex electrical behavior.

Methods: Optical mapping signals with varying complexity from sheep (N = 7) ventricular preparations were examined. Windows of activation centered on each action potential upstroke were derived using Hilbert transform phase. Upstroke morphology was evaluated for potential multiple activation components and peaks of upstroke signal derivatives defined activation time. Spatially and temporally clustered activation time points were grouped in to wave fronts for individual processing. Each activation time point was evaluated for corresponding repolarization times. Each wave front was subsequently classified based on repetitive or non-repetitive events. Wave fronts were evaluated for activation time minima defining sites of wave front origin. A visualization tool was further developed to probe dynamically the ensemble activation sequence.

Results: Our framework facilitated activation time mapping during complex dynamic events including transitions to rotor-like reentry and ventricular fibrillation. We showed that using fixed AT windows to extract AT maps can impair interpretation of the activation sequence. However, the phase windowing of action potential upstrokes enabled accurate recapitulation of repetitive behavior, providing spatially coherent activation patterns. We further demonstrate that grouping the spatio-temporal distribution of AT points in to coherent wave fronts, facilitated

Abbreviations: AT, Activation time; APD'min, Minimum action potential duration limit; APD'max, Maximum action potential duration limit; APD''min, Refined minimum action potential duration limit; APD''max, Refined maximum action potential duration limit; eAT, Electrical activation time; ERP, Effective refractory period; ERPm*in*, Minimum effective refractory period; F, Fluorescenceπ, Constant Pi; σ_L, Longitudinal conductivity; T, Number of frames; φ, Phase; $\theta(dF/dt)$, Signal derivative threshold; $\theta_{dF/dt}$, Signal derivative threshold after outlier removal; $\theta''_{t,CB}$, Conduction block parameter; pAT, Phase window activation time; RT, Repolarization time; SNR, Signal to noise ratio; t, Time; σ_S, Transmural conductivity; σ_T, Transverse conductivity; uAT, Unified window activation time; X, Horizontal image dimension; Y, Vertical image dimension.

interpretation of isolated conduction events, such as conduction slowing, and to derive dynamic changes in repolarization properties. Focal origins precisely detected sites of stimulation origin and breakthrough for individual wave fronts. Furthermore, a visualization tool to dynamically probe activation time windows during reentry revealed a critical single static line of conduction slowing associated with the rotation core.

Conclusion: This comprehensive analytical framework enables detailed quantitative assessment and visualization of complex electrical behavior.

KEYWORDS

optical mapping, fibrillation, pacing, electrophysiology, image processing

1 Introduction

Chaotic electrical activity in the ventricles of the heart form the precursor to sudden cardiac death, a major public health problem. Our understanding of arrhythmic behavior and electrical remodeling in cardiac diseases at the organ level continues to grow with advancements of recording instruments. Optical mapping using potentiometric fluorescent probes excels in the compromise over resolution and imaging field of view (Himel and Knisley, 2007). Yet, spatio-temporal complexity of electrical signals recorded during chaotic electrical events such as in cardiac arrhythmias, imposes constraints to accurately interpret the electrical behavior. Increased frequency of activity often leads to concomitant slowing of overall conduction, increased variance of conduction velocities and a loss of synchronization (Kleber et al., 1986; Akar et al., 2007); the latter, impacting negatively the signal amplitude (Fast and Kleber, 1995). Moreover, multiple complex arrhythmic patterns may co-exist, originate from numerous sources and transition from one behavior to another over time. As a result, algorithmic activation time (AT) detection, visualization and interpretation are challenging and a unified approach encompassing a broad range of signal complexities is lacking.

The first 20 s following the induction of ventricular fibrillation in pig showed chaotic electrical impulse propagation evolving towards steadily more organized states (Rogers et al., 1997a; Rogers et al., 1997b). To understand and quantify waveform complexity, a multiplicity metric was developed to determine the repetitiveness of propagating wave fronts, which are dependent on their orientation, size and regularity. Chen et al. (2000) later showed using frequency analysis and phase mapping that regions of the ventricles in rabbit maintained periodic activity at frequencies exceeding the surrounding tissue. From this, they determined that high frequency periodic sources were responsible for driving complex fibrillatory behavior in the periphery, underlying ventricular fibrillation. However, the life-time of rotors when measuring from the epicardial surface are variable and rarely lasting more than two rotations in healthy myocardium (Kay et al., 2006). In this case, rotors were identified as the point of phase singularity, where contours of all phases converge to form the center of rotation (Winfree, 1989). More recently, it was demonstrated that the point of phase convergence could also assume a line, which aligned with functional gradients or structural boundaries (Arno et al., 2021). The wavelet hypothesis was evaluated using *in silico* models and suggested that multiple wavelets could be sustained in homogeneous tissue, but preferentially block or lead to wave break with increased heterogeneity (Fenton et al., 2002). Short-lived and intermittent renewal of rotor sources or the constant wave break and regeneration of wavelets describe at least part of the fundamental complexity of fibrillatory behavior. But this is further confounded in tissue by structural heterogeneities, particularly in pathological conditions resulting in increased electrical uncoupling.

Phase analysis of electrograms and optical mapping studies of tachyarrhythmic events has proven effective at identifying the substrate region implicated in classical rotor theory, but is less adapted currently for applications to assess macroreentry or non-reentrant events. Frequency analysis requires multiple electrical events to determine the periodicity and regularity of activity. However there remains an unmet need to provide a unified approach to spatially resolve electrical propagation patterns and to investigate wave front behavior in an individualized manner, irrespective of the underlying mechanism.

AT mapping has been used successfully to track critical excitatory pathways underlying stable ventricular tachycardia (Takahashi et al., 2004). Child et al. (2015) developed the reentry vulnerability index from an activation-repolarization time metric between the proximal and distal ends of the same wave front. Requiring only a short-coupled stimulation protocol, the vulnerability index provided maps of the relative probability of reentry without needing to induce the arrhythmia. Focal sources of activation can also be readily located as local sites of AT minima. Although surface mapping methods cannot distinguish between focal sources originating from the mapped surface or deeper layers and are therefore termed sites of activation breakthrough. That being said, optical mapping signals originate from a near-surface tissue volume and are therefore an integral of electrical responses from several cell layers (Fedorov et al., 2010). As a result, optical action potential upstroke morphology depends on the sequence that the different cell layers are activated and provides an approximation of the subsurface electrical wave orientation (Hyatt et al., 2008). Moreover, the depth contribution of optical signals can be varied by modifying the wavelength of excitation light (Walton et al., 2010); A palette of voltage-sensitive dyes extending in to the near-infrared range continue to be developed (Matiukas et al., 2007). The versatility, effective resolution, signal morphology and additional depth information afforded by optical mapping necessitates a dedicated framework for analysis of complex tachyarrhythmia.

The objective of this study was to establish a novel analytical framework for assessing electrical complexity recorded by optical mapping. Specifically, aims were to: Conserve image resolution; avoid temporal signal complexity reduction; conserve multiple upstroke events; To achieve spatial coherence of AT; To perform classification of repetitive/non-repetitive activity and to spatially classify wave fronts by their source. We present a comprehensive

pipeline based on a novel unified method to assess the activation sequence adapted for arrhythmic and transitional electrical behavior. We compared experimental recordings with an *in silico* model of reentry induced in a three-dimensional ventricular slab geometry. Optical mapping signals were derived from the *in silico* model to apply processing and analyses on signals with appropriate morphology, consistent with optical mapping experiments (Hyatt et al., 2005; Walton et al., 2012).

2 Methods and materials

2.1 *In silico* model

A finite element model of a three-dimensional ventricular wedge, measuring 5 cm × 5 cm in the epicardial plane and 1 cm transmural thickness, was created at a spatial resolution of 200 μm isotropic. Fibre orientation was set to vary by 120from the endocardial to the epicardial surfaces. The Ten Tusscher ionic model (Ten Tusscher and Panfilov, 2006) was implemented to simulate ventricular arrhythmia. Monodomain simulations were performed using the openCARP simulation environment (Plank et al., 2021) with baseline conductivity values of 0.03, 0.02 and 0.02 S/m for longitudinal (σ_L), transverse (σ_T) and transmural (σ_S) directions. Using time steps of 0.05 ms throughout, a planar wave was generated by stimulating one transmural surface of the slab with shortening coupling intervals at 0, 325, 525 and 715 ms. A rotating wave was then generated by applying a cross field stimulus during the recovery phase of the central portion of the model at 860 ms (Skouibine et al., 2002). To emulate experiments and signal morphology specific to optical mapping, the cardiac arrhythmia research package (Vigmond et al., 2003) was used to generate epi-fluorescent optical signals from electrical simulations, as described previously (Bishop et al., 2006).

2.2 Tissue acquisition

Hearts were obtained from sheep (N = 8, 2 years old) weighing 40–50 kg in accordance with the guidelines from Directive 2010/63/EU of the European Parliament on the protection of animals used for scientific purposes and the local ethical committee. Healthy sheep (N = 7) and a sheep (N = 1) with chronic myocardial infarction following coronary embolization (see Pallares-Lupon et al., 2022) were premedicated with ketamine (20 mg/kg) and acepromazine (0.02 mL/kg), anesthesia was induced by propofol (2 mg/kg) and maintained under isoflurane, 2%, in air/O2 (50/50%) after intratracheal intubation. Sheep were euthanized by intravenous injection with pentobarbital (30 mL/50 Kg) and hearts were rapidly excised, cannulated and flushed with cardioplegic solution, containing (mM): NaCl, 110; CaCl2, 1.2; KCl, 16; MgCL2, 16; NaHCO3, 10 and glucose, 9.01 at 4°C.

2.3 Preparations of sheep myocardium

Coronary-perfused ventricular wedges were prepared by dissection in to two different configurations, based on the major coronary artery perfused: right ventricle (right coronary artery) and left ventricle (left anterior descending and circumflex arteries (Moreno et al., 2019)). In each case, cannulation of the coronary circulation was applied at the ostia, arising from the aortic root. Perfusion leaks at cut surfaces were carefully tied-off and preparations mounted on to a frame, exposing the endocardial surfaces. Wedges were submersed and perfused with a saline solution gassed with 95%/5% O2/CO2 and containing (mM): NaCl, 130; NaHCO3, 24; NH2PO4, 1.2; MgCl2, 1; glucose, 5.6; KCl, 4; CaCl2, 1.8, at 37°C and pH7.4.

2.4 Optical mapping

Preparations were imaged using optical mapping of the endocardial surfaces after being mechanically-uncoupled using 15 μM blebbistatin, and loaded with the voltage-sensitive dye, Di-4-ANEPPS (Cytocybernetics, United States). Endocardial surfaces were illuminated with monochromatic LEDs at 530 nm (Cairn Research Ltd, Kent, United Kingdom). Optical images (100 × 100 pixels) of signals passed through a 650 ± 20 nm band-pass filter were acquired using a Micam Ultima CMOS camera (SciMedia United States Ltd, CA, United States) at 1 kHz with a spatial resolutions of 0.7 × 0.7 mm.

2.5 Pacing protocols

To demonstrate the analysis pipeline, an optical mapping acquisition for the induction of reentry composed of a single rotor was recorded from the right ventricle. Figure 1A shows two parallel 4 cm platinum line electrodes (Cardialen Inc, United States) were sutured to the endocardial surface at the atrioventricular ring and along the apico-anterior border of the preparation (approximately 5 cm apart). The preparation was paced by a train of pulses at twice the threshold at a fixed frequency of 2 Hz from the posterior border. Depolarization and repolarization fronts were near planar in between, and perpendicular to the line electrodes. With a delay of 220 ms from the last planar stimulation pulse, an electrical cross-field shock at 80 V was applied between the parallel electrodes, creating a voltage gradient of 16 V/cm. This was found to fall in the critical window of repolarization for induction of self-sustaining arrhythmic activity by the cross-field shock-on-T wave mechanism (Frazier et al., 1989) (Figure 1B). Following tachyarrhythmia induction, pacing was discontinued.

To observe transitioning dynamic electrical behavior from basal pacing rates to ventricular arrhythmia, left ventricles from a set of 5 sheep were optically mapped during increasingly shortened coupling intervals of pacing (S1S2S3S4 protocol). Following a stimulus train of ten beats (S1) at a frequency of 1.5 Hz, short coupled pulses were delivered just above the effective refractory period (ERP), with a precision of 5 ms. The ERP was determined by testing stimulation responses of tissue at decreasing coupling intervals starting from the interval of the preceding stimulation pulse. Therefore, S2 responses were tested for the following intervals (ms): 667, 600, 500, 450, 430, 410, 400, 390, . . ., decreasing by 10 ms until loss of capture. Intervals would then be stepped up 5 ms at a time until capture was reestablished. The pacing regime was continued, until a maximum S4 short-coupled stimuli and either ventricular fibrillation was initiated or a loss of capture.

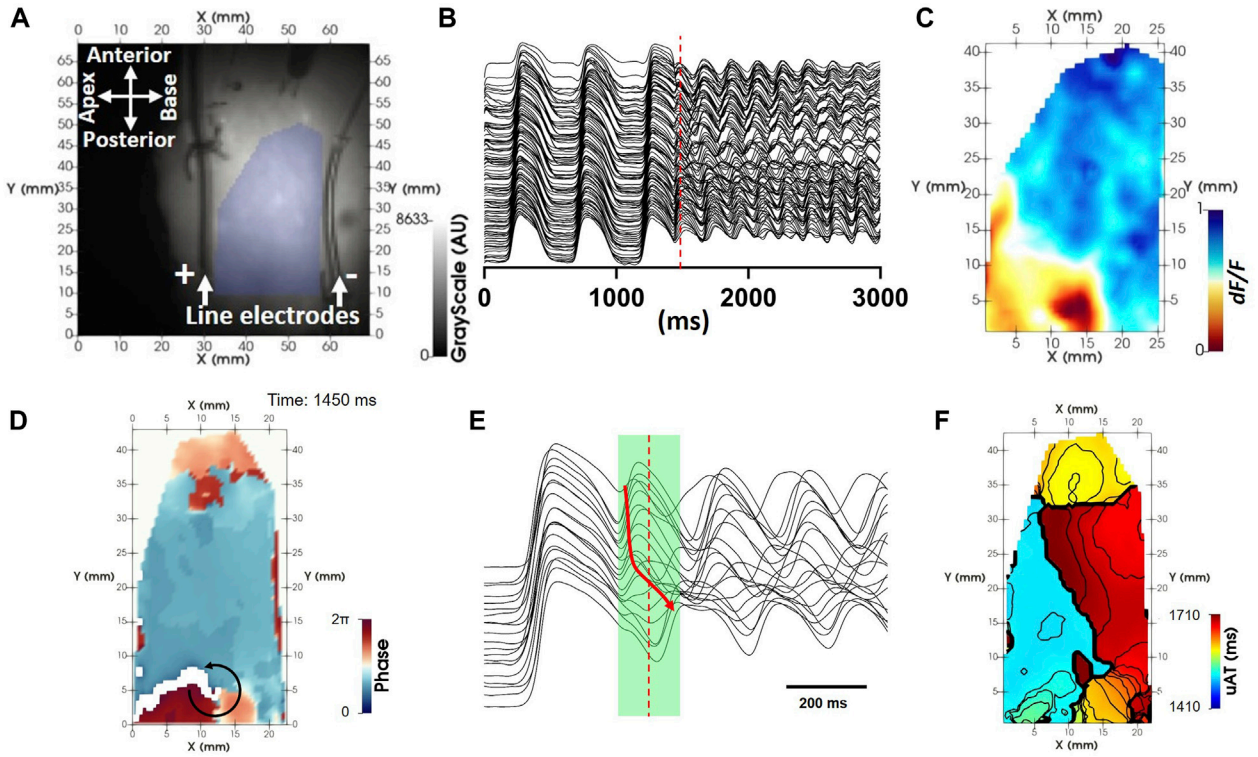

FIGURE 1
uAT mapping extracted from a fixed time window during reentry. **(A)** Background optical mapping image of the endocardial surface from a coronary-perfused right ventricle. The region of interest lying in between two line electrodes for reentry induction is highlighted by blue shading. **(B)** Example pre-processed optical mapping signals extracted from the full region of interest. **(C)** A snapshot of the dynamic voltage-dependent optical signal (*F/dF*) during reentry [time indicated by the red dashed line in **(B)**]. **(D)** An instantaneous phase map derived using the Hilbert transform showing evidence for a repetitive propagating wave front [red dashed line in **(B)**]. **(E)** Example pre-processed optical mapping signals extracted from pixels along the circular black arrow in **(D)**. A green shaded region indicates a uniform time window used to derive uAT points using the uniform window method for calculation of activation time. The red arrow shows the principle sequence of activation. **(F)** uAT map corresponding to the fixed time window shown in B during reentry. Isolines are spaced 10 ms.

2.6 Signal processing methods

All pre-conditioning and post-processing procedures were performed using custom-built software developed in our lab using the programming environment PV wave. Each specific processing and analytical procedure described below is detailed using universal pseudocode in the Supplementary Material.

2.7 Pre-conditioning of optical mapping signals

We consider optical mapping data as a time-series containing T image matrices, each with dimensions *X*, *Y*. Prior to initiating the analysis pipeline described herein, all voltage-sensitive fluorescent signals (F) first underwent filtering using a forwards-backwards butterworth digital filter with a low-pass cut-off at 60 Hz, spatial averaging using a 3 × 3 pixel uniform average filter and a 3-frame uniform running-average temporal filter. Signals were inverted and the magnitude of fluorescent changes normalized from 0 to 1 in each pixel (Figure 1C). A region of interest (Figure 1A) was defined for each experiment to identify foreground pixels and exclude background pixels containing noise (set to zero).

The tachyarrhythmia induced by cross-field shock-on-T example (Figure 1B) is used to illustrate the signal processing pipeline proposed herein. Phase mapping of the tachyarrhythmia showed a circuitous activation pattern (Figure 1D; Supplementary Video S1), which appeared to repeat over several consecutive APs (Figure 1E). ATs were sought from optical mapping signals during the arrhythmic episode using a uniform time window across all pixels (green shaded region in Figure 1E) for comparison with the proposed novel approach. ATs derived from a uniform window, uAT, failed to recapitulate a circuitous activation sequence (Figure 1F). The uniform time window was manually validated to incorporate the beginning of the earliest AP upstroke and the end (peak) of the latest upstroke during a single reentrant cycle.

2.8 Novel post-processing pipeline for analysis of complex optical mapping signals

The proposed method herein is a novel framework for AT-based processing and analysis of complex signals. The comprehensive pipeline is summarized in Figure 2 in to three main sections: 1) Deriving AT; 2) Associating AT points to common wave fronts and 3) classification and quantification of electrical behavior.

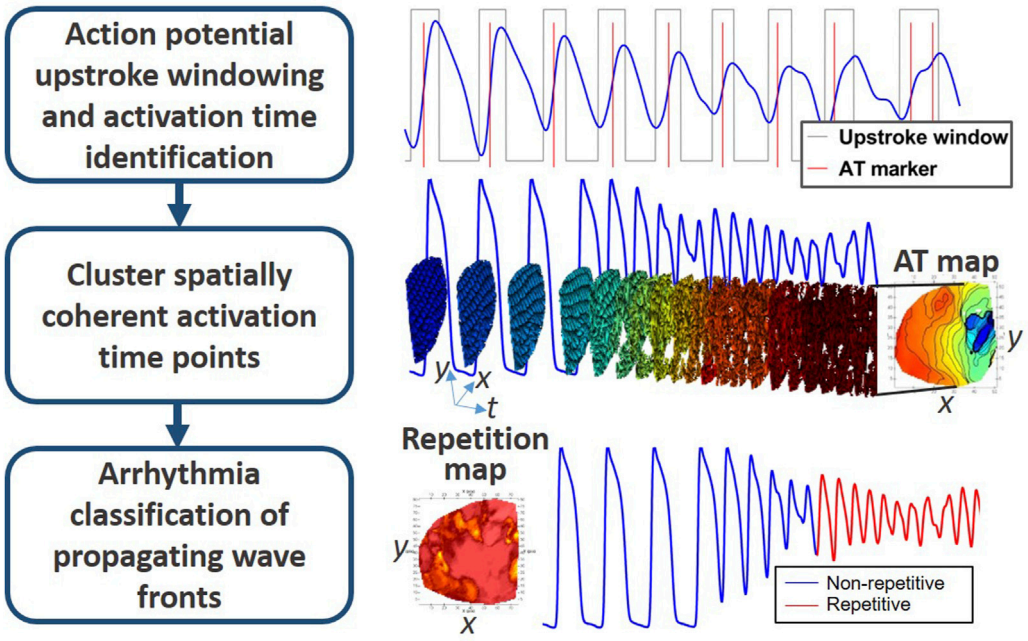

FIGURE 2
Schematic workflow of the novel pAT mapping framework.

2.8.1 Deriving AT

2.8.1.1 Pixel-independent optical action potential upstroke windowing

Time windows centered on action potential upstrokes were sought in a non-uniform, pixel-independent manner. All signals were temporarily mean-subtracted for computation of phase (φ) using a Hilbert Transform, with a negative phase-shift of 90°. Considering φ ranges from 0 to 2 π, taking $\varphi>\pi$, provided positive deflections of φ coinciding with, and encompassing action potential upstrokes from an experimental recording (Figure 3A) and a simulation of myocardial reentry (Figure 3B). Deriving φ using the Hilbert Transform is robust for periodic signals but fails when signals are non-periodic. Therefore, phase computation was applied to signal segments (Supplementary Figure S1). Further splitting of segments and phase computation was applied iteratively until segments reached a minimum duration of 128 ms. The resultant phase of the full-length signal was determined by assigning a value of 2π at all instances where $\varphi>\pi$ was observed in any corresponding segments. To avoid overpopulation of false positive phase detection, a second filtering step was applied. Windows where $\varphi = 2\pi$ were rejected if the corresponding optical signals showed linear regression ≤0 or a maximal derivative below a predefined derivative threshold ($\theta(dF/dt)$), defined either manually, or through automation (Section 2.8.1.2 Automated definition of a signal derivative threshold for AT). The time of maximal derivative of fluorescent signals during each phase-derived upstroke window defined AT using the novel method (pAT).

2.8.1.2 Automated definition of a signal derivative threshold for AT

Derivatives of optical mapping signals are highly susceptible to influences by noise. Thus a minimum, $\theta_{dF/dt}$ (>0) should be assigned to increase the probability of detecting true depolarizing events. Either a user-defined threshold can be employed based on the impact of background noise or alternatively, we propose an automated approach that approximates a single derivative threshold value that can be applied across all unmasked pixels and upstroke windows. The maximal derivative for each phase-derived time window from each pixel were identified. To reduce the influence of noise, outliers of maximum derivative values were removed using the False Discovery Rate method (Motulsky and Brown, 2006), where $\theta'_{dF/dt}$ equals the maximum desired false discovery rate of 1%.

2.8.1.3 Defining AT

The fundamental approach of defining pAT by the maximal derivative is the same as described for conventional methods (Walton et al., 2012), however we apply two additional constraints. These are: 1) That ATs are sought on a pixel-independent and upstroke window-independent basis and 2) Upstroke morphology is evaluated to identify a maximum of two AT points per upstroke. For the latter, Upstroke morphology was characterized from derivative profiles of the upstroke signal. The two largest first-order derivative maxima exceeding $\theta'_{dF/dt}$ were considered potential AT points (Figures 3A, B). If two potential AT points were detected, the signal derivative was further evaluated to determine of the derivative maxima are attributed to the same or separate depolarization events. The valley depth of the signal derivative between the two largest derivative maxima was measured relative to the amplitude of the smaller of the two maxima. The current study assumed a minimum valley depth of 75% to consider the upstroke morphology to be the result of two independent activation events (Fedorov et al., 2010). Otherwise, only the time of the largest derivative maxima was determined to be a pAT.

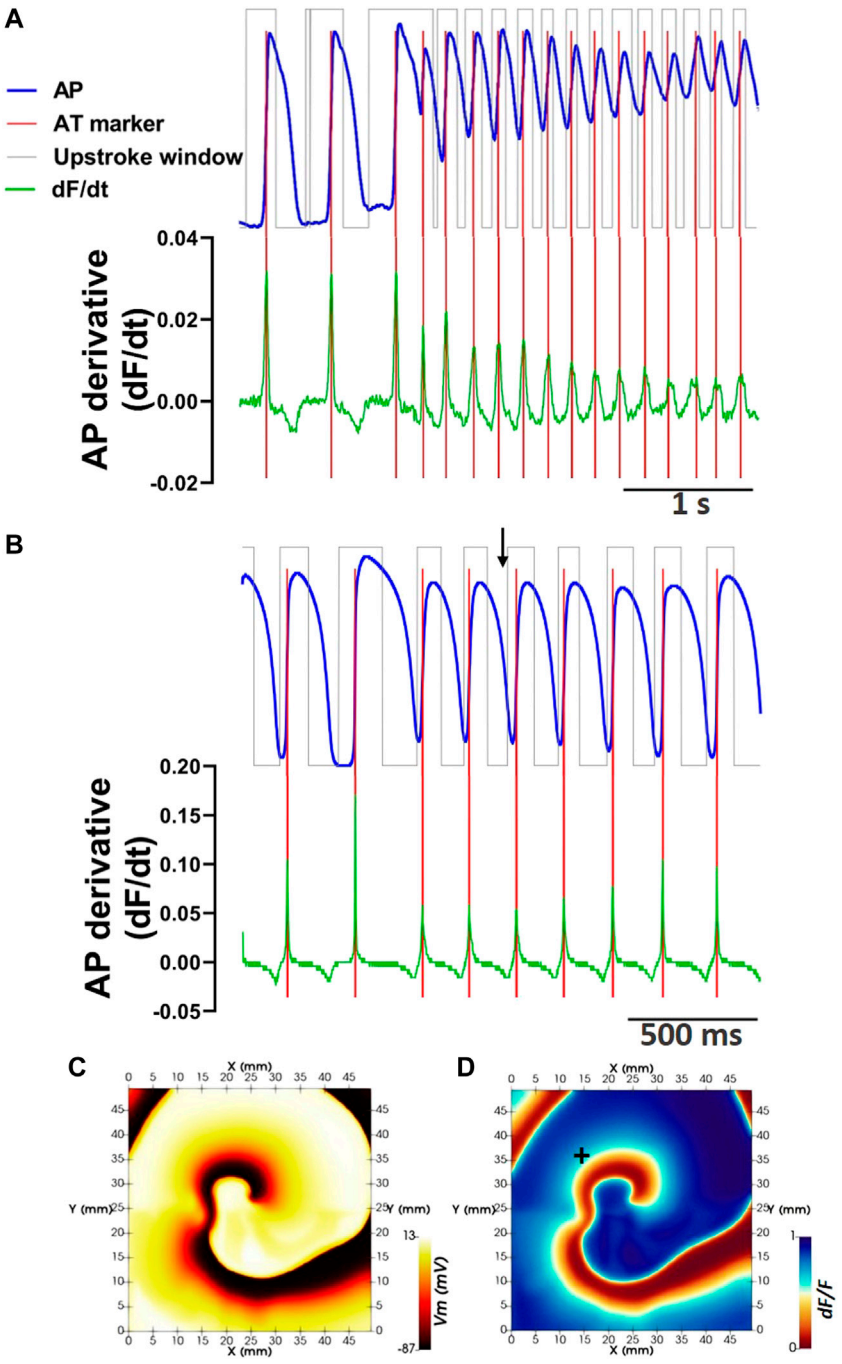

FIGURE 3
Defining phase window-independent upstroke morphology and pAT using the signal derivative. **(A)** Extraction of the pre-processed optical action potential signal during reentry from pixel coordinate (20,10). Corresponding phase windows of pAT are superimposed. The derivative of the corresponding signal is shown. Pronounced derivative peaks falling within phase windows indicate pAT (red lines). **(B)** Similarly, an optical action potential signal and corresponding derivative extracted from an *in silico* model of reentry. **(C)** Membrane voltage (*Vm*) map extracted from the epicardial surface of the electrical *in silico* model at the time indicated by a black arrow in **(B)**. **(D)** Corresponding *F/dF* computed from the *in silico* model. In silico optical signal in B extracted from pixel indicated by +.

To store and manipulate pAT values, a new pAT matrix with dimensions *X*,*Y*,*T* was considered. For each pixel and upstroke window pAT values were soughtafter as described above and the pAT matrix was updated in the corresponding pixel (*x*,*y*) and frame corresponding to pAT, *t*, with a value of 1.

2.8.2 Associating pAT points to common wave fronts

Wave fronts were identified by grouping spatially and temporally associated pAT points in the pAT matrix using an adapted connected components algorithm. A wave front was defined as a single object composed of all propagating fronts

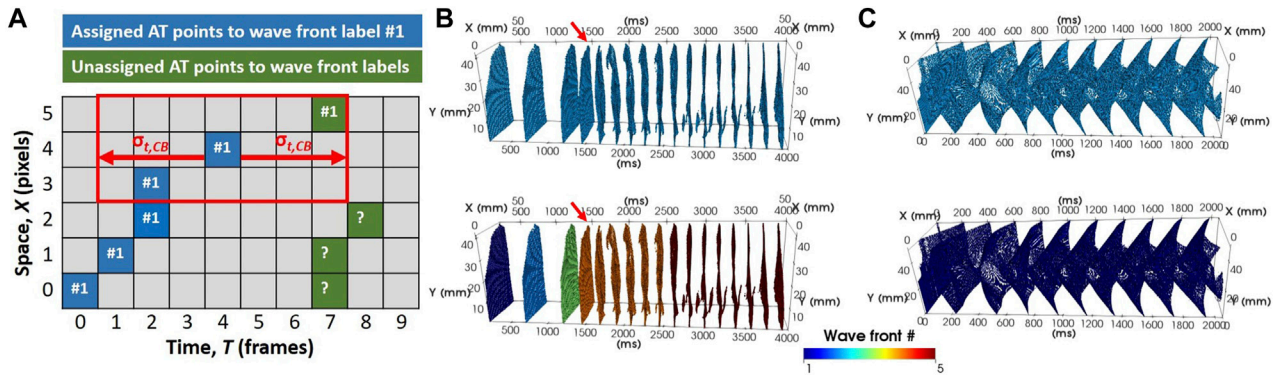

FIGURE 4
Adapted connected components algorithm for wave front clustering. **(A)** A schematic diagram illustrates pAT points on a space-time plot. In the example, wave front label assignment has been made for all pAT points in the first 4 frames to label #1. Let the current pAT point be evaluated for connectivity be at pixel 4, frame 4 on the space-time plot. The red box illustrates the space-time bounds of eligible connectivity. In this case, the currently unassigned pAT point at pixel 5, frame 7 lies within the connectivity boundary and will be assigned to wave front label #1. **(B)** A spatio-temporal distribution of pAT points for the first 4 s of pacing and reentry induction in experiments (upper panel). pAT points are assigned colors based on their wave front label assignment (lower panel). **(C)** Similarly, pAT points of the *in silico* model from the moment of reentry induction (upper panel) and wave front label assignment (lower panel).

that spatially and temporally converge. With this definition, a single wave front therefore may originate from multiple source locations. Connectivity within the pAT matrix is assessed by iterating through pAT points. Connectivity in the spatial domain only considered the immediate neighboring pixels in an 8-point neighborhood. However, wave front propagation from one pixel to its neighbor can be susceptible to conduction delays far exceeding a single time frame (Figure 4A). This required determining the maximum pAT gradient that could be considered as slowed but successful impulse propagation versus conduction block. A threshold of the delay defining conduction block ($\theta_{t,CB}$) may be a user-defined parameter, based on known literature of the species and conditions applied. However, we propose an alternative method to compute $\theta_{t,CB}$ automatically based on real experimental conditions and individual behavior of the tissue. First we describe how $\theta_{t,CB}$ is obtained automatically, followed by the procedure to derive adaptive connected component labels of individual wave fronts.

2.8.2.1 Automated definition of the conduction block parameter

The automated conduction block parameter is defined using an experiment-specific reference acquisition during progressively shortened stimuli (Section 2.5 Pacing protocols). An automated conduction block parameter, $\theta_{t,CB}$, assesses local conduction delays in an 8-point neighborhood. The parameter $\theta_{t,CB}$ was defined as the maximum conduction delay (to the nearest 1 ms) observed with a number of occurrences equal to the number of short-coupled stimuli applied (i.e., for a S1S2S3S4 stimulation protocol, $\theta_{t,CB}$ was defined as the largest common activation gradient observed between four pixel pairs during all stimuli.

2.8.2.2 Connected components labelling of wave fronts

A connected components labelling scheme was applied to the pAT matrix (Figure 4). The following iterative procedure was applied incrementally (looping fastest through *X*, then *Y*, then *T*) across all detected pAT points.

1) Assign label value 1 to the element corresponding to the first indexed pAT point.
2) Let the current pAT point be found at (*x*, *y*, *t*). Evaluate connectivity with adjacent unlabeled pAT points in a local 8-point spatial neighborhood and over the time interval extending from t–$\theta_{t,CB}$ to t + $\theta_{t,CB}$. In the absence of unassigned pAT points, go directly to (3). If pAT points not yet assigned a label exist, assign the same label value as *pAT* (*x,y,t*), and add the neighboring pAT point coordinates for matrix *X,Y,T* as the first elements in a queue; then go to (3).
3) Remove the original indexed pAT element from the queue and repeat (2) until there are no more elements in the queue. Go to (4).
4) Increment label by 1. By looping fastest through *X*, then *Y*, then *T* to the next unassigned pAT point of the pAT matrix; then go to (2).

2.8.3 Characterisation and classification of electrical behavior

2.8.3.1 Mapping wave front pAT

Each wave front identified by their unique label number was assessed independently for activation and repolarization distribution characteristics. Activation time maps of dimensions X,Y were derived for individual wave fronts. Iterating through each pixel, the earliest pAT point with the corresponding wave front label was plotted on the wave front label AT map. In cases where biphasic upstroke morphologies identified a second short-coupled pAT point (Section 2.8.1.3 Defining pAT), a second wave front label AT map was created to conserve information regarding local disassociated conduction patterns.

2.8.3.2 Mapping wave front repolarization characteristics

Repolarization time (RT) was similarly identified in a pixel- and label-wise manner. From any given pAT, the corresponding optical action potential was evaluated for the signal's recovery from excitation. The RT is measured from a user-defined percentage

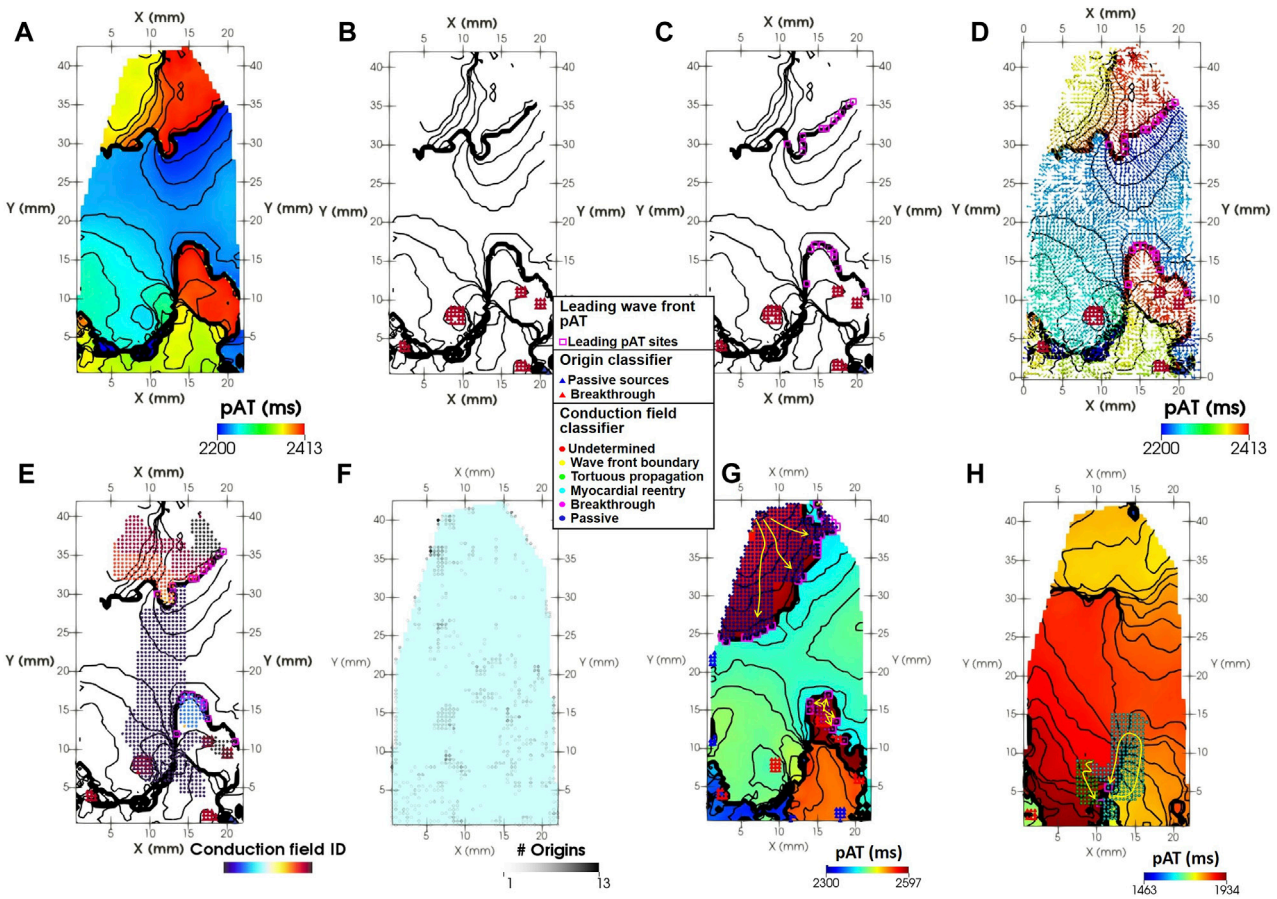

FIGURE 5
Spatial classification of activation sources. **(A)** A dynamic pAT map (left panel). **(B)** Origins of activation for breakthrough (red triangles) and passive (blue triangles) sources. **(C)** Leading pAT points of the active wave front (pink squares). **(D)** Conduction vectors oriented in the direction of local propagation overlaid on **(C)**. **(E)** The conduction fields of leading pAT points. **(F)** Number of accumulated breakthrough or passive origins throughout wave front #4. **(G)** A pAT map shows leading wave front pAT sites (purple squares) with conduction fields emanating from a single breakthrough (red triangles) and passively from outside of the imaged field of view. **(H)** The leading wave front during tachyarrhythmia was also maintained by reentrant propagation through myocardial pathways or regions of tortuous propagation. Yellow arrows indicate the local direction of propagation.

drop in signal amplitude from the action potential peak (for example, 80% of repolarization). The time window to search for RT was constrained to APD limits (*APD*'min and *APD*'max) measured from the earliest pAT of the corresponding action potential. Provisionally, limits used were user-selected for suitability to the species, state and experimental conditions implemented. However, for any individual wave front, a second set of minimum and maximum action potential duration limits (APD"min and *APD*"max) were established for the n^{th} pAT. Universal psuedocode is provided in the supplemental materials detailing *APD*"min and *APD*"max definitions. Within the refined APD limits the RT was determined based on the normalized signal amplitude of the full analyzed time window. It should be noted however that baseline elevation is a common occurrence when electrical activity becomes increasingly dyssynchronous at a local level. Therefore, signals during episodes of ventricular fibrillation, and particularly those capturing a transition from stable rhythm to fibrillatory behavior may not necessarily repolarize to the same baseline as signals during non-arrhythmic events. Therefore signals during arrhythmia initiation may have dynamic baselines, rendering the true level of repolarization challenging to define. For such cases, an alternative definition of RT is proposed based on the time of minimum signal derivative (Salama et al., 1989; Salama et al., 1994). Similar to pAT, RTs for each wave front were projected to maps *RT* [*X*,*Y*]. Corresponding APD maps were subsequently derived by subtracting pAT from the RT of corresponding pixels.

2.8.3.3 Classification of repetitive and non-repetitive wave fronts

Wave fronts were assessed for repeated excitation of the same regions of tissue over two or more cycles and wave front labels were classified as either repetitive or non-repetitive, accordingly. Firstly, each pixel of a given wave front was assessed for incidences of pAT repetition. If a majority of pixels for a given wave front had repetitiveness of pAT points, then this wave front was designated with a repetition classification. This classification scheme imposed the following criteria: A minimum cycle length between repetitive excitation events, defined by *ERPmin*, was necessary to identify as persistent behavior. *ERPmin* was defined as the shortest pacing interval during reference recordings using S1S2S3S4 stimulation where available. Otherwise, *ERPmin* was defined manually based on experience with the relevant species and disease state. If the majority of pAT points do not show repetition, impulse propagation events were assumed to self-

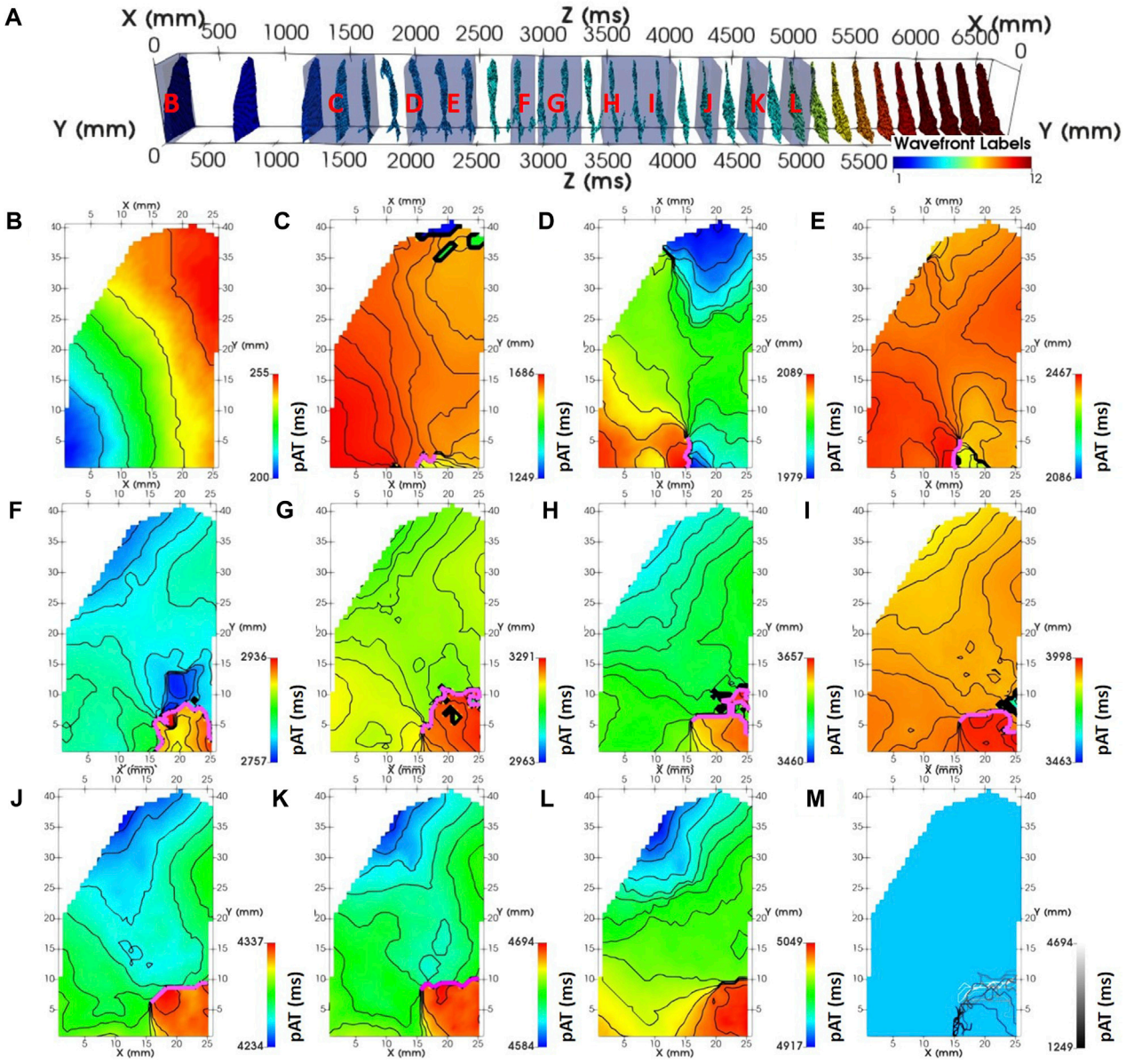

FIGURE 6
Dynamic mapping of experimental complex activity. **(A)** A spatio-temporal distribution of pAT points spanning pacing, induction and reentry phases of the experimental optical acquisition. pAT maps were dynamically probed for wave front labels (#): 1 **(B)**, 3 **(C)**, 5 **(D–F)**, 6 **(G–K)**, and 7 **(L)**. Lines of conduction slowing where the direction of maximal gradient exceedes 50 ms are annotated (pink lines). pAT windows are labelled in panel **(A)** (red). **(M)** Lines of conduction slowing superimposed. Lines are colored according to their average AT.

terminate without re-excitation and the wave front was classified as non-repetitive. It should be noted that classification at this stage does not distinguish classical reentry from macroreentry, for example. Similarly, there is no inference of the source of the identified non-repetitive activity, which may have single or multiple origins, or be driven by sinus rhythm/pacing/automaticity/etc., A detailed description in the form of pseudocode for the implementation of the reentry classification procedure can be found in the Supplementary Material.

2.8.3.4 Identifying origins of activation

Origins of activation presenting as sites of breakthrough on the imaged surface were evaluated throughout the full duration of each wave front label. Provisionally, pAT origins were found by assessing the spatio-temporal distributions of pAT minima (Supplementary Figure S3 for an example). Local pAT minima were determined as sites absent of preceding pAT points during an interval of *ERPmin* within the local 8 point neighborhood. However, considering pAT minima within a local neighborhood did not discriminate between multiple equivalent pAT points with a common origin such as when broad regions of tissue are activated simultaneously. These manifest either as a true breakthrough event or as false-positives due to continuity of propagation from a source peripheral to the region. Therefore false positive pAT origins were assessed using a connected components analysis to spatially group pAT minima points. Any of the points from the same pAT cluster

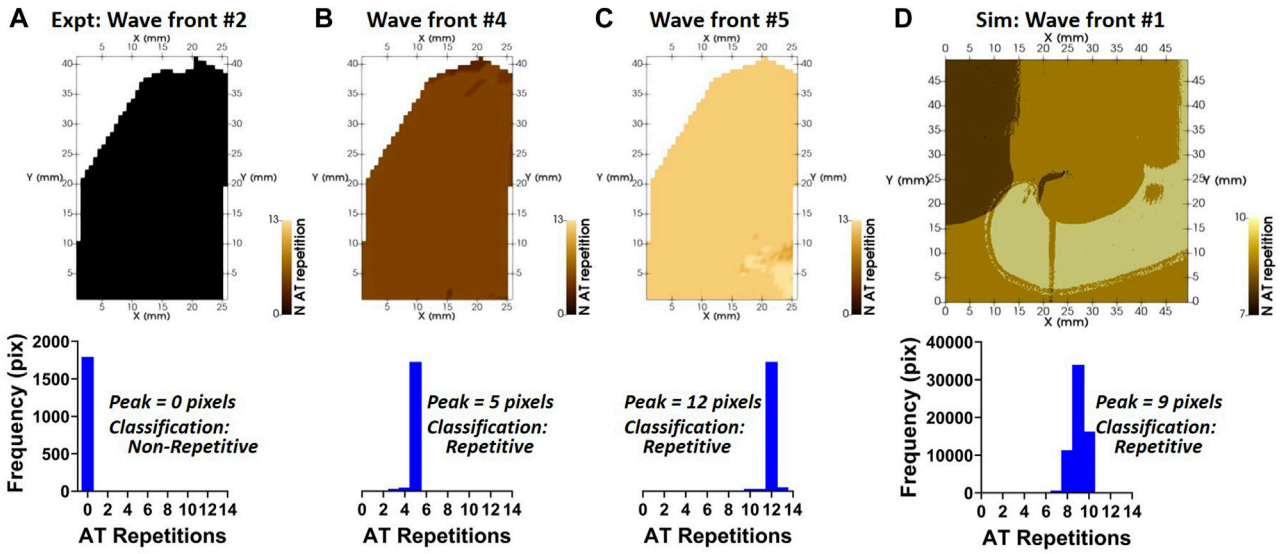

FIGURE 7
Repetitive/non-repetitive classification of wave fronts. **(A—D)** Wave fronts shown in Figure 5 were classified as repetitive or non-repetitive. The spatial distribution of the number of repetitions of activation for each wave front (upper panels) and their histograms (lower panels) are shown. Labels were classified as repetitive if the histogram peak of activation repetitions was ≥1.

with preceding pATs in the ERPmin interval and across an 8-point neighborhood would identify the whole pAT cluster as a false positive breakthrough sites.

Maps counting the occurrence of origins with dimensions [X,Y] were generated for each wave front such that $Origin_{x,y} = Origin_{x,y} + 1$. Complementary maps of the same dimensions were generated to show the location of the breakthrough center. The centeral pixel of origin pAT clusters were identified by averaging all horizontal and all vertical components of pAT point coordinates in each cluster to define mean focal origins.

2.8.3.5 Dynamically probing complex activation and repolarization sequences

Thus far, we have shown how to compute and visualize activation and repolarization sequences for individual labels. However, we should consider that activation or repolarization events can occur simultaneously for different wave fronts located in distinct regions. Moreover, we only map the earliest pAT points for each wave front, ignoring re-excitation in repetitive wave front labels. Therefore, a single pAT map per wave front does not allow understanding of the interactions between wave fronts or transitions to persistent reentrant behavior. Moreover, a single AT map is not compatible with reentrant activity, which inherently has strong overlap of the activation sequence between cycles, particularly when wave fronts are out of phase and discordant. Thus, a dynamic method was developed to interrogate and visualize the ensemble spatial components in a stack of maps, each covering sub-windows of time for activation or repolarization sequences. Firstly, an image stack of dynamic maps with dimensions [X,Y] were generated based on the following steps: The first map was constructed by mapping the earliest time points (using the desired pAT or RT matrix). From the earliest time point, advancing in time through the matrix, the rest of the map was filled with time points until the first instance where the map already contained a time point. A new map was initialized firstly by populating the map with all values from the previous map. Then the time of the next matrix time points were found and replaced the values in the corresponding pixel of the new map. A new map was again initialized with the previous map values and the same procedure repeated until the full time window of interest of the time point matrix was mapped.

2.8.3.6 Dynamic classification of activation sources of the leading wave front

Thus far, wave front labels have been broadly classified by their repetitive or non-repetitive sequences. But this is insufficient to understand the mechanisms underlying the arrhythmic event, such as myocardial reentry, macroreentry or short-coupled fast focal behavior, for example. Moreover, tachyarrhythmia are often unstable and evolving. Therefore a second detailed classification scheme is proposed to assess spatially and temporally the underlying source of activation for each pAT. In other words, which conduction source drove local propagation? Potential sources of conduction included: Passive activation from outside of the field of view; a breakthrough site on the imaged surface; a myocardial reentrant source; sources emanating from sites of discontinuous (tortuous) propagation and sources emanating from a wave front boundary.

Each pAT was individually classified by activation source in dynamic pAT maps (Figure 5A). Prior to classification, we identified if origins of activation (see Section 2.8.3.4 Identifying origins of activation) reflect breakthrough sites or origins of passive activation located at the periphery of the masked region of interest (Figure 5B). Pixels were selected for classification by identifying maximum pAT values along the leading wave front edges (Figure 5C). In addition, as shown in Figure 5D, local vectors of conduction normal to pAT contours were determined across the dynamic map using a finite different method (Cantwell et al., 2015). In order to identify the origin of each pAT value, the full surface area of tissue involved in the activation sequence (conduction field) leading directly to each maximum pAT site were identified as follows:

1) The first pAT from the leading wave front, found at (x,y,t) was annotated with a unique conduction field label.
2) Evaluate connectivity with adjacent unlabeled pAT points in a local 8-point spatial neighborhood. Neighboring pAT values within the time interval extending from $t-\theta_{t,CB}$ to t were considered. In the absence of eligible pAT neighbors, go directly to (3). Eligible pAT points were evaluated for conduction vectors intersecting pAT (x,y,t). Unlabelled intersecting pAT pixels were assigned the same conduction field label value as pAT (x,y,t) and the neighboring pAT point coordinates for matrix X,Y,T were added as the first elements in a queue; then go to (3).
3) Remove the last pAT coordinates from the queue and repeat (2) until there are no more elements in the queue. Repeat from (1) for the next leading wave front pAT value.

A classification scheme determined the origins of each identified conduction field driving the leading wave front pAT sites (Figure 5E). Evaluating each pAT point in conduction field, identify pAT points matching the following criteria for each class.

1) Breakthrough: One or more pAT points co-localize with one or more breakthrough activation origins (Figures 5F, G).
2) Passive: One or more pAT points co-localize with one or more passive activation origins (Figures 5F, G).
3) Myocardial reentry: Any number of conduction field pAT points with neighboring pAT points of the same conduction field with differences in pAT values > ERPmin (Figure 5H).
4) Tortuous propagation: One or more conduction field pAT points with neighbors within the time interval extending from $t-\theta_{t,CB}$ to t, but absent of intersecting conduction vectors (Figure 5H).
5) Wave front boundary: One or more conduction field pAT points absent of intersecting conduction field neighbors and neighboring pAT points from a different wave front label.

2.9 Statistical analyses

The performance and robustness of the signal processing pipeline was evaluated by varying the signal-to-noise ratio (SNR) of optical mapping recordings during tachyarrhythmia induction (N = 5, see Supplementary Figures S4–S8 for examples at baseline conditions). Non-parametric analyses of variance Friedman tests were used to identify statistical differences of signal characteristics and signal processing outputs across SNR populations. A multiple comparison assessment was also performed to compare results for individual SNR populations versus the baseline SNR population (established using a cut-off of 60Hz for a butterworth lowpass filter). Spatial correlations by pixel-to-pixel linear regression analyses were used for simulation data to compare eAT with uAT and pAT maps. Statistical differences of linear regression values between uAT and pAT performance was evaluated using the paired t-test. For all tests, statistical significance was determined when $p < 0.05$.

3 Results

3.1 AT mapping

Figure 4B showed that the pAT matrix derived from the experimental example was composed of distinct wave front labels with the conduction block parameter set to 76 ms. The experimental example acquisition of tachyarrythmia analyzed was 6,700 ms. The analysed arrhythmic episode was 5,211 ms in length, 14 out of 28 beats were classified as repetitive activity. Mean cycle lengths were 186 ms. Image stacks of pAT maps incrementing through the pAT matrix from the experimental example recording enabled dynamic visualization of the full activation sequence (Supplementary Video S1). Figure 6 shows extracts of pAT maps from the image stack and the corresponding time windows (Figure 6A). Figure 6B shows the pAT map for wave font #1 during steady-state pacing prior to the induction of reentry. Total pAT across the region of interest was 56 ms and composed of a regular near-planar wave front that propagated unperturbed from the lower left to upper right of the pAT map. A sub-region of pAT points from wave front #4, approximately 200 ms after the shock were projected on to a pAT map (Figure 6C). In contrast to uAT mapping (Figure 1F) pAT found a preferential activation of the lower left region of the map, coinciding with the region of early activation during basal pacing. The wave front subsequently propagated in a counter clockwise movement with a maximal local pAT gradient of 75 ms/mm observed between neighboring pixels and where pAT contours converged to a single site at the core of the circular movement. Over 20 arrhythmic cycle lengths, every second cycle of the arrhythmic episode was plotted as pAT maps (Figures 6D–6L), until a distinct near-planar wave front was observed (Figure 6L). The AT sequence was consistently characterized by a counter clockwise rotation. It was observed that each reentrant cycle was accompanied by a region of local pAT gradients >50 ms/mm, indicating conduction slowing. The locally enhanced pAT gradient was primarily vertically orientated at the bottom of the pAT map during wave front #4 (Figures 6C–E), but shifted towards the right border of the pAT map coincided with the transition to wave front #5 (Figure 6M).

3.2 Origins of activation

In an additional experimental preparation, the ventricular wedge from sheep was paced at a frequency of 6 Hz (Supplementary Figure S3). pAT minima were identified for each wave front label (Supplementary Figure S3). The activation sequence globally propagated from a single region of the myocardial surface from left to right (Supplementary Figure S3B). Yet the earliest pAT region was shared between two sites (Supplementary Figure S3C). These coincided with two electrodes used for bipolar stimulation. However, two sites of origin distal to the stimulation location were also observed. Initial computation revealed pAT origin clusters, indicating simultaneous activation of areas exceeding a single pixel (Supplementary Figure S3D). Supplementary Figure S2E shows the pAT origin clusters reduced to the estimated center-most pixel, representing a local single pAT origin site.

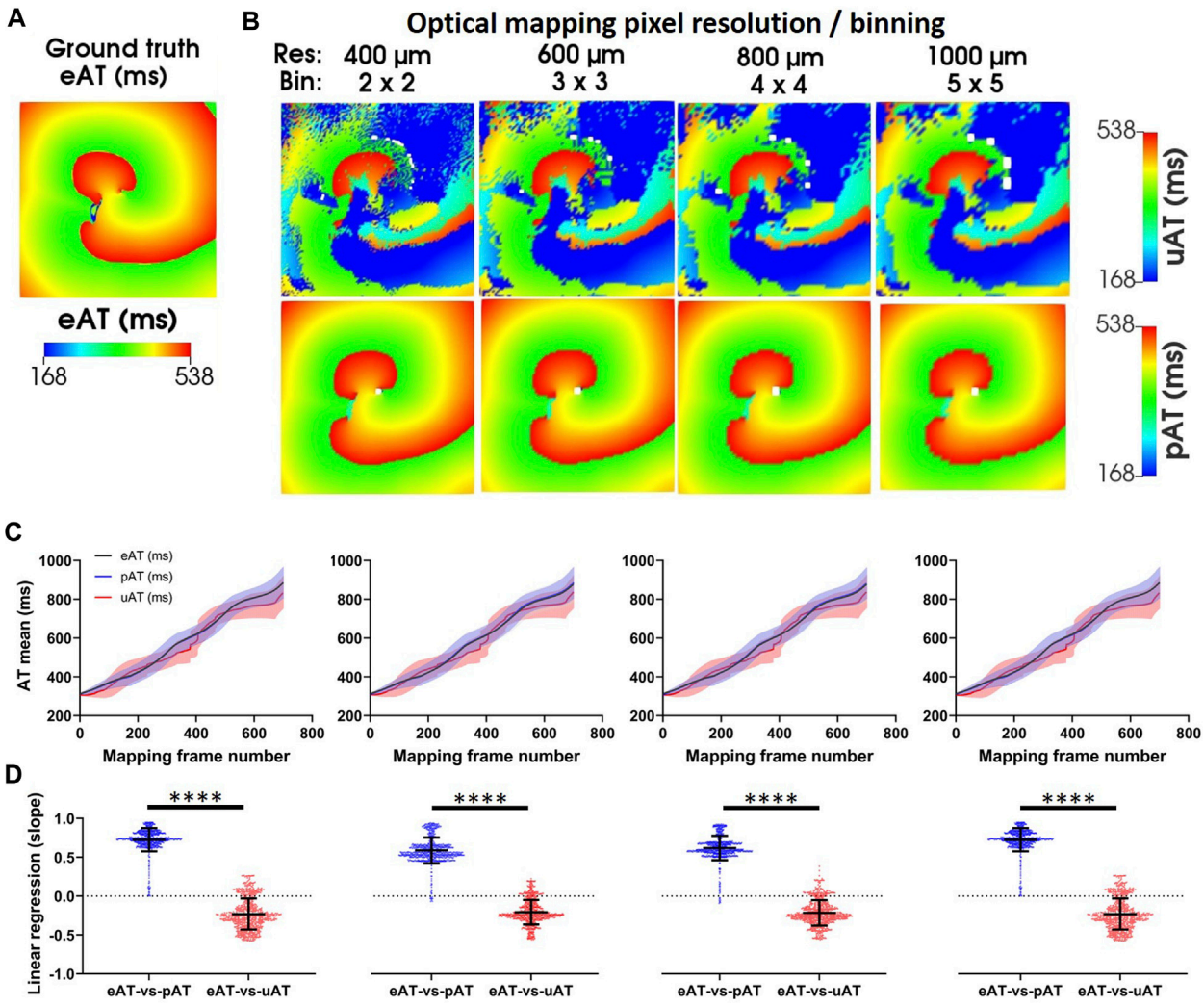

FIGURE 8
Simulations of pAT mapping and image resolution. **(A)** Ground truth eAT derived from a simulation of the underlying electrical action potential. **(B)** Optical mapping signals were derived from electrical simulations in **(A)**. The effects of image resolution evaluated on uAT and pAT derived from optical mapping signals. Optical mapping signals were derived from downsampled electrical simulations to simulate reduction of image resolution from 400 µm to 1,000 µm. **(C)** Mean ± standard deviation eAT, uAT, and pAT from dynamic AT maps of the full simulation. **(D)** Linear regression of pixel-to-pixel correlations of eAT with uAT and pAT.

3.3 Mapping repolarization properties

Supplementary Figure S4A shows pAT values derived from recordings of multiple short-coupled stimuli and ectopic activity at the onset of self-sustained tachyarrhythmia following S1S2S3S4 pacing (see Section 2.5 Pacing protocols). This pacing regime is composed of irregular coupling intervals that gave way to highly varying total pATs ranging from 42 ms (S1) to 334 ms (ectopic beat A). Despite the irregular coupling intervals and total pAT exceeding the shortest coupling interval (S3-S4, 215 ms), RTs could be determined across the imaged field of view (Supplementary Figure S4B). A user-defined window of 80–400 ms following pAT was used to refine repolarization time estimates. Resulting RT gradients (maximum–minimum) ranged from 72 ms (S1) to 424 ms (ectopic beat A). Pixels assigned both pAT and RT values were subsequently used to derive APD (Supplementary Figure S4C).

3.4 Wave front classification

Labelled wave fronts derived from the experimental and simulated acquisitions underwent classification in to repetitive and non-repetitive activation sequences. Figure 7A shows a map and histogram of pAT repetitiveness for wave front #2 of the example experimental recording under basal stimulation. Zero pixels observed repetitive pAT points with intervals exceeding a minimum ERP parameter, which was set to 200 ms. In this case, we did not have recordings of short-coupled stimulation intervals to identify the local ERP. Therefore, a minimum ERP parameter was estimated to equate 80% of the minimum action potential duration (250 ms) during basal stimulation. Wave front #2, was consequently classified as a non-repetitive activation sequence. Wave front #4, which was initiated by the cross-field shock and the activation sequence was maintained for a period of 1,018 ms. Wave front #4 was found to have almost uniform repetitiveness of 5 pAT repetitions across all pixels

(Figure 7B). A dominance of pAT repetition across pixels underlay the classification of wave front #4 as repetitive. Similarly, wave front #5 was classified as repetitive with a predominance of 12 repeated pAT points during a total activation period of 2,297 ms (Figure 7C). Concordantly, a computer model of repetitive behavior was accurately classified as repetitive through computation of the dominant pAT repetitiveness factor (Figure 7D). Local classification of the origin driver provided insight in to the spatial organization of arrhythmia and the temporal evolution underlying transitions between activation sequences, notably from wave front #4 to #5.

In the experimental example, origins of activation were detected following the onset of the tachyarrhythmic episode (wave front #4) both as breakthrough sites and at the periphery of the imaged tissue (Figure 5A). In part, breakthrough sites contributed to the progression of the wave front in the lower portion of the pAT map as observed by overlapping conduction fields with breakthrough sites (Figure 5B). The upper portion of the pAT map was primarily driven by passive impulse propagation emanating from outside of the imaged tissue in the upper left corner. Figure 5C shows that the wave front was also driven by myocardial reentry and tortuous propagation in the regions of slowest conduction. Throughout the full arrhythmic episode, there was a predominance of passively activated wave front (74.1%). This was primarily attributed to propagation extending from the top of the mapped area throughout the recorded arrhythmia episode. However, 22.3% was attributed to breakthrough sites of origin, observed as an important mechanism for maintenance of re-excitation of the lower portion of the map during wave front #4 and #5. To a lesser extent, the tissue was maintained through myocardial reentrant pathways and sites of tortuous propagation.

3.5 Robustness of phase window-derived AT mapping

The core methodology of this processing and analytical pipeline centers on the capacity of pAT mapping to reliably and reproducibly detect AT points in complex dynamic electrical behavior. For comparison to experimental measurements, a repetitive activation sequence was induced in a computational model. A pAT matrix was constructed over the duration of the simulated time window of 2 s (Figure 4C). The activation sequence was established to be a single wave front (#1), indicating a self-sustained arrhythmia. Figure 8A shows an activation map of the underlying electrical action potential (eAT), representing the ground truth activation sequence. A clockwise rotating activation sequence was observed on the eAT map. Figure 8B shows equivalent maps for uAT and pAT at varying image resolutions. Maps of uAT shows a complex and fragmented activation sequence with a total AT (95%–5% AT) of 362 ms, compared to 185 ms for eAT. However, pAT much more closely resembled the spiral activation sequence of the ground truth. Total AT for pAT was 192 ms. Sensitivity of the signal processing pipeline was tested on a series of simulations following down sampling of the ground truth electrical simulation and generation of optical signals with reduced resolution from 400 μm to 1,000 μm. Both uAT and pAT was compared across the down sampled simulated data sets, but there was no impact on the overall activation sequences detected using mapping methods (Figure 8C) and linear regression analysis comparing eAT with uAT and pAT showed consistently significantly higher correlations with eAT than uAT (Figure 8D).

Our signal processing framework relies on robust automated determination of $\theta_{t,CB}$ using a reference recording during S1S2S3S4 stimulation, the separation of pAT points in to coherent wave front labels and the capacity to reliably classify repetitive wave front activity. Table 1 summarizes the experimental parameters for implementation in five cases from left ventricles of sheep. The shortest stimulation interval ranged from 190–260 ms across all cases. Despite this variation, the conduction block parameter remained consistent with a mean (±standard deviation) of 59.2 ± 17.0 ms. Supplementary Figures S5–S9 showed pAT distributions, wave front labelling and pAT maps of each case during the transition from the end of a train of S1 pulses to short-coupled stimulation and to post-stimulation events. Despite broad total pAT events overlapping with stimulation intervals, activation sequences elicited by each stimulation pulse were successfully isolated and grouped in to individual wave fronts for each experimental case. Table 1 shows that signal-to-noise ratios of recordings were progressively reduced from >37.2 to 12.1 to evaluate pAT-sensitivity to noise (Figures 9A, B). Lowering signal-to-noise ratios reduced signal regularity indices significantly when limiting signal filtering to low pass filter cut-off 180 Hz. Concordantly, phase-derive AT window estimation also observed marginal reduction of regularity indices. Despite reduced quality of signals and signal windowing, output parameters were only significantly influenced by noise amplification using lowpass filter cut-offs >180Hz. Decreases in the estimations of $\theta_{t,CB}$ and augmented $\theta"_{dF/dt}$ were observed. Similarly, the number of wave fronts detected, pAT points and breakthrough sites were preserved using filtering cut-off <180Hz (Figure 9C).

3.6 pAT mapping of tachyarrhythmia in chronic myocardial infarction

The endocardial surface of the structurally remodeled was imaged by optical mapping (Figures 10A, B). Figure 10C showed that optical mapping signals were observed within the infarct zone indicating surviving functional myocardium and conduction within the structurally remodeled region, although SNR was reduced (Figure 10D). Nevertheless, a pAT matrix was derived. $\theta_{t,CB}$ was automatically detected as 62 ms and *ERPmin* was 180 ms. These parameters enabled coherent wave front allocation throughout the mapped surface during S1S2S3S4 stimulation and tachyarrhythmia onset (Figure 10E). Planar wave front propagation from the posterior left ventricular free wall induced by S2 (Figure 10F) was followed by passive activation from the anterobasal region (Figure 10G). Simultaneously, impulse propagation from S3 stimulation collided with the passive wave at the infarct zone (Figure 10H). This was followed by apex-to-base propagation in to the posterolateral base (Figure 10I). The excitatory wave front continued to advance to the anterior base and anterior apex (Figure 10J), colliding with an S4-driven impulse. From the late activated apical scar region, the wave front emanated towards the base along a narrow trajectory with an antero-lateral aspect

TABLE 1 Repeated use and robustness of the novel pAT mapping framework in experimental cases. Ventricular arrhythmia was induced in five experiments using an S1S2S34 induction protocol.

Lpf cut-off frequency (Hz)	60	80	100	120	140	160	180	200	220	240	*p*-Value
Stimulation protocol											
Minimum interval of short-coupled S1S2S3S4 stimuli (ms)	224 ± 23.4	224 ± 23.4	224 ± 23.4	224 ± 23.4	224 ± 23.4	224 ± 23.4	224 ± 23.4	224 ± 23.4	224 ± 23.4	224 ± 23.4	NS
Mean signal characteristics											
SNR	>37.2	37.2 ± 6.1	23.1 ± 4.2	18.4 ± 3.7	16.0 ± 3.4	14.6 ± 3.3	13.7 ± 3.2	13.0 ± 3.2*	12.5 ± 3.1**	12.1 ± 3.1***	<0.0001
AP signal Dominant frequency (Hz)	1.7 ± 0.4	1.7 ± 0.4	1.7 ± 0.4	1.7 ± 0.4	1.7 ± 0.4	1.7 ± 0.4	1.7 ± 0.4	1.7 ± 0.4	1.7 ± 0.4	1.7 ± 0.4	NS
AP signal regularity index	0.62 ± 0.09	0.60 ± 0.09	0.60 ± 0.09	0.59 ± 0.09	0.59 ± 0.09	0.59 ± 0.09	0.59 ± 0.09*	0.58 ± 0.09**	0.58 ± 0.09***	0.58 ± 0.09****	<0.0001
pAT characteristics											
pAT window dominant frequency (Hz)	2.2 ± 1.2	2.2 ± 1.2	2.2 ± 1.2	2.2 ± 1.2	2.2 ± 1.2	2.2 ± 1.2	2.2 ± 1.2	2.2 ± 1.2	2.2 ± 1.2	2.2 ± 1.2	NS
pAT window regularity index	0.37 ± 0.12	0.35 ± 0.12	0.35 ± 0.11	0.33 ± 0.12	0.33 ± 0.12	0.32 ± 0.12	0.32 ± 0.12*	0.31 ± 0.12**	0.33 ± 0.16*	0.33 ± 0.15**	0.0004
$\theta^{\circ}_{dF/dt}$	0.00039 ± 0.00013	0.00045 ± 0.00015	0.00049 ± 0.00016	0.00053 ± 0.00018	0.00057 ± 0.00019	0.00060 ± 0.00020	0.00062 ± 0.00021*	0.00064 ± 0.00023**	0.00066 ± 0.00024***	0.00068 ± 0.00024****	<0.0001
$\theta_{t,CB}$ (ms)	59.2 ± 17.0	56.2 ± 14.8	53.6 ± 13.7	54.0 ± 13.9	51.6 ± 12.6	52 ± 12.7	49.6 ± 12.3*	48.8 ± 12.1*	48.4 ± 11.6*	44.4 ± 12.3*	0.0002
N wave fronts	19.8 ± 15.0	17.8 ± 15.3	15.4 ± 13.2	14.2 ± 12.9	15.2 ± 13.9	16.4 ± 13.2	11.2 ± 2.7	13.8 ± 13.2*	16.0 ± 12.9	15.6 ± 13.6	0.0156
N AT points	216,810 ± 179,447	223,596 ± 174,066	230,518 ± 167,108	239,869 ± 160,573	248,019 ± 157,367	257,069 ± 155,073	273,621 ± 152,972	275,621 ± 150,720	284,561 ± 151,429	291,159 ± 151,319**	0.0015
N breakthrough sites	2,461 ± 1899	2,580 ± 1839	2,601 ± 1719	2,657 ± 1701	2,733 ± 1,685	2,758 ± 1,698	2,740 ± 1858	2,980 ± 1901	3,112 ± 1846**	3,222 ± 1832***	0.0004
Wave front repetitiveness											
N Non-sustained wave fronts	17.2 ± 15.7	15.2 ± 16.3	12.6 ± 13.8	12.0 ± 12.6	12.2 ± 13.6	13.8 ± 14.3	8.8 ± 3.3	12.0 ± 13.1	13.6 ± 13.3	13.8 ± 14.4	NS
N sustained wave fronts	3.6 ± 1.5	4.2 ± 1.3	3.6 ± 1.5	4.2 ± 1.9	4.2 ± 1; 3	4.2 ± 1.3	3.2 ± 1.3	3.3 ± 1.2	3.4 ± 1.5	4.4 ± 1.3	NS
Classification of the origins of the local wave front											
Breakthrough (%)	9.7 ± 1.3	10.6 ± 1.4	10.7 ± 1.1	11.2 ± 1.9	10.4 ± 0.8	10.3 ± 0.6	9.9 ± 0.6	10.1 ± 0.5	10.1 ± 0.6	10.2 ± 0.7	NS
Passive (%)	4.3 ± 1.3	4.5 ± 1.4	4.6 ± 1.3	4.8 ± 1.3	4.6 ± 1.1	4.5 ± 1.1	4.5 ± 1.1	4.6 ± 1.2	4.5 ± 1.0	4.5 ± 0.9	NS
Myocardial reentry (%)	0.5 ± 0.5	1.0 ± 1.2	1.5 ± 1.8	1.9 ± 2.3	2.1 ± 2.6	2.4 ± 3.0	2.6 ± 3.3*	3.1 ± 3.8**	3.1 ± 4.0*	3.6 ± 4.0**	0.0001
Tortuous propagation (%)	85.5 ± 2.7	83.8 ± 3.4	83.2 ± 3.5	82.0 ± 4.1	82.9 ± 4.1	82.9 ± 4.1	82.9 ± 4.4	82.2 ± 4.7	82.3 ± 4.4*	81.6 ± 4.2**	0.0157
Wave front boundary (%)	0.018 ± 0.026		0.008 ± 0.012	0.038 ± 0.076	0.008 ± 0.011	0.015 ± 0.018	0.023 ± 0.024	0.02 ± 0.021	0.019 ± 0.027	0.0273 ± 0.035	NS

Data are mean ± standard deviation and $N = 5$ for all cases. Statistical significance was considered if $p < 0.05$. *$p < 0.0332$, **$p < 0.0021$, ***$p < 0.0002$, ****$p < 0.0001$.

10.3389/fphys.2023.734356

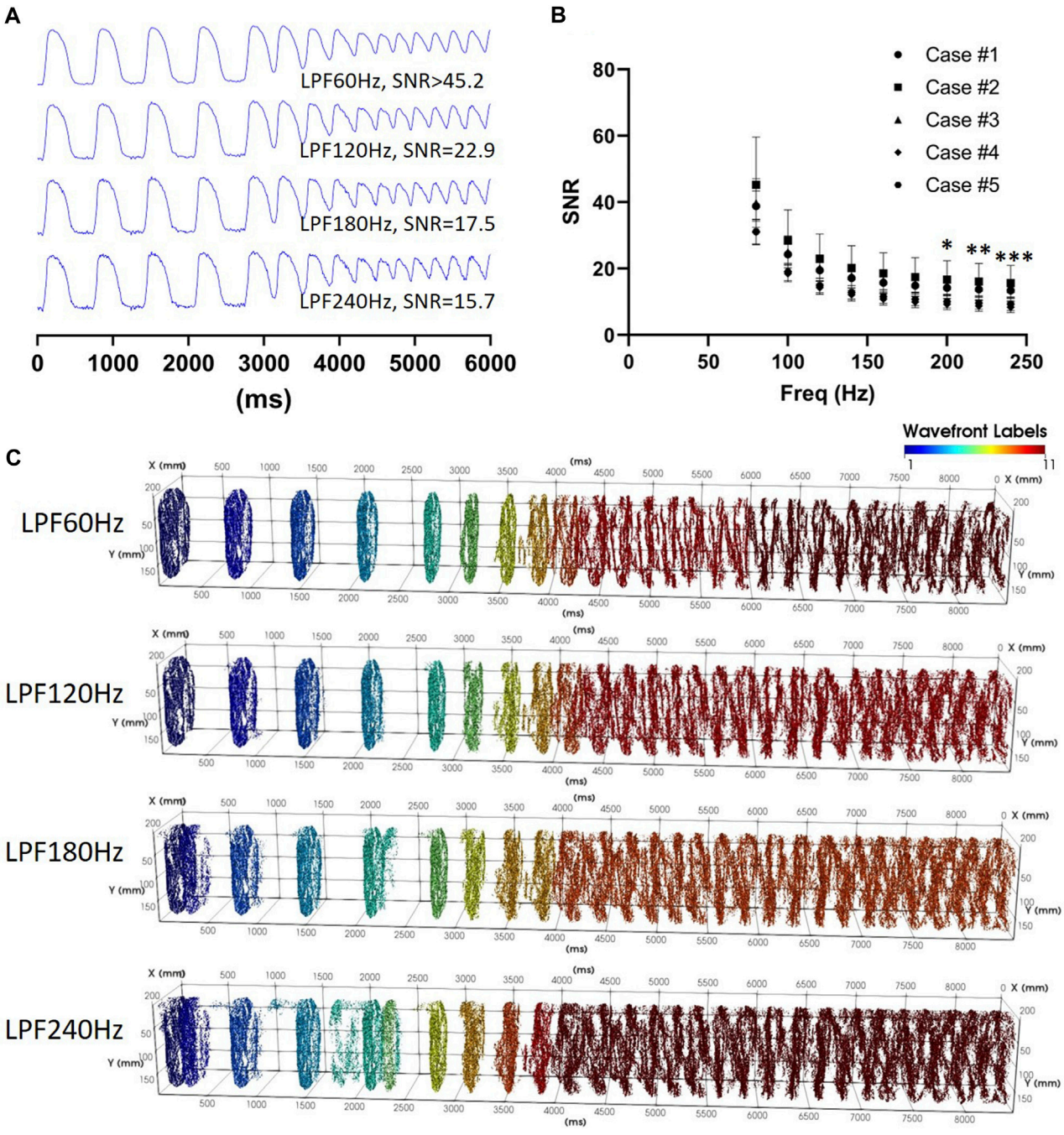

FIGURE 9
Influences of the signal-to-noise ratio. **(A)** Action potential traces with varying lowpass filter cut-off frequencies. **(B)** Mean ± standard deviation signal-to-noise ratios for experimental optical mapping recordings during S1S2S3S4 stimulation and tachyarrhythmia induction (N = 5). **(C)** Spatio-temporal distribution of pAT points corresponding to recordings used in A.

(Figure 10K). The wave front successfully propagated to the base where it diverged towards the posterior and anterior left ventricle (Figure 10L). Figure 10M showed both wave fonts circumventing the lateral left ventricle to again converge at the apical scar region in a figure of eight formation. Interestingly, pAT mapping of the scar tissue region was incomplete in Figure 10H requiring almost 200 ms to maximally activate (Figure 10I). The pAT map could distinguish individual pathways of fast and slow conduction within the structurally remodeled tissue.

4 Discussion

The framework for a novel analytical approach has been developed for AT mapping of complex electrical behavior recorded using optical mapping. A first critical aspect was to accurately probe activation events. For each image pixel, a Hilbert Transform phase analysis revealed the time intervals of action potential upstrokes. In turn, pAT events were elucidated for each upstroke based on signal morphology and slope profile. The spatio-temporal distribution of pAT events were

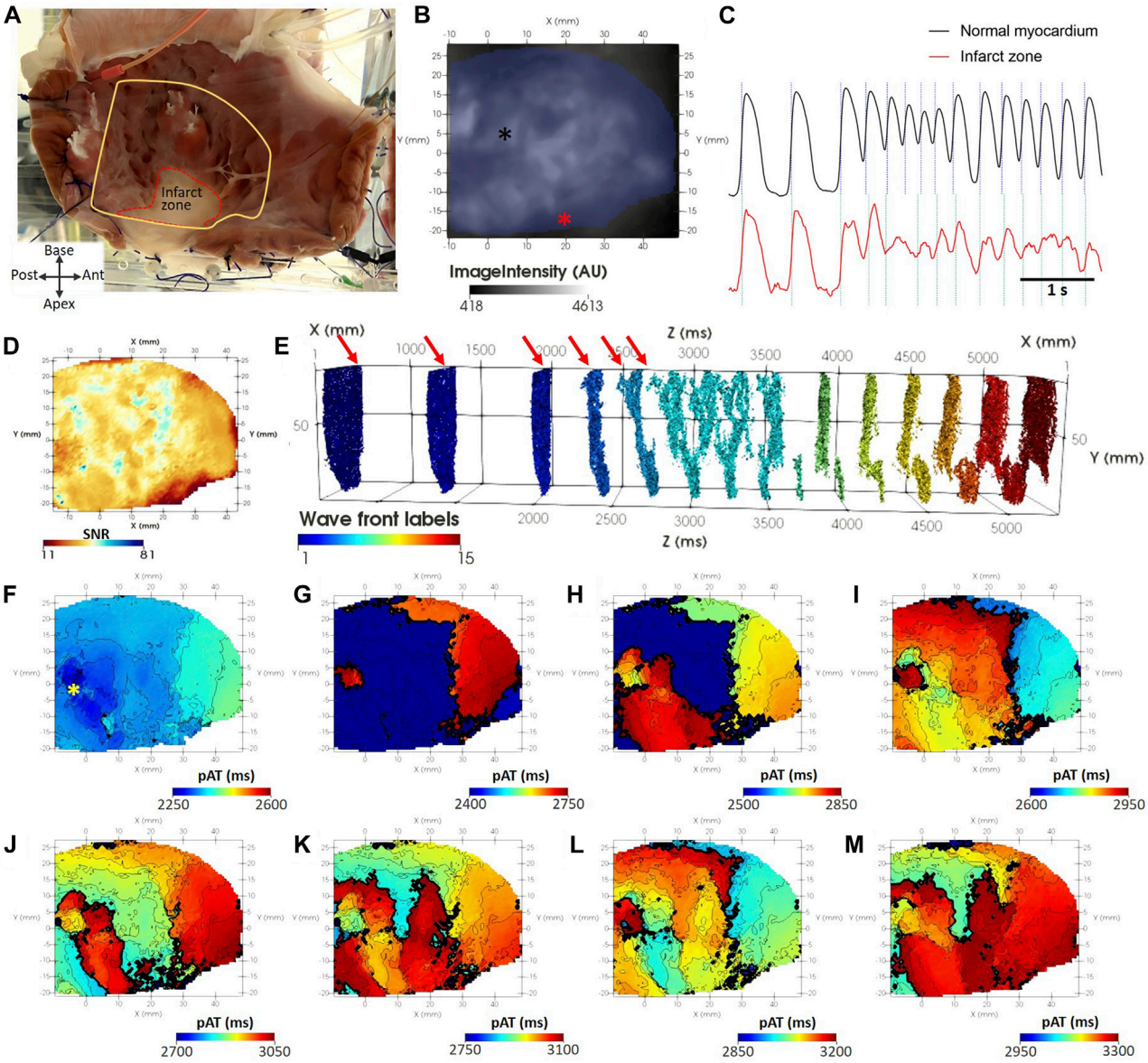

FIGURE 10
pAT mapping tachyarrhythmia in chronic myocardial infarction. **(A)** The endocardial surface was subject to optical mapping, encompassing a region of scar in the ventricular apex. **(B)** Background optical mapping signals. **(C)** Optical mapping traces taken from normal myocardium [black asterisk in **(B)**] and the scar region [red asterisk in **(B)**]. **(D)** Map of SNR from the same optical mapping recording. **(E)** pAT matrix with labelled wave fronts and indicating the timing stimulation pulses (red arrows). **(F–M)** Progressive pAT maps during the onset of tachyarrhythmia.

assigned groups corresponding to individual wave fronts. This enabled individualized analysis of the conduction properties of wave fronts. The corresponding time of repolarization and spatial distributions were also derived. Moreover, each wave front could be classified in to probable repetitive or non-repetitive propagating fronts. An approach for dynamically viewing the ensemble activation sequence throughout complex events was developed. This aided detailed interrogation of wave front interactions and classification of the wave front progression based on the underlying source of impulse propagation, irrespective of the complexity and irregularity of electrical organization. In addition, the pAT algorithm was thoroughly evaluated for sensitivity to SNR and image resolution. Finally, the algorithm was further tested on an experimental model of chronic myocardial infarction in sheep.

The aim of our pAT-based analysis of complex optical mapping signals is 2-fold: i) To accurately deduce the propagation sequence while conserving a high spatial resolution and ii) To thereby inform on the critical properties of arrhythmia and functional pro-arrhythmic factors. pAT maps can report on the source of activation for any given pAT point (Figures 5, 8). Moreover, pacing modalities are important tools for manipulating the AT or RT sequences to characterize functional substrates, induce arrhythmia or entrain and arrest arrhythmic behavior. Generally, high pacing frequencies or variable stimulation intervals are applied, which incurs further complexity to interpret and isolate the relevant AT events. Generally, AT mapping relies on adequately selecting a time window of interest, identification of a suitable time reference and robust interpretation of the signal

morphology. Depending on the approach selected to probe ATs, conflicting information can often times be produced (Walton et al., 2012; Tomek et al., 2021). This effect can be further confounded when signal complexity increases (Bishop et al., 2007; Asfour et al., 2011; O'shea et al., 2019). Therefore, identifying a robust approach to appropriately identify the window of activation and accurately interpret AT irrespective of the signal complexity underlay signal processing automation without prior understanding of the signal morphology.

Enhancing the versatility of our processing pipeline, this framework provided automatic determination of some critical properties of optical signals, such as maximal pAT gradients that determine thresholds of conduction block and tissue refractoriness. Moreover, automated assignment of such parameters can be derived on an individual basis for optical mapping images. This will enable the analytical procedure to adapt dynamically to changing conditions, such as rhythm or effects of ion channel-targeting drug treatments. Furthermore, the approach for determination of pAT was developed to maximally retain propagating wave front information by evaluating the upstroke morphology and signal derivative (Figure 3). The maximum derivative of the action potential upstroke is known to precisely reflect AT on the imaged surface of tissue (Walton et al., 2012). Moreover, the orientation of the wave front relative to the imaged surface can be inferred from the normalized amplitude of the maximal derivative on the upstroke, termed V_F* (Zemlin et al., 2008). V_F* is a byproduct of the derivation of pAT in our processing pipeline, which can therefore be exploited when implementing this framework. Biphasic upstroke morphologies have been shown to correspond to propagation through distinct myocardial pathways found within the tissue volume contributing to the same optical signal (Fedorov et al., 2010). Secondary pAT components likely inform on remnant late propagating electrical impulses (Kertes et al., 1984). Clinically, late potentials with slow conduction are thought to underlie numerous electrical disorders (Haïssaguerre et al., 2019a; Haïssaguerre et al., 2019b). In this context, information-loss through signal reduction to a single AT event for any given upstroke would likely exclude the critical arrhythmic pathway in favor of the principal propagating wave front.

Optical mapping has seen substantial development over recent years, particularly in the event of near-infrared voltage-sensitive dyes (Matiukas et al., 2007). Using near-infrared excitation wavelengths incur several differences to more conventional blue/green excitation optical mapping. Firstly, longer wavelength light better penetrates biological tissue as a result of reduced absorption and scattering properties. This can more easily result in substantial transillumination light if a photodetector (CCD/CMOS camera, for example) was simultaneously imaging the opposite surface to the one being illuminated (Baxter et al., 2001). Moreover, reduced attenuation and scatter increases the overall optical integration volume contributing to fluorescence. This means that a larger sub-surface volume of tissue contributes to the optical signal in epi-fluorescence mode and to an even greater extent when imaging transilluminated light. This further contributes to blurring of the optical action potential upstroke. Despite this, we showed in (Walton et al., 2012) that AT, defined as the maximal derivative of the optical action potential upstroke effectively approximates the true electrical AT irrespective of the excitation light wavelength in the range of 530 nm (green) to 660 nm (near-infrared). To our knowledge, there are no known alternatives of the fundamental approach to define AT that further improves this estimation. This strongly supports the versatility of the framework that we propose and its compatibility with near-infrared imaging, as well as transilluminated signals. We further demonstrated that image resolution has no impact on pAT computation and that the proposed pipeline is relatively insensitive to signal noise; an important factor that often depends on the experimental conditions and choices of voltage-sensitive dyes used.

Arrhythmia events can occur suddenly or as a result of gradual adaptation over several heart beats. Therefore, to prevent further information loss our pipeline avoids other forms of signal reduction such as ensemble averaging of action potentials. Yet, analysis of each propagation event may be complicated by interference from adjacent and spatially overlapping wave fronts and repolarization times. That being said, the interactions of independent wave fronts and particularly the influence of repolarization heterogeneity and refractoriness on subsequent electrical responses is crucial to determine how arrhythmia is maintained. Therefore, in order to optimize the diagnostic yield when mapping the arrhythmia mechanism, this framework probes the pAT matrix (and subsequently derived RT matrix) both at the individual wave front level and through a customized dynamic window of the ensemble time-based data fields. This allowed substantial mechanistic insight in to the causal activation sequence and origin of the leading wave front at the individual pixel level. Probing the conduction field of aberrant wave fronts provides deep understanding of the regions of tissue involved and the source of the activity. This insight will aid to identify arrhythmia organization and improve investigations of optimal therapeutic interventions on arrhythmia sources.

We have presented our own analytical tools to evaluate and classify arrhythmic behavior within this framework. However, our tools also serve to extract detailed activation sequence data pertinent to existing analytical approaches. Isolating wave fronts is a necessary post processing step for the multiplicity metric (Rogers et al., 1997a; 1997b). Similarly, the reentry vulnerability index depends upon activation and repolarization times to estimate local sites susceptible to re-excitation. In our framework, wave front classification of the repetitiveness of activity rapidly provides insight of the life-time of persistent versus non-persistent activity, which may be used analogously with rotor life-time analysis (Kay et al., 2006). Figure 6 showed that local points of rotation of the activation sequence were associated with large pAT gradients (>50 ms/mm). Moreover, conduction field analysis of wave front origins did not rely on the gradient point or line and was therefore not hindered by complex gradient organization or discontinuity that can hamper phase singularity detection (Arno et al., 2021). Therefore, our framework provides a versatile unified solution to analyze spatio-temporal dynamics of cardiac arrhythmias.

4.1 Limitations

The current framework has been parametrized to analyze optical mapping signals derived from voltage-sensitive dyes, accommodating action potential signal morphologies. Yet, the foundational approach to window individual activation events based on phase responses can likely be applied more diversely across dynamic imaging and recording modalities. More so, this proof-of-principle study focused on data obtained only from sheep ventricles. However, each procedure of this pipeline was designed on the premise of being applicable to the

broader spectrum of species or anatomical regions (e.g., atria vs. ventricles) and therefore action potential morphologies. The capacity to adapt from the basal action potential to complex and non-periodic fibrillatory activity within the same recording, insensitivity to image resolution, noise-handling and application in pathological settings is a strong indicator of the framework's versatility and robustness.

Our analytical framework proposes a novel approach to estimate the threshold of conduction block, $\theta_{t,CB}$, although a single threshold value generalizes the conduction limitations across the imaged field of view. However, the maximal electrical impulse transmission delay across structural substrates is likely heterogeneous. Cases in this study showed that regions of high pAT gradients represents only a small subset of the total activation sequence (~5%, Supplementary Figure S3). The challenge is to identify the excitable gap corresponding to vulnerable sites. It is assumed that the ERP termination can be spatially determined as the action potential duration to 80% of repolarization under conditions of short-coupled stimulation. A delay of activation of the following paced action potential (activation latency) approximated excitability for each pixel. As a result, local activation delays associated with pathological remodeling, namely post-repolarization refractoriness are addressed (Coronel et al., 2012). The $\theta_{t,CB}$ parameter is used to separate wave fronts temporally. However, in the current framework, wave fronts that converge, i.e., those originating from independent sources are considered the same wave front. Convergence will be considered for wave fronts that are temporally aligned, i.e., wave front collision sites show pAT gradients inferior to $\theta_{t,CB}$. But tissue generally remains in refractoriness for much longer than $\theta_{t,CB}$ in our experience, meaning wave fronts colliding with local pAT gradients superior to $\theta_{t,CB}$ will be separated.

4.2 Conclusion

In conclusion, we provide a comprehensive framework for image processing of complex optical mapping signals, including tachyarrhythmias. An action potential upstroke-windowing scheme based on calculations of phase enabled pixel-wise and upstroke-independent identification of pAT events. This approach is highly robust against changing signal morphology, signal noise, changes to the signal baseline and transitional behavior between non-arrhythmic and arrhythmic states. A crucial component of the image processing pipeline furthermore identifies the spatial organization of pAT points and groups them in to individual wave fronts. A series of analytical and visualization tools permit detailed characterization in a beat-to-beat basis, irrespective of signal complexity.

Data availability statement

The raw data supporting the conclusion of this article will be made available by the authors, without undue reservation.

Ethics statement

The animal study was in accordance with the guidelines from Directive 2010/63/EU of the European Parliament on the protection of animals used for scientific purposes and reviewed and approved by the Direction générale de la recherché et de l'innovation Cellule Animaux utilize à des Fins Scientifiques-AFiS.

Author contributions

GR contributed to data analysis and reveiwing the manuscript contents. KK contributed to data analysis and reveiwing the manuscript contents. NP-L contributed to generation of experimental data. BB contributed to generation of experimental data. IE contributed to generation of experimental data. EV contributed to generation of experimental data. OB contributed to study design and reviewing the manuscript contents. RW contributed to data analysis, generation of data design study design and preparation of the manuscript.

Funding

This study received financial support from the French Government as part of the "Investments of the Future" program managed by the National Research Agency (ANR), Grant reference ANR-10-IAHU-04, funding from the European Research Area in Cardiovascular Diseases (ERA-CVD), grant reference H2020-HCO-2015_680969 (MultiFib), funding from the French Region Nouvelle Aquitaine, grant references 2016–1R 30113 0000 7550/2016-1R 30113 0000 7553, and ANR-19-ECVD-0006-01, and funding from the Leducq Foundation, grant reference 16CVD02 (RHYTHM).

Acknowledgments

We acknowledge Cardelien Inc., United States, for the generous supply of a defibrillation system for high energy shock delivery used in this study.

Conflict of interest

The authors declare that the research was conducted in the absence of any commercial or financial relationships that could be construed as a potential conflict of interest.

Publisher's note

Supplementary material

The Supplementary Material for this article can be found online at: https://www.frontiersin.org/articles/10.3389/fphys.2023.734356/full#supplementary-material

References

Akar, F. G., Nass, R. D., Hahn, S., Cingolani, E., Shah, M., Hesketh, G. G., et al. (2007). Dynamic changes in conduction velocity and gap junction properties during development of pacing-induced heart failure. *Am. J. Physiol. - Hear. Circ. Physiol.* 293, H1223–H1230. doi:10.1152/ajpheart.00079.2007

Arno, L., Quan, J., Nguyen, N. T., Vanmarcke, M., Tolkacheva, E. G., and Dierckx, H. (2021). A phase defect framework for the analysis of cardiac arrhythmia patterns. *Front. Physiol.* 12, 690453. doi:10.3389/fphys.2021.690453

Asfour, H., Swift, L., Sarvazyan, N., Doroslovacki, M., and Kay, M. (2011). "Preprocessing of fluoresced transmembrane potential signals for cardiac optical mapping," in Proceedings of the Annual International Conference of the IEEE Engineering in Medicine and Biology Society, EMBS. doi:10.1109/IEMBS.2011.6090042

Baxter, W. T., Mironov, S. F., Zaitsev, A. V., Jalife, J., and Pertsov, A. M. (2001). Visualizing excitation waves inside cardiac muscle using transillumination. *Biophys. J.* 80, 516–530. doi:10.1016/S0006-3495(01)76034-1

Bishop, M. J., Rodriguez, B., Eason, J., Whiteley, J. P., Trayanova, N., and Gavaghan, D. J. (2006). Synthesis of voltage-sensitive optical signals: Application to panoramic optical mapping. *Biophys. J.* 90, 2938–2945. doi:10.1529/biophysj.105.076505

Bishop, M. J., Gavaghan, D. J., Trayanova, N. A., and Rodriguez, B. (2007). Photon scattering effects in optical mapping of propagation and arrhythmogenesis in the heart. *J. Electrocardiol.* 40, S75–S80. doi:10.1016/j.jelectrocard.2007.06.020

Cantwell, C. D., Roney, C. H., Ng, F. S., Siggers, J. H., Sherwin, S. J., and Peters, N. S. (2015). Techniques for automated local activation time annotation and conduction velocity estimation in cardiac mapping. *Comput. Biol. Med.* 65, 229–242. doi:10.1016/j.compbiomed.2015.04.027

Chen, J., Mandapati, R., Berenfeld, O., Skanes, A. C., and Jalife, J. (2000). High-frequency periodic sources underlie ventricular fibrillation in the isolated rabbit heart. *Circ. Res.* 86, 86–93. doi:10.1161/01.RES.86.1.86

Child, N., Bishop, M. J. M. J., Hanson, B., Coronel, R., Opthof, T., Boukens, B. J. B. J., et al. (2015). An activation-repolarization time metric to predict localized regions of high susceptibility to reentry. *Hear. Rhythm* 12, 1644–1653. doi:10.1016/j.hrthm.2015.04.013

Coronel, R., Janse, M. J., Opthof, T., Wilde, A. A., and Taggart, P. (2012). Postrepolarization refractoriness in acute ischemia and after antiarrhythmic drug administration: Action potential duration is not always an index of the refractory period. *Hear. Rhythm.* doi:10.1016/j.hrthm.2012.01.021

Fast, V. G., and Kleber, A. G. (1995). Cardiac tissue geometry as a determinant of unidirectional conduction block: Assessment of microscopic excitation spread by optical mapping in patterned cell cultures and in a computer model. *Cardiovasc. Res.* 29, 697–707. doi:10.1016/0008-6363(96)88643-3

Fedorov, V. V., Glukhov, A. V., Chang, R., Kostecki, G., Aferol, H., Hucker, W. J., et al. (2010). Optical mapping of the isolated coronary-perfused human sinus node. *J. Am. Coll. Cardiol.* 56, 1386–1394. doi:10.1016/j.jacc.2010.03.098

Fenton, F. H., Cherry, E. M., Hastings, H. M., and Evans, S. J. (2002). Multiple mechanisms of spiral wave breakup in a model of cardiac electrical activity. *Chaos* 12, 852–892. doi:10.1063/1.1504242

Frazier, D. W., Wolf, P. D., Wharton, J. M., Tang, A. S. L., Smith, W. M., and Ideker, R. E. (1989). Stimulus-induced critical point. Mechanism for electrical initiation of reentry in normal canine myocardium. *J. Clin. Invest.* 83, 1039–1052. doi:10.1172/JCI113945

Haïssaguerre, M., Nademanee, K., Hocini, M., Cheniti, G., Duchateau, J., Frontera, A., et al. (2019a). Depolarization versus repolarization abnormality underlying inferolateral J-wave syndromes: New concepts in sudden cardiac death with apparently normal hearts. *Hear. Rhythm* 16, 781–790. doi:10.1016/j.hrthm.2018.10.040

Haïssaguerre, M., Nademanee, W., Hocini, M., Duchateau, J., André, C., Lavergne, T., et al. (2019b). The spectrum of idiopathic ventricular fibrillation and J-wave syndromes: Novel mapping insights. *Card. Electrophysiol. Clin.* 11, 699–709. doi:10.1016/j.ccep.2019.08.011

Himel, H. D., IV, and Knisley, S. B. (2007). Comparison of optical and electrical mapping of fibrillation. *Physiol. Meas.* 28, 707–719. doi:10.1088/0967-3334/28/6/009

Hyatt, C. J., Mironov, S. F., Vetter, F. J., Zemlin, C. W., and Pertsov, A. M. (2005). Optical action potential upstroke morphology reveals near-surface transmural propagation direction. *Circ. Res.* 97, 277–284. doi:10.1161/01.RES.0000176022.74579.47

Hyatt, C. J., Zemlin, C. W., Smith, R. M., Matiukas, A., Pertsov, A. M., and Bernus, O. (2008). Reconstructing subsurface electrical wave orientation from cardiac epi-fluorescence recordings: Monte Carlo versus diffusion approximation. *Opt. Express* 16, 13758–13772. doi:10.1364/oe.16.013758

Kay, M. W., Walcott, G. P., Gladden, J. D., Melnick, S. B., and Rogers, J. M. (2006). Lifetimes of epicardial rotors in panoramic optical maps of fibrillating swine ventricles. *Am. J. Physiol. - Hear. Circ. Physiol.* 291, H1935–H1941. doi:10.1152/ajpheart.00276.2006

Kertes, P. J., Glabus, M., Murray, A., Julian, D. G., and Campbell, R. W. F. (1984). Delayed ventricular depolarization - correlation with ventricular activation and relevance to ventricular fibrillation in acute myocardial infarction. *Eur. Heart J.* 5, 974–983. doi:10.1093/oxfordjournals.eurheartj.a061617

Kleber, A. G., Janse, M. J., Wilms-Schopman, F. J. G., Wilde, A. A., and CoRonel, R. (1986). Changes in conduction velocity during acute ischemia in ventricular myocardium of the isolated porcine heart. *Circulation* 73, 189–198. doi:10.1161/01.CIR.73.1.189

Matiukas, A., Mitrea, B. G., Qin, M., Pertsov, A. M., Shvedko, A. G., Warren, M. D., et al. (2007). Near-infrared voltage-sensitive fluorescent dyes optimized for optical mapping in blood-perfused myocardium. *Hear. Rhythm* 4, 1441–1451. doi:10.1016/j.hrthm.2007.07.012

Moreno, A., Walton, R. D. R. D., Constantin, M., Bernus, O., Vigmond, E. J. E. J., and Bayer, J. D. J. D. (2019). Wide-area low-energy surface stimulation of large mammalian ventricular tissue. *Sci. Rep.* 9, 15863. doi:10.1038/s41598-019-51364-w

Motulsky, H. J., and Brown, R. E. (2006). Detecting outliers when fitting data with nonlinear regression - a new method based on robust nonlinear regression and the false discovery rate. *BMC Bioinforma.* 7, 123. doi:10.1186/1471-2105-7-123

O'shea, C., Holmes, A. P., Yu, T. Y., Winter, J., Wells, S. P., Parker, B. A., et al. (2019). High-throughput analysis of optical mapping data using electromap. *J. Vis. Exp.* 148, e59663. doi:10.3791/59663

Pallares-Lupon, N., Bayer, J. D., Guillot, B., Caluori, G., Ramlugun, G. S., Kulkarni, K., et al. (2022). Tissue preparation techniques for contrast-enhanced micro computed tomography imaging of large mammalian cardiac models with chronic disease. *J. Vis. Exp.* 180, e62909. doi:10.3791/62909

Plank, G., Loewe, A., Neic, A., Augustin, C., Huang, Y. L., Gsell, M. A. F., et al. (2021). The openCARP simulation environment for cardiac electrophysiology. *Comput. Methods Programs Biomed.* 208, 106223. doi:10.1016/j.cmpb.2021.106223

Rogers, J. M., Usui, M., KenKnight, B. H., Ideker, R. E., and Smith, W. M. (1997a). A quantitative framework for analyzing epicardial activation patterns during ventricular fibrillation. *Ann. Biomed. Eng.* 25, 749–760. doi:10.1007/BF02684159

Rogers, J. M., Usui, M., KenKnight, B. H., Ideker, R. E., and Smith, W. M. (1997b). Recurrent wavefront morphologies: A method for quantifying the complexity of epicardial activation patterns. *Ann. Biomed. Eng.* 25, 761–768. doi:10.1007/BF02684160

Salama, G., Rosenbaum, D. S., Kanai, A., Cohen, R. J., and Kaplan, D. T. (1989). "Data analysis techniques for measuring spatial inhomogeneity in repolarization using optical transmembrane potentials," in Annual International Conference of the IEEE Engineering in Medicine and Biology - Proceedings. doi:10.1109/iembs.1989.95692

Salama, G., Kanai, A., and Efimov, I. R. (1994). Subthreshold stimulation of Purkinje fibers interrupts ventricular tachycardia in intact hearts: Experimental study with voltage-sensitive dyes and imaging techniques. *Circ. Res.* 74, 604–619. doi:10.1161/01.RES.74.4.604

Skouibine, K., Wall, J., Krassowska, W., and Trayanova, N. (2002). Modelling induction of a rotor in cardiac muscle by perpendicular electric shocks. *Med. Biol. Eng. Comput.* 40, 47–55. doi:10.1007/BF02347695

Takahashi, T., van Dessel, P., Lopshire, J. C., Groh, W. J., Miller, J., Wu, J., et al. (2004). Optical mapping of the functional reentrant circuit of ventricular tachycardia in acute myocardial infarction. *Hear. Rhythm* 1, 451–459. doi:10.1016/j.hrthm.2004.05.005

Ten Tusscher, K. H. W. J., and Panfilov, A. V. (2006). Alternans and spiral breakup in a human ventricular tissue model. *Am. J. Physiol. - Hear. Circ. Physiol.* 291, H1088–H1100. doi:10.1152/ajpheart.00109.2006

Tomek, J., Wang, Z. J., Burton, R. A. B., Herring, N., and Bub, G. (2021). COSMAS: A lightweight toolbox for cardiac optical mapping analysis. *Sci. Rep.* 11, 9147. doi:10.1038/s41598-021-87402-9

Vigmond, E. J., Hughes, M., Plank, G., and Leon, L. J. (2003). Computational tools for modeling electrical activity in cardiac tissue. *J. Electrocardiol.* 36, 69–74. doi:10.1016/j.jelectrocard.2003.09.017

Walton, R. D. R. D., Benoist, D., Hyatt, C. J. C. J., Gilbert, S. H. S. H., White, E. E., and Bernus, O. (2010). Dual excitation wavelength epifluorescence imaging of transmural electrophysiological properties in intact hearts. *Hear. Rhythm* 7, 1843–1849. doi:10.1016/j.hrthm.2010.08.019

Walton, R. D. R. D., Smith, R. M. R. M., Mitrea, B. G., White, E., Bernus, O., and Pertsov, A. M. A. M. (2012). Extracting surface activation time from the optically recorded action potential in three-dimensional myocardium. *Biophys. J.* 102, 30–38. doi:10.1016/j.bpj.2011.10.036

Winfree, A. T. (1989). Electrical instability in cardiac muscle: Phase singularities and rotors. *J. Theor. Biol.* 138, 353–405. doi:10.1016/S0022-5193(89)80200-0

Zemlin, C. W., Bernus, O., Matiukas, A., Hyatt, C. J., and Pertsov, A. M. (2008). Extracting intramural wavefront orientation from optical upstroke shapes in whole hearts. *Biophys. J.* 95, 942–950. doi:10.1529/biophysj.107.117887

Frontiers in Physiology

Understanding how an organism's components work together to maintain a healthy state

The second most-cited physiology journal, promoting a multidisciplinary approach to the physiology of living systems - from the subcellular and molecular domains to the intact organism and its interaction with the environment.

Discover the latest Research Topics

See more →

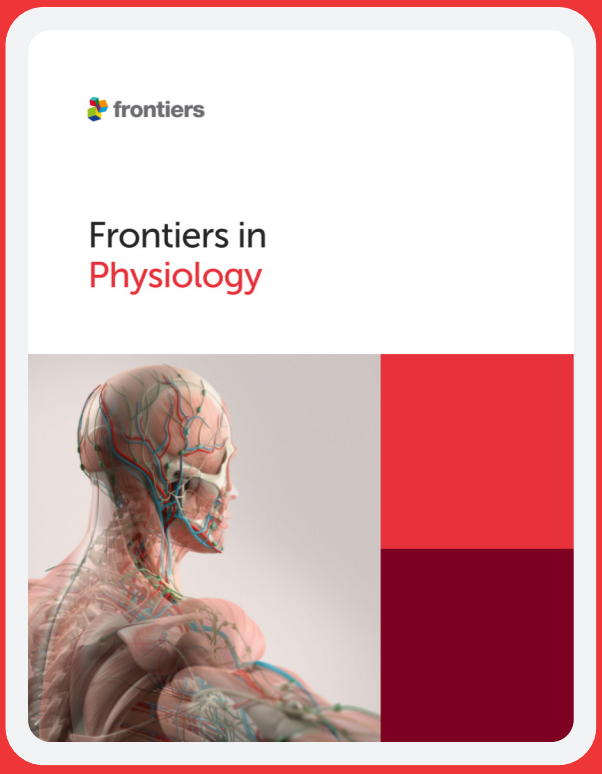

Frontiers

Avenue du Tribunal-Fédéral 34
1005 Lausanne, Switzerland
frontiersin.org

Contact us

+41 (0)21 510 17 00
frontiersin.org/about/contact